NASA/CR—2008-215440/PART1

Hydrogen Research for Spaceport and Space-Based Applications

Fuel Cell Projects

Tim Anderson and Canan Balaban
University of Florida, Gainesville, Florida

November 2008

NASA STI Program . . . in Profile

Since its founding, NASA has been dedicated to the advancement of aeronautics and space science. The NASA Scientific and Technical Information (STI) program plays a key part in helping NASA maintain this important role.

The NASA STI Program operates under the auspices of the Agency Chief Information Officer. It collects, organizes, provides for archiving, and disseminates NASA's STI. The NASA STI program provides access to the NASA Aeronautics and Space Database and its public interface, the NASA Technical Reports Server, thus providing one of the largest collections of aeronautical and space science STI in the world. Results are published in both non-NASA channels and by NASA in the NASA STI Report Series, which includes the following report types:

- TECHNICAL PUBLICATION. Reports of completed research or a major significant phase of research that present the results of NASA programs and include extensive data or theoretical analysis. Includes compilations of significant scientific and technical data and information deemed to be of continuing reference value. NASA counterpart of peer-reviewed formal professional papers but has less stringent limitations on manuscript length and extent of graphic presentations.

- TECHNICAL MEMORANDUM. Scientific and technical findings that are preliminary or of specialized interest, e.g., quick release reports, working papers, and bibliographies that contain minimal annotation. Does not contain extensive analysis.

- CONTRACTOR REPORT. Scientific and technical findings by NASA-sponsored contractors and grantees.

- CONFERENCE PUBLICATION. Collected papers from scientific and technical conferences, symposia, seminars, or other meetings sponsored or cosponsored by NASA.

- SPECIAL PUBLICATION. Scientific, technical, or historical information from NASA programs, projects, and missions, often concerned with subjects having substantial public interest.

- TECHNICAL TRANSLATION. English-language translations of foreign scientific and technical material pertinent to NASA's mission.

Specialized services also include creating custom thesauri, building customized databases, organizing and publishing research results.

For more information about the NASA STI program, see the following:

- Access the NASA STI program home page at *http://www.sti.nasa.gov*

- E-mail your question via the Internet to *help@ sti.nasa.gov*

- Fax your question to the NASA STI Help Desk at 301–621–0134

- Telephone the NASA STI Help Desk at 301–621–0390

- Write to:
  NASA Center for AeroSpace Information (CASI)
  7115 Standard Drive
  Hanover, MD 21076–1320

Hydrogen Research for Spaceport and Space-Based Applications

Fuel Cell Projects

Tim Anderson and Canan Balaban
University of Florida, Gainesville, Florida

National Aeronautics and
Space Administration

Glenn Research Center
Cleveland, Ohio 44135

November 2008

Level of Review: This material has been technically reviewed by NASA technical management.

Contents

Hydrogen Research for Spaceport and Space-Based Applications

Fuel Cell Projects

Tim Anderson and Canan Balaban
University of Florida
Gainesville, Florida 32611

Abstract

The activities presented are a broad based approach to advancing key hydrogen related technologies in areas such as fuel cells, hydrogen production, and distributed sensors for hydrogen-leak detection, laser instrumentation for hydrogen-leak detection, and cryogenic transport and storage. Presented are the results from research projects, education and outreach activities, system and trade studies. The work will aid in advancing the state-of-the-art for several critical technologies related to the implementation of a hydrogen infrastructure. Activities conducted are relevant to a number of propulsion and power systems for terrestrial, aeronautics and aerospace applications.

Fuel cell research focused on proton exchange membranes (PEM), solid oxide fuel cells (SOFC). Specific technologies included aircraft fuel cell reformers, new and improved electrodes, electrolytes, interconnect, and seals, modeling of fuel cells including CFD coupled with impedance spectroscopy. Research was conducted on new materials and designs for fuel cells, along with using embedded sensors with power management electronics to improve the power density delivered by fuel cells. Fuel cell applications considered were in-space operations, aviation, and ground-based fuel cells such as; powering auxiliary power units (APUs) in aircraft; high power density, long duration power supplies for interplanetary missions (space science probes and planetary rovers); regenerative capabilities for high altitude aircraft; and power supplies for reusable launch vehicles.

1. Remote Power Transmission Using High Power GaN HEMTs and Diodes for Regenerative Fuel Cells

Task PI: Dr. Steve Pearton, Material Science & Engineering, University of Florida

Co-Investigators: Dr. Fan Ren, Chemical Engineering, Dr. David Norton, Material Science & Engineering and Dr. Jenshan Lin, Electrical and Computer Engineering, University of Florida

Reporting Period: August 3, 2004 to June 31, 2007

Abstract

High power GaN-based diodes and High Electron Mobility Transistors (HEMTs) were developed on large-area substrates for use in future wireless power transmission systems. The substrates used included free-standing GaN, Si and re-usable Si-on-poly SiC substrates.

Introduction

There are compelling reasons for developing improved components and systems for **wireless power transmission (WPT)**. The applications of such systems would include unmanned aerial vehicles and unmanned drones with capability for very long duration surveillance, microwave powered aircraft and reusable aeronautical vehicles designed to provide cellular communication services. Orbital reflectors are envisaged to allow power transmission between two very distant locations. This ability to control the supply of power in a pinpoint fashion will reduce some of the problems caused by limitations of existing battery technology. Some of the technological barriers to realizing cost-effective, reliable WPT systems include the need for improved dc-rf converters in the transmitter, improved phased array antennas and rectennas and improved beam control and the need for high temperature stable operation without cooling.

GaN-based power diodes and transistors appear most suited for these power amplification applications. AlGaN HEMTs on Si substrates have achieved power-added efficiencies of 70% at 5.8 GHz, one of the desirable transmission frequencies. To meet the need for rectifiers and switching devices, we proposed development of Schottky GaN rectifiers and AlGaN/GaN HEMTs on large area, low-cost Si substrates.

Results and Discussion

We initially fabricated rectifiers on free-standing GaN substrates to determine the state-of-the-art performance in homoepitaxial devices and then moved to fabricate these devices on GaN grown on large area, low cost Si substrates and re-usuable Si-on-poly SiC substrates.

(i)Rectifiers on free-standing GaN substrates

Pd and Pt Schottky diodes were fabricated on free-standing 2 inch diameter GaN substrates prepared by a combination of hydride vapor phase epitaxy of ~350 μm onto sapphire, substrate removal and subsequent growth of 3 μm of epi GaN by Metal Organic Chemical Vapor Deposition. Vertical diodes with Ti/Al/Pt/Au back contacts annealed at 850 °C for 30 sec showed excellent rectification with an on/off ratio of ~100 at 1.5V/-10V. Both forward turn-on and reverse breakdown voltages showed negative temperature coefficients.

A variety of approaches have been used to produce free-standing GaN substrates with thicknesses up to ~400 μm. Here we report on the characteristics of Pt or Pd-gated bulk GaN diodes grown on Si using substrates obtained from Lumilog .The substrates were ~350 μm thick and were grown by high-rate vapor phase epitaxy on c-plane Al_2O_3 substrates and removed by differential heating. Another 3 μm of n-GaN was then grown on the top surface by Metal Organic Chemical Vapor Deposition (MOCVD). The material exhibits dislocation densities in the range 10^6-10^8 cm^{-2} as measured by cathodoluminescence (CL) contrast, several orders of magnitude lower than standard GaN grown on sapphire by MOCVD. Full-area back Ohmic contacts of Ti/Al/Pt/Au were deposited by e-beam evaporation and annealed at 850 °C for 30 sec. On some of the samples we also placed Ti/Al/Pt/Au Ohmic contacts on the front surface so we could compare vertical versus lateral device geometries. Schottky contacts of e-beam evaporated, unannealed Pt or Pd with diameters of 0.06-0.12 mm were placed on the front (Ga-face) surface. The Schottky contact was extended over an SiN_X passivation layer (2000Å thick) deposited by plasma enhanced chemical vapor deposition. An optical microscope image of the full 2 inch wafer prior to processing is shown at the top of Figure 1,while a charge-coupled device image of a processed device captured on a microscope are shown at the bottom of Figure 1 After final metal of e-beam deposited Ti/Au (300Å/1200Å) interconnection contacts was deposited, the devices were bonded to electrical feed-throughs and exposed to different gas ambients in an environmental chamber while the diode current-voltage(I-V) characteristics were monitored in the temperature range 25-450 °C.

The I-V characteristics from the vertical diodes are shown in Figure 2 in both linear and log form. These devices showed excellent rectification, with an on/off ratio of ~100 at 1.5V/-10V. Lateral geometry diodes showed similar magnitudes of reverse current, suggesting that surface contributions to the leakage current are dominant as we have seen previously on GaN rectifiers. The diode ideality factors derived from the forward I-V characteristics were ~2, indicating that recombination was the dominant current transport mechanism.
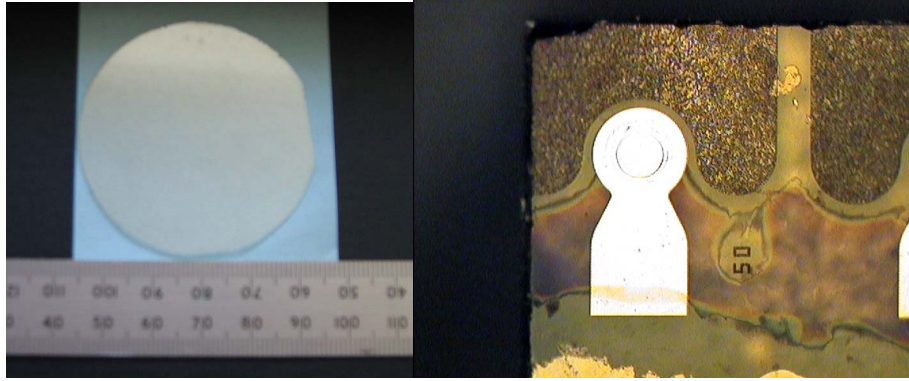
Figure 1. Optical micrograph of 2 inch diameter GaN wafer (top) and SEM micrograph of completed diode (bottom).
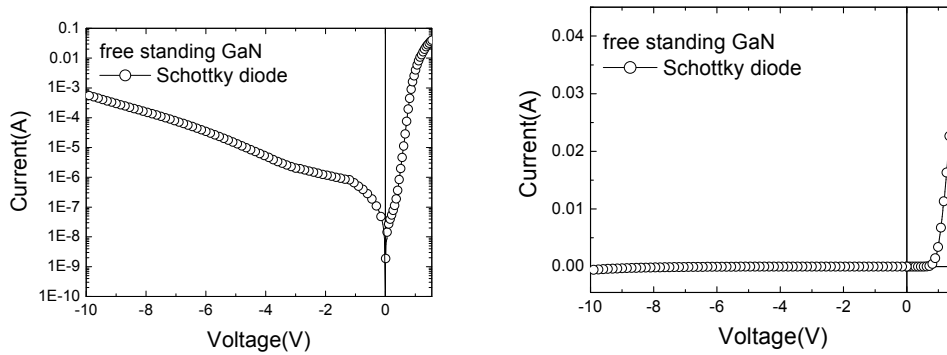

Figure 2. Room temperature I-V characteristics in both linear (right) and log (left) formats.

The reverse breakdown showed a much smaller negative temperature coefficient than in previous work showing the benefit of the reduced defect density in the material.

(ii) Rectifiers on GaN layers grown on large area Si substrates

Schottky rectifiers fabricated on GaN layers grown on 4 inch diameter Si substrates showed breakdown voltages (V_R) of ~300V at room temperature, on-state resistances (R_{ON}) of 40 mΩ.cm^2 and figure-of-merit $(V_B)^2/R_{ON}$ of 2.25 MW/cm^2. The reverse current is thermally activated with activation energies in the range 0.3-0.4 eV and is proportional to contact perimeter at reverse biases up to ~100V. This approach provides a low-cost alternative to GaN rectifiers on sapphire or SiC substrates while still maintaining good breakdown characteristics. Even with simple dielectric-overlap edge termination, the devices show reverse breakdown voltages in the 300V range and on/off ratios of 200 at +5/-200V.

Reverse I-V characteristics from two diodes are shown in Figure 3. The reverse breakdown voltage, defined as the voltage where the current density is 50 mA/cm^2 is around 300V and this was uniform to within approximately 5% over the wafer area.These devices showed excellent rectification, with an on/off ratio of ~200 at 5V/-200V. The figure-of-merit $(V_B)^2/R_{ON}$ was 2.25 MW/cm^2 at room temperature. The reverse current characteristics showed a consistent dip around 30-40V depending on the measurement temperature, as shown in Figure 4. This may be a result of the depletion region reaching the interface region between the GaN and the Si substrate. Up to 175 °C, the reverse breakdown showed a much smaller negative temperature

coefficient (~0.2V/K) than in previous work on GaN rectifiers on sapphire substrates, showing the benefit of the improved growth in the recent past. In the early stages of SiC rectifier development, the diodes also showed negative temperature coefficients of breakdown and the switch to the intrinsic positive coefficient was only seen as the defect density in the material was further improved. There have been no reports of positive temperature coefficient of breakdown for GaN, even for rectifiers fabricated on free-standing GaN.
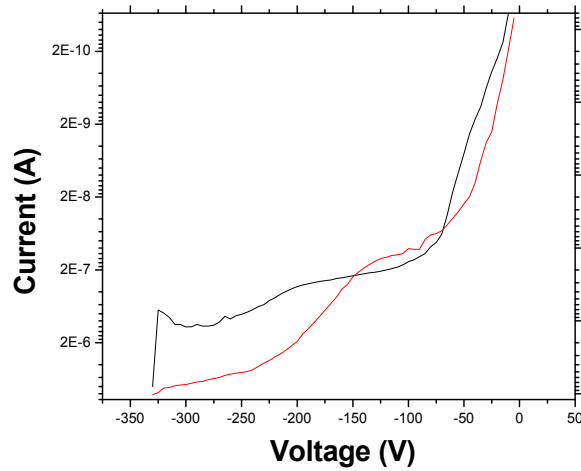

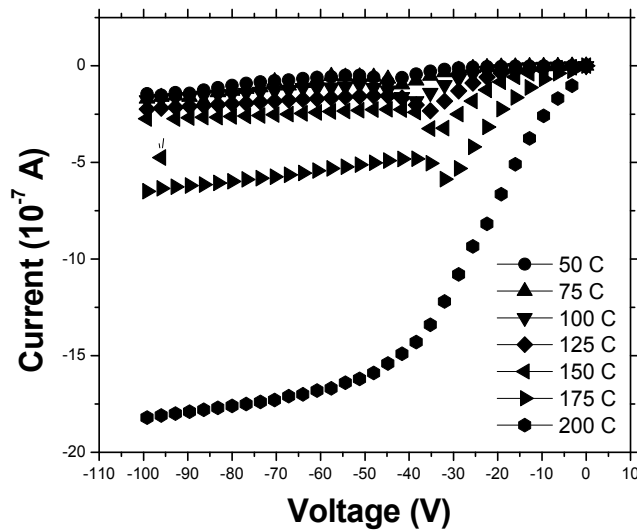Figure 3. Reverse I-V characteristic from two separate diodes, measured at 300K.

Figure 4. Reverse I-V characteristic as a function of measurement temperature.

The origin of the reverse current can be examined by looking at the dependence of current on perimeter/area ratio. At biases up to 100V, the reverse current was proportional to the perimeter of the rectifying contact, so that surface contributions are the most important in this voltage range. For biases close to breakdown, the current was proportional to the area of the rectifying contact. Under these conditions, the main contribution to the reverse current is from under this contact. An Arrhenius plot of reverse current density at various biases is shown in Figure 5. Much of the current is bias-dependent and may originate from generation-recombination at defects in the GaN, while there is also a temperature-dependent component. The straight sections correspond to activation energies in the range 0.3-0.4 eV, which is most likely the ionization energy of the most prominent surface states which contribute to the current conduction.
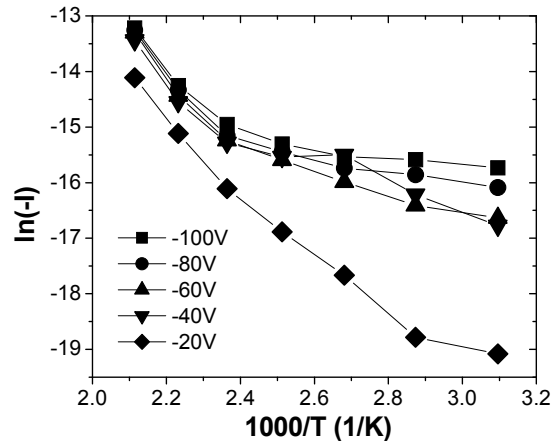

Figure 5. Arrhenius plot of reverse current density at different biases (64 µm diameter).

(iii) AlGaN/GaN High Electron Mobility Transistors on Si/SiO$_2$/poly-SiC Substrates

GaN and related alloys are typically grown on either sapphire or SiC substrates. The GaN has a significant lattice mismatch with both types of substrates, leading to a high density of threading dislocations in the nitride layer. The use of SiC substrates is preferred for electronic devices such as High Electron Mobility Transistors (HEMTs) because of the superior thermal conductivity, leading to less device self-heating and improved reliability and operating stability. AlGaN/GaN high electron mobility transistors (HEMTs) are very promising for high power, high temperature commercial applications in telecommunications, hybrid electric vehicles, power flow control and remote sensing. To reduce the cost of AlGaN/GaN HEMTs, there is a strong push to grow the layers on large, cheap substrates such as Si and impressive dc and rf power performance has been reported by several groups. Previous works confirmed that GaN HEMT on silicon achieve an excellent reliability because of the maturity of the substrate. However the thermal conductivity of the silicon substrate is not good enough to withstand very high power density. A limitation of the RF performances is observed. The use of Silicon-on-Polycrystalline SiC seems to be an appropriate alternative by combining the low cost approach of the Silicon and poly SiC bulk with the demand of better thermal dissipation. An even more intriguing approach involves the use of the Smart-Cut^{TM} technology involving re-usuable substrates. In this process a high resistivity Si wafer is implanted with a high dose of H$^+$ ions, then wafer bonded to a polycrystalline SiC substrate before heating to cause splitting of the Si substrate and reclaiming of the Si wafer for re-use. The AlGaN/GaN HEMT wafer is then grown on the Silicon-on-poly SiC (SopSiC) composite substrate.

The thermal conductivity of the composite substrate is comparable to that of polycrystalline SiC and superior to Si and simple thermal simulations of nitride HEMTs operating at power densities of 5-15 W/mm grown on such substrates indicate junction temperatures fairly similar to devices on polycrystalline SiC substrates. For power amplifier applications, ability to extract heat and the allowed thermal budget of operation is critical. High thermal conductivity substrates may make it possible to design a power amplifier without an auxiliary cooling system and lead to further cost savings (materials/operation) along with weight/volume reduction.

The starting substrates were 4 inch diameter high resistivity (111) Si and conducting polycrystalline SiC. The Si was initially oxidized and implanted with a high dose of H^+ ions, cleaned and bonded to the SiC wafer. Removal of the Si by Smart Cut^{TM} splitting was followed by reclaiming of the top Si wafer and surface preparation of the SopSiC wafer. The thermal conductivity of polycrystalline SiC is ~300 W/mK while that of crystalline SiC is 400 W/mK and (111) Si is 150 W/mK. The SopSiC wafer consists of the SiC substrate, followed by 0.1 µm of thermal SiO_2, ~0.2 µm of (111)Si.

The maximum drain-source current was ~250 mA/mm with a transconductance of 125 mS/mm for a device with 4 µm spacing between gate and drain. The drain current is in line with that expected for this sheet carrier density. The standard HEMT grown by MBE directly on single-crystal SiC substrates with a sheet carrier density of 1.5×10^{13} cm^{-2} showed roughly double this drain current. Figure 6 shows the I_{DS}-V_{DS} characteristics from 1x200 µm^2 gate length HEMTs-on- SopSiC. The devices exhibited breakdown characteristics, with values up to 250V for 32 µm source-drain spacing. The resulting breakdown fields were in the range $5\text{-}15 \times 10^4$ V/cm. By comparison, a HEMT grown directly on single-crystal SiC showed a breakdown voltage in the middle of this range.
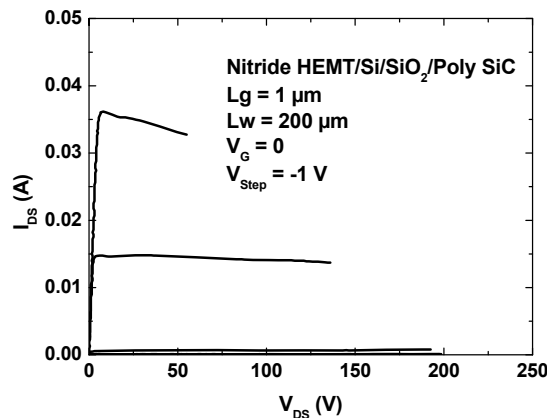
Figure 6. I_{DS}-V_{DS} characteristics from 1x200 µm^2 gate length HEMT-on- SopSiC.
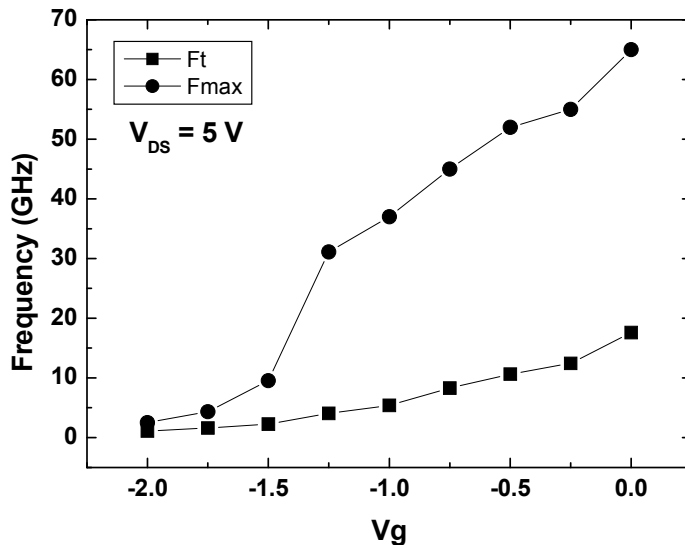
Figure 7. Variation of F_t and F_{max} as a function of gate voltage for a fixed drain-source voltage of 5V.

The HEMTs-on- SopSiC showed very good high frequency performance. Figure 7 shows the rf performance of a 0.7x200 μm^2 gate length device. We measured the variation of F_t and F_{max} as a function of gate voltage for a fixed drain-source voltage, as shown in Figure 7. The maximum values obtained were 18GHz for F_t and 65GHz for F_{max} at 0V gate voltage. This maximum corresponds to the maximum in g_m, as expected since F_t = gm/(2πC) ,where the total capacitance C=Cgs+Cgd. Initial load-pull measurements at 4GHz on the HEMTs on SopSiC templates showed a maximum power gain output of 10dBm at a power-added efficiency of ~35%. This is approximately 75% the performance of a standard HEMT on SiC substrate fabricated with the same mask-set.

Conclusions

In conclusion, GaN on Si rectifiers and AlGaN/GaN HEMTs on Si /SiC composite substrates appear well-suited to WPT systems. We also developed more thermally stable contacts for extended operation at 350 °C described elsewhere in this report.

Patents

No patent applications have been filed.

Publications

1. "Analysis and Design of AlGaN/GaN HEMT Resistive Mixers", T. Chang, W. Wu, J. Lin, S. Jang, F. Ren, S.J. Pearton, R. Fitch and J. Gillespie, Microwave and Optical Techn. Lett. 49, 1152 (2007).
2. "AlGaN/GaN high electron mobility transistors on Si/SiO$_2$/poly-SiC substrates", T.J. Anderson, F. Ren, L. Voss, M. Hlad, B.P. Gila, L. Covert, J. Lin, S.J. Pearton, P. Bove, H. Lahreche, and J. Thuret, J. Vac. Sci. Technol. B 24, 2302 (2006).
3. "Laser ablation of via holes in GaN and AlGaN/GaN high electron mobility transistor structures", Travis Anderson, Fan Ren, S.J. Pearton, Michael A. Mastro, Ron T. Holm, Rich L. Henry, Charles R. Eddy, Jr., Joon Yeob Lee, Kwan-Young Lee, and Jihyun Kim, J. Vac. Sci. Technol. B 24, 2246 (2006).
4. "A high efficiency class-F power amplifier using AlGaN/GaN HEMT", Sangwon Ko , Wenhsing Wu , Jenshan Lin , Soohwan Jang, Fan Ren, S.J. Pearton, Robert Fitch and James Gillespie, Microwave and Optical Technology Letters, 48, 1955(2006).
5. "Thermal Considerations in Design of Vertically Integrated Si/GaN/SiC Multichip Modules", T.J. Anderson, F. Ren, L. Covert, J. Lin and S.J. Pearton, J. Electrochem. Soc. 153 G906 (2006).
6. "Electrical Performance of GaN Schottky Rectifiers on Si Substrates", L. Voss, S.J. Pearton, F. Ren, P. Bove, H. Lareche and J.Thuret, J. Electrochem. Soc. 153, G681(2006).
7. "Si diffused GaN for enhancement mode GaN MOSFET on Si applications", S. Jang, F. Ren, S.J. Pearton, B.P. Gila, M. Hlad, C.R. Abernathy, H.S. Yang, C.J. Pan, J.I. Chyi, P. Bove, H. Lareche and J. Thuret, J. Electron. Mater. 35,685(2006).
8. "Comparison of laser wavelength operation for drilling of via holes in AlGaN/GaN HEMTs on SiC substrates", T. Anderson, F. Ren, L. Covert, J. Lin, S.J. Pearton, T. Dalrymple, C. Bozada, R. Fitch, N. Moser, R. Bedford and M. Schimpf", J.Electron. Mater. 35,675(2006).
9. "Thermal Simulations of three-dimensional Integrated Multichip Module with GaN power amplifier and Si modulator", T.J. Anderson, F. Ren, L. Covert, J. Lin and S.J. Pearton, J. Vac. Sci. Technol. 24,284 (2006).

Presentations

1. "AlGaN/GaN High Electron Mobility Transistors and Diodes Fabricated on Large Area Silicon on Poly-SiC (SopSiC) Substrates for Lower Cost and Higher Yield" T.J. Anderson, F. Ren, L. Voss, M. Hlad, B.P. Gila, S.J. Pearton, J. Kim, J. Lin, P. Bove, H. Lahreche, J. Thuret, and R. Langer, 2007 Mantech Conference, Austin, TX, May 2007.
2. "Microwave Performance of AlGaN/GaN High Electron Mobility Transistors on Si/SiO2/Poly-SiC Substrates", T. Anderson, F. Ren, L. Covert, J. Lin, S.J. Pearton, J. Thuret, P. Bove and H. Lahreche, TMS Annual Meeting and Exhibition, Orlando, FL, Feb 2007.
3. "AlGaN/GaN High Electron Mobility Transistors on Si/SiO2/poly-SiC Substrates", Travis Anderson, Fan Ren, Lars Voss, Mark Hlad, Brent Gila, S.J. Pearton, Lance Covert, Jenshan Lin, Julien Thuret, P. Bove and H. Lahreche, MRS Fall Meeting, Boston, Nov 2006.
4. "SiC Via Fabrication and Integration for Wide Bandgap HEMT/MMIC Devices", by R. Shul, M. Overberg, A. Baca, C. Sanchez, J. Stevens, L. Voss, K. Ip, S. Pearton, M. Martinez, M. Armendariz and G. Wouters, 210th Meeting of ECS, Cancun, Mexico, Nov 2006.
5. "Hydrogen sensitive Schottky diodes on free-standing GaN Rectifiers", L. Voss, B.P. Gila and S.J. Pearton, Hung-Ta Wang and F. Ren, 208th ECS Meeting, Los Angeles, CA Oct 2005.

Students From Research

Jon Wright and Travis Anderson were supported from this program. Jon is serving as a summer intern at NASA Glenn in Summer 2007 and will graduate with a Ph.D in Summer 2009. Travis is interning at Sandia National Labs this summer and will graduate with a Ph.D in Spring 2008.

Follow-on Funding

The PI's have completed a Phase I SBIR ward with Nitronex, Inc. on developing AlGaN/GaN HEMTs on Si substrates and that team has been invited to submit a Phase II proposal.

2. Remote Wireless Power Transmission for Regenerative Fuel Cells

Task PI: Dr. Jenshan Lin, Electrical and Computer Engineering, University of Florida

Co-Investigators: Dr. Fan Ren, Chemical Engineering, Dr. Steve Pearton, Material Science & Engineering

Graduate Student: Mingqi Chen, Electrical and Computer Engineering

Abstract

In this research task, the concept of wireless power transmission for NASA application has been explored and the challenges are identified from a system perspective. By transmitting at microwave frequency, the electromagnetic wave beam can be focused to improve overall efficiency. However, lightweight high power microwave devices and circuits operating with high efficiency are required. Among various semiconductor technologies, GaN has the best power density and power handling capability. High efficiency rectifier circuits using GaN diodes are used as examples and detailed analysis is presented.

Introduction

The concept of Wireless Power Transmission (WPT) has been around for more than a century since Tesla carried out his first experiment using 150 kHz radio wave at Colorado Springs, Colorado, in 1899. However, such a long wavelength radio wave is difficult to focus and the overall efficiency would be too low for practical use. Due to the challenge of generating high power at microwave frequencies, WPT was confined to being a highly futuristic research goal and was never really close to a practical implementation. Serious effort was not started until 1958 when high power microwave tubes capable of efficiently generating hundreds of kilowatts at 3GHz became available [1]. Rectenna (antenna and rectifier) circuits with high RF-to-DC conversion efficiency were also developed by Raytheon in 1960's. This attracted Air Force's interest to power aircrafts by microwave beam. Later in 1977, NASA and DOE were interested in using WPT to transmit collected solar power from satellite stations to earth.

In addition to the above applications, microwave wireless power transmission can be used to solve many problems related to energy. The electric power distribution grid system can use WPT to extend the coverage range beyond what transmission lines can reach [2]. For example, excess electric power generated in rural areas on earth can be transmitted through satellite relays to more populated areas [3]. As Earth rotates, excess electric power generated in the nightside can be relayed to the dayside by satellites. The WPT system can also be used to conveniently transmit electric power to remote islands without using power transmission lines [4].

As semiconductor technologies advanced in the past several decades, microwave tubes were replaced by compound semiconductor power devices. This makes it feasible to have a compact lightweight high power microwave source. By integrating an array of microwave devices on a substrate or a wafer, and distribute the power processing load among them, a very high power solid state system can be achieved [5]-[6]. The recent development of high breakdown voltage devices based on wide bandgap materials, e.g., GaN and SiC, further increases the power

handling capability by 10 folds [7]-[8]. The microwave WPT system will benefit from such technologies.

In addition to the device technology, there are several other challenges for the entire microwave WPT system, which involves the DC-to-RF conversion at energy source transmitter, the RF-to-DC conversion at receiver, and the radio propagation in between. The technology challenges include high power device, high efficiency power circuits, transmitter and receiver architectures, power combining techniques, large antenna array, radio propagation, packaging, and integration. Above all, the frequency planning for different use scenarios is an important issue.

As high power millimeter-wave solid state devices became available, experiments were carried out to realize WPT at higher frequencies (35-GHz) in the 90's [9]-[10]. This was done in order to reduce the size of the transmitting and receiving antenna and to increase the transmission range. The components required to generate high power levels at 35-GHz were expensive and the efficiency was also not good, compared to low frequency systems. However, as system needs arise and device technologies advance, WPT at higher frequencies may be practical in the near future.

The objective of this research task is to develop enabling technologies to build a novel WPT system using broadband transmission to improve the overall system efficiency. We will investigate the RF transmitter architecture that can achieve the highest DC-to-RF conversion efficiency. GaN-based devices, which have been proven to have the highest power density per unit device area at frequencies from a few GHz to millimeter-wave frequency, will be used to design and build the transmitter and the receiver. We will design high-efficiency transmitter circuits including power amplifiers and power oscillators. The DC electric energy will be converted to RF energy for transmission over a long distance. The transmitter circuits will be optimized for high DC-to-RF conversion efficiency. On the receiver side connecting to the Regenerative Fuel Cell (RFC), broadband high efficiency rectifiers will be designed and optimized for high RF-to-DC conversion efficiency.

Background

Fuel cells have been used in NASA's space missions. Fuel cells use hydrogen and oxygen to generate electricity. Once the fuels (hydrogen and oxygen) are consumed, the fuel cells can no longer generate the power. To ensure a successful mission, the spacecrafts must carry enough fuels. This means increased size and weight, which in turn increases the energy consumption during the mission. The regenerative fuel cell (RFC) can be recharged to restore the energy capacity. RFC will be used in NASA's future space projects including planetary solar electric aircraft, lunar base, and Mars base.

However, the recharging needs the electricity and the regenerative fuel cells have to be sent to a recharging station. In space missions, immediate availability of power is critical, especially during an emergency situation. The possibility of losing power during a mission presents a life-threatening risk. When this happens, emergency delivery of backup energy sources in time becomes extremely critical. The physical delivery of fuel cells takes time in space missions. Therefore, scientists have been searching a method to charge the regenerative fuel cells on site.

Experimental

Properties of Microwave Wireless Power Transmission
Beamed microwave power transmission has the following unique features as a means of transferring energy from one point to another:

- No need for massive cables for energy transportation from source to destination
- Transfer of energy at the speed of light and flexibility to change direction of energy transfer
- No energy is lost in transmission in space through vacuum and very little loss in Earth's atmosphere at lower frequencies
- Energy transfer between points is independent of gravitational force between the source and destination

Collection efficiency between the transmitter and the receiver through free space is directly related to the sizes of the transmitter and receiver apertures, the distance over which the energy is being sent, and frequency of the microwave beam. A relationship between these parameters has been studied and experimentally verified by Goubau and other. The relationship between the parameter τ and the aperture-to-aperture collection efficiency is described by Equation (1) and shown in Figure 1 [11]-[12].
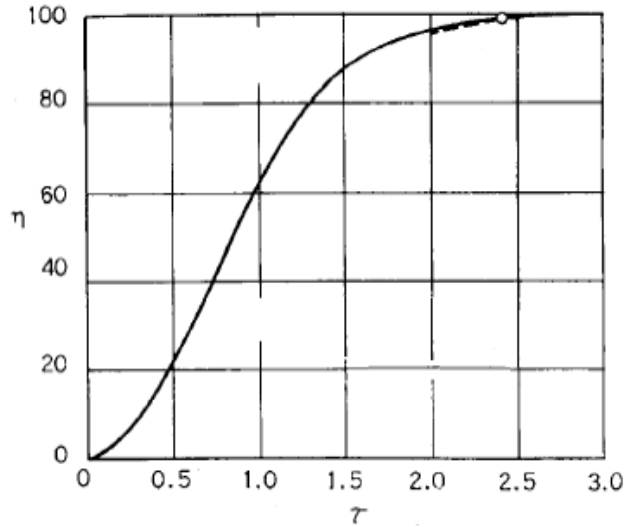
Figure 1. Collection efficiency between receiver and transmitter apertures as a function of parameter τ.

$$\tau = \frac{\sqrt{A_t A_r}}{\lambda D}$$

(1)

A_t is the transmitter area aperture. A_r is the receiver area aperture. λ is the wavelength of microwave beam. D is the separation between the two apertures. Collection efficiency is also affected by atmospheric attenuation which depends on operating frequency and weather conditions.

In order to achieve very high collection efficiency, the transmitted beam characteristic should be truncated Gaussian tapered distribution with very low sidelobe levels. A tapered distribution results in a higher power density at the transmitter aperture. The choice of the taper depends on the system constraints of collection efficiency, sidelobe levels, peak power density, and size of the apertures. A tapered Gaussian distribution at the transmitter results in a similar distribution at the receiver. Conversion efficiency at the receiver is strongly related to the power density distribution across the receiver aperture. With the assumption of a uniform taper at the transmitter, the directivity can be expressed as,

$$D_0 = \frac{4\pi A_{tm}}{\lambda^2}$$
(2)

This directivity expresses the gain factor of focused microwave beam compared to isotropic radiation. A_{tm} is the maximum effective transmitter area. For aperture antennas, A_{tm} is same as A_t. The magnification is reduced by decay of field strength over a distance D

$$\frac{1}{4\pi D^2}$$
(3)

Using Equation (2) and (3), the peak power density at the center of the receiver aperture at a distance D from the transmitter can be expressed as

$$P_{d,center} = \frac{A_t P_t}{\lambda^2 D^2}$$
(4)

where $P_{d,center}$ is the peak density of receiver power which is achieved at the center of the aperture. Power density and achieved DC output power across the receiver follow the same distribution as the transmitter. Gaussian distribution at the receiver is specified in terms of peak power density and half power beam width (*HPBW*) in degrees, which can be approximately written as [13],

$$HPBW = \sqrt{\frac{32400}{D}} = \sqrt{\frac{32400\lambda^2}{4\pi A_t}}$$
(5)

Using *HPBW*, the half power beam radius can be achieved for the Gaussian distribution on the receiver aperture, which can be expressed as

$$r_{hp} = HPBW \frac{\pi}{360} D$$
(6)

The Gaussian power density distribution on the receiver aperture is given by

$$P_d(r) = P_{d,center} \exp\left[(-\frac{r^2}{r_{hp}^2}) \ln(2) \right]$$
(7)

Total power received can be obtained by integrating the power density distribution over the aperture area. Average power density is given by total power divided by the total area, which can be written as

$$P_{d,average} = \frac{\int P_d(r).dA_{rx}}{A_{rx}}$$

(8)

Equation (8) shows that for a given total received power, a high value of $P_{d,average}$ requires a smaller receiver aperture. Power handling capability of the receiver is typically limited by the power density rating of the rectifying elements. Power handling capability of rectifying diodes is related to their breakdown voltage. Rectifying elements are one of the bottlenecks to achieve high efficiency at higher power density. To increase the power handling capability of this bottleneck, it is required to use diodes that give high efficiency at higher power levels. GaN diodes with very high power handling capability can serve as a good candidate for WPT systems involving very high power density transmission.

WPT System Configuration

WPT system can be viewed as a system that transfers electrical power from one location to another without support of actual cables. WPT system can be integrated to other systems at relatively low implementation cost. It was estimated that power carried through a microwave beam can be four times less expensive than electricity produced by photovoltaic panels [14]. Most important requirement for a WPT system is to achieve high overall transfer efficiency (DC-to-DC). WPT system consists of three major building blocks as shown in Figure 2.
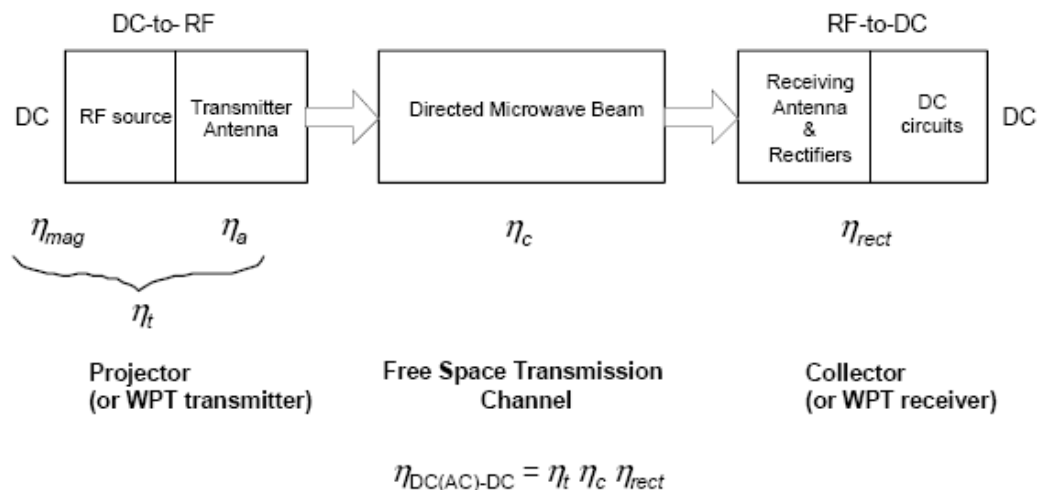
Figure 2. System block diagram of wireless power transmission.

The first block converts the DC (or AC) power to microwave energy. Microwave energy is then radiated through an array of antennas and converted to a focused beam. This focused beam is then transmitted across free space towards the collector antenna. Microwave energy is then collected using receiver antenna which is then rectified back to DC power. Overall efficiency of the WPT system is a combination of these three factors: DC-to-RF conversion efficiency (η_t), collection efficiency (η_c), and RF-to-DC rectification efficiency (η_r). To achieve the maximum system efficiency, it is required to maximize the efficiency of individual stages. Efficiency of a

system can be expressed as the ratio of useful output power to the total input power delivered to the system:

$$Efficiency = \frac{P_{out}}{P_{in}} \times 100 \ \%$$

(9)

For the transmitter, it is required to achieve high levels of microwave power from DC. Vacuum tube devices such as magnetron can efficiently convert DC power into RF power. Magnetrons with DC-to-RF conversion efficiency in the range of 70 to 85% are available in lower frequency ranges of 1-5 GHz. Magnetrons are cheap devices and can provide high power levels at good efficiency compared to typical solid-state FET device. Suitable choice of antenna type and size is required for both transmitter and receiver end. Slotted waveguide antenna can be used at the transmitter end when magnetrons are used as RF sources. Slotted waveguide antennas are a suitable choice for transmission of RF power when magnetrons are used as the RF source. These antennas have high efficiency and high power handling capability. Such structures can also provide a low cost solution.

Efficiency of antenna is defined as the ratio of antenna gain and directivity. A large number of antenna and sources need to be used to achieve sufficiently high RF power levels. The radiated RF power should be efficiently collected by a receiver antenna which is usually larger in size compared to transmitter antenna. For constant collection efficiency (τ) at fixed operating frequency, the product of transmitter and receiver aperture areas is also a constant as described in Equation (1). Transmitter antenna size can be maximized to enhance the beamed characteristics but is limited by the approximation of far field region of operation which depends on the separation between the receiver and the transmitter. Typically, the receiver aperture should be larger than the transmitter to efficiently collect the radiated energy. An array of smaller antenna elements connected to the rectifier circuit can be used to comprise the whole receiver system. In order to reduce the number of array elements, it is required to collect higher power per array element, which implies higher power handling capability of the devices. RF-to-DC conversion efficiency of a Schottky barrier diode at higher power level is limited by the breakdown voltage. GaN diodes, which have high breakdown voltage, were proven to be suitable candidates for rectification of high RF input power levels.

Effect of Diode Parameters on RF-To-DC Conversion Efficiency

Diode conversion efficiency η_d is a key measure to determine the overall efficiency of the WPT system. Diode efficiency is defined as the following:

$$\eta_d = \frac{\text{dc output power}}{\text{RF power incident on the diode}}$$

(10)

Efficiency of the rectifier circuit at a particular frequency depends on the electrical parameters of the diode. A diode model suggested in [15]-[16] is used to predict the behavior of rectification efficiency.
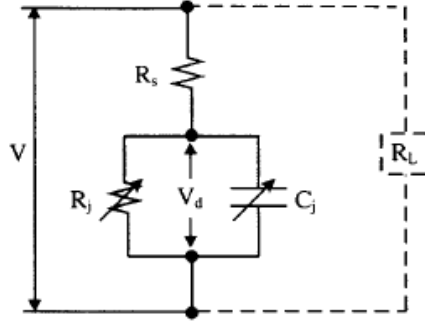
Figure 3. Equivalent circuit model of Schottky barrier diode.

In Figure 3, R_s is the series resistance, V_{bi} is built in potential, C_{jo} is the zero bias junction capacitance and V_o is the DC voltage level across the load resistance R_L. This model takes into account the electrical parameters of the diode and the loss at the fundamental frequency of operation only. Effect of other harmonics is assumed to be negligible. A dynamic variable θ_{on} which depends on the input power applied to the diode is defined as,

$$\tan\theta_{on} - \theta_{on} = \frac{\pi R_s}{R_L\left(1 + \dfrac{V_{bi}}{V_o}\right)}$$

(11)

Closed form equations for efficiency were determined [85] and the RF-DC rectification efficiency can be expressed as,

$$\eta_d = \frac{1}{A + B + C}$$

(12)

$$A = \frac{R_L}{\pi R_s}\left(1 + \frac{V_{bi}}{V_o}\right)^2\left[\theta_{on}\left(1 + \frac{1}{2\cos^2\theta_{on}}\right) - 1.5\tan\theta_{on}\right]$$

(13)

$$B = \frac{R_L R_s C_j^2 \omega^2}{2\pi}\left(1 + \frac{V_{bi}}{V_o}\right)\left[\frac{\pi - \theta_{on}}{\cos^2\theta_{on}} + \tan\theta_{on}\right]$$

(14)

$$C = \frac{R_L}{\pi R_s}\left(1 + \frac{V_{bi}}{V_o}\right)\frac{V_{bi}}{V_o}(\tan\theta_{on} - \theta_{on})$$

(15)

Equations (12)-(15) give an estimate of the maximum achievable efficiency for diode with fixed parasitic values when the RF input power level is changed. To get an estimate of the efficiency values with varying R_L, V_o can be kept constant in Equation (11) and θ_{on} can be determined for different R_L values. An example of GaN diode used in this work had R_s=19.5 Ω, C_{jo}=1.4pF and V_{bi}=1.3 V. For the chosen V_o and R_L values, output DC power available at load can be determined using Equation (16). Corresponding values of efficiency with available DC output power level gives the amount of input RF power level, as shown in Equation (17).

$$Power_{DC} = \frac{V_0^{\,2}}{R_L} \qquad (16)$$

$$Power_{RF} = \frac{Power_{DC}}{\eta_d} \qquad (17)$$

Efficiency versus load resistance R_L for three different values of V_o (20-V, 25-V, and 30-V) is plotted in Figure 4. Efficiency versus input power level is shown in Figure 5.
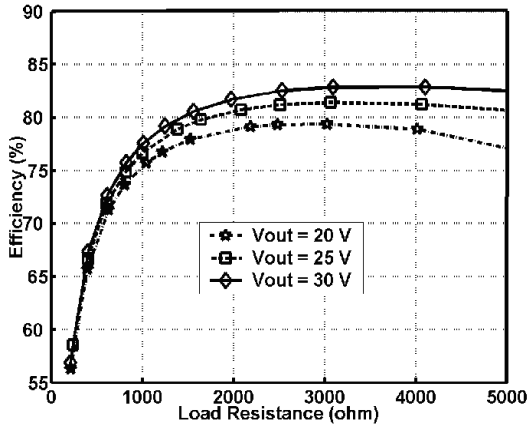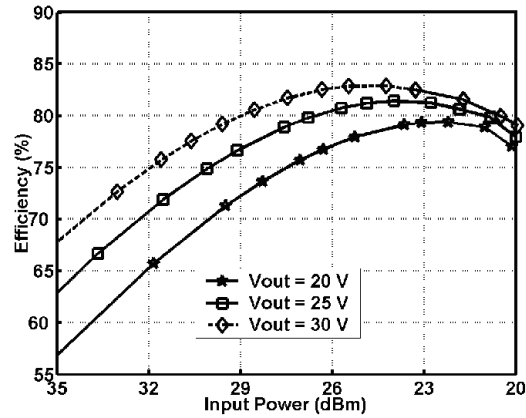

Figure 4. Efficiency vs. load resistance.   Figure 5. Efficiency vs. input power level.

RF-to-DC conversion efficiency increases with an increase in R_L for constant V_o and then saturate with further increase in R_L values. A larger chosen value of V_o helps to achieve better efficiency. Considering the achievable efficiency, R_L and V_0 values input RF power level can be obtained. A list of R_L, efficiency and corresponding input power level is shown in Table 1. It can be seen that maximum achievable efficiency increases with an increase in R_L value when RF power level is simultaneously decreased. Maximum efficiency of around 80% can be achieved for R_L values greater than 2000 Ω and input power level of around 25 dBm.

Table 1. Input power level versus corresponding efficiency and R_L values

V_0 = 20V			V_0 = 25V			V_0 = 30V		
Load Resistance (Ω)	Eff. (%)	Input Power (dBm)	Load Resistance (Ω)	Eff. (%)	Input Power (dBm)	Load Resistance (Ω)	Eff. (%)	Input Power (dBm)
210	56.80	38.75	238	58.5	36.50	216	51.4	35.17
408	67.30	35.15	400	66.5	33.65	400	65.7	31.83
617	72.60	33.00	610	72.0	31.52	633	71.3	29.47
825	75.70	31.60	820	74.8	30.00	808	73.6	28.27
1000	77.50	30.60	1000	76.6	29.10	1044	75.7	27.04
1250	79.20	29.60	1380	78.8	26.80	1250	76.7	26.28
1560	80.50	28.55	1640	79.8	25.90	1500	77.9	25.25
1970	81.70	27.50	2080	80.7	25.50	2190	79.1	23.63
2530	82.50	26.30	2530	81.2	24.85	2485	79.3	23.07
3090	82.80	25.45	3060	81.4	24.00	3030	79.4	22.20
4100	82.60	24.20	4070	81.2	22.75	4120	78.9	21.00
5150	82.40	23.30	5110	80.6	21.80	5050	77.0	20.12

Theoretical estimation of achieved efficiency was also desired for changing V_o conditions when R_L was kept constant. Different values of θ_{on} were obtained from Equation (11) and efficiency was calculated using Equation (12). The corresponding input power level was calculated from efficiency, R_L and V_o values. Plots of efficiency versus V_o and input power level are shown in Figures 6 and 7, respectively.
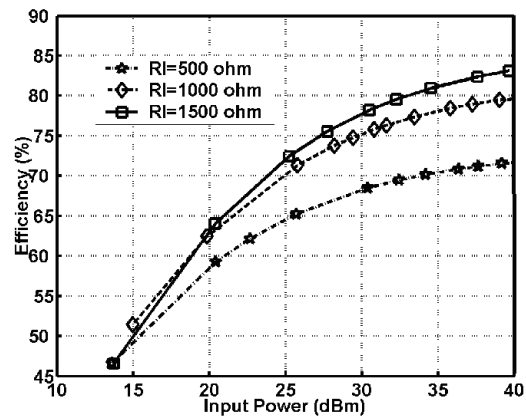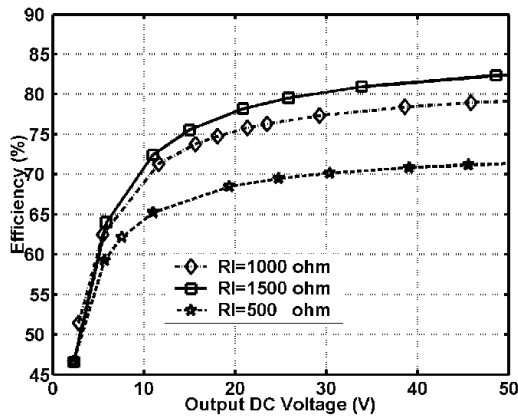

Figure 6. Efficiency vs. DC output voltage.   Figure 7. Efficiency vs. input power.

RF-to-DC conversion efficiency increases with an increase in V_o for constant R_L. In actual devices, efficiency starts to fall when V_o becomes higher than half the breakdown voltage of the device. Considering the achievable efficiency, R_L and V_o values of the input RF power level can be obtained using Equations (16) and (17). A list of R_L, efficiency and corresponding input power levels is shown in Table 2. It can be seen that the maximum achievable efficiency increases with an increase in R_L value when RF power level is increased. Maximum efficiency of around 80% was achieved for V_o values greater than 30V and input power level of around 35 dBm.

Table 2. Input power level versus corresponding efficiency and V_o values

R_L = 500 Ω			R_L = 1000 Ω			R_L = 1500 Ω		
Output Voltage (V)	Eff. (%)	Input Power (dBm)	Output Voltage (V)	Eff. (%)	Input Power (dBm)	Output Voltage (V)	Eff. (%)	Input Power (dBm)
2.32	46.64	13.63	2.85	51.40	15.00	2.35	46.5	13.75
5.72	59.20	20.43	5.50	62.40	19.86	5.90	64.0	20.40
7.60	62.17	22.69	11.63	71.30	25.78	11.00	72.4	25.30
11.00	65.24	25.73	15.64	73.70	28.22	15.00	75.5	27.75
19.40	68.47	30.40	18.09	74.70	29.42	20.90	78.2	30.50
24.80	69.47	32.48	21.39	75.70	30.82	25.90	79.5	32.30
30.40	70.15	34.20	23.52	76.30	31.61	33.90	80.90	34.5
39.10	70.83	36.25	29.28	77.30	33.45	48.65	82.30	37.6
45.63	71.18	37.35	38.64	78.40	35.80	62.00	83.00	40.0
54.68	71.53	39.22	45.90	78.90	37.27			

Results presented in Table 2 show that efficiency increases with an increase in the output voltage level, when the input power level is increased. In order to achieve highest efficiency, a large load and a high input power level are required. This observation is in contrast to the observation from Table 1, where highest efficiency was achieved at higher load resistance values but at lower input power levels. The two behaviors contrast with each other and it can be concluded that there exists an optimum load resistance value for a desired input power level that gives the highest RF-to-DC rectification efficiency. It was concluded that a resistance R_L = 1000 Ω gives highest efficiency of 80% when operated at a power level of around 30 dBm.

Results and Discussion

In order to achieve good efficiency at higher frequency, junction capacitance plays an important role. GaN HEMTs have lower junction capacitance compared to ring diodes. Diode behavior can be achieved using a HEMT by connecting the drain and gate node of the device. Due to the layout of the device, it was difficult to connect the gate and drain together without introducing unwanted parasitic inductances. Therefore, only the gate-source diode was used. DC and small signal parameters were measured and diode model was derived using Agilent IC-CAP modeling software. Diode model parameters are I_s = 7.1 nA, N = 3.8, R_s = 19.5 Ω, BV>45V, C_{jo} = 1.4pF. A plot of measured and modeled forward bias characteristics of the HEMT diodes is shown in Figure 8.
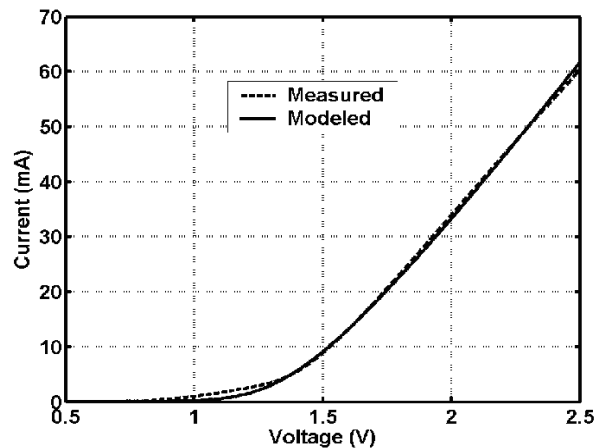

Figure 8. Forward DC I-V characteristics of HEMT diode.

A half wave voltage doubler configuration has been used owing to its ability to achieve higher voltage output as compared to a single rectifier diode [17]. Figure 9 shows the schematic of the rectifier circuit.
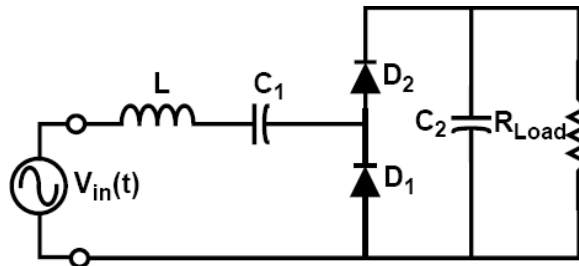

Figure 9. Schematic of the voltage doubler rectifier circuit.

In Figure 9, one Schottky diode is placed in parallel with the input RF signal. This lowers the input impedance and makes the design of matching network easier. During the negative half of the input cycle, diode D_1 is forward biased whereas D_2 is reverse biased. The capacitance C_1 is then charged to the peak voltage of the incoming signal. During the positive half of the input cycle, D_1 is off whereas D_2 is on. At node X, the incoming RF signal now increases the voltage already present on C_1 and therefore increases the voltage across the load. Capacitor C_2 acts as low-pass filter which reflects the microwave energy arising from the diode thereby producing DC voltage across R_{Load}. Figure 10 shows a photo of the AlGaN/GaN HEMT device used as a diode and the fabricated circuit on FR4 board (relative permittivity = 4.4, thickness = 1.58 mm).
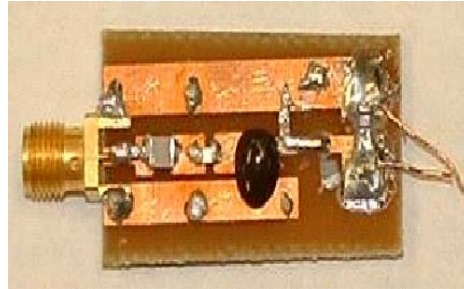

Figure 10. Photo of fabricated circuit board on FR4 substrate.

Two metal traces are put on each side of the signal trace to ease connections of shunt elements to ground. The traces are connected to the ground plane on the back using via holes. Wire-bonding is used to connect the diodes to the metal traces. The effect of bond wire inductance was taken into account during the design. GaN diodes used in this work have a breakdown voltage of about 45-V and a relatively high ideality factor. The ideality factor of these devices is ~3.8 which makes them not as suitable for use at lower input power levels.

The circuits were measured using a power amplifier to boost the input RF power level from the signal generator up to 30-dBm. Figure 11 shows a plot of the maximum achieved RF-to-DC conversion efficiency and corresponding DC output voltage level versus input power level with R_{Load} = 1000 Ω, at the frequency of 900 MHz.
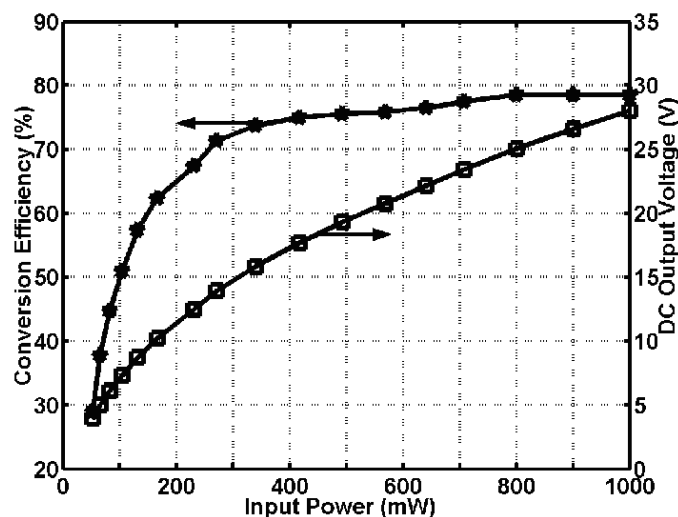

Figure 11. Measured RF-to-DC conversion efficiency and DC
output voltage versus RF input power (R_{Load} = 1000 Ω).

To evaluate the use of the rectifier circuit to achieve even higher voltage levels, a load impedance of 5.4-kΩ was used. At 1-W input power, the circuit achieved an output voltage of 51-V at 900-MHz but conversion efficiency decreased to 51%. Figure 12 shows the variation of RF-to-DC conversion efficiency and corresponding DC output voltage level versus input power level with R_{Load} = 5.4-kΩ.
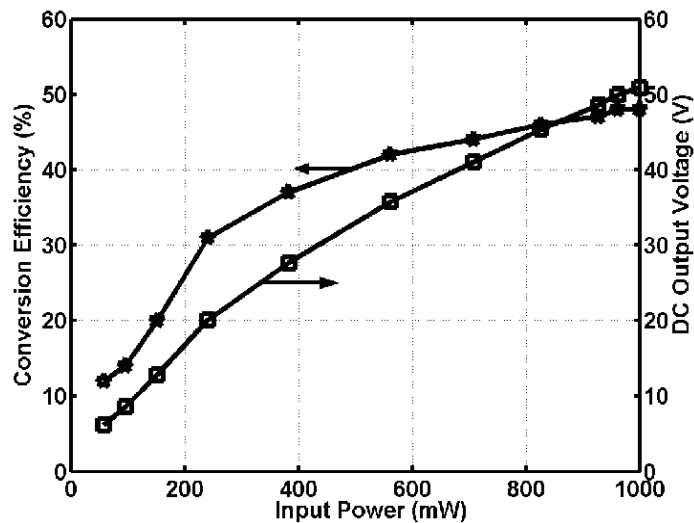
Figure 12. Measured RF-to-DC conversion efficiency and DC output voltage versus input power
(R_{Load} = 5.4-kΩ)
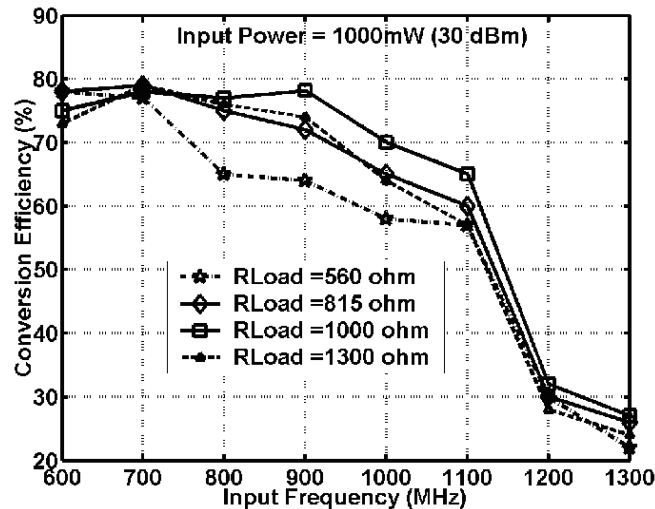
Figure 13. Measured RF-to-DC conversion efficiency versus frequency
for different values of load resistance.

To evaluate the frequency response of the circuit, measurements were performed for a frequency range of 600-MHz to 1300-MHz with a constant input power level of 1-W. Efficiency remained better than 65% up to 1100-GHz for load impedance of 1000-Ω. At up to 1000-MHz, efficiency better than 60% was achieved for load impedance ranged from 815-Ω to 1.3-kΩ, as shown in Figure 13.

Another test board was built with similar configuration. Inductance and capacitance values at the input side were tuned to make the circuit operate optimally at little higher frequencies. Efficiency response of the new test board was measured between 1-GHz– 1.7-GHz. Efficiency values of better than 63% were achieved up to 1.4 GHz for load impedance of 815 Ω. Figure 14 shows the achieved efficiency versus frequency for an input power level of 1W for different values of load impedances.
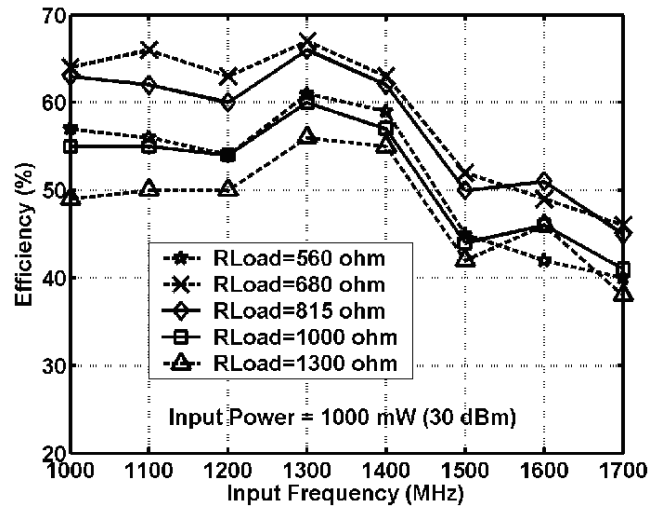

Figure 14. Measured RF-to-DC conversion efficiency versus frequency
for different values of load resistance.

Conclusions

Concept of applying wireless power transmission for NASA application has been explored in this research task. System-level analysis is presented. To achieve a practical WPT system, high power density semiconductor devices and high efficiency circuits operating at microwave frequency and above are needed. GaN devices and circuits that can handle high power at high frequency are good candidates to be used for microwave WPT systems.

A high power high efficiency RF-to-DC rectifier was fabricated using GaN Schottky diodes. The circuit achieves high output DC voltage and good RF-to-DC conversion efficiency. Conversion efficiency of 79% is achieved at 900-MHz at an input power level of 1-W. The circuit can also achieve high output DC voltage level of around 50-V at increased load condition (R_{Load} = 5.4-kΩ), at the expense of a reduction in conversion efficiency. Use of such high power rectifiers in a receiver system with high power density levels at the transmitting and receiving antenna can reduce the number of receiver array elements in microwave wireless power transmission systems.

Patents

None

Publications

Journals

1. T. Chang, W. Wu, J. Lin, S. Jang, F. Ren, S. Pearton, R. Fitch, and J. Gillespie, "Analysis and Design of AlGaN/GaN HEMT Resistive Mixers," *Microwave and Optical Technology Letters*, Vol. 49, No. 5, pp. 1152-1154, May 2007.
2. S. Ko, W. Wu, J. Lin, S. Jang, F. Ren, S. Pearton, R. Fitch, and J. Gillespie, "A High Efficiency Class-F Power Amplifier using AlGaN/GaN HEMT," *Microwave and Optical Technology Letters*, Vol. 48, No. 10, pp. 1955-1957, October 2006.
3. T.J. Anderson, F. Ren, L. Voss, M. Hlad, B.P. Gila, L. Covert, J. Lin, S.J. Pearton, P. Bove, H. Lahreche, J. Thuret, "AlGaN/GaN high electron mobility transistors on Si/SiO2/poly-SiC substrates," *J. Vac. Sci. Technol. B – Microelectronics and Nanometer Structures*, 24(5), pp. 2302-2305, September/October 2006.
4. T.J. Anderson, F. Ren, L. Covert, J. Lin, S.J. Pearton, "Thermal Considerations in Design of Vertically Integrated Si/GaN/SiC Multichip Modules," *Journal of The Electrochemical Society*, Vol. 153, No. 10, G906-G910, July 31, 2006.
5. T.J. Anderson, F. Ren, L. Covert, J. Lin, S. J. Pearton, T.W. Dalrymple, C. Bozada, R.C. Fitch, N. Moser, R.G. Bedford and M. Schimp, "Comparison of Laser Wavelength Operation for Drilling of Via Holes in AlGaN/GaN HEMTs on SiC substrates," *Journal of Electronic Materials*, Vol. 35, No. 4, pp. 675-679, April 2006.
6. T.J. Anderson, F. Ren, L. Covert, J. Lin, S. J. Pearton, "Thermal Simulations of 3-D integrated Multi-Chip Module with GaN Power Amplifier and Si Modulator," *J. Vac. Sci. Technol. B – Microelectronics and Nanometer Structures*, 24(1), pp. 284-287, January/February 2006.

Conference Papers

1. J.S. Kim, W. Wu, J. Lin, A. Verma, S. Jang, F. Ren, S. Pearton, R. Fitch, J. Gillespie, "A High-Efficiency GaN/AlGaN HEMT Oscillator Operating at L-Band," *Proceedings of IEEE Asia-Pacific Microwave Conference*, pp. 631-634, December 2006.
2. J. Lin, A. Verma, J. Kim, S. W. Ko, W. Wu, F. Ren, S. Jang, S.J. Pearton, "Microwave Wireless Power Transmission – A System Perspective," *ECS Transactions, Vol. 3, No. 5, State-of-the-Art Programs on Compound Semiconductor and Wide Bandgap Semiconductor Materials and Devices*, pp. 127-140, October 2006. (Invited).
3. F. Ren, T.J. Anderson, L. Voss, M. Hlad, B.P. Gila, A. Verma, W. Wu, L. Covert, J. Lin, S.J. Pearton, P. Bove, H. Lahreche, and J. Thuret, "GaN Based Material Growth and Devices for Microwave Power Transmission Systems," *Proceedings of the 3rd International Symposium on Sustainable Energy System*, pp. 116-118, September 2006. (Invited).
4. T.J. Anderson, F. Ren, L. Covert, J. Lin, "Thermal Simulations of 3-D integrated Multi-Chip Module with GaN Power Amplifier and Si Modulator," *Proceedings of 208th Meeting of the Electrochemical Society*, pp. 94-102, 2005.

Presentations

1. T. Anderson, F. Ren, L. Covert, J. Lin, S. Pearton, J. Thuret, P. Bove, H. Lahreche, "Microwave performance of AlGaN/GaN High Electron Mobility Transistors on Si/SiO2/poly-SiC Substrates," Recent Developments in Semiconductor, Electro Optic and Radio Frequency Materials Symposium, in TMS 136th Annual Meeting & Exhibition, Orlando, FL, Feb. 25-Mar. 1, 2007. (Refereed conference abstract)

2. J. Lin, "Self-Powered Wireless Nano-Sensor for Hydrogen Leak Detection and Wireless Power Transmission," Radio Science Symposium for A Sustainable Humanosphere, Kyoto, Japan, March 20-21, 2006. (Invited)
3. J. Lin, "Wireless Power Transmission" in Energy Colloquium, University of Florida, November 1, 2004. (Invited)

Students from Research

1. Ashok Verma (PhD May 2006) – Maxim
2. Sang Won Ko (PhD August 2007) – Skyworks
3. Travis Anderson (PhD student, exp. May 2008)
4. Tien-Yu Chang (PhD student, exp. May 2008)
5. Jaeshin Kim (PhD student)
6. Mingqi Chen (PhD student)

Funding Obtained by Leveraging NASA Grant

SBIR Phase I award with Nitronex, Inc. on developing AlGaN/GaN HEMTs on Si substrates. The team has been invited to submit a Phase II proposal.

Collaborations

Dr. Shigeo Kawasaki, Kyoto University, Japan – Modeling of GaN devices
Dr. Wayne Johnson, Nitronex Inc. – GaN materials and devices

References

1. W.C. Brown, "The history of power transmission by radio waves," IEEE Transactions on Microwave Theory and Techniques, Vol. 32, No. 9, pp. 1230-1242, September 1984.
2. S.S. Ahmed, T.W. Yeong, and H.B. Ahmed, "Wireless power transmission and its annexure to the grid system," IEE Proceedings – Generation, Transmission and Distribution, Vol. 150, No. 2. pp. 195-199, March 2003.
3. A.P. Smakhtin, V.V. Rybakov, "Comparative analysis of wireless systems as alternative to high-voltage power lines for global terrestrial power transmission," Proceedings of the 31st IEEE Intersociety Energy Conversion Engineering Conference, Vol. 1, 485-488, August 11-16, 1996.
4. A. Celeste, P. Jeanty, G. Pignolet, "Case study in Reunion Island," Acta Astronautica, Vol. 54, pp. 253-258, 2004.
5. D.B. Rutledge, Z.B. Popovic, R.M. Weikle, II, M. Kim, K.A. Potter, R.C. Compton, R.A. York, "Quasi-optical power-combining arrays," IEEE MTT-S International Microwave Symposium Digest, Vol. 3, pp. 1201-1204, May 8-10, 1990.
6. J. Lin, T. Itoh, "Two-dimensional quasi-optical power-combining arrays using strongly coupled oscillators," IEEE Transactions on Microwave Theory and Techniques, Vol. 42, No. 4, pp. 734-741, April 1994.
7. R.J. Trew, "SiC and GaN Transistors – Is There One Winner for Microwave Power Applications?" Proceedings of the IEEE, Vol. 90, No. 6, pp. 1032-1047, June 2002.
8. G.T. Dang, A.P. Zhang, F. Ren, X.A. Cao, S.J. Pearton, H. Cho, J. Han, J.-I. Chyi, C.-M. Lee, C.-C. Chuo, S.N.G. Chu, R.G. Wilson, "High voltage GaN Schottky rectifiers," IEEE Transactions on Electron Devices, Vol. 47, No. 4, pp. 692-696, April 2000.

9. P. Koert, J. Cha, and M. Macina, "35 and 94 GHz rectifying antenna systems," *in SPS'91-Power from Space Digest*, pp. 541-547, Paris, France, 1991.

10. T.W. Yoo and K. Chang, "Theoretical and Experimental developments of 10 and 35GHz rectenna," *IEEE Trans. Microwave Theory Tech.*, Vol. 40, pp. 1259-1266, June 1992.

11. W.C. Brown, and E.E. Eves, "Beamed Microwave Power Transmission and its Application to Space," IEEE Trans. Microwave Theory Tech., Vol. 40, No. 6, pp. 1239-1250, June 1992.

12. G. Goubau and F. Schwering "On the guided propagation of electromagnetic wave beams," IRE Trans. Antennas Propagation, Vol. 9, pp. 248-256, May 1961.

13. C.A. Balanis, *Antenna Theory – Analysis and Design*, Wiley Publication, 3rd ed., 2005.

14. G. Pignolet, *Wireless Power Transportation.* Paris: Centre National d'Études Spatiales, Université de La Réunion, 1999.

15. B. Strassner and K. Chang, "Highly Efficiency C-Band Circularly Polarized Rectifying Antenna Array for Wireless Microwave Power Transmission," *IEEE Tran. Microwave Theory Tech.*, Vol. 51, pp. 1347-1356, June 2003.

16. J.O. McSpadden, L. Fan and K. Chang, "Design and Experiments of a High-Conversion Efficiency 5.8GHz Rectenna," *IEEE Trans. Microwave Theory Tech.*, Vol. 46, No. 12, pp. 2053-2060, Dec. 1998.

17. G. Ivensky, M. Shvarstas, and S.B. Yaakov, "Analysis and Modeling of a Voltage Doubler Rectifier Fed by a Piezoelectric Transformer," *IEEE Tran. Power Electronics*, Vol. 19, pp. 542-549, Mar.

3. Rational Design of Higher Conductivity Solid Oxide Electrolytes

Task PI: Dr. Eric Wachsman, Materials Science and Engineering

Co-Investigators: Dr. Simon Phillpot, Materials Science and Engineering, Dr. Juan C. Nino, Materials Science and Engineering and Dr. Susan B. Sinnott, Materials Science and Engineering

Graduate Students: Doh Won Jung with Dr. Wachsman, Omar Shobit with Dr. Nino, and Aidhy Dilpuneet with Dr. Philpot and Dr. Sinnott

Research Period: August 3, 2004 to March 31, 2008

Abstract

A judicious combination of electronic-structure calculations and molecular dynamics simulations was used to fully characterize the structure of cubic δ-Bi_2O_3. We found that the intrinsic oxygen vacancies in the structure align in a combined manner in the <110> and <111> directions to form a defect-fluorite superstructure containing eight non-primitive cubic cells, containing a total of 80 atoms. This structure is consistent with that determined previously from neutron scattering. We characterize the oxygen diffusion process and find that the high polarizability of the Bi ions is crucial for obtaining oxygen diffusion; by contrast, the polarizability of the O ions does not appear to play a role in diffusion.

Introduction

In recent years, highly ionically conductive materials have received increased attention for applications in energy conversion, chemical processing, sensors, and combustion control. These applications typically require conduction of oxygen ions, which narrows the candidate materials to solid oxide electrolytes.[1] High oxygen diffusivity has been observed in oxides which exhibit large tolerance for atomic disorder. Several investigations have focused on cubic fluorite structured oxides due to their relatively open structure.[2] The most successful oxide electrolytes have been those based on fluorite-structured δ-Bi_2O_3 and acceptor-doped group IVB oxides (i.e., ZrO_2, HfO_2, CeO_2 or ThO_2).[3] Optimization of these materials led to 8 mol% yttria-stabilized zirconia (YSZ) becoming the favored electrolyte for solid oxide fuel cells (SOFCs).[4] YSZ is purely an ionic conductor, even at reducing atmospheres, however, its high operational temperature (~1000°C) restricts its usage to multi-MW SOFC systems (e.g.: electrical generation plants).[5] Smaller SOFC stacks (3-5kW) require ionically conductive materials that can operate in intermediate temperature (IT) range, i.e., 400-800°C,
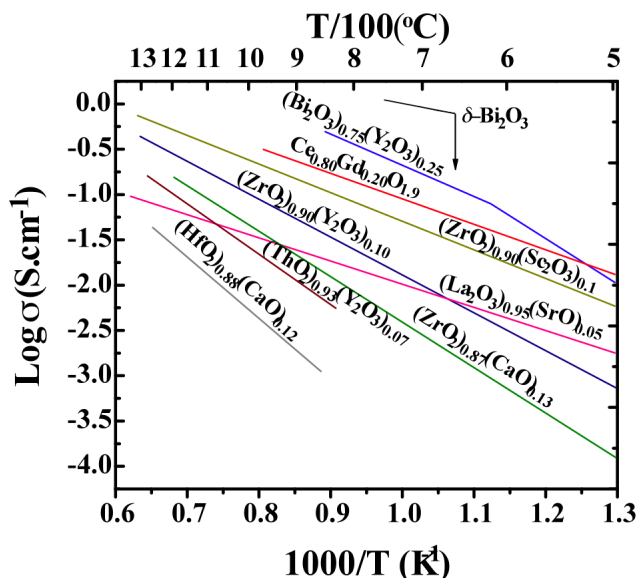

Figure 1. Comparison of the electrical conductivity of various fluorite structured oxides.[6]

without compromising the internal resistance of the cell. To date, candidate materials for operation in IT range includes cubic-stabilized δ-Bi$_2$O$_3$ and acceptor-doped ceria.[2,6]

A summary of the ionic conductivity of different fluorite structured oxides is shown in Figure 1 as an Arrhenius plot. It can be seen that δ-Bi$_2$O$_3$ and yttria-stabilized Bi$_2$O$_3$ exhibit the highest ionic conductivity among all oxygen ion conducting materials. However, these oxides possess a number of disadvantages, including thermodynamic instability in reducing atmospheres, volatilization of Bi$_2$O$_3$ at moderate temperatures, a high corrosive activity, and low mechanical strength. Hence, the applicability of these oxides in electrochemical cell is considerably limited. It is crucial therefore to develop oxygen ion conducting ceramics with sufficient conductivity at lower temperatures, while concomitantly improving their stability issues. In this study we have addressed this problem in two ways: (a) theoretically, through computational analysis of oxygen ion migration in simulated fluorite structures and (b) empirically, by developing novel cerium oxide (ceria) and cubic-stabilized bismuth oxide electrolytes, each with the highest conductivities reported in the literature (Figure 1). This report describes the results of our investigations.

Computational Study

Cubic δ-Bi$_2$O$_3$ was used as a model fluorite-structured ceramic to investigate the effects of lattice structure on conductivity because: (a) δ-Bi$_2$O$_3$ has two intrinsic vacancies per unit-cell instead (see Figure 2) unlike other fluorite systems which require doping to introduce oxygen vacancies; (b) the Coulombic and size effects arising due to the difference in the valence and radius of a dopant are absent, allowing the effects of the oxygen vacancies on the structure to be explored in isolation. In addition, Dy$_2$O$_3$ and WO$_3$ co-doped Bi$_2$O$_3$ has been reported[1] to have the highest conductivity among all the fluorite based solid electrolytes. Hence, δ-Bi$_2$O$_3$ is seen as a promising material for application in SOFCs.
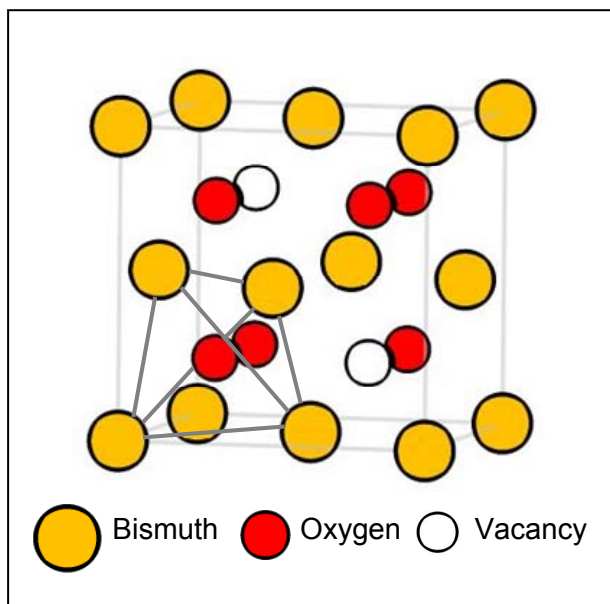

Bismuth Oxygen Vacancy

Figure 2. Conventional unit cell of δ-Bi$_2$O$_3$. A tetrahedron formed by four bismuth atoms with an oxygen atom inside it.

However, there are some fundamental issues which need to be addressed in cubic δ-Bi$_2$O$_3$: primarily, the ordering of the vacancies, the effect of the ionic polarizability of cation and anion on oxygen conductivity, the structural changes occurring due to vacancies within the unit-cell, the oxygen diffusion mechanism and most importantly, the basic defect structure of cubic δ-Bi$_2$O$_3$. Hence, these formed the objectives of this research. Previously, it had been observed experimentally that the oxygen conductivity of δ-Bi$_2$O$_3$ decreases with doping.[2] A direct proportional dependence of oxygen conductivity on dopant polarizability and radius are observed to be the two contributing factors in decreasing its oxygen conductivity.[2,3] Distinguishing the two effect is not possible by experiments; MD simulations can be used to separating them. In MD, for a given system of doped δ-Bi$_2$O$_3$, it is possible to keep either the radius or polarizability can be kept constant while the other is varied.

DFT was used to predict the most stable ordering mechanism of the vacancies and understand the system size dependence on the ordering mechanism. Using DFT calculations, Walsh et al.[4] had earlier predicted that <100> ordering mechanism as the most favorable one, a contradiction to any of the earlier predicted ones.[5,7-9] We have repeated their unit-cell system calculations and extended that work to 2x2x2 unit-cell systems. We have found that ordering mechanism is dependent on the size on the system considered. DFT is further used to understand the electronic charge distribution of the bismuth ions.

Optimization of Stabilized Bismuth Oxide

Stabilized cubic bismuth oxides (δ-Bi_2O_3) exhibit the highest known ionic conductivity.[10-13] The conductivity of δ-Bi_2O_3 is one to two orders of magnitude higher than YSZ at corresponding temperatures.[14] However, δ-Bi_2O_3 transforms to monoclinic α-phase on cooling below 730°C. Therefore, the application of δ-Bi_2O_3 is limited to the narrow temperature range of 730°C-824°C. Fortunately, the face centered cubic phase of δ-Bi_2O_3 can be stabilized down to room temperature by doping with other oxides.[15] However, due to the mismatch in ionic radii between the host and dopant cations, structure stabilization has resulted in the reduction of ionic conductivity.

Verkerk et al. assumed that the stabilization of relatively loose high temperature δ-Bi_2O_3 is possible by a contraction of this structure due to the dopant.[16] He observed that the effect of Ln_2O_3 or Y_2O_3 content which is required to stabilize δ-Bi_2O_3 is a dominant factor to obtain maximum ionic conductivity. For the case of singly doped Bi_2O_3, the highest ionic conductivity was obtained by the fcc phase of Er_2O_3 stabilized Bi_2O_3.[16]

Besides the singly doped Bi_2O_3 system, several ternary Bi_2O_3-based oxides have been synthesized and characterized.[17,18] Meng et al. showed that the fcc structure in Bi_2O_3-based solid solutions with two rare-earth oxide dopants could be stabilized down to room temperature, with much lower total dopant concentration than that of a singly doped oxide.[17] This cooperative effect was attributed to the increase in entropy of the resulting ternary system as a consequence of mixing.[17] It was observed that the existence of second dopant in smaller concentration stabilized the fcc structure and led to an increase in conductivity, especially in the lower temperature regions.

Verkerk et al. examined oxygen ion conductivity of Dy_2O_3 doped Bi_2O_3.[16] They found that the fcc structure was stabilized for samples containing 28.5-50 mol% Dy_2O_3.[16] Takahashi et al. investigated WO_3 doped Bi_2O_3 system and found that though the fcc structure had high oxide ion conductivity, it was stable over a rather narrow composition range of 22-28 mol% WO_3 in Bi_2O_3.[19] In both systems the highest conductivity was obtained with the minimum dopant concentration required to stabilize the fcc phase, i.e., $(DyO_{1.5})_{0.285}(BiO_{1.5})_{0.715}$ and $(WO_3)_{0.22}(BiO_{1.5})_{0.78}$.[16,19] It is thought that smaller dopant concentrations lead to higher conductivity because of fewer mismatches in ionic radii between the host and dopant cations. Hence, higher ionic conductivity is expected by double doping because the mismatch in ionic radii can be minimized by lower total dopant concentration.

However, stabilized bismuth oxides go through an order-disorder transition, which is reflected by a change in activation energy, at a temperature in the neighborhood of 600°C.[20-22] Although it is crucial to maximize the ionic conductivity of stabilized bismuth oxides, for practical applications involving isothermal operation in the intermediate temperature range, it is also very important to prevent the degradation of ionic conductivity.

Wachsman et al. shows that the radii and polarizability of the dopant cations affects the conductivity and stability of the disordered oxygen sublattice.[13] In order to better understand how different dopants affect conductivity and stability, a systematic study of bismuth oxides which were stabilized with different rare earth oxides, RE_2O_3 (RE = La, Nd, Sm, Gd, Dy, Ho, Er, Tm, or Yb) as well as Y_2O_3 were carried out. Most samples were synthesized with the same composition of 25 mol% dopant, e.g., $(RE_2O_3)_{0.25}(Bi_2O_3)_{0.75}$. Based on his result, cubic structure was obtained with Dy_2O_3, Ho_2O_3, Y_2O_3, Er_2O_3, Tm_2O_3 and Yb_2O_3. However, larger-radii rare-earth dopants (La^{3+} through Gd^{3+}) resulted in formation of the rhombohedral phase with 25 mol% amount. In order to examine the effect of different dopants on the aging process, cubic stabilized bismuth oxides with six different dopants were investigated. The stability for the disordered anion sublattice was enhanced as dopant radii and polarizability increased within the fcc phase-stability window. Due to its large radii and high polarizability, Dy provided the greatest stability for the disordered anion lattice and allowed the least conductivity decay.[13] Further, the highly polarizable cations within the immobile cation sublattice can deform to allow diffusing ions to 'squeeze' through small gaps. Thus, highly polarizable cations can be incorporated as dopants into bismuth oxide to enhance conductivity.

In this work, Dy and W were chosen as dopants among the potential dopants to stabilize the fluorite structure of Bi_2O_3. It is expected that W also enhance ionic conductivity and provide better stability for the disordered anion lattice as a second dopant.[23] The ordering rate was found to be a function of dopant size, concentration and polarizability. Consequently, understanding both effects (i.e., dopant-host radius and polarizability mismatches) is crucial to the development of highly conductive bismuth oxide based electrolytes for low (<600°C) temperature SOFCs. Considering these facts, Dy_2O_3 and WO_3, which has highly polarizable dopant cation, will be incorporated into bismuth oxide to achieve a structurally stable electrolyte with high conductivity. The results of this study will allow the mapping of conductivity, dopant concentration, and order-disorder transition temperature so that a specific dopant concentration can be chosen to obtain a desired conductivity at a given operating temperature.

For a long time, $(ErO_{1.5})_{0.2}(BiO_{1.5})_{0.8}$ (20ESB) was considered in the literature to have the highest conductivity among the stabilized δ-Bi_2O_3.[20] However, in our previous work,[11] bismuth oxide electrolytes doubly doped with Dy_2O_3 and WO_3 (DWSB) were found to have even higher conductivity. The effect of double doping on conductivity behavior is still not well understood. It is therefore necessary to optimize the total dopant concentration as well as the dopant ratio to obtain the highest achievable conductivity for this particular dopant system.

Optimization of Acceptor-Doped Ceria

In the last few decades, ceria based electrolytes have gained much attention as an alternative of YSZ in SOFCs. As seen in Figure 1, ionic conductivity of gadolinium-doped ceria is about one order of magnitude higher than that of YSZ. In addition, they exhibit good thermal stability which makes them superior to yttria-stabilized Bi_2O_3.

In these fluorite oxides, the incorporation of aliovalent cation dopants (usually, divalent or trivalent) results in the formation of oxygen vacancies. For example in the case of trivalent dopant cation (D_2O_3), the mass-action reaction equation can be seen as

$$D_2O_3 \xrightarrow{\quad 2AO_2 \quad} 2D'_A + 3O^\times_O + V^{\bullet\bullet}_O \qquad [1]$$
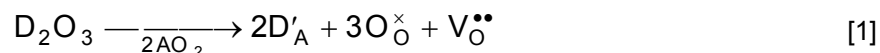
It follows that an increase in the doping concentration leads to an increase in the concentration of oxygen vacancies. In addition, since th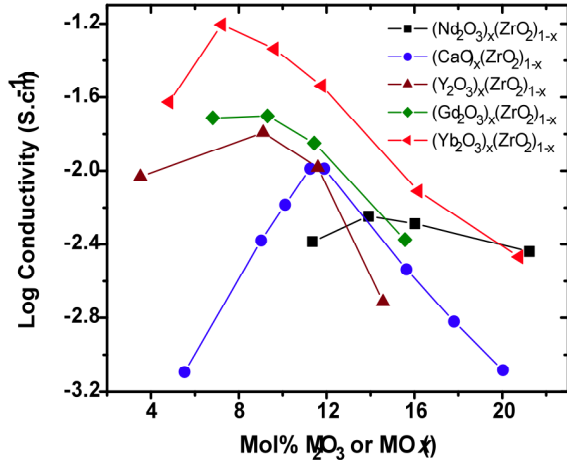e ionic conductivity in these materials is primarily dependent on the concentration of oxygen vacancies, an increase in ionic conductivity is expected. However, it reaches maximum and then decreases beyond certain dopant concentration. This is the general behavior observed in all the oxide systems (Figure 3). The observed peak positions are not the same for the host material with different dopants. It has been argued that the observed decrease in conductivity in the higher dopant content regime is due to the interactions between oxygen vacancies and dopant cations. Such interactions can be attributed to the electrostatic attraction between the two oppositely-charged defects. Also involved is the elastic interaction that relieves the local stresses associated with both defects. Thus, the binding energy of the defects depends primarily on the electrostatic and elastic interactions between the defects.

Figure 3. Variation of ionic conductivity of stabilized ZrO_2 as a function of dopant concentration at $807^{\circ}C$.[24]

These interactions lead to the formation of local defect structures such as $\left(D_A' - V_O^{\bullet\bullet} - D_A'\right)$ and $\left(D_A' - V_O^{\bullet\bullet}\right)^{\bullet}$ which effectively reduce the number of mobile oxygen ions, thus leading to a decrease in the ionic conductivity of the electrolyte. Thus, in order to design an electrolyte that shows improved conductivity among doped ceria electrolytes, it is imperative to understand the interactions between the dopant cations and oxygen vacancies in the crystal lattice at intermediate temperatures.

According to the theory of electrical conduction, diffusion of oxygen ions within the fluorite structure can be seen as a thermally activated process with a characteristic activation energy barrier.[25] The ionic conductivity dependence on the temperature can be expressed by the following empirical equation:

$$\sigma T = \sigma_o \exp\left(-\Delta H / kT\right) \qquad [2]$$

where T is the absolute temperature, σ_o is the pre-exponential factor, ΔH is the activation enthalpy, and k is the Boltzmann's constant. At intermediate temperatures, E_A consists of migration enthalpy (ΔH_m) of the oxygen ion, and the association enthalpy (ΔH_a) of the local defect structures. From previous research it has been found that in the dilute regime, ΔH_m is independent of dopant concentration. Thus, to enhance the grain ionic conductivity, the minimization of the association of defects is required.

In addition, σ_o can be written as:

$$\sigma_o = 4e^2 k^{-1} a^2 \nu_o N_o \exp\left(\frac{\Delta S_a + \Delta S_m}{k}\right) \qquad [3]$$

where e is the electronic charge, a is the oxygen vacancy jump distance, ν_o is an appropriate lattice vibration frequency, ΔS_m is the activation entropy of diffusion, and ΔS_a is the activation

entropy of association.[26] Since ΔS_m is considered to be constant when the host lattice is determined, thus maximization of ΔS_a lead to the increase in σ_o, which consequently increases the ionic conductivity.

As mentioned before, the association energy (ΔH_a) is a function of the Coulombic attraction between oxygen vacancies and dopant cations and the elastic strain field around the defect complex. Kim studied the effect of ionic radius and valence of the dopant cation on the ionic conductivity of the ceria solid solution.[27] Empirical equations were derived for the lattice parameters of fluorite-related oxides doped with aliovalent cations considering the charge effect as well as the difference of ionic radius between the host and dopant ions. In order to better understand the relationship between the association enthalpy and dopant ionic radius, a critical ionic radius, r_c, was proposed. The r_c was defined as the ionic radius of the dopant that neither causes expansion nor contraction of the fluorite lattice. For trivalent dopant cation in host ceria, r_c was calculated to be 0.1038 nm.[27] This value is very close to the ionic radius of the dopant corresponding to the maximum electrical conductivity as shown in Figure 4. To further enhance the grain ionic conductivity, a co-doping scheme provides an experimental scenario for testing this hypothesis. Using co-dopants in the host ceria also increases the randomness in the system, and suppresses the ordering of the defects. This consequently enhanced the association configuration entropy of the system and thereby increases the pre-exponential factor, which is critical for the improvement of the grain ionic conductivity.

Based on the critical dopant ionic radius concept, experiments were conducted using Lu^{3+} and Nd^{3+} as trivalent co-dopants, taking into consideration their ionic radius. They are added in a proportion such that the weighted average dopant ionic radius matches r_c. For example if x_A and x_B are the proportion of A and B co-dopants, then they must satisfy the following equation:

$$x_A r_A + x_B r_B = (x_A + x_B) r_c \qquad [4]$$

where r_A and r_B are the ionic radius of trivalent dopant A and B with VIII coordination. By doing so, it was expected that the positive elastic strain due to larger dopant cation can be compensated by the negative elastic strain due to smaller dopant cation. This in turn prevents any distortion in fluorite lattice, which is usually present in singly doped ceria systems. Polycrystalline samples of $Lu_x Nd_y Ce_{1-x-y} O_{2-\delta}$ (where $x+y$ = 0.05, 0.10, 0.15, and 0.20) were prepared by conventional solid oxide reaction from a stoichiometric mixture of Lu_2O_3, Nd_2O_3, and CeO_2 powders. The ratio of the amount of co-dopants (x/y) to be added was calculated using equation [4] and was found to be 1.16. Details about the experimentations can be found in the experimental section of this work.

As we compare our grain ionic conductivity of $Gd_{0.10}Ce_{0.90}O_{2-\delta}$ with literature, it was observed that it varies with the processing techniques used to synthesize the powder. Figure 5 shows the comparison of grain ionic conductivity of $Gd_{0.10}Ce_{0.90}O_{2-\delta}$ taken after different sources. Figure 5 shows the grain ionic conductivity comparison of our processed singly doped ceria with that from literature. It can be seen that our grain ionic conductivity data for $Gd_x Ce_{1-x} O_{2-\delta}$ is lower than the literature. Similar is the case with $Sm_x Ce_{1-x} O_{2-\delta}$. However, our grain ionic conductivity data for $Nd_x Ce_{1-x} O_{2-\delta}$ is quite higher than that from literature. The main cause for this mismatch is may be due to the segregation of dopant cations near the grain boundaries. In addition, microstructure might also affect the grain ionic conductivity of the electrolyte.

Upon examination of the experimental procedure followed in each reported investigation, a strong correlation between the processing conditions and the conductivity is observed. It can be inferred that besides composition, processing related variables such as grain size distribution, dopant redistribution within the grain, grain impurities, and extended grain defects can greatly affect the grain ionic conductivity of the electrolytes. Thus, in order to understand the separate effect of grain microstructure on the observed conductivity, a detailed investigation on the $Gd_{0.10}Ce_{0.90}O_{2-\delta}$ microstructure was performed.
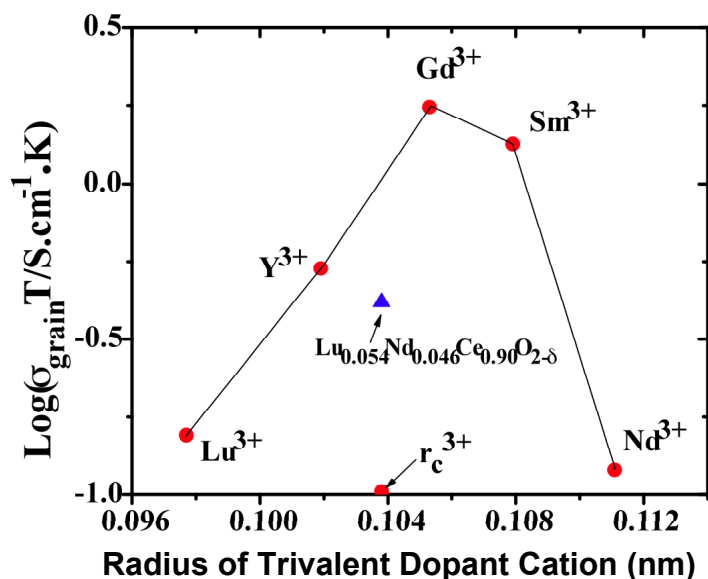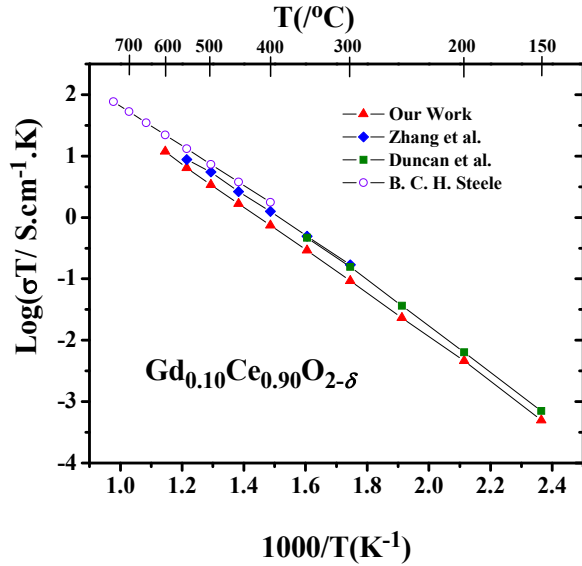

Figure 4. Bulk ionic conductivity of doped ceria at 400°C as a function of dopant cation ionic radius, r_c^{3+} shown in the figure is critical radius of the trivalent cation. Bulk ionic conductivity data of $Y_{0.10}Ce_{0.90}O_{2-\delta}$ and $Nd_{0.10}Ce_{0.90}O_{2-\delta}$ were taken after Zhang et al.[28] and Li et al.[29] respectively. Bulk ionic conductivity data of $Gd_{0.10}Ce_{0.90}O_{2-\delta}$ and $Lu_{0.10}Ce_{0.90}O_{2-\delta}$ are our work. Ionic radii data is taken Shannon.[30]

In addition to the microstructural optimization, a co-doping strategy based on average atomic number was used to investigate the effect on the grain ionic conductivity. Recent density function theory (DFT) work by Andersson et al. has shown that the total interaction energy values for the oxygen vacancy sitting in first nearest neighbor site and the next to nearest neighbor (NNN) site for Pm^{3+} dopant are almost the same (Figure 6).[17] Based on interaction energy values determined between the oxygen vacancy and different dopant ions, it was suggested that for Pm^{3+}, and for ions to the right of the Pm^{3+} in the lanthanide series, oxygen vacancy interacts strongly with the dopant cation when it occupies NN position of the dopant cation. Moreover, cations with an atomic number less than the Pm^{3+} in the lanthanide series usually hold oxygen vacancies in the NNN position of the dopant cation. Thus, around Pm^{3+} there a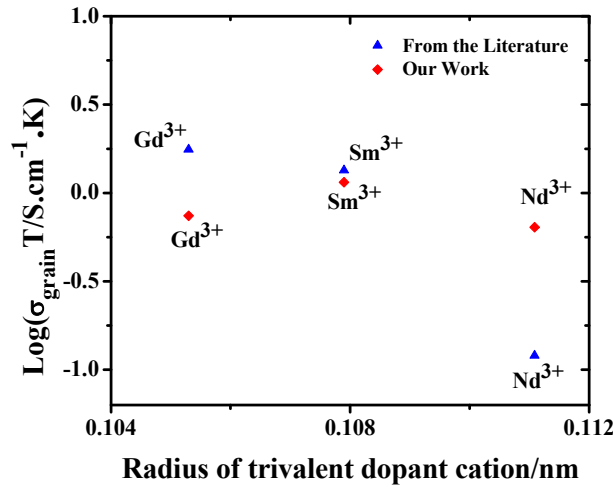re no site preferences for oxygen vacancies, which consequently increases the number of equi-interaction energy oxygen sites in the fluorite crystal lattice through which oxygen vacancies can diffuse. Therefore, oxygen diffusion in Pm^{3+} doped ceria is more relaxed in comparison to other doped ceria materials. However, Pm is radioactive and cannot be used for electrolyte applications.

Figure 5. Comparison of grain ionic conductivity of (a) our $Gd_{0.10}Ce_{0.90}O_{2-\delta}$ with that from Steele[31], Zhang et al.[28] and Duncan et al.[32] (b) our singly doped ceria, at 400°C with data for $Gd_{0.10}Ce_{0.90}O_{2-\delta}$, $Sm_{0.10}Ce_{0.90}O_{2-\delta}$ and $Nd_{0.10}Ce_{0.90}O_{2-\delta}$ taken from Steele[31], Zhan et al.[33] and Li et al.[29], respectively.

The ideal dopant should have an effective atomic number around Pm^{3+} (61) which shows ionic radius of 1.093 Å[13]. Thus, as suggested by Andersson et al., a co-dopant scheme, using Sm^{3+} and Nd^{3+}, may be useful way of testing this hypothesis. In terms of ionic radii such co-doping can be seen as having an effective dopant ionic radius of 1.094 Å (which is close to Pm^{3+} ionic radius of 1.093 Å).[30]

Based on the effective atomic number concept, in this work the effect of co-dopant pair Sm^{3+} and Nd^{3+} on the grain ionic conductivity of ceria-based electrolytes was also investigated. Both dopants were added to host ceria in a proportion such that the weighted average of the dopant atomic number matches that of Pm. Phase-pure powders of $Sm_xNd_xCe_{1-2x}O_{2-\delta}$ (where $2x = 0.01 - 0.20$) were prepared using conventional solid state synthesis.
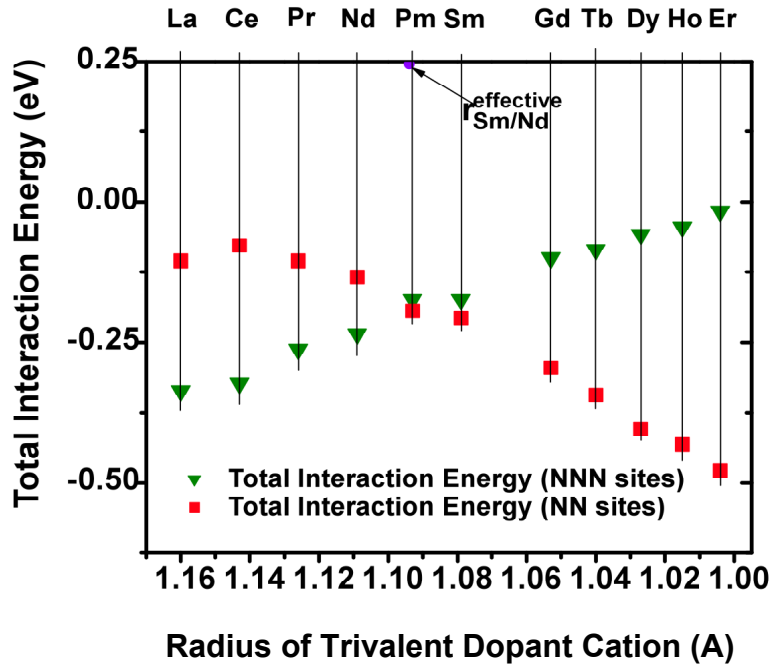
Figure 6. Total interaction energy for different trivalent dopant cation with oxygen vacancy for nearest neighbor oxygen vacancy configuration and next to nearest neighbor oxygen vacancy configuration (modified after Andersson et al.).[34]

Computational Modeling

Experimental

In the MD simulations, to describe the inter-atomic interactions, we adopted the empirical potential function of Jacobs and Macdonaill[5] in which interactions are described by:

$$V(r) = \frac{Z_1 Z_2 e^2}{r} + A\,\mathbf{exp}(-r/\rho) + B\,\mathbf{exp}(-r/\sigma) - C/r^6 \qquad (1)$$

The first term in the potential describes the Coulombic interactions; r is the distance between two ions of charges Z_1 and Z_2, respectively. The second and third terms are short ranged repulsive interaction, parameterized by A, B, ρ, σ. The last term is the attractive van der Waals interaction characterized by C. The parameters A, B, ρ, σ and C were fitted to experimental values of pertinent physical properties, including the lattice parameter, high frequency dielectric constant for α and γ phases, and the cohesive energies. The polarizability of the ions was accounted for via the shell model.[35]

In the DFT calculations, we used the GGA exchange-correlation functional in PW91 form.[36] The projector augmented wave method (PAW)[37] was applied to the core electrons (Bi [Xe]$4f^{14}5d^{10}$), O[He]). A plane wave cutoff of 500eV was used with a k-points grid of 6*6*6 for 1x1x1 systems and 3*3*3 k-points grid for 2x2x2 systems. The positions of the atoms were optimized such that the force on each atom had converged to less than 0.0005 eV/Å. Periodic boundary conditions were applied in all the three directions. The system was allowed to relax until the forces and the volume had equilibrated.

Results and Discussion

Oxygen diffusion is temperature dependent

To lay the basic foundation that diffusion is a temperature dependent process and as a check to our simulations, we performed MD simulations of pure δ-Bi$_2$O$_3$ at a series of increasing temperatures. Figure 7 shows the mean square displacement (MSD) of oxygen ions at different temperatures. It is clear that our potential and simulations replicate the basic phenomenon that the MSD, which is proportional to the oxygen diffusion constant, increases with temperature.
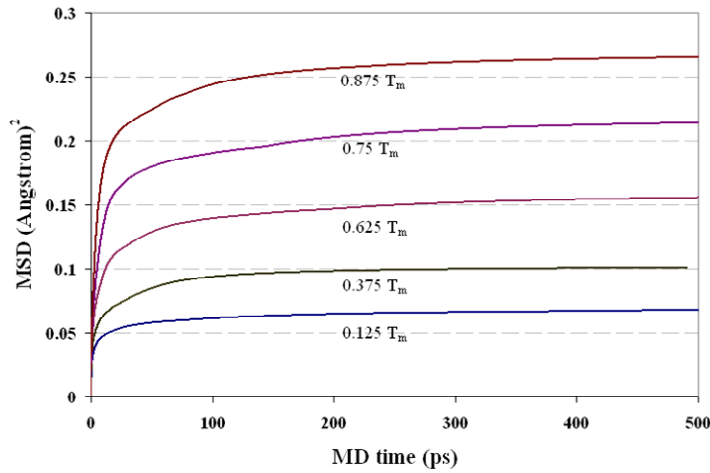

Figure 7. Oxygen MSD as a function of temperature: oxygen diffusion increases with temperature.

Polarizable and non-polarizable δ-Bi$_2$O$_3$

As mentioned above, the polarizability of Bi and O ions in δ-Bi$_2$O$_3$ was treated as a simulation variable. In the MD simulations, the shell model [10] was used to distinguish non-polarizable from polarizable ions. Atomic polarizability is captured in the shell model, in which the atom is described as a heavy core and a mass-less shell of charge, Y, attached to the core by a spring of force constant, k. The electronic polarizability of an ion, $\langle$, is given by $\langle = Y^2/k$.

Using these two models, we have found that the oxygen diffusion varies considerably. Figure 8 shows the oxygen MSD of non-polarizable and polarizable δ-Bi$_2$O$_3$. For simulations using non-polarizable ions there is essentially no oxygen diffusion; by contrast when the ions are polarizable, there is considerable oxygen diffusion. We analyzed this difference and found that, non-polarizable ion, a configuration of vacancies is set up in the material that prohibits further oxygen diffusion.
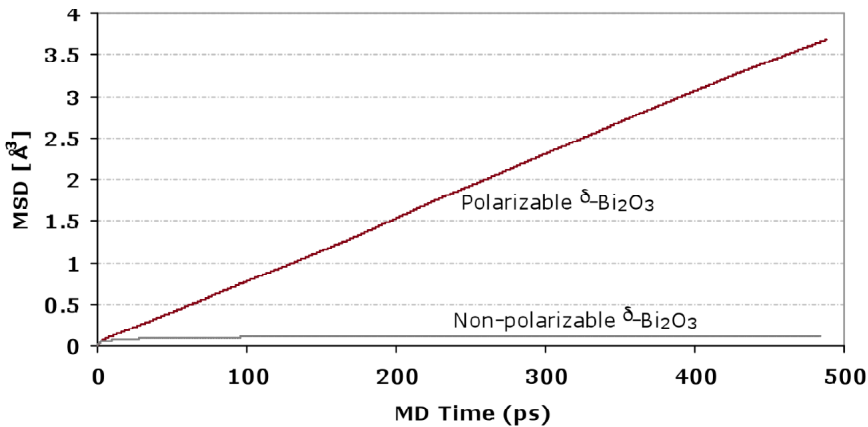

Figure 8. MSD of oxygen in polarizable and non-polarizable δ-Bi$_2$O$_3$. A constant increase in MSD is observed for diffusion in polarizable δ-Bi$_2$O$_3$ compared to non-polarizable δ-Bi$_2$O$_3$, where diffusion stops eventually and the structure locks down by combined vacancy ordering in <110> and <111> directions.

As a result the system diffusion gets locked down into a fixed structure. We call this the "equilibrated" non-polarizable δ-Bi_2O_3 system. To develop a highly conducting system, it is very important to understand this locked structure (equilibrated non-polarizable δ-Bi_2O_3 structure) from the atomic viewpoint. Therefore, a complete analysis of the ordering mechanism of vacancies was performed.
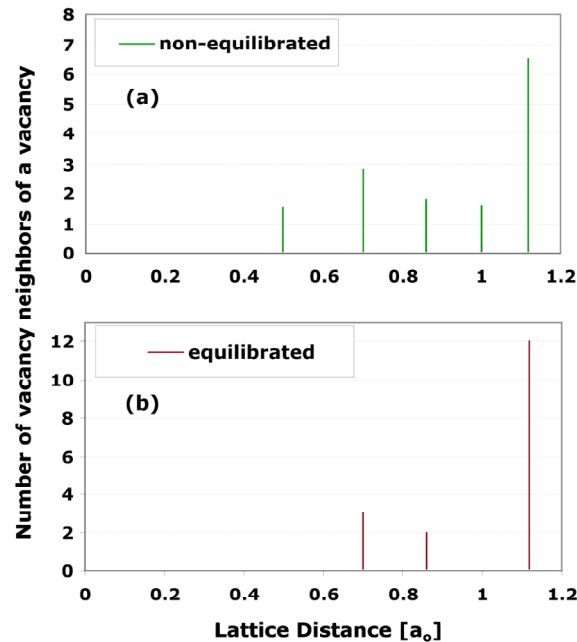

Figure 9. Pair distribution function for vacancy neighbors in Bi_2O_3: (a) non-equilibrated and (b) equilibrated. In the non-equilibrated structure, the vacancy neighbors are at first, second, third, etc. distances in accord with the expectation for randomly distributed vacancies. In the equilibrated structure there are no vacancy-vacancy first **nearest** neighbors, consistent with <110><111> vacancy ordering.
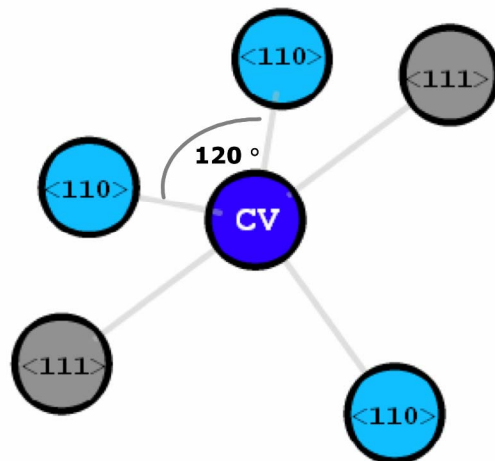

Figure 10. A central vacancy (CV, dark blue) is surrounded by three vacancies in <110> directions (light blue) and two vacancies along <111) directions (gray).

Ordering of the Vacancies

To understand the ordering of the vacancies, we concentrated on the vacancy-vacancy neighbors. Before starting the simulation, the vacancies were randomly distributed throughout the system. The system was then allowed to equilibrate for a long enough time to allow significant oxygen diffusion. After the simulation, the system was then quenched to remove the signature of any thermal vibration. This final system was then used to analyze the structure. A vacancy-vacancy PDF of the non-equilibrated (initial) and equilibrated (final) structure is shown in Figure 9. Figure 9a shows the average number of vacancies around each vacancy as a function of distance. In contrast to the non-equilibrated PDF, the equilibrated PDF has some peaks missing. Particularly, at a distance of $0.5a_o$, which corresponds to a first nearest neighbor in the oxygen cubic sub-lattice, no vacancy has a vacancy neighbor. This shows that no two vacancies like to sit together at $0.5\ a_o$ (<100>) direction. Similarly, the peak is absent at $1.0\ a_o$. However, there are peaks at $0.7a_o$ and $0.86a_o$, which correspond to second (<110>) and third (<111>) nearest neighbors respectively. This configuration of the vacancies is the same for every vacancy throughout the structure. This pattern is shown on Figure 10; every vacancy has three second nearest vacancy neighbors (shown in light blue color) in three different (110) planes and two <111> vacancies (shown in grey color) directed in opposite directions. From our MD simulations, we determined that it is the combined ordering of the vacancies in <110> and <111> directions that gives the final ordered structure.

To confirm that this vacancy ordering is indeed the lowest energy structure, we have performed different DFT calculations on 2x2x2 super-structure with vacancy ordering in <100>, <110>, <111> and a combined ordered structure as mentioned observed, i.e., vacancy ordering in <110> and <111> directions. Table I shows the relative energies of the four different structures. As expected, DFT also predicted the combined ordered <110> and <111> structure as the minimum energy structure. This structure is consistent with that determined previously by the neutron scattering experiment.[38]

To understand the bonding in this structure, we have examined the electron density in the structure. The electron density contour maps for the individually ordered structures in <100>, <110> and <111> were found to be consistent with the Walsh et al. [4] In particular, when the cube containing an octahedral bismuth is contains either <100> or <110> ordering, the Bi electron lone-pair charge is directed towards the vacancies. By contrast, for the case of <111>, the electron distribution is found to be evenly distributed. The distribution of the electron lone-pair charge in the combined vacancy ordered structure, i.e., <110> and <111> maintains the same charge distribution as observed in the individual vacancy ordered structures. However, in the combined vacancy-ordered structure, there are two different environments around the Bi atoms, i.e., some Bi atoms are surrounded by <110> ordering and some by <111>; there are thus two different kinds of the Bi atoms, which result in two different electron lone-pair charge distributions. The presence of either of the two different charge distributions does not affect the other. The two different electron lone-pair charge distributions around Bi are shown in Figure 11. The charge distribution is represented in two (110) planes perpendicular to each other (for clarity, the planes in the oxygen sub-lattice are also shown). (110) planes in the Bi centered <111> ordered oxygen sub-lattice are shown in Figures 11a and 11b. Due to the symmetric ordering of vacancies in this cubic sub-lattice, the electron lone-pair charge is equally distributed to form the Bi-O bonds of equal length.

Table I. Relative stability of the ordered structures
in 2x2x2 system confirming that the <110>, <111>
vacancy structure is indeed the lowest in energy

Ordering	Relative Energy (eV/Bi)
<100>	0.000
<110>	0.066
<111>	0.542
<110> <111>	-0.225
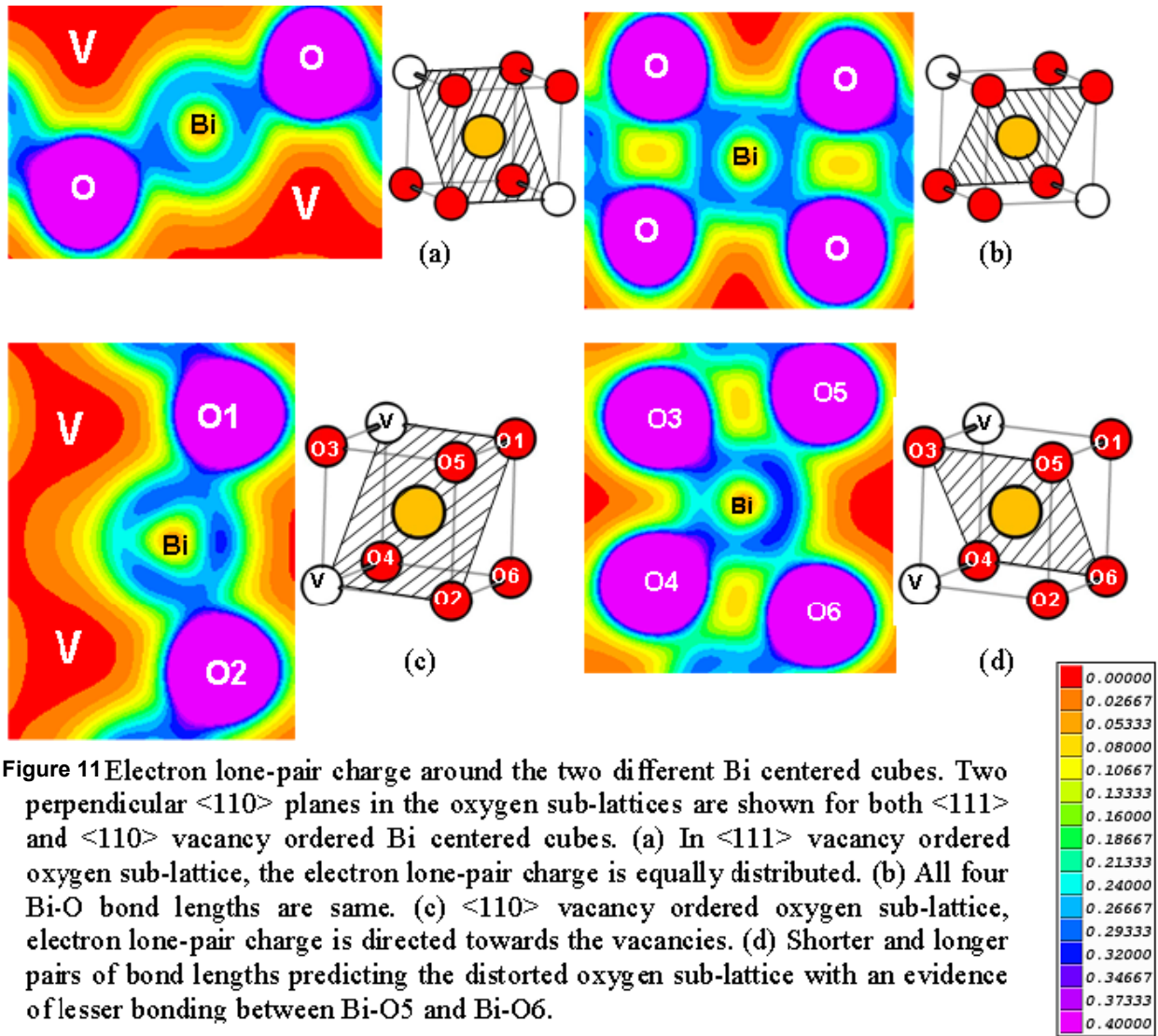
Figure 11 Electron lone-pair charge around the two different Bi centered cubes. Two perpendicular <110> planes in the oxygen sub-lattices are shown for both <111> and <110> vacancy ordered Bi centered cubes. (a) In <111> vacancy ordered oxygen sub-lattice, the electron lone-pair charge is equally distributed. (b) All four Bi-O bond lengths are same. (c) <110> vacancy ordered oxygen sub-lattice, electron lone-pair charge is directed towards the vacancies. (d) Shorter and longer pairs of bond lengths predicting the distorted oxygen sub-lattice with an evidence of lesser bonding between Bi-O5 and Bi-O6.

In contrast, the Bi centered <110> ordered oxygen sub-lattice has different bond lengths which occur in pairs. The two perpendicular (110) planes for <110> ordered sub-lattice are shown in Figures 11c and 11d. The plane containing the two vacancies here (in Figure 11c) has the Bi-O bond length same as in the <111> ordered oxygen sub-lattice. However, in the perpendicular plane, two of the Bi-O bonds are shorter and two are longer, thus showing the distorted Bi centered <110> oxygen sub-lattice. As expected, there is a directional distribution of the electron lone-pair charge towards the vacancies. In this distorted sub-lattice, there is further an evidence of weaker bonding between the Bi-O5 and Bi-O6.

Tetrahedron Expansion and Contraction

There are numerous ways in which the structure of δ-Bi_2O_3 can be visualized. It is particularly instructive to consider the tetrahedra formed by four bismuth atoms, in the interior of which is either an oxygen atom or the vacancy. Every Bi atom forms eight tetrahedra, six of which have oxygen atoms inside them, two have vacancies inside them. The Bi-Bi interatomic distances depend on whether an oxygen atom or a vacancy is present inside the tetrahedron. Figure 12 shows the non-equilibrated and equilibrated Bi-Bi PDF. In the non-equilibrated structure PDF, every bismuth atom has twelve first nearest Bi neighbors shown by the first peak. However, in the equilibrated structure PDF, we observed that the peak gets equally divided into two smaller peaks. These two different Bi-Bi separations correspond to a lattice distance of $0.67a_o$ and $0.76a_o$.
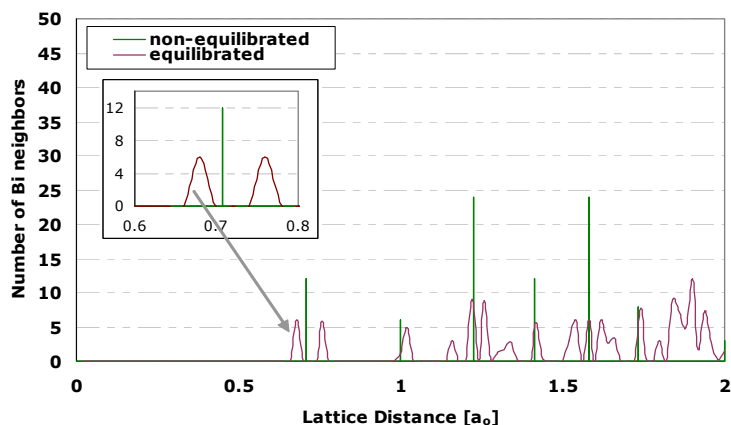

Figure 12. Bi-Bi pair distribution function. In the non-equilibrated structure (green) the Bi ions form a perfect fcc lattice. In the equilibrated structure (purple) the sharp fcc peaks are split. In particular, in the non-equilibrated structure all 12 Bi neighbors of a Bi atom lie at the fcc distance of 0.707 lattice parameters. In the equilibrated structure, this peak is split into 6 long Bi-Bi bonds and 6 short Bi-Bi bonds.

To understand this variation, we analyzed the vacancy effect and found that if an oxygen atom is present inside the tetrahedron (Figure 13a) then four out of the six Bi-Bi inter-atomic distances became shorter and two became longer. On the other hand, if a vacancy is present (Figure 13b), all the six Bi-Bi inter-atomic distances became long. When an oxygen atom and the vacancy are neighbors, the two tetrahedrons share a longer Bi-Bi distance between them (Figure 13c). The two distinct Bi-Bi inter-atomic distances arise purely from the Columbic interactions. The two long Bi-Bi distances in oxygen centered tetrahedron are from the two adjacent tetrahedrons where the vacancies are present.
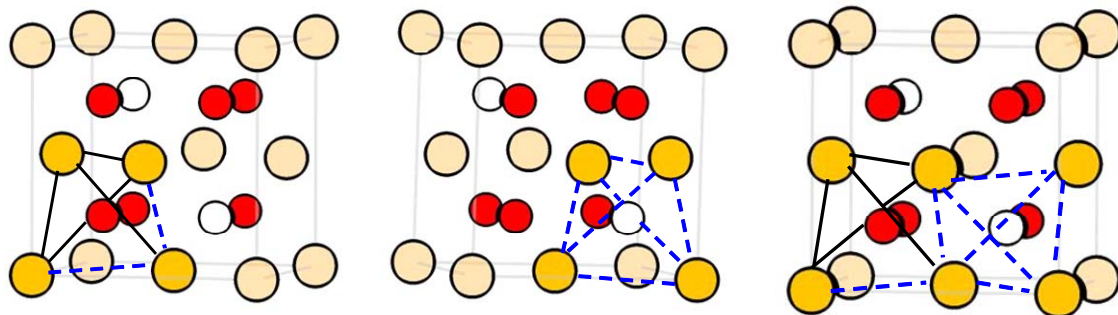
Figure 13. Tetrahedron expansion and contraction due to a vacancy and an oxygen atom respectively: (a) Oxygen present inside the tetrahedron, the oxygen-tetrahedron has four short and two long Bi-Bi interatomic distances; (b) Vacancy inside the tetrahedron, the vacancy-tetrahedron has six long Bi-Bi interatomic distances; (c) A vacancy tetrahedron juxtaposed with an oxygen tetrahedron share a long Bi-Bi inter-atomic distance. (To highlight the tetrahedron, the rest of the Bi atoms are lightened in color)

Oxygen Diffusion Migration

We have carried out the MD simulations to identify the oxygen diffusion mechanism in δ-Bi_2O_3. We have performed the simulations on non-polarizable δ-Bi_2O_3, the diffusion mechanism simulations on polarizable δ-Bi_2O_3 are still underway. In the non-polarizable δ-Bi_2O_3 we have found that the oxygen diffuses in the <100> direction (see Figure 14). Two diffusing oxygen atoms are shown in Figure 14.
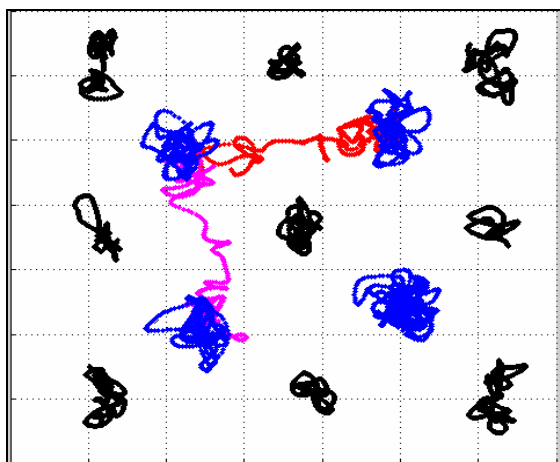
Figure 14. Oxygen diffusion mechanism: two oxygen diffusion instances (in pink and red) occur in the <100> direction in a unit cell. The blue and black colors show vibrations of non-diffusing oxygen atoms and the Bi atoms, respectively.

Effect of Electronic Polarizability

As mentioned earlier, the oxygen conductivity increases when the atoms are made polarizable. This is physically reasonable, since the electric field polarizes the atoms and makes the oxygen diffusion easier. However, it is important to understand the polarizable effect of both the cation and anion individually. We have observed that oxygen polarizability is not necessary for high conduction. On the other hand, a gradual increase in oxygen conductivity occurs with the increase in the bismuth polarizability (see Figure 15), showing that the Bi polarizability determines the oxygen diffusivity.

Figure 15. Oxygen MSD for varying bismuth polarizability. A gradual increase in oxygen MSD occurs with greater Bi polarizability.

Development of Stable, High Conductivity Bismuth Oxide Electrolytes
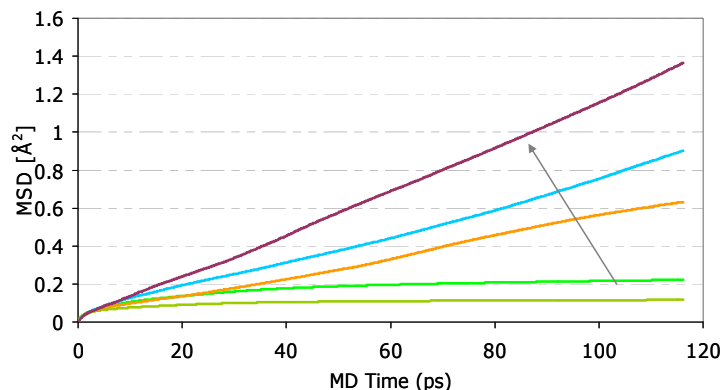
Experimental

Sample Preparation

Disks of $(DyO_{1.5})_x$-$(WO_3)_y$-$(BiO_{1.5})_{1-x-y}$ composition were fabricated by solid state synthesis. Disks of $(ErO_{1.5})_{0.2}(BiO_{1.5})_{0.8}$, 20ESB, were also prepared for comparison of conductivity results. Based on previous results,[11] the effect of double doping on conductivity is "non-ideal." First, six different compositions were investigated; $(DyO_{1.5})_{0.15-x}(WO_3)_x(BiO_{1.5})_{0.85}$ (where x=0.05, 0.075, 0.10), $(DyO_{1.5})_{0.10-x}(WO_3)_x(BiO_{1.5})_{0.90,}$ (where x=0.03, 0.05, 0.07). The former three compositions, with a fixed 15 mol% total dopant concentrations, are 10D5WSB, 7.5D7.5WSB and 5D10WSB. The latter three compositions, with a fixed 10 mol% total dopant concentrations, are 7D3WSB, 5D5WSB and 3D7WSB. Subsequently, various compositions with 2:1 dopant ratio between Dy and W (8D4WSB, 9D4.5WSB, 10D5WSB, 11D5.5WSB, 12D6WSB and 14D7WSB) were also prepared in order to optimize composition with respect to ionic conductivity.

In addition, three DWSB compositions of the preferred (highest conductivity) 2:1 ratio were selected to further investigate the long term stability of DWSB compositions, namely: 8D4WSB, 10D5WSB and 12D6WSB.

A stoichiometric mixture of Bi_2O_3 (99.9995% pure), Dy_2O_3 (99.99% pure) and WO_3 (99.8% pure), from Alfa Aesar, were mixed and ball-milled with zirconia ball media in a high-density polyethylene bottle for 24 hours. After drying, the mixed powders were calcined at 800°C for 16 hours. Agglomerated powders were ground using mortar and pestle and sieved to get uniform particle sizes. The powders were pressed uniaxially into a disk-shaped 0.8 cm diameter die using 1500 lb to get disk-shaped pellets, and pressed again to increase the density of electrolyte through cold isostatic pressing at 200 MPa. The pellets were subsequently sintered in air at 890°C for 16 hours. The lattice structure of the calcined powders was identified by means of X-ray diffraction analysis using CuK_α radiation.

After sintering, the specimens were polished to acquire an even surface and the desired thickness (3 mm). Engelhard gold paste mixed with isopropanol was brushed onto both sides of the electrolytes and the organic additives were evaporated at 120°C for 1 hour. Subsequently, the electrodes were sintered at 800°C for 1 hour. Pt(or Ag) wires with circular Ag mesh were attached to the cells by mechanical contact.

Conductivity Measurement

Conductivity measurements were obtained by electrochemical impedance spectroscopy (EIS) using a Solartron 1260 over the frequency range of 0.1 Hz to 10 MHz. The frequency response analyzer was used in standalone mode for unbiased testing and interfaced to a computer using Zplot software. Due to the small sample impedances at high temperature, a nulling technique was necessary to remove any artifacts caused by inductive responses of the test leads and the equipment. The impedance of the leads without a sample was obtained and subtracted from the sample (plus lead) measurements. The measurements were performed between 200°C and 700°C in air atmosphere. Activation energies were calculated from Arrhenius conductivity plots.

Results and Discussion

Optimization of doubly doped Bi$_2$O$_3$ electrolytes with higher conductivity
First, various compositions with different dopant ratio between Dy and W were investigated. Dopant content ratio of 2:1, 1:1, 1:2 were conducted. Figure 16a shows XRD patterns of various DWSB compositions with the same 15 mol% total dopant concentration. 10D5WSB and 7.5D7.5WSB had a single phase, while 5D10WSB had mixed phase. In addition, 7D3WSB had a single phase among DWSB compositions with 10 mol% total dopant concentration. From a viewpoint of solid solution range, WO$_3$ doped Bi$_2$O$_3$ system had narrow range of fcc phase compared with Dy$_2$O$_3$ doped Bi$_2$O$_3$ system.[16,19] Based on this XRD patterns and respective solubility range of dopant, it appears that Bi$_2$O$_3$ has a wider solubility range with Dy$_2$O$_3$ than WO$_3$. In this respect, it is expected that Dy mol content should be much larger than W content in order to obtain a pure fcc phase and consequently higher ionic conductivity.

For this reason, in addition, DWSB electrolytes with the same 2:1 mol dopant ratio between Dy and W were prepared afterwards (6D3WSB, 7D3.5WSB, 8D4WSB, 9D4.5WSB, 10D5WSB, 11D5.5WSB, 12D6WSB and 14D7WSB). The total dopant concentration ranges from 9 mol% up to 21 mol%. Figure 16b shows XRD patterns of these DWSB electrolytes. All compositions were found to be pure fcc phase except for 6D3WSB and 7D3.5WSB. Therefore, 8D4WSB is the composition with the minimum dopant content for stabilizing fcc structure, with a 2:1 dopant ratio. Conductivity measurements were performed on specimens with single fcc phase.
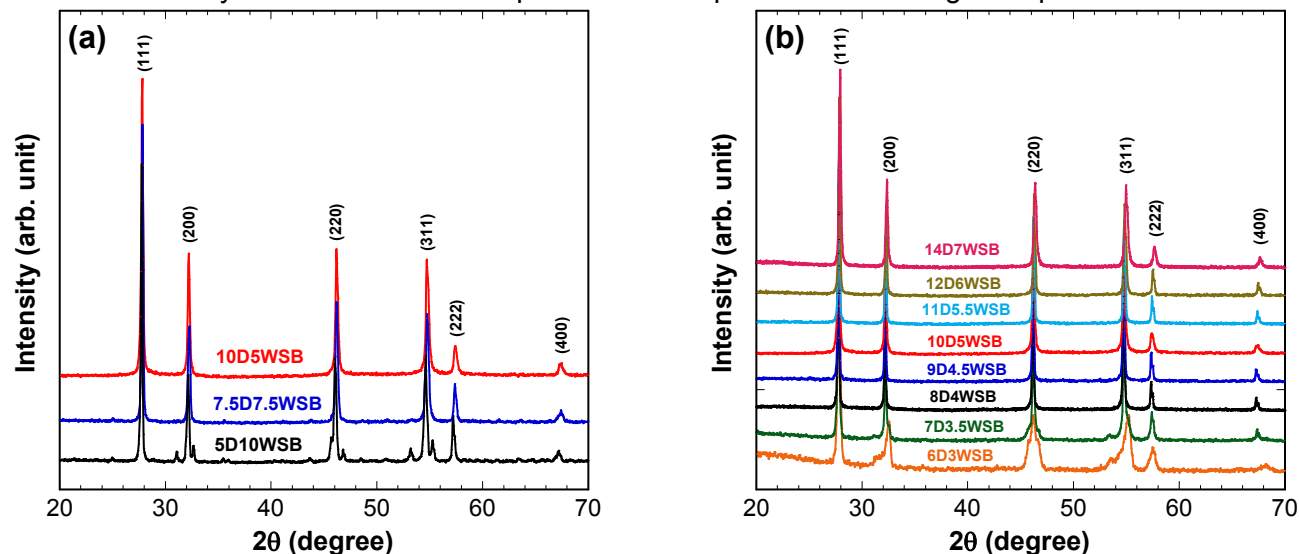

Figure 16. X-ray diffraction patterns of DWSB with (a) fixed 15 mol% total dopant concentration and (b) 2:1 mol dopant ration between Dy and W.

Firstly, the bulk conductivities of three DWSB electrolytes (10D5WSB, 7.5D7.5WSB, and 7D3WSB) were plotted in Figure 17. Among these compositions, 10D5WSB showed higher conductivity. The conductivity of 10D5WSB was 0.487, 0.066 and 2.23×10^{-4} S/cm at 700, 500, and 300°C respectively. Even though 10D5WSB and 7.5D7.5WSB had same total dopant concentrations, the Arrhenius behavior was different. DWSB shows two different conductivity activation energies (Figure 17 and Table 2) with lower activation energies above ~600°C and higher activation energies below ~600°C. This may be attributed to the order-disorder phenomenon, which is a general trend in stabilized bismuth oxide systems.[39,40]
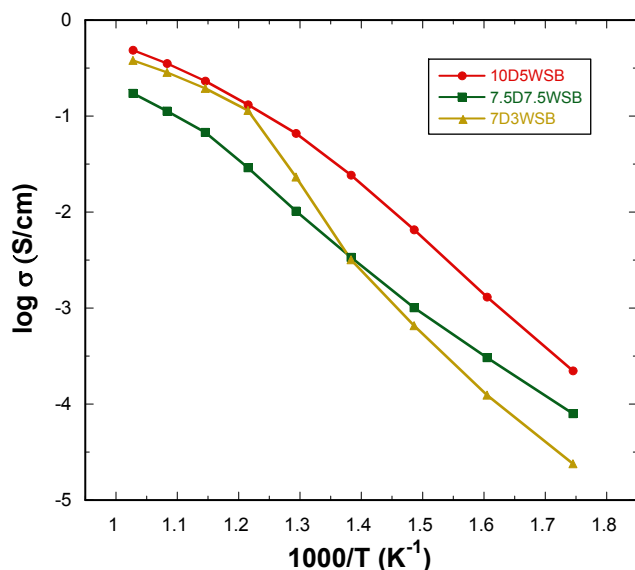

Figure 17. Arrhenius plot of conductivities for 10D5WSB, 7.5D7.5WSB and 7D3WSB.

While 10D5WSB had higher conductivity than 7.5D7.5WSB, the former composition had larger disparity between two activation energies than the latter composition. Therefore, this observation also indicates that dopant ratio plays an important role in obtaining higher ionic conductivity. In addition, an abrupt change in activation energy was observed for the case of 7D3WSB. The disparity between these two activation energies decreases as the total dopant concentration increases.

Secondly, considering the phase stability and solubility limit, bismuth oxide doubly doped with dysprosium (Dy) and tungsten (W) in a 2:1 ratio were investigated. Figure 18a shows the conductivity values of various DWSB compositions with 2:1 mol dopant ratio as a function of total dopant concentration at 500°C. This figure shows a trend wherein the highest conductivity is achieved with the lowest total dopant concentration. In addition, it is obvious that ionic conductivity value increases linearly as total dopant concentration decreases with fixed dopant ratio at this temperature. According to the literature,[16,19] highest conductivity was obtained with the lowest dopant concentration for Bi_2O_3 stabilized by single dopant ($(DyO_{1.5})_{0.285}(BiO_{1.5})_{0.715}$ and $(WO_3)_{0.22}(BiO_{1.5})_{0.78}$). Among DWSB formulations tested in this study, 8D4WSB is the composition with minimum total dopant concentration for stabilizing the fcc δ-Bi_2O_3 phase. The conductivity of $(DyO_{1.5})_{0.285}(BiO_{1.5})_{0.715}$ is 0.0071 S/cm and 0.144 S/cm at 500°C and 700°C, respectively.[16] In addition, the conductivity of $(WO_3)_{0.22}(BiO_{1.5})_{0.78}$ is 0.01 S/cm and 0.062 S/cm at 500°C and 700°C, respectively.[19] Therefore, it is evident that double doping made the reduction of dopant concentration to stabilize the structure and consequently led higher ionic conductivity.

The bulk ionic conductivities of various DWSB electrolytes and 20ESB are plotted as log σ vs. 1000/T in Figure 18b. Conductivity values of these compositions are also compared with 20ESB[20] and YSZ[41] in this Arrhenius plot. It is observed that most DWSB compositions with the same 2:1 dopant ratio have even higher conductivities than 20ESB, GDC and YSZ.[20,41-42] In this work, 20ESB has conductivities of 0.397, 0.027 and 5.78×10^{-5} S/cm at 700°C, 500°C and 300°C, respectively. Verkerk et al. examined the ionic conductivity of 20ESB and showed that 20ESB had an ionic conductivity of 0.37 and 0.023 S/cm at 700°C and 500°C.[20]

This indicates that the conductivity of 20ESB prepared in this work is comparable to literature value. In addition, the conductivity of 10GDC is 0.0095 S/cm and that of 10YSZ is 8.25×10^{-4} S/cm at 500°C.[41] Notably, the conductivities of 8D4WSB, the highest conductivity composition, are 0.569, 0.098, and 2.50×10^{-4} S/cm at 700°C, 500°C, and 300°C respectively. Therefore, the conductivity of 8D4WSB is approximately 4 times higher than that of 20ESB at 500°C and 300°C, and 1.5 times higher than that of 20ESB at 700°C. Significantly, at 500°C, 8D4WSB is 4 times more conductive than 20ESB, 10 times more conductive than 10GDC and 100 times more conductive than 10YSZ.[20,41-42] These results may allow significant reduction in electrolyte operating temperature and make this DWSB composition a very promising SOFC electrolyte for low temperature applications.

Like other stabilized bismuth oxide systems, a change in activation energy for the DWSB compositions was observed. Table 1 shows the values of activation energy measured for low and high temperatures. The temperature dependence of ionic conductivity can be expressed by the following empirical equation:

$$\ln(\sigma T) = \ln A - E_a / kT \qquad [1]$$
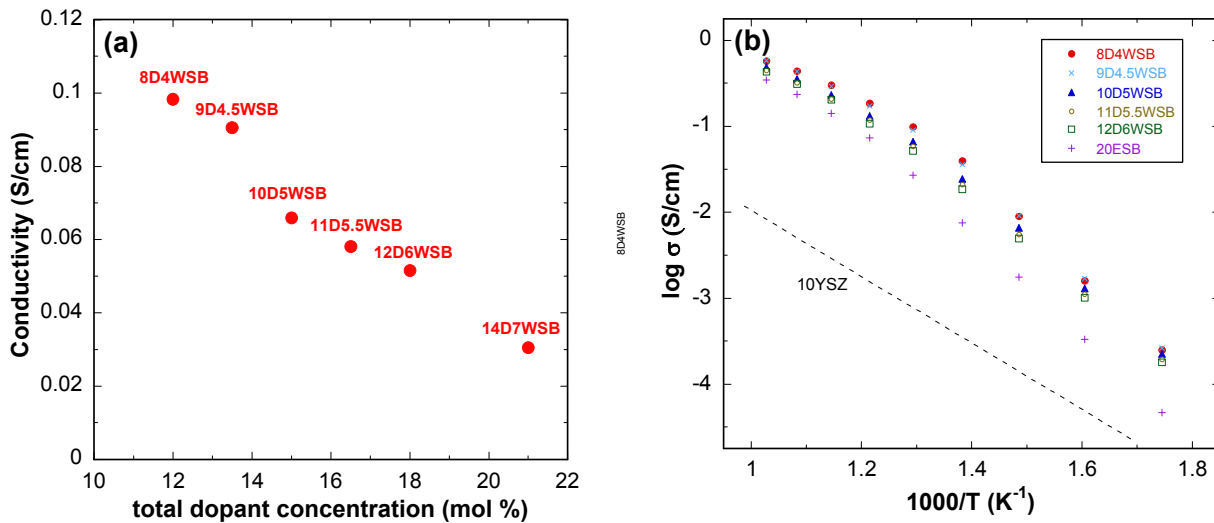
Figure 18. (a) Effect of total dopant concentration on conductivity for a 2:1 ratio of Dy to W in DWSB at (a) 500°C and (b) Arrhenius plot of conductivities for 8D4WSB, 9D4.5WSB, 10D5WSB, 11D5.5WSB, 12D6WSB and 20ESB; the dashed line represents the conductivity of 10YSZ.

Table 2. Conductivity activation energies of various DWSB compositions.

Composition	E_a (eV) Low temperature (≤550 °C)	E_a (eV) High temperature (≥550 °C)	ΔE_a (eV)
8D4WSB	1.1385	0.5961	0.5424
9D4.5WSB	1.1247	0.6329	0.4918
10D5WSB	1.0988	0.6813	0.4175
11D5.5WSB	1.0955	0.6890	0.4065
12D6WSB	1.0874	0.7110	0.3764

where σ is the oxygen ion conductivity, A is a pre-exponential constant, T is the absolute temperature, k is the Boltzmann constant and E_a is the activation energy for oxygen diffusion.

As the total dopant concentration increases, the disparity between these two activation energies decreases. This change in activation energy is attributed to an order-disorder transition of the oxygen sublattice.[16,43] That is, at high temperature above order-disorder transition temperature, the disordered state of oxygen sublattice is maintained. On the other hand, at relatively low temperature below this transition temperature, the oxygen sublattice is becoming ordered with degradation of ionic conductivity. Disparity of activation energy implies aging rate of this electrolyte. So, above the order-disorder temperature, lowering total dopant concentration to increase conductivity is reasonable, but below this temperature, there may be a trade-off between conductivity and long-term stability.

Long Term Stability of Bi_2O_3 Based Electrolytes Using Dy and W as Dopants

It is reported that stabilized bismuth oxides undergo an order-disorder transition of the oxygen sublattice at about 600°C.[39-40] Therefore, we should investigate the effect of dopant concentration on the ordering rate and consider the order-disorder transition temperature for this DWSB electrolyte system. In order to further investigate the ordering phenomenon, three DWSB compositions of the preferred (highest conductivity) 2:1 ratio were selected for long-term stability tests, namely: 8D4WSB, 10D5WSB and 12D6WSB.

In order to observe the effect of dopant concentration on conductivity under isothermal operation, time-dependent conductivity for various DWSB compositions annealed at (a) 700°C, (b) 600°C and (c) 500°C is shown in Figure 19. Especially, time-dependent conductivity of 20ESB annealed at 500°C was added in Figure 19c. In all compositions, the initial conductivity was maintained when the sample was annealed at 700°C, which is significantly higher than the expected order-disorder transition temperature of ~600°C. That is, all DWSB compositions tested were stable at 700°C in terms of conductivity. However, the conductivity of samples decayed when annealed at 600°C and 500°C. Especially, at 500°C, conductivity decay rate is fastest in all compositions. Among them, the conductivity of 8D4WSB decayed rapidly at 500°C because of the lower total dopant concentration.

Nevertheless, a big improvement of long-term stability was achieved through 10D5WSB compared with 20ESB. As shown in Figure 19c, the conductivity of 10D5WSB annealed at 500°C for 100 hours is more than two times as high as that of 20ESB. With respect to this result, 10D5WSB is a promising electrolyte composition because its initial conductivity is comparable to that of 8D4WSB and its aging rate is less than other compositions. However, the merit of double doped stabilized bismuth oxide was rather compromised due to the decrease of conductivity. So, above the order-disorder temperature, lowering total dopant concentration to increase conductivity is reasonable, but below this temperature, there may be a trade-off between conductivity and stability. Therefore, for applications involving isothermal operation in the IT range, especially at 500°C for several hundreds of hours, the long-term stability of DWSB system needs to be enhanced. In addition, the methodology to enhance the long-term stability at temperature below transition temperature was necessary.
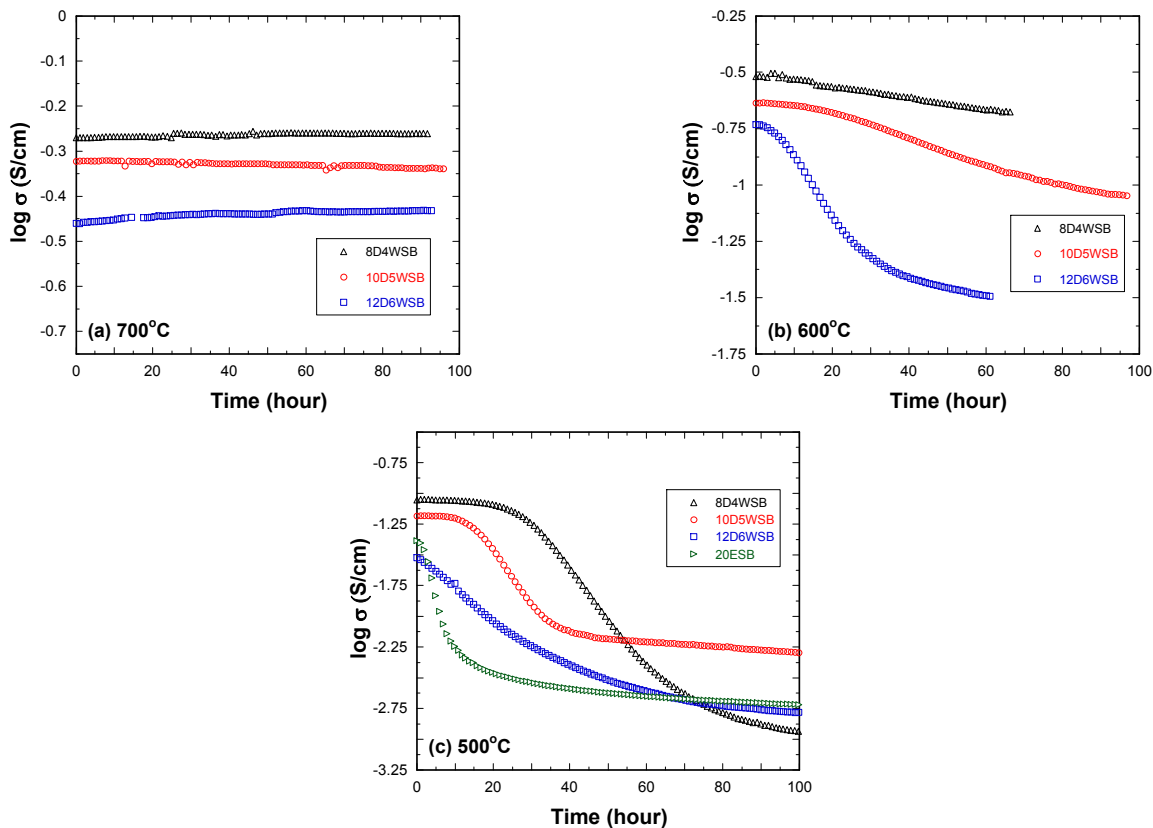
Figure 19. Isothermal comparison of time-dependent conductivity for 8D4WSB, 10D5WSB and 12D6WSB annealed at (a) 700°C, (b) 600°C, and (c) 500°C; 20ESB is added in (c).

We found that DWSB compositions experienced the fastest degradation of conductivity at 500°C in the IT range. In order to observe conductivity behavior with time below 500°C for DWSB electrolyte system, the long term test was also conducted for 8D4WSB composition at 400°C and 300°C. Figure 20a shows time dependent conductivity of 8D4WSB annealed at different temperatures including previous temperature range of 500-700°C. In addition, Figure 20b shows the relative conductivity of 8D4WSB at various temperatures as a function of time to compare conductivity degradation rate at various temperatures. On the contrary to 500°C operation, we observed less conductivity degradation relatively at 400°C and 300°C. Further, the degradation rate at 300°C was much less than that at 400°C and only small conductivity degradation was observed at 300°C. This trend implies that exponentially slower kinetics, decreasing with temperature would impact on conductivity. It is thought that slower kinetics has more dominant effect than thermal energy on conductivity at low temperature below about 400°C. Therefore, as temperature decreased, 8D4WSB had lower initial conductivity because conductivity is controlled by diffusion process, but experienced less conductivity degradation due to the slower kinetics of phase transformation or ordering phenomenon.

As discussed earlier, conductivity degradation remains an issue even though an increase in initial conductivity was achieved in this DWSB system. To begin with, X-ray diffraction was performed to identify the presence of phase change for 8D4WSB composition annealed at different temperatures for 100 hours. After 100 hour annealing test, each sample was polished to remove the gold electrode and XRD patterns were obtained.

Figure 21 shows the XRD patterns of 8D4WSB annealed at 300-500°C for 100 hours including the pattern of as-sintered pellet. This figure shows that 8D4WSB maintains cubic fluorite structure at 300°C and 400°C, but second phase was formed at 500°C. This indicates that 8D4WSB is stable at 300°C and 400°C while not stable at 500°C with respect to phase stability.
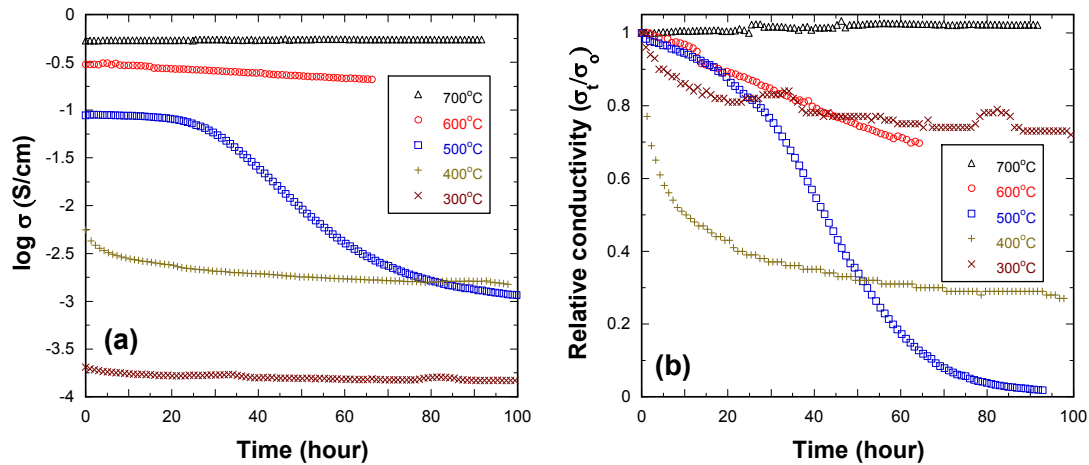

Figure 20. (a) Time dependent conductivity and (b) relative conductivity for 8D4WSB annealed at various temperatures as a function of time.

Wachsman et al. observed that the conductivity of $(ErO_{1.5})_{0.2}(BiO_{1.5})_{0.8}$ (20ESB) decreased with time when this sample was annealed at ~500°C without apparent phase change [15]. Wachsman et al. extensively investigated aging process without involving a phase transformation for cubic stabilized bismuth oxides using differential scanning calorimetry (DSC) or differential thermal analysis (DTA), transmission electron microscopy (TEM) and neutron diffraction.[40,44] They found that this aging phenomenon is attributed to the formation of an ordered structure, as observed by TEM and neutron diffraction.[40,44] However, this process was not detected by XRD. Jiang et al. also insisted that aging phenomenon for ordered structure is most rapid ~500°C. It was expected that ordering phenomenon is solely responsible for conductivity degradation at 500°C for this DWSB system before XRD characterization was performed. However, XRD pattern of 8D4WSB annealed at 500°C for 100 hours showed an indication of phase change. This may be attributed to phase destabilization through less dopant concentration. It indicates that both ordering phenomenon and phase transformation should be considered simultaneously in this DWSB system at 500°C.

As shown in Figure 19c, DWSB compositions experience the fastest degradation of conductivity at 500°C. Figure 22 shows XRD patterns of various DWSB compositions including 20ESB annealed at 500°C for 100 hours.
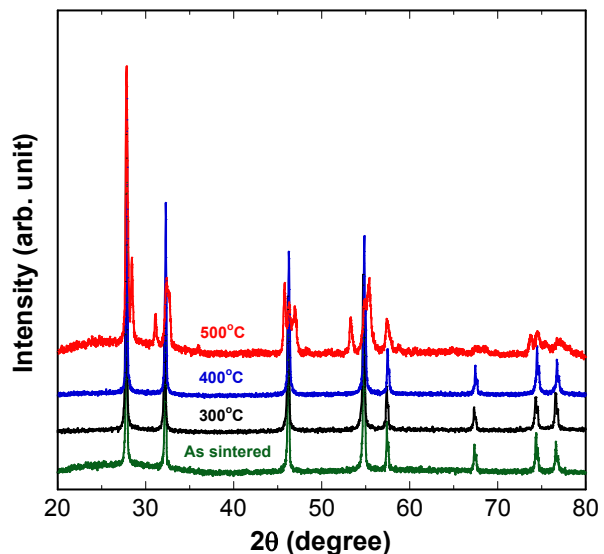

Figure 21. XRD patterns of 8D4WSB annealed at various temperatures for 100 hours.

In order to compare the amount of second phase, all XRD patterns were normalized based on (111) main peaks. We observed that 8D4WSB had the mixture of fcc phase and another second phase after 100 hour annealing at 500°C. 10D5WSB or 12D6WSB also experienced this phase change; however, the amount of second phase remarkably decreased as total dopant concentration increased. On the other hand, 20ESB did not show phase change during 100 hour annealing at 500°C as shown in Figure 22. This is consistent with our previous result.[39] Most of the conductivity decay in 20ESB at 500°C occurred in the first 10 hours and no second phase was observed by XRD. It implies that conductivity mechanism is also dependent on dopant type. Therefore, the ordering phenomenon is solely responsible for conductivity degradation of 20ESB at 500°C.

To identify the second phase of 8D4WSB annealed at 500°C, a few compositions of $(WO_3)_x(BiO_{1.5})_{1-x}$ (x=0.222, 0.24, 0.25, and 0.30) were synthesized. Figure 23 shows the XRD patterns of various $(WO_3)_x(BiO_{1.5})_{1-x}$ (x=0.222, 0.24, 0.25, and 0.30) as-calcined compositions. Takahashi et al. investigated WO_3 doped Bi_2O_3 system and also attained fcc structure with 22-28 mol% WO_3.[19] Watanabe et al. also examined the solid solubility region of this system.[45] It was believed that an fcc phase $Bi_7WO_{13.5}$ ($=7Bi_2O_3 \cdot 2WO_3$, 22.22 mol% WO_3) exists stably and yields high oxide-ion conduction.[19] However, Watanabe revealed that $Bi_7WO_{13.5}$ decompose around 650°C.[45] This implies that an fcc phase of $Bi_7WO_{13.5}$ is not stable in the intermediate temperature range we are aiming for operating. As shown in Figure 23, all tungsten doped bismuth oxide tested in this study had mixed phases of tetragonal ($7Bi_2O_3 \cdot WO_3 \equiv Bi_{14}WO_{24}$) and orthorhombic ($Bi_2O_3 \cdot WO_3 \equiv Bi_2WO_6$). The amount of each phase was dependent on the doping amount of WO_3. This result is consistent with Watanabe's measured solid solubility region in the system Bi_2O_3-WO_3.[45] However, we didn't get a single fcc phase as opposite to other literature results.[19, 45] It is probably due to the difference of processing. While they conducted quenching to obtain high temperature modification structure, we didn't conduct quenching when we cooled down the temperature. A single fcc phase through quenching doesn't guarantee a stable structure when it is annealed in intermediate temperature. Nevertheless, as-calcined XRD patterns of $(WO_3)_x(BiO_{1.5})_{1-x}$ provided a clue about the second phase of Figure 22. The second phase was identified as the mixture of tetragonal ($7Bi_2O_3 \cdot WO_3 \equiv Bi_{14}WO_{24}$) and orthorhombic ($Bi_2O_3 \cdot WO_3 \equiv Bi_2WO_6$) phase.
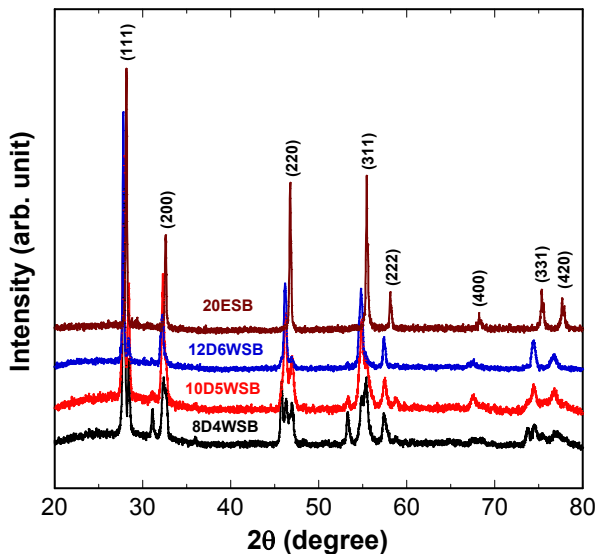

Figure 22. XRD patterns for 8D4WSB, 10D5WSB, 12D6WSB and 20ESB annealed at 500 °C for 100 h.

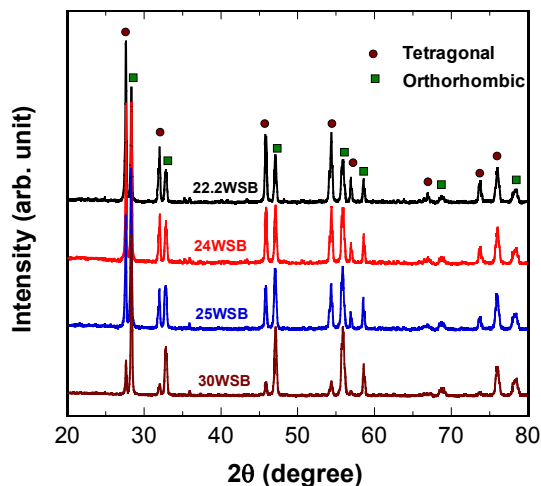Figure 23. XRD patterns of $(WO_3)_x(BiO_{1.5})_{1-x}$. (x=0.222, 0.24, 0.25 and 0.30)

Therefore, it is thought that there is a decomposition of (WO_3)-$(BiO_{1.5})$ cubic phase when DWSB compositions with less total dopant concentration are annealed at 500°C for some periods of time.
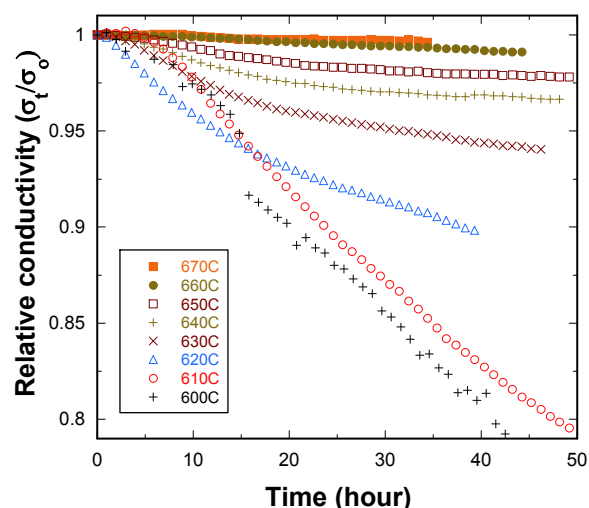

Figure 24. Relative conductivity for 8D4WSB as a function of time at various temperatures.
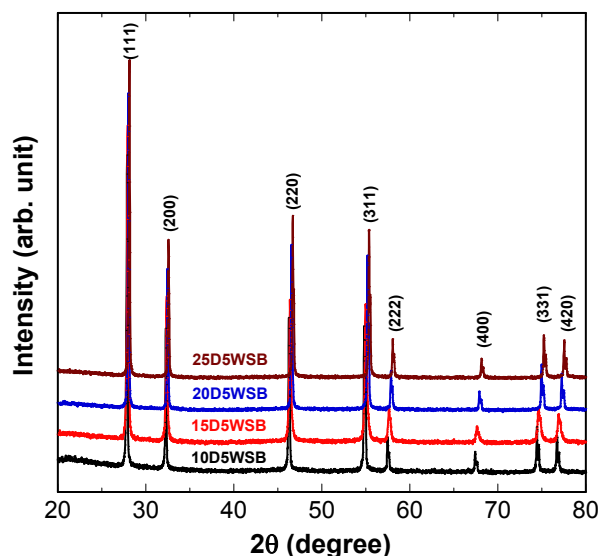

Figure 25. XRD patterns of 10D5WSB, 15D5WSB, 20D5WSB and 25D5WSB.

In order to obtain a more precise order-disorder transition temperature for this DWSB system, long term tests for 8D4WSB were performed at temperatures between 600°C and 670°C. The initial ionic conductivity was maintained when it was annealed above 600°C, but a little decay was observed at temperatures near to 600°C. To investigate the conductivity trend in more detail, relative conductivity is plotted in Figure 24.

Enhancement of Long Term Stability at 500°C (Increase of Dy Content)

10D5WSB maintained the highest conductivity after 100 hour annealing at 500°C as shown in Figure 24 and Table 3. In addition, we observed that a decomposition of (WO_3)-$(BiO_{1.5})$ cubic phase is responsible for the second phase formed during annealing at 500°C for DWSB compositions. Based on these results, we increased the Dy dopant concentration while keeping the W dopant concentration as 5 mol%. We synthesized 15D5WSB, 20D5WSB and 25D5WSB through solid state reaction. In addition, $(DyO_{1.5})_{0.25}(BiO_{1.5})_{0.75}$, 25DSB, was also synthesized to compare this Dy-doped Bi_2O_3 with other DWSB compositions. Figure 25 shows XRD patterns of various DWSB compositions with same 5 mol.% W content. These compositions had a pure fcc structure and obeyed Vegard's law. The lattice parameter decreased linearly with the increase of Dy concentration. Conductivity measurements were performed on these compositions.

The bulk conductivities of various DWSB electrolytes (10D5WSB, 15D5WSB, 20D5WSB and 25D5WSB) were plotted in Figure 26. As predicted by XRD patterns, we observed that initial conductivity decreased as Dy concentration increased. This also results from the decrease of lattice parameter with the increase of dopant concentration. Table 3 shows activation energy at low and high temperature regime for these compositions. On the other hand, the difference in activation energy decreased with the increase of Dy concentration like previous DWSB compositions with the same 2:1 dopant ratio. Especially, we obtained almost straight Arrhenius behavior from 25D5WSB.

Long-term stability tests were also performed for newly prepared DWSB compositions including 25DSB under 500°C operation for about 300 hours. Particularly 25D5WSB was annealed at

500°C for 500 hours. Figure 27 shows time-dependent conductivity behavior for these compositions with previous 10D5WSB.

As total dopant concentration increased, the long term stability was enhanced while compromising its initial conductivity. Consequently, 25D5WSB could provide a lot improved long term stability at 500°C operation for 500 hours.

Therefore, conductivity degradation was considerably minimized by manipulating dopant concentration of DWSB system. In order to obtain optimum electrolyte composition, which satisfies both criteria of conductivity and stability for low temperature applications, the mechanism of conductivity degradation should be examined thoroughly.
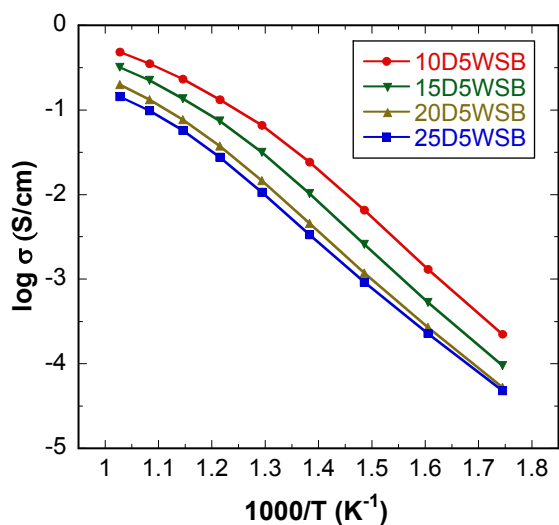
Figure 26. Arrhenius plot of conductivities for 10D5WSB, 15D5WSB, 20D5WSB and 25D5WSB.
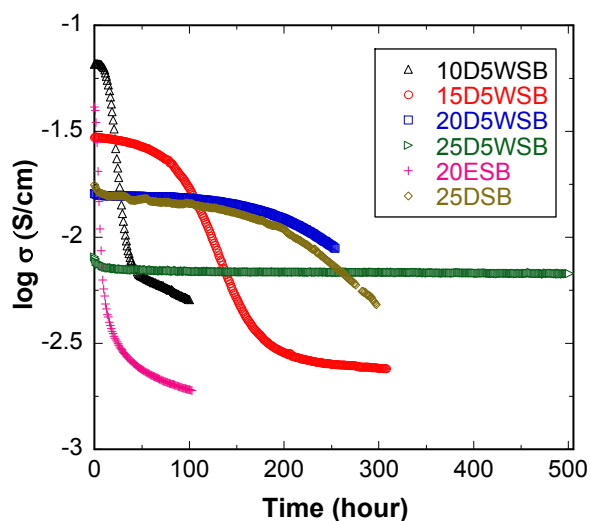
Figure 27. Time-dependent conductivity for 10D5WSB, 15D5WSB, 20D5WSB, 25D5WSB, 20ESB and 25DSB annealed at 500°C.

Table 3. Conductivity activation energies for 10D5WSB, 15D5WSB, 20D5WSB and 25D5WSB.

Composition	E_a /eV (≤550°C)	E_a /eV (≥550°C)	ΔE_a (eV)
10D5WSB	1.0988	0.6813	0.4175
15D5WSB	1.1571	0.7579	0.3992
20D5WSB	1.1381	0.8449	0.2932
25D5WSB	1.0990	0.8354	0.2636

Conclusions

1. 8D4WSB composition with minimum total dopant concentrations has highest ionic conductivity.

2. The conductivity of DWSB electrolytes increases linearly as the total dopant concentration decreases with fixed dopant ratio.

3. The disparity in activation energy decreases as the total dopant concentration increases.

4. From the viewpoint of stability, above the order-disorder temperature, lowering total dopant concentration is appropriate, but below this temperature, there is a trade-off between conductivity and stability.

5. DWSB compositions experienced the fastest conductivity degradation rate at 500°C.

6. 8D4WSB composition is a very promising electrolyte in the whole temperature range except for 500°C operation.

7. Order-disorder transition temperature for this DWSB system was investigated.

8. The long term stability was a lot enhanced by increasing the total dopant concentration at 500°C

Development of Ionic Conductivity Optimized Acceptor-Doped Ceria

Experimental
All the polycrystalline ceramic samples were prepared by conventional solid oxide reaction method, starting from stoichiometric mixtures of respective oxides powders (all with 99.99% purity). The weighed powders were mixed by ball-milling in de-ionized water with 1% dispersant for 24 hour and subsequently dried in the oven at 120°C for 16 h. The calcination temperature and time for all the powders was optimized to be 1450°C for 10 h. After the calcination, agglomerated powders were ball milled for 24 h and and subsequently dried in the oven at 120 °C for 16 hour. Using polyvinyl alcohol (~1%wt) as a binder, powders were then uniaxially pressed into disk-shaped pellets (8 mm diameter and 3 mm thickness) under a pressure of 130 MPa. The green pellets were then pressed in the cold isostatic press (CIP) under a pressure of 200 MPa for 3 minutes. The geometrical density of all the green pellets was determined to be 61% of theoretical density or above. The green pellets were then finally sintered in air at 1550°C for 10 h. Densities of all the sintered samples were measured in water using Archimedes's principle and were estimated to be 98% of theoretical density or above.

The as-sintered pellets were then polished to obtain planar surfaces. Pt paste (CL11- 5349, Heraeus) was brushed onto both sides of the cylindrical shaped pellets to serve as the electrode. The pellets were then cofired at 900°C for 1 h. Pt wires (99.9% pure) with diameter 0.127 mm were attached to the cell using Pt paste to perform ionic conductivity measurements. For impedance measurement at different temperatures, each sample was individually heated in a glass reactor which was placed inside a small tube furnace. The thermocouple was kept right next to the sample to minimize the temperature measurement errors. The complex impedance (Z) of the samples was measured using the two-point probe electrochemical impedance spectroscopy technique (Solartron 1260) over the frequency range of 10 MHz to 0.10 Hz. Measurements were taken in air, in the temperature range of 250°C to 700°C.

Results and Discussion

Co-doping Strategy Based on Critical Dopant Ionic Radii (r_c)

To ensure the complete dissolution of dopant in CeO_2, phase analysis was performed using the X-Ray diffraction (XRD) technique. Figure 28 shows the XRD patterns measured at room temperature for all the compositions of $Lu_xNd_yCe_{1-x-y}O_{2-\delta}$. It can be observed that all compositions studied are single phase with a cubic fluorite structure like pure CeO_2.

The effect of total dopant concentration ($x+y$) on the lattice constant a_o of the cubic fluorite structure of $Lu_xNd_yCe_{1-x-y}O_{2-\delta}$ was studied. The a_o of the calcined powders of $Lu_xNd_yCe_{1-x-y}O_{2-\delta}$ and $Lu_xCe_{1-x}O_{2-\delta}$ with different total dopant concentrations was calculated using maximum likelihood estimation method with tungsten as an internal standard. Figure 29 shows the variation of the elastic strain present in the cubic fluorite lattice of $Lu_xNd_yCe_{1-x-y}O_{2-\delta}$, $Nd_xCe_{1-x}O_{2-\delta}$ and $Lu_xCe_{1-x}O_{2-\delta}$ as a function of total dopant concentration. The lattice constant data for the different compositions of $Nd_xCe_{1-x}O_{2-\delta}$ were taken after Stephens et al.[46] Elastic strain is calculated using the following equation:

$$\text{Elastic strain} = \frac{a_o - a}{a} \qquad [5]$$
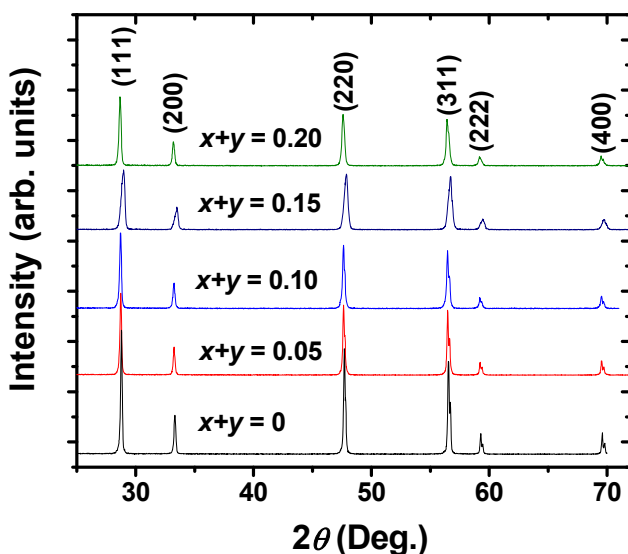
Figure 28. XRD patterns of $Lu_xNd_yCe_{1-x-y}O_{2-\delta}$ solid solution.
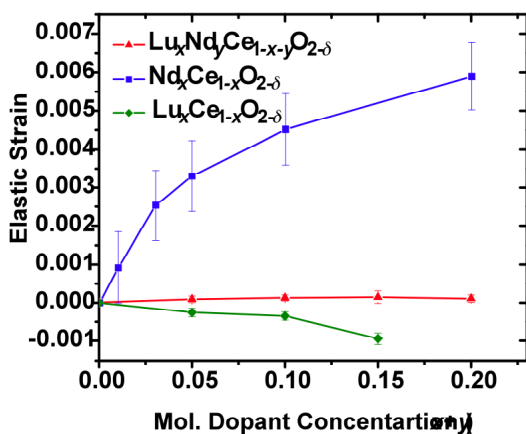
Figure 29. Elastic strain as a function of dopant concentration. Lattice parameter data for $Nd_xCe_{1-x}O_{2-\delta}$ were taken after Stephens et al.[46]

where a is the lattice constant of a pure ceria. Positive and negative elastic strain is respectively observed upon the separate addition of Nd^{3+} and Lu^{3+}. By contrast, there is almost no elastic strain present in the fluorite lattice of $Lu_xNd_yCe_{1-x-y}O_{2-\delta}$, even at high dopant concentrations. This validates the hypothesis that, when combined, the positive elastic strain generated by the addition of the larger Nd^{3+} dopant ion is compensated by the negative elastic strain caused by the addition of smaller Lu^{3+} dopant ion.

The grain ionic conductivity was determined using the two-point probe electrochemical impedance spectroscopy technique. The complex impedance measurements were taken in air, in the temperature range of 250°C to 700°C using (Solartron 1260) over the frequency range of 32 MHz to 0.10 Hz.

It was assumed that the electronic contribution to the overall conductivity was negligible. This assumption was reasonable, since all the measurements were done below 800°C in air.
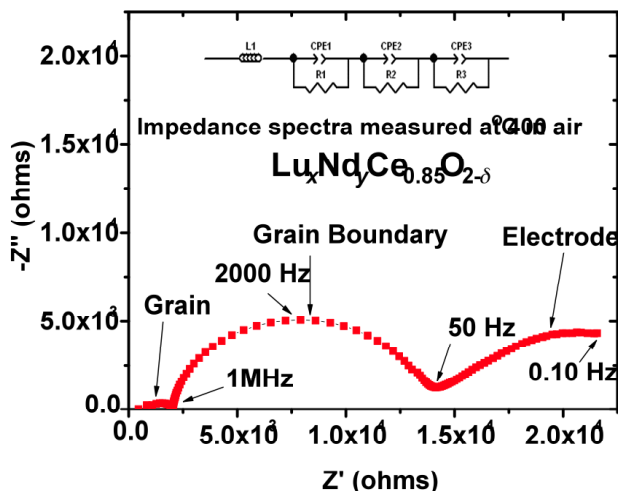
Figure 30. Impedance spectra and analog equivalent circuit for a polycrystalline electroded ceramic pellet.

Previous research indicates that Ce^{4+} has a high tendency to reduce to Ce^{3+} at high temperatures (>1000°C).[47] Figure 30 shows the impedance response for the electroded $Lu_{0.081}Nd_{0.069}Ce_{0.85}O_{2-\delta}$ ceramic at 400°C in air. In the figure, three main features can be observed: incomplete depressed arc at high frequency and two distinct arcs at low frequency. The low frequency arc was attributed to electrode polarization while the remaining two arcs at high frequencies correspond to grain and grain boundary polarization processes. The negative $-Z''$ at high frequencies may be attributed to stray inductance from the test setup.

The ideal frequency response of the intra-grain polarization (bulk conductivity) of an electroded polycrystalline electrolyte can be modeled by a resistor-capacitor (RC) pair in parallel. However,
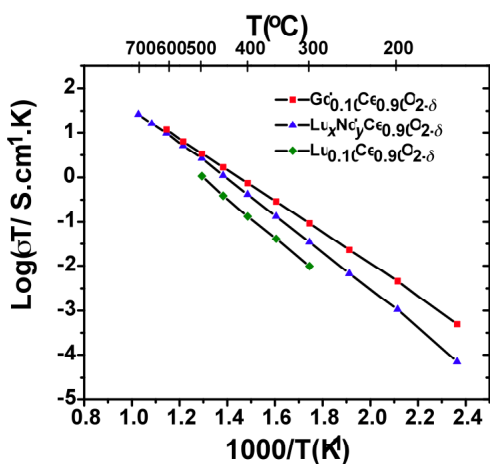
Figure 31. Arrhenius plots for the bulk ionic conductivity of $Lu_{0.054}Nd_{0.046}Ce_{0.90}O_{2-\delta}$, $Lu_{0.10}Ce_{0.90}O_{2-\delta}$ and $Gd_{0.10}Ce_{0.90}O_{2-\delta}$ systems in air.

in the present case due to microstructural inhomogeneities among different grain, instead of capacitor a constant phase element (CPE) is used to model the experimental data. The grain ionic conductivity was calculated from the observed impedance spectra using the equivalent circuit also shown in Figure 30, where L1, R1, R2, R3, CPE1, CPE2 and CPE3 represent the inductance of the experimental set-up, grain resistance, grain boundary resistance, electrode resistance, constant phase element of the grain, constant phase element of the grain boundary and constant phase element of the electrode respectively. From the impedance analysis, bulk ionic conductivities of different compositions of doped ceria electrolyte were determined. The conductivities exhibited Arrhenius behavior i.e., the data obeyed the familiar relationship stated as [2].

The fit of the data to equation [2] is generally quite good with correlation coefficient for a linear least squares fits of between 0.9995 and 0.9999 (Figure 31).

Figure 4 in the beginning compares the bulk ionic conductivity data of co-doped ceria with that of singly doped ceria, taken at 400^oC. It is important to note that, for that figure, grain ionic conductivity data for singly doped ceria is taken from the literature. It can be seen that $Lu_xNd_yCe_{0.90}O_{2-\delta}$ exhibits higher grain ionic conductivity than $Lu_{0.10}Ce_{0.90}O_{2-\delta}$, and $Nd_{0.10}Ce_{0.90}O_{2-\delta}$. This behavior is in accordance with the large elastic strain present in the fluorite lattice of $Lu_{0.10}Ce_{0.90}O_{2-\delta}$ and $Nd_{0.10}Ce_{0.90}O_{2-\delta}$ compare to $Lu_xNd_yCe_{0.90}O_{2-\delta}$. However, as shown in Figure 4, $Lu_xNd_yCe_{1-x-y}O_{2-\delta}$ exhibits lower grain ionic conductivity than $Gd_xCe_{1-x}O_{2-\delta}$. This may be explained by the high polarizability of Gd^{3+}. The weighted average dielectric polarizability of Lu^{3+} and Nd^{3+} for the above experimental conditions is calculated to be 4.27 $Å^3$. This value is less than that of Gd^{3+} having a dielectric polarizability of 4.37 $Å^3$.[48]
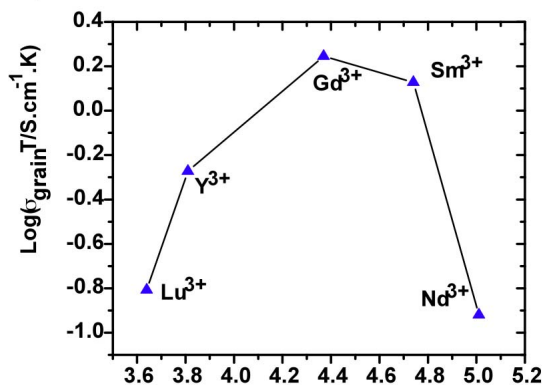
Figure 32. Grain ionic conductivity of doped ceria at 400^oC as a function of polarizability of dopant cation. Conductivity data of $Y_{0.10}Ce_{0.90}O_{2-\delta}$, $Gd_{0.10}Ce_{0.90}O_{2-\delta}$, $Sm_{0.10}Ce_{0.90}O_{2-\delta}$, and $Nd_{0.10}Ce_{0.90}O_{2-\delta}$ were taken after Zhang et al.[28], Steele[31], Zhan et al[33] and Li et al.[29] respectively. Data for $Lu_{0.10}Ce_{0.90}O_{2-\delta}$ is our work.

Figure 32 shows a plot of the grain ionic conductivity data of rare earth elements doped ceria at 400^oC as a function of dielectric polarizability of dopant cation. From the figure, it is clear that high ionic conductivity of Gd^{3+} doped CeO_2 is not only because the ionic radius of Gd^{3+} ($r^{3+}_{Gd,VIII}$= 0.1053 nm) lies near the critical ionic radius ($r^{3+}_{c,VIII}$= 0.1038 nm) but also due to the high polarizability of Gd^{3+}. Data for dielectric polarizability for this plot is taken from Shannon.[48]

Effect of the Grain Size on Grain Ionic Conductivity

Design of experiments (DOE) was utilized to optimize the microstructure and to study the effects of different processing variables, or factors, (i.e., ball milling speed and time, sintering temperature and time, etc.) on the grain size. The use of DOE allows for determination of interactions between factors.[49] It estimates the effects of a factor at several conditions of the other factors, yielding conclusions that are valid over a range of experimental situations. For each factor, a theoretical range was established in which experiments will be performed. Based on the range of each factor, 8 sets of experiments were designed with different processing variables (shown in Table 4).

Phase pure powder of $Gd_{0.10}Ce_{0.90}O_{2-\delta}$ was synthesized using the conventional solid oxide route method. Calcination temperature and time for the powder was optimized at 1450^oC for 10 hour. Microstructural analysis of $Gd_{0.10}Ce_{0.90}O_{2-\delta}$ pellets was performed using scanning electron microscopy (SEM). The sintered ceramic pellets of $Gd_{0.10}Ce_{0.90}O_{2-\delta}$ were polished using 0.3 μm abrasive paper to obtain a glossy surface for SEM. The polished pellets were then thermally etched at temperature 100^oC below their respective sintering temperature for 1 hour. Figure 33 shows the scanning electron micrograph of GDC2 and GDC5 pellets. Almost zero porosity was observed in both the samples.

The grain size measurement was performed using mean lineal intercept, or Heyn's technique. The mean lineal intercept length is the average length of a line segment that crosses a

sufficiently large number of grains. It is determined by laying a number of randomly placed test lines on the image and counting the number of times that grain boundaries are intercepted. Mathematically, it is defined as:

$$MLI = \frac{L}{N}$$

[5]

where L is the length of the test line, N is the total number of grain boundary intersections and *MLI* is the mean lineal intercept shows the average grain size with standard error for different $Gd_{0.10}Ce_{0.90}O_{2-\delta}$ ceramic pellets processed with different conditions.

The estimated effect of each factor and their interaction was determined and is shown in Table 5. It was found that ball milling time does not significantly affect grain growth when compared to other factors. The ANOVA analysis was performed on the remaining factors and their interactions. On comparing the Fisher distribution of each factor and their interactions with the value of $F_{0.05,1,2}$ (18.51), it can be seen that sintering time, temperature and their interaction are the main factors affecting the grain size during the sintering process (see Table 6).
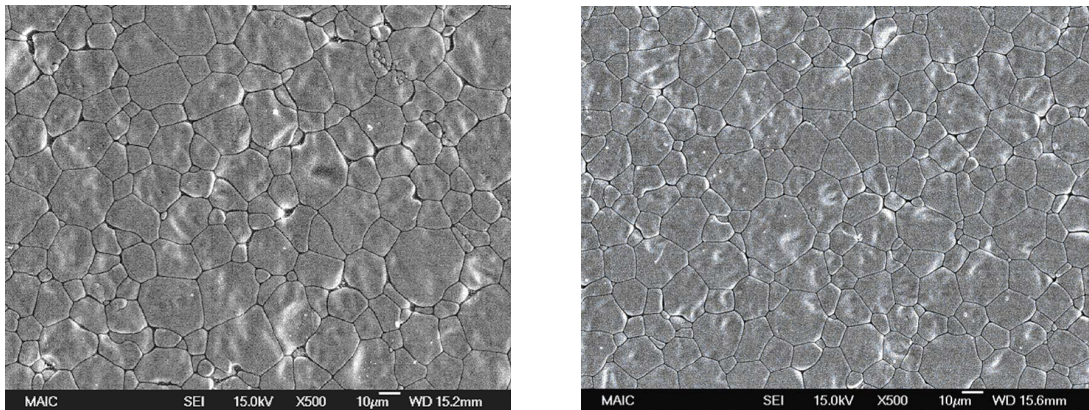
Figure 33. Scanning electron micrograph of GDC2 (left) and GDC5 (right).

The regression model for predicting grain size was determined and is shown in equation [6],

$$\hat{y} = 9.8 + 4.38\left(\frac{A-1600}{50}\right) + 1.25\left(\frac{B-15}{5}\right) + 0.58\left(\frac{A-1600}{50}\right)\left(\frac{B-15}{5}\right)$$

[6]

where A is sintering temperature (^{o}C), B is sintering time (h), and y is grain size (μm).
Figure 34 shows the grain ionic conductivity comparison of different grain size $Gd_{0.10}Ce_{0.90}O_{2-\delta}$ samples. It was observed that the grain ionic conductivity remains almost constant and is independent of the size of the grain within the tested range.

Table 4. Fractional factorial design to optimize the microstructure of $Gd_{0.10}Ce_{0.90}O_{2-\delta}$

Sample	Ball milling Time (h) after calcination	Ball milling Speed (rpm) after calcinations	Sintering Time (h)	Sintering Temperature (^{o}C)	Grain Size (μm)	Standard Error
GDC1	24 (+)	103 (+)	10 (+)	1550 (+)	4.60	0.05
GDC2	24 (+)	103 (+)	20 (-)	1650 (-)	15.62	0.22
GDC3	24 (+)	124 (-)	10 (+)	1650 (-)	12.76	0.17
GDC4	24 (+)	124 (-)	20 (-)	1550 (+)	5.98	0.06
GDC5	48 (-)	103 (+)	10 (+)	1650 (-)	12.10	0.10
GDC6	48 (-)	103 (+)	20 (-)	1550 (+)	6.29	0.06
GDC7	48 (-)	124 (-)	10 (+)	1550 (+)	5.01	0.05
GDC8	48 (-)	124 (-)	20 (-)	1650 (-)	16.52	0.38

Table 5. Estimated effect of each individual factor and their interactions

Process Variable	Estimated Effect (EE)	Regress. Coeff. (EE/2)	Contrast (EE/0.25)
Overall Average			
Ball milling Time (A)	0.255	0.128	1.02
Ball milling Speed (B)	0.400	0.200	1.60
Sintering Temperature (C)	8.755	4.378	35.02
Sintering Time (D)	2.490	1.245	9.96
AB + CD	1.160	0.580	4.64
BC + AD	0.350	0.175	1.40
AC + BD	-0.105	-0.053	-0.42

Table 6. The Analysis of Variance (ANOVA) Table for the 2^{4} factorial design

Source of Variation	Sum of Squares (SS)	Deg. of Freedom (df)	Mean Square (SS/df)	F_{o} (Fisher Dist.)
Ball Milling Speed (B)	0.32	1	0.32	4.20
Sintering Temp. (°C)	153.30	1	153.30	2015.78
Sintering Time (D)	12.40	1	12.40	163.05
CD	2.69	1	2.69	35.39
BC	0.25	1	0.25	3.22
Error (SS_{E})	0.15	2	0.08	
Total (SS_{T})	169.11	7		
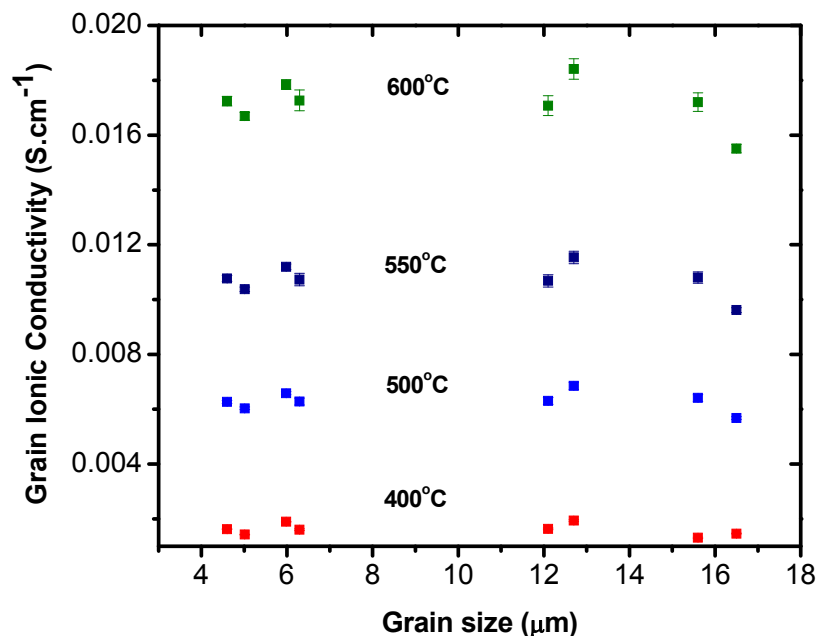
Figure 34. Grain ionic conductivity comparison of different grain size $Gd_{0.10}Ce_{0.90}O_{2-\delta}$ samples.

Effect of Atomic Number on the Grain Ionic Conductivity of Co-Doped Ceria Electrolytes

Figure 35 shows the XRD patterns measured at room temperature for all the compositions of $Sm_xNd_xCe_{1-2x}O_{2-\delta}$. Tungsten was used as an internal standard in the powder sample. It can be

Figure 35. XRD patterns of $Sm_xNd_xCe_{1-2x}O_{2-\delta}$ measured at room temperature.

observed that with the increase in the total dopant content ($2x$), (111) and (200) peaks of the material shift to the lower 2θ angles while (110) peak positions of standard tungsten remain stable in all the compositions. This clearly indicates the lattice expansion of doped ceria with the increase in dopant content. The lattice parameter of $Sm_xNd_xCe_{1-2x}O_{2-\delta}$ was calculated using extrapolation technique. In Figure 36 the lattice parameter of $Sm_xNd_xCe_{1-2x}O_{2-\delta}$ is plotted as a function of total dopant content ($2x$). For comparison, the lattice parameter data of $Nd_{2x}Ce_{1-2x}O_{2-\delta}$ as a function of dopant content is also shown taken after Stephen et al.[46] It can be observed that $Nd_{2x}Ce_{1-2x}O_{2-\delta}$ shows quadratic lattice expansion with dopant content. The non-linear part of the $Nd_{2x}Ce_{1-2x}O_{2-\delta}$ lattice parameter expansion was attributed to the formation of local defect structures while linear segments depend upon the distribution of the dopant cations within the host lattice. The lattice parameter of $Sm_xNd_xCe_{1-2x}O_{2-\delta}$ varies linearly with dopant concentration (Vegard's law). This indicates that the probability of the formation of local defect structure is lower in $Sm_xNd_xCe_{1-2x}O_{2-\delta}$ than in $Nd_{2x}Ce_{1-2x}O_{2-\delta}$.

Figure 37a shows the grain ionic conductivity of $Sm_xNd_xCe_{1-2x}O_{2-\delta}$ as a function of dopant content. It can be observed that the grain ionic conductivity increases with increase in dopant

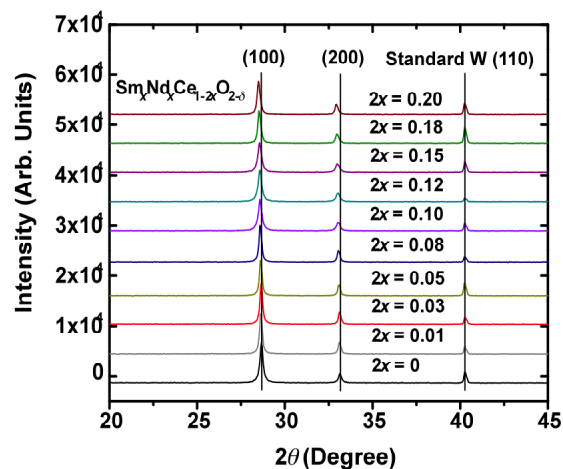content. However, after reaching a maximum it begins to drop beyond certain dopant content. This is attributed to the formation of the local defect structures at higher dopant concentration. For comparison, the grain ionic conductivity of $Gd_xCe_{1-x}O_{2-\delta}$ is also plotted as a function of dopant content (after Zhang et al.[28]). It can be seen that the $Sm_xNd_xCe_{1-2x}O_{2-\delta}$ exhibits higher grain ionic conductivity than that of $Gd_xCe_{1-x}O_{2-\delta}$. This can be attributed to the increase in the number of equi-interaction energy sites in $Sm_xNd_xCe_{1-2x}O_{2-\delta}$ which promote the relaxed diffusion in the material. Thus, we report the grain ionic conductivity of $Sm_{0.05}Nd_{0.05}Ce_{0.90}O_{2-\delta}$ as 12.2×10^{-3} S.cm^{-1} which is considerably higher than that of GDC (~10.7×10^{-3} S.cm^{-1}) at 550°C. In addition, total doping content was also optimized for $Sm_xNd_xCe_{1-2x}O_{2-\delta}$ to achieve the highest grain ionic conductivity. In this effort, we observed that the $Sm_{0.075}Nd_{0.075}Ce_{0.85}O_{2-\delta}$ is the best material for intermediate temperature SOFCs applications.

Figure 37b compares the grain ionic conductivity of all the doped ceria electrolytes as a function of dopant ionic radius. It can be seen that the $Sm_{0.05}Nd_{0.05}Ce_{0.90}O_{2-\delta}$ is the best among all the doped ceria materials while $Sm_{0.10}Ce_{0.90}O_{2-\delta}$ exhibits higher grain ionic conductivity than that of $Gd_{0.10}Ce_{0.90}O_{2-\delta}$.

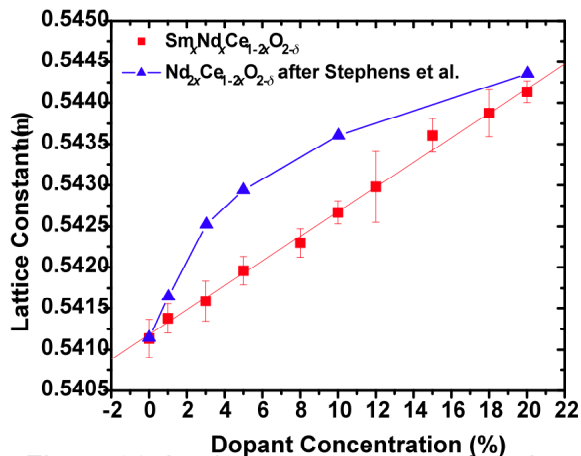Figure 36. Lattice parameter as a function of dopant content for $Sm_xNd_xCe_{1-2x}O_{2-\delta}$ and $Nd_{2x}Ce_{1-2x}O_{2-\delta}$ taken after Stephens et al.[18]
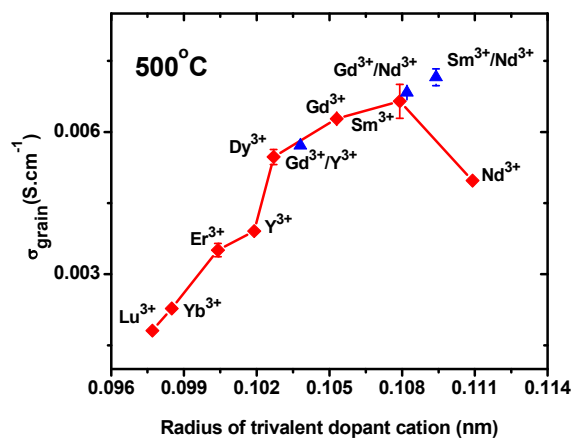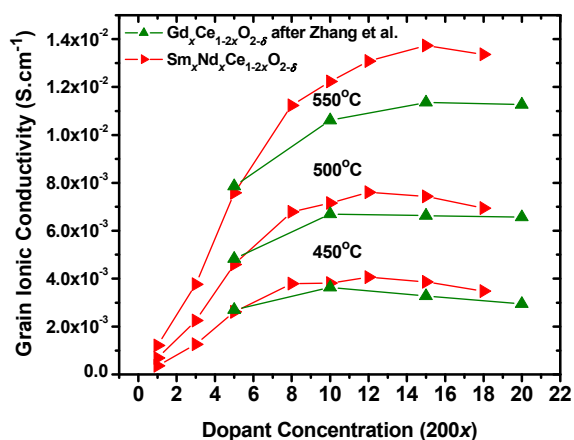

Figure 37. Grain ionic conductivity dependence on total dopant content ($2x$) in $Sm_xNd_xCe_{1-2x}O_{2-\delta}$ and $Gd_{2x}Ce_{1-2x}O_{2-\delta}$.[28] (b) Comparison of grain ionic conductivity of 10 mol% doped ceria electrolytes in air.

Conclusions

1. The $Lu_xNd_yCe_{1-x-y}O_{2-\delta}$ system was investigated as a test case for a co-dopant strategy for enhancing the grain ionic conductivity of ceria electrolytes based on the critical dopant ionic radius r_c concept. Lu^{3+} and Nd^{3+} were added as co-dopants such that the weighed average dopant ionic radius matched r_c for all the compositions. The lattice elastic strain of the $Lu_xNd_yCe_{1-x-y}O_{2-\delta}$ compounds was calculated from precise lattice parameter measurements and was found to be negligible when compared to $Lu_xCe_{1-x}O_{2-\delta}$ and $Nd_xCe_{1-x}O_{2-\delta}$. It was observed that the $Lu_xNd_yCe_{1-x-y}O_{2-\delta}$ exhibits higher grain ionic conductivity than either of $Lu_xCe_{1-x}O_{2-\delta}$ and $Nd_xCe_{1-x}O_{2-\delta}$. These results indicate that the co-dopant strategy based on critical dopant ionic radius can lead to the enhancement of the grain ionic conductivity for ceria based electrolytes.

2. The grain size effect on the grain ionic conductivity of doped ceria electrolyte was investigated. Design of experiment was utilized to optimize the microstructure and to study the effects of different processing variables, or factors, on the grain size. $Gd_{0.10}Ce_{0.90}O_{2-\delta}$ was used as a test material. On comparing the grain ionic conductivity of the different grain size $Gd_{0.10}Ce_{0.90}O_{2-\delta}$ ceramic samples, it was observed that the grain ionic conductivity is independent of grain size within the tested range (4-16 μm).

3. Based on the effective atomic number concept, in this work the effect of co-dopant pair Sm^{3+} and Nd^{3+} on the grain ionic conductivity of ceria-based electrolytes was investigated. This novel approach was based on computational work which suggests using co-dopant with an average effective atomic number of Pm (62). By doing so, the increase in the number of equi-interaction energy sites of oxygen vacancy was expected, which as a result, promoted relaxed oxygen diffusion. This in turn increased the ionic conductivity of the material. Co-doped electrolytes of $Sm_xNd_xCe_{1-2x}O_{2-\delta}$ were processed with different total dopant content. The grain ionic conductivity of $Sm_xNd_xCe_{1-2x}O_{2-\delta}$ was found to be quite higher in comparison with that of $Gd_{2x}Ce_{1-2x}O_{2-\delta}$.

Publications

1. "Doubly doped Bi_2O_3 electrolytes with higher conductivity," D. Jung, K.L. Duncan and E.D. Wachsman, *Solid State Ionic Devices IV*, *ECS Transactions*, E. Wachsman, V. Birss, F. Garzon, R. Mukundan, and E. Traversa, Ed., Vol. 1 [7] pp. 63 (2006).

2. "Development of Higher Ionic Conductivity Ceria Based Electrolyte," S. Omar, E.D. Wachsman, and J.C. Nino, *Solid State Ionic Devices IV*, *ECS Transactions*, E.D. Wachsman, F.H. Garzon, E. Traversa, R. Mukundan, and V. Birss, Ed., Vol. 1 [7] pp. 73-82 (2004).

3. "A Co-Doping Approach towards Enhanced Ionic Conductivity in Fluorite-Based Electrolytes," S. Omar, E.D. Wachsman, and J.C. Nino, *Solid State Ionics*, 177 [35-36] pp. 3199-3202 (2006).

Presentations from Research

1. **Characterization of Oxygen Vacancy Clusters in Bi_2O_3 using Molecular Dynamics Simulations**- The American Ceramics Society: The 30th International Conference and Exposition on Advanced Ceramics and Composites, Cocoa Beach, Florida. January 22-27, 2006.

2. **Oxygen Vacancy Behavior in Cubic Bismuth Oxide** (Poster) - Florida Chapter of American Vacuum Society (FLAVS), March 12-16, 2006.

3. **Study of the Structure of Cubic Bismuth Oxide using Molecular Dynamics Simulation** (Poster) – International Center for Materials Research Conference on Oxide Materials, Bangalore India, December 2007.

4. **Oxygen Diffusion Mechanism in Cubic Bismuth Oxide using Molecular Dynamics Simulations** - The 31st International Cocoa Beach Conference & Exposition on Advanced Ceramics and Composites, Daytona Beach, Florida, January 2007.

5. **Atomic Level Processes in Solid Oxide Fuel Electrolytes** – Third Annual Meeting of the Florida Society for Materials Simulation, University of South Florida, 7th July 2007.

6. **"Effect of dopant concentration of doubly doped Bi_2O_3 electrolyte on ionic conductivity and anion ordering**", D. Jung, M.A. Camaratta, K.L. Duncan, and E.D. Wachsman, 31st International Conference & Exhibition on Advanced Ceramic & Composites, Daytona Beach, Florida, USA, January 21-26, 2007.

7. "**Optimization of doubly doped Bi_2O_3 electrolyte composition",** D. Jung, K.L. Duncan, and E.D. Wachsman, 30th International Conference & Exhibition on Advanced Ceramic & Composites, Cocoa Beach, Florida, USA, January 24, 2006.

8. "**A study on doubly doped Bi_2O_3 electrolytes with higher conductivity**", D. Jung, K.L. Duncan, and E.D. Wachsman, 208th Electrochemical Society Meeting, Los Angeles, California, USA, October 19, 2005.

9. "**Microstructural Effects on the Grain Ionic Conductivity of $Gd_{0.10}Ce_{0.90}O_{2-\delta}$**", S. Omar, H. El-Shall, E.D. Wachsman, and J.C. Nino, 31st International Conference & Exhibition on Advanced Ceramic & Composites, Daytona Beach, Florida, USA, January 21-26, 2007.

10. "**Effect of Microstructure on the Grain Ionic Conductivity of Ceria based Electrolytes**", S. Omar, H. El-Shall E.D. Wachsman, and J.C. Nino, 2006 MRS Fall Meeting, Boston, Massachusetts, USA, November 27-December 1, 2006.

11. "**A Co-Doping Approach towards Enhanced Ionic Conductivity in Fluorite-Based Electrolytes**", S. Omar, E.D. Wachsman, and J.C. Nino, European Materials Research Society Spring Meeting, Nice, FRANCE, June 1st , 2006.

12. "**Effect of Co-Doping on the Electrical Properties of Ceria Electrolyte**", S. Omar, E.D. Wachsman, and J.C. Nino, 30th International Conference & Exhibition on Advanced Ceramic & Composites, Cocoa Beach, Florida, USA, January 24, 2006.

13. "**Development of Higher Ionic Conductivity Ceria Based Electrolyte**", S. Omar, E.D. Wachsman, and J.C. Nino, 208th Electrochemical Society Meeting, Los Angeles, California, USA, October 19, 2005.

Graduate Students

Dilpuneet S. Aidhy (Ph. D.)
Doh Won Jung (Ph. D.)
Shobit Omar (Ph. D.)

Acknowledgments

References

1. N. Jiang, E.D. Wachsman and S.H. Jung, "A Higher Conductivity Bi_2O_3-Based Electrolyte," Solid State Ionics, 150 347-353 (2002).
2. N. Jiang and E.D. Wachsman, "Structural Stability and Conductivity of Phase-Stabilized Cubic Bismuth Oxides," *J. Am. Cer. Society*, 82 3057-3064 (1999).
3. E.D. Wachsman, S.Boyapati and N. Jiang, "Effect of Dopant Polarizability on Oxygen Sublattice Order in Phase-Stabilized Cubic Bismuth Oxides," *Ionics*, 1-6 (2001).
4. A. Walsh, G.W. Watson, D.J. Payne, R.G. Edgell, J. Guo, P. Glans, T. Learmonth and K.E. Smith, "Electronic Structure of the Alpha and Delta Phases of Bi_2O_3: A Combined *Ab Initio* and X-Ray Spectroscopy Study," *Physical Review B*, 73 235104-235101-235112 (2006)
5. P.W.M. Jacobs and D.A. Macdonaill, "Computational Simulations of Delta-Bi_2O_3.1. Disorder," *Solid State Ionics*, 23 279-293 (1987).
6. S. Omar, Wachsman, E. D., and Nino, J.C., "A co-doping approach towards enhanced ionic conductivity in fluorite-based electrolytes," *Solid State Ionics* **177** [35-36] 3199-3203 (2006).
7. E.D. Wachsman, S. Boyapati and M.J. Kauffman, "Modelling of Ordered Structures of Phase-Stabilized Cubic Bismuth Oxides," *J. Am. Cer. Society*, 83 1964-1968 (2000).
8. P.D. Battle, C.R.A. Catlow, J. Drennan and A.D. Murray, "The Structural -Properties of the Oxygen Conducting Delta-Phase of Bi_2O_3," *Journal of Physics C- Solid State Physics*, 16 L561-L566 (1983).
9. A.A. Zav'yalova and R.M. Imamov, "Cubic Structure of delta-Bismuth sesquioxide," *Kristallografiya*, 14 331-333 (1969).
10. E.D. Wachsman, *Journal of European Ceramics,* **24** 1281 (2004).
11. N. Jiang, E.D. Wachsman and S.H. Jung, *Solid State Ionic*s, **150** 347 (2002).
12. S. Boyapati, E.D. Wachsman and N. Jiang, *Solid State Ionics,* **140** 149 (2001).
13. E.D. Wachsman, S. Boyapati and N. Jiang, *Ionics*, **7** 1 (2001).
14. N. Minh, *J. Am. Ceram. Soc.* **76**(3) 563 (1993).
15. T. Takahashi and H. Iwahara, *J. Appl. Electrochem.,* **2** 97 (1972).
16. M.J. Verkerk and A.J. Burggraaf, *J. Electrochem. Soc.*, **128** 75 (1981).
17. G.Y. Meng, C.S. Chen, X. Han, P.H. Yang and D.K. Peng, *Solid State Ionics*, **28** 533 (1988).
18. D. Mercurio, M. Elfarissi, B. Frit, J.M. Reau and J. Senegas, *Solid State Ionics*, **39** 297 (1990).
19. T. Takahashi and H. Iwahara, *J. Appl. Electrochem.*, **3** 65 (1973).
20. M.J. Verkerk, K. Keizer and A.J. Burggraaf, *J. Appl. Electrochem.*, **10** 81 (1980).
21. H.T. Cahen, T.G.M. Van Den Belt, J.H.W. De Wit and G.H.J. Broers, *Solid State Ionics*, **1** 411 (1980).
22. M.J. Verkerk and A.J. Burggraaf, *Solid State Ionics*, **3-4** 463 (1981).
23. N. Jiang, Thesis, Aug., Stanford University (1994).
24. T. Takahashi, *Physics of Electrolytes*. Academic Press: London, 1972; Vol. 2, pp. 980-1049.
25. J.A. Kilner, and Brook, R.J., "A Study of Oxygen Ion Conductivity in Doped Nonstoichiometric Oxides," *Solid State Ionics* **6** [3] 237-252 (1982).
26. H. Inaba, and Tagawa, H., "Ceria-based solid electrolytes - Review," *Solid State Ionics* **83** [1-2] 1-16 (1996).
27. D.J. Kim, "Lattice-Parameters, Ionic Conductivities, and Solubility Limits in Fluorite-Structure Hf-4+O2, Zr-4+O2, Ce-4+O2, Th-4+O2, V-4+O2 Oxide Solid-Solutions," *Journal of the American Ceramic Society* **72** [8] 1415-1421 (1989).
28. T.S. Zhang, Ma, J., Kong, L.B., Chan, S.H., and Kilner, J.A., "Aging behavior and ionic conductivity of ceria-based ceramics: a comparative study," *Solid State Ionics* **170** [3-4] 209-217 (2004).
29. L.P. Li, Lin, X. M., Li, G.S., and Inomata, H., "Solid solubility and transport properties of Ce1-xNdxO2-delta nanocrystalline solid solutions by a sol-gel route," *Journal of Materials Research* **16** [11] 3207-3213 (2001).

30. R.D. Shannon, "Revised Effective Ionic-Radii and Systematic Studies of Interatomic Distances in Halides and Chalcogenides," *Acta Crystallographica Section A* **32** [Sep1] 751-767 (1976).
31. B.C. H. Steele, "Appraisal of Ce1-yGdyO2-y/2 electrolytes for IT-SOFC operation at 500°C," *Solid State Ionics* **129** [1-4] 95-110 (2000).
32. H. Duncan, and Lasia, A., "Influence of the electrode nature on conductivity measurements of gadolinia-doped ceria," *Solid State Ionics* **176** [15-16] 1429-1437 (2005).
33. Z.L. Zhan, Wen, T.L., Tu, H.Y., and Lu, Z.Y., "AC impedance investigation of samarium-doped ceria," *Journal of the Electrochemical Society* **148** [5] A427-A432 (2001).
34. D.A. Andersson, Simak, S.I., Skorodumova, N.V., Abrikosov, I.A., and Johansson, B., "Optimization of ionic conductivity in doped ceria," *Proceedings of the National Academy of Sciences of the United States of America* **103** 3518 (2006).
35. B.G. Dick and A.W. Overhauser, "Theory of the Dielectric Constant of Alkali Halide Crystals," *Physical Review*, 112 90-103 (1958).
36. J.P. Perdew and Y. Wang, "Accurate and Simple Analytic Representation of the Electron-Gas," *Physical Review B*, 45 13244-13249 (1992).
37. P.E. Blochl, "Projector Augmented Wave," *Physical Review B*, 50 17953-17979 (1994).
38. S. Boyapati, E.D. Wachsman and N. Jiang, "Effect of Oxygen Sub-lattice Ordering on Interstitial Transport Mechanism and Conductivity Activation Energies in Phase- Stabilized Cubic Bismuth Oxide," *Solid State Ionics*, 140 149-160 (2001).
39. N. Jiang and E.D. Wachsman, *J. Am. Ceram. Soc.*, **82** (11) 3057 (1999).
40. E.D. Wachsman, S. Boyapati, M.J. Kaufman and N. Jiang, *J. Am. Ceram. Soc.*, **83**(8)1964 (2000).
41. B.C.H. Steele, in: High Conductivity Solid Ionic Conductors, ed. T. Takahashi, (World Scientific, Singapore) (1989).
42. B.C.H. Steele, *Solid State Ionics*, **129** 95 (2000).
43. E.D. Wachsman, N. Jiang, D.M. Mason and D.A. Stevenson, *Proc. Electrochem. Soc.*, **89** (11) 15 (1989).
44. S. Boyapati, E.D. Wachsman and B.C. Chakoumakos, *Solid State Ionics,* **138** 293 (2001).
45. A Watanabe and A. Ono, *Solid State Ionics*, **174** 15 (2004).
46. I. E. L. Stephens, and Kilner, J. A. ""Ionic conductivity of Ce1-xNdxO2-x/2," Solid State Ionics 177 [7-8] 669-676 (2006).
47. G. B. Balazs, and Glass, R. S., "Ac-Impedance Studies of Rare-Earth-Oxide Doped Ceria," *Solid State Ionics* **76** [1-2] 155-162 (1995).
48. R. D. Shannon, "Dielectric Polarizabilities of Ions in Oxides and Fluorides," *Journal of Applied Physics* **73** [1] 348-366 (1993).
49. D. C. Montgomery, *Design and Analysis of Experiments*. John Wiley & Sons Inc.: New York, 2001; pp. 218-276.

4. A Test Bed for Impedance Measurements on PEM Fuel Cells
and
5. Interpretation Models for Impedance Response of PEM Fuel Cells

Task PI: Mark E. Orazem, Chemical Engineering, University of Florida

Collaborators: Dr. Jason Weaver, Chemical Engineering, Dr. Lisa McElwee-White, Chemistry, Dr. Eric Wachsman, Material Science & Engineering, Dr. James Klausner, Mechanical & Aerospace Engineering, Dr. Jacob Chung, Mechanical & Aerospace Engineering and Dr. Renwei Mei, Mechanical & Aerospace Engineering, University of Florida

Graduate Student: Sunil Roy, Chemical Engineering, University of Florida

Research Period: August 8, 2004 to March 31, 2008

Abstract

A test station for impedance measurements on PEM fuel cells was created. The test bed has capability of *in-situ* electrochemical characterization techniques such as cyclic voltammetry (CV) and linear sweep voltammetry (LSV) (for catalyst area characterization and hydrogen crossover measurement respectively) and durability analysis (fluoride ion and peroxide concentration measurement in the effluent of the fuel cell) in addition of the impedance measurements. The fuel cell test bed will permit study of typical fuel cell assemblies in future years. The test station was used to collect impedance data and the data were analyzed using a Voigt measurement model. The inductive loops found at low frequency were found to be consistent with the Kramer-Kronig relation once the fuel cell achieved steady-state operation. The present work confirmed that the low-frequency inductive loops could be attributed to processes occurring in the fuel cell.

Impedance models were developed to account for reaction mechanisms that may be responsible for the inductive impedance response often seen at low frequencies in PEM fuel cells. Models that incorporate only the hydrogen oxidation and oxygen reduction reactions cannot account for these inductive features. Inductive loops can be predicted by models that account for formation of hydrogen peroxide as an intermediate in a two-step oxygen reduction reaction. Inductive loops can also be predicted by models that account for Pt dissolution and associated deactivation of catalytic activity. These interpretations are supported by experimental evidence. Interpretation of impedance spectra in terms of side reactions may prove useful for predicting the lifetime of fuel cell performance.

In addition, a more sensitive manner of using impedance spectroscopy was established to gain an insight into the problem of flooding which adversely affects the performance of the fuel cell. A comprehensive model for base-level noise in impedance measurements for normal (non-flooded) conditions was developed and actual noise in flooded conditions was calculated by transient fixed-frequency measurements. A comparison of the actual noise to the base-level noise was used to detect onset of flooding.

Introduction

The objective of this work was to create a test bed for PEM fuel cells suitable for evaluating the new catalysts, membranes, and flow configurations. The long-term objective was to enhance the application of impedance spectroscopy as a tool for electrochemical characterization of fuel cells. The first portion of the project encompasses experimental investigations, which deal with collecting impedance data on the fuel cell and analyzing it for rectifying possible errors in the impedance measurement. In the second portion, interpretation models were developed based on the physics, transport, and kinetic mechanisms for impedance response. The expected outcomes of this work will provide better insight about the fuel cell and thus will guide improved system design and enhancing efficiency. The rate constants will give information about durability of the system, which is one of the most crucial issues in commercialization of fuel cells. The impedance technique was also used to detect of flooding which adversely affects the performances of the fuel cell.

Background: Relevance to NASA

1. This work is intended to enhance NASA research efforts in PEM fuel cells by making impedance spectroscopy a more useful tool.
2. The fundamental information obtained will guide research to enhance performance of fuel cells.
3. Integration of impedance data with interpretation models will provide meaningful parameters related to electrochemical, thermodynamic and transport processes in PEM fuel cells.

Motivation

The impedance response reported by Makharia et al[1] for a PEM fuel cell (see Figure 1) shows a pure inductance at very high frequency (which can be attributed to instrument artifacts), a small 45° region (associated with mass transfer), a capacitive loop at intermediate frequencies, and an inductive loop at low frequency. To date, no quantitative explanation has been reported concerning the low-frequency inductive loop. The impedance response at low frequency is usually attributed to side reactions and intermediates involved in overall reaction of the fuel cell, relaxation of adsorbed oxygenated intermediate species, and diffusion. The low-frequency inductive loop can also be due to non-stationary behavior of the fuel cell. The objective is to explore whether the inductive loop at low frequency is due to processes occurring in the fuel cell such as side reactions and intermediates or is due to non-stationary behavior of the fuel cell. The following experimental and theoretical approaches were used to achieve this objective.
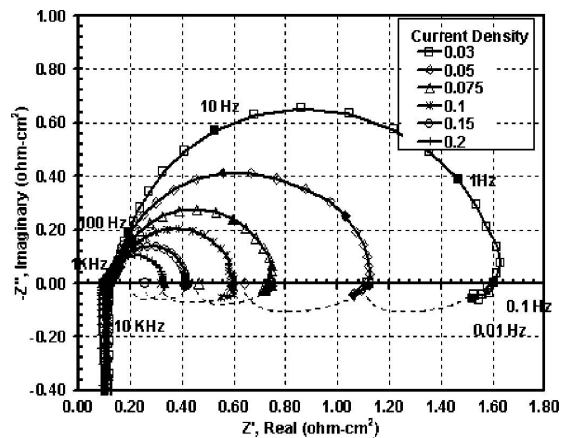
Figure 1. Impedance data reported by Makharia et al.[1] for H_2/O_2 operations at constant current density (A/cm^2).

Experimental Details

The membrane electrode assembly (MEA) employed a 0.0308 mm (2 mils) thick Nafion N112 membrane with an active surface area of 5 cm^2. The catalyst layers of the MEA were platinum supported on carbon with a Pt catalyst loading of 0.4 mg/cm^2 on both the anode and the cathode sides. The material of the flow channel used was graphite with the outlet lower than the inlet to facilitate removal of condensed water. Hydrogen gas was used as fuel and compressed air was used as oxidant for experiments. Compressed N_2 was used for purging of the fuel cell before and after experiments. Barnstead E-Pure Water System was used as a source of deionized water to the anode and the cathode humidifiers. The 850C fuel-cell test station (supplied by Scribner Associates, Southern Pines, NC) was used to control reactant flow rates and temperatures. The test station was connected to a computer by an interface for data acquisition.

Impedance measurements were performed using two different systems. Scribner Associates 850C Fuel Cell Test Stand contains an electronic load and frequency response analyzer. Impedance measurements obtained with the 850C were compared to impedance collected using a FC350 impedance analyzer (provided by Gamry Instruments Inc., Warminster, PA). The Gamry FC350 drove a Dynaload electronic loads series RBL 100V-60A-400W. All electrochemical measurements were performed with a two-electrode cell in which the anode was used as a pseudoreference electrode. The impedance measurements were conducted in galavanostatic mode for frequency range of 10 kHz to 1 mHz with a 10 mA peak-to-peak sinusoidal perturbation. The corresponding potential perturbation ranged from 0.04 mV to 0.4 mV. The frequencies were spaced in logarithmic progression with 10 points per frequency decade. Impedance scans were conducted in auto-integration mode with a minimum of 2 cycles per frequency measured.

Results and Discussion

I. Error Analysis of the Impedance data by Measurement Model

The impedance data collected were analyzed by a measurement model[2] to identify the stochastic and bias error structure. The measurement model method for distinguishing between bias and stochastic errors is based on using a generalized model as a filter for non-replicacy of impedance data. The model is composed of a superposition of line-shapes, which can be arbitrarily chosen subject to the constraint that the model satisfies the Kramers-Kronig relations. The measurement model is used first to filter lack of replication of repeated impedance scans.

The statistics of the residual errors yields an estimate for the variance (or standard deviation) of stochastic measurement errors. This experimentally-determined variance is then used to weight subsequent regression of the measurement model to determine consistency with the KK relations. If the data can be represented by a model that is itself consistent with the KK relations, the data can be considered to be consistent.

Typical results after the measurement model analysis are presented in Figure 2 for the impedance response of a single 5 cm^2 PEM fuel cell with hydrogen and air as reactants. The results presented as Figure 2a were obtained using a Scribner 850C fuel cell test station, and the results presented as Figure 2b were obtained using a Gamry FC350 impedance instrument coupled with a Dynaload RBL: 100V-60A-400W electronic load. The arrow points to the nominal zero-frequency impedance obtained from the slope of the polarization curve, and the solid lines correspond to a fit of the measurement model.
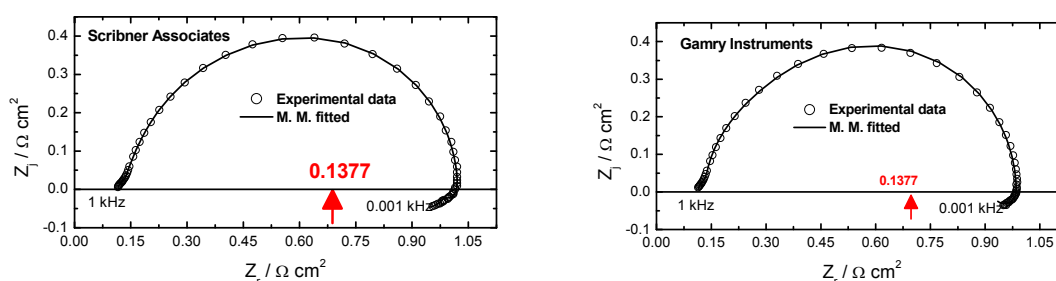

Figure 2. Comparison of impedance data obtained for a PEM Fuel cell. Symbols represent experimental data and solid lines represent the measurement model fit. The arrow points to the nominal zero-frequency impedance obtained from the slope of the polarization curve. a) Data collected at 0.2 A cm^2 using the Scribner 850C; b) Data collected at 0.2 A/cm^2 using a Gamry FC350 impedance instrument coupled with a Dynaload RBL: 100V-60A-400W electronic load.

The ability to fit the data with a measurement model demonstrates that, independent of the instrumentation used, the low-frequency features could be found to be consistent with the Kramers-Kronig relations. Therefore, the low-frequency inductive loops could be attributed to process characteristics and not to non-stationary artifacts.

II. Impedance Model Development

Three impedance models were investigated for interpretation of low-frequency inductive loops. In the first model, a single-step ORR at cathode and single step HOR at anode was proposed. In the second model, hydrogen peroxide formation in two steps ORR kinetics at cathode along with single step HOR at anode was proposed while in the third model ORR coupled with the platinum dissolution at cathode catalyst along with single step HOR at anode was proposed.

The mathematical model used to assess the influence of proposed reactions on the impedance response is summarized briefly in this section. The mass transfer problem was simplified significantly by assuming that the membrane properties were uniform, that issues associated with flooding and gas-phase transport could be neglected, and that the heterogeneous reactions took place at a plane, e.g., the interface between the catalyst active layer and the proton exchange membrane. This preliminary approach does not account for the spatial distribution of the catalyst particles in the catalyst layer, but this simplified treatment is sufficient to explore the role of specific reaction on impedance features, such as low-frequency inductive loops.

Model 1: Simple Reaction Kinetics

A single-step ORR

$$O_2 + 4H^+ + 4e^- \rightarrow 2H_2O \tag{1}$$

was assumed to take place at the cathode.
The single step HOR

$$H_2 \rightarrow 2H^+ + 2e^- \tag{2}$$
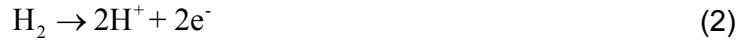
was assumed to take place at the anode.

Model 2: Hydrogen Peroxide Formation

In this case, the ORR was assumed to take place in two steps. The first reaction involves formation of hydrogen peroxide H_2O_2 that reacts further to form water, i.e.,

$$O_2 + 2e^- + 2H^+ \rightarrow H_2O_2 \tag{3}$$

and

$$H_2O_2 + 2e^- + 2H^+ \rightarrow 2H_2O \tag{4}$$

Model 3: Platinum Dissolution

Platinum dissolution was proposed to take place in two steps, according to an electrochemical reaction in which PtO is formed,

$$Pt + H_2O \rightleftharpoons 2H^+ + 2e^- + PtO \tag{5}$$

followed by a chemical dissolution of PtO, i.e.,

$$2H^+ + PtO \rightarrow Pt^{+2} + H_2O \tag{6}$$

The dissolution of PtO was assumed to occur according to

$$r_{PtO} = K_3 \bar{\gamma}_{PtO} \tag{7}$$

The formation of platinum oxide was assumed to have an indirect influence on the oxygen reduction reaction by changing the effective rate constant for the reaction. Thus,

$$K_{eff} = K_{Pt} + (K_{PtO} - K_{Pt})\gamma_{PtO} \tag{8}$$

where K_{Pt} is the rate constant on a platinum surface and K_{PtO} is the rate constant on a platinum oxide surface. It was assumed that $K_{PtO} << K_{Pt}$. The ORR was assumed to take place according to reaction (1).

Response Analysis of Models

Mathematical expressions were developed for the impedance response of a fuel cell that accounted for the reaction mechanisms described above. These models were compared to the experimental polarization and impedance data.

The method employed was to calculate the polarization curve that matched closely the experimental results and then to use the same parameters to estimate the impedance response at different currents. Direct regression was not employed as the model does not account explicitly for the non-uniform reaction rates caused by the serpentine flow channels. Constant values for the double layer capacitance, the Tafel slope, ionic resistance in the catalyst layer, membrane resistance, and oxygen permeability were used, as reported in the literature.[3] The impedance response for all simulations corresponded to a frequency range of 10 kHz to 0.001 mHz.

Model 1 accounts well for the capacitive loops, but cannot account for the low-frequency inductive loops. The impedance response for the model with the hydrogen peroxide formation (Model 2) consisted of one high-frequency capacitive loop and one low-frequency inductive loop. The impedance response for the model accounting for platinum dissolution (Model 3) also consisted of one high-frequency capacitive loop and one low-frequency inductive loop.
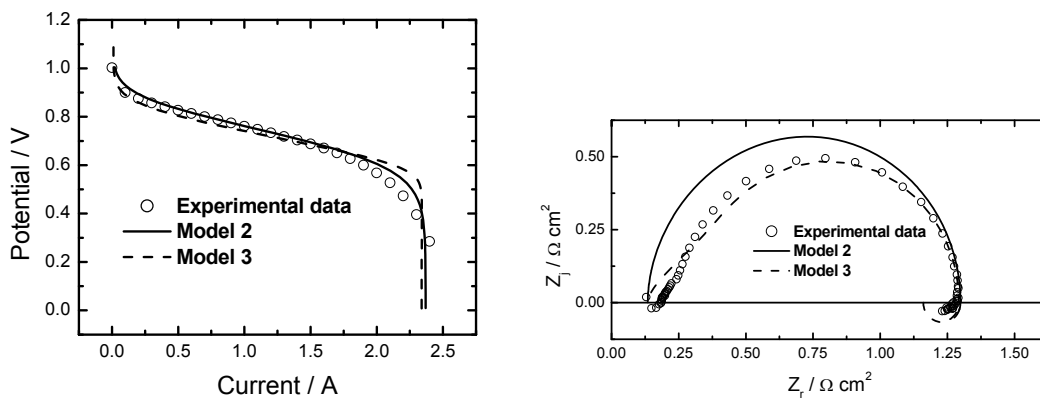

Figure 3 Polarization curves generated with the Model 2 and Model 3 and compared with the experimental data.

Figure 4 Impedance response generated with the Model 2 and Model 3 and compared with experimental data for low current density.
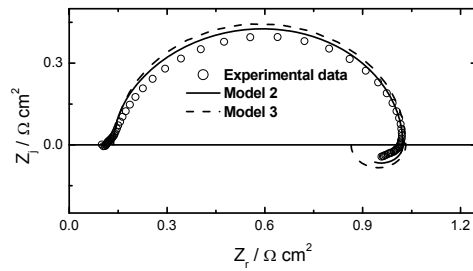
Figure 5 Impedance response generated with the Model 2 and Model 3 and compared with experimental data for intermediate current density.
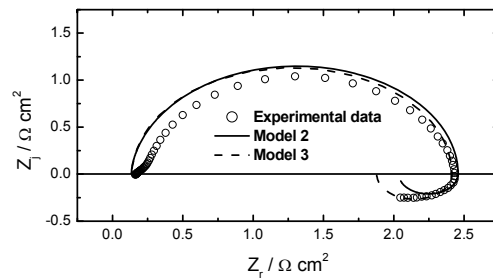
Figure 6 Impedance response generated with the Model 2 and Model 3 and compared with experimental data for high current density.

The polarization curve generated with Models 2 and 3 is presented in Figure 3. The presence of the side reactions in the model has no discernable influence on the polarization curve as these reactions are assumed to be taking place at a low rate as compared to the dominant hydrogen oxidation and oxygen reduction reactions. The impedance response was generated for all three region of the polarization curve. Figure 4 represents the impedance response predicted with the model in the low current density, Figure 5 represents the impedance response in the intermediate current density, and Figure 6 represents the impedance response in the high current density. As shown in Figures 4, 5, and 6, impedance measurements are much more sensitive to the presence of the side reactions. Both models 2 and 3 were found to be capable of yielding low-frequency inductive loops.

III. To Detect Onset of Flooding

In the final part, impedance was used to gain an understanding into problem of water management issues such as flooding of fuel cell. The approach demonstrates how the stochastic character of flooding may be exploited to detect onset of flooding without the need to regress impedance spectra. The research presented has potential to give guidelines for efficient fuel-cell operation.
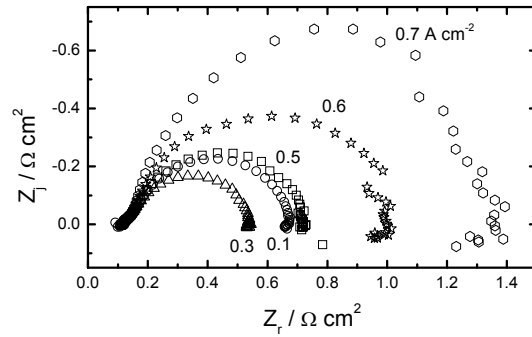
Figure 7 Impedance data recorded with the 850C for H_2 as reactant at the anode and air as oxidant at the cathode. The anode, the cathode, and cell temperatures were set at 40C.
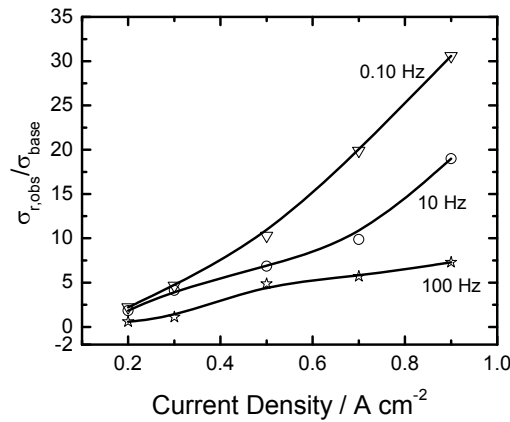
Figure 8 Normalized standard deviations calculated from the fixed-frequency impedance measurement as a function of current density with frequency as a parameter for real part.

The impedance response is presented in Figure 7 with current density as a parameter. The impedance spectra were well-shaped for low current densities however the spectra at higher current densities where the flooding was probable, have a lots of scattering. Noise in the EIS response was much pronounced and visible at high current density. This noise may be attributed to flooding of the fuel cell. The low-frequency impedance response at higher current densities has significant scatter; whereas, the low-frequency impedance response at lower current densities has comparatively less scatter. The enhanced disturbance in the low-frequency impedance response at higher current densities may be attributed to stochastic processes such as flooding.

To calculate the noise in above impedance measurements, the impedance was recorded as a function of time for different current densities and frequencies. The standard deviations in the impedance data were calculated using a moving average method to account for the systematic changes. A model for the standard deviation of impedance measurements in the absence of

flooding, was established by measurement model analysis was applied to a large set of impedance data. To develop the model for the error structure, the standard deviations were fitted as a function of frequency and impedance value. It was found that the standard deviations were constant for high frequency range whereas an exponential increase in the standard deviations was discerned for low frequency range.

The standard deviations of real part impedance as a ratio of actual noise, and the base-noise level calculated using the error structure are presented in Figure 8. At a current density of 0.3 A cm^{-2}, the ratio was approximately equal to that obtained in the absence of flooding. At higher current densities, the ratio of the calculated and the non-flooding standard deviations was greater than unity. As shown in Figure 8, the standard deviation of the impedance data increased with an increase in the operating current. The increased noise levels are seen at a frequency of 100~Hz as well as at lower frequencies. At large current densities and at low frequencies, the standard deviation calculated for the real part of the impedance was more than 10 times that obtained in the absence of flooding. The standard deviation for the imaginary part of the impedance was less sensitive to flooding. Interestingly, the standard deviation in the imaginary part of the impedance has no clear dependency on flooding. The standard deviation of the real part particularly at low frequency, can, however, be used to detect onset of flooding.

IV. Evaluation of Interfacial Capacitance

Interfacial capacitance is an important parameter which characterizes double-layer charging of an interface of electrode and electrolyte for any electrochemical system. Very limited or no information is reported about evaluation of the capacitance. We used graphical methods suggested by Orazem et al.[4] to extract interfacial capacitance from impedance data collected as a function of several operational parameters such as current densities, time, and temperature. It was found that values of the capacitance decreased with an increase in current densities and time. The decreases in interfacial capacitance with higher current density can be attributed to an excess amount of water i.e., flooding. The interfacial capacitance is usually scaled as effective surface area of electrode therefore the decreases in values of interfacial capacitance can be a representative of decrease in electrochemical active surface area of electrodes, which can arise due to water accumulation at higher current density. The decrease in interfacial capacitance with time can be ascribed to decrease in an effective surface area due to catalyst dissolution and deactivation.

Conclusions

The work presented here has demonstrated the value of combining experimental investigation and a modeling effort to interpret the processes occurring in the fuel cell by impedance techniques. The inductive loops found at low frequency were found to be consistent with the Kramer-Kronig relations once the fuel cell achieved steady-state operation. The formalism of the measurement model error analysis provides a means for determining whether a steady state has been achieved. The present work confirms that the low-frequency inductive loops can be attributed to processes occurring in the fuel cell. Kramers-Kronig-consistent inductive loops were observed in the entire range (current density) of operation of the fuel cell. The results were independent of the impedance instrumentation used.

Three analytic impedance models were derived from consideration of specific reaction sequences proposed to take place in PEM fuel cells to interpret the low-frequency inductive loops. The model that accounted only for hydrogen oxidation and oxygen reduction could not account for the low-frequency inductive loops observed in experimental data. Models that accounted for additional reactions, i.e., formation of hydrogen peroxide and formation of PtO

with subsequent dissolution of Pt, could predict low-frequency inductive loops. These models were supported by complementary experiments, and the results show that either of these reaction mechanisms could account for the experimentally observed low-frequency inductive loops. These models can also be used to predict such variables as the fractional surface-coverage of the proposed intermediates.

Impedance spectroscopy was coupled with a measurement-model-based error analysis to detect onset of flooding. This method is particularly attractive because it is extremely sensitive and a well-defined baseline noise level can be established for the non-flooding condition. Scattering in impedance spectra especially at higher current densities were recorded. The ratio noise in flooded condition and non-flooded condition in the real part of the impedance confirmed that the flooding was severe in higher current densities. This work has provided an example that error analysis approach improves the sensitivity of the EIS to onset of flooding and can provide direct insight into operation of the PEM Fuel cell.

The interfacial capacitance was evaluated by impedance techniques emphasizing graphical methods, which can give very important information about fuel cell operations such as flooding and catalyst degradation.

References

1. R. Makharia, M.F. Mathias, and D.R. Baker, "Measurement of Catalyst Layer Electrolyte Resistance in PEFCs using Electrochemical Impedance Spectroscopy," J. Electrochem. Soc., 152 (5) (2005), A970-A977.

2. P. Agarwal, M.E. Orazem, and L.H. Garcia- Rubio, "Measurement Models For Electrochemical Impedance Spectroscopy: 3. Evaluation of Consistency with the Kramers-Kronig Relations," J. Electrochem. Soc., 142 (1995), 4159-4156.

3. T.E. Springer, T.A. Zawodzinski, M.S. Wilson, S. Gottesfeld, "Characterization of Polymer Electrolyte Fuel Cells using AC Impedance Spectroscopy", J. Electrochem. Soc., 143 (1996), 587-599.

4. M.E. Orazem, N. Pebere, and B. Tribollet, "Enhanced Graphical Representation of Electrochemical Impedance data," J. Electrochem. Soc., 153 (2006) B129 B136.

Journal Publications

1. S.K. Roy and M.E. Orazem, "Error Analysis of the Impedance Response of PEM Fuel Cells," *Journal of the Electrochemical Society,* **154** (2007), B883-B891.

2. S.K. Roy, M.E. Orazem, and B. Tribollet, "Interpretation of Low-Frequency Inductive Loops in PEM Fuel Cells," *Journal of the Electrochemical Society,* **154** (2007), B1378-B1388.

Manuscripts in preparation

1. S.K. Roy and M.E. Orazem, "Analysis of Flooding as a Stochastic Process in PEM Fuel Cells by Impedance Techniques," manuscript in preparation with submission expected in April 2008.

2. S.K. Roy and M.E. Orazem, "Application of Impedance Techniques to Estimate Interfacial Capacitance of PEM Fuel Cells," manuscript in preparation with submission expected in May 2008.

Refereed Conference Proceedings

1. S.K. Roy and M.E. Orazem, "Deterministic Impedance Models for Interpretation of Low-Frequency Inductive Loops in PEM Fuel Cells," in *Proton Exchange Membrane Fuel Cells 6*, T. Fuller, C. Bock, S. Cleghorn, H. Gasteiger, T. Jarvi, M. Mathias, M. Murthy, T. Nguyen, V. Ramani, E. Stuve, T. Zawodzinski, editors, *ECS Transactions,* **3:1**, (2006), 1031-1040.

2. S.K. Roy and M.E. Orazem, "Stochastic Analysis of Flooding in PEM Fuel Cells by Electrochemical Impedance Spectroscopy," in Proton Exchange Membrane Fuel Cells 7, T. Fuller, H. Gasteiger, S. Cleghorn, V. Ramani, T. Zhao, T. Nguyen, A. Haug, C. Bock, C. Lamy, and K. Ota, editors, *Electrochemical Society Transactions,* **11:1**, (2007), 485-495.

Non-Refereed Conference Proceedings

1. S.K. Roy and M.E. Orazem, "Interpretation of Low-Frequency Inductive Loops in PEM Fuel Cell Impedance Data in Terms of Reactions Influencing the Life-Time of Fuel Cell Performance," Proceedings of the 2007 NHA Annual Hydrogen Conference, the National Hydrogen Association, Washington, DC, 2007.

Presentations

2. S.K. Roy and M. E. Orazem, "Application of Measurement Models to Impedance Data of PEMFC," presented at the 209th Meeting of The Electrochemical Society, Denver, Colorado, May 7-12, 2006.

3. S.K. Roy and M.E. Orazem, "Interpretation of Low-Frequency Inductive Loops in PEM Fuel Cell Impedance Data," presented at the 210th meeting of the Electrochemical Society, Cancun, Mexico, October 29 - November 3, 2006.

4. S.K. Roy and M.E. Orazem, "Interpretation of Low-Frequency Inductive Loops in PEM Fuel Cell Impedance Data in Terms of Reactions Influencing the Life-Time of Fuel Cell Performance," NHA Annual Hydrogen Conference, March 19-22, 2007.

5. M.E. Orazem, "An Integrated Approach to Impedance Spectroscopy," invited plenary lecture presented at the Seventh International Symposium on Electrochemical Impedance Spectroscopy, Argelés sur Mer, France, June 3-8, 2007.

6. M.E. Orazem and S.K. Roy, "On Modeling the Impedance Response of PEM Fuel Cells," Invited lecture, presented at the International Conference "Polymer Batteries Fuel Cells-PABFC-2007" on the occasion of Professor Scrosati's 70th birthday, Rome, Italy, June 11-15, 2007.

7. S. Roy and M. Orazem, "Stochastic Analysis of Flooding in PEM Fuel Cells by Electrochemical Impedance Spectroscopy," presented at the 212th Meeting of the Electrochemical Society, Washington DC, October 7-12, 2007.

8. S.K. Roy and M.E. Orazem, "Guidelines for Evaluation of Error Structure for Impedance Response of PEM Fuel Cells," to be presented at the 213th Meeting of the Electrochemical Society, Phoenix, Arizona, May 18-23, 2008.

Student Supported by Research

Sunil Roy, PhD (May 2008)
Michael Matlock, MS (May 2006)

6. Simulation and Modeling for the Improvement on the Thermal Fluid Management of PEM Fuel Cell

Task PI: Principal Investigators: Dr. Renwei Mei, Mechanical and Aerospace Engineering, University of Florida
Co-Investigator: Dr. James F. Klausner, Mechanical and Aerospace Engineering, University of Florida
Collaborators: Dr. Mark Orazem, Chemical Engineering, Dr. Chang-Won Park, Chemical Engineering, Dr. James Klausner, Mechanical & Aerospace Engineering, and Dr. Jacob Chung, Mechanical & Aerospace Engineering, University of Florida
Graduate Student: Yanxia Zhao, Mechanical and Aerospace Engineering, University of Florida

Research Period: August 8, 2004 to June 31, 2007

Sub-Task 1: Effects of Geometrical Parameters on Improving the Transversal Mass Transport in PEM Fuel Cells

Abstract

In this work, we develop a computational model using Lattice Boltzmann Equation (LBE) method to investigate the fluid transport on the anode side of Polymer Electrolyte Membrane (PEM) fuel cells, with an emphasis on the mass transfer enhancement. The LBE method is powerful in handling complex geometries, such as flow through porous substrate and around obstructions in a flow channel. The specific geometric details of a porous structure can be simulated in the computational model. A 3-dimensional LBE code is developed to solve the flows in the channel and the porous media in the gas diffusion layer (GDL) simultaneously. Multiple flow enhancers (obstructions in the flow channel) are placed in the channel to enhance the transversal flow across the GDL. Many small particles are placed in the GDL to simulate the porous substrate. The mass flow rate, the velocity field and the pressure distribution are analyzed. The effects of flow enhancers are assessed. The results show that the transversal flow across the GDL can be enhanced by placing flow enhancers in the channel. Increasing flow enhancer size can significantly increase the transversal flow rate, with high pressure-loss through the flow channel. The results also demonstrate that the location of flow enhancers in the flow channel have a remarkable impact on the transversal flow rate. The transversal flow rate increases as the GDL porosity increases. This computational model can be used to optimize the designs of the flow channel geometry.

Nomenclature

f	single particle mass distribution function
ξ	particle velocity vector
$\boldsymbol{u}$	fluid velocity
p	pressure
t	time
ρ	mass density
x	spatial position vector
$f^{(0)}$	equilibrium distribution function
$\widetilde{f}_\alpha$	post-collision distribution function
$\boldsymbol{\lambda}$	relaxation time

v	kinematic viscosity
e_α	discrete particle velocity in LBE model
w_α	weighting factor
$f_\alpha^{(eq)}$	equilibrium distribution function in discretized particle velocity space
c_s	speed of sound
δt	time step
δx	space step
τ	dimensionless relaxation time

I. Introduction

Polymer Electrolyte Membrane (PEM) fuel cells are able to generate electricity with high power densities and operate at low temperature. Therefore it is attractive for transportation applications and stationary power applications. In a PEM fuel cell, the hydrogen molecules on the anode disassociate into H^+ ions and electrons. The ions transport across the membrane to the cathode and to react with the oxygen to form water. The electrons are removed to power an electrical device.

One of the difficulties to achieve high power density is that the reaction rate is limited by the diffusion rates of hydrogen fuel and oxygen through the channels and gas diffusion layer (GDL). To overcome the limitation caused by ineffective transversal mass transport, novel flow channel geometries have recently been developed, such as straight channels, serpentine channels, multiple channels in parallel type and interdigitate channels [1, 2]. Much effort has been devoted to the numerical computations for the flow distribution and fuel gas diffusion in order to gain insights and improve the design. Most of numerical computations use the conventional computational fluid dynamics (CFD) method by numerically solving the mass, energy and Navier-Stokes equations and treated the flow in the GDL using Darcy's law. In their simulation, Gurau et al. [3] developed a two-dimensional mathematical model for the entire sandwich of PEM fuel cell. Yi et al. [4] investigated the convective water transport across the membrane by a pressure gradient, temperature distribution in the solid phase along the flow channel, and heat removal by natural convection and coflow and counterflow heat exchangers. Dutta et al. [5] performed three-dimensional computations for flow between channels in PEM fuel cell with a serpentine flow path. Bernig et al. [6] studied the three-dimensional distribution of flow velocities, species concentration, mass transfer rates, electric current and temperature. Kazim et al. [1] demonstrated the superiority of the interdigitated flow field design over the conventional flow field design. Soong et al. [2] studied the partially blocked fuel channel with baffle plates transversely inserted in the channel. However, in conventional computational fluid dynamics (CFD) method, the transversal flow through porous media in the GDL is often modeled using Darcy's law, which requires empirical input such as permeability, ignores the specific geometric details of the porous structure, and may not account completely for the interaction between the porous GDL and the enhancer. In contrast, the method of Lattice Boltzmann Equation (LBE) can handle complex geometry (such as porous media and multiple flow enhancers) with ease. The geometric details of porous structure can be simulated, if desired, so that the need for empirical inputs can be eliminated. LBE method has been used in simulating various kinds of flow problems in fluid dynamics. Since it is kinetic based, it can potentially be easily integrated with the multi-phase multi-component electrochemistry on the membrane side.

In this work, we develop a 3-dimensional computational model using LBE method that is applied simultaneously to solve the flows in the channel and the porous media in the GDL. The transversal flow rate, the velocity field and the pressure distribution are analyzed. The effects of

flow enhancer location, shape, size and GDL porosity are investigated. The results may provide guidelines for effective designing of the flow enhancer.

II. Model Development

II.1. Flow field model

Hydrogen fuel and oxygen (air) in PEM fuel cells mainly flow in the direction that is parallel to the channel while the direction of the flow across the GDL is transversal. The desired transversal transport of the fuel and oxygen in a flat channel is primarily associated with the transversal diffusion. When an object is placed in the channel, the flow in the channel is forced to induce a transversal component so that the transport of the fuel/oxygen across the GDL can be greatly enhanced. However, there are numerous geometrical parameters in this problem that could affect the performance of the flow enhancer. They are:

- location of the enhancer
- size of the enhancer
- shape of the enhancer

In order to address those issues effectively, a 3-dimensional computational model is developed using LBE method to study the fluid transport on the anode side of PEM fuel cells. The Q19D3 [9, 10] lattice model is used in the simulation. The computational domain consists of the flow channel and GDL (Fig. 1) so that the transversal flow across the GDL can be investigated. The GDL is typically a carbon-based porous substrate, which is in contact with the flow field in flow channels. Since the flow in GDL is in the creeping flow region, the effect of the porous substrate is simulated using many small spheres placed in GDL. The solid objects including channel walls and particles in the GDL are identified in the discretized space and stored.
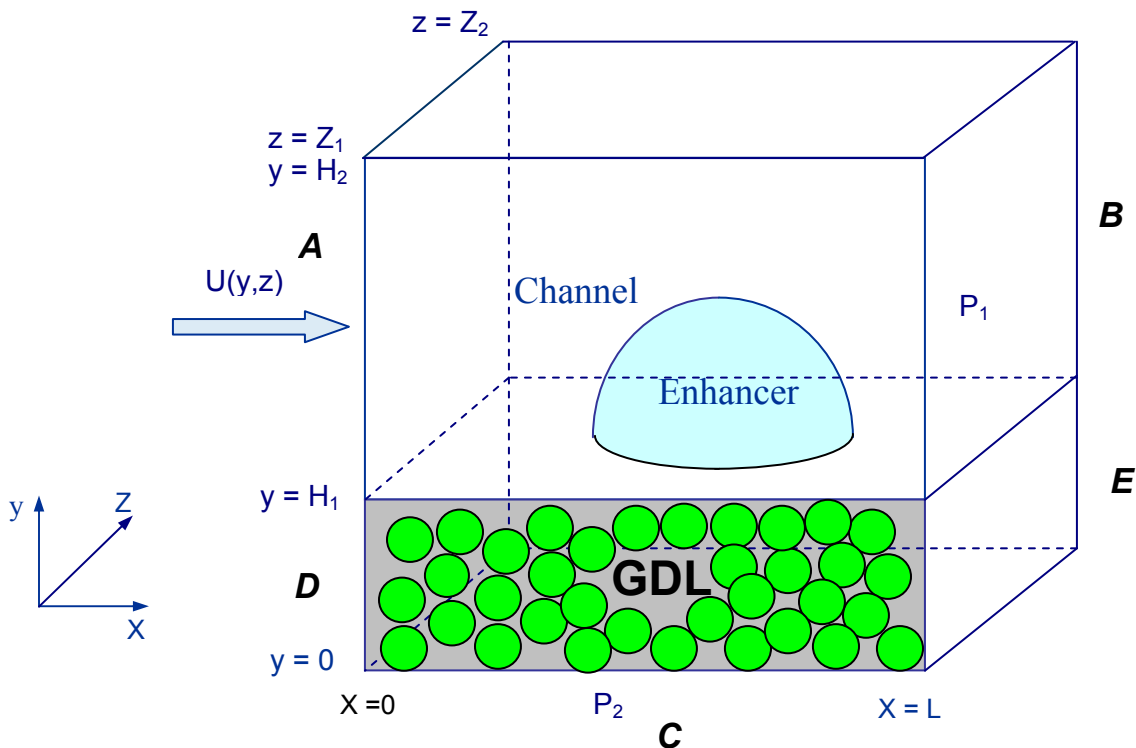

Fig. 1. PEM half-cell model with flow enhancers.

In this study, a fully developed velocity profile at the inlet of the channel (A) is specified based on the solution to a duct flow, UFD(y, z) (YX: put reference based on F. White's Viscous Flow book). Pressure values at the outlet of the channel (B) and on the lower boundary of GDL (C) are specified. Periodic boundary conditions are specified at the inlet (D) and outlet (E) of the GDL. No-slip boundary conditions are imposed at all other boundaries of the channel and particles in the GDL. The boundary conditions are as follows:

    For the flow channel:
        At x = 0, $H_1 < y < H_2$, $Z_1 < z < Z_2$ $U = U_{FD}(y, z)$
        At x = L, $H_1 < y < H_2$, $Z_1 < z < Z_2$ $P = P_1$
        where $U_{FD}(y, z)$ is the fully-developed velocity profile in a pressure drive duct flow.
    For the GDL:
    At x = 0 and x = L, $0 < y < H_1$, $Z_1 < z < Z_2$ periodic boundary conditions
        At y = 0, $0 < x < L$, $Z_1 < z < Z_2$ $P = P_2$
    No-slip boundary conditions are imposed for the following boundaries:
        $y = H_2$, $0 < x < L$, $Z_1 < z < Z_2$
        $z = Z_1$ and $z = Z_2$, $0 < x < L$, $0 < y < H_2$
   and   surfaces of flow enhancers and GDL spheres.

II.2. Lattice Boltzmann Equation Method

Conventional methods of computational fluid dynamics (CFD) compute pertinent flow field, such as velocity u and pressure p, by numerically solving the Navier-Stokes equations in space x and time t. In contract, the Boltzmann equation is a kinetic method, which deals with the single particle distribution function $f(x, \xi, t)$, where ξ is the particle velocity, in phase space (x, ξ) and time t, from which the macroscopic quantities (flow mass density ρ and velocity u) are obtained through moment integration of $f(x, \xi, t)$.

One popular kinetic model is the Bhatnagar-Gross-Krook (BGK) model with the single relaxation time approximation [8]:

$$\frac{\partial f}{\partial t} + \xi \cdot \nabla f = -\frac{1}{\lambda}\left[f - f^{(0)}\right] \tag{1}$$

where ξ is the particle velocity, $f^{(0)}$ is the equilibrium distribution function, and λ is the relaxation time to account for viscous effects. The mass density ρ and momentum density ρu are the first $(D+1)$ hydrodynamic moments of the distribution function f and $f^{(0)}$, where D is the dimension of velocity space. To solve for f numerically, Eq. (1) is first discretized in the velocity space ξ using a finite set of velocities $\{\xi_\alpha\}$ without affecting the conserved hydrodynamic moments

$$\frac{\partial f_\alpha}{\partial t} + \xi_\alpha \cdot \nabla f_\alpha = -\frac{1}{\lambda}[f_\alpha - f_\alpha^{(eq)}] . \tag{2}$$

Where $f_\alpha^{(eq)} = f^{(0)}(\boldsymbol{x}, \xi_\alpha, t)$ is the equilibrium distribution function of the ξ-th discrete velocity ξ_α. For 3-D flows, there are several cubic lattice models, such as the 15-bit (Q15D3), 19-bit (Q19D3), and 27-bit (Q27D3) models [9], which have been used in the literature. We found that

Q19D3 model is the best in terms of computational reliability and efficiency [10]. The equilibrium distributions for the Q9D2, Q15D3, Q19D3, and Q27D3 models are all of the same form

$$f_\alpha^{(eq)} = \rho\, w_\alpha\, [1 + \frac{3}{c^2}\, \mathbf{e}_\alpha \cdot \mathbf{u} + \frac{9}{2c^4}\, (\mathbf{e}_\alpha \cdot \mathbf{u})^2 - \frac{3}{2c^2}\, \mathbf{u} \cdot \mathbf{u}] \qquad (3)$$

where w_α is a weighting factor and $\mathbf{e}_\alpha$ is a discrete velocity, $c = \delta x/\delta t$ is the lattice speed, and δx and δt are the lattice constant and the time step respectively. With the velocity space discretized, the mass density and velocity are evaluated as following:

$$\rho = \sum_\alpha f_\alpha = \sum_\alpha f_\alpha^{(eq)} \qquad (4a)$$

$$\rho u = \sum_\alpha e_\alpha f_\alpha = \sum_\alpha e_\alpha f_\alpha^{(eq)} \qquad (4b)$$

Equation (2) is further discretized in space, $\mathbf{x}$, and time, t, into

$$f_\alpha(\mathbf{x}_i + \mathbf{e}_\alpha \delta t,\, t + \delta t) - f_\alpha(\mathbf{x}_i,\, t) = -\frac{1}{\tau}[f_\alpha(\mathbf{x}_i, t) - f_\alpha^{(eq)}(\mathbf{x}_i, t)] \qquad (5)$$

where $\tau = \lambda/\delta t$. The viscosity is $v = (\tau - \frac{1}{2})c_s^2 \delta t = (\tau - \frac{1}{2})/3$. The scheme is second order accurate. Equation (5) can be solved in the following two steps:

collision step: $\qquad \widetilde{f}_\alpha(\mathbf{x}_i, t) = f_\alpha(\mathbf{x}_i, t) - \frac{1}{\tau}[f_\alpha(\mathbf{x}_i, t) - f_\alpha^{(eq)}(\mathbf{x}_i, t)] \qquad (6a)$

streaming step: $\qquad f_\alpha(\mathbf{x}_i + \mathbf{e}_\alpha \delta t,\, t + \delta t) = \widetilde{f}_\alpha(\mathbf{x}_i,\, t) \qquad (6b)$

where $\widetilde{f}_\alpha$ denotes the post-collision state of $f_\alpha(\mathbf{x}_i, t)$. It is noted that the collision step is completely local, and the streaming step is uniform and is extremely simple. Eqn. (6) is explicit, easy to implement, and straightforward to parallelize.

Because the LBE method uses uniform Cartesian meshes, and the solid-fluid interfaces are usually handled by using the bounce-back scheme [11], it has the computational advantages in simulating systems of moving or stationary particles with sharp edges and handling complex geometries. For 3-dimensional lattice Boltzmann BGK model, the pressure boundary conditions are handled by employing the extrapolation scheme [12].

To investigate the effects of flow enhancers on the fluid transport in PEM fuel cells, a total of $N_x \times N_y \times N_z$ = 75 x 95 x 47 grid points lattices are used. The radius of small spheres in GDL is selected as r = 3.5 lattice units. The dimensionless relaxation time is τ = 0.8 so that v = 0.1. Velocity at the inlet of the channel is specified as parabolic profile with Umax = 0.00157 in lattice unit. The Reynolds number for the channel flow is Re = Umax(Nz-2)/v = 0.71. After the flow field is obtained, the total transversal flow rate on the bottom of the GDL is evaluated so that we can

assess various factors affecting the transversal flow rate. The dimensionless transversal flow rate $\dot{m}$ is evaluated as following:

$$\dot{m} = -\int_{Z_1}^{Z_2}\int_0^L \rho V dx dz \Big/ \int_{Z_1}^{Z_2}\int_{H_1}^{H_2} \rho U dy dz \qquad (7)$$

II. Results

A typical example is considered first. A semi-sphere flow enhancer is placed in the region considered (Fig. 2). Fuel flows across the GDL and channel. The radius of semi-sphere is r = 15 lattice units. The pressure at the outlet of the channel and on the lower boundary of GDL are selected as $P_1 = P_2 = 1.001$. The porosity in GDL is $\varepsilon = 0.7536$. For comparison purpose, three cases are studied: duct with no flow enhancer; flow enhancer on top of the duct; and flow enhancer on the bottom of duct. The results for dimensionless transversal flow rate are given in Table 1. It is seen that flow enhancers in the channel can noticeably enhance the transversal flow rate. It is also noted that the transversal flow rate is a little higher if the flow enhancer is placed at the bottom of the channel than at the top. However, the difference is so small that other factors should be investigated in order to improve the design of the flow system. Those factors include: background pressure, flow enhancer location, shape, size and GDL porosity.
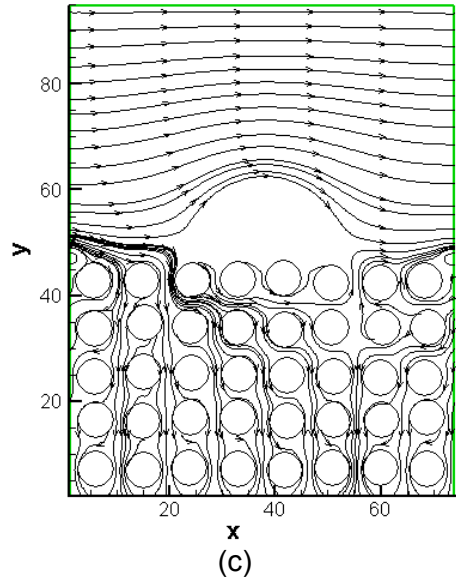

(a)   (b)

(c)
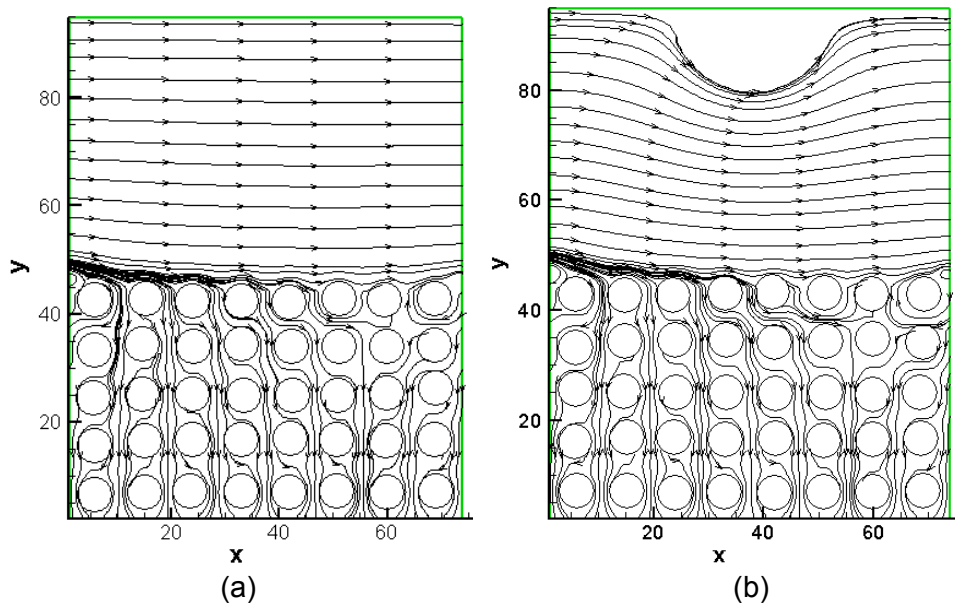
Fig. 2 Streamlines for the flow in channel and GDL with flow enhancer. (a) No flow enhancer; (b) Flow enhancer is on the upper boundary of channel; (c) Flow enhancer is on the lower boundary of channel.

Table 1. Transversal flow rate with enhancers

	No enhancer (case a)	Enhancer on top (case b)	Enhancer on bottom (case c)
Transversal flow rate $\dot{m}$	1.47e-2	1.97e-2	2.0e-2

III.1. Effects of pressure P1 and P2 on transversal flow rate

Fig. 3 shows the effects of the channel outlet pressure on the transversal flow rate while the lower boundary pressure is fixed at $P_2 = 1.01$. The radius of semi-sphere flow enhancer is again r = 15 lattice units. The semi-sphere flow enhancer is placed above GDL as Fig. 2 (c). A linear relationship between the channel outlet pressure and the transversal flow rate is observed. This is expected since for the fixed flow rate coming to the flow channel, higher pressure at one of the outlet will simply force more mass to go through the other outlet. The linear relationship is an indication that the flow is driven by pressure to overcome the viscous effect.
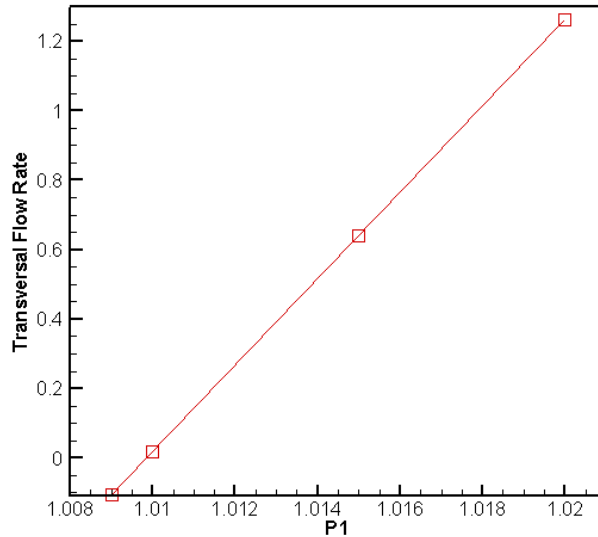
Fig. 3 Effects of channel outlet pressure P_1 on transversal flow rate.

Fig. 4 shows the effects of increasing GDL lower boundary pressure P_2 on transversal flow rate with the channel outlet pressure $P_1 = 1.01$. Again a linear relationship exists between the GDL lower boundary pressure and the transversal flow rate. As expected, an increase of the pressure on the lower boundary side of GDL leads to high transversal flow rate.
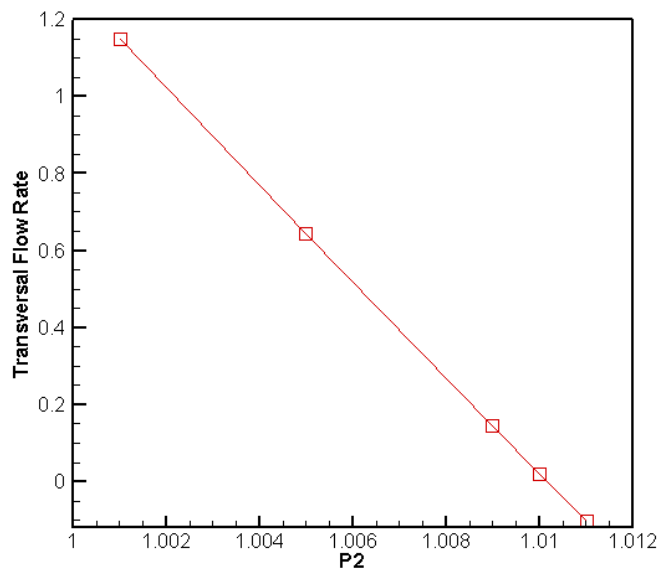

Fig. 4 Effects of GDL lower boundary pressure P_2 on transversal flow rate.

III.2. Effects of flow enhancer location on the transversal flow rate

Fig. 2 and Table 1 show the flow field and transversal flow rate results when the enhancer is placed at the top and bottom of the channel. Next consideration is given to the effect of arbitrary location of the enhancer on the transversal flow rate. Fig.5 shows transversal flow rate when the distance between the GDL and the lower boundary of flow enhancer increases. The pressure at the outlet of the channel and on the lower boundary of GDL are still at $P_1 = P_2 = 1.001$. The transversal flow rate first increases as the flow enhancer moves upwards. It reaches a maximum when the flow enhancer is placed near the middle of the channel. The transversal

flow rate then decreases as the flow enhancer moves to the upper boundary of channel. It indicates that an optimum location for the flow enhancer in the channel exists.
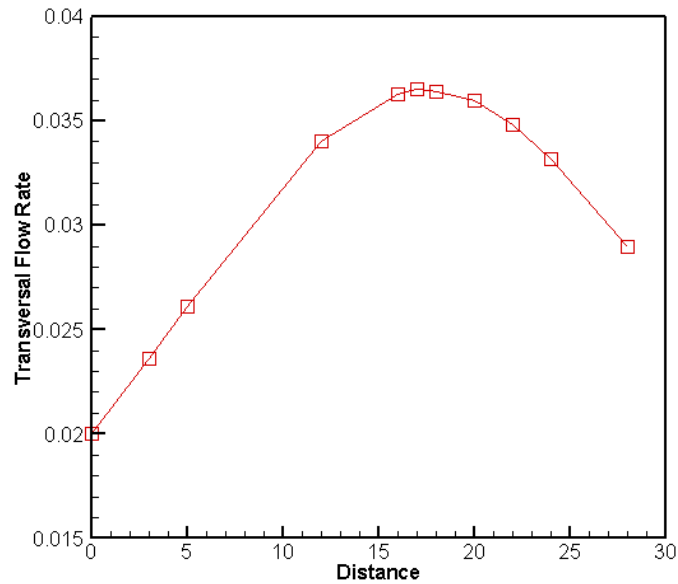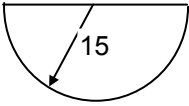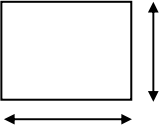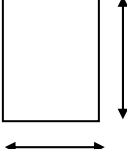

Fig. 5 Effects of distance between the GDL and the flow enhancer on transversal flow rate

III.3. Effects of flow enhancer shape on the transversal flow rate

Table 2 shows the transversal flow rate for flow enhancers with different shape. The flow enhancers are placed on the upper boundary of the channel as Fig. 2 (b). The volume of the flow enhancers is purposely kept same. The pressure at the outlet of the channel and on the lower boundary of GDL are $P_1 = P_2 = 1.001$. For cases (a) and (b), the height is the same while case (b) possesses sharp edges as opposed to smooth spherical shape in case (a). The transversal flow rate in case (b) is a little higher than in case (a). It is hypothesized that the singular nature of the flow around the sharp edge in case (b) caused large disturbance than in case (a) so that the resulting transversal flow rate $\dot{m}$ is higher. For cases (b) and case (c), both possess sharp edges. However, case (c) has a height that is almost twice of that in case (b). This definitely causes much stronger transversal disturbance to the fuel flow in the channel and results in much higher transversal flow rate $\dot{m}$.

Table 2 Effects of flow enhancer shape on transversal flow rate

	Case a	Case b	Case c
Flow enhancer shape	15	15 21.7 Lz = Lx = 21.7	31.4 15 Lz = Lx = 15
Transversal flow rate $\dot{m}$	0.0197	0.0222	0.0358

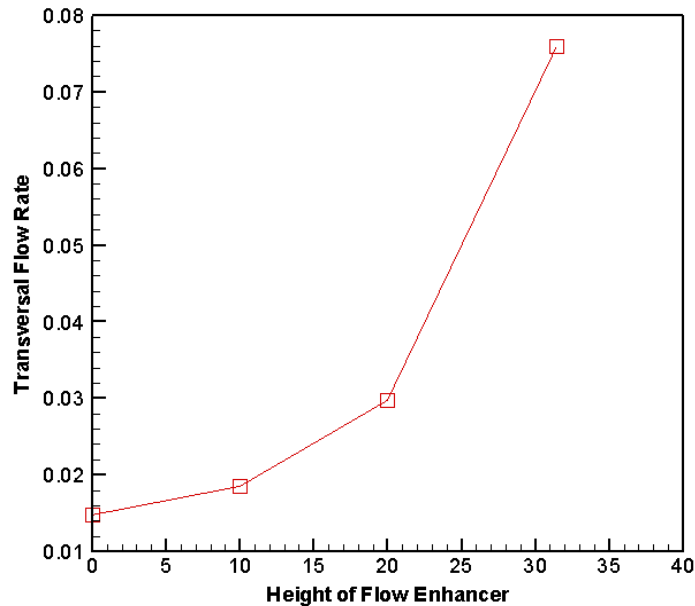**III.4. Effects of flow enhancer size on transversal flow rate**

Fig. 6 Effects of flow enhancer height on transversal flow rate.

Since it is seen in section 3.3 that a rectangular flow enhancer has stronger influence on the transversal flow rate than a hemisphere, case (c) is selected to investigate the effect of the height of the flow enhancer on transversal flow rate $\dot{m}$. The flow enhancer is placed on the upper wall of the channel. The size of flow enhancers is Lx = 15 and Lz = 42 lattice units, while the height is varied. The pressure at the outlet of the channel and on the lower boundary of GDL is selected as $P_1 = P_2 = 1.001$. `As expected, Fig. 6 shows that increasing flow enhancer height drastically increases transversal flow rate due to the larger disturbance it causes. However, this is not accomplished without a price. As shown in Fig. 7, the pressure loss (between the inlet A and outlet B in Fig. 1) also increases drastically as the height of the flow enhancer increases.
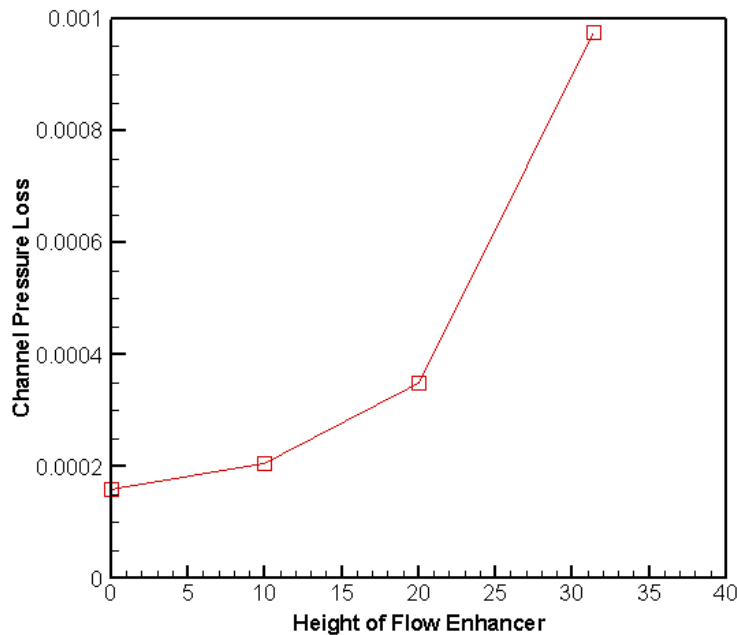

Fig. 7 Effects of flow enhancer height on pressure-loss through the flow channel.

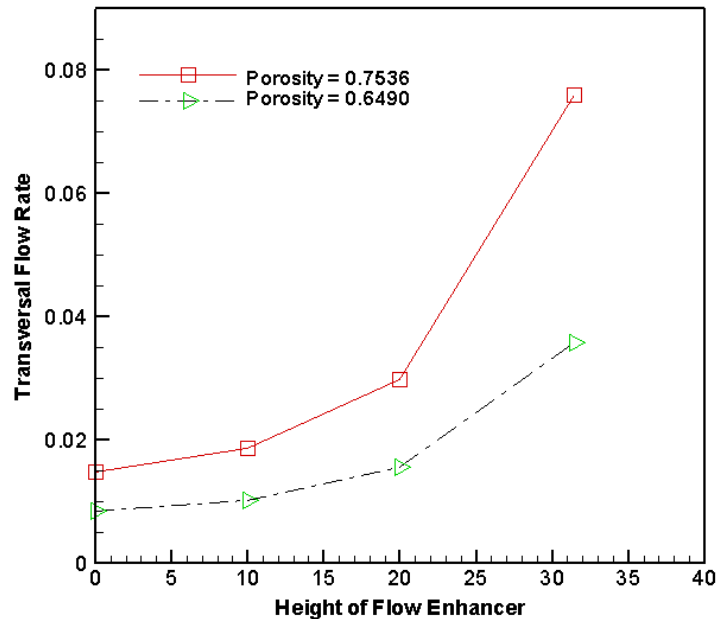### III.5. Effects of GDL porosity on transversal flow rate

Fig. 8 Effects of GDL porosity on transversal flow rate.

The porosity in the GDL in the previous discussions is relatively high. Hence the numerical values presented so far are useful in the qualitatively assessing the relative influence of various geometric factors. To ensure that the general conclusions are valid, a lower porosity is also considered by reducing the spacing between small spheres in the GDL. Fig. 8 shows the variations of the transversal flow rate vs the height of the enhancer considered in Section 3.4 at two different values of porosity. The size of flow enhancers is l_x = 15 and l_z = 42 lattice units. The pressure at the outlet of the channel and on the lower boundary of GDL are P_1 = P_2 = 1.001. Very similar behavior is observed as porosity changes. In general, the flow rate is reduced when porosity is reduced due to increased blockage in the GDL. Since the present study focuses on the effects of the enhancer on improving the transversal flow rate, the results in Fig. 8 show that: i) the present model is qualitatively correct; and ii) the results and conclusions in the previous sections are generally valid as the porosity further decreases,

IV. Conclusions

A 3-dimensional computational model using LBE method is developed to investigate the fluid transport on the anode side of PEM fuel cells, with the capabilities for simulating specific geometric details of GDL porous structure. The flows in the channel and the porous media in the GDL are solved simultaneously. Transversal flow rate across GDL can be enhanced by placing flow enhancers in the channel. Increasing the height of flow enhancers can increase the transversal flow rate significantly with high pressure-loss through the flow channel. The location of flow enhancers in the flow channel has an impact on the transversal flow rate. The transversal flow rate reaches maximum when flow enhancers are placed in the middle of the flow channel. The transversal flow rate decreases as the GDL porosity decreases.

IV. Patents, Publications, Presentations and Students from Research

IV.1. Publications

Yanxia Zhao, Renwei Mei, James F. Klausner, Effects of Geometrical Parameters on Improving the Transversal Mass Transport in PEM Fuel Cells, Proceedings of FEDSM2006, 2006 ASME Joint U.S. - European Fluids Engineering Summer Meeting, July 17-20, Miami, FL

IV.2. Students from Research

Yanxia Zhao: Recived MSc. Moved to Nevada. Switched major to statistics.

V. Acknowledgements

We would like to thank Dr. Mark Orazem, Dr. Chang-Won Park, Dr. James Klausner, and Dr. Jacob Chung for technical discussions.

VI. References

[1]   A. Kazim, H.T. Liu, P. Forges, Modeling of performance of PEM fuel cells with conventional and interdigitated flow fields, J. Applied Electrochemistry 29 (1999) 1409.
[2]   C.Y. Soong, W.M. Yan, C.Y. Tseng, H.C. Liu, F. Chen, H.S.Chu, Analysis of reactant gas transport in a PEM fuel cell with partially blocked fuel flow channels, J. Power Sources 143 (2005) 36.
[3]   V. Gurau, H. Liu, S. Kakac, Two-dimensional model for proton exchange membrane fuel cells, AIChE J. 44(11)(1998) 2410-2422.
[4]   J.S. Yi, T.V. Nguyen, An along-the-channel model for proton exchange membrane fuel cells, J. Electrochem. Soc. 145 (4)(1998) 1149-1159.
[5]   S. Dutta, S. Shimpalee, J.W.Van Zee, Numerical prediction of mass-exchange between cathod and anode channels in a PEM fuel cell, Int. J. Heat and Mass Transfer 44 (2001) 2029.
[6]   T. Berning, D.M. Lu, N. Djilali, Three-dimensional computational analysis of transport phenomena in a PEM fuel cell, Journal of Power sources 106 (2002) 284-294.
[7]   M. Grujicic, C.L. Zhao, K.M. Chittajallu, J.M. Ochterbeck, Cathode and interdigitated air distributor geometry optimization in polymer electrolyte membrane (PEM) fuel cells, Materials Science and Engineering B 108, 241-252 (2004).
[8]   P.L. Bhatnagar, E.P. Gross, M. Krook, A model for collision processes in gases, I. Small amplitude processes in charged and neutral one-component system. Phys Rev 94 (1954) 511.
[9]   Y.H. Qian, S. Succi, S.A. Orszag, Recent advances in lattice Boltzmann computing, in Annual Reviews of Computational Physics, Vol. III (D. Stauffer, Ed., World Scientific, Singapore), pp. 195-242 (1995).
[10] R. Mei, W. Shyy, D. Yu, L.-S. Luo, Lattice Boltzmann method for 3-D flows with curved boundary, J. Computational Physics 161,680-699 (2000).
[11] I. Ginzbourg and D. d'Humieres, Local second-order boundary methods for lattice Boltzmann models, J. Stat. Phys. 84,927 (1996).
[12] R.S. Maier, R.S. Bernard, D.W. Grunau, Boundary conditions for the lattice Boltzmann method, Phys. Fluids 8(7), July 1996.

Sub-Task 2: A Filter-Based, Mass-Conserving Lattice Boltzmann Method for Immiscible Multiphase Flows

Abstract

A filter-based two-distribution function lattice Boltzmann method for immiscible multiphase flows with volume conservation is proposed based on He-Chen-Zhang's LBE multiphase model (referred as HCZ model) [Journal of Computational Physics 152 (1999) 642-663]. The original HCZ model is capable of maintaining a thin interface but is prone to generating unphysical oscillations in surface tension and index function at moderate values of density ratio. With a filtering technique, the monotonic variation of the index function across the interface is maintained. Kim's surface tension formulation for diffuse-interface method [Journal of Computational Physics 204 (2005) 784-804] is then used to remove unphysical oscillation in the surface tension. Furthermore, as the density ratio increases, the effect of velocity divergence term neglected in the original HCZ model causes significant unphysical mass sources near the interface. The long time accumulation of the modeling and/or numerical errors in the HCZ model also results in the error of mass conservation of each dispersed phase. A mass correction procedure is devised to improve the performance of the method in this regard. For flows over a stationary and a rising bubble, and capillary waves with density ratio up to 100, the present approach yields solutions with interface thickness of about 5-6 lattices and no long-time diffusion, significantly advancing the performance of the LBE method for multiphase flow simulations.

I. Introduction

Multiphase flows often possess large property jumps across interfaces, resulting in multiple time and length scales [1][2]. In addition, the interface shapes and locations are not known a priori, form moving boundaries, and need to be treated as part of the solution. Substantial efforts have been made in the research community in developing techniques for such fluid flow problems. Both continuum (Navier-Stokes) [3]-[6] and kinetic (such as lattice Boltzmann) [7]-[9] models have been employed. Overall, the continuum approach has received substantially more attention, including sharp and smooth interface methods [1][10][11], Eulerian, Lagrangian and hybrid approaches [1][6]. The lattice Boltzmann equation (LBE) approach has been successfully developed to treat numerous fluid flow problems, e.g., porous media flows [12], free surface flows [13], reacting flows [14], and numerous high Reynolds number flows [7].

In the context of the LBE method for isothermal immiscible multiphase flow, various interfacial characteristics can be incorporated into the LBE model utilizing a kinetic framework. Employing the diffuse-interface approach [13], the LBE multiphase method does not track the interface explicitly and can handle complex phase topology, including breakup and merger. The phase interface is modeled as a thin zone spanning several lattices over which the fluid/flow properties vary smoothly. The surface tension is modeled as a volumetric force that acts on the fluids only over a thin zone across the interface. The volumetric force is represented in the spatial density gradient (or index function) manner. For immiscible multiphase flows without phase change, this interface modeling in the LBE requires that the interface thickness does not smear off, and dispersed phase mass is conserved, with long time evolution. The numerical methods used in this modeling should also be numerically stable for large flow/fluid property jump across the interface.

Some of the popular LBE multiphase models include Shan-Chen's (hereinafter refereed as SC) inter-particle potential model [9][17], free energy model by Swift et al.[19], He-Shan-Doolen's

model (hereinafter referred to HSD model) from kinetic theory of dense fluid [21], and an extension by He-Chen-Zhang (the HCZ model) [8]. In the SC model, the interface is modeled through non-local fluid particle interaction. It is incorporated into the lattice Boltzmann equation through an additional forcing term added to the macroscopic velocity [9][17]. The SC model has been successfully applied in some multiphase flow simulations, including stationary droplet [9], oscillation of a capillary wave [17] and drag and virtual mass forces in bubbly suspensions [18]. However, in this model, temperature is not consistent with the thermodynamics definition, the surface tension coefficient cannot be freely chosen according to the fluid property, and the viscosities of all phases must be the same. The free energy model of Swift et al. [19] does not suffer from such limitations as in SC model. It has been successfully used to simulate some multiphase flows, such as stationary bubble/droplet, capillary wave, and phase separation in a narrow capillary [19], two-dimensional bubble in Poiseuille flow [20]. However the Galilean invariance cannot be maintained in this model [22]. In the HSD model the kinetic theory of dense gases is applied to model phase segregation and surface tension. It overcomes the limitations of the SC model while maintaining the Galilean invariance. The major drawback of the HSD model is its numerical instability for flows with large gradients arising from interfacial forcing terms. This drawback of the HCZ model, shared by all LBE multiphase models, has not been adequately addressed in the literature. In the HCZ model, introducing a second lattice Boltzmann equation alleviates the numerical instability. In this second lattice Boltzmann equation the large gradient term is multiplied by a term that is proportional to the Mach number. The first lattice Boltzmann equation is used to track interfaces and its function is similar to that of a fixed grid (Eulerian) method, such as the level set method and the volume-of-fluid method. With the improved numerical stability, the Rayleigh-Taylor instability with density ratio up to about 20 [8] and the two-phase Rayleigh-Benard convection with a deformable interface [25] have been successfully simulated using the HCZ model. The computational results also show that the HCZ model is comparable in accuracy with macroscopic CFD method [22]. The detailed assessments for these three major LBE multiphase models can be found in Nourgaliev et al.'s work [22].

Recently these LBE multiphase models have been extended to flows with large density ratios. Inamuro et al. [24] used free energy model with a projection method for pressure correction to simulate multiphase flows with large density ratio. Zheng et al. [16] also used free energy model, and two lattice Boltzmann equations for flows with large density ratio, like those in the HCZ model, to capture interface and represent momentum evolution. Lee and Lin's model [13] for multiphase flows with large density ratio differs only slightly from the HCZ model. Instead of using index function, Lee and Lin directly used density as the macroscopic variable calculated from the interface-capturing lattice Boltzmann equation. They also used a potential form for surface tension formulation and hybrid discretizations for the forcing terms.

While these models can handle larger density ratios between phases, their capability of maintaining non-diffuse interface thickness for long time evolution, as in the HCZ model (See Fig. 5 in [8]), has not been adequately examined. If the interface diffuses in time, the interfacial forcing terms associated with spatial density (or index function) gradients, and hence the interfacial physics being modeled, will change accordingly. The non-diffuse interface thickness is thus very important for interfacial dynamics simulation using the LBE method.

Another critical factor for immiscible multiphase flows is mass conservation. In the LBE multiphase models, due to numerical modeling and/or numerical errors, a dispersed phase volume may change with time even though its density remains the same, leading to incorrect mass and momentum distributions. This problem is worsened as the density ratio increases

because the numerical error due to the forcing term calculations becomes larger. To date, this issue has not been investigated in the literature.

In this paper the HCZ model is adopted because of its capability of maintaining non-diffuse interface thickness for long time evolution. In order to address the above-mentioned issues, several new treatments have been incorporated. Specifically, a nonlinear filter technique [33] and a new surface tension formulation from diffuse-interface method [31] are used to remove the unphysical oscillations caused by the surface tension treatment. The interfacial compressibility effect, which was neglected in the original HCZ model, can lead to unphysical mass sources/sinks near interface regions when density ratio is large. This aspect is considered in our approach. Furthermore, a correction step is introduced to keep the mass of the dispersed phase conserved.

In the following, the numerical methods associated with the HCZ model, including the interfacial compressibility effect, the surface tension formulation, the filter technique for index function, and the mass correction for the dispersed phase are presented in Section 2. The performance of the improved LBE technique is assessed in Section 3 by simulating flows around a stationary and a rising bubble, and capillary waves. We will finish the paper with a summary and conclusion.

II. The LBE Method and the Proposed Improvement

II.1. The HCZ Model With Interfacial Compressibility Effect

In the HCZ multiphase model [8] two lattice Boltzmann equations are used to describe the evolutions of index function and pressure. The index function is used to tracks interfaces between different phases. These two lattice Boltzmann equations were derived from two discretized Boltzmann equations:

$$\frac{\partial f_\alpha}{\partial t} + \mathbf{e}_\alpha \cdot \nabla f_\alpha = -\frac{f_\alpha - f_\alpha^{eq}}{\tau} + \frac{(\mathbf{e}_\alpha - \mathbf{u}) \cdot \nabla \psi(\phi)}{\phi RT} f_\alpha^{eq} \tag{1}$$

$$\frac{\partial g_\alpha}{\partial t} + \mathbf{e}_\alpha \cdot \nabla g_\alpha = -\frac{g_\alpha - g_\alpha^{eq}}{\tau} + (\mathbf{e}_\alpha - \mathbf{u}) \cdot \left[\Gamma_\alpha(\mathbf{u})(\mathbf{F} + \mathbf{G}) - (\Gamma_\alpha(\mathbf{u}) - \Gamma_\alpha(0)) \nabla \psi(\rho) \right] \tag{2}$$

The hydrodynamic properties can be obtained from the distribution functions f and g

$$\phi = \sum_\alpha f_\alpha \qquad p_h = \sum_\alpha g_\alpha \qquad \rho RT \mathbf{u} = \sum_\alpha \mathbf{e}_\alpha g_\alpha \tag{3}$$

where ϕ is index function, p_h is hydrodynamic pressure , $\mathbf{u}$ is macroscopic velocity, T is temperature, R is gas constant. In Eq. (1), f_α denotes $f(\mathbf{x}, \mathbf{e}_\alpha, t)$, which is the distribution function in the direction of the αth discrete velocity $\mathbf{e}_\alpha$, τ is dimensionless relaxation time, and $\mathbf{x}$ represents physical space coordinate, $f_\alpha^{(eq)}$ is the corresponding equilibrium distribution function in the discrete velocity space

$$f_\alpha^{eq} = \phi \Gamma(\mathbf{u}), \tag{4}$$

where ϕ is the index function and $\Gamma(\mathbf{u}) = \frac{1}{(2\pi RT)^{D/2}} \exp\left[-\frac{(\boldsymbol{\xi} - \mathbf{u})^2}{2RT} \right]$. In Eq. (2), the distribution function g is defined from the distribution function f by

$$g_\alpha = RT f_\alpha + \Gamma(0) \psi(\rho) \tag{5}$$

The corresponding equilibrium distribution function g_α^{eq} is

$$g_\alpha^{eq} = RT f_\alpha^{eq} + \Gamma(0) \psi(\rho). \tag{6}$$

The functions ψ in Eq. (1), (2) and (5) represent exclusively the volumetric effect, and are defined by

$$\psi(\rho) = p_h - \rho RT \qquad (7)$$

$$\psi(\phi) = p_{th} - \phi RT \qquad (8)$$

where p_{th} is thermodynamic pressure calculated from equation of state. He et al. [8] used Carnahan-Starling equation of state in their model [26][27]

$$p_{th} = \phi RT \frac{1 + \dfrac{b\phi}{4} + \left(\dfrac{b\phi}{4}\right)^2 - \left(\dfrac{b\phi}{4}\right)^3}{\left(1 - \dfrac{b\phi}{4}\right)^3} - a\phi^2 , \qquad (9)$$

where a and b are two constants. From the van der Waals theory, if fluid temperature is lower than its critical point, phase segregation appears due to the molecular attraction. In the p-V-T state diagram, the curve plotted from Eq. (9) has a mechanical unstable portion, which represents the different separated phases [8]. Therefore, Eq. (9) plays a key role in phase segregation in the HCZ model.

Generally the gradient of $\psi(\rho)$ in Eq. (2) can be very large across interfaces because of the sharp change of phase densities. By introducing another distribution function g, the effect of the gradient of $\psi(\rho)$ is alleviated to some extension by multiplying $\Gamma(\boldsymbol{u}) - \Gamma(\boldsymbol{0})$, which is proportional to Mach number under the limit of incompressibility.

In the HCZ model, the following incompressibility assumption is used when deriving Eq. (2) (See He et. al's paper for details [8])

$$\frac{D\psi}{Dt} = \frac{\partial \psi}{\partial t} + \boldsymbol{\xi} \cdot \nabla \psi = \frac{\partial \psi}{\partial t} + \boldsymbol{u} \cdot \nabla \psi + \boldsymbol{\xi} \cdot \nabla \psi - \boldsymbol{u} \cdot \nabla \psi = \frac{d\psi}{dt} + (\boldsymbol{\xi} - \boldsymbol{u}) \cdot \nabla \psi \qquad (10)$$

in which $\dfrac{d\psi}{dt} = \dfrac{d\psi}{d\rho}\dfrac{d\rho}{dt} = \dfrac{d\psi}{d\rho}\left(\dfrac{\partial \rho}{\partial t} + \boldsymbol{u} \cdot \nabla \rho\right) = 0$ was assumed. Although $\nabla \cdot \boldsymbol{u} = 0$ is correct theoretically for individual phases, this condition is not exactly satisfied across interfaces during computations [34]. The effect of $\nabla \cdot \boldsymbol{u}$ which represents the compressibility effect across interface therefore should remain in the LBE model. To include $\nabla \cdot \boldsymbol{u}$ into the present model, the expression $\psi(\rho) = p_h - \rho RT$ given by Eq. (7) needs simplification. The material derivative of $\psi(\rho)$ has two components: one is the material derivative of the hydrodynamic pressure $\dfrac{dp_h}{dt}$, and the other is the product of $(-RT)$ with the material derivative of density $\dfrac{d\rho}{dt}$. In these material derivatives, the unsteady terms are generally much smaller than the convection terms in one lattice time step because, for macroscopic flows, one dimensionless time step is much larger than one lattice time step, which means there is no significant change contributed from the unsteady effect. Therefore the dominant terms in these two material derivatives are the convection ones. We then can have

$$\frac{dp_h}{dt} = \frac{\partial p_h}{\partial t} + \boldsymbol{u} \cdot \nabla p_h \approx \boldsymbol{u} \cdot \nabla p_h$$

$$RT\frac{d\rho}{dt} = RT\frac{\partial \rho}{\partial t} + RT\boldsymbol{u} \cdot \nabla \rho \approx \boldsymbol{u} \cdot \nabla \rho = \boldsymbol{u} \cdot \nabla(\rho RT) \qquad (11)$$

Using dimensional analysis, Lee and Lee [13] found that the spatial derivative of hydrodynamic pressure is much smaller than that of (ρRT). Thus the hydrodynamic pressure term in $\dfrac{d\psi(\rho)}{dt}$ can be neglected

$$\frac{d\psi}{dt} = \frac{dp_h}{dt} - RT\frac{d\rho}{dt} \approx -RT\frac{d\rho}{dt} = -RT\left[\frac{\partial\rho}{\partial t} + \boldsymbol{u}\cdot\nabla\rho\right] = -RT\left[\frac{\partial\rho}{\partial t} + \nabla\cdot(\rho\boldsymbol{u})\right] + \rho RT\nabla\cdot\boldsymbol{u}. \tag{12}$$

Instead of assuming $\dfrac{d\rho}{dt} = \dfrac{\partial\rho}{\partial t} + \boldsymbol{u}\cdot\nabla\rho = 0$, we take $\dfrac{\partial\rho}{\partial t} + \nabla\cdot(\rho\boldsymbol{u}) = 0$. The material derivative of $\psi(\rho)$ can then be simplified as

$$\frac{d\psi}{dt} \approx \rho RT\nabla\cdot\boldsymbol{u} \tag{13}$$

The Eq. (10) can then be rewritten as

$$\frac{D\psi}{Dt} = (\boldsymbol{\xi} - \boldsymbol{u})\cdot\nabla\psi + \rho RT\nabla\cdot\boldsymbol{u} \tag{14}$$

With this additional term, the lattice Boltzmann equation for the distribution function g can be written as

$$\frac{\partial g_\alpha}{\partial t} + \boldsymbol{e}_\alpha\cdot\nabla g_\alpha$$
$$= -\frac{g_\alpha - g_\alpha^{eq}}{\tau} + (\boldsymbol{\xi} - \boldsymbol{u})\cdot\left[\Gamma(u)(\boldsymbol{F}_s + \boldsymbol{G}) - (\Gamma(u) - \Gamma(0))\nabla\psi(\rho)\right] + \Gamma(0)\rho RT\nabla\cdot\boldsymbol{u} \tag{15}$$

It is worth noting that the interfacial compressibility effect can be amplified when the density ratio is large since the last term in Eq. (15) is proportional to the product of density and the velocity divergence, i.e., $\rho RT\nabla\cdot\boldsymbol{u}$.

The forces F and G in Eq. (2) are surface tension and body forces, respectively. In the HCZ model the surface tension is modeled as

$$\boldsymbol{F} = \kappa\rho\nabla\nabla^2\rho \tag{16}$$

The lattice Boltzmann equations of THE HCZ model can be obtained by discretizing Eqs. (1) and (2) in physical space [28]. In order to obtain the second order accuracy and maintain the explicit computational scheme, He et al. [8] further introduced two new variables, which are

$$\overline{f}_\alpha = f_\alpha - \frac{(\boldsymbol{e}_\alpha - \boldsymbol{u})\cdot\nabla\psi(\phi)}{2RT}\Gamma_\alpha(u)\delta_t, \tag{17}$$

$$\overline{g}_\alpha = g_\alpha - \frac{1}{2}(\boldsymbol{e}_\alpha - \boldsymbol{u})\left[\Gamma_\alpha(u)(\boldsymbol{F}_s + \boldsymbol{G}) - (\Gamma_\alpha(u) - \Gamma_\alpha(0))\nabla\psi(\rho)\right]\delta_t \tag{18}$$

Including the last term in Eq. (15), the new variable $\overline{g}_\alpha$ can be rewritten as

$$\overline{g}_\alpha = g_\alpha - \frac{1}{2}(\boldsymbol{e}_\alpha - \boldsymbol{u})\left[\Gamma_\alpha(u)(\boldsymbol{F}_s + \boldsymbol{G}) - (\Gamma_\alpha(u) - \Gamma_\alpha(0))\nabla\psi(\rho)\right]\delta_t - \frac{1}{2}\Gamma(0)\rho RT\nabla\cdot\boldsymbol{u} \tag{19}$$

The lattice Boltzmann equations in terms of these two new variables are

$$\overline{f}_\alpha(\boldsymbol{x} + \boldsymbol{e}_\alpha\delta_t, t + \delta_t) - \overline{f}_\alpha(\boldsymbol{x}, t)$$
$$= -\frac{\overline{f}_\alpha(\boldsymbol{x}, t) - f_\alpha^{eq}(\boldsymbol{x}, t)}{\tau} - \frac{2\tau - 1}{2\tau}\frac{(\boldsymbol{e}_\alpha - \boldsymbol{u})\cdot\nabla\psi(\phi)}{RT}\Gamma_\alpha(u)\delta_t \tag{20}$$

$$\bar{g}_\alpha\left(\boldsymbol{x}+\boldsymbol{e}_\alpha\delta_t,t+\delta_t\right)-\bar{g}_\alpha\left(\boldsymbol{x},t\right)=-\frac{\bar{g}_\alpha\left(\boldsymbol{x},t\right)-g_\alpha^{eq}\left(\boldsymbol{x},t\right)}{\tau}$$
$$+\frac{2\tau-1}{2\tau}\left\{\left(\boldsymbol{e}_\alpha-\boldsymbol{u}\right)\cdot\left[\Gamma\left(u\right)\left(\boldsymbol{F}_s+\boldsymbol{G}\right)-\left(\Gamma\left(u\right)-\Gamma\left(0\right)\right)\nabla\psi\left(\rho\right)\right]+\Gamma\left(0\right)\rho RT\nabla\cdot\boldsymbol{u}\right\}\delta_t \tag{21}$$

The macroscopic variables can be calculated from the moments of the new distribution functions

$$\phi=\sum\bar{f}_\alpha, \tag{22}$$

$$p_h=\sum\bar{g}_\alpha-\frac{1}{2}\boldsymbol{u}\cdot\nabla\psi\left(\rho\right)\delta_t \tag{23}$$

$$\rho RT\boldsymbol{u}=\sum\boldsymbol{e}_\alpha\bar{g}_\alpha+\frac{1}{2}RT\left(\boldsymbol{F}_s+\boldsymbol{G}\right)\delta_t. \tag{24}$$

Density and viscosity can be computed through a linear interpolation from ϕ

$$\rho=\rho_l+\frac{\phi-\phi_l}{\phi_h-\phi_l}\left(\rho_h-\rho_l\right) \tag{25}$$

$$v=v_l+\frac{\phi-\phi_l}{\phi_h-\phi_l}\left(v_h-v_l\right) \tag{26}$$

The above formulation is equivalent to the following macroscopic equations [29]

$$\frac{\partial\phi}{\partial t}+\nabla\cdot\left(\phi\boldsymbol{u}\right)=-\lambda\nabla\cdot\left[\frac{\phi}{\rho}\nabla p\left(\rho\right)-\nabla p\left(\phi\right)\right] \tag{27}$$

$$\frac{1}{\rho RT}\frac{\partial p}{\partial t}+\nabla\cdot\boldsymbol{u}=0 \tag{28}$$

$$\rho\left[\frac{\partial\boldsymbol{u}}{\partial t}+\left(\boldsymbol{u}\cdot\nabla\right)\boldsymbol{u}\right]=-\nabla p+\nabla\cdot\left[\rho v\left(\nabla\boldsymbol{u}+\boldsymbol{u}\nabla\right)\right]+\kappa\nabla\nabla^2\rho+\boldsymbol{G} \tag{29}$$

For D2Q9 lattice Boltzmann model, the function $\Gamma\left(\boldsymbol{u}\right)$ in Eq. (4) is

$$\Gamma\left(\boldsymbol{u}\right)=w_\alpha\left[1+\frac{3\boldsymbol{e}_\alpha\cdot\boldsymbol{u}}{c^2}+\frac{9\left(\boldsymbol{e}_\alpha\cdot\boldsymbol{u}\right)^2}{2c^4}-\frac{3\boldsymbol{u}^2}{2c^2}\right] \tag{30}$$

where $c=\delta x/\delta t$, δx and δt are lattice units in length and time respectively; w_α is weighted coefficient given by

$$w_0=\frac{4}{9},\quad w_1=w_3=w_5=w_7=\frac{1}{9},\quad w_2=w_4=w_6=w_8=\frac{1}{36}, \tag{31}$$

and the discrete velocities $\left(\boldsymbol{e}_\alpha\right)$ are as follows

$$e_0=0$$
$$\boldsymbol{e}_\alpha=c\left[\cos\left(\left(\alpha-1\right)\pi/4\right),\sin\left(\left(\alpha-1\right)\pi/4\right)\right]\qquad\text{for }\alpha=1,3,5,7 \tag{32}$$
$$\boldsymbol{e}_\alpha=\sqrt{2}c\left[\cos\left(\left(\alpha-1\right)\pi/4\right),\sin\left(\left(\alpha-1\right)\pi/4\right)\right]\quad\text{for }\alpha=2,4,6,8$$

The kinetic viscosity is independent of surface force and is related to the non-dimensional relaxation time as

$$v=\left(\tau-0.5\right)RT\delta_t \tag{33}$$

Zhang et al. [29] have used the following integral relationship to analytically relate surface tension σ with the coefficient κ:

$$\sigma=\kappa I\left(a\right)=\kappa\int_{-\infty}^{\infty}\left(\frac{\partial\phi}{\partial z}\right)^2 dz \tag{34}$$

where z is a direction normal to a flat interface.

In Eq. (21), the last term $\left[\Gamma(\boldsymbol{u})-\Gamma(\boldsymbol{0})\right]\nabla\phi$ can be written as

$$\left[\Gamma(\boldsymbol{u})-\Gamma(\boldsymbol{0})\right]\nabla\phi = w_\alpha\left[\frac{3\boldsymbol{e}_\alpha\cdot\boldsymbol{u}}{c^2}+O\left(\boldsymbol{u}^2\right)\right]\nabla\phi \tag{35}$$

Since the high order term $O\left(\boldsymbol{u}^2\right)$ is proportional to square of Mach number, they can be neglected under the low Mach number condition.

II.2. Surface Force Formulation

The surface tension in the HCZ model is calculated from Eq. (16). With this formulation, Rayleigh-Taylor instability is successfully simulated [8]. However the surface tension from this formulation changes its direction across interfaces, which is illustrated via a stationary bubble (density ratio 3, viscosity ratio 1) in Fig. 1. The surface tension of this bubble calculated from Eq. (16) is plotted along the vertical central cross-section. The surface tension changes its direction across the bubble interface, generating a wiggle over the interface region. This surface tension wiggle can lead to significant velocity and pressure changes over the interface, and always causes numerical instability at large density ratio, even though its effect on numerical stability is limited as density ratio is small.

Although the surface tension in the HCZ model results from intermolecular attraction [8], it is modeled as a body force (See Eq. (21)). Thus other continuum surface force formulation can be used to reduce such unphysical oscillations caused by the surface tension. Since the LBE multiphase models can be considered as one of diffuse-interface methods [30], Kim's formulation for diffuse-interface model [31] is used in this work to replace the surface tension formulation in the HCZ model,

$$F_s = -\kappa\nabla\cdot\left(\frac{\nabla\phi}{|\nabla\phi|}\right)|\nabla\phi|\nabla\phi \tag{36}$$

where κ is the coefficient calculated from Eq. (34). The same discretization form of Kim's formulation [31] is adopted for Eq. (36). With this new surface tension formulation, the surface tension for the same stationary bubble is shown in Fig. 2. No unphysical wiggles in the surface tension profile exist.

II.3. A Filter Technique for Index Function

The surface tension calculated from Kim's formulation does not have unphysical wiggle only if monotonic variation of the index function is maintained (See Eq. (36)). To ensure the monotonic variation of the index function across the interface, a filter technique used for solving convection-diffusion equation by finite difference [33] is applied to the HCZ model to remove local extremes. The idea of this filter technique is explained as follow.

If the index function has a local extreme with respect to its neighbors, its value would increase (decrease) to the minimum (maximum) value of its neighbors. The filtering algorithm proceeds by first scanning the index function on a node and its neighbors. If it is a local extreme with respect to its neighbors, a correction is made on this node and additional corrections on its neighbors to maintain index function conservation.

Let $\phi_{(I,J)}$ represents the index function on a tested node, $\phi_{(I,J)}$ represents the index function on its eight neighbors, $\phi_{(i,j)\min}$ represent the index function on a neighbor node with minimum value,

and $\phi_{(I,J)}$ represent the index function on a neighbor node with maximum value. Then the filter technique can be described as

if ($\phi_{(I,J)}$ < all $\phi_{(I,J)}$ on its neighbor points)

        distance=abs($\phi_{(I,J)} - \phi_{(i,j)\min}$)

  $\phi_{(I,J)}$ = $\phi_{(i,j)\min}$

        all $\phi_{(i,j)} \neq \phi_{(i,j)\min}$ on neighbor points = $\phi_{(I,J)}$ − distance/7.0

else if ($\phi_{(I,J)}$ > all $\phi_{(I,J)}$ on its neighbor points)

        distance=abs($\phi_{(I,J)} - \phi_{(I,J)}$)

  $\phi_{(I,J)}$ = $\phi_{(i,j)\max}$

        all $\phi_{(i,j)} \neq \phi_{(i,j)\max}$ on neighbor points = $\phi_{(I,J)}$ + distance/7.0

endif

By adjusting the index functions on its neighboring points, this filter algorithm ensures the conservation of the index function. By using this filter local minima/maxima as well as the associated oscillations are removed and monotonic variation of the index function can be maintained. Since the filter is only implemented on the nearest and the next nearest neighbor points, the diffusion effect of the filter is limited to only in one lattice. Another advantage of this filter is that it is easy to implement and has much less computational overhead.

II.4. Mass Correction

For all the LBE multiphase models described in Section 1, the macroscopic volumes of different phases are calculated from distribution functions. There is no intrinsic mechanism to enforce mass conservation within each phase (assuming constant density in individual phases) in LBE multiphase modeling. Since computational errors, such as large gradient calculations across interfaces, can accumulate and propagate over the whole computational domain, the macroscopic mass may not conserve after long time computing. This issue has not ever been addressed in any LBE multiphase models.

In the HCZ model the density profile is determined by the index function whose evolution is governed by Eq. (20). The dispersed phase volume can be obtained from the index function distribution. On the macroscopic level, the index function evolution equation Eq. is equivalent to Eq. (27). On the RHS of Eq. (27), $p\phi$ is the thermodynamics pressure in term of the index function ϕ, while $p(\rho)$ is the hydrodynamic pressure in term of the density ρ. Due to the presence of interfaces, the RHS of Eq. (27) may not be negligibly small in the region near the interface, especially for high density-ratio flows [34]. This term can result in non-conservation of volume/mass that can accumulate over time and destabilize the computation.

In order to ensure the mass conservation, a correction step is required for high density ratio. In this paper the volume of the dispersed phase, V, is corrected using the method described in [35]

$$\frac{\partial \phi}{\partial \tau} = \left(V - V_0\right)\left|\nabla \phi\right| \tag{37}$$

where V is the dispersed phase volume before the correction, V_0 is the initial volume of the dispersed phase, and τ is an artificial time. Eq. (37) is computed till the steady state $V=V_0$ is reached. This correction step is based on the consideration that the density of the fluid in each phase remains the same. If the density changes due to, e.g., pressure variation, then a

generalization of the above procedure needs to be devised. Eq. (37) can also be recast in another form as

$$\frac{\partial \phi}{\partial \tau} + \boldsymbol{u} \cdot \nabla \phi = 0 \qquad (38)$$

where $\boldsymbol{u} = (V_0 - V)\frac{\nabla \phi}{|\nabla \phi|}$. This is an advection equation. Thus high-order schemes can be used for this equation to avoid spatial oscillations across discontinuities. In this paper, a finite volume method is used to solve Eq. (38) with the second order essentially non-oscillatory (ENO) scheme for the advection term. In discretizing Eq. (38) in space, the lattice node is located at the center of a computational cell. The second order ENO scheme for the advection term discretization is illustrated at the east surface of a computational cell:

$$\left.\frac{\partial \phi}{\partial x}\right|_{e1} = \frac{\phi_E - \phi_P}{\Delta x}, \qquad \left.\frac{\partial \phi}{\partial x}\right|_{e2} = \frac{\phi_P - \phi_W}{\Delta x} \qquad \text{if} \quad u \geq 0$$

$$\left.\frac{\partial \phi}{\partial x}\right|_{e1} = \frac{\phi_P - \phi_E}{\Delta x}, \qquad \left.\frac{\partial \phi}{\partial x}\right|_{e2} = \frac{\phi_E - \phi_{EE}}{\Delta x} \qquad \text{if} \quad u < 0 \qquad (39)$$

$$\left.\frac{\partial \phi}{\partial x}\right|_{e} = \min\left(\text{abs}\left(\left.\frac{\partial \phi}{\partial x}\right|_{e1}, \left.\frac{\partial \phi}{\partial x}\right|_{e2} \right) \right)$$

where P is the lattice node and also the center of the finite volume; E is the east lattice node next to P; W is the west lattice node next to P. The time derivative is discretized using first order Euler's scheme.

III. Numerical Assessment of the Proposed Techniques

III.1. Single Mode Rayleigh-Taylor Instability (RTI) With Density Ratio 9

The original HCZ model has been successfully employed to simulate the RTI without surface tension [8]; the comparison with theoretical analysis [36] is very good. At low density ratio, say 3, the jump properties across the interface do not show noticeable numerical instability. In this study, the same RTI problem at a higher density ratio of 9 is used to assess the performance of the extended HCZ model by comparing with the original HCZ model.

The computation is performed in a 2D rectangular domain of width W with no-slip condition on the top and bottom walls and periodic boundary condition on the sides. The kinetic viscosities of both fluids are set to be same. The dimensionless parameters, Reynolds number and Atwood number, used to describe the problem, are defined as $\mathrm{Re} = \frac{\sqrt{Wg}W}{\nu}$ and $At = \frac{\rho_h - \rho_l}{\rho_h + \rho_l}$, where g is gravity, ρ_h and ρ_l are the densities of heavy and light fluids, respectively. The time scale in this problem is $T = \sqrt{W/g}$. For an otherwise flat interface, an initial perturbation of 10% amplitude (normalized by the wavelength) in the interface is specified at t=0 in order to promote the growth of the instability. The more detail computational setup can be found in [8].

The theoretical growth rate based on linear analysis [36] and numerical growth rate presently obtained are shown in Fig. 3. The good agreement between the numerical and theoretical growth rate indicates that the extended HCZ model is capable of capturing accurately the physics of this complex flow [8][32].

Fig. 4 shows the evolution of the interface from 10% initial perturbation computed on a 256×1024 grid with Re=2048 and At=0.8 (density ratio 9). In the early stage (t/T<1.0), the interface evolution of both the HCZ and the extended HCZ are almost identical. However at later stage (t/T~1.5), the HCZ model creates significant oscillations in the near interface region. After t/T=1.5, the numerical instability in the HCZ model causes the simulation to blow up. Comparing with the HCZ model, the extended HCZ model at t/T=1.5 performs much better in the interfacial region in the entire period of simulation. The oscillations near the interface of the original HCZ solution can be clearly seen from the density profile along the central vertical section of the computational domain, as shown in Fig. 5. Clearly, the use of the filter in the extended HCZ model has improved the numerical stability.

To further systematically examine the performance of the present extended HCZ multiphase model, besides the single mode RTI, computations for stationary bubbles, capillary waves and rising bubbles are carried out in the following sections for larger density ratio up to 100.

III.2 Stationary Bubble

III.2.1. A stationary bubble with diameter d=40 lattices

The computational parameters for this stationary bubble are listed below:

$$La = \frac{\rho_h \sigma d}{\mu_h^2} = 100, \quad \frac{\rho_h}{\rho_l} = 100, \quad \frac{\mu_h}{\mu_l} = 10$$

The computation of this case was performed on a computational domain of 201x201 lattices. A circular bubble of diameter 40 is placed at the center of the domain with the periodic boundary condition for all boundaries. The surface tension is set to 0.27777 in this case. The dimensionless time is defined as $t_{ch} = \frac{\mu d}{\sigma}$, which is equal to 480 lattice time steps for this case.

Ideally the velocity should be zero everywhere and the pressure drop across the interface balances the surface tension force dictated by the Young-Laplace equation:

$$\Delta p = \frac{\sigma}{R}, \qquad \text{for 2D bubbles}. \tag{40}$$

The theoretical pressure jump in this case is $\Delta p = \sigma / R = 0.1388$. However due to numerical errors causing imbalance of interfacial stresses, a stationary bubble simulated by continuum surface force methods always has a spurious velocity field. As one of the continuous interface method, the LBE method is no exception. The spurious velocity of this stationary bubble is shown in Fig. 6a. Fig. 6b shows the pressure variation across the bubble. Significant unphysical oscillation associated with the original HCZ model is now essentially removed by using the new surface tension formulation with the filter technique.

The density profiles at dimensionless time t=0, and t=100 (48000 lattice time steps) are shown in Fig. 7a. Very little variation in the density profile is observed. The interface thickness is maintained within 5-6 lattices, and does not diffuse out with time during the simulation. Furthermore the computed density profiles remain to be monotonic across interfaces (See Fig. 4b), which is a significant improvement over the original HCZ model.

III.2.2. Effect of grid resolution on the accuracy of computed pressure jump

There are several ways to characterize the computational accuracy of the interfacial problems. In several studies, the dimensionless maximum absolute value of the spurious velocity is often used as an indication of the error in the solution for stationary bubble case [37]. For LBE method, because the lattice speed and lattice spacing are all of unity while the resolution of the computation is dictated by the number of lattice across the bubble, it is not possible to maintain the same dimensionless parameters while varying the resolution [38]. Thus an alternative measure for the accuracy of the numerical solution based on the pressure variation is used. Following [39], an average pressure drop is defined as follows,

$$\Delta p_{num} = \frac{1}{N_d} \sum_{i,j=1}^{N_d} \left(p_{i,j} - p_{ref} \right) \tag{41}$$

where N_d is the number of lattice nodes lying within the bubble and p_{ref} is the liquid static pressure far away from the bubble. Because of possible numerical oscillation, the region of the bubble is defined as the region where $\rho \geq 1.01 \rho_g$. For a sharp interface, the theoretical value for Δp_{exact} is given by Eq. (40). Hence $\left(1 - \frac{\Delta p_{num}}{\Delta p_{exact}} \right)$ will measure the relative error of the LBE solution in capturing the pressure jump across the interface.

Two stationary bubble cases with different grid resolutions inside the bubbles but same Laplace number (La=100) are computed. Density ratio and viscosity ratio are 100 and 10 respectively. One bubble has 40 lattices in diameter and the other has 80 lattices. The evolutions of the maximum spurious velocity with dimensionless time are shown in Fig. 8. The maximum spurious velocities in both cases approach to constants, indicating the computational steady states are reached. Table 1 lists the relative error of the pressure drop, $\left(1 - \frac{\Delta p_{num}}{\Delta p_{exact}} \right)$, for these two cases with different grid resolution. The value for the fine grid case is about half of that for the coarse grid case, indicating that the computation carried out on the fine grid has better accuracy.

The effect of different Laplace numbers on the computational error is also examined. It is found that for La=100 and La=1000 there is no appreciable difference in $\left(1 - \frac{\Delta p_{num}}{\Delta p_{exact}} \right)$ as shown in Table 2. Table 3 and Table 4D show the effect of density and viscosity ratios on the solution accuracy. It is observed that they do not cause significant changes in $\left(1 - \frac{\Delta p_{num}}{\Delta p_{exact}} \right)$. The present finding is similar to that reported in [37] for a stationary bubble by using Navier-Stokes solvers.

III.3. Capillary Wave

The second test case is a capillary wave, a small-amplitude motion of two superposed viscous fluids with same viscosity [40]. In this test, gravity is not considered. Initially the interface between two stationary fluids is set up as a wave with a small-amplitude H_0, as shown in Fig. 9. It damps off with time due to the interaction between viscous force and surface tension. The no-slip boundary condition is used on the top and bottom boundaries and the periodic boundary condition is used on the lateral boundaries. In this problem, the length scale is taken as k^{-1}, in

which k is the wave number defined as $k = \dfrac{2\pi}{NX}$ and NX is the domain width. The time scale is taken as ω_0^{-1}, in which ω_0 is the frequency defined as $\omega_0 = \dfrac{\sigma k^3}{\rho_1 + \rho_2}$.

Based on these time and length scales, the dimensionless time and viscosity which characterize the wave motion are

$$t' = \omega_0 t, \qquad \bar{\varepsilon} = \frac{\nu k^2}{\omega_0} \tag{42}$$

where ν is the kinematic viscosity of the fluid. With these dimensionless time and viscosity, the theoretic solution for the dimensionless amplitude $a = H / H_0$ given by [40] is

$$a(t') = \frac{4(1-4\beta)\bar{\varepsilon}^2}{8(1-4\beta)\bar{\varepsilon}^2 + 1} erfc\left(\sqrt{\bar{\varepsilon}t'}\right) + \sum_{i=1}^{4} \frac{z_i \omega_0^2}{Z_i \left(z_i^2 - \bar{\varepsilon}\omega_0\right)} \exp\left[\frac{\left(z_i^2 - \bar{\varepsilon}\omega_0\right)t'}{\omega_0}\right] erfc\left(z_i \sqrt{\frac{t'}{\omega_0}}\right) \tag{43}$$

where z_i are the four complex roots of the following equation

$$z^4 - 4\beta\sqrt{\bar{\varepsilon}\omega_0}z^3 + 2(1-6\beta)\bar{\varepsilon}\omega_0 z^2 + 4(1-3\beta)\left(\bar{\varepsilon}\omega_0\right)^{3/2} z + (1-4\beta)\left(\bar{\varepsilon}\omega_0\right)^2 + \omega_0^2 = 0 \tag{44}$$

and $Z_i = \prod\limits_{j=1, j\neq i}^{4} \left(z_j - z_i\right)$. The parameter β is given by $\beta = \dfrac{\rho_1 \rho_2}{\left(\rho_1 + \rho_2\right)^2}$.

The test parameters taken here are $\omega_0 = 1.13 \times 10^{-3}$, $\bar{\varepsilon} = 0.116$, and ρ_h / ρ_l is 100. The initial velocity is zero for the whole domain and the distribution functions are assigned to the corresponding equilibrium values. The time evolution of the wave amplitude is shown in Fig. 10. The time evolution of the dimensionless amplitude agrees well with that given by the exact solution. The slight difference between them in the early stage may be caused by the numerical initial condition used in implementing the extended HCZ LBE model.

III.4. Two-Dimensional Rising Bubble

Two-dimensional single bubbles rising in an initially quiescent fluid due to the buoyancy force are simulated to assess the efficacy of the extended HCZ LBE model in capturing the dynamics of the two-phase flow. In this problem the effects of gravity and the surface tension determine the final steady bubble shape. Clift et al. [41] gave a bubble shape diagram in terms of Eötvos number, Morton number and Reynolds number, defined as

$$\text{Reynolds number (Re)} = \frac{\rho_h U_{ref} d}{\mu_h} \tag{45}$$

$$\text{Morton number } (M) = \frac{g\mu_h^4}{\rho_h \sigma^3} \tag{46}$$

$$\text{Eötvos number (Eo)} = \frac{\rho_h g d^2}{\sigma}. \tag{47}$$

The simulations carried out here are 2D planar bubbles. The computational domain is a rectangle consisting of 151x801 lattices. A circular bubble is initially placed at i=76, j=201 lattice node with a radius R=20 lattices. The initial velocity is set to zero for the whole domain. The no-slip boundary condition is imposed on the top and bottom and the periodic boundary condition is used for the lateral boundaries. The density ratio and viscosity ratio are 100 and 10 respectively here.

Three groups of dimensionless parameters are chosen

(1) Eo=0.971, M=1.26e-3, Re=5.19
(2) Eo=9.71, M=0.4, Re=6.92
(3) Eo=97.1, M=100, Re=9.78

For the first case, the bubble shape should almost be a circle in a 2D simulation. However, without the mass-correction, the bubble volume increases with time (Fig. 11a). At later stages, the bubble shape even changes from a circle to an ellipse due to larger rising velocity. The bubble thus cannot reach its steady state. When the correction step is applied, the bubble volume remains constant and its shape remains almost a circle during the rising process as shown in Fig. 11b.

In this rising bubble simulation, the interfacial compressibility effect is included in the extended HCZ LBE multiphase model. As shown in Eq. (21) and discussed in section 2.1, the interfacial compressibility effect cannot be neglected when density ratio is large. If the last term in Eq. (21) is not included, some unphysical mass sources/sinks will be generated along the interface and mass conservation will not be maintained. Fig. 12a shows the streamlines inside and outside this rising bubble without the last term in Eq. (21). Fig. 12b shows the streamlines of the flow inside and outside the rising bubble with the inclusion of the last term in Eq. (21). It can be clearly observed that there are mass sources/sinks next to the interface inside the bubble if the interfacial compressibility effect is not included; and these mass sources/sinks can be entirely removed when the interfacial compressibility effect is included. Fig. 13 shows the volume and velocity history for this case with mass correction. The volume of this bubble does not change with time and the bubble velocity increases at early time steps and then reaches its steady state value.

(a)   (b)   (c)
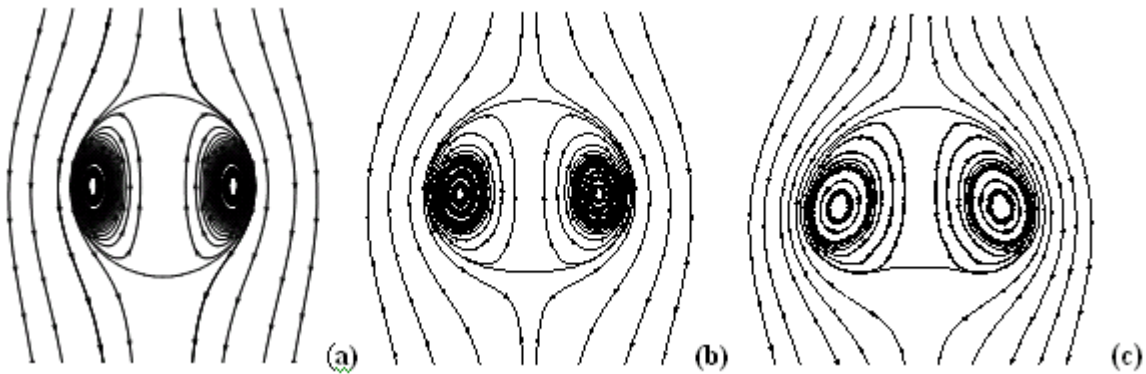
Fig. 14Fig. 14 shows the computed bubble shapes for all these three cases. Typical bubble shapes are captured using the extended HCZ LBE model.
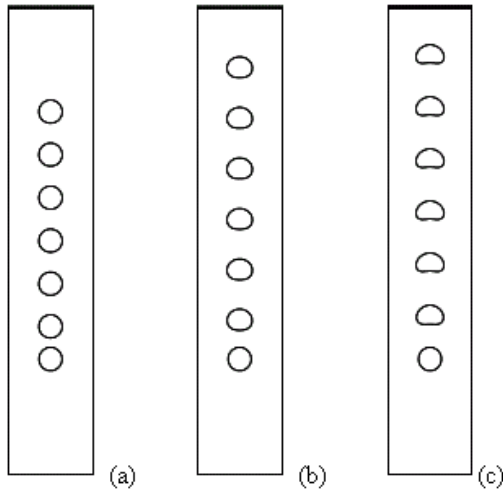
Fig. 15Fig. 15 shows the corresponding time evolutions of these bubbles. Due to larger shape deformation, the dimpled-ellipsoidal bubble rises faster than the other two bubbles.

Fig. 16 shows the velocity histories of these three bubbles. Because of the larger shape deformation comparing to cylindrical and ellipsoidal bubbles, the velocity of the dimpled-ellipsoidal bubble exhibits larger oscillations at the early rising stages. At later rising stages, all three bubble velocities do not change significantly, indicating their steady states are reached.

Fig. 17 shows the density profiles of these three bubbles on the central vertical cross section at T=0, 15 and 30 respectively. From these density profiles, it can be observed that the interfaces do not diffuse out, and interface thickness is maintained within 5-6 grids. Thus the capability of THE HCZ model for non-diffused interface thickness is still maintained when density ratio is up to O(100). This feature of this model is very desirable for interfacial dynamics.

Fig. 18 shows the evolution of another rising bubble during a period of six dimensionless time steps with Eo=97.1, M=0.971, Re=31.2, density ratio 100 and viscosity ratio 10. In the present planar 2D planar simulation, the bubble undergoes complex deformation dynamics and breaks into two larger bubbles with four satellites at the dimensionless time t=6.

IV. Conclusions

In this paper, a new filter-based LBE method for immiscible multiphase flows is developed based on the HCZ model. A surface tension formulation from diffuse-interface methods is adopted to replace that in the HCZ model and to reduce unphysical oscillations in surface tension across interfaces. The compressibility effect and mass correction are added to the HCZ model to preserve the phase volume and remove unphysical mass sources/sinks. A filtering technique is used to maintain monotonic variation of index function across interfaces that results in significant reduction of unphysical wiggles in surface tension profile. The performance of the extended HCZ LBE model is assessed using computations of single mode RTI, stationary bubbles, capillary wave, and rising 2D planar bubbles. The computational results demonstrate that the extended HCZ model can be used to simulate flows with large density ration up to O(100) while maintaining the interface thickness to within 5-6 grids through a very long period of time.

The mass conservation issue from the long time accumulation of the modeling and/or numerical errors in the HCZ model is investigated in this paper. The corresponding mass correction

procedure is applied to maintain the mass conservation on the macroscopic level, i.e. correcting the index function via Eq. (38). Although this correction yields correct physics, it counts the most computational time in one lattice time step. This step causes significant reduction of the efficiency of the LBE method. To maintain the efficiency of the LBE method, further efforts should be made to directly correct the mesoscopic distribution functions, rather than the macroscopic index function. However, correcting distribution functions could be much more difficult because, on one lattice node, more distribution functions (for example, nine distribution functions in D2Q9 model) need to be corrected on the mesoscopic level rather than one index function on the macroscopic level.

Further efforts are needed to treat multiphase flows with much higher density ratio of 1000 because as the density ratio becomes higher, the gradient of $\psi(\rho)$ in Eq. (21) can still generate numerical instability in pressure and velocity.

V. Patents, Publications, Presentations and Students from Research

V.1. Publications

1. Jianghui Chao, Renwei Mei, Rajkeshar Singh, Wei Shyy, 2007, "A Filter-Based, Mass-Conserving Lattice Boltzmann Method for Immiscible Multiphase Flows", submitted to International Journal of Numerical Method for Fluid Flow.

V.2. Presentations

Multi-Scale Computational Fluid Dynamics with Interfaces
Jianghui Chao, Renwei Mei, and Wei Shyy
59TH ANNUAL MEETING OF THE DIVISION OF FLUID DYNAMICS
Marriott Tampa Waterside, November 19-21, 2006, Tampa, Florida

V.3. Students from Research

Jianghui Chao: Received PhD. Post-doc at the University of Florida

VI. Acknowledgements

VII. References

[1]   Shyy W., Udaykumar H.S, Rao M.M, and Smith R.W. *Computational fluid dynamics with moving boundaries.* Taylor & Francis: Washington, DC, 1996 (revised printing 1997, 1998, 2001).
[2]   Shyy W. Computational modeling for fluid flow and interfacial transport. Elsevier: Amsterdam, Netherlands, 1994 (revised printing 1997).
[3]   Scardovelli R., Zaleski S. Direct numerical simulation of free-surface and interfacial flow. Annual Review of Fluid Mechanics 1991; 31: 567-603.

[4]   Tryggvason G., Bunner B., Esmaeeli A., Juric D., Al-Rawahi A., Tauber W., Han J., Nas S and Jan Y.-J. A front-tracking method for the computations of multiphase flow. Journal of Computational Physics 2001; 169: 708-759.

[5]   Osher S., Fedkiw R.P. Level set methods: an overview and some recent results. Journal of Computational Physics 2001; 169: 463-502.

[6]   Shyy W. Multiphase computations using sharp and continuous interface techniques for micro-gravity applications. Computes Rendus Mecanique 2004; 332: 375-386.

[7]   Chen S., Doolen D. Lattice Boltzmann method for fluid flows. Annual Review of Fluid Mechanics 1998; 30: 329-364.

[8]   He X., Chen S., Zhang R.A lattice Boltzmann scheme for incompressible multiphase flow and its application in simulation of Rayleigh-Taylor instability. Journal of Computational Physics 1999; 152: 642-663.

[9]   Shan X., Chen H. Lattice Boltzmann model of simulating flows with multiple phases and components. Physical Review E 1993; 47: 1815-1819.

[10]   Ye T., Mittal R., Udaykumar H.S, and Shyy W. An accurate Cartesian grid method for viscous incompressible flows with complex immersed boundaries. Journal of Computational Physics 1999; 156: 209-240.

[11]   Ye T., Shyy W., Chung J.C. A fixed-grid, sharp-interface method for bubble dynamics and phase change. Journal of Computational Physics 2001; 174: 781-815.

[12]   Chen S., Diemer K., Doolen G.D., Eggert K., Fu C., Gutman S., Travis B.J. Lattice gas automata for flow through porous media. Physica D 1991; 47: 72-84.

[13]   Lee T., Lin C.A. stable discretization of the lattice Boltzmann equation for simulation of incompressible two-phase flows at high density ratio. Journal of Computational Physics 2005; 206: 16-47.

[14]   Filippova O., Hänel D. A novel lattice BGK approach for low Mach number combustion. Journal of Computational Physics 2000; 158: 139-160.

[15]   Singh R., Shyy W. Three-dimensional adaptive Cartesian grid method with conservative interface restructuring and reconstruction. Journal of Computational Physics 2007; 224: 150-167

[16]   Zheng H.W., Shu C., Chew Y.T. A lattice Boltzmann model for multiphase flows with large density ratio. Journal of Computational Physics 2006; 218: 353-371.

[17]   Shan X., Chen H. Simulation of non-ideal gases and liquid-gas phase transitions by the lattice Boltzmann equation. Physical Review E 1994; 49: 2941-2948.

[18]   Sankaranarayanan K., Shan X., Kevrekidis I.G., Sundaresan S. Analysis of drag and virtual mass forces in bubbly suspensions using an implicit formulation of the lattice Boltzmann method. Journal of Fluid Mechanics 2002; 452: 61-96.

[19]   Swift M., Osborn W., Yeomans J. Lattice Boltzmann simulation of nonideal fluids. Physical Review Letter 1995; 75: 830-833.

[20]   Holdych D.J., Georgiadis J.G., and Buckius R.O. Migration of a van der Waals bubble: lattice Boltzmann formulation. Physics of Fluids 2001; 13: 817-825.

[21]   He X., Shan X., Doolen G.D. A discrete Boltzmann equation model for non ideal gases. Physical Review E 1998; 57: R13-R16.

[22]   Nourgaliev R., Dinh T., Theofanous T., Joseph D. The lattice Boltzmann method: theoretical interpretation, numerics and implications. International Journal of Multiphase Flow 2003; 29: 117-169.

[23]   Gonnella G., Orlandini E., Yeomans J.M. Lattice-Boltzmann simulation of complex fluids. International Journal of Modern Physics 1997; 8: 783-792.

[24]   Inamuro T., Ogata T., Tajima S., Konishi N. A lattice Boltzmann method for incompressible two-phase flows with large density difference. Journal of Computational Physics 2004; 198: 628-644.

[25] Chang Q., Iwan J., Alexander D. Application of the lattice Boltzmann method to two-phase Rayleigh-Benard convection with a deformable interface. Journal of Computational Physics 2006; 212: 473-486.

[26] Carnahan N.F, Starling K.E. Intermolecular repulsions and the equation of state for fluids. AIChE Journal 1972; 81: 1184.

[27] Carnahan N.F., Starling K.E. Equation of state for non-attracting rigid spheres. Journal of Chemical Physics 1969; 51: 635.

[28] He X., Luo L. On the theory of the lattice Boltzmann method: From the Boltzmann equation to the lattice Boltzmann equation. Physical Review E 1997; 56: 6811-6817.

[29] Zhang R., He X., Chen S. Interface and surface tension in incompressible lattice Boltzmann multiphase model. Computer Physics Communications 2000; 129: 121-130.

[30] Anderson D.M., McFadden G.B., Wheeler A.A. Diffuse-interface methods in fluid mechanics. Annual Review of Fluid Mechanics 1998; 30: 139-165.

[31] Kim J. A continuous surface tension force formulation for diffuse-interface models. Journal of Computational Physics 2005; 204: 784-804.

[32] Singh R.K., Chao J., Popescu M., Tai C-F., Mei R., Shyy W. Multiphase/multi-domain computations using Continuum and Lattice Boltzmann methods. Journal of Aerospace Engineering 2006; 19: 288-295.

[33] Shyy W., Chen M., Mittal R., Udaykumar H. On the suppression of numerical oscillations using a non-linear filter. Journal of Computational Physics 1992; 102: 49-62.

[34] Yang X., James A., Lowengrub J., Zheng X., Cristini V. An adaptive coupled level-set/volume-of-fluid interface capturing method for unstructured triangular grids. Journal of Computational Physics 2006; 217: 364-394.

[35] Son G. A numerical method for bubble motion with phase change. Numerical Heat Transfer, Part B 2001; 39: 509-523.

[36] Chandrasekhar S. Hydrodynamic and hydromagnetic stability. Dover: New York, 1981.

[37] Singh R. Three-dimensional marker-based multiphase flow computation using adaptive Cartesian grid techniques. PhD dissertation, University of Florida, 2006.

[38] Chao J. Multiscale computational fluid dynamics and heat transfer with interface. PhD dissertation, University of Florida, 2006.

[39] Brackbill J.U., Kothe D.B, and Zemach C. A continuum method for modeling surface tension. Journal of Computational Physics 1992; 100: 335-354.

[40] Prosperetti A. Montion of two superposed viscous fluids. Physics of Fluids 1981; 24: 1217-1223.

[41] Clift R., Grace J.R, and Weber M. Bubbles, drops and Particles. Academic Press: New York, 1978.

Table 1 Effect of grid resolution on computed pressure drop for Laplace number 100. The data were taken after 100 dimensionless time steps and the density and viscosity ratios were set to 100 and 10 respectively.

Grid resolution	$1-\dfrac{\Delta p_{num}}{\Delta p_{exact}}$
40 lattice in bubble diameter	0.08
80 lattice in bubble diameter	0.04

Table 2 Effect of Laplace number on the ratio of numerical pressure drop to theoretical pressure drop: Bubble diameter is 40 lattices. The data were taken at non-dimensional time = 100. Density ratio is 100 and dynamics viscosity ratio is 10.

Laplace number	$1-\dfrac{\Delta p_{num}}{\Delta p_{exact}}$
100	0.08
1000	0.08

Table 3 Effect of density ratio on pressure drop: Bubble diameter is 40 lattice units. Viscosity ratio was set to 10 for Laplace number = 100 and the data were taken at non-dimensional time = 100.

Density ratio = $\dfrac{\rho_1}{\rho_2}$	$1-\dfrac{\Delta p_{num}}{\Delta p_{exact}}$
1	0.06
10	0.07
100	0.08

Table 4 Effect of viscosity ratio on pressure drop: Bubble diameter is 40 lattice units. Laplace number = 100 and density ratio is 100. The data were taken at non-dimensional time = 100.

Viscosity ratio = $\dfrac{\mu_1}{\mu_2}$	$1-\dfrac{\Delta p_{num}}{\Delta p_{exact}}$
10	0.08
100	0.07
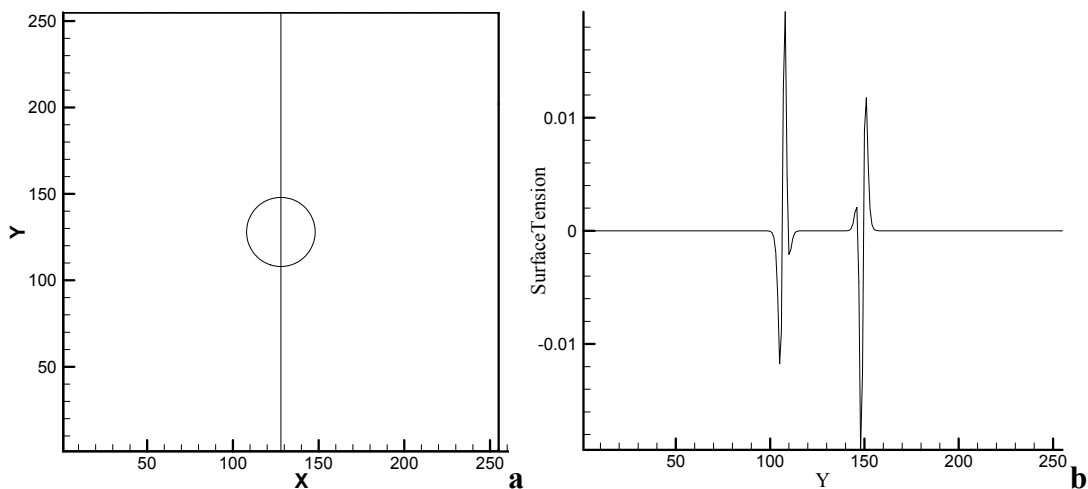
Fig. 1 Surface tension profile for a stationary bubble computed from He et al.'s method.
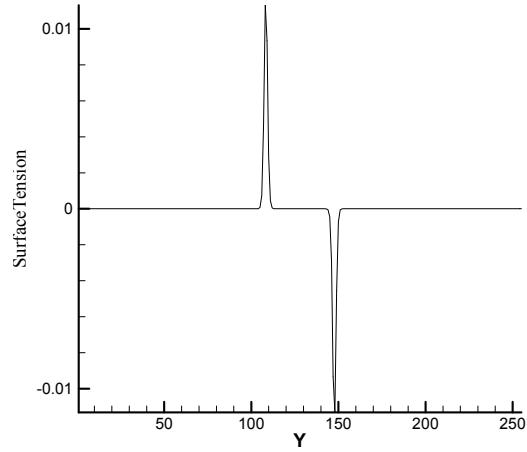
Fig. 2 Surface tension calculated by Kim's formulation.
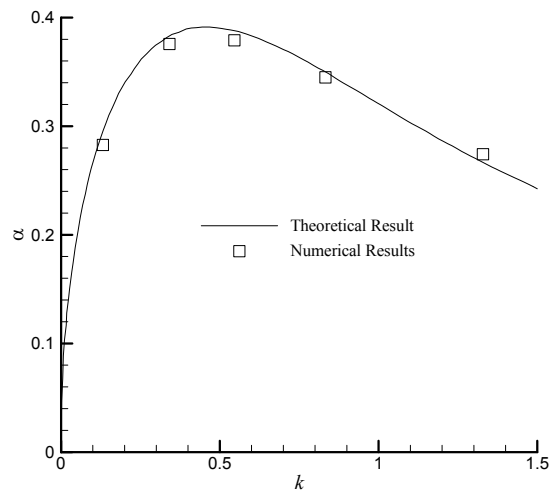
Fig. 3 The growth rate α (measured in units of $\left(g^2/v\right)^{1/3}$) of a disturbance vs. its wave numbers $k = 2\pi/W$ (measured in units of $\left(g/v^2\right)^{1/3}$).
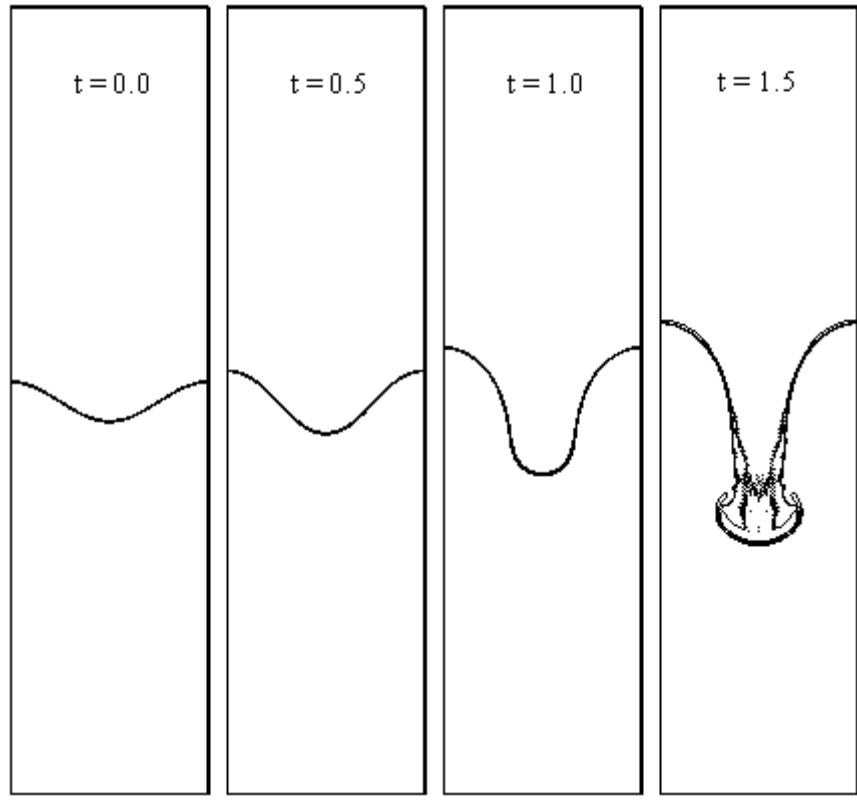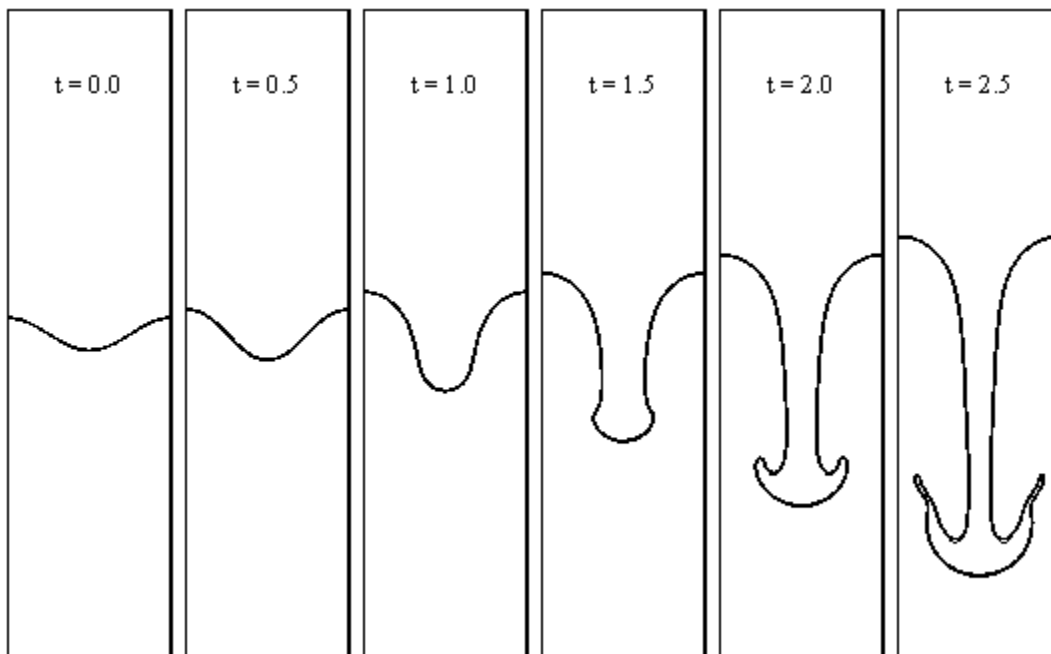
Fig. 4a

Fig. 4b

Fig. 4 Evolution of the fluid interface from a single mode perturbation for *At*=0.8 and *Re*=2048.
The time is measured in units of $\sqrt{Wg}$, where *W* is the domain width and *g* is gravity.
Fig. 4a Results from the HCZ model result. Fig. 4b Results from the extended HCZ model.
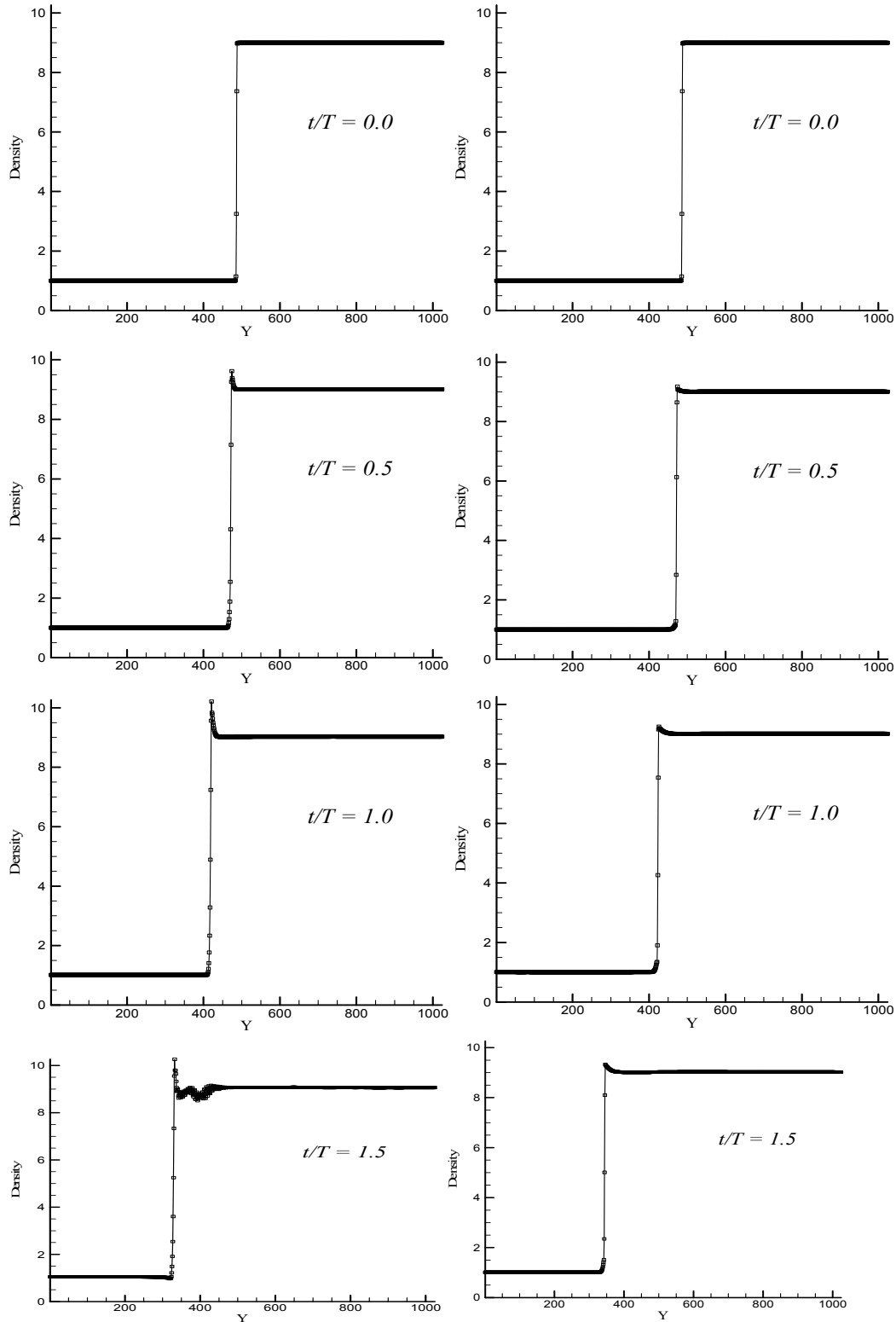
Fig. 5 Density profile across the central vertical section of the computational domain at four different time steps. The horizontal axis is the computational grid. The left panel shows the density profiles of the HCZ model and the right one shows the density profiles of the extended HCZ model. *Re*=2048 and *At*=0.8.
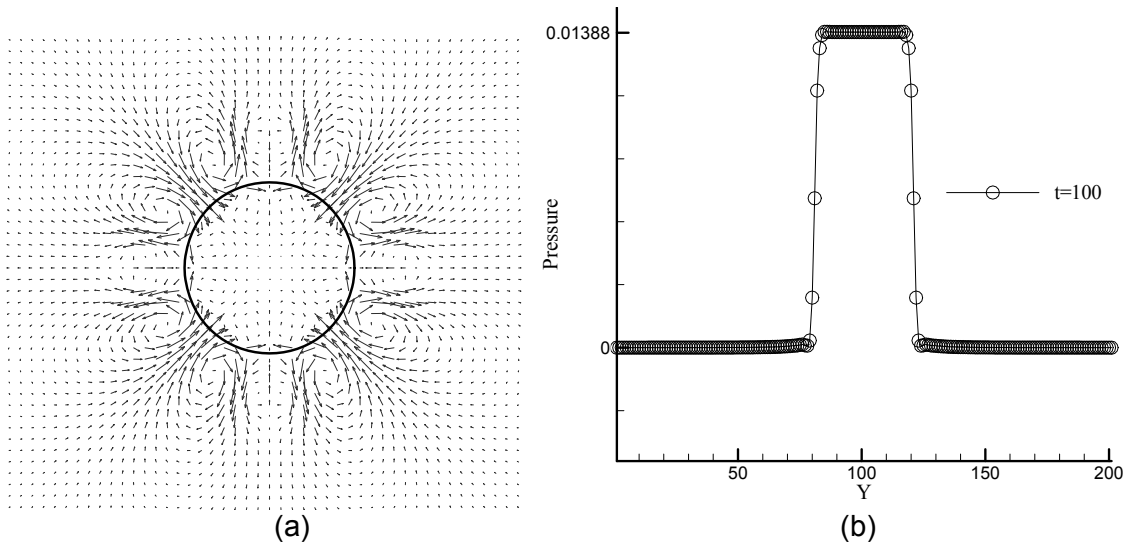
Fig. 6 Stationary bubble computation, *La*=100, density ratio 100, viscosity ratio 10. (a) Spurious currents of magnitude Ca=5.03 x 10^{-3}, (b) computational pressure at t=100 for theoretical pressure jump 0.1388.
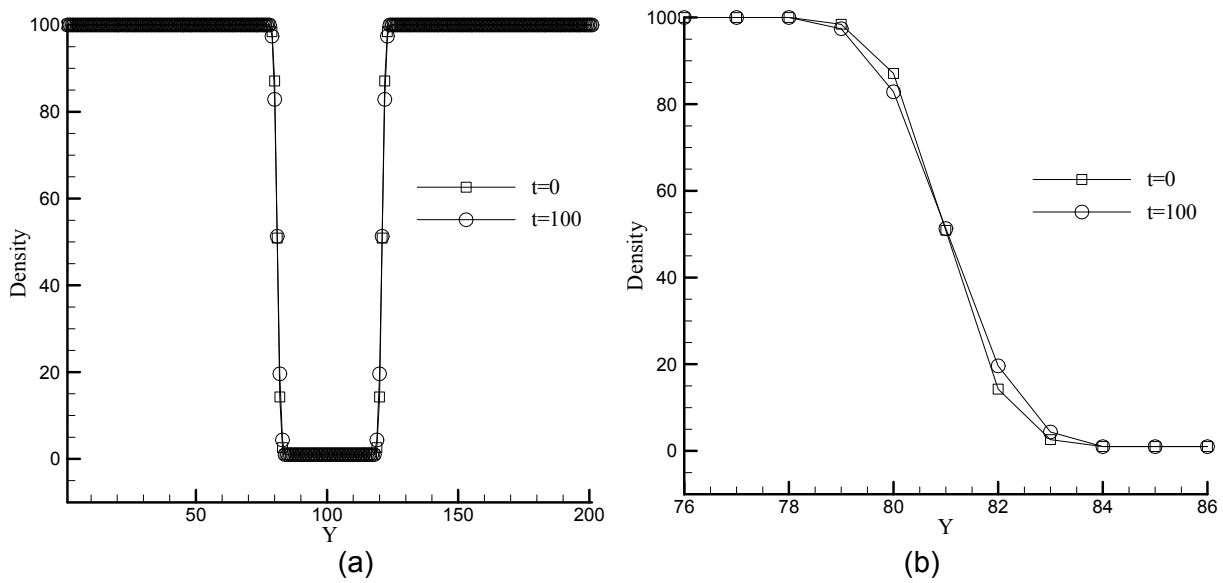
Fig. 7 (a) Density profiles of the stationary bubble with diameter 40, *La*=100, density ratio 100, and viscosity ratio 10; (b) the zoomed-in density profile at the bubble interface.
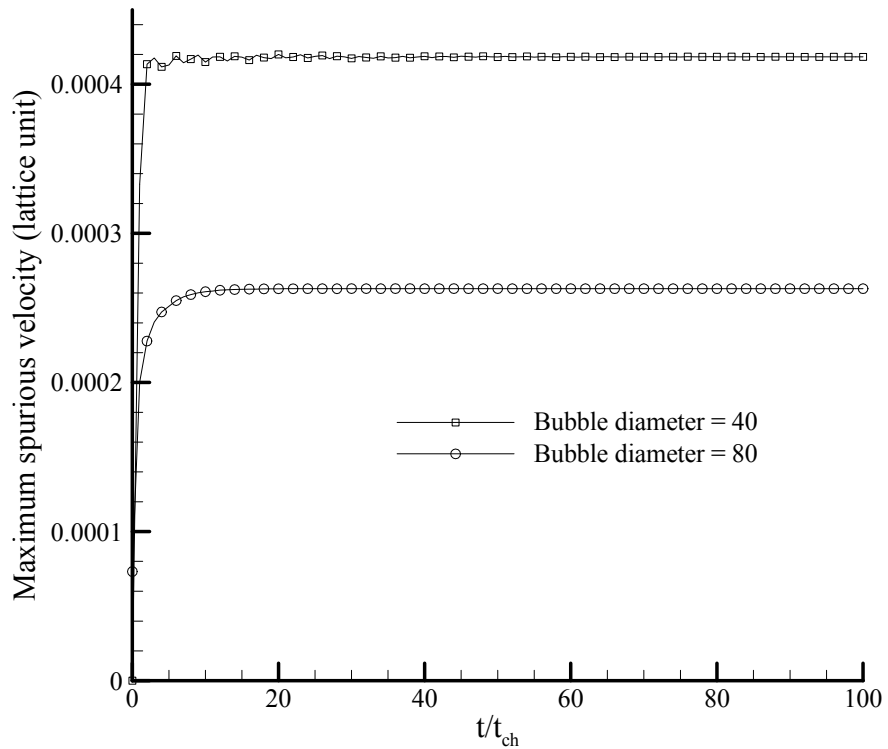
Fig. 8 Maximum spurious velocities for these two grid resolutions, *La*=100, density ratio 100, viscosity ratio 10.
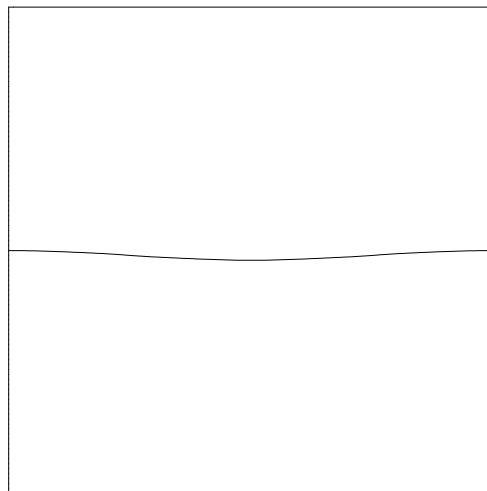
Fig. 9 Initial interface profile for a capillary wave simulation, $\omega_0 = 1.13 \times 10^{-3}$, $\bar{\varepsilon} = 0.116$, density ratio 100.
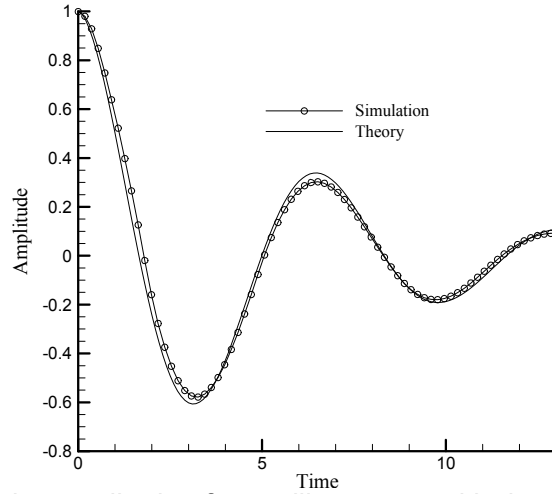
Fig. 10 Time evolution of the amplitude of a capillary wave with density ratio 100.

(a) (b)
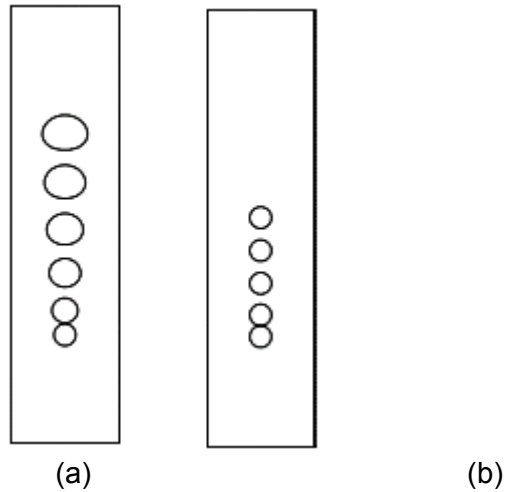
Fig. 11 Rising bubble with Eo=0.971, Mo=1.26e-3, density ratio=100, viscosity ratio=10. The time steps in this figure are t=0, 4, 8, 12, 16, and 20. (a) bubble shapes without mass correction, (b) bubble shapes with mass correction.

(a) (b)
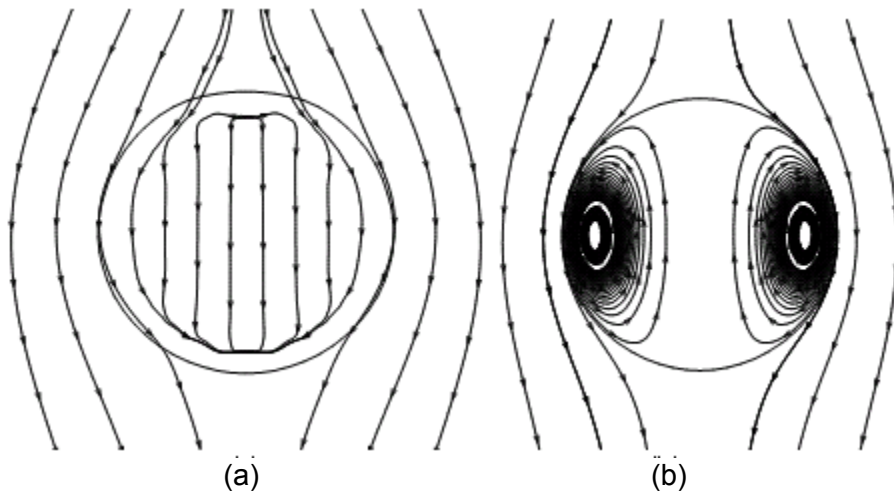
FIG. 12 Streamlines around the bubble at t=20 in Fig. 11b, (a) without accounting for the compressibility effect; (b) with accounting for the compressibility effect.
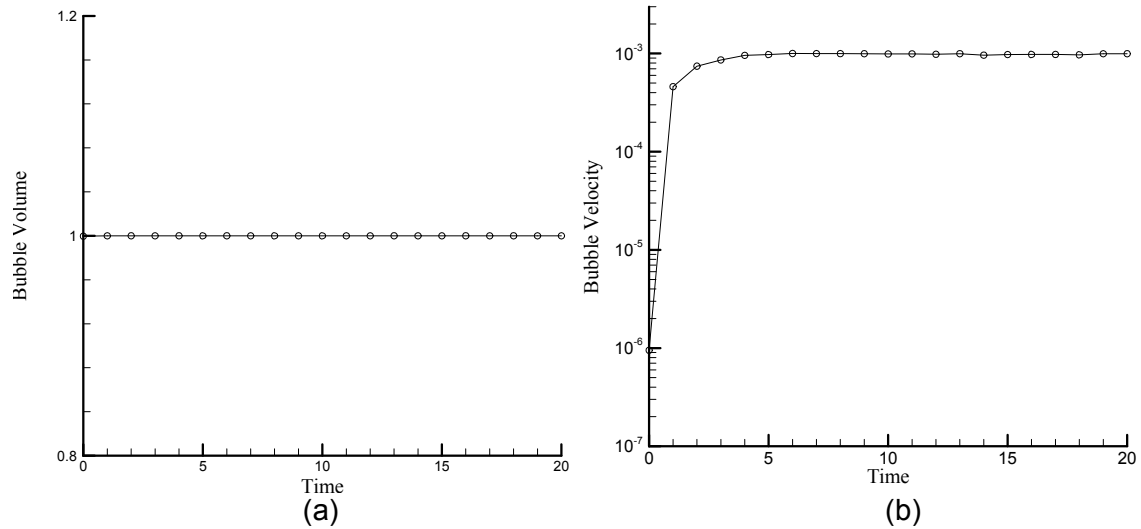
Fig. 13 Time evolution of the volume (a) and velocity (b) of the rising bubble with mass correction, as shown in Fig. 11b.
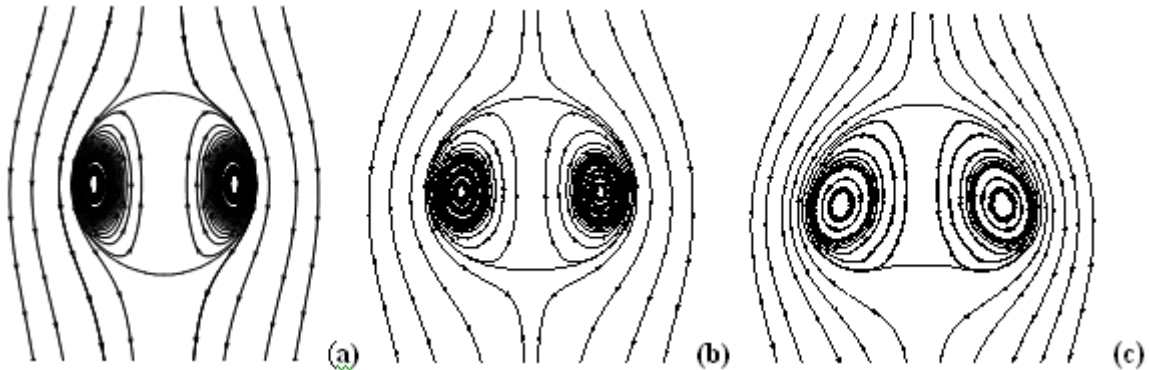
Fig. 14 Computed bubble shapes, density ratio 100, viscosity ratio 10. (a) Cylindrical, Eo=0.971, M=1.26e-3, Re=5.19; (b) Ellipsoidal Eo=9.71, M=0.4, Re=6.92; , (c) Dimpled-ellipsoidal, Eo=97.1, M=100, Re=9.78.
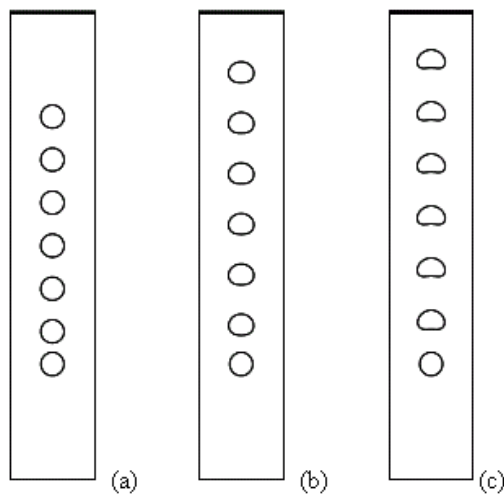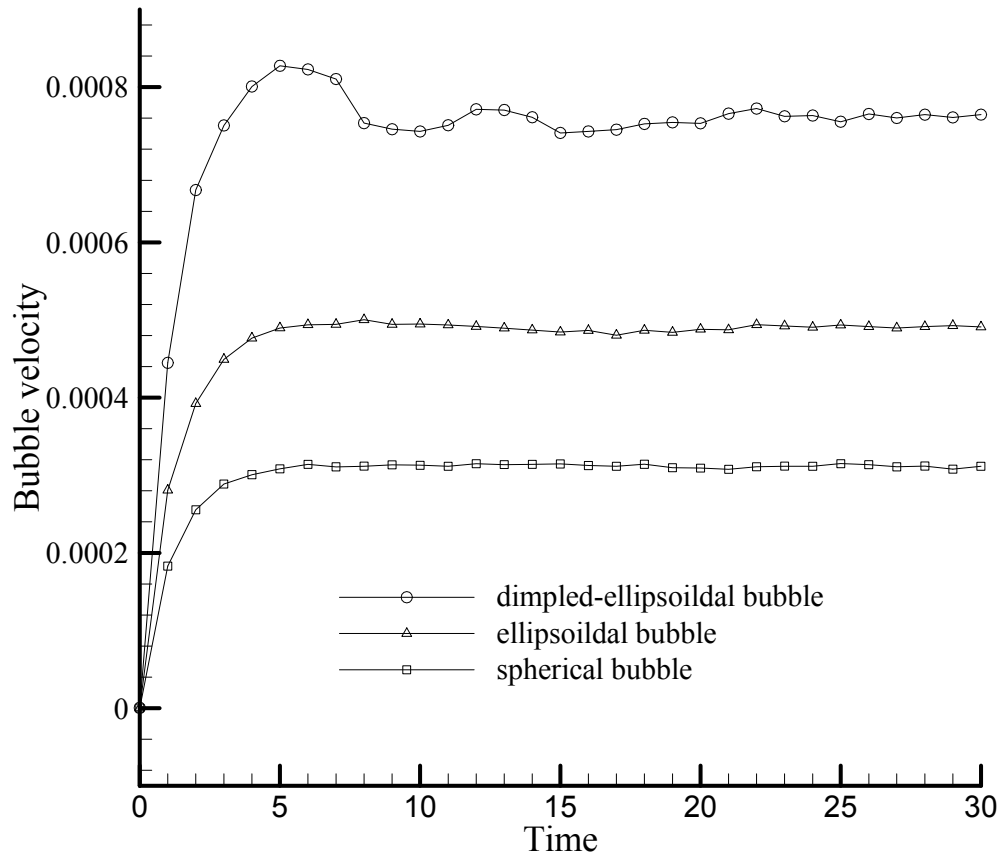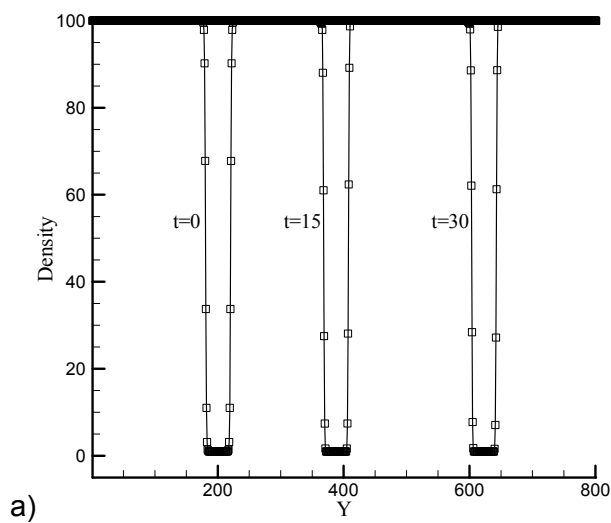

Fig. 15 Time evolutions of rising, density ratio 100, viscosity ratio 10. (a) Cylindrical, Eo=0.971, M=1.26e-3, Re=5.19; (b) Ellipsoidal Eo=9.71, M=0.4, Re=6.92; , (c) Dimpled-ellipsoidal, Eo=97.1, M=100, Re=9.78.

Fig. 16 Time evolutions of bubble velocities, density ratio 100, viscosity ratio 10. (a) Cylindrical, Eo=0.971, M=1.26e-3, Re=5.19; (b) Ellipsoidal Eo=9.71, M=0.4, Re=6.92; , (c) Dimpled-ellipsoidal, Eo=97.1, M=100, Re=9.78.
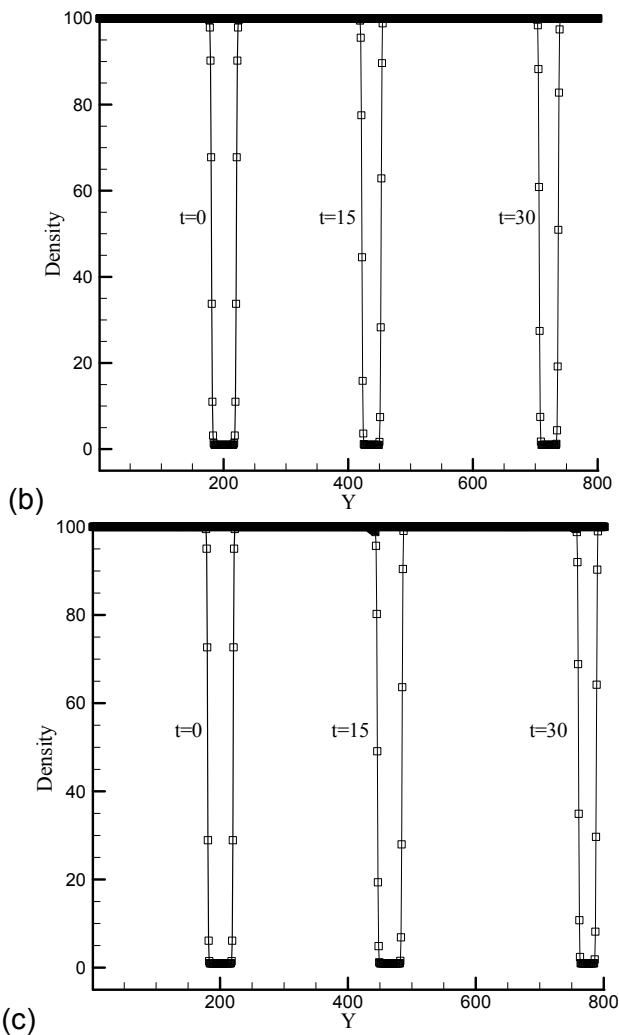

a)

(b)

(c)

Fig. 17 Density profiles of rising bubbles, density ratio 100, viscosity ratio 10. (a) Cylindrical, Eo=0.971, M=1.26e-3, Re=5.19; (b) Ellipsoidal Eo=9.71, M=0.4, Re=6.92; , (c) Dimpled-ellipsoidal, Eo=97.1, M=100, Re=9.78.
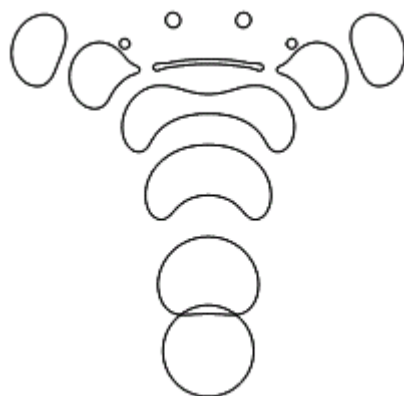

Fig. 18 Time evolutions of a rising bubbles, density ratio 100, viscosity ratio 10, with Eo=97.1, M=0.971 and Re=31.2.

7. Thermal-Fluid Transport Issues for High Power Density and Gravity Independent Aviation and Space Applications of PEM Fuel Cells

Task PI: Dr. J. N. Chung, Mechanical and Aerospace Engineering, University of Florida
Graduate Student: Renqiang Xiong, Mechanical and Aerospace Engineering
Collaborators: Dr. James Klausner, Mechanical and Aerospace Engineering, Dr. Renwei Mei, Mechanical and Aerospace Engineering, Dr. Mark Orazem, Chemical Engineering

Abstract

The power density and gravity independence of a fuel cell are closely related to the pressure-driven single-phase and two-phase flows in the fluid transport micro-channels. To enrich the current fundamental knowledge of micro-scale fluid dynamics, experimental investigations were performed in this project to provide fundamental information to support fuel-cell optimal designs for high power densities and space applications.

The pressure drops of liquid flow in straight and serpentine micro-channels with hydraulic diameters of 0.209, 0.412, and 0.622 mm were evaluated. To segregate the bends and entrance effects individually from the total pressure drop, for each size, three types of micro-channels: straight short, straight long and long serpentine, were fabricated. An in-house micron-resolution particle image velocimetry system (micro-PIV) was built at the University of Florida and used to obtain the detailed velocity vector field in micro-scale channels. The friction factor result shows that the conventional theory is still valid under the current channel size. The additional pressure drop is consistent with the flow structure around the bend measured by the micro-PIV.

Adiabatic nitrogen-water flow patterns and void fractions in straight micro-channels were experimentally investigated. Gas and liquid superficial velocities were varied from 0.06-72.3 and 0.02-7.13 m/s, respectively. The instability of flow patterns was observed. Four groups of flow patterns including bubbly-slug flow, slug-ring flow, dispersed-churn flow and annular flow were observed in micro-channels of 0.412 and 0.622 mm while in the micro-channel of 0.209 mm, the bubbly-slug flow became the slug-flow and the dispersed-churn flow disappeared. The current flow regime maps showed that the transition lines shifted to a higher gas superficial velocity due to a dominant surface tension effect as the channel size was reduced. The regime maps presented by other authors for mini-channels were found not applicable for micro-channels. The void fractions hold a non-linear relationship with the homogeneous void fraction as oppose to the relatively linear trend for the mini-channels. A new correlation was developed to predict the non-linear relationship that fits most of the current experimental data and those of the 0.1 mm diameter tube reported by Kawahara et al. (2002) within ±15%.

Nomenclature

A	Area [m^2]
A_i	Area of interrogation window [μm^2]
B	Coefficient in Eq. (2.6)
Bo	Bond number
C	Coefficient in Eq. (4.4)

C_v	Volumetric concentration [μm^{-3}]
C_0	Coefficient in Eq. (4.1)
Ca	Capillary number
dP/dz	Pressure gradient [Pa/m]
D	Diameter [mm]
f	Fraction factor
fre	Frequency [1/s]
g	Gravity acceleration [m/s^2]
j	Superficial velocity [m/s]
K	Pressure drop defect
K_b	Bend loss coefficient
L	Length [mm]
L_d	Entrance length [m]
m	Mass transfer rate [g]
n	Refraction index
N	Total number
NA	Numerical aperture
P	Pressure [Pa]
Q	Flow rate [ml/min]
Re	Reynolds number
S	Depth of micro-channels [mm]
t	Time [s]
u	Local velocity at x direction [m/s]
U	Mean velocity [m/s]
V_{gj}	Mean drift velocity [m/s]
W/w	Width [mm]
We	Weber number
X	Martinelli parameter
x	The coordinate along the length
x^+	Dimensionless entrance length
y	The coordinate along the width
Z_m	Measurement depth [μm]

Greek letters

Δ	Variable difference
α	Aspect ratio
β	Homogeneous void fraction
Γ	Circulation [mm^2/s]
δ	Differential value
λ	Wavelength of light in a vacuum [μm]
μ	Viscosity [kg/m·s]
θ	Light collection angle
ρ	Density [kg/m^3]
σ	Surface tension [N/s]

Subscripts

b	90° bend
c	Cross-section
dev	Developing and developed flow
exp	Experimental result

fd	Fully developed
G/g	Gas
GS	Superficial gas
h	Hydraulic diameter
i	Particle image
io	Inlet and outlet
L/l	Liquid
LS	Superficial liquid
l	Long straight micro-channel
m	Other type of flow patterns
p	Fluorescent particles
s	Serpentine micro-channel
sh	Short straight micro-channel

1. Introduction

The power density and gravity independence of a fuel cell are closely related to the pressure-driven single-phase and two-phase flows in the fluid transport micro-channels. Micro-scale fluid dynamics usually refers to the dynamics of fluid flow in the devices with length scales less than one millimeter. Studies of such fluid-related phenomena have long been an important part of the fluid mechanical component (Batchelor 1977). Due to the availability of MEMS fabrication methods (Ho and Tai 1998; Stone & Kim 2001), methods for fabricating individual and integrated flow configurations with length scales on the order of tens and hundreds of microns and smaller, micro-scale fluid dynamics research has received enormous recent attention and been widely applied in many fields such as biotechnology (Beebe et al. 2002), cooling of IC chips (Zhang et al. 2002), micro-fuel cell (Heinzel et al. 2002) and lab on a chip (Erickson and Li 2004). In many applications, a valuable feature of microflows is that the dynamics in a single channel can be replicated in many channels, so understanding the fundamental knowledge of fluid motion and associated transport processes in micro-channels is quite important for the micro-scale fluid transport system design.

In this study, we experimentally and numerically investigated many flow features of pressure-driven single- and two-phase flow in micro-channels to enrich the current fundamental knowledge of micro-scale fluid dynamics.

1.1 Research Background

Micro-scale flows can be manipulated using many kinas of external fields such as pressure, electric, magnetic, capillary, etc. Pressure-driven flow is an indispensable component in micro-scale fluid dynamics research. It is widely used in micro-heat exchanger (Brandner et al. 2000), and the pressure drop is a critical parameter to design the micro-pumps. For single phase liquid flow in straight micro-channels, many scientists have published numerous papers on the relationship between the friction factor and Re number in the past fifteen years. Some of them found for a liquid flow an increase of the friction factor with the Re number including Wu and Little (1983), Peng and Peterson (1996), Mala and Li (1999), Qu et al. (2000), and Li et al. (2003). They attributed it to surface roughness effect or the early transition to turbulent flow (Re=300-500) in straight micro-channels. However, recent studies showed general agreement with theoretical macro-scale predictions for friction factors including Judy et al. (2002), Wu and Cheng (2003), Hetsroni et al. (2005), and Kohl et al. (2005). They attributed the deviation from the theoretical prediction in the previous literatures to the size and measurement uncertainties or not count the entrance effect. Hence, the relationship is not clear yet. The studies for liquid

flow in serpentine micro-channels just started (Lee et al. 2001; Maharudrayya et al. 2004). It becomes a concern in the field of micro-fuel cell.

Most measurements of microflows have been performed with optical microscopes. An adaptation of particle image velocimetry known as micro-PIV can yield a spatial resolution of the flow field of approximately one micron (Santiago et al. 1998). Due to the high expense of purchasing such a commercial system, around $500,000, building an in-house micro-PIV system became timely to speed up the progress of micro-scale fluid dynamics research at the University of Florida.

Two-phase flow in micro-channels is also a major research subject in micro-scale fluid dynamics. Recent researches show that the surface tension becomes dominant when the channel size decreases which may result in a big change in the flow pattern and flow map, even the void fraction (Kawahara et al. 2002). A study of the size effect on those flow features need to be performed to provide a clear image of the micro-scale two-phase flow.

Micro-bubble dispenser is one of the fundamental elements in a lab-on-a-chip system. It can be integrated with other microfluidic components including valves, pumps, actuators, switches, sensors, mixers, filters, separators, heaters, etc. to succeed with chemical synthesis, analysis, and reactions using only very small fluids volumes (Stone et al. 2004). Recent studies have reported several bubble dispensers but with complex structures (Ganan-Calvo and Gordillo 2001; Garstecki et al. 2004). New dispensers with simple structures that are easy to be scaled up or multiplexed need to be designed and tested.

1.2 Research Objectives

This research is performed to provide fundamental understand for the following flow features in micro-scale:
1)   Friction factor, entrance effect and bend effect for a liquid flow in micro-channels.
2)   Flow structure around the bend and its correspondence to the additional pressure drop.
3)   Flow patterns, time-averaging void fraction and two-phase frictional pressure drop for gas-liquid two-phase flow in micro-channels
4)   Micro-bubble dispenser with a simple structure to generate uniform micro-bubbles.
To reach the above objectives, several micro-channels and bubble dispensers need to be fabricated and a micron-resolution particle image velocimetry system needs to be built to obtain the flow structure in micro-scale.

1.3 Justifications

For the application of fuel cells in aviation, the grand challenge is meeting the specific power density requirement of 10 kW/kg while maintaining the notorious fuel cell high energy efficiency of more than 50%. The current average specific power density for land applications is around 0.3 kW/kg. Based on basic principles of transport physics, miniaturization of the reactor transport scale and maintaining high rates of feed and product flows are the obvious strategies to dramatically increase the power density for meeting the aviation requirement. For both high-gravity (launch and reentry accelerations) and microgravity environment (near-earth orbit), the water management, two-phase flow, and gas separation have been identified as critical issues for the development of PEM fuel cells for space applications.

2. Entrance Flow and Bend Effect

Flow characteristics of pressure-driven de-ionized water were investigated in straight and serpentine micro-channels with miter bends. The micro-channels had rectangular cross-sections with hydraulic diameters of 0.209, 0.412, and 0.622 mm. To evaluate bend loss coefficient in the serpentine micro-channel and micro-scale size effect on it, the additional pressure drop due to the miter bend must be obtained. This additional pressure drop can be achieved by subtracting the frictional pressure drop in the straight micro-channel from the total pressure drop in the serpentine micro-channel. Since currently there still has a debate on the relationship between the friction factor and Re number in the straight micro-channel, the frictional pressure drop had to be obtained experimentally here. Three groups of micro-channels were fabricated to remove the inlet and outlet losses. The experimental results show that after considering the measurement uncertainties the experimental Poiseuille number can be well predicted by the conventional laminar incompressible flow theory when Re number is less than some value around 1500, the discrepancy observed by the former researchers can be attributed to not accounting for the additional pressure drop in the entrance region. The onset of transition to turbulence might be at 1500-1700. For serpentine micro-channels, the additional pressure drop can be divided into two regions. One is Re<100. It's very small since no circulation exists. The other one is Re larger than some value in 100-200. At this time the circulation appears and develops at the inner and outer wall of the bend. The additional pressure drop increases sharply with Re number. The bend loss coefficient was observed to decrease and tend to be a constant with decreasing Re number. It's found to be larger than the predicted value for macro-channel turbulent flow and related with the channel size when flow separation appears, namely Re>100-200.

2.1 Introduction and Background

In recent years, the proliferation of MEMS and micro-fluidic devices has resulted in the use of micro-channels in many applications including propulsion and power generation of micro air vehicles, micro-scaled cooling systems of electronic devices, micro satellites, etc. Because of the wide range of uses for micro-channels, it is important to be able to well predict their behavior which requires a good knowledge of flow characteristics in straight and serpentine micro-channels (Ho and Tai 1998).

Flow characteristics in circular and non-circular macro-ducts with curved bends have been extensively studied (Humphrey et al. 1981; Berger et al. 1983; Bradshaw et al. 1987) in the past years. However, there were limited literatures on single phase flow characteristics in the channels with miter bends in the past. Streeter (1961) reported the bend loss coefficient for miter bend was taken to be around 1.1 for engineering applications, which was usually for turbulent flow. Yamashita et al. (1984, 1986) and Kushida et al. (1985) studied three-dimensional flow and heat transfer in miter-bend experimentally and numerically. They found a decreasing trend of the bend loss coefficient with Re number in laminar and turbulent flow region and analyzed the effects of Re number and aspect ratio on the flow structures. Though significant attention has been paid to the flow in macro-systems with bends, research on flow characteristics in micro-systems with bends has recently been started. In most practical applications the micro-channels are not straight due to required turns and sometimes it is complicated and expensive to keep the micro-channel straight.

To minimize the pressure losses in the flow through the micro-channels for optimum design, flow characteristics in serpentine micro-channels with miter bends must be also well understood. Lee et al. (2001) researched on the gas flow in micro-channels having the dimensions $20 \times 1 \times 5810 \ \mu m^3$ with bends of miter, curved and double-turn. They found the flow rate through the channel with the miter bend was the lowest at a certain inlet pressure and the

largest drop was found in the miter bend with the lowest flow rate. They also found the secondary flow could develop in micro-channels, contrary to expectations. Maharudrayya et al. (2004) studied the pressure losses and flow structures of laminar flow through serpentine channels with miter bends by a CFD code but they didn't consider the micro-scale effect. After literature review, it can be seen that the experimental work of liquid flow in serpentine micro-channels with miter bends and the micro-scale size effect on flow characteristics have never been reported before.

As we know, the additional pressure loss due to the miter bend in serpentine channels was usually related with the flow separation and reattachment around the bend. To evaluate the bend loss coefficient, the additional pressure drop must be achieved. It can be calculated by subtracting the frictional pressure drop of straight micro-channels from the total serpentine micro-channel pressure drop. Hence, the issue of frictional pressure drop in straight micro-channels was involved in this work too.

For recently 15 years, many scientists have published numerous papers on the flow characteristics in straight micro-channels. Some of them found flow characteristics in the straight micro-channel were quite different with those predicted by the conventional laminar flow theory. One of the important flow performances was the relationship between the friction factor and Re number. For liquid flow in straight micro-channels, an increase of friction factor with Re number under certain conditions was found by the scientists including Wu and Little (1983), Peng and Peterson (1996), Mala and Li (1999), Papautsky et al. (1999), Qu et al. (2000), Pfund et al. (2000), and Li et al. (2003). Wu and Little's (1983) friction factor measurements appear to correlate with surface roughness, as the results agreed well with theory for smooth channels, but the agreement decreased as the roughness increased. In an effort to understand the influence of geometrical parameters (specifically, hydraulic diameter and aspect ratio) on flow resistance, Peng et al. (1994) considered water flows in rectangular machined steel grooves enclosed with a fiberglass cover. A large range of Re were obtained (50 to 4000), and a geometrical dependence was observed. For the most part, the friction factor increased with increasing H/W and also with increasing D_h (holding H/W constant). Nonlinear trends between pressure drop and flow rate were observed for Re as low as 300 by Mala and Li (1999), specially for water flowing through a 0.13 mm diameter stainless steel micro-tube. At small Re number (Re<100) the measured friction factors were consistently higher in stainless steel and fused silica micro-tubes. Measured flow friction for trapezoidal channels was 8 to 38% higher than macroscale predictions for the range of parameters studied by Qu et al. (2000), and a dependence on D_h and Re was also observed. However, there were some other scientists finding general agreement with theoretical macroscale prediction for friction factor including Flockhart and Dhariwal (1998), Jiang et al. (1995), Sharp et al. (2000) and Wilding et al. (1994), Xu et al. (2000), Judy et al. (2002), Wu and Cheng (2003), Hetsroni et al. (2005), and Kohl et al. (2005). Jiang et al. (1995) got a linear relationship between flow rate and pressure drop in micro-channels with various cross-sectional shapes. In the circular case, the friction factor matched theoretical predictions within 10%-20%.

Wilding et al. (1994) found the result for water flowing in silicon micro-machined channels agreed well with theory for at least the lower Re number (Re around 17 to 126) tested. Flockhart and Dhariwal (1998) found a good agreement between the numerical calculations for flow in trapezoidal channels and the experimental results for Re<600. Sharp et al. (2000) found the microscale measurements of the friction factor generally agree with the macroscale laminar theory to within ±2% experimental error over all Re numbers up to transition (around 50<Re<2000), for water flowing through circular fused silica micro-channels with hydraulic diameter 0.075 to 0.242 mm. This group attributed the deviation from the theoretical prediction

in the previous literatures to the size and measurement uncertainties. Hence, the relationship between the friction factor and Re number in straight micro-channels is not clear yet. The frictional pressure drop in straight micro-channels can't be calculated by a universal formulation and need to be achieved experimentally here.

In our research, three groups of micro-channels were fabricated. Each group has three micro-channels with the same size: straight long, straight short and single serpentine with miter bends. The straight long and straight short micro-channels were used to achieve the reliable frictional pressure drop in straight micro-channels, and the serpentine micro-channels were used to get the additional pressure drop due to the miter bend. The main objective of this study is to achieve this additional pressure drop and bend loss coefficient to evaluate flow characteristics in serpentine micro-channels, and compare it with the bend loss coefficient in macro-channels. The Poiseuille number for straight micro-channels can also be achieved experimentally and compared with the previous conclusions.

2.2 Experimental Setup
2.2.1 Micro-channels Fabrication

Fig. 2-1 a) to d) shows the photographs of straight and serpentine micro-channels and schematic of the straight micro-channel used in this work. The micro-channel was laser etched in a silicon plate and then a Pyrex thin cover glass plate was anodically bonded on the top of the plate. The micro-channel plates have two dimensions of $30 \times 12 \times 2$ mm^3 (straight long and serpentine) and $11 \times 12 \times 2$ mm^3 (straight short). Two small connection tubes which can be inserted into the inlet and outlet assembly were connected with the small reservoirs. Each of the serpentine micro-channels had five straight micro-channels with the same size and eight miter bends. A microscope (Olympus BX50), a $10 \times$ objective lens and a CCD camera with pixel size 6.45 μm were used to measure the dimensions of the micro-channels' rectangular cross-sections, which were listed in Table 2-1.

2.2.2 Apparatus

Fig. 2-2 shows schematic and 3-D assembly drawing of the experimental apparatus used to investigate the pressure-driven de-ionized water flow in straight and serpentine micro-channels. It includes a syringe infusion pump (Cole-Parmer Instrument), 60ml syringe (Mcmaster), micro-filter (Swagelok), pressure transducers (Kavlico), straight and serpentine micro-channel test sections and computerized data acquisition system. The de-ionized water at the flow rate from 0.1 to 70ml/min, which can be set on the panel of the infusion pump with an accuracy of $\pm 0.5\%$, was driven to the micro-channel test section. The 2 μm micro-filter can remove any particles or bubbles which may block the micro-channel before the flow enters into the test section.

Owing to the unavailability of appropriate internal pressure sensors which would allow in situ measurements, two pressure transducers with $\pm 0.5\%$ FS accuracy were installed at the inlet and outlet of the micro-channel to measure the upstream and downstream pressure and then sent to the data acquisition system. To get the accurate pressure at the upstream, two pressure transducers with different measurement range were used. The one with large measurement range (0-150 PSI) was used for smaller micro-channels/larger flow rates, and the other one with small range (0-15 PSI) were used for larger micro-channels/smaller flow rates.
The data started recording when the pressures didn't change heavily for some time, which can be considered as steady state. The digital pressure output signals (0.5-4.5 V) were collected by an A/D data acquisition board (Measurement Computing PCI-DAS6034). This board has 16

single ended or 8 differential channels, 16 bits resolution and the maximum sampling rate can be 200 KS/s. For the signal range of ±5 V, the absolute accuracy is ±10.9 LSB. A Labview program can read the signals from the board, show the pressure data in real time and save them to a data file. The test sections were placed horizontally, and all experiments were conducted at room temperature. Since the pressure measurements were made between the inlet and outlet, which is beyond the actual length of the micro-channel, there should be contraction and expansion losses in pressure drop from the inlet to micro-channel and micro-channel to the outlet. In our work, the pressure drops for the short and long straight micro-channels were measured separately. The short micro-channel has the entrance effect while the long micro-channel has the friction effect more, so the difference of these two pressure drops can be considered as the pressure drop due to the straight friction factor. Besides these two effects, the serpentine micro-channel has one more effect, bend effect. This effect is introduced by the flow separation around the corner and will be evaluated individually at the late section.

2.3 Data Reduction and Analysis

For a laminar flow in a macro-scale rectangular channel, the length of the developing flow in the entrance region can be estimated by the following equation given by Shah and London (1978):

$$L_d = \left(0.06 + 0.07\alpha - 0.04\alpha^2\right)\mathrm{Re}\,D_h \tag{2.1}$$

Table 2-2 shows the minimum and maximum L_d/D_h for the flow rate range in our experiment and the L/D_h for the current short and long channels. It is clear that for a substantial number of cases, the flows are not fully developed under the current experimental conditions. The follow addresses the estimation of the friction factor for both entrance and fully developed flows.

For a fully developed laminar flow in a macro-scale rectangular channel with an aspect ratio α, Shah and London (1978) used a power series for the friction factor and fitted the coefficients using their experimental data as below:

$$(f\,\mathrm{Re})_{fd} = 96(1 - 1.3553\alpha + 1.9467\alpha^2 - 1.7012\alpha^3 + 0.9564\alpha^4 - 0.2537\alpha^5) \tag{2.2}$$

This empirical equation can approximate the two-dimensional theoretical exact solution (Nguyen and Wereley 2006) for the fully developed friction factor with an error less than 0.05%. For the current micro-channels, the aspect ratio range is from 0.9 to 0.97, so the corresponding theoretical Poiseuille numbers $(f\mathrm{Re})_{fd}$ for the fully developed flow are around 57. However, the current micro-channels may not be long enough for the flow to become fully developed under laminar flow conditions. Actually in many practical applications, flows generally can not reach the fully developed state in micro-channels as they are relatively short due to space limitations in micro-systems.

For a developing flow, its pressure drop is higher than the fully developed flow. As a result, the pressure drop from the inlet of the channel to a downstream location x in the entrance region is the sum of the fully developed pressure drop and the pressure drop defect given by the equation below (Kakac et al. 1987):

$$\Delta P_{dev} = \left[(f\,\mathrm{Re})_{fd}\,x^+ + K\left(x^+\right)\right]\frac{\rho U^2}{2} \tag{2.3}$$

$$x^+ = \frac{x}{\text{Re} \cdot D_h}$$ (2.4)

where $K(x^+)$ is the pressure drop defect given by:

$$K\left(x^+\right) = \left[f_{app} \text{Re} - (f \text{Re})_{fd} \right] x^+$$ (2.5)

$$f_{app} \text{Re} = 4 \left\{ \frac{3.44}{\left(x^+\right)^{0.5}} + \frac{K(\infty)/\left(4x^+\right) + (f \text{Re})_{fd}/4 - 3.44/\left(x^+\right)^{0.5}}{1 + B\left(x^+\right)^{-2}} \right\}$$ (2.6)

where f_{app} is the apparent friction factor and Eq. (2.6) is given in Kalkac et al. (1987). According to White (1991), the constant B in Eq. (2.6) is equal to 2.93×10^{-4}. As plotted in Fig. 2-3, the pressure drop defect $K(x^+)$ for the current micro-channels begins at the value of 0 for $x^+ = 0$ and increases asymptotically to the fully developed constant value $K(\infty)$ which has a dependence upon the channel aspect ratio for rectangular channels as suggested by Shah and London (1978).

$$K(\infty) = 0.6796 + 1.2197\alpha + 3.3089\alpha^2 - 9.5921\alpha^3 + 8.9089\alpha^4 - 2.9959\alpha^5$$ (2.7)

Eq. (2.7) determines the fully developed $K(\infty)$ for a rectangular channel with an uncertainty of 0.04%. So the pressure drop for the straight short, ΔP_{sh}, and straight long channel, ΔP_l, can be expressed as:

$$\Delta P_{sh} = \Delta P_{io} + \Delta P_{dev}\left(x = L_{sh}\right)$$ (2.8)

$$\Delta P_l = \Delta P_{io} + \Delta P_{dev}\left(x = L_l\right)$$ (2.9)

where ΔP_{io} is the inlet and outlet assembly losses due to changes in tubing diameter, tees and elbows as indicated in Fig. 2-1(e). Straight short and straight long micro-channels have the same channel size but different channel length.

Since the inlet and outlet pressure losses are proportional to U^2, the inlet and outlet losses are the same for both lengths of the channels under a given Re number because that both have two ends placed in the same inlet and outlet assembly. ΔP_{sh} and ΔP_l are the measured pressure drops for the straight short and straight long channels, respectively. Hence, the experimental friction factor that takes the entrance effect into consideration is estimated by the following equation:

$$f_{exp} = \left\{ \frac{\Delta P_l - \Delta P_{sh}}{\rho U^2/2} - \left[K(L_l) - K(L_{sh})\right] \right\} \frac{D_h}{L_l - L_{sh}}$$ (2.10)

For the serpentine micro-channels, the measure pressure drop can be expressed as:

$$\Delta P_s = \Delta P_{io} + \Delta P_{dev}\left(x = L_s\right) + N \cdot \Delta P_b$$ (2.11)

where ΔP_s is the measured pressure drop for the serpentine channel and ΔP_b is the additional pressure drop due to the miter bend. N is the number of miter bends. So ΔP_b and the bend loss coefficient, K_b, can be written as:

$$\Delta P_b = \frac{\dfrac{\Delta P_s - \Delta P_l}{\rho U^2 / 2} - \left[\left\{ \dfrac{\Delta P_l - \Delta P_{sh}}{\rho U^2 / 2} - \left[K(L_l) - K(L_{sh}) \right] \right\} \dfrac{L_s - L_l}{L_l - L_{sh}} + K(L_s) - K(L_l) \right]}{N \Big/ \dfrac{\rho U^2}{2}} \qquad (2.12)$$

$$K_b = \frac{\dfrac{\Delta P_s - \Delta P_l}{\rho U^2 / 2} - \left[\left\{ \dfrac{\Delta P_l - \Delta P_{sh}}{\rho U^2 / 2} - \left[K(L_l) - K(L_{sh}) \right] \right\} \dfrac{L_s - L_l}{L_l - L_{sh}} + K(L_s) - K(L_l) \right]}{N} \qquad (2.13)$$

According to the error propagation analysis, the uncertainty of the friction factor and bend loss coefficient can be expressed as:

$$\frac{\delta(f\,\mathrm{Re})}{f\,\mathrm{Re}} = \left(\left[2\frac{\delta D_h}{D_h} \right]^2 + \left[\frac{\delta A}{A} \right]^2 + \left[\frac{\delta Q}{Q} \right]^2 + \left[\frac{\delta(\Delta P / \Delta L)}{\Delta P / \Delta L} \right]^2 \right)^{1/2} \qquad (2.14)$$

$$\frac{\delta K_b}{K_b} = \left(\left[2\frac{\delta A}{A} \right]^2 + \left[2\frac{\delta Q}{Q} \right]^2 + \left[\frac{\delta(\Delta P_b)}{\Delta P_b} \right]^2 \right)^{1/2} \qquad (2.15)$$

The uncertainty range of the friction factor and bend loss coefficient can be calculated to be $\pm 10.2 - \pm 15.1\%$ and $\pm 12.3\% - \pm 16.1\%$.

2.4 Results and Discussion
2.4.1 Friction Factor

Fig. 2-4 shows the comparison between the experimental pressure gradients without removing the entrance effect, $(\Delta P_l - \Delta P_{sh})/(L_l - L_{sh})$, and theoretical results for the current micro-channels. The dot lines represent the pressure gradients predicted by the 2-D conventional laminar incompressible flow theory, which shows a linear relationship with Re number theoretically. However, as the Re number increases, the measured pressure gradients shows a non-linear relationship with Re number. Some former researchers attribute it to the early transition to turbulence at Re=700. However, from Fig. 2-5, we can conclude it doesn't result from the early transition to turbulence but may from not accounting for additional pressure drop in the entrance region of the channel.

Fig. 2-5 shows the comparison between the experimental friction factor calculated by Eq. (2.10) and theoretical results predicted by Eq. (2.2). The solid line represents the predicted friction factor for fully developed flow, and the vertical bars denote the measurement uncertainty. From Fig. 2-5, we can see after the experimental uncertainties are considered, the experimental results show agreement with standard laminar incompressible flow predictions when Re<1500.

It's believed that the consistent offset observed by the previous researchers is the result of unaccounted for bias in experimental setups. When Re equals to 1500-1700, fRe begins to deviate from the theoretical value which may suggest the transition to turbulence.

2.4.2 Bend Loss Coefficient

For laminar flow, the additional pressure drop is related with the flow separation which need energy to be maintained and results in an additional pressure drop not associated with frictional losses.

As we know, in micro-channels, the flow usually keeps in laminar flow region, so the flow pattern along the miter bend affects the additional pressure drop pretty much. Maharudrayya et al. (2004) used CFD simulation and obtained the flow pattern along a miter bend at different Re numbers. When Re=100, there is no eddies around the inner and outer wall. While Re=210, significant recirculation at the inner and outer wall appears. The size and intensity of both vortices increase with increasing Re number.

Fig. 2-6 shows the experimental additional pressure drop under different Re numbers. It can be divided into two regions. One is Re<100. There is no eddies and the additional pressure drop is very small for all of the channels. The other one is the circulation appears on the inner and outer wall and develops with increasing Re number. The critical Re number is in the range 100-200. At this time the additional pressure drop increases sharply. The experimental results also show the additional pressure drop increases with decreasing hydraulic diameters. From Fig. 2-6, the additional pressure drop of the micro-channel with hydraulic diameter 0.209 mm is around 0.5 atm when Re number reaches around 850, which is approximately equal to the frictional pressure drop of the same size straight micro-channel with 23.7 mm length, 101% of the current total length. Hence, the additional pressure drop due to the miter bend is also a big source of the micro-channel pressure drop, especially for small size and short length micro-channels.

Since the pressure drop for channel 1 is pretty high, Re number can only reach around 850 and the upstream pressure will exceed the measurement range of the transducer. Here the bend loss coefficients are calculated by using Eq. (2.13) and compared at Re number from 47-2268, which is shown in Fig. 2-7. The solid line represents the bend loss coefficient of the miter bend, 1,1, reported by Streeter (1961). From Fig. 2-7, we can see bend loss coefficients of the micro-channels are all larger than 1.1. It is a similar conclusion with that of Yamashita et al. (1984), the bend loss coefficient in laminar flow region is larger than that in turbulent region. The second characteristic is it's dependent of Re number and decreases with increasing Re number, which is also different with turbulent flow. For macro-channel turbulent flow at larger Re number, K_b almost won't change with Re number. When Re is larger than some value in 1300-1500, K_b almost keeps constant and changes in the range of ±10%. The last characteristic is the size effect on K_b. It's larger for smaller channel when there is flow separation, namely Re>100-200. After considering the measurement uncertainty, these two curves still have difference. The quantitative relationship needs more experiments and simulation to be determined.

2.5 Summary

The investigation of a pressure-driven water flow in straight micro-channels and in serpentine micro-channels with miter bends was conducted experimentally. A short straight and a long straight micro-channel with the same channel size were fabricated and used to isolate the inlet and outlet assembly extra pressure losses. The following conclusions were obtained:

1) The experimental friction factors show good agreement with the classical laminar incompressible flow predictions after considering the measurement uncertainties when the Re is less than 1500. When the Re is larger than 1500, the onset of transition to turbulence may take place. For laminar flows in micro-channels, the frictional pressure drops in the developing entrance region can still be predicted by the classical macro-scale equations for developing flows. In general, the frictional pressure drop in a micro-channel can be estimated by macro-scale theories and correlations.

2) In serpentine micro-channels, the additional pressure drop due to miter bends can be divided into two groups. The first group is for Re<100 where there is no eddies and the additional pressure drop is very small for all of the channels. The other group is for flows with the Reynolds numbers exceeding the threshold values that are in the range of 100-300. When the Reynolds is higher than the threshold value, we found the flow separation and formation of vortices that appear on the inner and outer wall around the miter bend. These vortices increase in strength with increasing Re number that causes the bend pressure drop to increase sharply with the Re number. The experimental results also show the bend pressure drop increases with decreasing hydraulic diameters. Bend loss coefficient K_b is a function of the Re number only when Re<100, a function of the Re number and channel size when Re>100, and almost keeps constant and changes in the range of $\pm10\%$ when Re is larger than some value in 1000-1500. The trend of the experimental pressure drop is consistent with the flow structure change.

The flow structures around the serpentine micro-channel can also be achieved by a relatively new laser diagnostic technique – micron-resolution particle image velocimetry (Micro-PIV), which is present in Chapter 5 in details.

Table 2-1. Dimensions of three groups of micro-channels

Channel group No.	Width $W\pm2$ μm	Depth $S\pm2$ μm	Hydraulic Diameter D_h (mm)	Total length of the micro-channels $L\pm0.3$ mm		
				Long Channel L_l (mm)	Short Channel L_{sh} (mm)	Serpentine Channel L_s (mm)
Channel 1	213	206	0.2094	23.6	4.1	118
Channel 2	419	406	0.4124	23.5	4	117.5
Channel 3	630	615	0.6224	23.8	4.2	119

Table 2-2. Comparison of current pipe lengths with those of entrance regions.

Re	L_d/D_h	L/D_h (Straight short)			L/D_h (Straight long)		
		Channel 1	Channel 2	Channel 3	Channel 1	Channel 2	Channel 3
47	4.23	19.58	9.70	6.74	112.7	56.98	38.24
2268	204.12						

(a)   (b)

(c)

(d)

(e)
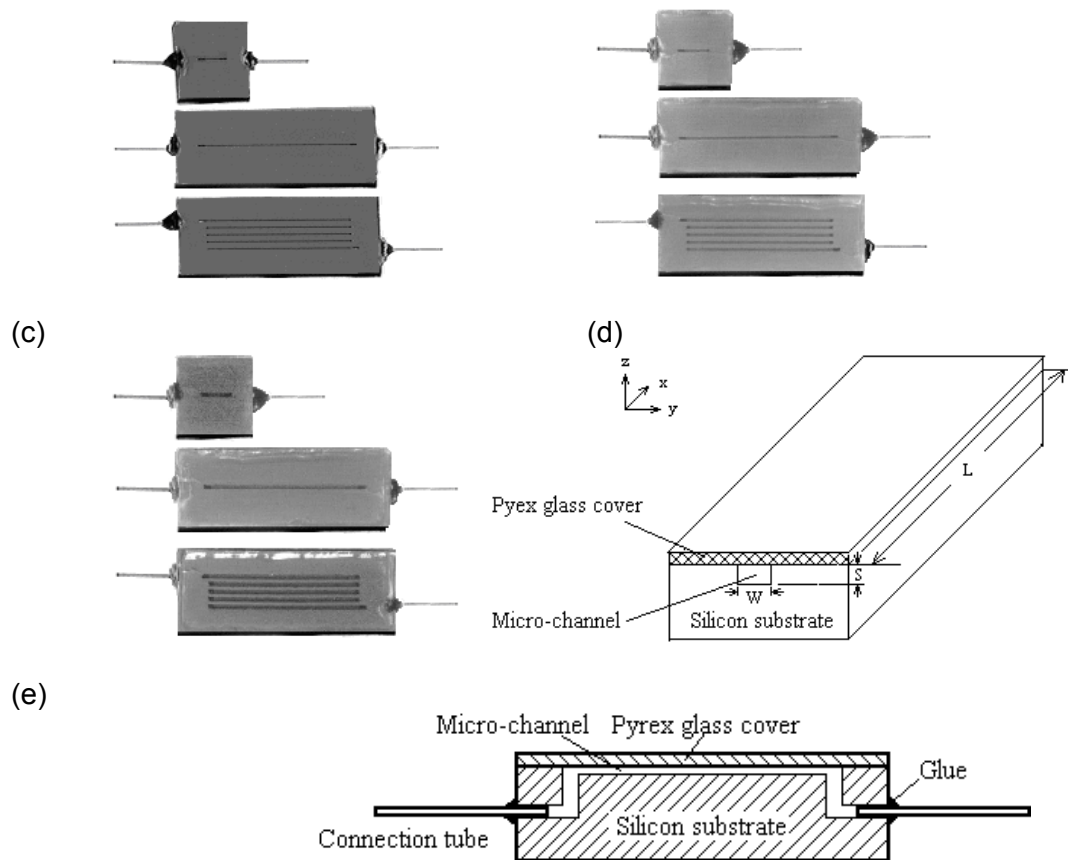
Figure 2-1. (a) Photograph of a group of micro-channels (D_h = 0.209 mm) (b) D_h = 0.412 mm (c) D_h = 0.622 mm (d) Schematic of the straight micro-channel (e) Schematic showing inlet and outlet elbows.
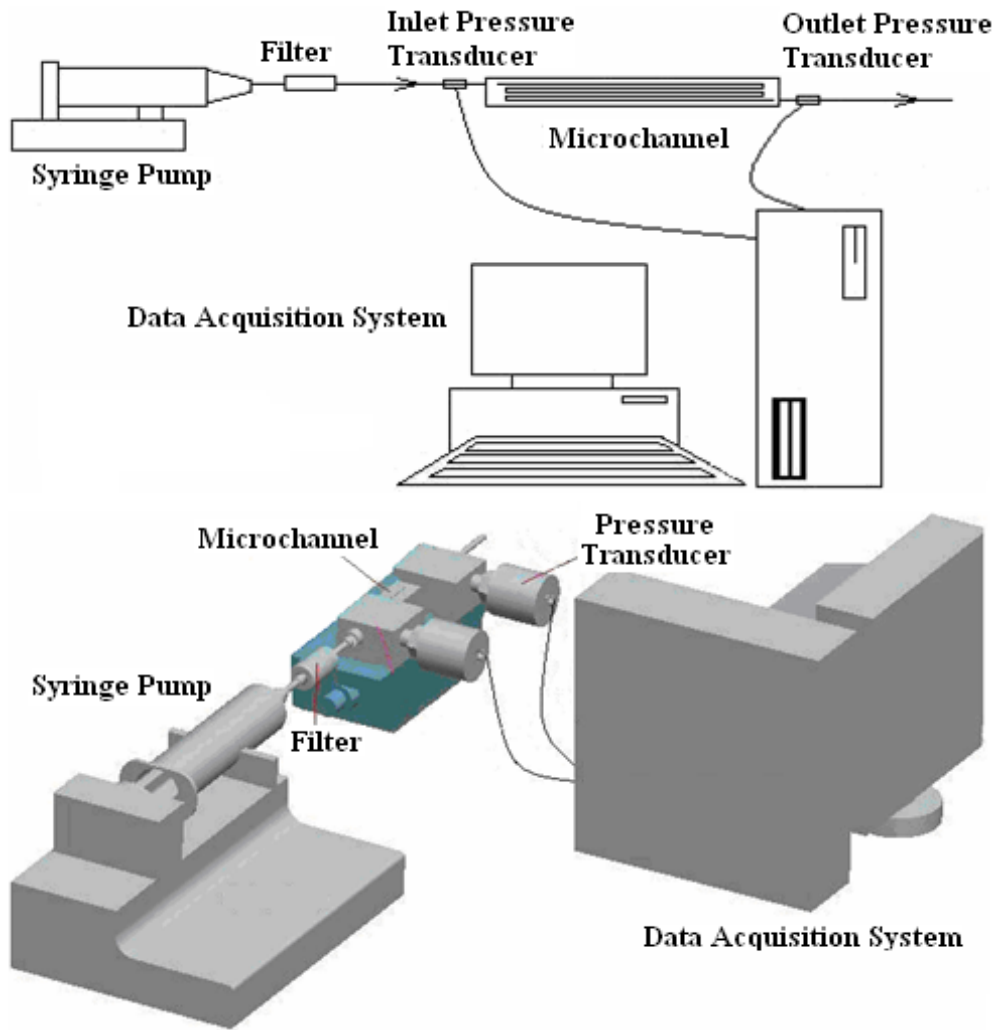
Figure 2-2. Schematic of experimental apparatus.
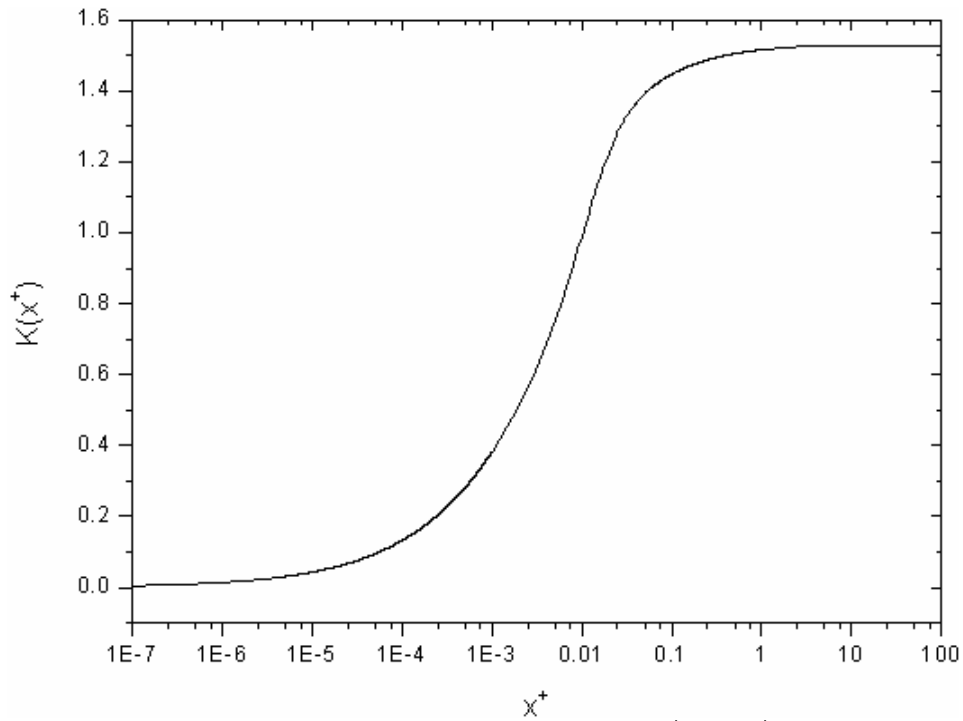
Figure 2-3. Pressure drop defect $K(x^+)$ vs. x^+.
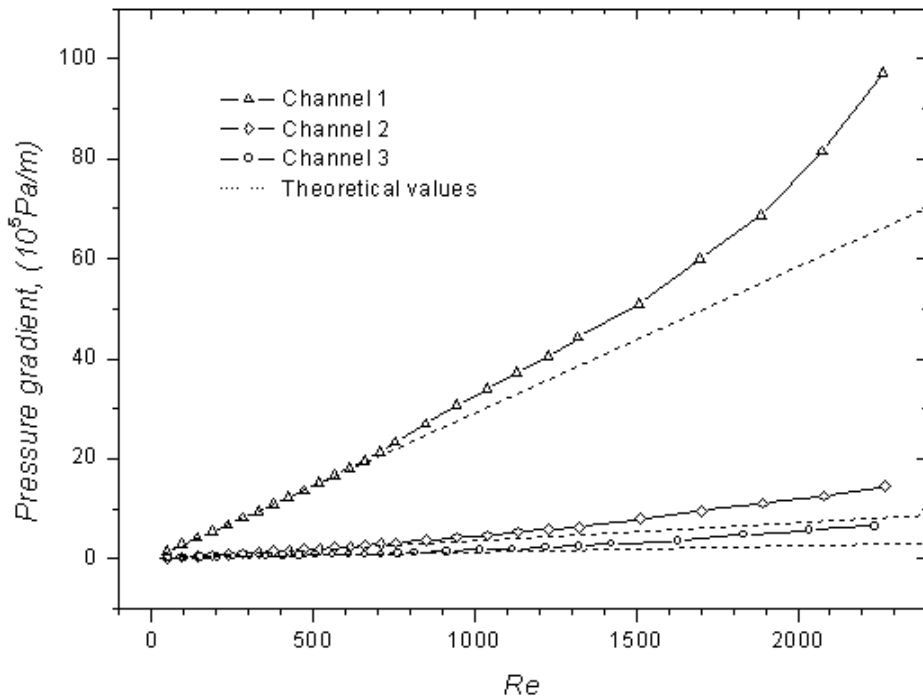
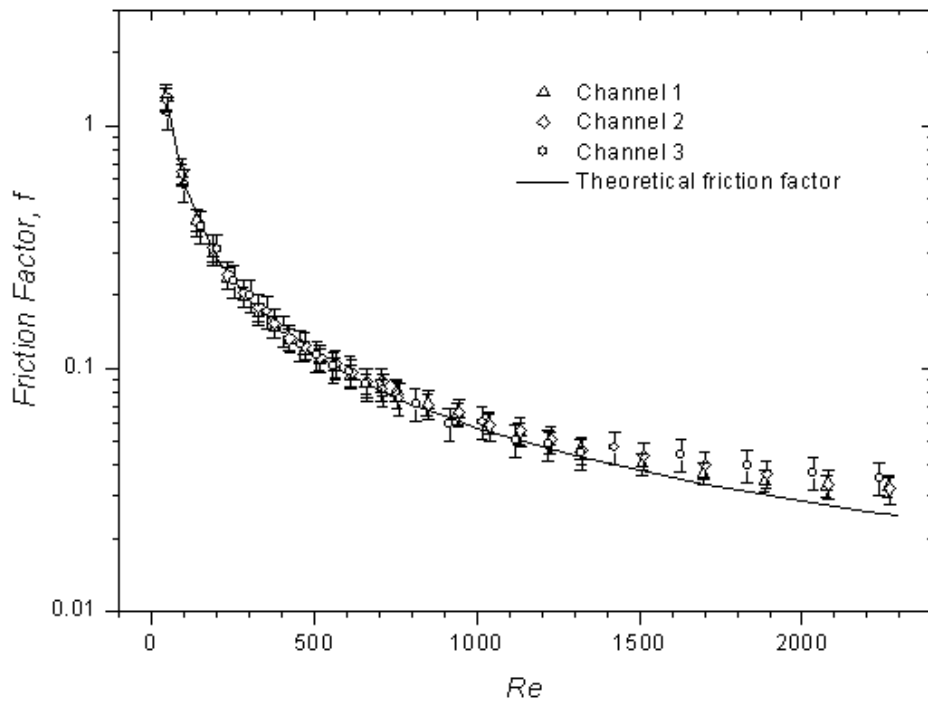Figure 2-4.   Experimental pressure gradients without removing the entrance effect $(\Delta P_\lambda - \Delta P_{sh})/(L_\lambda - L_{sh})$ vs. Re number.

Figure 2-5. Experimental friction factor vs. Re number in straight micro-channels.
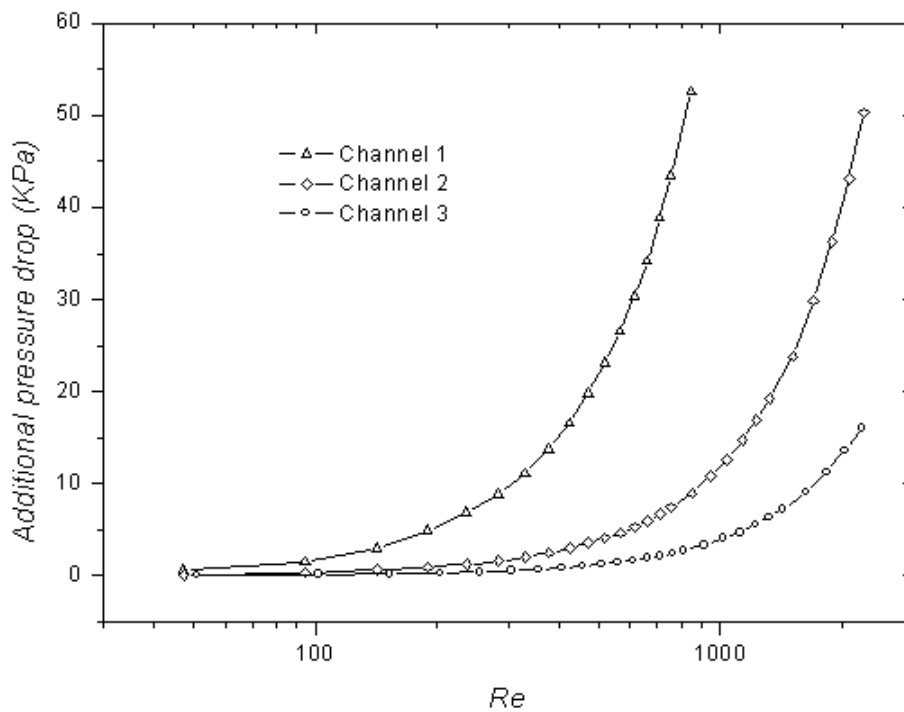
Figure 2-6. Bend additional pressure drops vs. Re number in serpentine micro-channels.
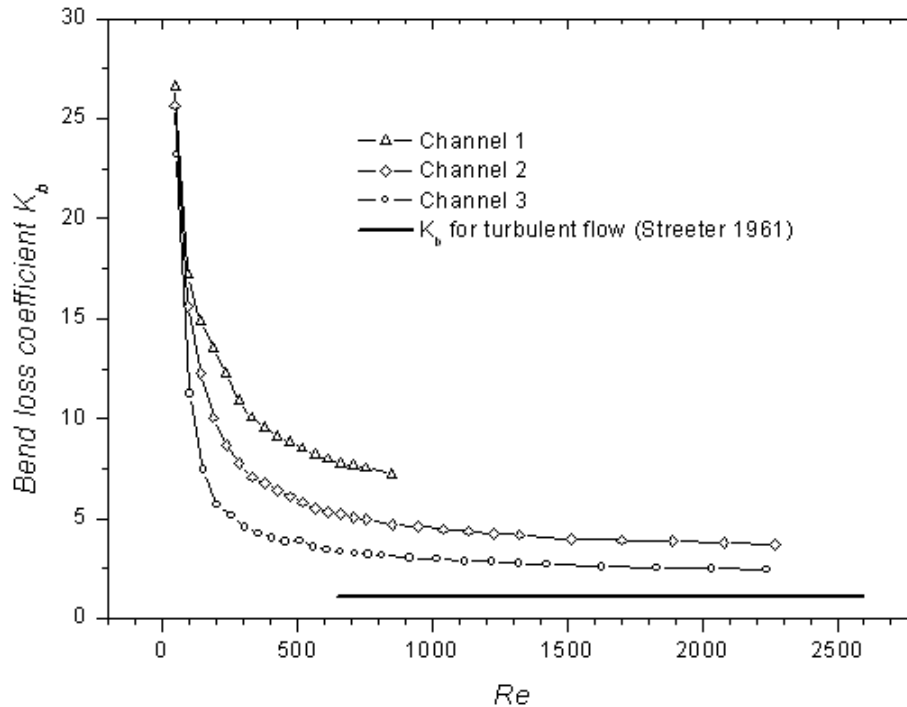
Figure 2-7. Bend loss coefficients vs. Re number in serpentine micro-channels.

3. Flow Structures around a Bend

From chapter 3, we know the bend additional pressure drop is related to the flow structure around the bend, here a micron-resolution particle image velocimetry (micro-PIV) system was built and used to obtain the detailed velocity vector field in a serpentine micro-channel. The micro-PIV system was verified first by the velocity profile in a straight micro-channel of 0.209 mm. It was found that the vortices around the outer and inner walls of the bend do not form when Re<100. Those vortices appear and continue to develop with the Re number when Re>100, and the shape and size of the vortices almost remain constant when Re is larger than a value in 1000-1500. The results are compatible with those in chapter 3.

3.1 Introduction and Background

In curved channels, the centrifugal force drives the more rapid fluid toward the concave part of the curved channel while the fluid in the convex part is slowing down causing a secondary flow at a right angle to the main flow. The magnitude of the secondary flow increases with a decreasing bend radius and increasing fluid velocity. As expected, the curved channel will cause a much higher friction loss than that of the corresponding straight tube for both laminar flow and turbulent flow. In previous works, the researchers used computational method or color dye to visualize the flow structure. Here a relatively new experimental technique, microscopic particle image velocimetry (micro-PIV) was used to measure the velocity field. The micron-resolution Particle Image Velocimetry (μPIV) system was first developed by Santiago et al. (1998) to investigate microscale fluid flow. He used an epi-fluorescent microscope with a continuous Hg-arc lamp, and a Princeton Instruments' intensified CCD camera to record the flow around a nominally 30 μm diameter cylinder in a Hele-Shaw flow cell. A bulk velocity of 50 μms⁻¹ was measured with a spatial resolution of 6.9×6.9×1.5 μm, based upon the size of the first correlation window and the depth-of-field of the microscope.

Later, the system was modified by Meinhart et al. (1999) to measure higher speed flow using the pulsed laser. It is becoming one of the most versatile experimental tools in microfluidic research. Though μPIV has evolved from conventional PIV, there are several important factors which differentiate μPIV from conventional PIV.

One hardware difference is the method of illumination in μPIV, i.e. volume illumination. The conventional PIV used a light sheet to illuminate a single plane of the flow with the thickness less than the depth of field of the image recording system. Volume illumination is an alternative approach, whereby the test section is illuminated by a volume of light. This illumination model may be necessary for obtaining 2-D measurements when optical access is limited to only one direction or in micro-scale geometries in which alignment of the light sheet is difficult. It is advantageous when one is interested in measuring flows through micro electromechanical systems for which optical access is limited to one direction and the length scale is of the order of micrometers (Meinhart et al. 2000a). The small length scales associated with microfluidic devices require that the thickness of the measurement plane should be only a few micrometers. Since it is difficult to form a light sheet that is only a few micrometers thick and virtually impossible to align such a light sheet with the optical plane, volume illumination is the only feasible illumination method for most micro-PIV applications. One shortcoming for volume illumination is it causes significant background noise and limits the particle concentration by reducing the signal to noise ratio (Gui et al. 2002; Meinhart et al. 2000b).

Image processing and advanced interrogation algorithms can be used to enhance image quality and to increase the signal-to-noise ratio. The images taken in micro-PIV are usually in worse condition, i.e. lower signal-to-noise ratio, than those in the conventional PIV. Errors in PIV measurements can be reduced by improving the experimental conditions and by using advanced interrogation algorithms such as the average correlation method. Ensemble average correlation method is a time-averaged PIV algorithm developed by Meinhart et al. (2000b) to improve the signal to noise ratio, especially in case of the volume illumination. This algorithm can only be applied to steady or periodic flow fields. Since most typical microfluidic devices are working in steady flow conditions, the time averaged velocity field is sufficient to resolve the micro-scale flow. The central difference image correction algorithm (Wereley and Gui 2003) is a very effective and accurate method, especially for making measurements in regions of high velocity gradient. This method is a combination of the central difference interrogation algorithm developed by Wereley and Meinhart (2001), the continuous window shifting technique developed by Gui and Wereley (2002) and the modified image correction algorithm originally introduced by Huang et al. (1993). This central difference image correction method shows the significant reduction in the evaluation error, i.e. the bias and random errors, when compared to other more traditional methods.

Another important difference is the size of seed particles. Since a seed particle should be small enough compared to the dimension of the microfluidic device not to disturb the flow pattern, relatively small seed particles are required in μPIV. However, when the particle diameter is much smaller than the wavelength of the illumination light, scattering from the particles is too weak to image them using elastic scattering, i.e. the frequency of the scattered light is the same as that of the incident light. An inelastic scattering technique such as fluorescence can be used to increase the signal-to-noise ratio by filtering the background light.

Brownian motion is another factor to be considered in μPIV since Brownian motion becomes significant when the particle or the flow velocity is very small, and eventually causes errors in the velocity measurement and increases the uncertainty in the particle location. Brownian motion has two major effects on μPIV measurements.

One effect decreases the accuracy in estimating the particle displacement between the two light pulses, i.e. the time interval. Brownian motion also can cause errors in estimating the particle location during the illumination exposure. The latter problem can be solved readily by using pulsed lasers which reduce the exposure time so significantly (to 5 ns) that Brownian motion has no effect (Nguyen and Wereley 2002). The former error can be reduced by increasing the time interval. Though long time interval values generally have been avoided in PIV evaluation because of the larger evaluation error associated with the longer time interval, this problem can be minimized with advanced interrogation algorithms such as the central difference interrogation. Also the Brownian motion error is further reduced by a factor of $1/\sqrt{N_i}$ when N_i particle images are averaged in a single interrogation spot.

In this chapter, the main objective is to 1) build an in-house micro-PIV system and 2) achieve the flow structures under different Re numbers to explain the pressure drop data in chapter 3.

3.2 Micro-PIV System
3.2.1 Laser Beam Alignment

Two Nd:YAG laser machines(Continuum Minilite II) were used to create the illumination source. Some useful information of the laser is listed in Table 3-1. To make the two lasers illuminate approximately the same region, a laser beam alignment component is constructed to combine these two lasers in the same optical axis. Fig. 3-1 shows the top view of the optical layout of the laser beam alignment component. A half waveplate (Newport) changes the vertical polarization of laser B to be horizontal polarization while laser A still keeps the vertical polarization. The beam merger, a dielectric polarizer (Newport), reflects the laser with vertical polarization, namely laser A and transmits the laser with horizontal polarization, namely laser B. A beam stop absorbs the light that transmits the beam merger. A linear and rotation stage A with high precision was fixed beneath the beam merger and another linear high precision positioning stage B was fixed beneath the laser B output. Rotate stage A to change the incline angle of laser A and make the intensity of the reflection beam maximum. After that, adjust stage B to make laser B merge into the optical axis of laser A. A beam expander including two spherical concave and convex lenses (Newport) expands the size of the laser beam after the beam merger. Adjusting the distance between these two lenses can change the expanded laser beam size. The reason why the spherical lenses were used here is to create volume illumination for micro-PIV measurement.

3.2.2 Timing Scheme

Since the laser beams are pulsed and the pulse width is so short, 3-5 nsec from Table 3-1, the CCD camera shutter is required to keep open to make the frame exposed during the pulse width. And one frame is required to be exposed once. Hence a timing scheme is required to externally control the two lasers and CCD camera.

To externally control the laser, turn the real panel FLASHLAMP and Q-SWITCH switch of the laser machine Minilite II from INT to EXT. It will disable the internally generated signals which respectively fire the flash lamp and open the Q-switch. At the same time, these switches let the Minilite II accept TTL signals into the FLASHLAMP TRIG IN and Q-SWITCH TRIG IN BNC ports to trigger flash lamp firing and Q-switch opening. The Q-switch delay can adjust the output pulse energy.

For Minilite II, the delay of about 152 µs yields highest energy laser pulse. The time delay between the two lasers' firing the flash lamp is quite important and should be chose carefully since it sets the interframing time.

A specialized CCD camera (Cooke Sensicam QE), 1376x1040 pixels, was used to record the flow field. It uses thermo-electrical cooling to cool down to -12 °C, which lowers the readout noise low to 4 e-rms so the weak fluorescent signal can be measured. The interframing time low to 500 ns make it enough to measure the flow with high Reynolds number up to 2000. To externally control the CCD camera, set the operation mode to double shutter in the software and use a coaxial cable to connect the TRIG IN BNC ports with the timing controller. The double exposure is controlled via an external TTL trigger signal from the controller.

A timing controller (Labsmith LC 880) was used to realize the timing scheme. It has 8 input and 8 output channels. It is also able to send a trigger-pulse delay from 50 ns to 1370 s and trigger-pulse duration from 7.7 ms to 1370 s with the resolution of 10 ns. A RS232 interface connects the controller with the computer to make remote control. Connect the two lasers (4 output ports) and the CCD camera (1 output ports) with the controller, and TTL trigger signals can be sent to them via some coaxial cables. Fig. 3-2 shows the timing diagram for the two lasers and CCD camera. How to program LC 880 to realize this time scheme refers to the Appendix.

When the shutter trigger signal falls, the shutter opens after a very short period. The integration time for image one will be finished some time after the trigger signal rises again and the integration time for image two starts. What we need control is to send two laser pulses by setting a proper time delay from the trigger signal to make one pulse be in the integration time of image one and the other pulse in the integration time of image two, so in each integration time the image will be exposed once, which is called double frames double shutter. The interfaming time can be shortened by sending the first pulse at the end of the image one's integration time and the second pulse at the beginning of the image two's integration time. After testing the CCD camera, we find the minimum interframing time for our CCD camera can reach 300 ns which is enough short for our experiment. Another important issue is the rising duration of the trigger signal must be long enough for the CCD to read out the two images.

3.2.3 Fluorescent Particles Image

To visualize the flow field in the micro-channel, fluorescent particles, polymer micro-spheres (Duke Scientific R500), are seeded in the flow. These micro-spheres have a measured mean diameter of 0.49 µm and approximate a number of 1.5×10^{11} per mL. They also have the excitation maxima of 542 nm and the emission maxima of 612 nm with 70 nm stokes shift. A filter cube (Olympus U-MWIG), assembled in the microscope (Olympus BX50), reflects the light with wavelengths between 520 and 550 nm, exciting TMRM (maximum excitation at 548 nm), and transmits fluorescence through a high-pass filter (565 nm). The process of taking fluorescent particles image was that the expanded laser beam was delivered into the microscope, where the filter cube directs the beams to the objective lens. The objective lens relays the light onto the micro-channel, where it illuminates the entire flow volume. Fluorescent particles in the cone of illumination absorb the illumination light, λ = 532 nm, and emit a distribution of red light, λ = 612 nm. The emitted red light can go through the filter cube and is recorded onto the CCD camera while the reflected green light from the background is filtered out by the filter cube. According to the timing scheme, the CCD camera shutter was opening when the lasers came. Hence two consecutive fluorescent particles images were recorded.

Fig. 3-3 (a) and (b) show the real images and schematics of a straight micro-channel with the hydraulic diameter of 209 μm and a serpentine micro-channel having a rectangular cross-section 650×100 μm with hydraulic diameter of 0.173 mm.

3.2.4 Measurement Depth

Fig. 3-4 shows the schematic of micro-PIV used to investigate the pressure-driven de-ionized water flow in serpentine micro-channels. Fig. 3-5 and Fig. 3-6 show the photo of the system and the laser beam alignment component. Firstly the fluorescent particles were seeded into the de-ionized water flow. Two Nd:YAG lasers were directed to the same optical path by optical lenses and expanded by a beam expander made up of a concave and a convex lens. The 0.69 μm particles absorb green light (~542 nm) and emit red light (~612 nm). The emitted light is imaged through a 10× objectives lens (NA = 0.3) and passed to the fluorescent filter cube, where the green light from background reflection is filtered out and the red fluorescence from the sub-micron particles is passed to the 0.5× lens and recorded on the CCD camera. With the micro-PIV technique, the depth of field is described by Meinhart et al. (2000a) as:

$$z_m = \frac{3n\lambda}{NA^2} + \frac{2.16D_p}{\tan\theta} + D_p \tag{3.1}$$

where n is the index of refraction of the immersion medium between the microfluidic device and the objective lens, λ is the wavelength of light in a vacuum, NA is the numerical aperture of the objective lens, D_p is the diameter of the PIV particle and θ is the small light collection angle. In our case, n was 1, λ was 612 nm, NA was 0.3, d was 0.69 μm and tanθ was 0.31. Therefore, the depth of field was calculated to be 26.06 μm. The concentration of the fluorescent particles solution was prepared to ensure at least 5-10 seed particles in each interrogation volume. The necessary minimum seed density was estimated using the equation (Li et al. 2006):

$$N_p = C_v A_i (2z_m) \tag{3.2}$$

where N_p is the desired minimum number of particles in each interrogation volume; C_v is the volumetric concentration of the fluorescent particle solution; A_i is the area of each interrogation window. The interrogation windows in current experiments measure 42 μm square. Adjacent interrogation windows were overlapped by 50%, yielding a spatial resolution of 21 μm. To achieve this spatial resolution required a volumetric particle concentration of approximately 0.0082%. This volume fraction of seed particles is small enough to neglect any two-phase effects, and the working fluid can be considered a single-phase fluid. In this work, this time delay is set to be 1-15 μs for the micro-channel flow at different Re numbers, so the particles move approximately 1/4th of an interrogation window between pulses. The interrogation windows measure 32 camera pixels square, thus the particles moves approximately 8 pixels between laser pulses. Assume that the measured velocity is accurate to within 1/5th of a pixel. It results in an experimental uncertainty of less than ±2.5% (Prasad et al. 1992).

3.3 System Validation

To validate the micro-PIV system, the velocity field is initially obtained at room temperature in the straight micro-channel of 0.209 mm at low Re numbers. The time delay between consecutive frames is 5 ms. An interrogation window of 32×32 pixels and a grid size of 16×16

pixels are used. The analytical solution for the velocity profile at the PIV measurement depth can be formulated as:

$$u(y) = -\frac{W^2}{2\mu}\frac{dP}{dx}\left[\frac{y}{W} - \frac{y^2}{W^2} - \left(\frac{2}{\pi}\right)^3 \sum_{k=0}^{\infty}\frac{(-1)^k}{(2k+1)^3}\frac{\cosh\left[(2k+1)\frac{\pi z_m}{2W}\right]}{\cosh\left[(2k+1)\frac{\pi S}{2W}\right]}\cos\left[(2k+1)\frac{\pi(2y-W)}{2W}\right]\right] \quad (3.3)$$

where *dp/dx* is the pressure gradient, *W* and *S* are the width and depth of the micro-channel respectively. Fig. 3-7(a)-(b) shows the results of PIV analysis for the square micro-channel of 0.209 mm and comparison with the theoretical profile computed from Eq. (3.3). The average discrepancy between our PIV measurements and the predicted velocities is averagely about 4% for the center line ±70 μm while about 10% for the measurements closet to the wall due to the near-wall effect.

3.4 Results and Discussions
3.4.1 Flow structures around the miter bend

Figure 3-8 shows a typical image and velocity vector field generated by the micro-PIV system. The focus of the flow field in Fig. 3-8 is the effects of the 90° turning on the flow micro-structures around the miter bend in the serpentine micro-channel at Re = 500. We note that the main stream velocity increases while the flow is rounding the corner. It is also apparent that micro-structures of flow recirculation have formed around the outer corner and immediately after the inner corner (flow separation). A detailed visualization and discussion on the onset and development of induced vortices around the outer and inner corners with the Re number are given below. Fig. 3-9(a-e) shows the enlarged velocity fields at the outer corner for the Reynolds numbers ranging from 100 to 1500. Fig. 3-9(f-j) shows the enlarged velocity fields at the inner corner for the same Reynolds numbers. Fig. 3-10 shows the corresponding streamlines computed from the experimental velocity vectors. For the induced micro flow structures at the outer corner, there is basically no recirculation for Re = 100 and only some fluctuations in the flow adjacent to the wall due to the wall roughness are captured by the PIV. At Re = 300, a very small vortex located at (x = 0.2 mm, y = 0.95 mm) is seen, but its circulatory motion is not fully developed. It is clear that at Re = 500, the recirculation vortex is fully developed and located at (x = 0.3 mm, y = 1.07 mm). As the Reynolds number is further increased to 1000 (Fig. 3-10(d)) and then to 1500 (Fig. 3-10(e)), the locations of recirculation vortices stay at the same point and only the size and strength are increased with the Reynolds number.

For flow structures near the inner corner, the micro flow structures that form due the flow separation always start right after the sharp edge as the flow separates. Again, there is basically no separation vortex for Re = 100. The separation vortex is very clear for Re = 300. As the Reynolds number is further increased, the size and strength of the separation vortex are also increased accordingly. However, the growth of the vortex seems saturated after Re = 1000 as there is no significant difference in the size between Re = 1000 and Re = 1500 but the strength continues to increase as discussed later. For Re = 1000, the inner corner vortex approximately occupies 20% of the width of the channel in the downstream of the bend.

In summary, micro-structured recirculation vortices are induced when the flow is making the turn in a serpentine micro-channel. These vortex structures are responsible for the bend additional pressure drops for the serpentine micro-channel as compared to a straight micro-channel. The following presents the measured pressure drops and discussions for serpentine channels.

3.4.2 Circulation Calculation

In order to further substantiate the relatively large bend pressure drops, we calculated the circulation, $\wp$, for every induced vortex from the velocity field given in Fig. 3-9. The circulation, $\wp$, that is the strength of the vortex is defined as:

$$\Gamma = \iint \left(\nabla \times \vec{V} \right) \cdot d\vec{A}$$

(3.4)

The results of the calculated vortex circulation are given in Table 3-2. In general, the outer vortices are three to six times stronger than the inner vortices. Fig. 3-11 shows the total vortex circulations as a function of the Reynolds number. The total circulation is the sum of the absolute values of the inner and outer vortices. The similar trends between the total vortex circulation (Fig. 3-11) and the bend pressure drop of D_h = 0.209 mm channel (Fig. 3-6) serve to confirm the measured data.

3.4.3 Shear strain
For further understanding the micro-structures of the flow, the flow shear strain rate distributions were computed based on the Eq. (3.5) and plotted in Fig. 3-11.

$$\varepsilon_{xy} = \frac{1}{2} \left(\frac{\partial u}{\partial y} + \frac{\partial v}{\partial x} \right)$$

(3.5)

As we examine Fig. 3-11, the shear strain rates generally increase with the Reynolds number and there is an uneven distribution pattern with highest rates concentrated along the inside wall and they peak around the sharp edge. Before the vortices appear, the velocity only changes much around the bend, so we can see bright color around the bend when Re = 100. After the vortices appear, the velocity also changes a lot from the vortex to the main stream, so we can see the color change around the vortex structure.

3.5 Summary

A micron-resolution particle image velocimetry system has been built. The minimum interframing time can be set to 200 ns which make the system has the ability to measure the velocity up to 10 m/s. The flow structure in a serpentine micro-channel with miter bends was conducted experimentally. The following conclusions were obtained:

1) The Micro-PIV system is verified by the flow field in the micro-channel with the hydraulic diameter of 0.209 mm.
2) The flow micro structures around the bend of a serpentine micro-channel can be divided into three categories depending on the flow Reynolds number. When Re<100, there is no induced flow recirculation and flow separation. When Re>100, vortices and flow separation appear and further develop. The outer corner vortex develops along the wall of the channel, and the vortex center moves slightly from the upper stream to the down stream with the increasing of the Re number. The inner wall vortex due to flow separation develops immediately after the flow makes the turn. When Re is around 1000, the inner wall vortex approximately occupies 20% of the width of the channel in the downstream side of the bend. When Re>1000-1500, the shape and size of the outer and inner vortices become almost constant.

3) The shear strain rates generally increase with the Reynolds number and there is an uneven distribution pattern with highest rates concentrated along the inside wall and they peak around the sharp edge. After the vortices appear, the velocity also changes a lot from the vortex to the main stream, so we can see the color change around the vortex structure.

Table 3-1. Specification of the Nd:YAG laser
(Continuum Minilite II).

Parameters	Value
Wavelength	532 nm
Energy	25 mJ
Pulse width	3-5 nsec
Polarization	Vert.
Beam size	<3 mm
Divergence	<3 mradx
Repetition Rate	1-15 Hz

Table 3-2. Calculated vortex circulation

Re	Inner Wall Vortex Strength (mm^2/s)	Outer Wall Vortex Strength (mm^2/s)
100	0.082	-0.41
300	4.10	-12.47
500	10.97	-77.48
1000	28.10	-203.9
1500	97.99	-266.9
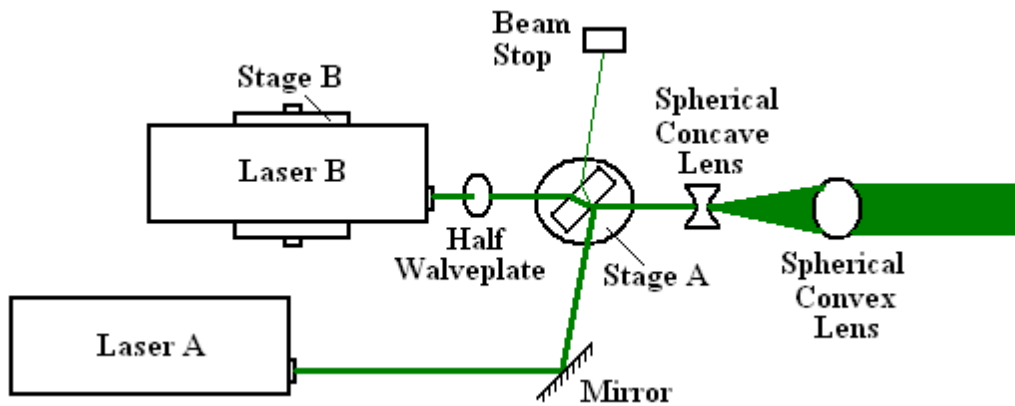
Figure 3-1. Top view of the optical layout of the laser beam alignment.
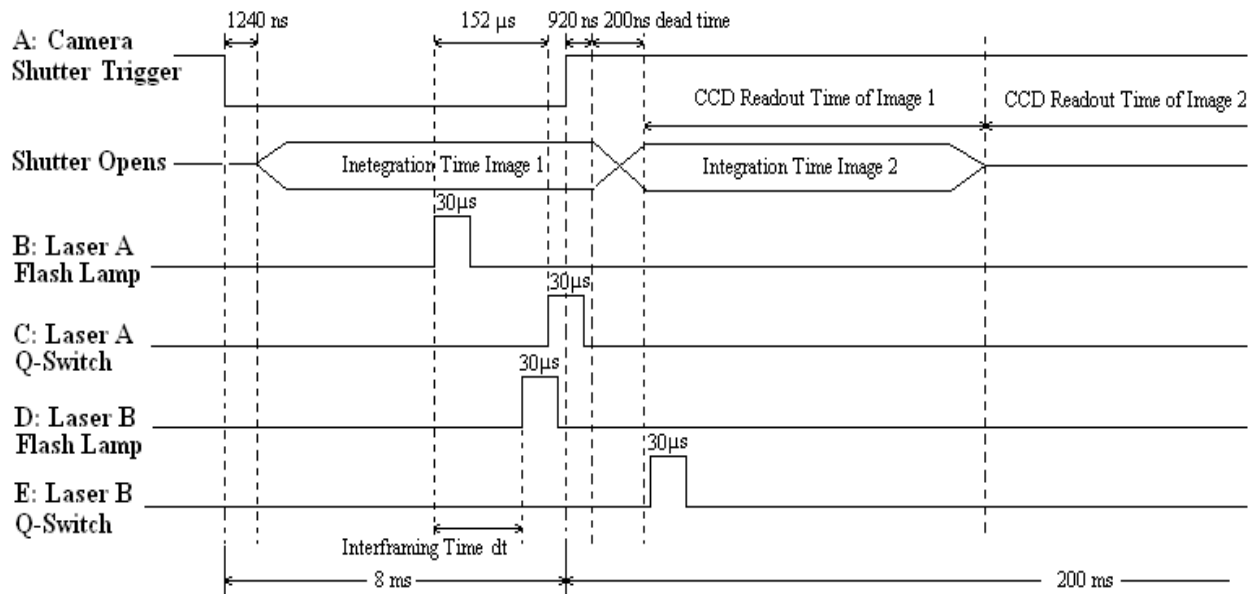
Figure 3-2. Timing diagram for the two lasers and CCD camera.

a)
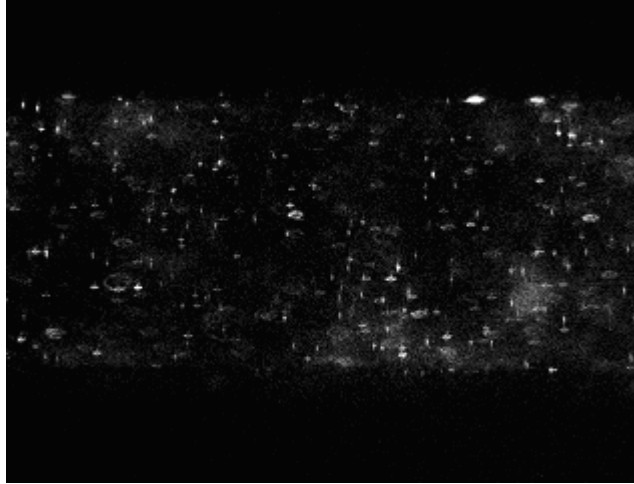
b)
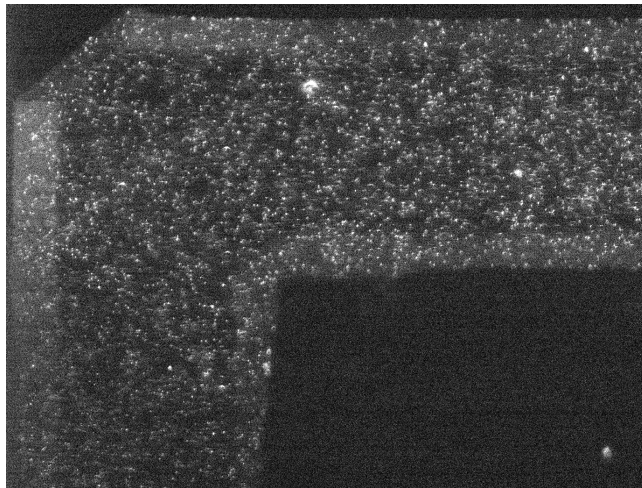
Figure 3-3. a) A real image of the straight micro-channel with hydraulic diameter of 0.209 mm and b) the serpentine micro-channel with hydraulic diameter of 0.172 mm (a 10× objectives used; white spots are the fluorescent particles).
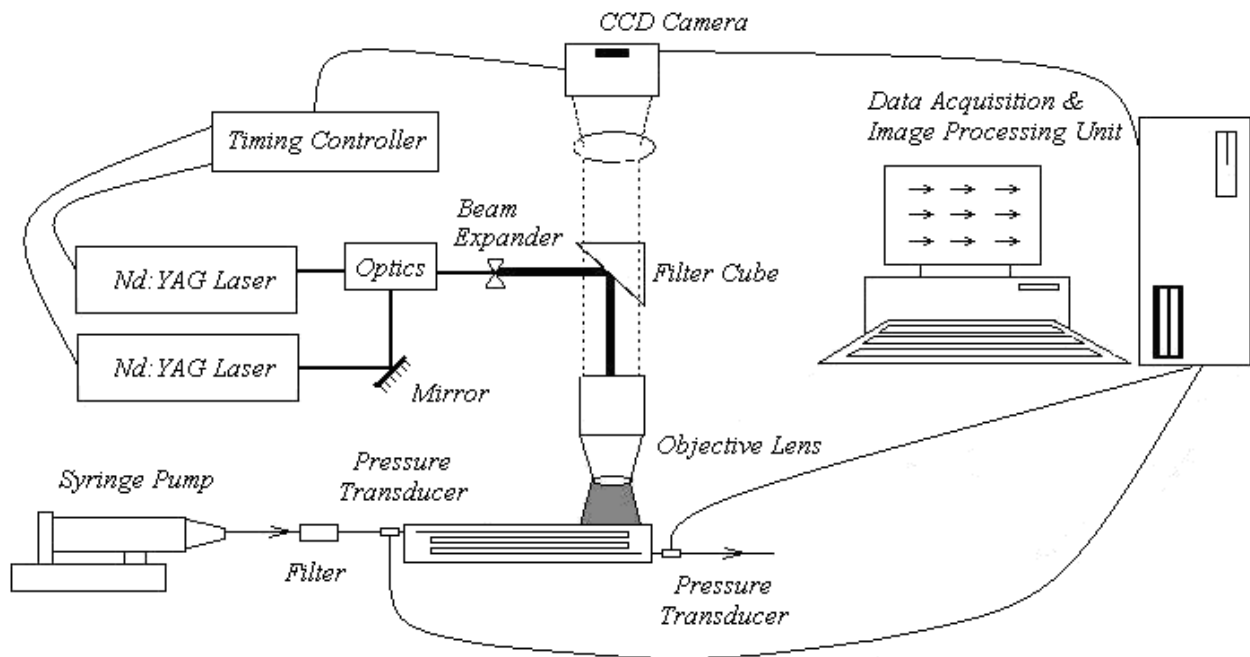
Figure 3-4. Schematic of the experimental apparatus.
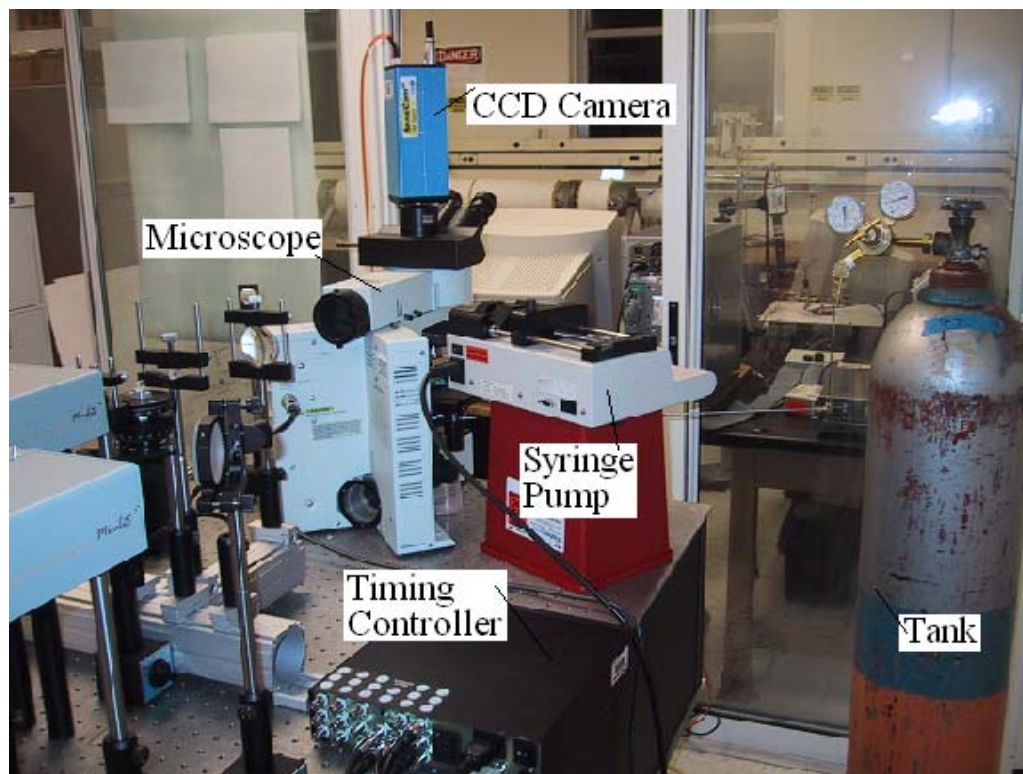
Figure 3-5. Photo of the optical subsystem.
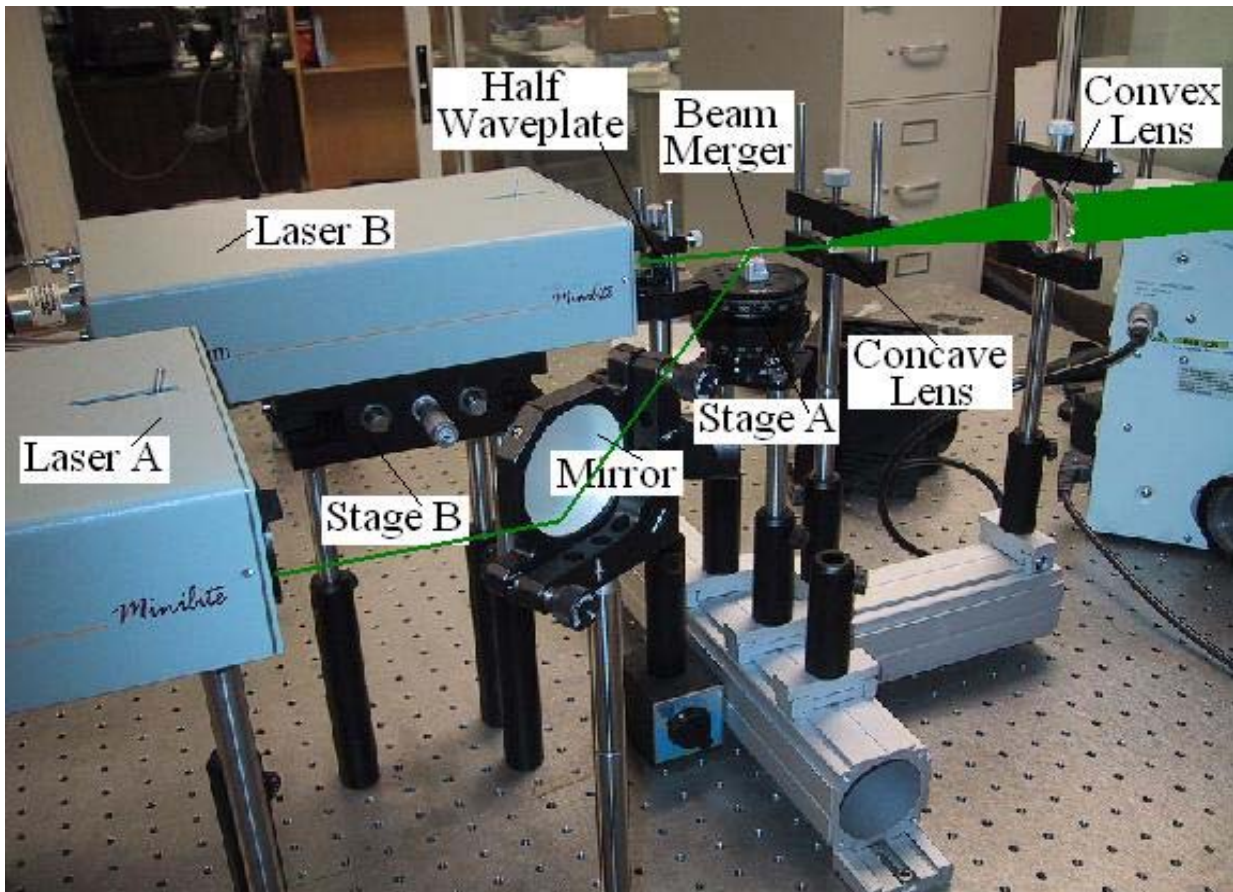
Figure 3-6. Photo of the laser beam alignment component.

a)
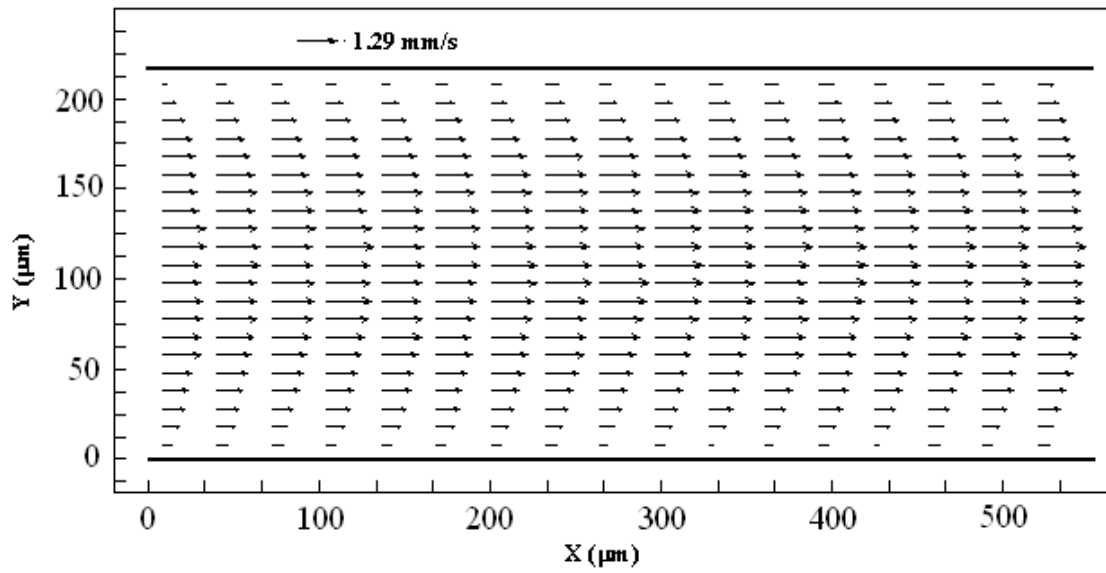
b)
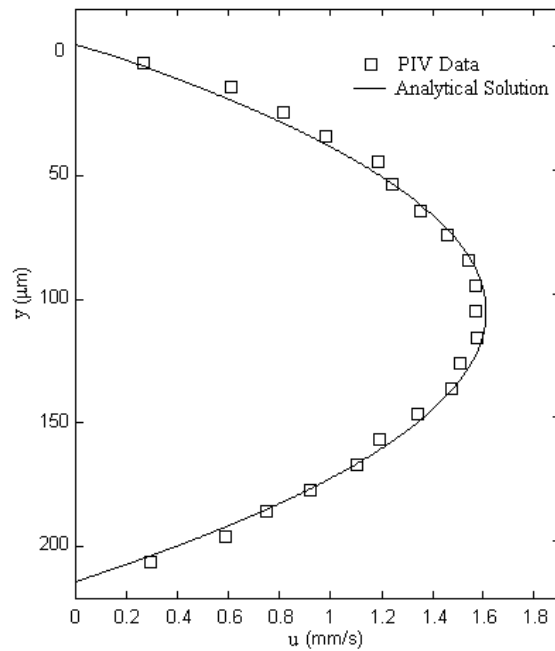
Figure 3-7. Micro-PIV results for low speed flow. a) Velocity vectors (112 pairs of images were ensemble-averaged) b) Comparison of the measurements with the theoretical profile (*Re* = 0.3).
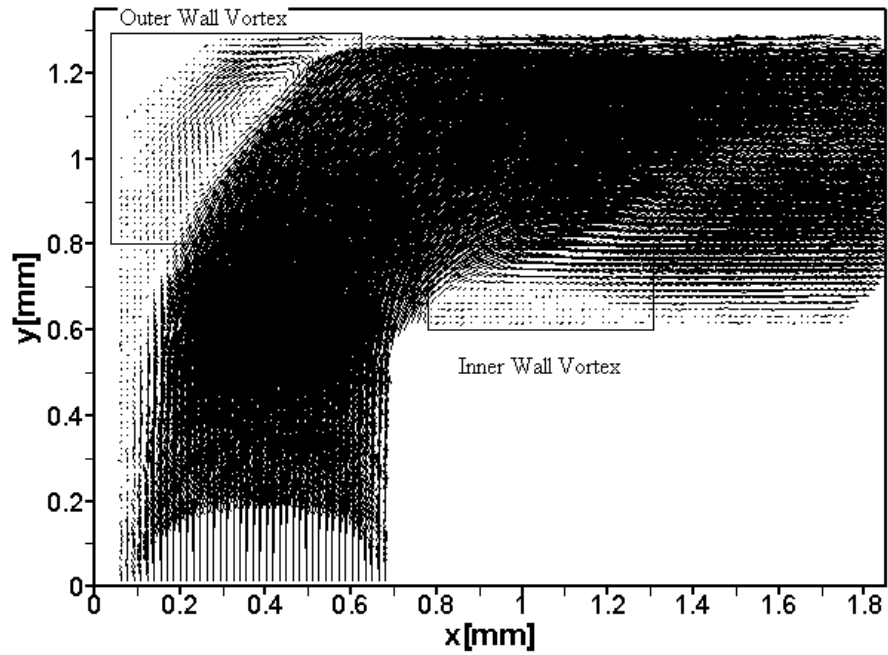
Figure 3-8. Typical velocity vector in the serpentine micro-channel at *Re* = 500.

e)

f)

g)

h)

i)

j)
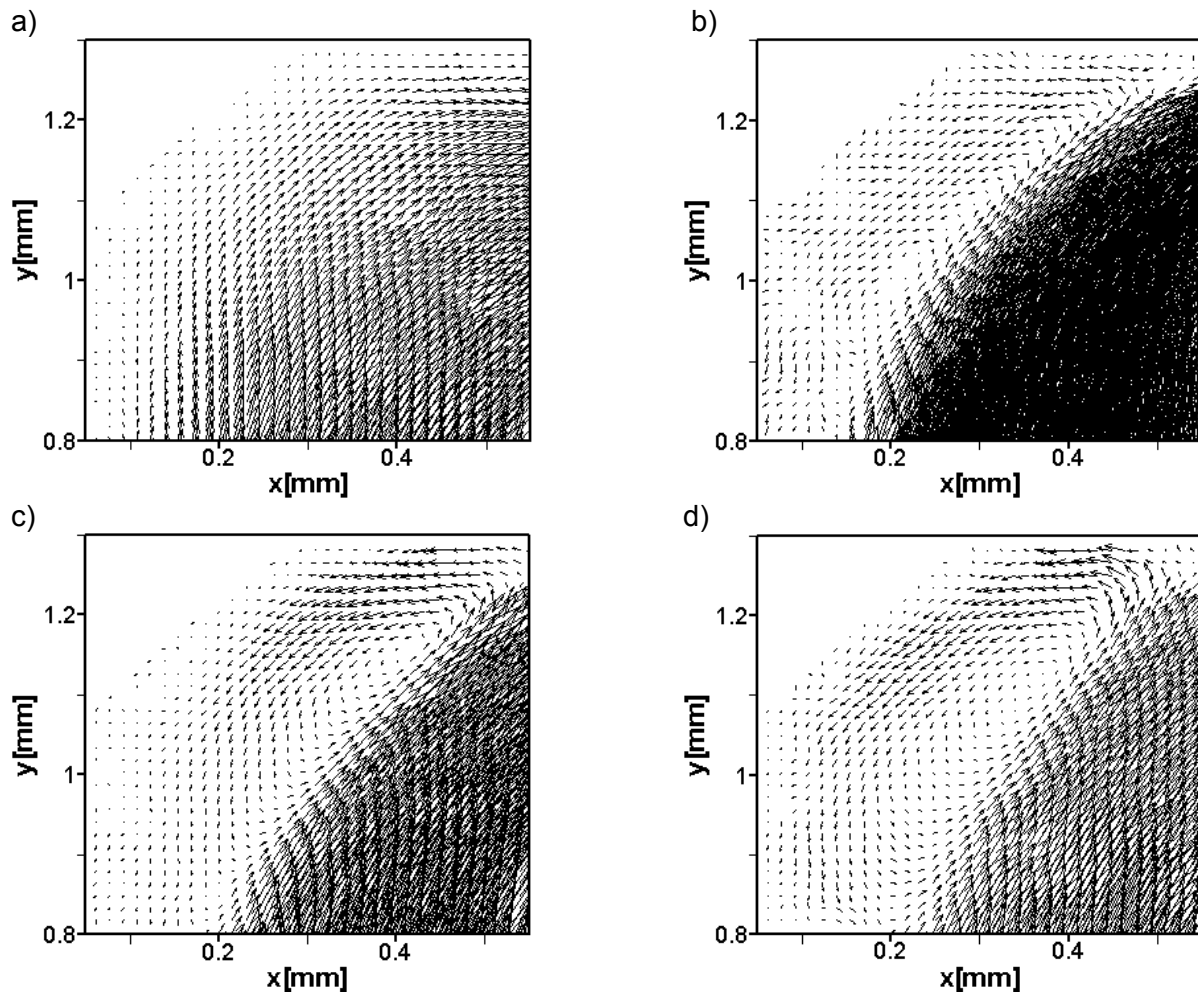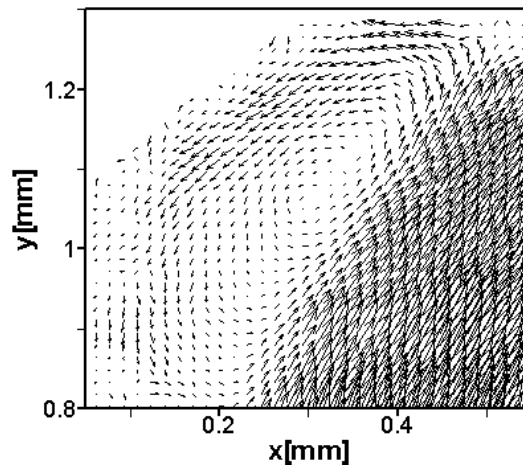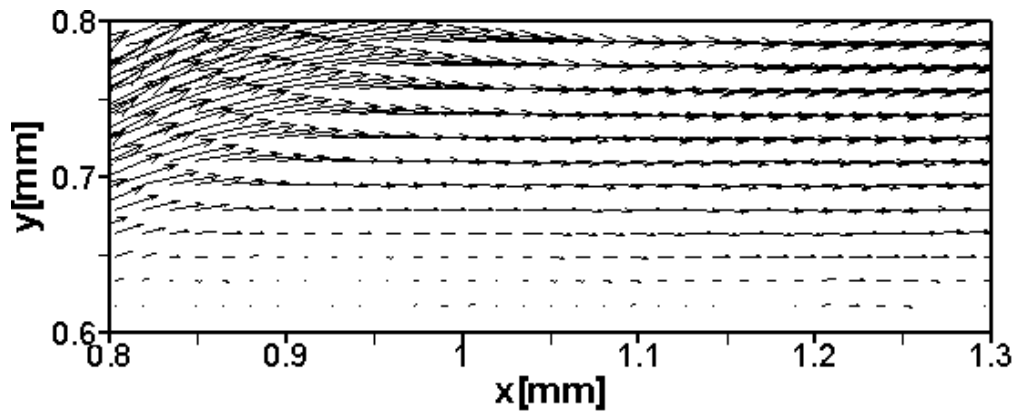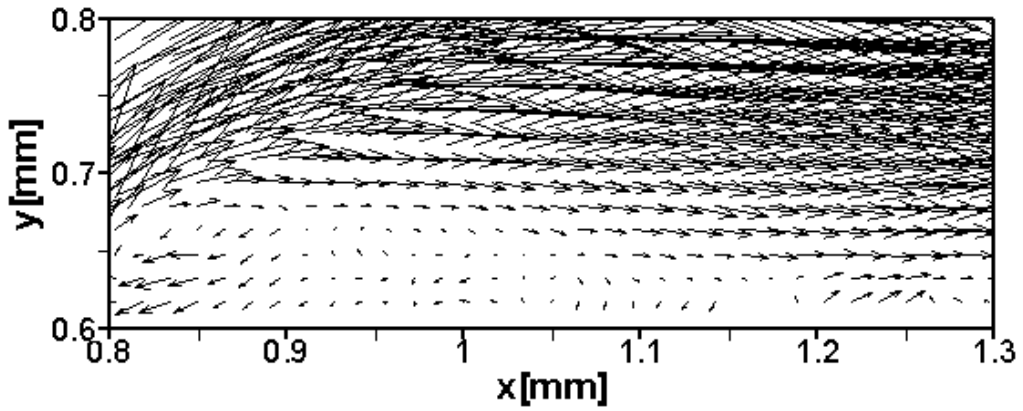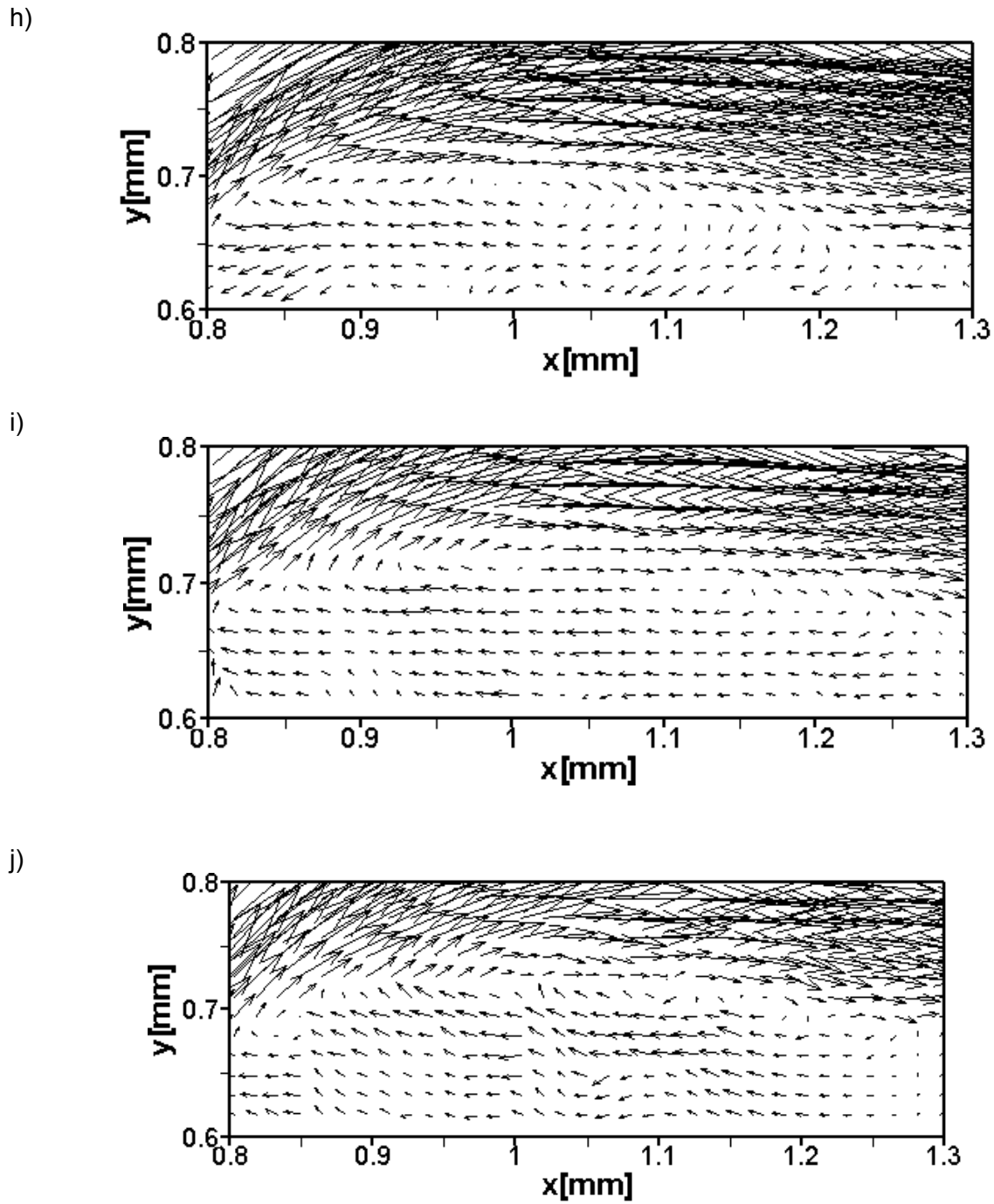
Figure 3-9. Flow structure at the outer wall (a) *Re* = 100 (b) *Re* =300 (c) *Re* = 500 (d) *Re* = 1000 (e) *Re* = 1500 and at the inner wall (f) *Re* = 100 (g) *Re* =300 (h) *Re* = 500 (i) *Re* = 1000 (j) *Re* = 1500

a)
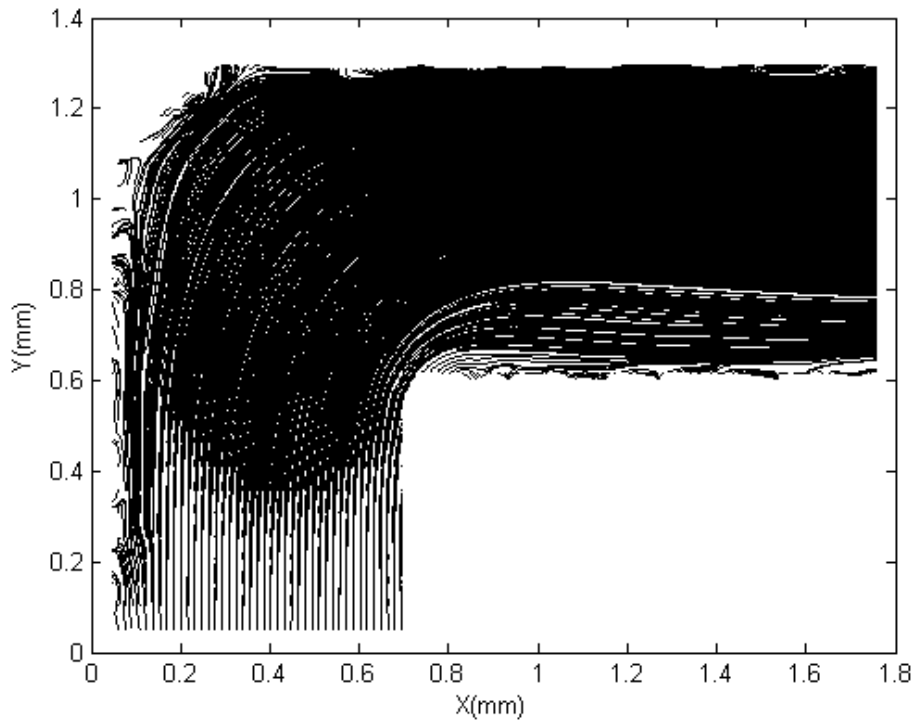
b)
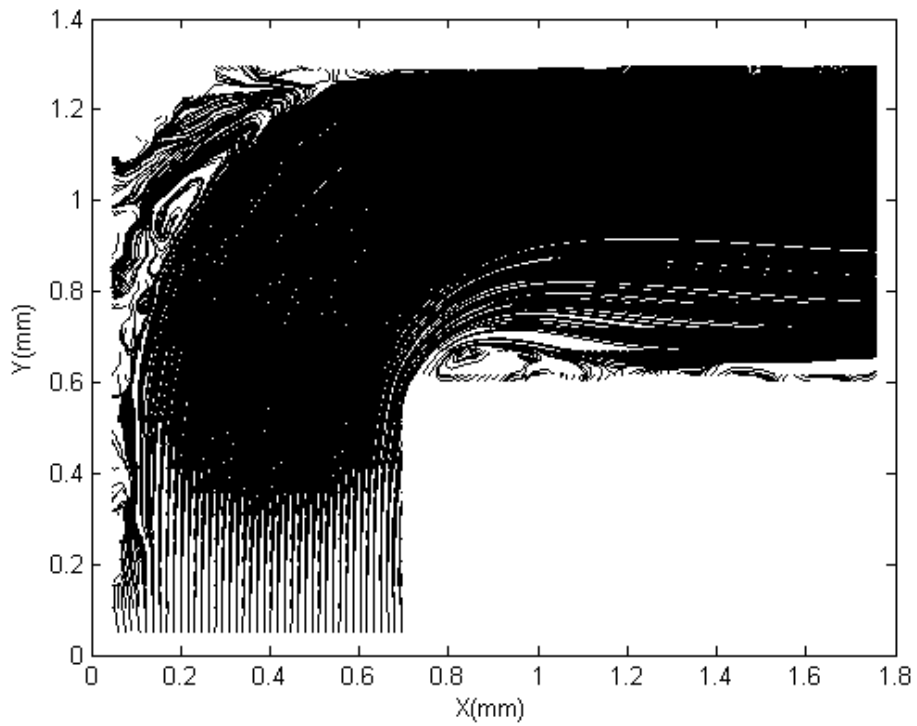
c)
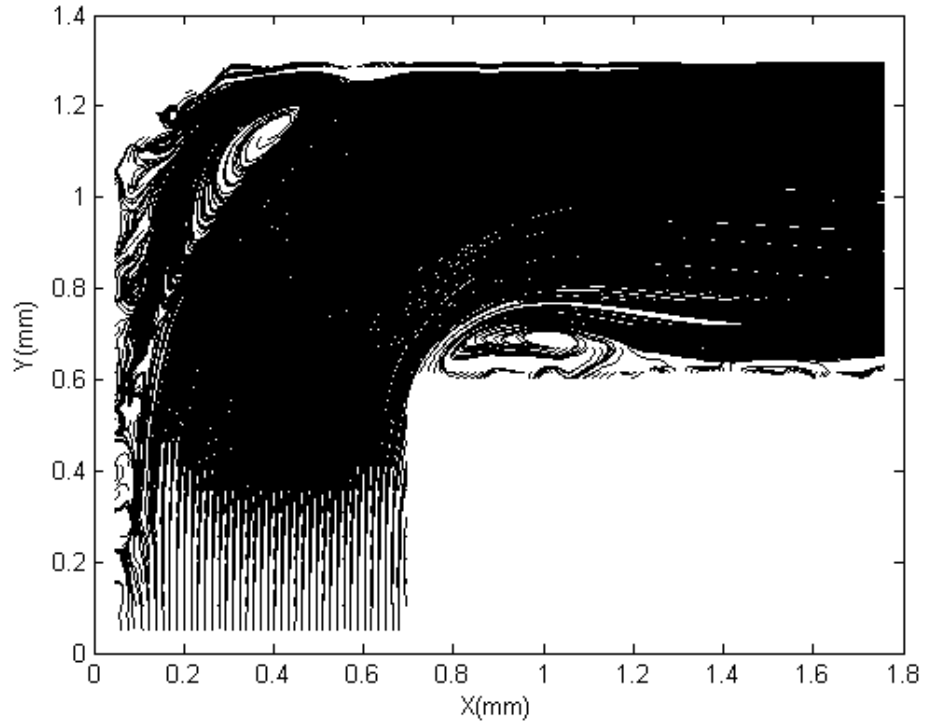
d)
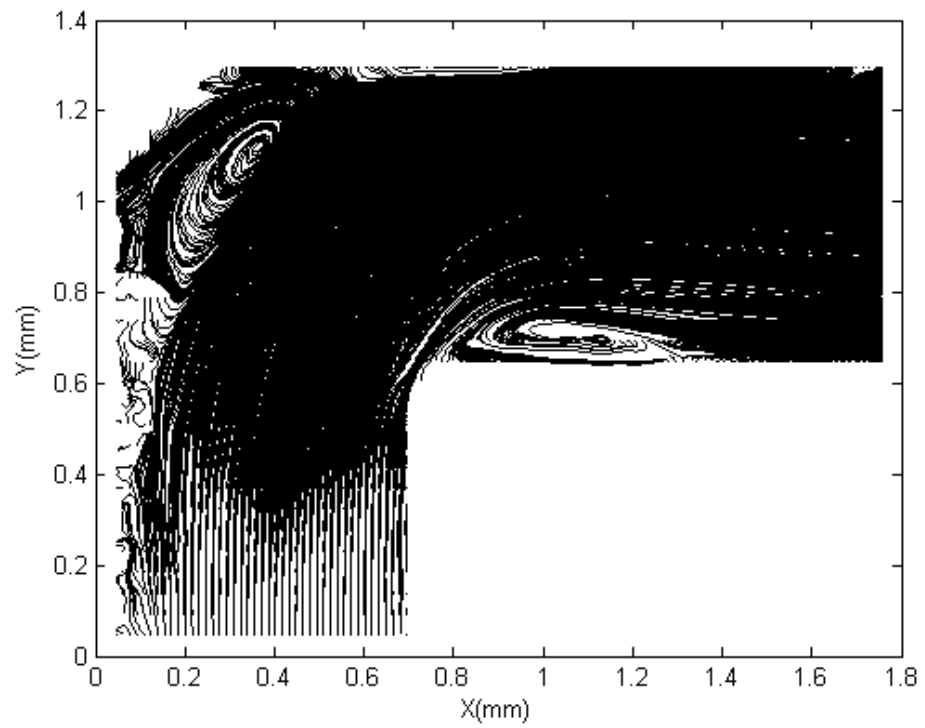
e)
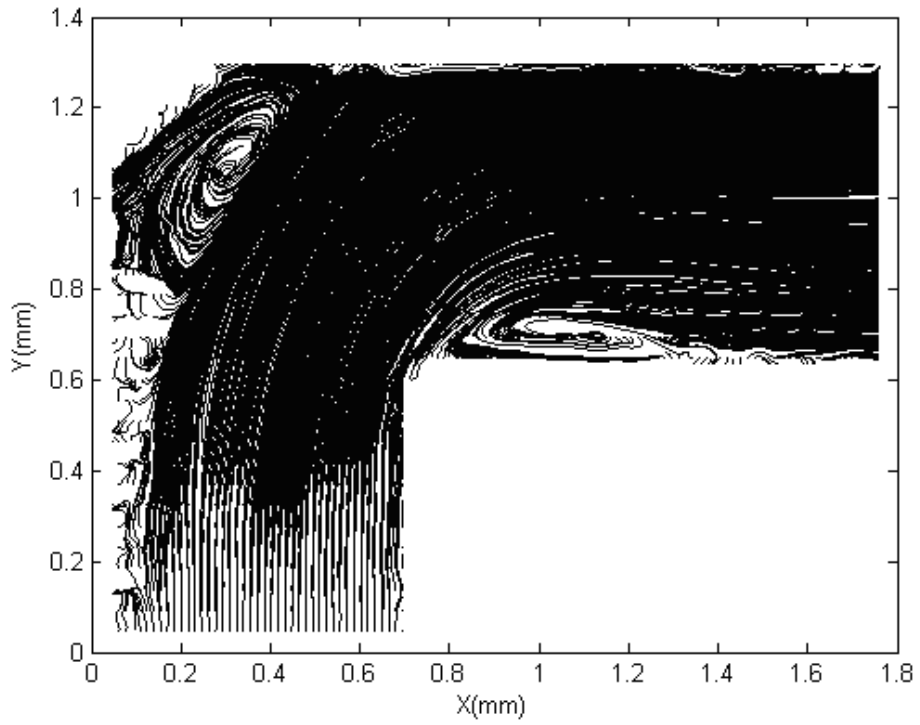
Figure 3-10. Streamline of (a) *Re* = 100, (b) *Re* = 300, (c) *Re* = 500, (d) *Re* = 1000, and (e) *Re* = 1500.

a) *Re* = 100
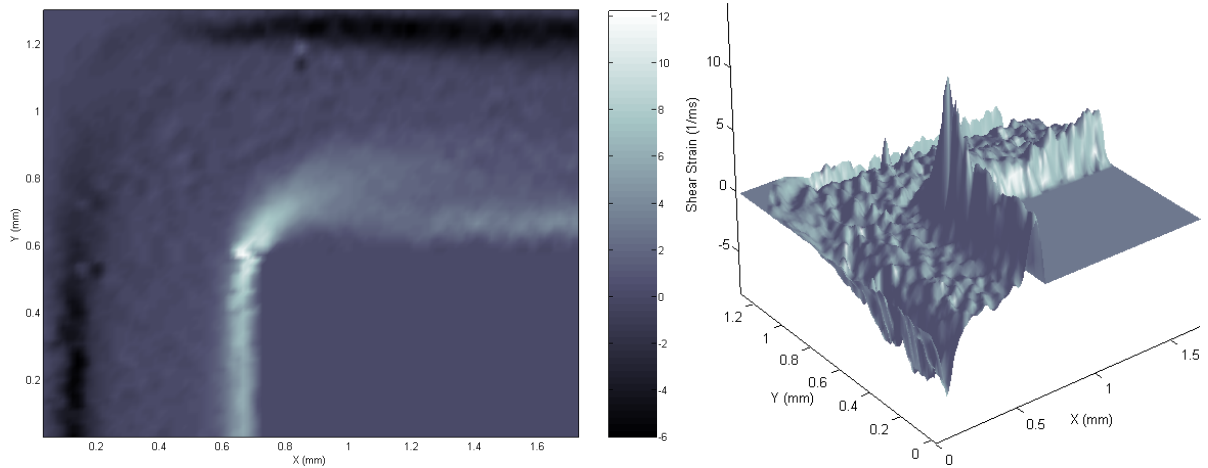
b) *Re* = 300
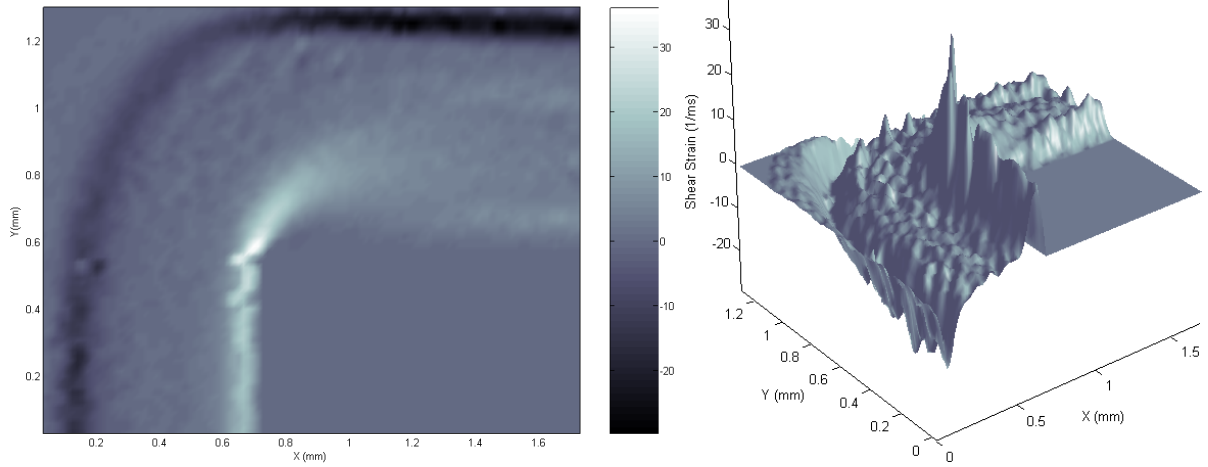
c) *Re* = 500
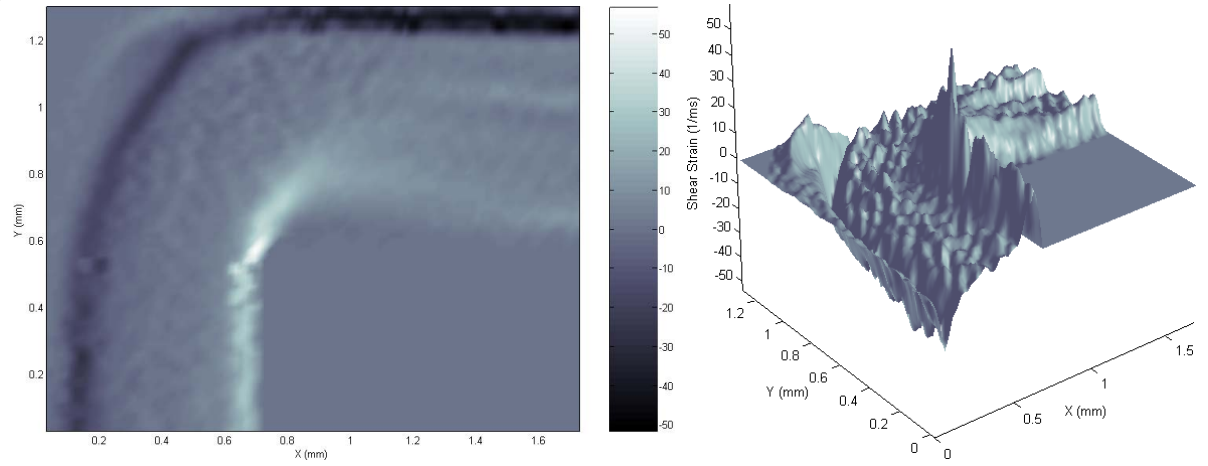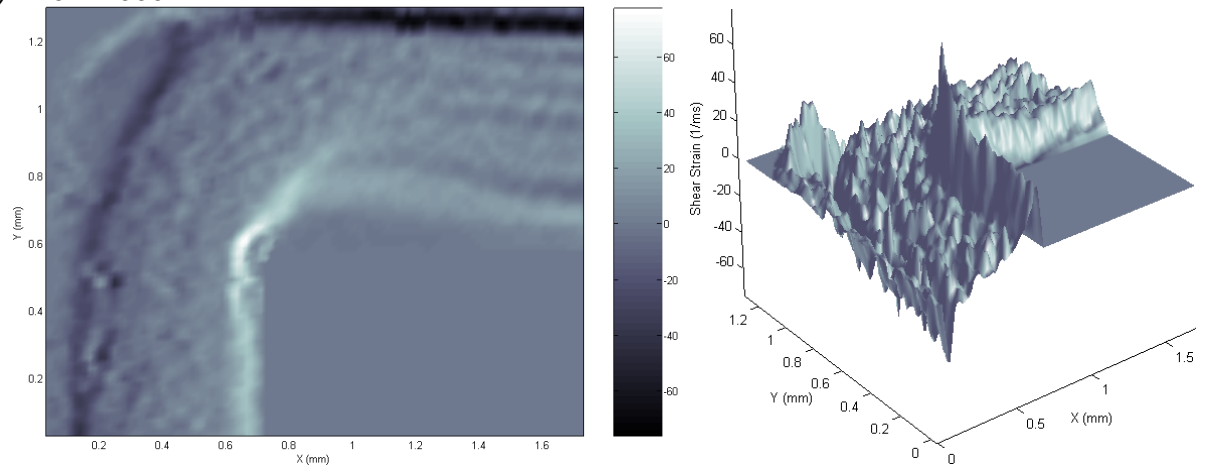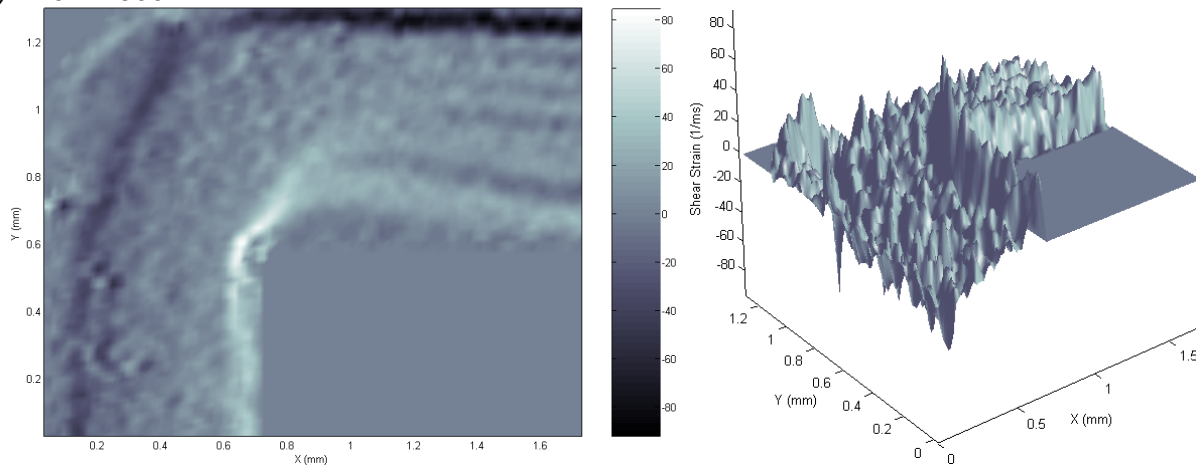
d) *Re* = 1000

e) *Re* = 1500

Figure 3-11. Distribution patterns of shear strain rates. (a) *Re* = 100, (b) *Re* = 300, (c) *Re* = 500, (d) *Re* = 1000, (e) *Re* = 1500.

4. Adiabatic Gas-Liquid Two-Phase Flow

In this chapter, adiabatic gas-liquid flow patterns and void fractions in micro-channels were experimentally investigated. Using nitrogen and water, experiments were conducted in rectangular micro-channels with hydraulic diameters of 0.209, 0.412, and 0.622 mm, respectively. Gas and liquid superficial velocities were varied from 0.06-72.3 and 0.02-7.13 m/s, respectively. The main objective is focused on the effects of micro-scale channel sizes on the flow regime map and void fraction. The instability of flow patterns was observed. Four groups of flow patterns including bubbly-slug flow, slug-ring flow, dispersed-churn flow and annular flow were observed in micro-channels of 0.412 and, 0.622 mm. In the micro-channel of 0.209 mm, the bubbly-slug flow became the slug-flow and the dispersed-churn flow disappeared. The current flow regime maps showed the transition lines shifted to higher gas superficial velocity due to a dominant surface tension effect as the channel size was reduced. The regime maps presented by other authors for mini-channels were found not applicable for micro-channels. Time-averaged void fractions were measured by analyzing 8000 high speed video images for each flow condition. The void fractions hold a non-linear relationship with the homogeneous void fraction as oppose to the relatively linear trend for the mini-channels. A new correlation was developed to predict the non-linear relationship that fits most of the current experimental data and those of the 0.1 mm diameter tube reported by Kawahara et al. within ±15%. Two-phase frictional pressure drop can be predicted within ±10% by Lee and Lee's model.

4.1 Introduction and Background

The flow patterns of adiabatic liquid-gas two-phase flow in the macro-channel have been extensively studied in the past (Mandhane et al. 1974, Taitel and Dukler 1976). Since the buoyancy effect is suppressed by the surface tension, the flow patterns in the mini/micro channel are different from those observed in the macro-channel (Ghiaasiaan and Abdel-Khalik 2001). Recently many researchers published research results on the gas-liquid two-phase flow patterns in micro/mini channels. Wilmarth and Ishii (1994) researched on adiabatic concurrent vertical and horizontal two-phase air-water flows through narrow rectangular channels with gap widths of 1 and 2 mm. Five flow regimes (stratified smooth, plug, slug, dispersed bubbly, wavy annular) and three transition regions (elongated plug, elongated slug, cap-bubbly) were

identified for the horizontal flow. Mishima and Hibiki (1996) measured the flow regimes, void fraction and frictional pressure loss for air-water flow in vertical capillary tubes with inner diameters from 1 to 4 mm. Bubbly flow, slug flow, churn flow and annular flow were observed. Churn flow was never observed in the 1 mm channel. Coleman and Garimella (1999) studied air-water flows in four round tubes with 1.3, 1.75, 2.6, and 5.5 mm inner diameters. Eight flow patterns (bubble, dispersed, elongated bubble, slug, stratified, wavy, annular-wavy, and annular) were observed. Triplett et al. (1999) investigated the air-water two-phase flow patterns in circular channels with 1.1 and 1.45 mm inner diameters and in semi-triangular channels with hydraulic diameters of 1.09 and 1.49 mm. The results showed bubbly, churn, slug, slug-annular and annular patterns can be observed but they poorly agreed with the previous transition models and correlations for macro-channels. Chen et al. (2002) presented the nitrogen-water two-phase flow regimes in circular channels with 1.0 and 1.5 mm. Five flow patterns (bubbly, slug, bubble-train slug, churn, and annular) were found. Kawahara et al. (2002) investigated the two-phase nitrogen-water flow patterns in a 0.1 mm diameter circular tube. Intermittent and semi-annular flows were observed while bubbly and churn flows were not observed. Qu et al. (2004) studied the nitrogen-water two-phase flow in a rectangular micro-channel with a gap of 0.406 mm.

The results revealed the dominant flow patterns were slug and annular flows, with the bubbly flow occurring only occasionally and stratified, and the churn flow was never observed.

Void fraction is also an important issue in heat transfer and flow characteristics for gas-liquid two-phase flows. Armand et al. (1946) investigated the void fraction for the horizontal and vertical air-water flow in macro-channels and gave a correlation widely used by others. Zuber and Findlay (1965) built a model named drift flux model to correlate the void fraction data in two-phase flow. This model relates the gas velocity with the mixture mean velocity, distribution parameter C_0 and the mean drift velocity V_{gj}, which can be given by:

$$\frac{j_G}{\alpha} = C_0\left(j_G + j_L\right) + V_{gj} \tag{4.1}$$

C_0 depends on the pressure, the channel geometry and the flow rate for a given flow pattern. Ali et al. (1993) found that the mean drift velocity V_{gj} can be neglected in narrow channels due to the inability of the bubbles to rise through the stagnant liquid and reported that the void fraction in narrow channels with the hydraulic diameter around 1 mm can be approximately given by the Armand-type correlation with a different distribution parameter. Chung et al. (2004) investigated the void fraction in a 0.1 mm diameter circular tube and a square micro-channel with a hydraulic diameter of 0.096 mm and found the void fraction was independent of the channel geometry in their experiment. Kawahara et al. (2002) experimentally achieved a non-linear relationship between the measured void fraction and the homogeneous void fraction in a 0.1 mm diameter tube. According to the above literature review, more experimental data for the flow patterns and void fraction in the channels of sizes from 1 to 0.1 mm need to be obtained to understand the flow performance in micro-channels.

To evaluate the frictional pressure drop of two-phase flow, there were a lot of models and correlations to predict it for macro-channels, mini-channels and micro-channels. Table 4-1 listed the previous two-phase pressure drop correlations. Triplett et al. (1999) researched on the two-phase pressure drop for the channels with hydraulic diameter of 1.1 and 1.45 mm. He found the homogeneous model provided the best agreement with experimental data for bubbly and slug flow patterns, but all of the widely used correlations significantly over predicted the frictional

pressure drop for annular flow. Kawahara et al. (2002) found Lee and Lee's model present the good agreement (within ±10%) with experimental data for his circular channel of 0.1 mm diameter. Zhao and Bi (2001) found the Lockhart-Martinelli correlation well predicted the two-phase pressure drop for the triangular channels with hydraulic diameters of 0.866, 1.443 and 2.886 mm.

In this chapter, three near-square micro-channels with the hydraulic diameters of 0.209, 0.412, and 0.622 mm were fabricated by laser etching to investigate the nitrogen-water two phase flow patterns, regime maps and time-averaged void fraction. The main objectives of this study are to (1) obtain the flow patterns using a high speed CCD video camera, construct flow regime maps for three micro-channels with superficial velocities of nitrogen and water ranging from 0.06 to 72.3 m/s and 0.02 to 7.13 m/s, respectively, and investigate the size effect on the flow regime maps, (2) compare the new flow maps with the mini-channel flow map based on the Weber number model, (3) evaluate the time averaged void fraction for each micro-channel and compare them with previous correlations, and build an empirical correlation for micro-channels based on current data. Check the predictive ability of the new correlation by using existing time-averaged void fraction data in the literature, (4) obtain the two-phase frictional pressure drops and evaluate the present pressure drop models.

Since the majority of publications in the literature were dealing with the air-water flows, the current work is aimed at providing fundamental understanding and design information for nitrogen-water two-phase flows in micro-channels due to their close relationship with the PEM fuel cells that are receiving top priority for their central role in the hydrogen economy.

4.2 Experimental Apparatus

Fig. 4-1a and 4-1b shows the schematic of the experimental apparatus and the mixer used to investigate the adiabatic nitrogen-water two-phase flow in micro-channels. It includes a syringe infusion pump (Cole-Parmer Instrument), 60 ml syringe (McMaster), micro-filter (Swagelok), nitrogen gas cylinder, regulator (McMaster), flow meters (Omega), valves (Swagelok), Fiber-Lite MI-150 high intensity illuminator (Dolan-Jenner), micro-channels, high speed CCD camera (Redlake), and computerized image acquisition system.

The de-ionized water with flow rates ranging from 0.5 to 46 ml/min, which can be set on the panel of the infusion pump, was driven to the micro-channel test section. The 2 μm micro-filter can remove any particles or bubbles before the flow entered into the micro-channel. The nitrogen gas was released from the compressed gas cylinder. After the regulator, the gas pressure was reduced to 0-30 PSI. The gas flow rate was measured by two volume flow meters with ranges of 0-50 and 0-2610 SCCM, respectively. The mixer was fabricated as a bubble generator. A needle with a 0.2 mm inner diameter was connected to the 1/8 inch gas tube. It was inserted onto the centerline of the 1/8 inch liquid tube. After going through the 1/8 inch gas tube and the needle, the gas flow was mixed with the de-ionized water coming from the 1/8 inch liquid tube and directed into the micro-channel. The superglue was used to bond the micro-channel to the 1/8 inch tube, and it can be easily removed by the superglue remover, so the micro-channel can be replaced easily to make up different test sections. Two pressure transducers with a ±0.5% FS accuracy were installed at the inlet and outlet of the micro-channel respectively to measure the upstream and downstream pressure. The data acquisition system started recording when the flow can be considered as steady state. The test sections were placed horizontally. All experiments were conducted in room temperature and under atmospheric pressure at the discharge of the test section. Flow visualization was achieved by the high speed CCD camera, which can operate at a frame rate up to 8000 fps and a shutter

speed of 1/8,000 s. In this work, the frame rate of 1000 fps and a shutter speed of 1/2,000 s were used. The resolution of the camera was 240(H)×210(V) pixels. Two Fiber-Lite illuminators provided the high intensity light, which was directed onto the test section by two optical fiber light guides. An adjustable microscopic magnification lens was used to magnify the test section. The view field was near the outlet of the micro-channel to minimize the entrance effect, and the view field length was 1.48 mm.

Fig. 4-2 shows the photograph of three size micro-channels and schematic of the micro-channel used in the experiment. The micro-channel was laser etched in a silicon substrate and then a Pyrex thin cover glass plate was anodically bonded on the top of the substrate. Two small connection tubes which can be inserted into the inlet and outlet assembly were connected with the small reservoirs. A microscope (Olympus BX50), a 10× objective lens and a CCD camera were used to measure the dimensions of the micro-channels.

In order to facilitate a meaningful discussion, the relative dominance of the forces involved in the two-phase flow is analyzed through six dimensionless groups. These are defined as follows: $Bo = g(\rho_L - \rho_G)D_h^2/\sigma$, $Ca = \mu_L j_L/\sigma$, $\mathrm{Re}_{GS} = \rho_G j_G D_h/\mu_G$, $\mathrm{Re}_{LS} = \rho_L j_L D_h/\mu_L$, $We_{GS} = \rho_G j_G^2 D_h/\sigma$, and $We_{LS} = \rho_L j_L^2 D_h/\sigma$. Here g is gravitational acceleration, ρ is density, Dh is hydraulic diameter of the channel, σ is surface tension, μ is viscosity, and j is superficial velocity. The subscripts "L", "G" mean the variables are based on liquid, gas flow respectively and "LS", "GS" mean the dimensionless numbers are based on superficial liquid, superficial gas flow respectively. Table 4-2 lists the ranges of those dimensionless parameters for the three channels under experimental conditions. For comparison purposes, parallel values for a 10 cm macro-scale channel are also provided to focus on the scale effects.

With the information given in Table 4-2, we can examine the major differences on the relative importance of various forces involved in a gas-liquid flow between the macro and micro scales. For the flow rates used in our experiments, both the surface tension and the viscous forces are at least two to three orders of magnitude smaller than the gravitational and inertia forces for the macro-scale channel as indicated in Table 4-2. Whereas for the three micro channels in our experiments, it is very clear that the gravitational and viscous force are dominated by the surface tension and inertia forces by at least two orders of magnitude. Comparing between the macro and micro scales, we can conclude that the major change in the force balance is the surface tension which is negligibly small in the macro scale and then becomes dominant in the micro scale while the inertia force is important in both scales as it is proportional to the momentum of the flow only. As a result, the following results and discussion are based on the scenario that the two-phase micro-channel flow is dominated by the balance between surface tension and inertia.

4.3 Results and Discussions
4.3.1 Two-Phase Flow Patterns

The high speed CCD camera can record a continuous video for 8 s with a frame rate of 1000 fps. Since the frame rate was set at 1000 fps, one image was recorded for every 1 ms. For a specific channel size and each flow condition, a total of 8000 images were obtained in one continuous video. From the recorded images, the dynamic structures of the two-phase flow were obtained and the instability of the flow pattern was observed: At a certain gas and liquid superficial velocity, the micro-channel two-phase flow pattern changes with time at a fixed downstream location. Moving the viewing window from the end of the channel to the middle of

the channel, the same phenomenon was found. A scale bar was thought to be helpful in estimating the size of flow structures.

It was developed by multiplying the pixel size of the camera by the number of pixels and then dividing it by the magnification factor. For example, in our experiment the pixel size of the CCD camera was 7.4 μm and the magnification factor was around 1.1 in this experiment, so the actual 100-μm length was covered in 15 pixels in the image, and the uncertainty was 2-3 μm. A variety of flow patterns appeared such as "single-phase liquid", "bubbly flow", "slug flow", "bubble-train slug flow", "liquid ring flow", "liquid lump flow", etc. Only limited numbers of typical flow pattern images from our experiment are given in Fig. 4-3. According to the appearance of the transition flow patterns such as the "liquid ring flow", "liquid lump flow", and "disruption tail of the slug", the entire flow patterns in the present micro-channels can be categorized into four basic flow patterns based on the balance between the inertia and surface tension.

As indicated by the values of Webber numbers in Table 4-1, the relative dominance between inertia and surface tension covers a wide span ranging from where surface tension is three orders of magnitude larger than the inertia to where it is two orders of magnitude smaller. The four basic flow patterns are explained below:

1) *Bubbly-Slug flow*: This regime is dominated by the surface tension force. It mainly has the "slug flow", and occasionally "bubbly flow" would show up. Transitional flow patterns of "liquid ring flow" and "liquid lump flow" do not appear here. It usually appears at a low gas flow rate. The "slug flows" were separated by a thick liquid bridge. The width of nitrogen gas slugs is slightly smaller than that of the channel due to the existing smooth and thin liquid film on the walls. Occasionally, some spherical bubbles, whose diameters are much smaller than the width of the channel, appear.
2) *Slug-Ring flow*: This regime is controlled by the balance between the surface tension force and the inertia force, also called the transition regime. Surface tension force and inertia force are comparable to each other in this region. It mainly features the "slug flow", "liquid ring flow", "bubble-train slug flow", and occasionally "bubbly flow". It often appears at intermediate gas flow rates. The liquid bridge sometimes is thick and forms the "slug flow", while other times it is quite thin and forms the "bubble-train slug flow", and even at times it disappears half and forms the "liquid ring flow". The ring-shaped liquid film is smooth and axi-symmetrically distributed around the channel inner wall. The nose of the slug is flatter than that observed in a bubbly-slug flow.
3) *Dispersed-Churn flow*: In this regime, the flow is strongly influenced by the inertia force but not totally dominated. The main characteristic feature is a mixture of small vapor slugs and liquid chunks. It has no stable "slug flow". Dispersed-churn flow is also called bubbly/slug, liquid/slug, and ring/slug by other researchers. It normally appears at the intermediate liquid and gas flow rates. For example, among the dispersed-churn flows from the recorded images, we can see the "disruption tail of the slug" flow pattern usually followed by some very small shedding bubbles.
4) *Annular flow*: This regime is totally dominated by the inertia force. It mainly consists of the flow pattern of "gas core with a smooth interface", and occasionally the "liquid lump flow". It usually appears at a low to intermediate liquid flow rate together with a high gas flow rate. The water film flows along the channel inner wall while the nitrogen gas core flows through the center of the channel. The gas-liquid interface is smooth due to the weak interaction between the gas and liquid at the interface in the micro-channel, which is different from the wavy interface observed in mini-channels and macro-channels.

Fig. 4-4 shows the instable temporal pressure measurement at the upstream and downstream for a slug-ring flow. This instability of P_{in} can be attributed to or cause the density wave oscillation in the micro-channel, which was also found in parallel channels and believed to be intrinsic to the test module itself (Qu and Mudawar 2004). The density oscillation could change the gas inertia force $\rho_G j_G^2$ at the interface. That could be the reason why the time instability of flow patterns observed in the micro-channel.

4.3.2 Flow Regime Maps

Based on the images and pattern distinctions discussed above, we have summarized our observations using two-phase flow regime maps. Traditionally, the regime map was developed with the superficial velocities of water and nitrogen, j_L and j_G, as the vertical and horizontal coordinates, respectively. Instead of the superficial velocities, we decided to use the respective gas and liquid Webber numbers as the coordinates for the regime maps.

Essentially, the Webber number is the dimensionless superficial velocity square and physically it represents the ratio of inertia to surface tension that is the guiding parameter for two-phase flow patters in micro-channels. Fig. 4-5 shows the regime maps for the three channel sizes. The solid lines are used to indicate the boundaries between different flow patterns. Figs. 4-5(a) and 4-5(b) provide the two-phase flow regime maps for the current micro-channels with hydraulic diameters of 0.622 mm and 0.412 mm, respectively. Fig. 4-5(c) shows the flow regime map for the micro-channel with a hydraulic diameter of 0.209 mm.

In general, for the lager channels (0.622 and 0.412 mm), the regime maps are relative similar as shown in Figs. 4-5(a) and 4-5(b). They all have bubbly-slug flows located in the lower left corner representing very small Webber numbers that correspond to a total dominance by the surface tension force. For higher gas velocities that are associated with larger gas Webber numbers and dominance by the inertia force, the flow pattern becomes he annular flow and it is not very sensitive to the liquid velocities. Between the bubbly-slug flow and the annular flow, we found the slug-ring and dispersed-churn flows that corresponds to the relatively balance between the inertia and the surface tension and neither one is dominant. The slug-ring flow is under relatively more control by the surface tension while the disperse-churn is controlled more by the inertia as a larger inertia force offered by the higher liquid flow is needed to break the slug into dispersed fragments. This is why the disperse-churn flow is located above the slug-ring flow. While for the smallest channel (0.209 mm), the regime map displays some differences from those of the larger channels. We observed that the bubbly flow pattern was no longer present and the slug flow filled its place in the lower left corner, lower We_{LS} and We_{GS} (lower j_G and j_L). A plausible explanation is that as the channel size gets smaller the surface tension force holds a deeper control over the inertia for the same low gas flows that prevents the break up of the bridge between slugs to form bubbles. Therefore the slug flow resulted. The dispersed-churn flow was also absent in Fig. 4-5(c), the slug-ring flow took its place. Again, the reason is that the strong surface tension effect prevented break-down of the slugs and the disruption of the gas-liquid interface.

From the current experimental data, we also observed the boundary lines have a tendency to shift slightly to right, namely higher We_{GS} or gas superficial velocity, as the hydraulic diameter was decreased, which was different from what reported by Taitel et al. (1980) that the boundary line was not affected by tube diameter for circular vertical macro-tubes, or by Mishima and Ishii (1984) that the boundary line shifted to the left in vertical macro-tubes as the tube diameter was decreased.

This again may be explained by the stronger surface tension effect in micro-channels that requires a higher inertia force (boundary line moving to the right) to balance in order to maintain the same flow pattern. Tabatabai and Faghri (2001) reported a new flow map based on their theoretical study that accounted for surface tension effects in horizontal miniature and micro tubes. They showed an increasing ratio of gas superficial velocity to liquid superficial velocity with the decreasing of hydraulic diameter, which indicated a right shit of the transition boundary lines too.

4.3.3 Comparison with Prior Mini-channel Flow Map

Akbar et al. (2003) reviewed the flow maps in mini-channels with hydraulic diameter around 1 mm and concluded that there were some similarities between the flow regime transitions in mini-channels and channels operating under microgravity. They developed a flow map for circular and near-circular mini-channels based on the Weber number, which can be represented by the following expressions:

- Surface tension dominated region (including bubbly, plug, and slug flows):
  - For $We_{LS} \leq 3.0$, $We_{GS} \leq 0.11 We_L^{0.315}$
  - For $We_{LS} > 3.0$, $We_{GS} \leq 1.0$
- Annular flow region:
  $We_{GS} \geq 11.0 We_{LS}^{0.14}$, $We_{LS} \leq 3.0$
- Dispersed flow region:
  $We_{LS} > 3.0$, $We_{GS} > 1.0$

This model can reasonably explain the flow maps for circular and near-circular mini-channels with hydraulic diameter around 1 mm including the data of Mishima et al. (1996), Triplett et al. (1999), and Yang & Shieh (2001). However, it only provided a fair prediction to the data of Zhao and Bi (2001) due to the channel geometry effects. Fig. 4-6 shows the transition lines predicted by the Weber number model (solid lines) with the current data for the channel with D_h = 0.622 mm (dashed lines). A poor agreement was found. One of the possible reasons might be the significant sensitivity of gas-liquid flow patterns to the working fluid, channel geometry and channel size. Another possible reason may be related to some special flow characteristics associated specifically with micro-channels. The liquid and gas flow remain laminar even at high flow rates, and a weaker interaction between the liquid and gas at the interface in micro-channels than in mini-channels. We may conclude that the flow regime criteria developed for mini-channels should not be applied for micro-channels without further verification.

4.3.4 Time-Averaged Void Fraction

For each gas-liquid flow combination, the time-averaged void fraction can be estimated by analyzing its 8000 recorded images. The method of analyzing the time-averaged void fraction is described as follows. 22 data points were selected from the video image files for each channel size to cover the entire range of the homogeneous void fraction. It is noted that each data point corresponds to a specific homogeneous void fraction. The homogeneous void fraction is defined as $\beta = j_G/(j_G+j_L)$ which has a range between zero and one. The physical meaning of the homogeneous void fraction is that the actual void fraction is equal to the homogeneous void fraction when both phases have the same velocities in a dynamic equilibrium condition. The actual void fraction would deviate from the homogeneous void fraction for the dynamic non-equilibrium conditions investigated in the current study where the two phases have non-equal velocities (slip ratio) in different flow regimes. Each recorded image covers the flow pattern for a streamline distance of 1.48 mm.

The instantaneous void fraction on each image can be calculated by estimating the ratio of the volume occupied by the gas to that of the whole region on each image field. The time averaged void fraction was obtained by adding all the instantaneous void fractions and dividing the sum by the total number of images, the time-averaged void fraction, α, can be determined and expressed as follows:

$$\alpha = \frac{\sum\limits_{n=1}^{N} \alpha_n}{N} = \frac{\sum\limits_{i=1}^{N_l} \alpha_{l,i} + \sum\limits_{j=1}^{N_g} \alpha_{g,j} + \sum\limits_{k=1}^{N_m} \alpha_{m,k}}{N}, \quad N = N_l + N_g + N_m \qquad (4.2)$$

Eq. (4.2) represents a strategy that we divided the images into three major groups based on the number of images for a specific type. For the total recorded images, approximately, 90% of all the images belong to either pure liquid type or gas core with a smooth interface, and all other types such as "liquid ring flow", "liquid lump flow", and "bubbly flow" account for only 10%. As a result, we chose "pure liquid" (zero void fraction), "gas core with a smooth interface" and "all the rest types combined" as the three groups.

Therefore, in Eq. (4.2), $\alpha_{l,i}$, $\alpha_{g,j}$, $\alpha_{m,k}$ are the estimated void fractions for "pure liquid type", "gas core with a smooth interface type", and "any other type', respectively. N is the total number of the recorded images. N_l, N_g, N_m are the number of the images of "liquid", "gas core with a smooth interface", and "other types", respectively. According to the error propagation, the uncertainty of the estimated time-averaged void fraction, $\Delta\alpha$, can be expressed as:

$$\Delta\alpha = \sqrt{\left(\frac{N_l}{N}\Delta\alpha_l\right)^2 + \left(\frac{N_g}{N}\Delta\alpha_g\right)^2 + \left(\frac{N_m}{N}\Delta\alpha_m\right)^2} \qquad (4.3)$$

where $\Delta\alpha_l$, $\Delta\alpha_g$, $\Delta\alpha_m$ are the uncertainties of the void fractions for "liquid", "gas core with a smooth interface", and "all other flow pattern", respectively. Even though, the void fraction of "pure liquid" is zero, there is still an uncertainty associate with it because of possible trace amount of gas in the liquid core, but in general this uncertainty is very small compared to other types. Based on the above, we estimated that the range of uncertainties for the time averaged void fractions is from 3.1 to 9.8%.

Fig. 4-7 shows the measured time-averaged void fraction results for the present three micro-channels. Also shown in Fig. 4-7 is the data given by Kawahara et al. (2002) for a micro-tube with 0.1 mm in diameter. The dotted line represents the homogeneous void fraction β. Ali et al. (1993) suggested that the void fraction in narrow channels with a D_h around 1 mm can be correlated with the equation, $\alpha = 0.8\ \beta$. When applying this correlation to our results, we found that for the vast majority of our data, it overestimated the void fractions, especially for the smaller channels. The predictions become worse as the size of the channel is decreased further. The over-predictions are more than 100% for many data points. The time-averaged void fraction patterns for the smaller channels showed a non-linear relationship with the homogeneous void fraction. As explained before, when the channel sizes are smaller, the effects of surface tension are more prevalent, and allow the liquid film to bridge the gas core more easily, so the flow pattern is more likely to be bubbly-slug flow, which results in a lower time-averaged void fraction due to the absence of gas phase.

Based on our own data for the three micro-channel sizes (0.209, 0.412, and 0.622 mm) and those of Kawahara et al. (2002) for a 0.1 mm diameter micro-tube, we have developed an empirical correlation of the time-averaged void fraction for micro-channels with hydraulic diameters less than 1 mm.

The correlation is expressed in Eqs. (4.4) and (4.5).

$$\alpha_p = \frac{C\beta^{0.5}}{1-(1-C)\beta^{0.5}} \tag{4.4}$$

$$C = \frac{0.266}{1+13.8 \cdot e^{-6.88 D_h}} \tag{4.5}$$

where the unit of D_h is in mm. Fig. 4-8 shows the comparison between the predictions by the new correlation and the corresponding measured results. Fig. 4-9 is a plot of the α_p/α_d vs. β for all the data points in Fig. 4-8, where α_p and α_d are the void fraction predicted by the correlation and that of the measured data, respectively. 57 of our 66 data points fall within ±15%. Most of the outliers came from Kawahara et al's data (17 out of 26 outliers) which may be attributed to the lack of the total number of sample images (200-300) in their experiment resulting in higher uncertainties. If the uncertainty range was increased to ±35%, only 2 data out of 66 were out of the range.

4.3.5 Frictional Pressure Drop

Currently most of the two-phase pressure drop models are based on the model of Lockhart-Martinelli (1949), such as Mishima and Hibiki (1996), Lee and Lee (2001), Qu and Mudawar (2004). To compare our experimental data with the prediction of those models, the Martinelli parameter X should be determined experimentally first, which is defined as:

$$X = \frac{(dP/dz)_L}{(dP/dz)_G} \tag{4.6}$$

$(dP/dz)_L$ and $(dP/dz)_G$ are the frictional pressure drop of single phase liquid and vapor with the same mass flow rate respectively. Then insert X into the above models to get the two-phase frictional pressure drop. Fig. 4-10 shows the comparison between the experimental data of the micro-channel (D_h = 0.412 mm) and the value predicted by those models. From the figure, we can see Lockhart-Martinelli's model (C = 5) obviously underestimate the pressure drop here. Mishima and Hibiki's model can predict the pressure drop very well. All of the data fall in ±10% of the predicted value. Lee and Lee's model may also predict well, but it's worse than Mishima and Hibiki's model for out experimental data.

4.4 Summary

Nitrogen-water flow patterns in rectangular micro-channels with hydraulic diameters of 0.209, 0.412, and 0.622 mm were obtained and analyzed. Based on our experimental results and comparison with other results in the literature, the following conclusions can be obtained:

1) The phenomenon that micro-channel flow pattern changes with time at a fixed location under a certain gas and liquid superficial velocity was found, which can be attributed to the density wave oscillation in the micro-channel. According to the appearance of the transition flow patterns such as "liquid ring flow", "liquid lump flow" and "disruption tail of the slug", four flow patterns can be defined for micro-channels with the hydraulic diameters of 0.412 and 0.622 mm: bubbly-slug flow, slug-ring flow, dispersed-churn flow and annular flow. For the micro-channel with the hydraulic diameters of 0.209 mm, the bubbly-slug flow became the slug-flow and the dispersed flow disappeared.

2) The current flow regime maps show the transition boundary lines shift to high We_{GS} or gas superficial velocity with the decreasing of the hydraulic diameter. It can be explained by the strong surface tension effect in micro-channels.

   The micro-channel flow maps were compared with the mini-channel flow map based on the Weber number model, which showed poor agreement.

3) Time-averaged void fractions of each micro-channel were measured for 22 runs to cover the whole range of homogeneous void fraction. The data of each run were obtained from the analysis of 8000 flow pattern images captured at a certain gas and liquid superficial velocity. With the decreasing of the hydraulic diameter, the time-average void fraction showed a non-linear relationship with the homogeneous void fraction. A new empirical correlation was proposed to predict the non-linear relationship, and most of the current experimental data and Kawaraha's data fall within ±15% of the new correlation. The uncertainty of this measurement method was analyzed and the uncertainty range was approximately from 3.1 to 9.8% under the current experimental conditions.

4) Lockhart-Martinelli's model (C = 5) which was widely used to predict the two-phase frictional pressure loss in macro-channel obviously underestimate the pressure drop in micro-channel. Mishima and Hibiki's model formulated from experimental data of small channels can predict the pressure drop here very well. All of the data fall within ±10% of the predicted value. Lee and Lee's model can also predict well, but it's worse than Mishima and Hibiki's model for out experimental data.

<u>Table 4-1. Generalized two-phase frictional pressure-drop correlations.</u>

Correlation	Reference	Frictional pressure drop
1	Homogeneous model (1994)	$-\left(\dfrac{dP}{dz}\right)=\dfrac{2f_{tp}G^2}{\rho_l D_h}\left[1+x\dfrac{\rho_l-\rho_v}{\rho_v}\right]$
2	Lockhart-Martinelli (1949)	$-\left(\dfrac{dP}{dz}\right)=\dfrac{2f_l G^2(1-x)^2}{\rho_l D_h}\phi_l^2$ $\phi_l^2=\left(1+\dfrac{C}{X}+\dfrac{1}{X^2}\right)$ $X=\dfrac{(dP/dz)_l}{(dP/dz)_v}$ C = 20 for turbulent liquid-turbulent vapor C = 12 for laminar liquid-turbulent vapor C = 10 for turbulent liquid-laminar vapor C = 5 for laminar liquid-laminar vapor
3	Mishima and Hibiki (1996)	$-\left(\dfrac{dP}{dz}\right)=\dfrac{2f_l G^2(1-x)^2}{\rho_l D_h}\phi_l^2$ $\phi_l^2=\left(1+\dfrac{C}{X}+\dfrac{1}{X^2}\right)$ $C=21\left[1-e^{-319D_h}\right]$
4	Lee and Lee (2001)	$-\left(\dfrac{dP}{dz}\right)=\dfrac{2f_l G^2(1-x)^2}{\rho_l D_h}\phi_l^2$ $\phi_l^2=\left(1+\dfrac{C}{X}+\dfrac{1}{X^2}\right)$ $C=6.185\times10^{-2}\,\mathrm{Re}_{Lo}^{0.726}$ for laminar liquid-turbulent vapor
5	Qu and Mudawar (2004)	$-\left(\dfrac{dP}{dz}\right)=\dfrac{2f_l G^2(1-x)^2}{\rho_l D_h}\phi_l^2$ $\phi_l^2=\left(1+\dfrac{C}{X}+\dfrac{1}{X^2}\right)$ $C=21\left[1-e^{-319D_h}\right](0.00418G+0.0613)$

Table 4-2. Non-dimensional parameters for a macro-channel and micro-channels

	Bo	Ca	Re		We	
	(Ratio of gravitational force to surface tension force)	(Ratio of viscous force to surface tension force)	(Ratio of inertia force to viscous force)		(Ratio of inertia force to surface tension force)	
			Re_{LS}	Re_{GS}	We_{LS}	We_{GS}
10cm Channel	1354.3	0.00047-0.12	4665-1166276	6320-63200	2.21-138333	1.6-158
Channel 1	0.0117	0.00023-0.08	4.64-1670	7-1631	0.001-135	0.0005-32
Channel 2	0.0230	0.00035-0.04	14.1-1602	7-1838	0.005-63	0.0003-28
Channel 3	0.0525	0.00015-0.02	9.36-1436	7-2270	0.0014-34	0.0003-33
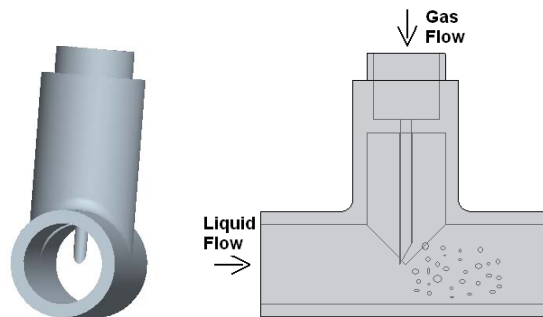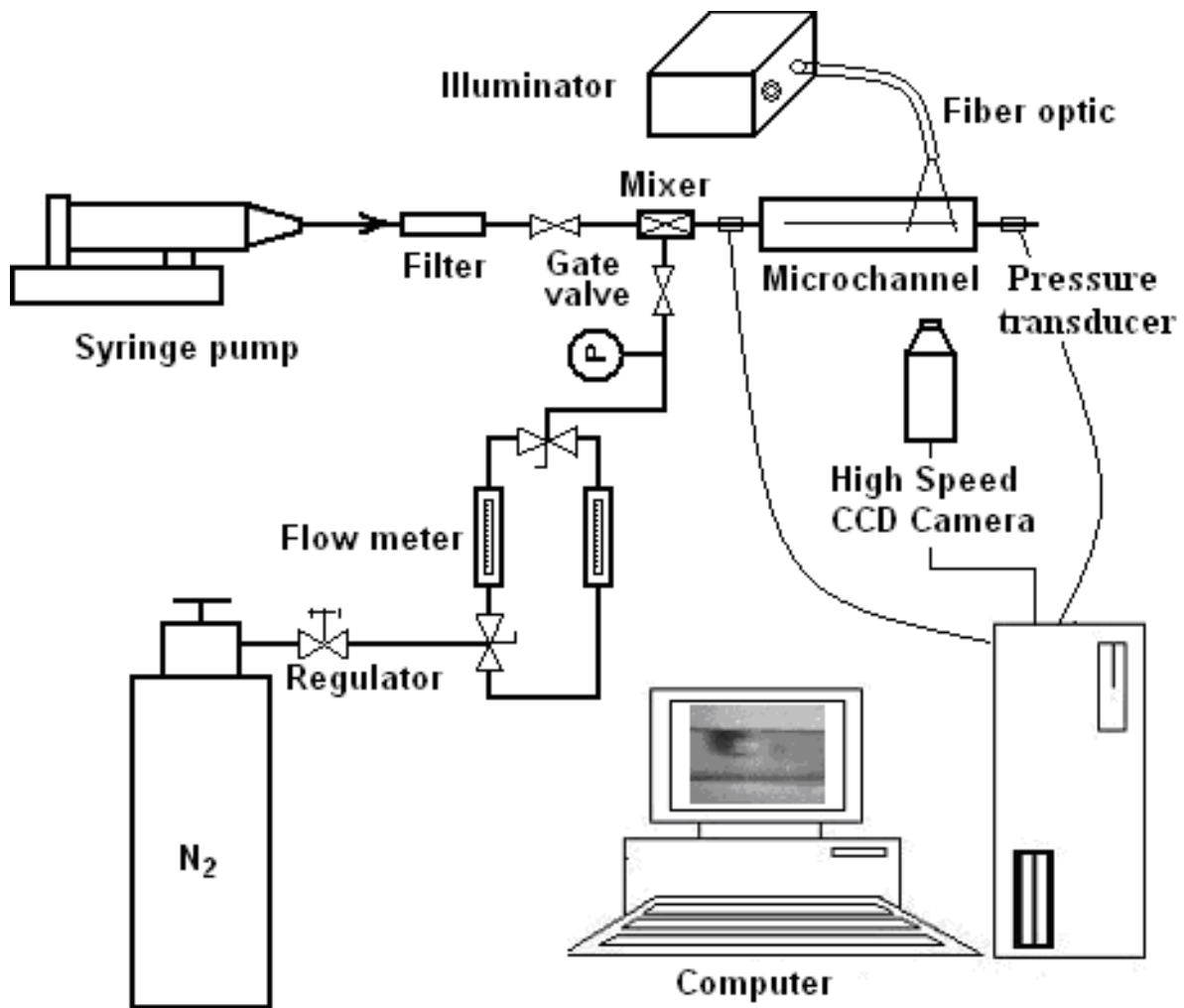
Figure 4-1a. Schematic of the experimental apparatus and the mixer.
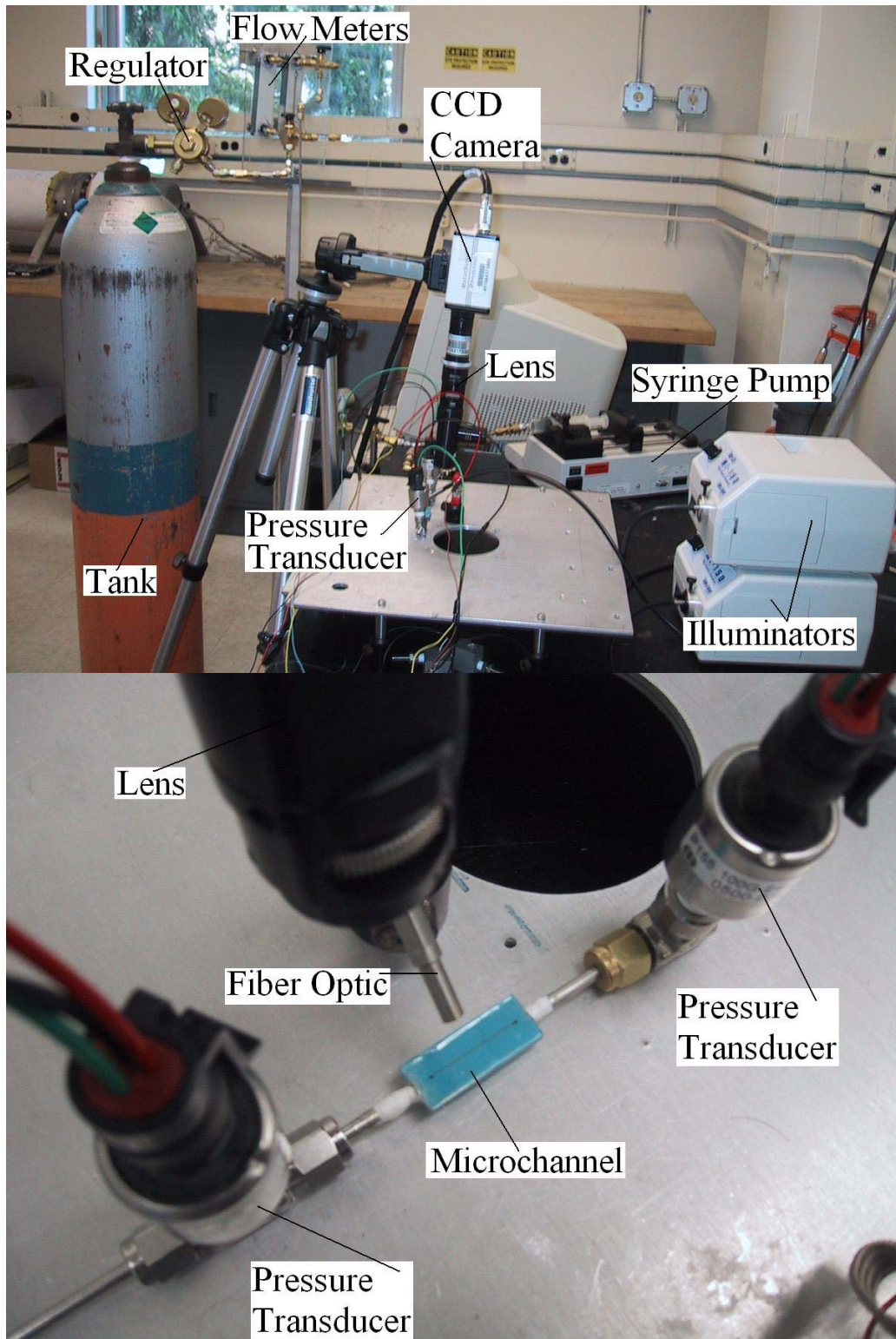
Figure 4-1b. Photoes of the experimental apparatus.
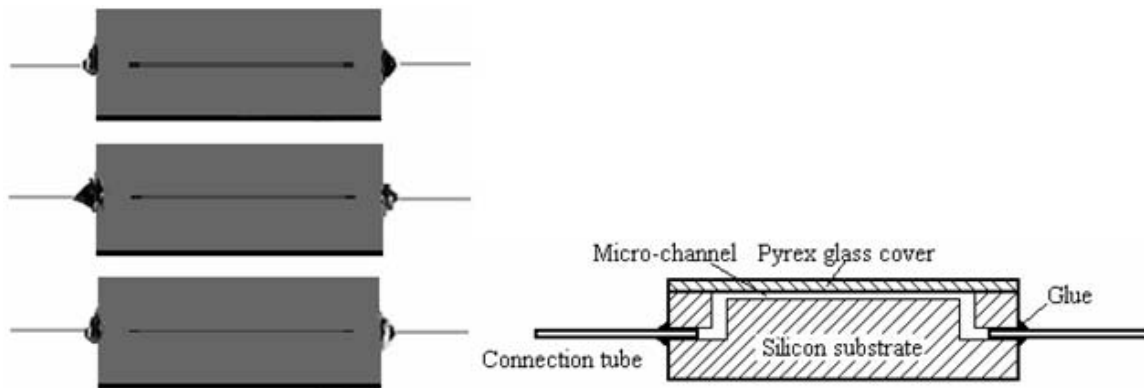
Figure 4-2. Photograph of micro-channels and schematic of the micro-channel.

a) Bubbly-Slug flow, j_L = 0.08 m/s, j_G = 0.17 m/s
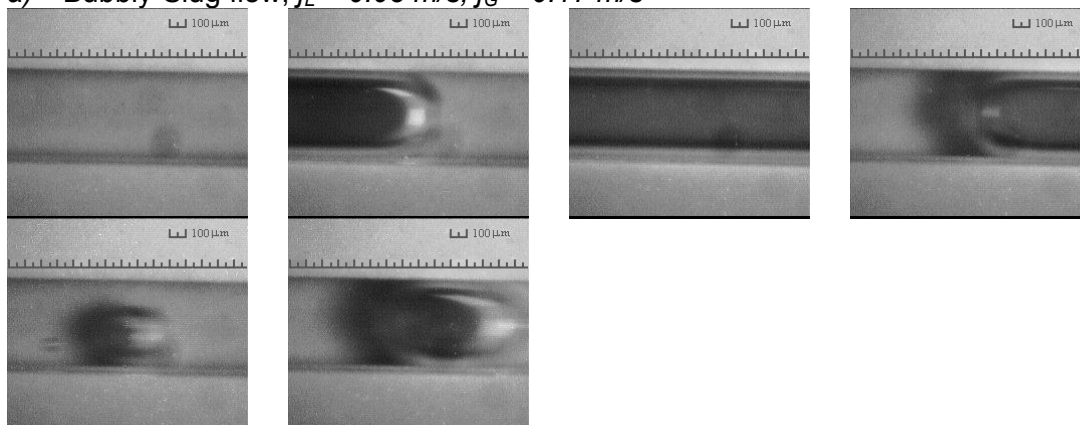
b) Slug-Ring flow, j_L = 0.215 m/s, j_G = 1.2 m/s
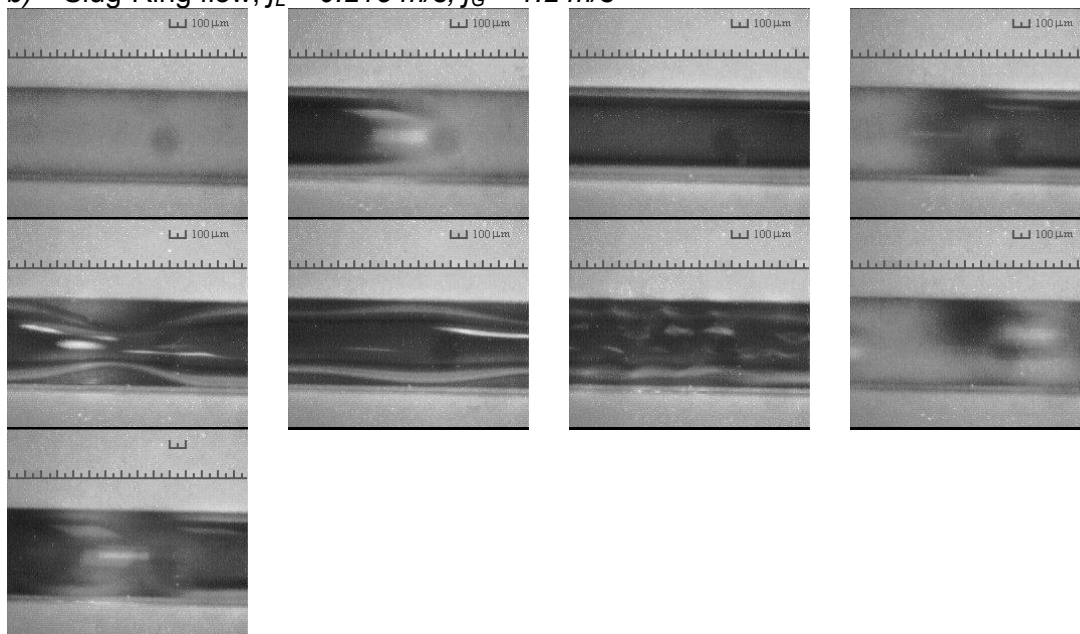
c) Dispersed-Churn flow, j_L = 0.473 m/s, j_G = 3.23 m/s
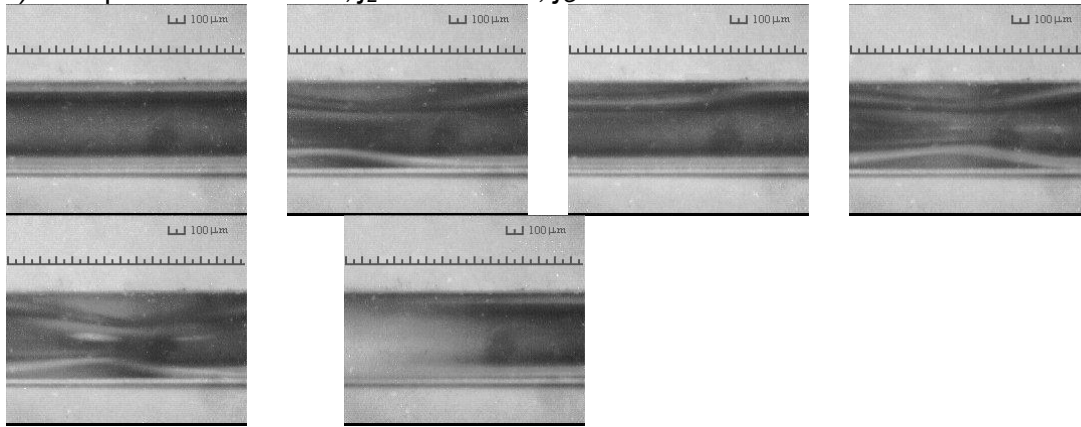
d) Annular flow, j_L = 0.172 m/s, j_G = 27.1 m/s
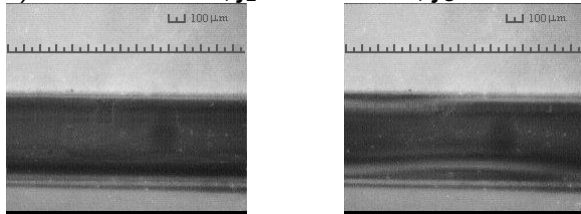
Figure 4-3. Typical flow patterns in the micro-channel: (a) Bubbly-Slug flow (b) Slug-Ring flow (c) Dispersed-Churn flow (d) Annular flow.
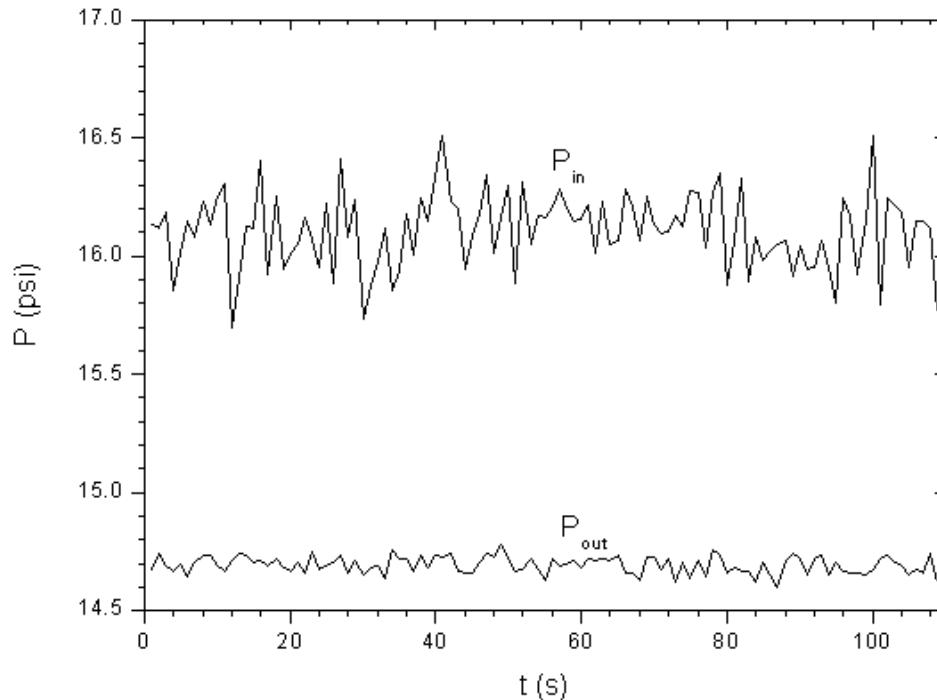
Figure 4-4. Temporal records of inlet and outlet pressures (Slug-Ring flow, j_L = 0.215 m/s, j_G = 1.2 m/s).

a)
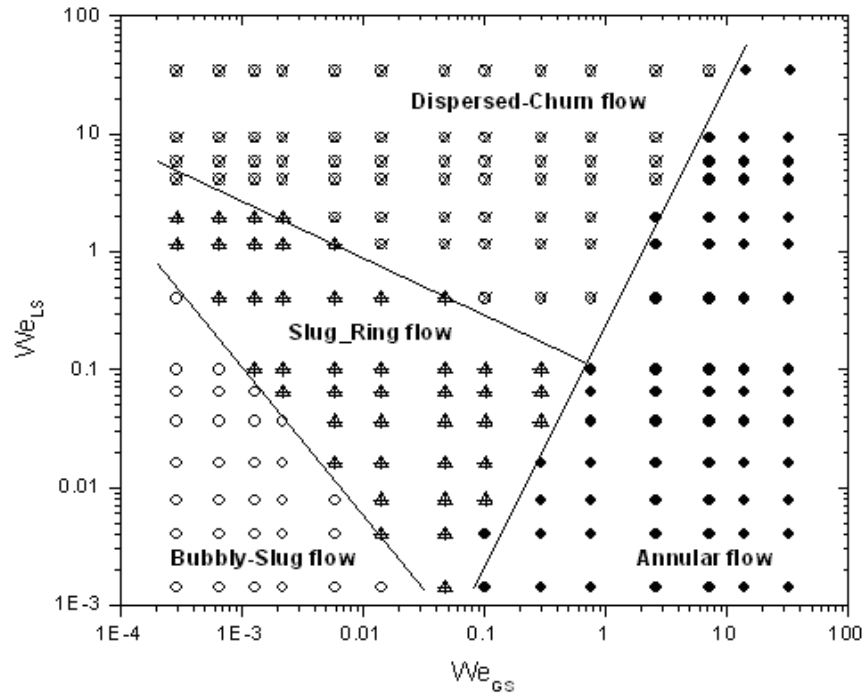
b)
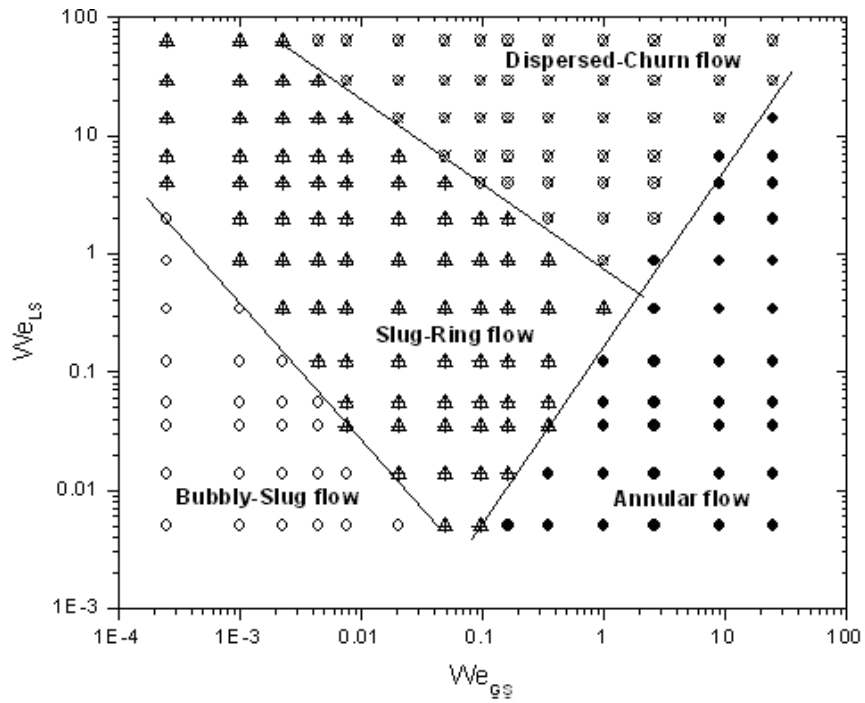
c)
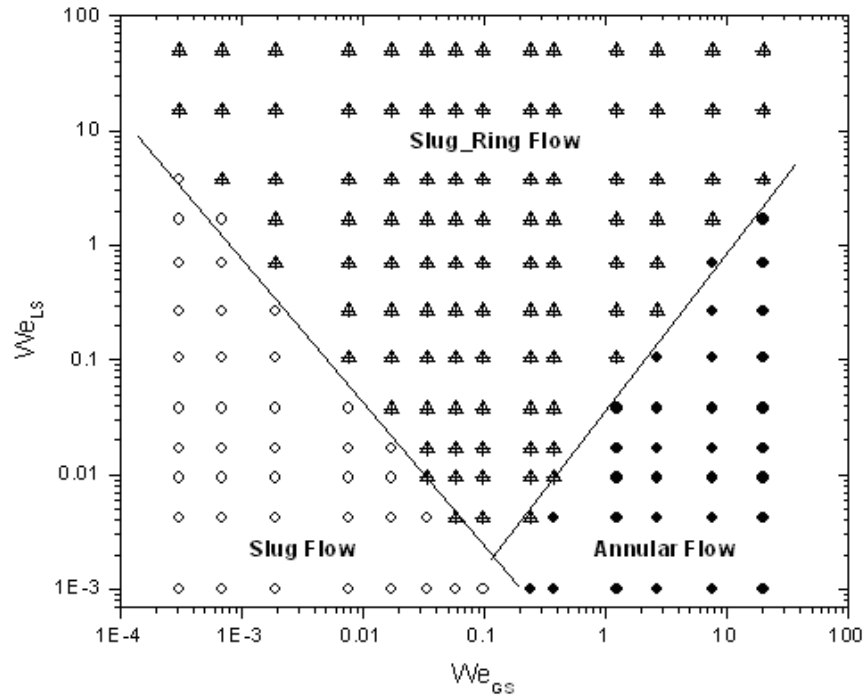
Figure 4-5. Flow regime maps for: (a) D_h = 0.622 mm (b) D_h = 0.412 mm (c) D_h = 0.209 mm.
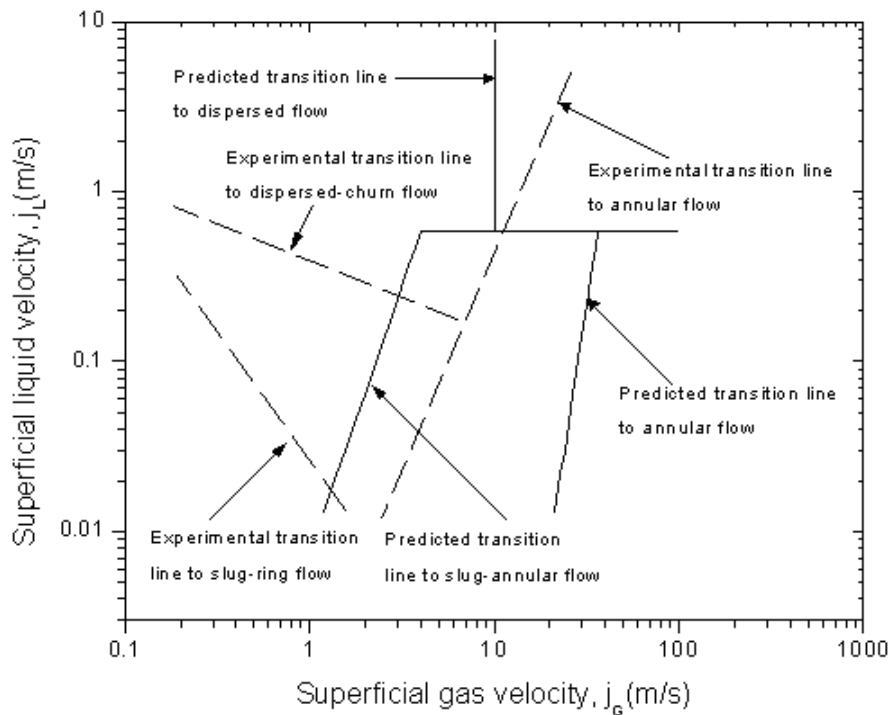
Figure 4-6. Flow map comparison between micro-channel and mini-channel predicted by the Weber number model.
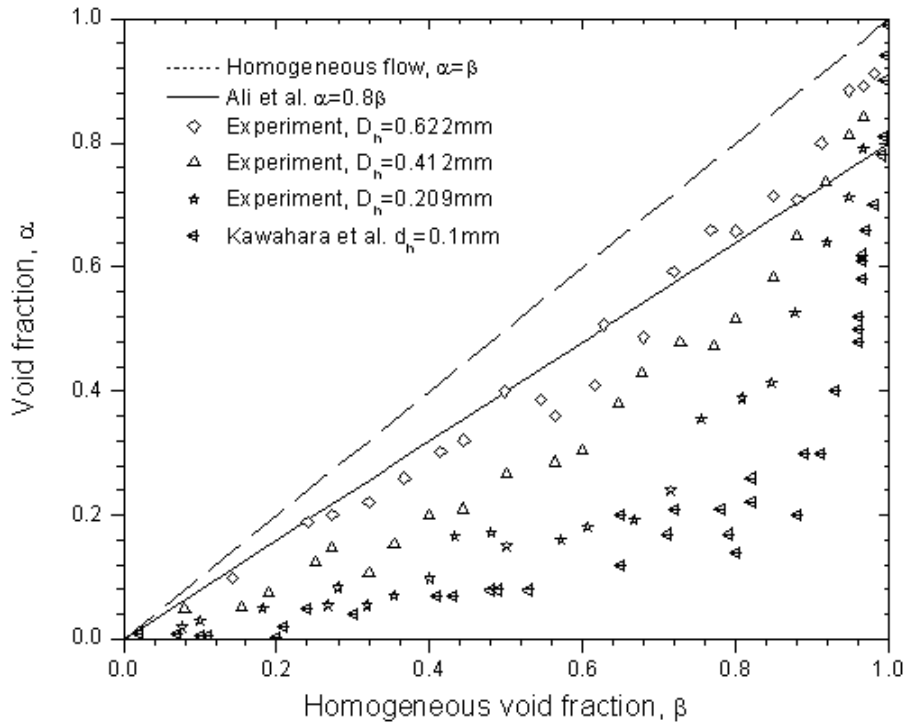
Figure 4-7. Measured time-averaged void fraction results vs. two previous correlations.
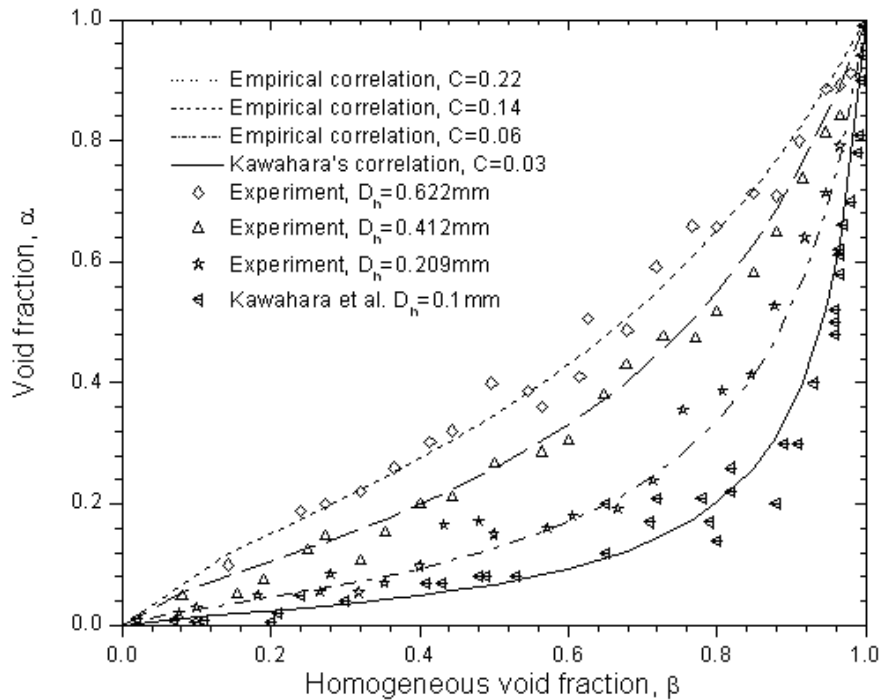
Figure 4-8. Comparison between the new correlation and experimental data.
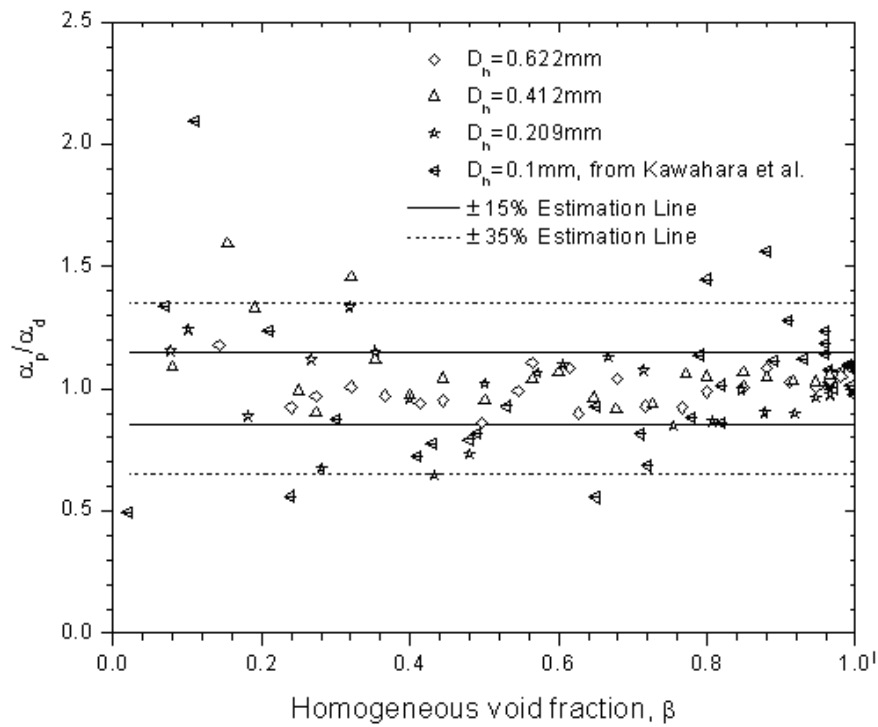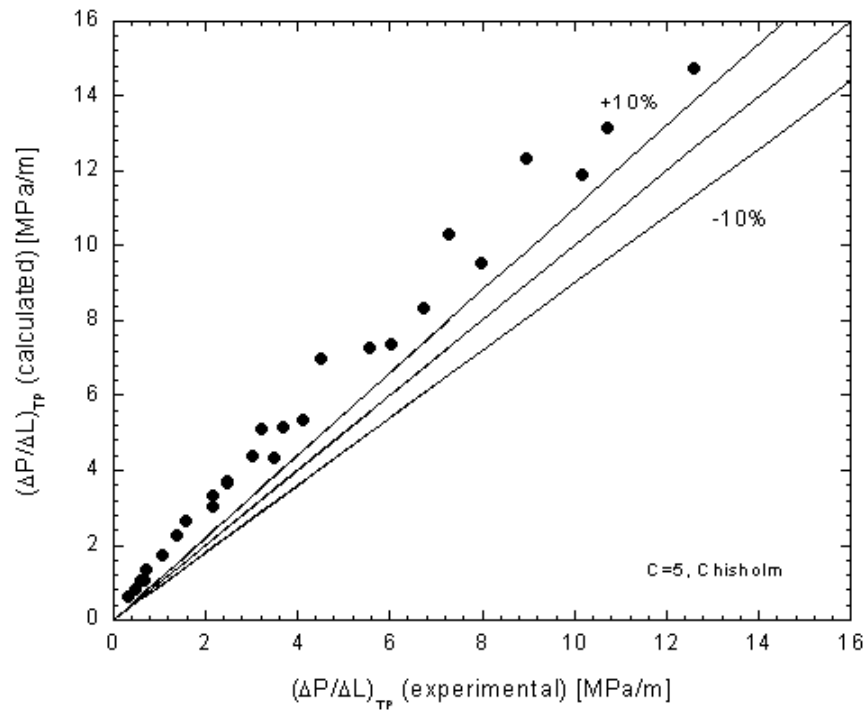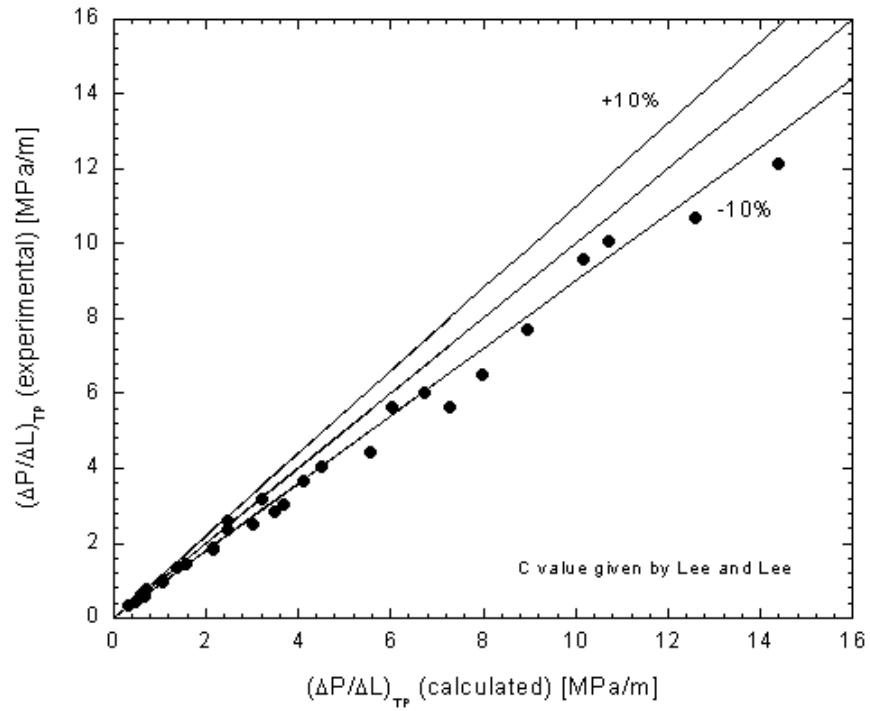
Figure 4-9. Ratio of predicted and experimental time-averaged void fraction vs. homogeneous void fraction β.
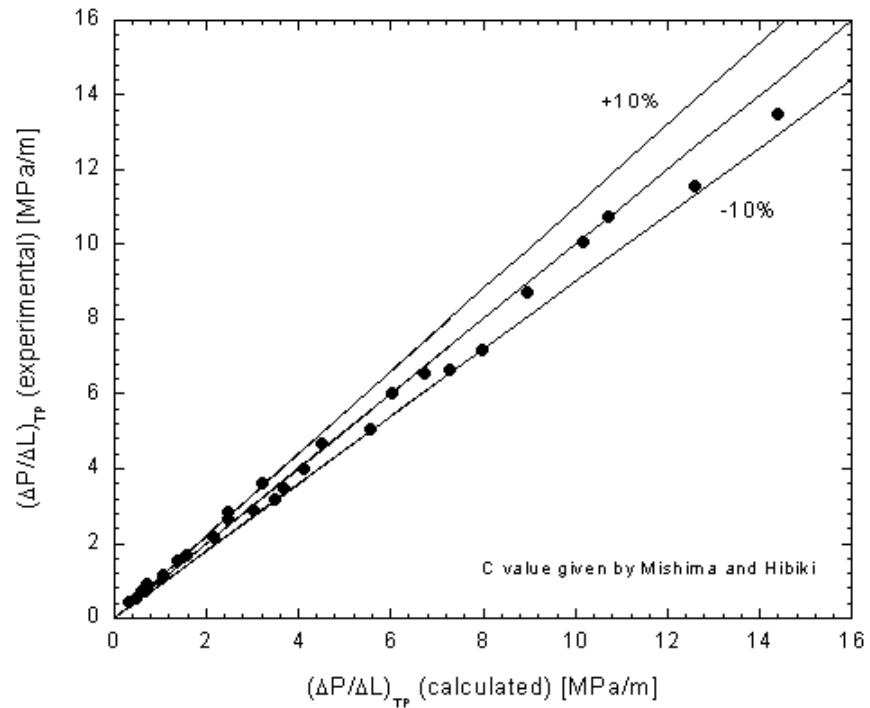
a)

b)

c)

Figure 4-10. Comparison between the experimental data and the models (D_h = 0.412 mm) a) Lockhart-Martinelli's model (C = 5) b) Lee and Lee's model c) Mishima and Hibiki's model.

5. Conclusion

1. For straight micro-channels, the experimental Poiseuille numbers show agreement with standard laminar incompressible flow predictions when the Re is less than a value around 1500. The discrepancy observed by the former researchers is the result of unaccounted bias in experiment setups, such as not accounting for increased pressure drop in the entrance region or unreliable inlet and outlet losses.

2. The flow micro structures around the bend of a serpentine micro-channel can be divided into three categories depending on the flow Reynolds number. When Re<100, there is no induced flow recirculation and flow separation. When Re>100, vortices and flow separation appear and further develop. The outer corner vortex develops along the wall of the channel, and the vortex center moves slightly from the upper stream to the down stream with the increasing of the Re number. The inner wall vortex due to flow separation develops immediately after the flow makes the turn. When Re>1000-1500, the shape and size of the outer and inner vortices become almost constant.

3. In serpentine micro-channels, the additional pressure drop due to miter bends can be divided into two groups. The first group is for Re<100 where there is no eddies and the additional pressure drop is very small for all of the channels. The other group is for flows with the Reynolds numbers exceeding the threshold values that are in the range of 100-300. When the Reynolds is higher than the threshold value, we found the flow separation and formation of vortices that appear on the inner and outer wall around the miter bend. These vortices increase in strength with increasing Re number that causes the bend pressure drop to increase sharply with the Re number. The experimental results also show the bend pressure drop increases with decreasing hydraulic diameters. Bend loss coefficient K_b is a function of the Re number only when Re<100, a function of the Re number and channel size when Re>100, and almost keeps constant and changes in the range of $\pm10\%$ when Re is larger than some value in 1000-1500. The trend of the experimental pressure drop is consistent with the flow structure change.

4. The phenomenon that micro-channel flow pattern changes with time at a fixed location under a certain gas and liquid superficial velocity was found, which can be attributed to the density wave oscillation in the micro-channel. According to the appearance of the transition flow patterns such as "liquid ring flow", "liquid lump flow" and "disruption tail of the slug", four flow patterns can be defined for micro-channels with the hydraulic diameters of 0.412 and 0.622 mm: bubbly-slug flow, slug-ring flow, dispersed-churn flow and annular flow. For the micro-channel with the hydraulic diameters of 0.209 mm, the bubbly-slug flow became the slug-flow and the dispersed flow disappeared. The current flow regime maps show the transition boundary lines shift to high We_{GS} or gas superficial velocity with the decreasing of the hydraulic diameter. It can be explained by the strong surface tension effect in micro-channels. The micro-channel flow maps were compared with the mini-channel flow map based on the Weber number model, which showed poor agreement.

5. Time-averaged void fractions of each micro-channel were measured for 22 runs to cover the whole range of homogeneous void fraction. The data of each run were obtained from the analysis of 8000 flow pattern images captured at a certain gas and liquid superficial velocity. With the decreasing of the hydraulic diameter, the time-average void fraction showed a non-linear relationship with the homogeneous void fraction. A new empirical correlation was proposed to predict the non-linear relationship, and most of the current experimental data and Kawaraha's (2002) data fall within $\pm15\%$ of the new correlation. The uncertainty of this measurement method was analyzed and the uncertainty range was approximately from

3.1 to 9.8% under the current experimental conditions. The results of this study provide basic information of the effects of length scale reduction on nitrogen-water two-phase flow characteristics in micro-scale channels that would be useful for the design of gas-liquid transport and their separation encountered in low-temperature fuel cells.

6. Patents, Publications and Presentations

6.1 Patents
There was no patent filed.

6.2 Publications and Presentations

Y. Ji, K. Yuan, J.N. Chung and Y.C. Chen, "Effects of transport scale on heat/mass transfer and performance optimization for solid oxide fuel cells", *Journal of Power Source,* Vol. 161, 380-391, (2006).

R. Xiong and J.N. Chung, "Flow Characteristics of Water in Straight and Serpentine Microchannels with Miter Bends", *Experimental Thermal and Fluid Science*, Vol. 31, pp. 805-812, (2007).

R. Xiong and J.N. Chung, An experimental study of adiabatic gas-liquid two-phase flow patterns and void fraction in micro-channels", *Physics of Fluids*, Vol. 19(3), Article 033301, (2007).

R. Xiong, M. Bai and J.N. Chung, "Formation of bubbles in a simple co-flowing microchannel", *Int. J. Micromechanics and Microengineering,* Vol. 17, 1002-1011, (2007).

R. Xiong and J.N. Chung, "An experimental study of flow micro structures and pressure drops in serpentine micro-channels", accepted for publication and available on-line, *Int. J. Heat and Mass Transfer,* (*2007)*.

R. Xiong, and J.N. Chung, "Size effect on adiabatic gas-liquid two-phase flow map and void fraction in micro-channels", ASME IMECE 2006, November 5-10, Chicago, IL. Paper no.: IMECE2006-13263.

R. Xiong, and J.N. Chung, "Flow characteristics of pressure-driven water in serpentine micro-channels", IMECE 2006, November 5-10, Chicago, IL. Paper no.: IMECE2006-13302.

R. Xiong, and J.N. Chung, "Adiabatic gas-liquid two-phase flow patterns in micro-channels", FEDSM 2006, July 17-20, Miami, FL. Paper no.: FEDSM2006-98476.

7. Students from Research

Renqiang Xiong, Ph.D., August, 2007, currently employed as a post-doctoral fellow in the School of Mechanical engineering at the Georgia Institute of Technology.

8. Funding Obtained by Leveraging NASA Grant

$200k, Office of Naval Research STTR Project entitled Dodecane Reforming for SOFCs, Phase II, August 2006 - March 2008, Funding through InnovaTek Inc. Richland, WA.

9. Collaborations

1. Dr. Jim Klausner and Dr. Renwei Mei, Department of Mechanical and Aerospace Engineering, University of Florida.
2. Dr. Mark Orazem, Department of Chemical Engineering, University of Florida.

10. Acknowledgments

11. References

Akbar M.K., Plummer D.A., Ghiaasiaan S.M., 2003, On gas-liquid two-phase flow regimes in microchannels, Int. J. Multiphase Flow, Vol. 29, pp. 855-865.

Ali M.I., Sadatomi M., Kawaji M., 1993, Two-phase flow in narrow channels between two flat plates, Can. J. Chem. Eng., Vol. 71, pp. 657-666.

Armand A.A., 1946, The resistance during the movement of a two-phase system in horizontal pipes, Izv.V.T.I., Vol. 1, pp. 16-21.

Brandner J., Fichtner M., Schygulla U., Schubert K., 2000, Improving the efficiency of micro heat exchangers and reactors, in Proc. 4th Int. Conf. Microreaction Technology, AIChE, March 5-9, Atlanta, GA, pp. 244-249.

Batchelor G.K., 1977, Developments in micro-hydrodynamics, in Theoretical and Applied Mechanics, ed. W Koiter. pp. 33-35.

Beebe D.J., Mensing G.A., Walker G.M., 2002, Physics and applications of microfluidics in biology, Auun Rev. Biomed. Eng., Vol. 4, pp. 261-286.

Berger S.A., Talbot L., Yao L.S., 1983, Flow in curved pipes, Annu. Rev. Fluid Mech., Vol. 15, pp. 461-512.

Bradshaw P., 1987, Turbulent secondary flows, Annu. Rev. Fluid Mech., Vol. 19, pp. 53-74.

Brutin D., Tadrist L., 2003, Experimental friction factor of a liquid flow in microtubes, Phys. Fluids, Vol. 15, pp. 653–661.

Cubaud T., Tatineni M., Zhong X.L., Ho C.M., 2005, Bubble dispenser in microfluidic devices, Phys. Rev. E, Vol. 72, 037302.

Chen W.L., Twu M.C., Pan C., 2002, "Gas-liquid two-phase flow in micro-channels", Int. J. Multiphase Flow, Vol. 28, pp. 1235-1247.

Chung P.M.-Y., Kawaji M., 2004, "The effect of channel diameter on adiabatic two-phase flow characteristics in microchannels", Int. J. Multiphase Flow, Vol. 30, pp. 735-761.

Coleman J.W., Garimella S., 1999, "Characteristics of two-phase patterns in small diameter round and rectangular tubes", Int. J. Heat Mass Transfer, Vol. 42, pp. 2869-2881.

Collier J.G., Thome J.R., 1994, Convective boiling and condensation, Third ed., Oxford University Press, Oxford.

Dreyfus R., Tabeling P., Williams H., 2003, Ordered and disordered patterns in two-phase flow in microchannels, Phys. Rev. Lett., Vol. 90, 144505.

Erickson D., Li D., 2004, Integrated microfluidic devices, Anal. Chim. Acta, Vol. 507, pp.11-26.

Flockhart S.M., Dhariwal R.S., 1998, Experimental and numerical investigation into the flow characteristics of channels etched in <100> silicon, J. Fluids Eng. Vol. 120, pp. 291-295.

Fu A.Y., Spence C., Scherer A., Arnold F.H., Quake S.R., 1999, A microfabricated fluorescence-activated cell sorter, Nat. Biotechnol., Vol. 17, pp. 1109-1111.

Ganan-Calvo A.M., Gordillo J.M., 2001, Perfectly monodisperse microbubbling by capillary flow focusing, Phys. Rev. Lett., Vol. 87, 274501.

Garstecki P., Fuerstman M.J., Stone H.A., Whitesides G.M., 2006, Formation of droplets and bubbles in a microfluidic T-junction - scaling and mechanism of break-up, Lab Chip, Vol. 6, pp. 437-446

Garstecki P., Gitlin I., DiLuzio W., Whitesides G.M., Kumacheva E., Stone H.A., 2004, Formation of monodisperse bubbles in a microfluidic flow-focusing device, Appl. Phys. Lett., Vol. 85, pp. 2649-2651.

Ghiaasiaan S.M., Abdel-Khalik S.I., 2001, Two-phase flow in micro-channels, Advances in Heat Transfer, Vol. 34, Academic Press, New York, pp. 145.

Gordillo J.M., Cheng Z.D., Ganan-Calvo A.M., Marquez M., Weitz D.A., 2004, A new device for the generation of microbubbles, Phys. Fluids, Vol. 16, pp. 2828-2834.

Gui L., Wereley S.T., 2002, "A correlation-based continuous window shift technique for reducing the peak locking effect in digital PIV image evaluation", Exp. Fluids, Vol. 32, pp. 506-517.

Gui L., Wereley S.T., Lee S.Y., 2002, Digital filters for reducing background noise in micro PIV measurement", Proc. of the 11th International Symposium on the Application of Laser Techniques to Fluid Mechanics, pp. 15.1, Lisbon, Portugal, July 8-11.

Guillot P., Colin A., 2005, Stability of parallel flows in a microchannel after a T junction, Phys. Rev. E, Vol. 72, 066301.

Haverkamp V., Hessel V., Loewe H., Menges G., Warnier J.F.M., Rebrov E.V., de Croon M.H.J. M., Schouten J.C., Liauw, M.A., 2006, Hydrodynamics and mixer-induced bubble formation in micro bubble columns with single and multiple-channels, Chem. Eng. Technol., Vol. 29, pp. 1015-1026.

Heinzel A., Hebling C., Muller M., Zedda M., Muller C., 2002, Fuel cells for low power applications, J. of Power Sources, Vol. 105, pp. 250-255.

Hetsroni G., Mostak A., Pogrebnyak E., Yarin L.P., 2005, Fluid flow in micro-channels, Int. J. Heat Mass Transfer, Vol. 48, pp. 982-1998.

Ho C.M., Tai Y.C., 1998, Micro-electro-mechanical systems (MEMS) and fluid flows, Annu. Rev. Fluid Mech., Vol. 30, pp. 579-612.

Humphrey J.A.C., Taylor A.M.K., Whitelaw J.H., 1981, Turbulent-flow in a square duct with strong curvature, J. Fluid Mech., Vol. 103, pp. 443-463.

Huang H.T., Fiedler H.E., Wang J.J., 1993, "Limitation and improvement of PIV, Part II: particle image distortion, a novel technique", Exp. Fluids, Vol. 15, pp. 263-273.

Jiang X.N., Zhou Z.Y., Yao J., Li Y., Ye X.Y., 1995, Micro-fluid flow in microchannel, In: Proc. the 8th Int. Conf. on Solid State Sensors, Actuators and Eurosensors IX, Sweden, pp. 317-320.

Judy J., Maynes D., Webb B.W., 2002, Characterization of frictional pressure drop for liquid flows through microchannels, Int. J. Heat Mass Transfer, Vol. 45, pp. 3477-3489.

Kakac S., Shah R.K., Aung W., 1987, Handbook of single-phase convective heat transfer, John Wiley and Sons, New York.

Kawahara A., Chung P.M.-Y., Kawaji M., 2002, Investigation of two-phase flow pattern, void fraction and pressure drop in a microchannel, Int. J. Multiphase Flow, Vol. 28, pp. 1411-1435.

Kohl M.J., Abdel-Khalik S.I., Jeter S.M., Sadowski D.L., 2005, An experimental investigation of microchannel flow with internal pressure measurements, Int. J. Heat Mass Transfer, Vol. 48, pp. 1518-1533.

Kushida G., Yamashita H., Izumi R., 1985, Study on three-dimensional flow and heat transfer in miter-bend (3st report, effects of Reynolds number and aspect ratio), Bulletin of JSME, Vol. 28, pp. 2000-2006.

Lee H.J., Lee S.Y., 2001, Pressure drop correlations for two-phase flow within horizontal rectangular channels with small heights", Int. J. Multiphase Flow, Vol. 27, pp. 783-796.

Lee S.Y.K., Wong M., Zohar Y., 2001, Gas flow in microchannels with bends, J. Micromecha. Microeng., Vol. 11, pp. 635-644.

Li H., Olsen M.G., 2006, MicroPIV measurements of turbulent flow in square microchannels with hydraulic diameters from 200 to 640 μm, Int. J. Heat Fluid Flow, Vol. 27, pp. 123-134.

Li Z.X., Du D.X., Guo Z.Y., 2003, Experimental study on flow characteristics of liquid in circular micro-tubes, Microscale Thermophys. Eng., Vol. 7, pp. 253-265.

Lockhart R.W., Martinelli R.C., 1949, "Proposed correlation of data for isothermal two-phase, two-component flow in pipes", Chem. Eng. Prog., Vol. 45, pp. 39-48.

Maharudrayya S., Jayanti S., Deshpande A. P., 2004, Pressure losses in laminar flow through serpentine channels in fuel cell stacks, J. of Power Sources, Vol. 138 (1-2), pp. 1-13.

Mala G.M., Li D., 1999, Flow characteristics of water in microtubes, Int. J. Heat Fluid Flow, Vol. 20, pp. 142-148.

Mandhane J.M., Gregory G.A. and Aziz K., 1974, "Flow pattern map for gas-liquid flow in horizontal pipes", Int. J. Multiphase Flow, Vol. 1, pp. 537-553.

Meinhart C.D., Wereley S.T., Gray M.H.B., 2000a, Volume illumination for two-dimensional particle image velocimetry, Meas. Sci. Technol., Vol. 11, pp. 809-814.

Meinhart C.D., Wereley S.T., Santiago J.G., 2000b, A PIV algorithm for estimating time-averaged velocity fields, J. Fluids Engineering, Vol. 122, pp. 285-289.

Meinhart C.D., Wereley S.T., Santiago J.G., 1999, PIV measurements of a microchannel flow, Exp. Fluids, Vol. 27, pp. 414-419.

Mishima K., Hibiki T., 1996, Some characteristics of air-water two-phase flow in small diameter vertical tubes", Int. J. Multiphase Flow, Vol. 22, pp. 703-712.

Mishima K., Ishii M., 1984, Flow regime transition criteria for upward two-phase flow in vertical tubes, Int. J. Heat Mass Transfer, Vol. 27, pp. 723-730.

Nguyen N.T., Wereley S. T., 2002, Fundamentals and applications of microfluidics. MEMS Series. Artech House, Norwood, MA.

Nguyen N., Wereley S.T., 2006, Fundamentals and applications of Microfluidics, 2nd Edition, Artech House, Boston.

Oak J., Pence D.V., Liburdy J.A., 2004, Flow development of co-flowing streams in rectangular micro-channels, Microscale Therm. Eng., Vol. 8, pp. 111-128.

Peng X.F., Peterson G. P., 1996, Convective heat transfer and flow friction for water flow in microchannel structures, Int. J. Heat Mass Transfer, Vol. 39, pp. 2599-2608.

Peng X.F., Peterson G.P., Wang B.X., 1994, Frictional flow characteristics of water flowing through rectangular microchannels, Exp. Heat Transfer, Vol. 7, pp. 249-264.

Pfund D., Rector D., Shekarriz A., 2000, Pressure drop measurements in a micro channel, AIChE J., Vol. 46 pp. 1496-1507.

Prasad A.K., Adrian R.J., Landreth C.C., Offutt P.W., 1992, Effect of resolution on the speed and accuracy of particle image velocimetry interrogation, Exp. Fluids, Vol. 13, pp. 105-116.

Qu W., Mala G.M., Li D., 2000, Pressure-driven water flows in trapezoidal silicon microchannels, Int. J. Heat Mass Transfer, Vol. 43, pp. 353-364.

Qu. W., Yoon S.M., Mudawar I., 2004, Two-phase flow and heat transfer in rectangular micro-channels", J. Electronic Packaging, Vol. 126, pp. 288-300.

Santiago J.G., Wereley S.T., Meinhart C.D., Beebe D.J., Adrian R.J., 1998, A particle image velocimetry system for microfluidics, Exp. Fluids, Vol. 25, pp. 316-319.

Sevilla A., Gordillo J.M., Martinez-bazan C., 2005, Bubble formation in a coflowing air-water stream, J. Fluid Mech., Vol. 530, pp. 181-195.

Shah R.K., London A.L., 1978, Advances in Heat Transfer, Suppl. 1, Academic Press, New York.

Sharp K.V., Adrian R.J., Beebe D.J., 2000, Anomalous transition to turbulence in microtubes, In: Proc. Int. Mech. Eng. Cong. Expo., 5th Micro-Fluidic Symp., Nov. 5-10, Orlando, FL.

Song H., Tice J.D., Ismagilov R.F., 2003, A microfluidic system for controlling reaction networks in time, Angew. Chem., Int. Ed., Vol. 42, pp. 768-772.

Stone H.A., Kim S., 2001, Microfluidics: basic issues, applications, and chanllenges, AIChE J., Vol. 47, pp. 1250-1254.

Stone H.A., Stroock A.D., Ajdari A., 2004, Engineering flows in small devices: microfluidics toward a lab-on-a-chip, Annu. Rev. Fluid. Mech., Vol. 36, pp. 381-411.

Streeter V. L., 1961, Handbook of fluid dynamics. McGraw-Hill, New York.

Tabatabai A., Faghri A., 2001, A new two-phase flow map and transition boundary accounting for surface tension effects in horizontal miniature and micro tubes, J. Fluids Eng.-Trans. ASME, Vol. 123, 958-966.

Taitel T., Barnea D., Dukler A.E., 1980, Modeling flow pattern transitions for steady upward gas-liquid flow in vertical tubes, AIChE J., Vol. 26, pp. 345-350.

Taitel Y. and Dukler A.E., 1976, A model for predicting flow regime transitions in horizontal and near horizontal gas-liquid flow", J. AIChE, Vol. 22, pp. 47-55.

Triplett K.A., Ghiaasiaan S.M., "Adbel-Khalik, S.I., Sadowski D.L., 1999, Gas-liquid two-phase flow in microchannels. Part I: two-phase flow patterns", Int. J. Multiphase Flow, Vol. 25, pp. 377-394.

Triplett K.A., Ghiaasiaan S.M., "Adbel-Khalik, S.I., Sadowski D.L., 1999, Gas-liquid two-phase flow in microchannels. Part II: void fraction and pressure drop", Int. J. Multiphase Flow, Vol. 25, pp. 395-410.

Wereley S. T., Gui L., 2003, A correlation-based central difference image correction (CDIC) method and application in a four-roll mill flow PIV measurement, Exp. Fluids, Vol. 34, pp. 42-51.

Wereley S.T., Meinhart C.D., 2001, Second-order accurate particle image velocimetry, Exp. Fluids, Vol. 31, pp. 258-268.

White F.M., 1991, Viscous fluid flow, 2nd edition, McGraw-Hill, New York.

Wilding P., Pfahler J., Bau H.H., Zemel J.N., Kricka L.J., 1994, Manipulation and flow of biological fluids in straight channels micromachined in silicon, Clin. Chem., Vol. 40, pp. 43-47.

Wilmarth T., Ishii M., 1994, "Two-phase flow regimes in narrow rectangular vertical and horizontal channels," Int. J. Heat Mass Transfer, Vol. 37, pp. 1749-1755.

Wu H.Y., Cheng P., 2003, Friction factors in smooth trapezoidal silicon microchannels with different aspect ratios, Int. J. Heat Mass Transfer, Vol. 46, pp. 2519-2525.

Wu P., Little W.A., 1983, Measurement of friction factors for the flow of gases in very fine channels used for microminiature Joule-Thomson refrigerators, Cryogenics, Vol. 23, pp. 273-277.

Xiong R., Chung J.N., 2007a, Flow characteristics of water in straight and serpentine microchannels with miter bends, Exp. Therm. Fluid Sci., Vol. 31, pp. 805-812.

Xiong R., Chung J.N., 2007b, An experimental study of the size effect on adiabatic gas-liquid two-phase flow patterns and void fraction in micro-channels, Phys. Fluids, Vol. 19, 033301.

Xu B., Ooi K.T., Wong N.T., Choi W.K., 2000, Experimental investigation of flow friction for liquid flow in microchannels, Int. Comm. Heat Mass Transfer, Vol. 27 pp. 1165-1176.

Xu J.H., Li S.W., Wang Y.J., Luo G.S., 2006, Controllable gas-liquid phase flow patterns and monodisperse microbubbles in a microfluidic T-junction device, Appl. Phys. Lett., Vol. 88, 133506.

Yamashita H., Kushida G., Izumi R., 1984, Study on three-dimensional flow and heat transfer in miter-bend (1st report, analysis of flow in laminar region), Bulletin of JSME, Vol. 27, pp. 1905-1912.

Yamashita H., Izumi R., Kushida G., Mizuno T., 1986, Fluid flow and heat transfer in a two-dimensional miter-bend (1st report, experiments and analysis), Bulletin of JSME, Vol. 29, pp. 4164-4169.

Yang C.Y., Shieh C.C., 2001, Flow pattern of air-water and two-phase R-134a in small circular tubes, Int. J. Multiphase Flow, Vol. 27, pp. 1163-1177.

Zhang L., Koo J.M., Jiang L., Asheghi M., Goodson K.E., Santiago J.G., Kenny T.W., 2002, Measurements and modeling of two-phase flow in microchannels with nearly constant heat flux boundary conditions, J. MEMS, Vol. 11, pp. 12-19.

Zhao T.S., Bi Q.C., 2001, Co-current air-water two-phase flow patterns in vertical triangular microchannels" Int. J. Multiphase Flow, Vol. 27, pp. 765-782.

Zheng B., Tice J.D., Ismagilov R.F., 2004, Formation of arrayed droplets of soft lithography and two-phase fluid flow, and application in protein crystallization, Adv. Mater., Vol. 16, pp. 1365-1368.

Zuber N., and Findlay J.A., 1965, Average volumetric concentration in two-phase flow systems, ASME J. Heat Transfer, Vol. 87, 453-459.

8. High Power Density Thermal Management of Proton Exchange Membrane Fuel Cells

Task PI: Dr. James F. Klausner, Mechanical and Aerospace Engineering, University of Florida
Co-Investigator: Dr. Renwei Mei, Mechanical and Aerospace Engineering, University of Florida
Graduate Student: Patrick Garrity, Mechanical and Aerospace Engineering, University of Florida

Research Period: August 2004 to May 2007

Abstract

The goal of this research task is to develop an advanced high power density thermal management system for Proton Exchange Membrane (PEM) Fuel Cells that will significantly increase the heat removal capacity, decrease the required pumping power, and keep the operating temperature within its optimal range while reducing the overall weight. The strategy will be to implement a two-phase flow passive cooling system using a microchannel evaporator plate. The passive cooling system will allow for the removal of the power consuming pump and improve the overall power density of the Fuel Cell. Due to the isothermal nature of two-phase flow, temperature gradients should be minimal, allowing the fuel cell to operate primarily within its optimal temperature range. The microchannel evaporator plate will provide high heat transfer rates, helping reduce temperature at the channel walls.

Introduction and Background

Fuel cells are expected to play a major role in energy production within the foreseeable future. Increasing concerns about pollution and possible anthropogenic global warming along with economic issues involving fossil fuels have accelerated an abundance of research for alternative energy systems that run on a cleaner, more economical energy source such as hydrogen. It is anticipated that the development and deployment of economical and reliable fuel cells could usher in the sustainable hydrogen age. Proton Exchange Membrane Fuel Cells (PEMFC) in particular are of significant interest to the automobile industry, as well as the avionics and space industry, among others due to the potential for high power density, relatively quick start up, rapid response to varying loads, and low operating temperatures. In addition, there is effectively no pollution produced during operation of PEM fuel cells as water and heat essentially make up the exhaust to the environment.

The basic principle of Proton Exchange Membrane Fuel Cells (PEMFC) is to convert hydrogen to electricity by passing the fuel across a solid polymer membrane, a thin plastic film that is permeable to protons but does not allow for the conduction of electrons, thus allowing for electron transport through an external electric circuit, see Fig. 1. This solid polymer membrane, also known as the electrolyte, is located between the anode and the cathode side of the cell. At the anode, the hydrogen makes contact with a thin layer of platinum catalyst and the electron is stripped away from the hydrogen. The liberated electrons continue along the external circuit while the protons travel through the electrolyte to the cathode side.

On the cathode side, protons coming from the anode encounter oxygen and the electrons from the external circuit in a catalyst electrode layer to form liquid water which is than drained away so as to not block the fuel cell.

In the case of PEM fuel cells, the polymer membrane is solid; reducing corrosion and electrolyte management problems, however, in order for the hydrogen ions to conduct through to the cathode, sufficient hydration is required. This is because the proton motion in these polymer membranes can occur only in the presence of water. The proton has to first bind with water to form hydronium ions, which are then drawn across the membrane by the existing electric field. This implies that every proton moving across the membrane carries along with it a certain number of water molecules. This phenomenon is referred to as electro-osmotic drag. If there is not enough water present, a high resistance to proton conduction takes place while on the other hand, if too much water is present, flooding will occur blocking the transport of reactants. This concept makes water management essential. Likewise, thermal problems can arise within the stacks that significantly lower the fuel cells efficiency. At low operating temperature, the resistance to proton conduction is low due to the promising hydration, but the oxygen reduction on the cathode side requires higher activation overpotential, reducing the current density. On the other hand when the temperature is too high, the water within the membrane will evaporate, increasing the mass transport resistance and in turn reducing the cells power output. You and Liu [1] have developed a two-phase flow transport model for the cathode side of PEM fuel cells. They have demonstrated that there exists an operating temperature for optimum performance that tends to be in the range of 70-80 °C. This low operating temperature, coupled with the large heat flux removal demand makes thermal management a difficult task and further supports the need for enhanced modes of thermal transport. However, there are also several advantages to this that make PEM fuel cells cutting edge in the context of lightweight, mobile energy sources. For instance, at low operating temperature, the fuel cell is capable of warming up quickly which can be beneficial for mobile applications. Other advantages include the elimination of expensive containment structures and less wear on system components, resulting in better durability. By implementing various heat removal methods such as two-phase heat transfer in a thermosyphon, this low operating temperature can make PEM fuel cells more practical to energy production.
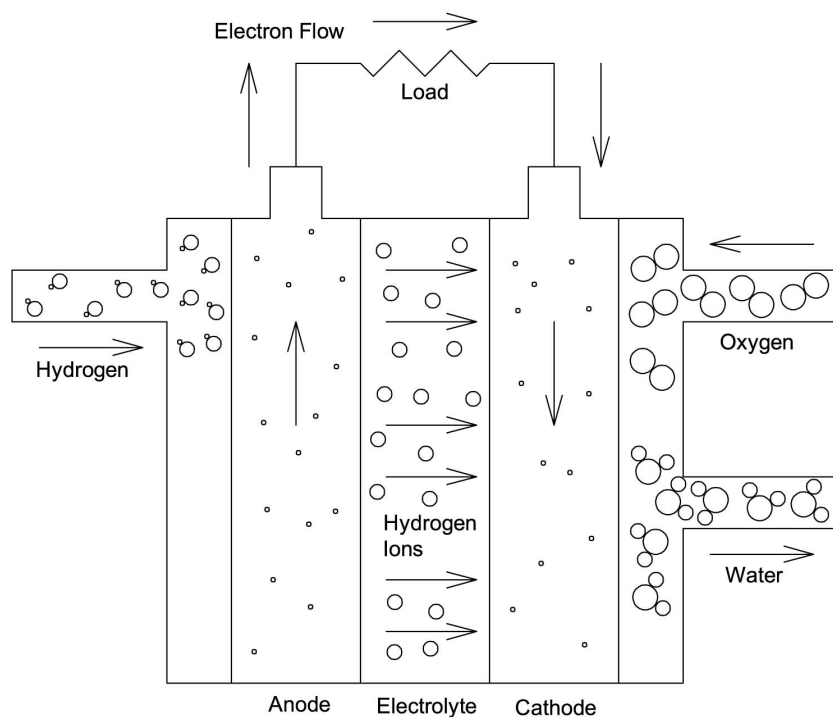

Figure 1: Operation of a PEM Fuel Cell.

With the hopes of optimizing efficiency, PEM fuel cells have recently been subject to en ever-increasing number of modeling efforts for the past 15 years. Accurate models describing the complex coupling of the heat, mass and momentum transfer within the stack are a crucial step in optimizing fuel cell efficiency with regards to thermal management. Coppo et al. [2] provides a 3-D computational model to describe the effects of temperature on operation of PEM fuel cells. It is shown that temperature affects the fuel cell differently depending on the current density. At low current density, $(0 \text{ A } cm^{-2} < J < 0.2 \text{ A } cm^{-2})$ reaction activation losses dominate, in the intermediate range of currents $(0.2 \text{ A} cm^{-2} < J < 0.7 \text{ A} cm^{-2})$, ohmic losses are preponderant, and finally, for higher currents, mass transport losses prevail. In the activation regime, or low current density operation, the optimal temperature is balanced between the effects of the cathode side activation overpotential and the open circuit resistance, i.e. an increase in temperature lowers the activation overpotential, which increases current density, however this simultaneously raises electrical resistance, reducing the power output. At slightly higher current densities, classified as the ohmic region, electro-osmotic drag becomes more significant causing the optimal temperature to be governed by membrane ionic conductivity and dissolved water diffusivity. Higher temperature decreases the ionic conduction due to the reduced hydration in the presence of electro-osmotic drag. On the other hand lowering the temperature decreases the dissolved water diffusivity. This causes the membrane hydration level to be less homogeneous, bringing about localized regions of low ionic conductivity. Finally, for high current density operation, also known as the mass transport limited regime, the optimal temperature is governed by the resistance to reactant transport that results from the high mass flow rates required to sustain the electrochemical reactions at a rapid kinetic pace. By increasing the operating temperature, the oxygen diffusivity within the gas diffusion layer as well as the ion-conducting polymer is amplified. Adversely the air/water concentration ratio influencing reaction kinetics decreases with temperature. The higher water content in the gas stream reduces oxygen concentration at the cell inlet. So even though the oxygen diffusivity is higher, less oxygen is available when the temperature is too high reducing the cathode overpotential and consequently cell voltage. Similarly, water diffusivity increases with temperature due to the strong temperature dependency of kinematic viscosity, contact angle, and surface tension. It should also be noted that there is a strong coupling between the liquid water and oxygen diffusion, since higher liquid water diffusion increases the water content in the gas stream. The resulting optimal temperature within the mass transport limited regime is governed by a balance of the coupled oxygen and liquid water diffusivities as well as the resulting saturation level at the oxygen at the cell inlet.

In conclusion, temperature strongly influences PEM fuel cell operation. Optimal operating temperatures will vary depending on the fuel cells output or current density and usually range from 70-80 °C. For optimal performance a thermal management system must be implemented that will remove the required heat load while keeping the fuel cell temperature within the optimal range.

The objective of this research is to implement a two-phase microchannel thermosyphon that will efficiently dissipate heat from the fuel cell providing compact, lightweight thermal management. By reducing the superheat within the microchannel plate, the working fluid may be chosen with a higher saturation temperature. As long as the fuel cell operates within the optimal range, a high saturation temperature is desired as it helps reduce the required surface area within the condenser, resulting in a compact, lightweight design. A large focus of this research includes the construction of a fundamental model to predict and optimize both the heat transfer within the evaporator plate as well as in the condenser. The final objective is to predict the onset of the system limiting instability observed at high heat flux. The combined models describing the heat

transfer and pressure drop characteristics of the evaporator plate and condenser should provide sufficient design tools that can predict and optimize the system performance while preventing any catastrophic failures that arise from instabilities.

Thermosyphon Experimental Facility

The experimental two-phase thermosyphon is shown in Fig. 2. The main test section consists of a 56 channel aluminum cooling plate. Each channel has a cross section of 1x1 mm and has a length of 115 mm. The cooling plate is covered with Lexan to allow for flow visualization. An imposed heat flux is placed on the cooling plate using a Minco foil heater, 127x127 mm, that covers the back of the cooling plate, and the maximum heater flux is 60 kW/m^2, based on the surface area of the heater. The heated surface area in contact with the liquid is 193.2 cm^2. During operation, the cooling plate is thoroughly insulated. The temperature difference between the insulation and ambient is used to evaluate the heat loss, which is based on calibration.
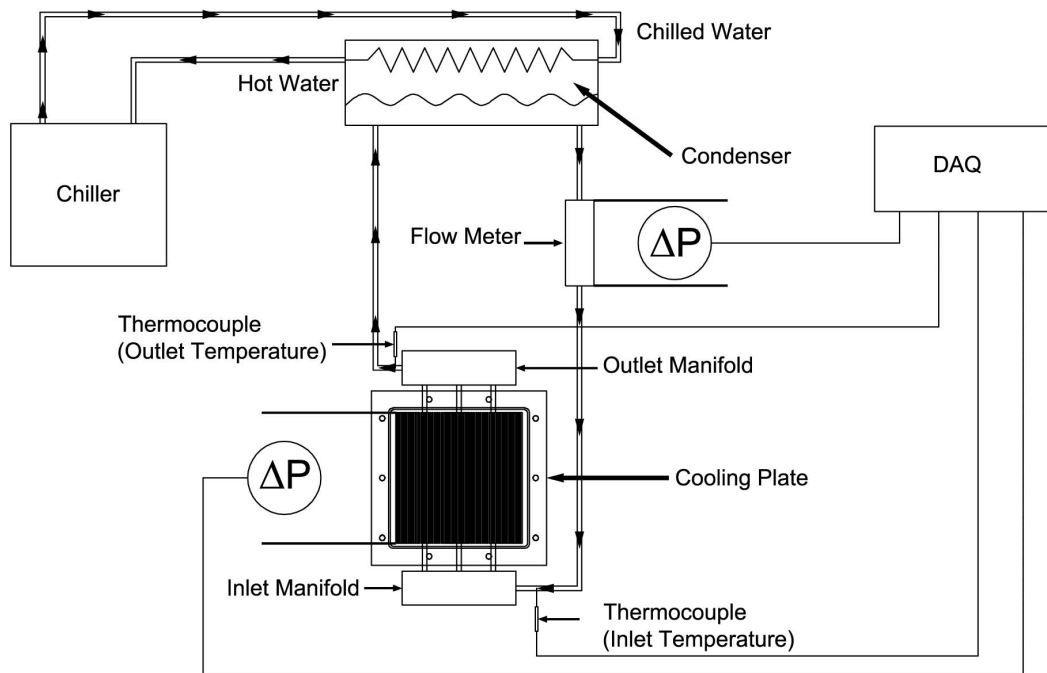
Figure 2: Experimental Two-Phase Thermosyphon.

An exploded view of the cooling plate assembly is shown in Fig. 3. The facility is filled with HFE-7100 which enters and discharges the cooling plate through an inlet and outlet manifold, respectively. The two-phase mixture discharges the cooling plate and rises to a water cooled condenser operating at 15 °C with a water flow rate of up to 46 g/s. The vapor is condensed, and the pure liquid phase flows out of the condenser and through a flow meter. The liquid discharge from the flow meter returns to the cooling plate. The inner diameter of the tubing carrying fluid between the condenser and cooling plate is 9.5 mm. The vertical height between the condenser outlet and manifold inlet is 114 cm, while the vertical height between the outlet manifold and condenser inlet is 102 cm. The test section and piping throughout the system are insulated with elastomeric foam.
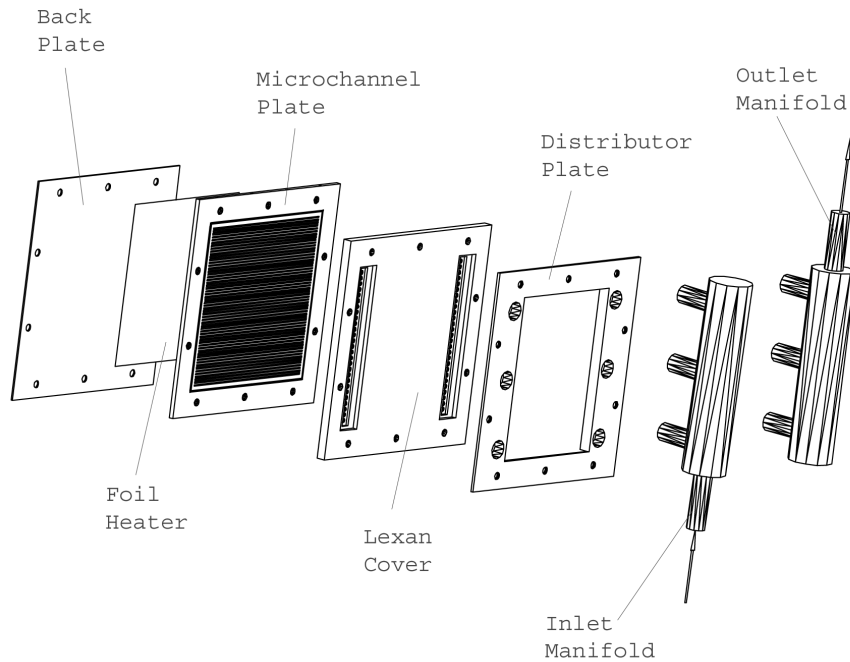
Figure 3: Exploded View of the Cooling Plate Assembly.

A venturi flow meter is implemented into the thermosyphon loop to measure the flow rate. The pressure drop across the venturi is measured with a Validyne differential pressure transducer with a diaphragm capable of measuring a pressure drop up to 9.2 kPa. The maximum pressure drop recorded was 6.9 kPa which corresponds to a flow rate of 30.0 g/s. The relationship between flow rate and pressure drop was determined through calibration over a range of 42 g/s. The uncertainty of the flow rate measurement is estimated to be ± 0.35 g/s.
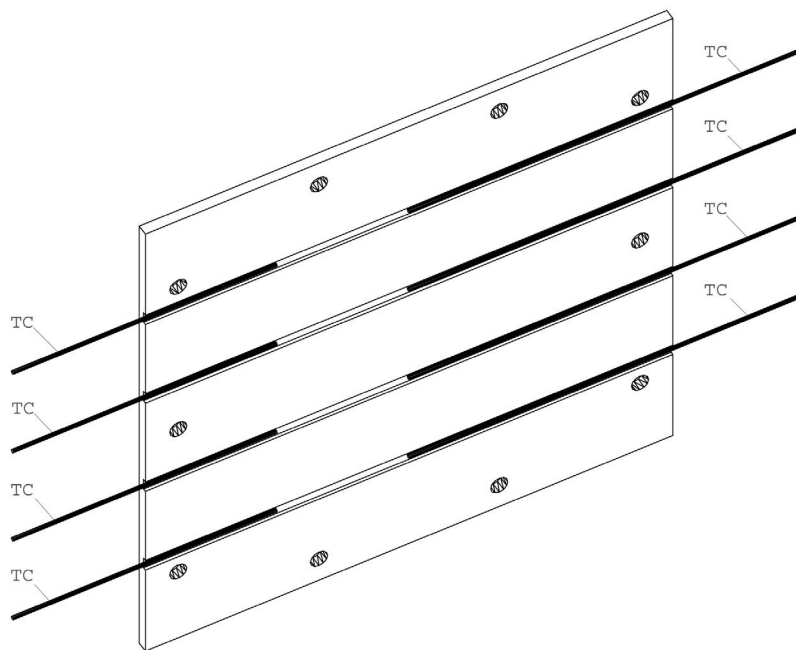
Figure 4a: Thermocouple Locations on Cooling Plate.

A second Validyne differential pressure transducer is used to measure the pressure drop across the cooling channel and has a range and uncertainty of 0-3.5 kPa and $\pm$0.01 kPa, respectively. Type E thermocouples have been inserted into the inlet and outlet manifolds to measure the fluid temperature. Also, 8 thermocouples have been embedded into the back of the cooling plate to measure wall temperature as depicted in Figs. 4 a and b. Each thermocouple has been calibrated and the uncertainty is estimated to be $\pm$0.1 $^\circ$C. The wall thickness between each thermocouple and the fluid is 1 mm. The thermocouples were bonded securely using Omegabond-200 high thermal conductivity adhesive. Each thermocouple has been labeled 1-8 for reference. All reported uncertainties are based on the standard deviation from the calibration.
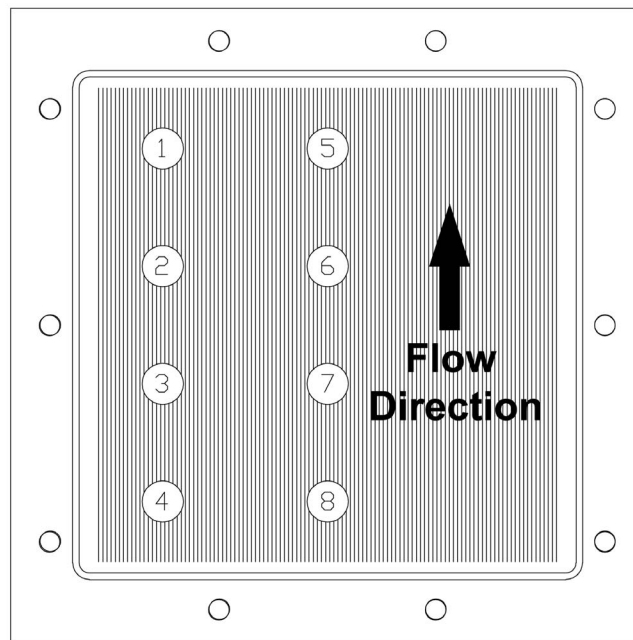
Figure 4b: Thermocouple Locations on Cooling Plate.

All signals were measured using digital data acquisition consisting of a Measurement and Computing CIO-EXP32 multiplexer and PCIM-DAS1602/16 16 bit analog to digital converter. A custom algorithm was developed to convert the measured voltages to pressure, temperature, and flow rate.

Experimental Protocol

HFE-7100 is added to the facility through the top of the condenser until the height of the fluid is just below the condenser coil. Liquid water at 15 $^\circ$C is then circulated through the condenser coil. The differential pressure transducers are then purged of air. The heat flux on the cooling plate is gradually raised so that vigorous boiling is observed through the channels. Once vigorous boiling is established for a half an hour, the condenser is purged of non-condensable gas. Following purging, the heat flux is reduced to zero so that the flow through the facility ceases. The heat flux is then raised in increments, and at each increment the flow rate and temperatures are allowed to reach a steady state. Measurements of pressure, flow rate, and temperature are made at each heat flux interval. The heat flux is raised until the flow becomes unstable, at which point large scale flow oscillations and flow reversal are easily visible.

The fluid leaving the condenser is subcooled to some degree. The degree of sub-cooling varies with heat flux, as shown in Fig. 5. At low heat flux, the fluid is below saturation throughout the

loop, and therefore higher heat flux results in a larger degree of subcooling. Once the fluid reaches saturation at the exit to the plate, the subcooling is decreased until significant vapor is generated at which point the subcooling increases once again. The condenser coils are located above the liquid level within the condenser. When the vapor condenses, it is highly subcooled and mixes with the bulk liquid in the storage area. Therefore, as more vapor flows through the condenser, the bulk fluid becomes more subcooled.
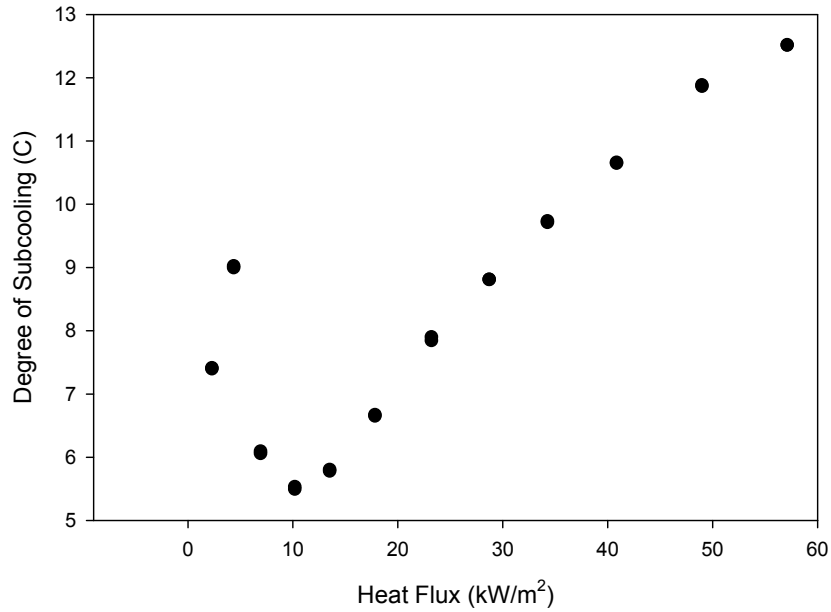

Figure 5: Degree of Inlet Sub Cooling Variation with Heat Flux for H1=1.33 m.

Results and Discussion
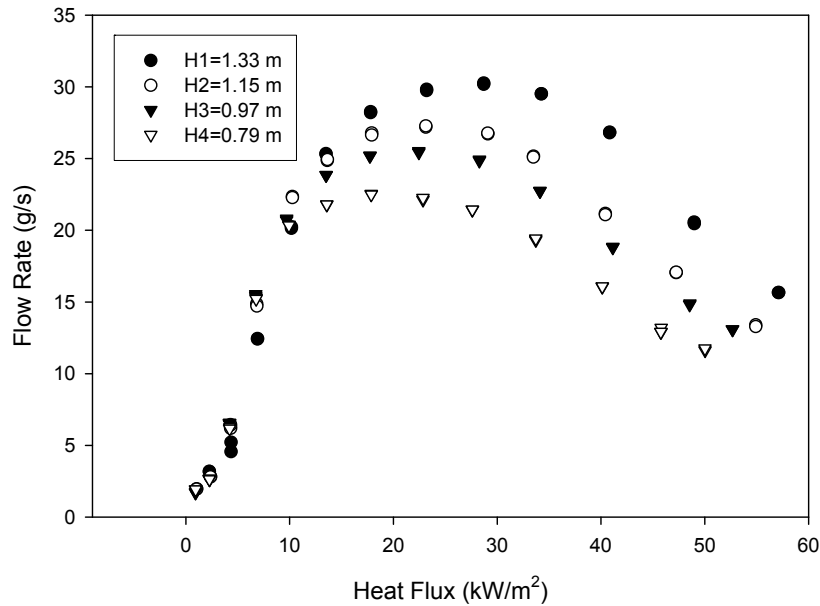
Figure 6: Measured Flow Rate vs. Heat Flux for Varying Condenser Heights.

Fig. 6 shows the measured flow rate circulating through the two-phase thermosyphon at various heat fluxes, where the heat flux is based on the heated area in contact with the liquid. Initially, there is a rapid rise in flow rate with increasing heat flux. This rapid rise in flow rate is due to an increase in vapor volume fraction in the riser, and thus the density difference between the down flow line and riser increases, which results in an increased flow rate. As the heat flux increases further, the increase in vapor volume fraction is marginal, but the increase in vapor quality is significant which results in increased friction. Thus, the mass flow rate peaks at 30 g/s, corresponding to a heat flux of approximately 28 kW/m^2 at the highest condenser height. As the heat flux is further increased, the mass flow rate decreases. The maximum achievable heat flux during these sets of experiments is 58 kW/m^2. At that point, the flow becomes unstable due to the onset of a Ledinegg instability.
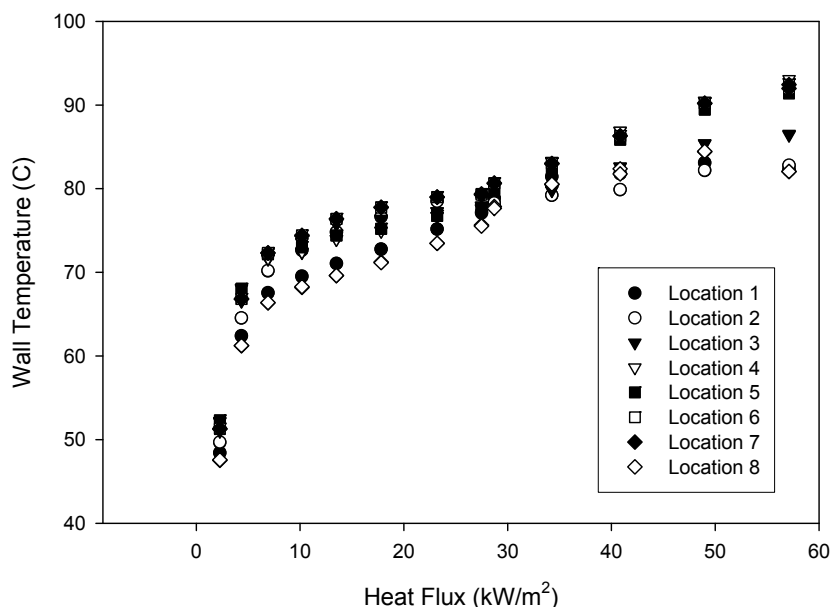
Figure 7: Wall Temperature at Various Locations for H1=1.33 m.

Fig. 7 shows the measured wall temperatures for thermocouple positions 1-8 at various heat fluxes for a condenser height of 1.33 m. The wall temperatures near the entrance to the cooling plate, which correspond to locations 4 & 8 from Fig. 4b, tend to be the highest. This is because the fluid enters the cooling plate as a pure liquid, and the heat transfer coefficient is lower than that near the exit of the cooling plate, where the vapor quality is relatively high. Also, the wall temperatures are slightly less near the side of the plate than at the central region. This is due to the fact that there is finite heat leakage at the edges of the plate. In general, the thermal performance of the two-phase thermal management system is quite good. The wall temperatures of the cooling plate vary from approximately 47 to 90 °C depending on the heat flux and location. The majority of heat loads provide wall temperatures that are very close to the optimum temperature range for PEM fuel cell membranes. Furthermore, PEM fuel cells currently only require a heat flux of 5 kW/m^2 [3] heat removal capacity. Therefore, the present system far exceeds the current need and has sufficient heat removal capacity for larger power density systems prior to the onset of Ledinegg instability.
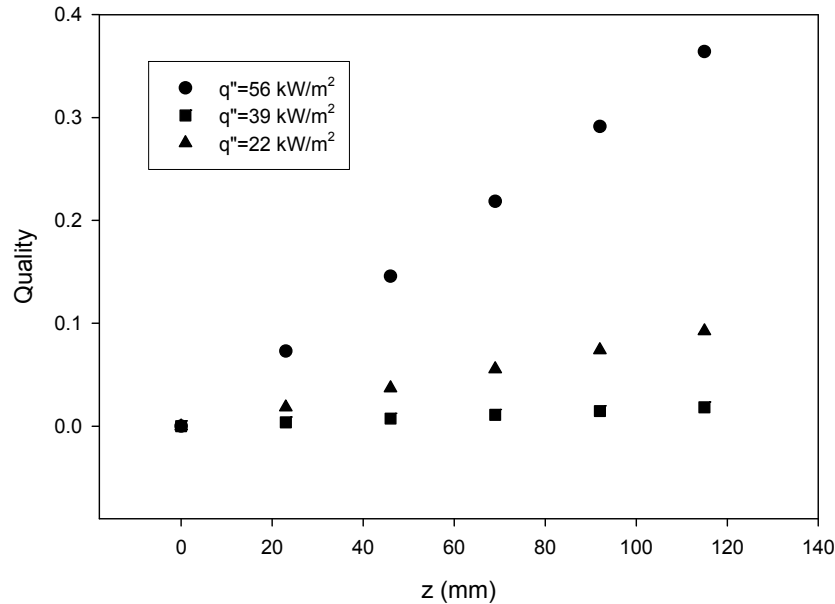
Figure 8: Variation in Vapor Quality with Channel Height for H1=1.33 m.

In order to elucidate how the variation of vapor quality influences the thermal field along the cooling plate, the axial variation of thermodynamic vapor quality is computed. Since the flow is subcooled entering the cooling plate, the change in sensible heat must be considered when evaluating the thermodynamic equilibrium vapor quality at any z-location along the cooling plate,

$$x(z) = \frac{\dot{q}_z - \dot{m}C_p(T(z)-T_i)}{\dot{m}h_{fg}}$$

where $\dot{q}_z$ is the rate of heat flow into the cooling plate from the entrance to the z-location, T(z) is the bulk fluid temperature at the z-location, T_{in} is the inlet fluid temperature, $\dot{m}$ is the mass flow rate, and h_{fg} is the latent heat of vaporization for the fluid. In order to evaluate T(z), the inlet and exit fluid temperatures are measured, and it is assumed that there is a linear change in the bulk fluid temperature along the z-direction. This assumption may not be exact, but since the maximum temperature change between the inlet and outlet is only 12 ˚C, it is acceptable for the estimation of the vapor quality x(z). The non-uniform heating is apparent from the measured wall temperatures shown in Fig. 7. The lateral heat flux toward the edges of the cooling plate is approximately 27% of the heat flux into the fluid. Fig. 8 shows the variation of vapor quality along the z-direction for various heat fluxes at the central region of the cooling plate. While the quality appears to be small for low heat flux, this approximation is based on thermodynamic quality and does not account for the localized subcooled boiling which produces net vapor generation at negative thermodynamic equilibrium quality. Also, the quality increases rather slowly for low heat flux. At higher heat flux, the flow begins to decrease in flow rate and a rapid increase in vapor quality is observed.

Instability Analysis

The steady state flow behavior of the fluid circulating through the two-phase thermosyphon system is shown in Fig. 6. As shown, at low heat loads the flow rate increases rapidly due to the increasing difference in pressure head between the riser and downcomer. This increase in pressure head results from the increasing vapor volume fraction. At slightly higher heat flux, the vapor quality becomes more significant and an increase in frictional pressure drop is observed. As the frictional pressure drop becomes more substantial, the flow rate actually begins to decrease. Although the vapor in the riser is at a high velocity, the low density and high friction give rise to a decrease in flow rate. The largest flow rate occurs when the condenser is situated highest from the microchannel evaporator plate. This is because a larger difference in pressure head between the riser and downcomer can be achieved for higher condenser heights.

The heat flux in Fig. 6 is taken from experiment ranging from zero to a maximum value, at which point the system goes unstable. The system limiting heat flux is plotted against condenser height in Fig. 9. As shown the system remains stable over a larger range of heat flux when the condenser is located highest above the microchannel evaporator plate.
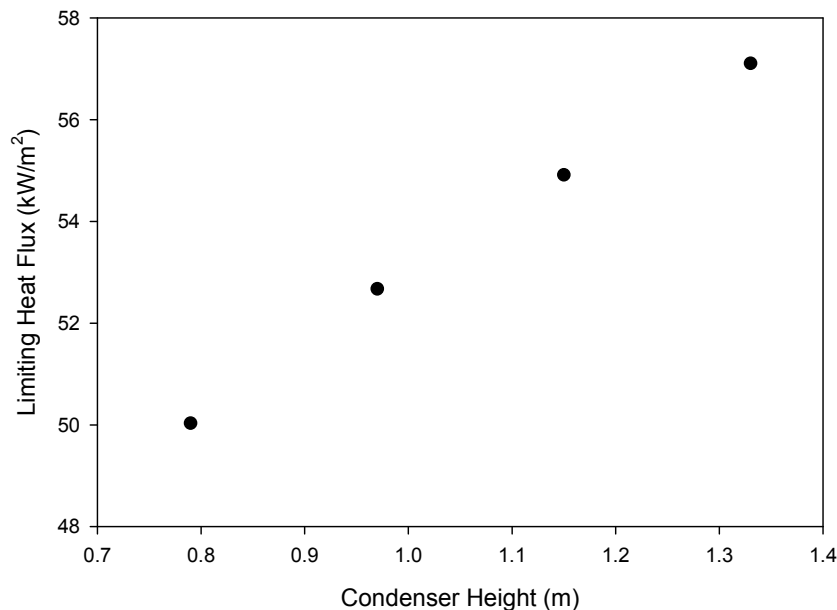

Figure 9: Limiting Heat Flux Resulting from Instability for Varying Condenser Heights.

Fig. 10 shows a histogram of the flow rate data taken immediately prior to instability for H=0.79 m. There is no obvious shape to the histogram and the kurtosis is significantly large. This suggests that the flow rate signal consists of one dominant frequency coupled with either several sinusoids at various frequencies, electronic noise, or a combination of both. The percent fluctuation is computed as the ratio of the standard deviation to the mean value and found to be 9%. The fluctuation phenomena are most likely a result of the bubble dynamics within the evaporator plate.
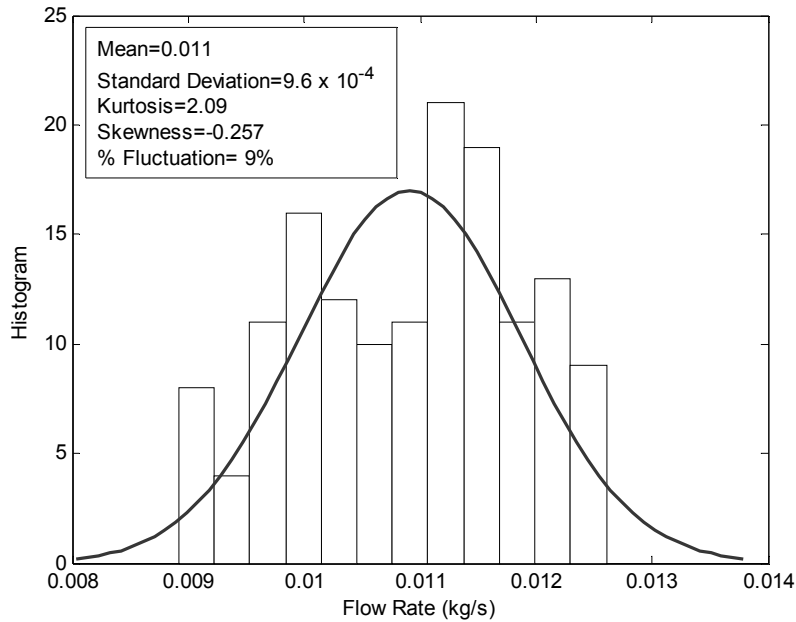
Figure 10: Histogram of Flow Rate Measurements for H4=0.79 m Immediately Prior to Instability.

Flow Modeling

In a closed loop natural circulation system, the pressure at the discharge of the condenser is the same as that at the return of the condenser. Therefore, in order to predict the system flow rate it is necessary to compute the pressure change around the flow loop and converge on a flow rate that insures the inlet and discharge pressure at the condenser match. The two phase pressure gradient may be expressed as,

$$\left(\frac{dP}{dz}\right)_{2\phi} = \left(\frac{dP}{dz}\right)_g + \left(\frac{dP}{dz}\right)_f + \left(\frac{dP}{dz}\right)_a \tag{1}$$

It consists of three components, gravitational, frictional, and accelerational, denoted by subscripts g, f, and a respectively. Each must be modeled accordingly to ensure proper representation of the flow behavior. The gravitational pressure gradient results from a body force acting on the fluid and is given by,

$$-\left(\frac{dP}{dz}\right)_g = \rho_m g \sin\theta \tag{2}$$

where ρ_m is the mixture density, g is the gravitational acceleration, and θ is an inclination angle. For upflow $\theta=\pi/2$ and $\theta=-\pi/2$ for downflow. The mixture density depends on the vapor volume fraction α,

$$\rho_m = \alpha\rho_v + (1-\alpha)\rho_l \tag{3}$$

where ρ is the density and the subscripts l and v refer to the liquid and vapor, respectively. In order to estimate the vapor volume fraction, the standard Zuber-Findlay drift flux model [4] for slug flow is used,

$$\alpha = \left(C_0 \left(1 + \left(\frac{1-x}{x} \right) \frac{\rho_v}{\rho_l} \right) + \frac{\rho_v}{Gx} V_{vj} \right)^{-1}$$

(4)

$$V_{vj} = 1.53 \left(g\sigma \frac{\left(\rho_l - \rho_v \right)}{\rho_l^2} \right)^{1/4}$$

(5)

where G is the mass flux and C_0=1.2. The pressure gradient associated with the acceleration of the fluid is derived from a momentum balance on a differential section of the tube in a constant cross section. The resulting expression for the change in velocity due to the change in vapor quality and vapor volume fraction is,

$$-\left(\frac{dP}{dz} \right)_a = G^2 \frac{d}{dz} \left(\frac{\left(1-x\right)^2}{\rho_l\left(1-\alpha\right)} + \frac{x^2}{\rho_v\alpha} \right)$$
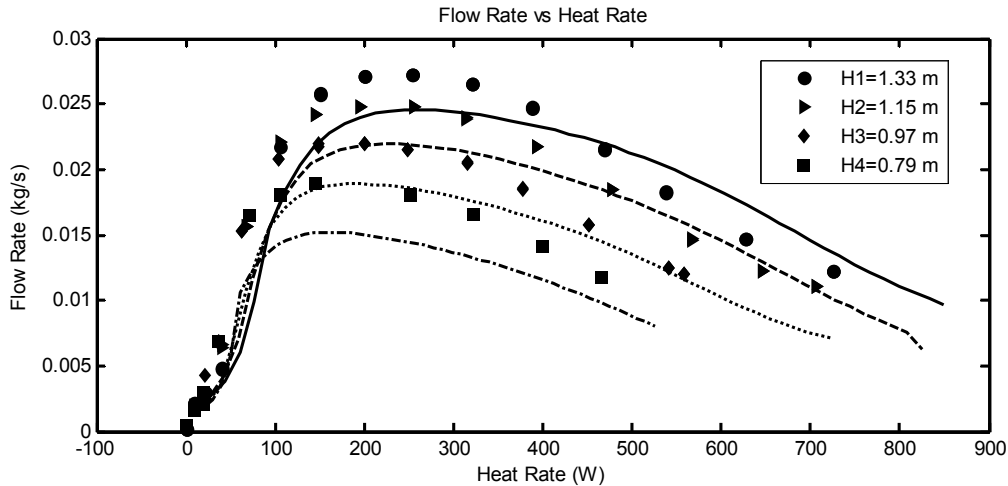
(6)

Figure 11: Measured vs. Predicted Flow Rate for Various Heat Flux

The frictional pressure gradient is modeled using the correlation from Mueller-Steinhagen and Heck [5]. This correlation considers the single-phase frictional pressure gradient for both liquid and vapor and uses superposition along with an empirical fit to model the two-phase frictional pressure gradient,

$$-\left(\frac{dP}{dz} \right)_f = F\left(1-x\right)^{1/3} + Bx^3$$

(7)

$$F = A + 2\left(B - A \right)x$$

(8)

where the superficial velocity of the liquid and vapor phases is used to evaluate A & B as,

$$A = f_l \frac{G^2}{2\rho_l d} \tag{9}$$

$$B = f_v \frac{G^2}{2\rho_v d} \tag{10}$$

Here, d is the hydraulic diameter, and the Darcy friction factor is computed as,

$$f_l = \begin{cases} \dfrac{64}{\mathrm{Re}_l}, \mathrm{Re}_l < 1187 \\ \dfrac{0.3164}{\mathrm{Re}_l^{1/4}}, \mathrm{Re}_l > 1187 \end{cases} \tag{11}$$

$$f_v = \begin{cases} \dfrac{64}{\mathrm{Re}_v}, \mathrm{Re}_v < 1187 \\ \dfrac{0.3164}{\mathrm{Re}_v^{1/4}}, \mathrm{Re}_v > 1187 \end{cases} \tag{12}$$

$$\mathrm{Re}_l = \frac{Gd}{\nu_l} \tag{13}$$

$$\mathrm{Re}_v = \frac{Gd}{\nu_v} \tag{14}$$
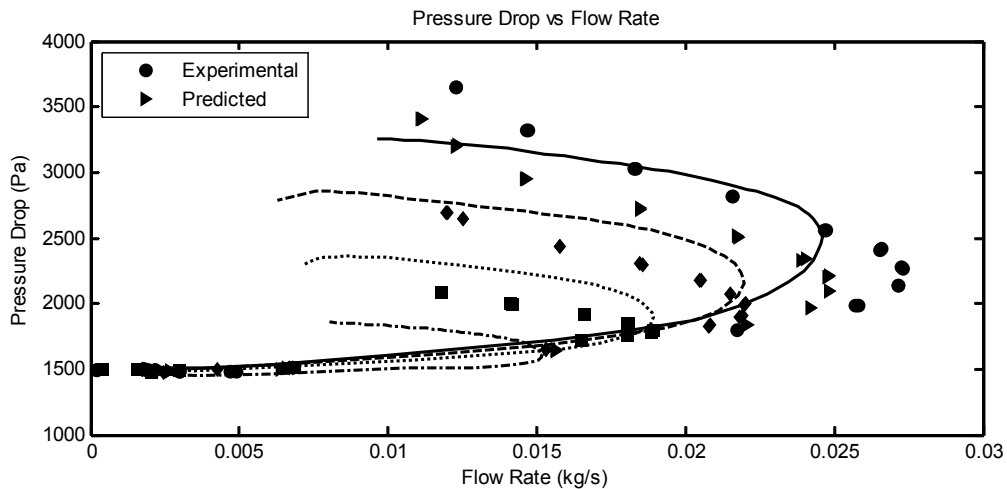
Figure 12: Measured vs. Predicted Pressure Drop Across the Microchannel Evaporator Plate for Various Heat Flux.

In order to compute the mass flow rate for a specified heat flux, an algorithm has been developed that searches for the flow rate that yields an equal pressure at the inlet and exit of the condenser. Fig. 11 shows a comparison between the measured and predicted mass flow

rate at various heat fluxes assuming a linear bulk fluid temperature profile along the microchannel plate. Very little difference is observed between the two predictions. The comparison between the measured and predicted pressure drop across the microchannel test section for various mass flow rates is shown in Fig. 12 that provides reasonable agreement. In general, the flow rate is slightly under-predicted, but considering the complexity of the system, the predicted flow rate and pressure drop is satisfactory for design purposes.
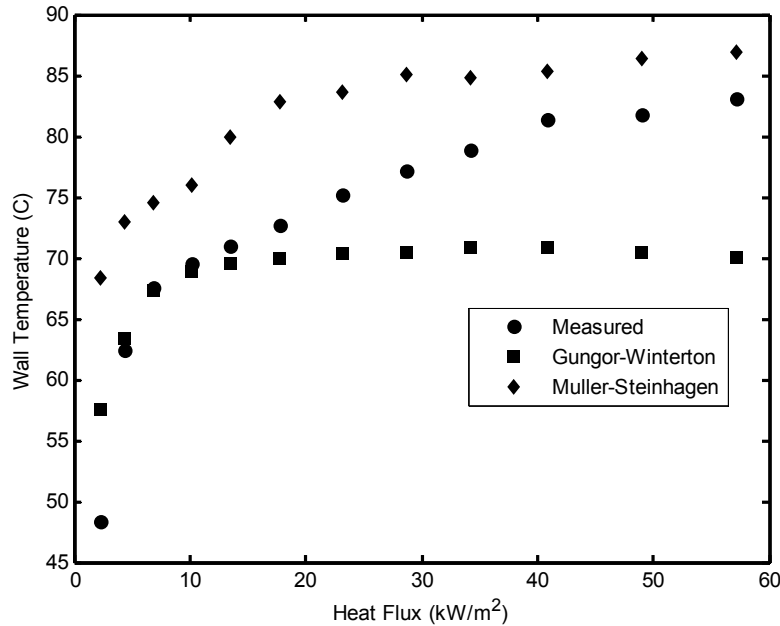
Figure 13a: Comparison Between Measured and Predicted Wall Temperature at Thermocouple Location 4 based on Measured Flow Rate and Vapor Quality.
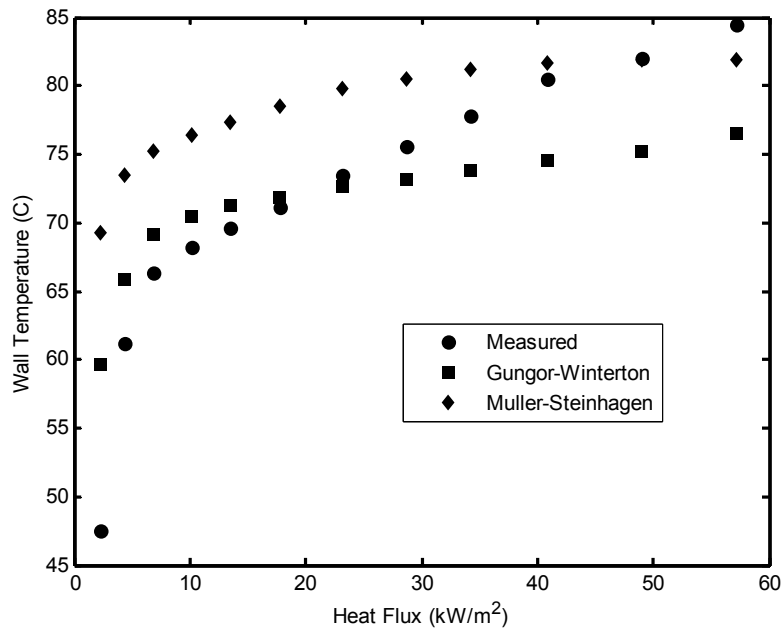
Figure 13b: Comparison Between Measured and Predicted Wall Temperature at Thermocouple Location 5 based on Measured Flow Rate and Vapor Quality.

Figures 13 a and b compare the measured wall temperatures at thermocouple locations 4 and 5, respectively, with those predicted using the Gungor-Winterton [6] and Mueller-Steinhagen [7] subcooled flow boiling correlations. The computations for these comparisons use the measured flow rate and vapor quality. The Gungor-Winterton [6] correlation gives better agreement at lower heat flux and vapor quality, and in general the data lie between both predictions. The wall temperatures were also computed using the predicted mass flow rates, and the results are virtually identical to those shown in Figures 13 a and b. This indicates that the predicted wall temperatures are not sensitive to small variations in vapor quality and mass flow rate. It is also noteworthy that flow boiling correlations developed for large diameter tubes are also satisfactory for the current microchannel plate design. The thermal-hydraulic models presented in this work allow the thermal field in the microchannel plate to be predicted from fundamental models without the need for experimental inputs.

Steady State Instability Modeling

Steady state instabilities, often labeled as flow excursion or Ledinegg instability, involve a sudden change in the flow rate to a lower value followed by oscillation and ultimately system failure. In forced convection the phenomena is governed by the slope of pressure gradient with respect to mass flux for both the internal characteristics; friction, acceleration, and gravity; and the external characteristics; the pumping mechanism. In the case of natural circulation, the pumping mechanism itself is the gravitational pressure head. Therefore the criterion for instability is simply,

$$\left.\frac{\partial P}{\partial G}\right|_f + \left.\frac{\partial P}{\partial G}\right|_a + \left.\frac{\partial P}{\partial G}\right|_g \leq 0 \,. \qquad\qquad (15)$$

From Eq. 15 it can be seen that in order for the flow to go unstable, the sum of the frictional, accelerational, and gravitational pressure gradients must be less than zero. Throughout the loop, the accelerational component of pressure drop is an order of magnitude smaller than the frictional and gravitational components and can be considered negligible here for discussion purposes.
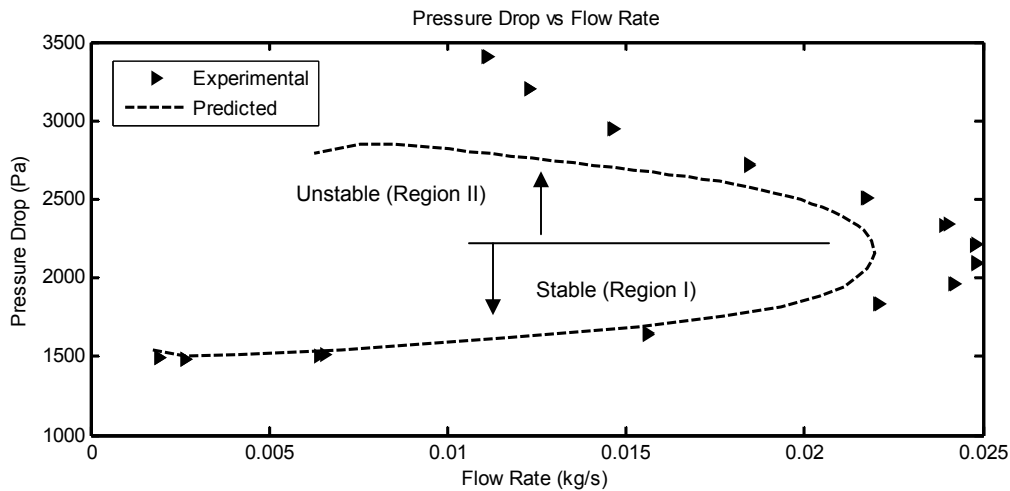
Figure 14: Pressure Drop across the Microchannel Plate for Varying Flow Rate at H=1.15 m.

At high heat flux where the instability occurs, the frictional pressure gradient within the microchannel plate is approximately 50 times the pressure gradient in the liquid section of the thermosyphon loop and 2.5 that in the two-phase upper section. Therefore the pressure drop across the microchannel plate, which is dominated by friction, gives a reasonable approximation of the frictional pressure drop with respect to mass flux throughout the system and is shown in Fig. 14 for illustration purposes.

In region-I, where the slope of the pressure drop as a function of flow rate curve is positive, a small perturbation decreasing the flow rate will result in increasing vapor quality and larger gravitational pumping potential. Simultaneously, the frictional pressure drop decreases due to decreased flow rate, and thus the flow rate will adjust back to its original value. Likewise, in region-I, the flow rate will return to its original value following a perturbation increasing the flow rate. Thus the flow is stable in region-I. In contrast, in region II the slope of the pressure drop as a function of flow rate curve is negative, and a small perturbation increasing the flow rate will result in decreasing vapor quality and gravitational pumping potential. Simultaneously, the frictional pressure drop is reduced. Thus further increases in flow rate and decrease in vapor quality can result, until the flow swings back to region I. However, the flow state does not remain in region I for long due to the high heat flux and rapid increase in vapor quality. A highly transient oscillatory mode is established until eventual dryout occurs.
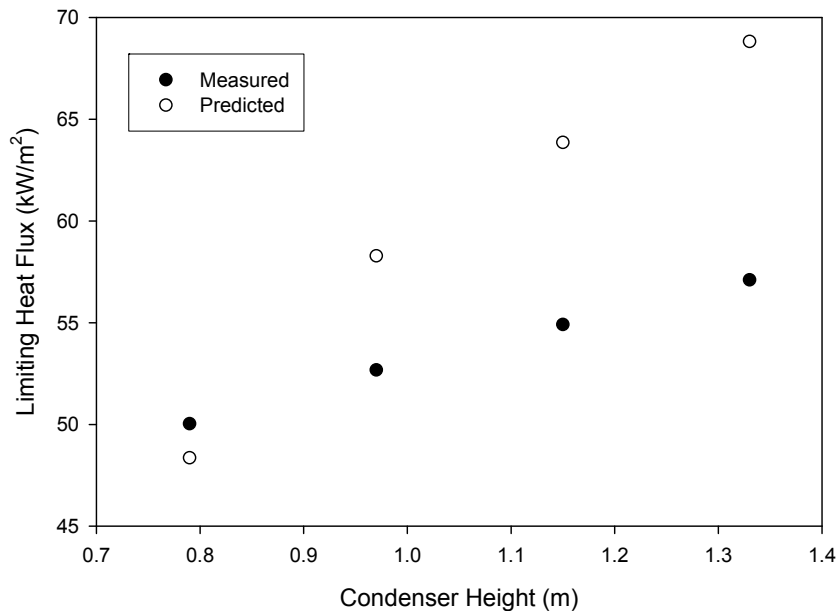
Figure 15: Measured vs. Predicted Heat Flux at the Onset of Instability.

Using the models presented previously for the three components of pressure drop, an instability model is constructed. After converging on a steady state flow rate, the 9% perturbation taken from Fig. 10 is introduced to the flow rate and the equations are solved again. Eq. 15 is evaluated for the entire range of heat flux and the lowest value of heat flux that satisfies Eq. 15 is taken to be the predicted heat flux at the onset of instability. Fig. 15 shows the measured vs. predicted values for heat flux when instability occurs providing reasonable agreement given the complex nature of two-phase flow. The relative error is computed to be ±14%. When the condenser height is high, more error is present. This could be due to excess flashing taking place at the outlet to the evaporator plate, giving rise to larger fluctuations in flow rate and increased friction.

Foam Testing for Airside Heat Transfer Enhancement

Three different aluminum foam samples manufactured by Energy Research and Generation Inc. are studied here along with three carbon foam samples manufactured by Koppers Inc. The samples are shown below in Figs. 16a and 16b and the properties are given in Table 1. The aluminum foams are identified by the manufacturer according to pore density, with values of 10, 20, and 40 pores per inch (PPI). The bulk density of all aluminum foam samples is 216 kg/m^3. The pore sizes for the 10, 20, and 40 PPI aluminum foams are 0.5, 1, and 2 mm, respectively. The three carbon foam samples are identified by the manufacturer as L1, D1, and 49-156. The respective pore sizes according to the manufacturer are 600, 650, and 726 μm. Due to the small pore size and large pressure drop required to convey air through the foams, they were modified by machining cylindrical air passages in the axial direction. In each case, 210 passages, 6 mm apart, each with a diameter of 4 mm, were machined into the foam providing for an axi-symmetric, homogeneous geometry. The modified L1, D1 and 49-156, foams have bulk densities of 374, 403, and 283 kg/m^3, respectively. Due to the large ratio of passage diameter to pore diameter, there is not a large pressure drop variation between carbon foam samples. It

is assumed throughout the analysis that convection heat transfer is dominated by air flow through the machined passages. Therefore the same surface area per unit volume, a, for each carbon foam sample is 331 m^{-1}and the porosity based on the flow passages is 0.328.

Figure 16a: Metal Foam Samples   Figure 16b: Carbon Foam Samples

The experimental facility displayed in Fig. 17 is used to measure the pressure drop and heat transfer coefficient with air blowing through the foam. As shown, a variable speed blower forces air through the foam sample in which a 16 mm diameter cylindrical cartridge heater is embedded at the centerline of the foam. A type E thermocouple is also embedded to measure the temperature at the heater surface. The foam sample outer diameter is 76 mm, and the inner diameter is 16 mm. The thickness of each sample is 25.4 mm. Validyne differential pressure transducers measure the pressure drop across the foam. Another Validyne differential pressure transducer measures the pressure drop from a pitot tube to obtain the mean air velocity. All analog signals were captured using a digital data acquisition system consisting of a Measurement and Computing CIO-EXP32 multiplexer and PCIM-DAS1602 16 bit analog to digital converter.

A custom algorithm was developed to convert measured voltages to pressure, temperature, and velocity.

The experimental facility is used to measure the heat transfer coefficient and pressure drop for each foam sample at different velocity increments. The pressure drop is measured adiabatically. Throughout the heat transfer experiments the heat flux remains fixed at 30.6 kW/m^{2}and the air velocity is increased in increments. The mean velocity ranges from approximately 1 to 9 m/s for the pressure drop and heat transfer experiments, beyond which point there is a substantial increase in pressure drop and only a marginal increase in the heat transfer rate. At each velocity increment, the wall temperature is observed until steady state is reached, at which point 500 data points are sampled at 1 Hz. The measurement is repeated 5 times to insure repeatability. The air velocity is then increased and the procedure is repeated. The uncertainty in temperature is estimated to be ±0.1 ˚C, the uncertainty for pressure drop is estimated to be ±18 Pa, and the uncertainty in velocity is estimated to be ±0.18 m/s.
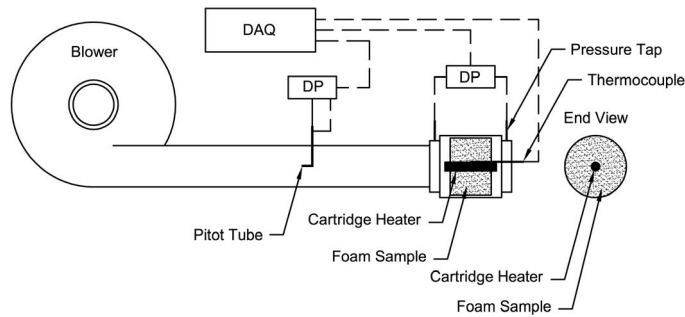
Figure 17: Experimental Facility

Experimental Results

For each foam sample considered the measured pressure drop and wall temperature are tabulated in Table 2. The measured pressure drop and wall temperature are also shown in Figs. 18-2 with varying air velocity. As observed, the pressure drop increases and the wall temperature decreases with increasing air velocity. At low velocity an incremental increase in velocity results in a large drop in wall temperature and a moderate increase in pressure drop. However, at relatively high air velocities, an incremental change in velocity results in a large increase in pressure drop and only moderate decrease in wall temperature.

Table 1: Foam Properties

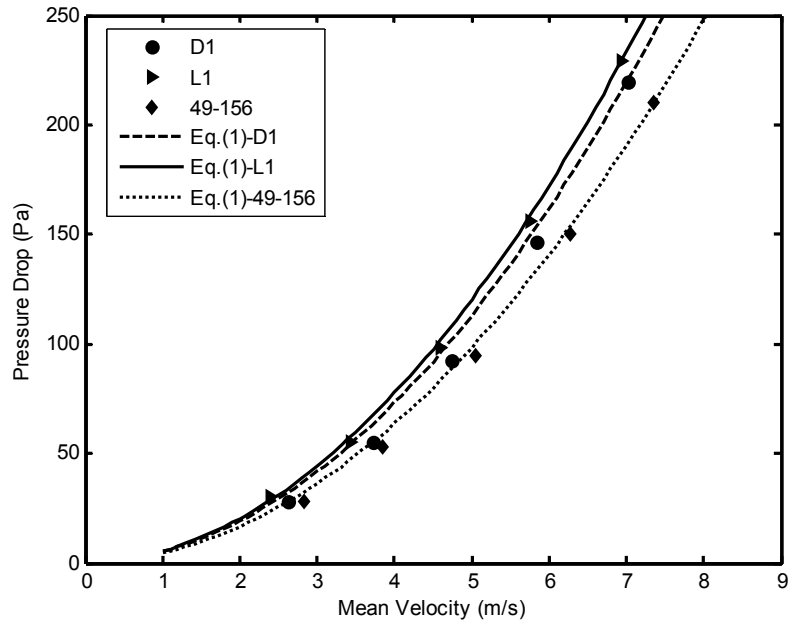| Foam Sample	K (m^2)	C_F	ε	ε_p	d_p (m)	k_{se} $\left(\frac{W}{mK}\right)$	a (m^{-1})
40 PPI	1.48×10^{-7}	0.054	0.915	NA	5.08×10^{-4}	9.78	804
20 PPI	2.23×10^{-7}	0.052	0.918	NA	1.02×10^{-3}	9.78	1770
10 PPI	3.29×10^{-7}	0.039	0.92	NA	2.03×10^{-3}	9.78	2760
49-156	5.42×10^{-7}	0.091	0.328	.8	7.26×10^{-4}	5	331
D1	5.42×10^{-7}	0.105	0.328	.7158	6.7×10^{-4}	8.9	331
L1	5.42×10^{-7}	0.112	0.328	.736	6.25×10^{-4}	7	331

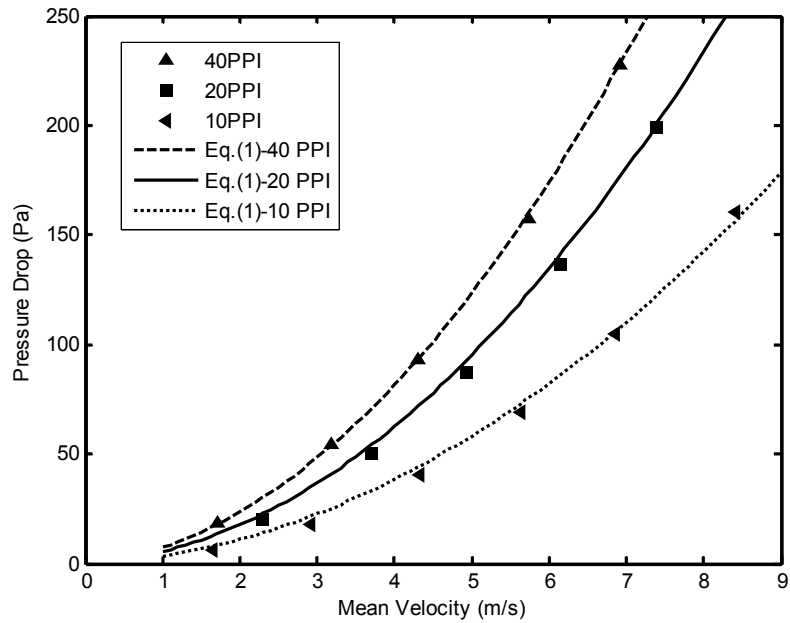Figure 18: Pressure Drop across Variation with Air Velocity.

Figure 19: Pressure Drop across Variation with Air Velocity.

The pressure drop for carbon and aluminum foams may be correlated using the Darcy-Forcheimer equation,

$$-\frac{dP}{dz} = \frac{\mu_f}{K} u_m + \frac{\rho_f C_F}{\sqrt{K}} u_m^2 \tag{1}$$

where K is the permeability, C_F is a dimensionless parameter that accounts for inertia effects, and u_m is the mean velocity. The permeability is determined from low Reynolds number $\left(\text{Re}_k < 15\right)$ pressure drop data, where $\text{Re}_k = \frac{U_m \sqrt{K}}{v_f}$ is the permeability based Reynolds number. C_F is then determined from the tabulated pressure drop data shown in Table 2. The measured K and C_F are listed in Table 1 for each foam. In the case of carbon foam, the difference in the pressure drop between data samples is not large because the majority of air flows through the machined passages. The small difference is attributed to flow through the interstitial pores.
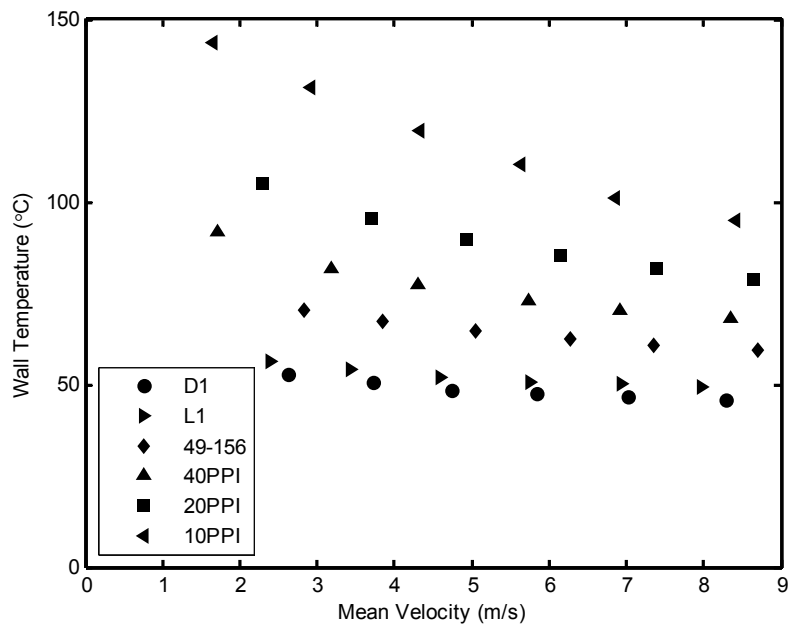

Figure 20: Wall Temperature Variation with Air Velocity.

Table 2: Pressure Drop and Heat Transfer Coefficient for Different Foams

49-156				D1			
u_m (m/s)	h_{sf} (W/m^2K)	T_w $(°C)$	ΔP (Pa)	u_m (m/s)	h_{sf} (W/m^2K)	T_w $(°C)$	ΔP (Pa)
2.83	68.4	70.4	27.9	2.62	105.5	52.8	28.2
3.85	80.1	67.5	53.0	3.72	127.0	50.7	54.9
5.04	99.6	64.6	94.5	4.73	160.2	48.6	92.4
6.28	125.0	62.4	150.3	5.83	187.5	47.5	146.7
7.36	144.5	60.9	209.9	7.02	218.8	46.5	220.0
8.69	171.9	59.6	297.7	8.29	242.2	46.0	315.5
L1				10 PPI			
u_m (m/s)	h_{sf} (W/m^2K)	T_w $(°C)$	ΔP (Pa)	u_m (m/s)	h_{sf} (W/m^2K)	T_w $(°C)$	ΔP (Pa)
2.39	99.6	56.3	30.1	1.66	4.7	143.4	6.2
3.42	117.2	54.3	55.2	2.92	5.2	131.4	18.1
4.60	148.4	52.0	98.1	4.33	6.0	119.4	40.4
5.76	171.9	50.8	155.8	5.62	6.8	110.5	69.4
6.94	195.3	50.1	229.0	6.85	7.8	101.2	104.9
7.98	218.8	49.5	305.8	8.42	8.7	94.9	160.7
20 PPI				40 PPI			
u_m (m/s)	h_{sf} (W/m^2K)	T_w $(°C)$	ΔP (Pa)	u_m (m/s)	h_{sf} (W/m^2K)	T_w $(°C)$	ΔP (Pa)
2.30	3.3	105.1	20.2	1.71	2.7	92.1	15.3
3.70	3.8	95.2	49.7	3.19	3.3	81.8	46.7
4.93	4.2	89.8	87.5	4.31	3.6	77.3	79.6
6.15	4.6	85.2	136.2	5.72	4.1	73.1	132.1
7.39	5.0	81.7	199.3	6.92	4.4	70.6	194.2
8.63	5.3	78.9	276.6	8.36	4.7	68.3	280.6

Heat Transfer Analysis

In order to extract the local heat transfer from the measured wall temperatures, the Brinkman extended Darcy momentum model and a two equation non-equilibrium heat transfer model proposed by Calmidi and Mahajan [8] are employed.

In this analysis it is assumed that all thermo-physical properties of the solid and fluid are independent of temperature. The foams are modeled as homogenous and axi-symmetric porous media, and the effects of radiation, natural convection, and thermal dispersion are negligible [9]. Assuming entry-region effects are minimal, the governing conservation equations can be expressed as [10],

Momentum

$$-\frac{dP}{dz}+\frac{\mu_f}{\varepsilon}\left(\frac{d^2u}{dr^2}+\frac{1}{r}\frac{du}{dr}\right)-\frac{\mu_f}{K}u=0 \ , \tag{2}$$

Energy (Solid)

$$(1-\varepsilon)k_s\left(\frac{d^2T_s}{dr^2}+\frac{1}{r}\frac{dT_s}{dr}\right)-h_{sf}a\left(T_s-T_f\right)=0 \tag{3}$$

Energy (Fluid)

$$\rho_f C_{p,f}u\frac{dT_f}{dz}=\varepsilon k_f\left(\frac{d^2T_f}{dr^2}+\frac{1}{r}\frac{dT_f}{dr}\right)+h_{sf}a\left(T_s-T_f\right) \ , \tag{4}$$

where μ_f is the dynamic viscosity of the fluid, ε is the porosity, K is the permeability, h_{sf} is the interstitial heat transfer coefficient, and a is the surface area per unit volume for the porous material. Here ρ_f and $C_{p,f}$ are the respective density and specific heat of the fluid, while k_f and k_s are the thermal conductivity of the fluid and solid, respectively.
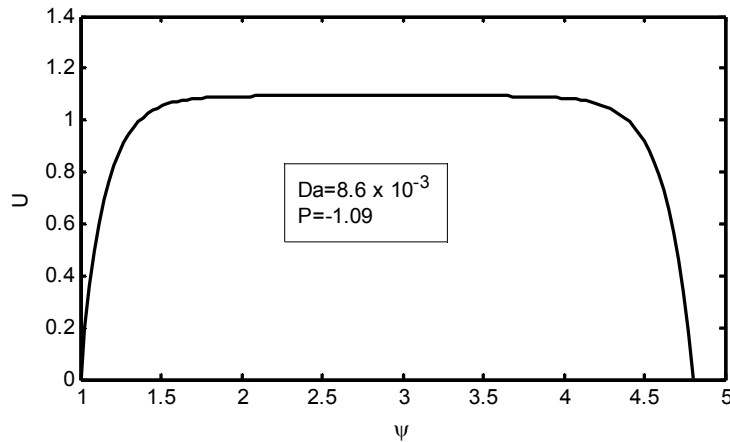
Figure 21: Dimensionless Velocity Profile.

During the experiments, the outer radius of the test section is insulated. The boundary conditions are, $u(r=R_1)=0$, $u(r=R_2)=0$, $T_s(r=R_1)=T_w$, $T_f(r=R_1)=T_w$, and $\frac{\partial T_f}{\partial r}(r=R_2)+\frac{\partial T_s}{\partial r}(r=R_2)=0$. The following dimensionless variables are introduced [9]:

$$Da=\frac{K}{R_1^2}; \quad \psi=\frac{r}{R_1}; \quad P=\frac{K}{\mu_f U_m}\frac{dP}{dz};$$

$$\theta=\frac{T-T_w}{q_w R_1/k_{se}}; \quad Bi=h_{sf}aR_1^2/k_{se}; \quad C=\frac{k_{fe}}{k_{se}}; \quad U=\frac{u}{u_m}$$

where u and u_m are the respective local and mean velocities, q_w is the applied heat flux along the inner radius, and $k_{fe} = \varepsilon k_f$ and $k_{se} = (1-\varepsilon)k_s$ are the effective thermal conductivities of the respective fluid and solid. Conservation equations (1-3) are non-dimensionalized as

$$U = -P + \frac{Da}{\varepsilon}\left(\frac{d^2U}{d\psi^2} + \frac{1}{\psi}\frac{dU}{d\psi}\right) \tag{5}$$

$$\left(\frac{d^2\theta_s}{d\psi^2} + \frac{1}{\psi}\frac{d\theta_s}{d\psi}\right) - Bi\left(\theta_s - \theta_f\right) = 0 \tag{6}$$

$$2U\left(\frac{1}{\left(\frac{R_2}{R_1} - 1\right)}\right) = C\left(\frac{d^2\theta_f}{d\psi^2} + \frac{1}{\psi}\frac{d\theta_f}{d\psi}\right) + Bi\left(\theta_s - \theta_f\right) \tag{7}$$

with boundary conditions, $U(\psi = 1) = 0$, $U(\psi = R_2/R_1) = 0$, $T_s(\psi = 1) = 0$, $T_f(\psi = 1) = 0$, and $\frac{\partial \theta_f}{\partial \psi}(\psi = R_2/R_1) + \frac{\partial \theta_s}{\partial \psi}(\psi = R_2/R_1) = 0$.
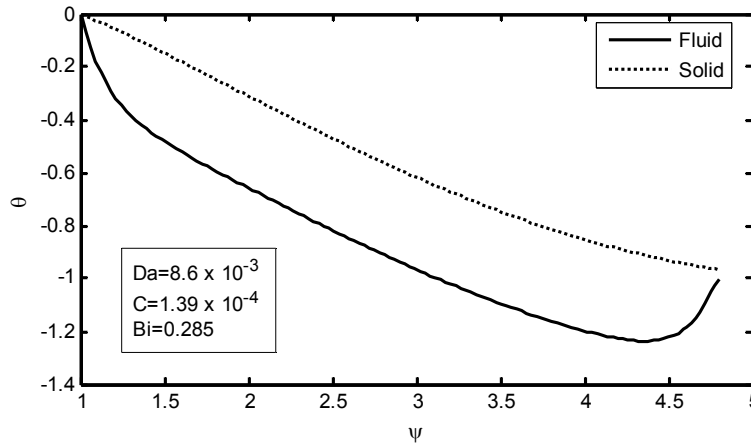
Figure 22: Dimensionless Fluid and Solid Temperature Profiles.

In order to solve the momentum equation, a guess is made for P, Eq. (2) is solved, and a check is made to insure $\frac{1}{A}\int_A UdA = 1$. If the integral is satisfied the solution is complete, otherwise a new guess is made for P and the procedure is repeated until the integral is satisfied.

Solutions to the governing conservation equations were obtained using the Thomas algorithm. For $\frac{R_2}{R_1} = 4.8$, $C = 1.39 \times 10^{-4}$, Bi=0.285, P=-1.09, and $Da = 8.6 \times 10^{-3}$ the computed dimensionless velocity profile is shown in Fig. 21 while that for temperature is shown in Fig. 22.

As observed, the velocity is uniform near the midpoint between R_1 and R_2 with a value close to the mean velocity. The solid foam temperature decreases monotonically in the radial direction.

The fluid temperature initially decreases in the radial direction, and then increases near the outer foam boundary. The increase in fluid temperature near the outer boundary is necessary to satisfy the adiabatic boundary condition at the outer wall.

When solving Eqs. (6 & 7) the heat transfer coefficient is not known a priori. Therefore, a guess is made for the heat transfer coefficient, h_{sf}, and solutions for Eqs. (6 & 7) yield $\theta_s(\psi)$ and $\theta_f(\psi)$. The bulk fluid temperature at any axial location is computed from

$$T_{b,f} = \frac{1}{AU_m} \int_A u T_f \, dA \tag{8}$$

and must match the bulk fluid temperature computed from an energy balance

$$T_{b,f}\Big|_{z=\frac{L}{2}} = T_{f,amb} + \frac{q_w \pi R_1 L}{2\dot{m} C_{p,f}}, \tag{9}$$

where $\dot{m}$ is the fluid mass flow rate and L is the heater length. Since the wall temperature is measured at $z = L/2$, the bulk fluid temperature is also evaluated at that location. The bulk fluid temperatures computed from Eqs. (8 & 9) are compared. If agreement is achieved, the guessed heat transfer coefficient is correct. If they do not agree, a new guess is made for the heat transfer coefficient and the computation is repeated until agreement is achieved.
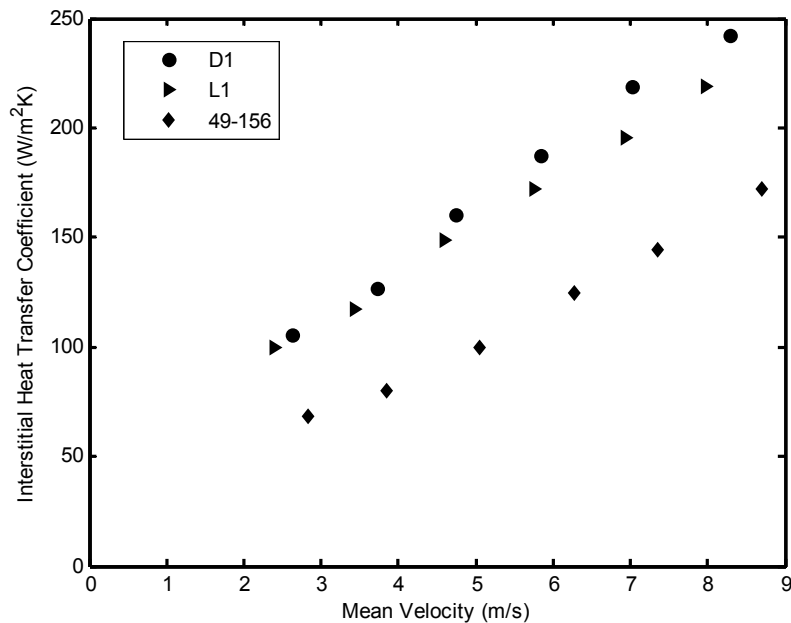
Results and Discussion

Figure 23: Interstitial Heat Transfer Coefficient Variation with Mean Fluid Velocity-Carbon Foams.
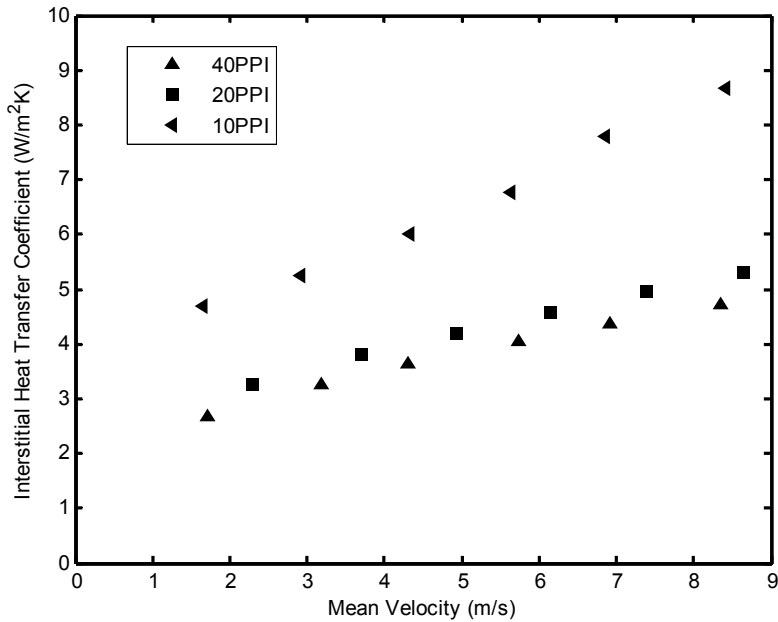
Figure 24: Interstitial Heat Transfer Coefficient Variation with Mean Fluid Velocity-Aluminum Foams.

The interstitial heat transfer coefficients computed for each of the six foams are summarized in Table 2. They are shown with varying air velocity in Figs. 23-24. As shown, the carbon foams have the largest interstitial heat transfer coefficient. Despite the low interstitial heat transfer coefficient, the aluminum foams are capable of handling a large heat load because they have large specific surface areas and large effective thermal conductivities. In order to correlate the interstitial heat transfer data, the permeability based Nusselt number is introduced, $Nu_K = \dfrac{h_{sf}\sqrt{K}}{k_f}$.

Fig. 25 shows the product of the Nusselt number and $a\sqrt{K}$ as a function of the Reynolds number for the three aluminum foams. It is observed that the data are well collapsed. The aluminum foam Nusselt number may be expressed as,

$$Nu_K = \frac{1}{a\sqrt{K}}\left(\frac{Re_K}{510.2} + 0.469\right) \tag{10}$$

For the carbon foam samples, it is assumed that all of the air passes through the machined channels, and ideally each foam sample should have the same interstitial heat transfer coefficient at the same Reynolds number. However, variations in the data are observed. These are explained by the fact that some air passes through the smaller interstitial pores of the foam. Thus, it is reasonable to expect that the data can be correlated using the foam porosity based on the interstitial pores. Fig. 26 shows the product of the Nusselt number and $(1-\varepsilon_p)^{-3/2}$ as a function of Reynolds number for the three carbon foams. As observed, the data are also well correlated, and the carbon foam Nusselt number may be expressed as

$$Nu_K = 3.8359(1-\varepsilon_p)^{3/2}\left(Re_K + 67.68\right) \tag{11}$$

The standard error between the measured and predicted pressure drops and interstitial heat

transfer coefficient for the aluminum and carbon foams are summarized in Table 3. As observed, the interstitial heat transfer coefficient is predicted with good accuracy.
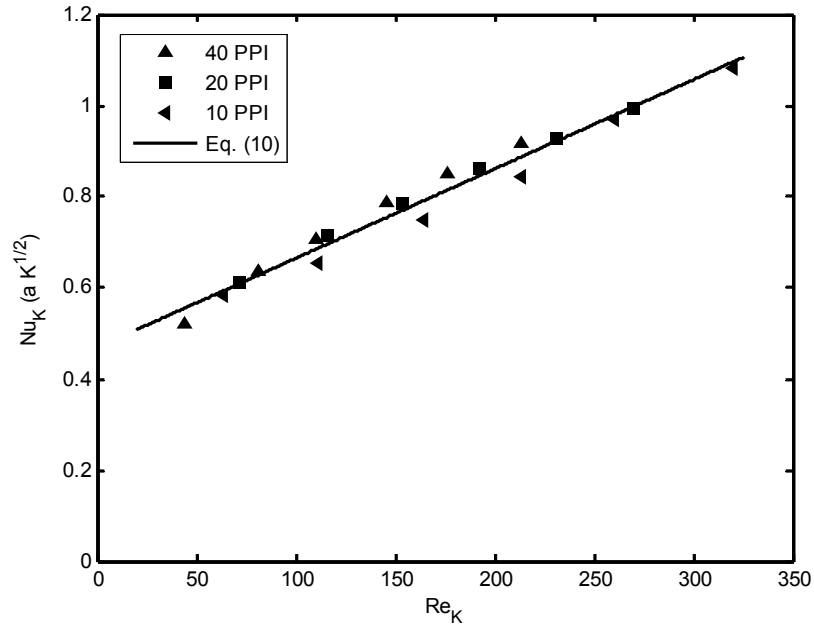

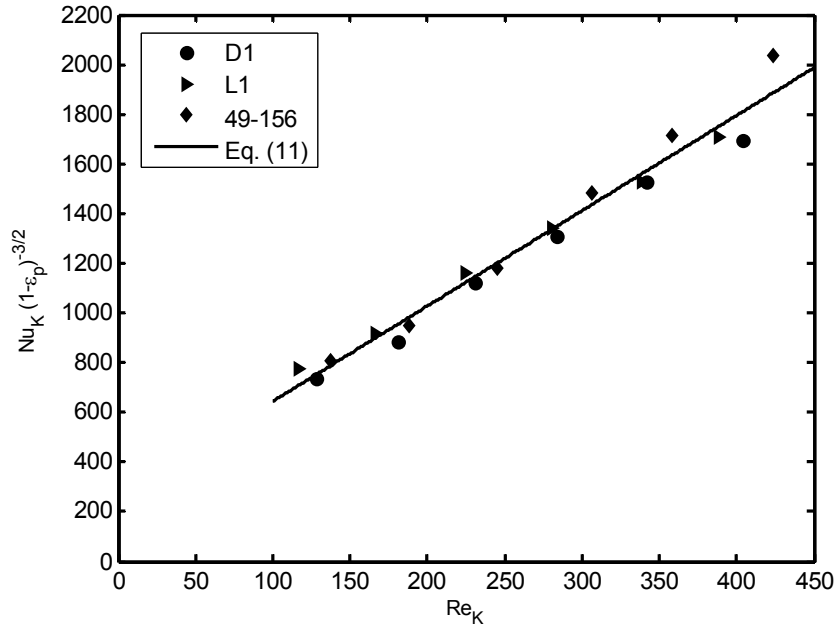Figure 25: Nusselt Number Correlation for Aluminum Foams.

Figure 26: Nusselt Number Correlation for Carbon Foams.

Table 3: Standard Error for Pressure Drop and Nusselt Number Correlations

	Standard Error (ΔP)	Standard Error (Nu_k)
10 PPI	0.111	.033
20 PPI	0.057	.014
40 PPI	0.011	.033
49-156	0.061	.038
D1	0.076	.040
L1	0.027	.032

Conclusions

A microchannel evaporative cooling plate has been developed to remove waste heat from PEM fuel cell stacks. The overall performance of the evaporator plate is excellent. The plate operates in a natural circulation two-phase thermosyphon, and the thermal capacity for the current microchannel plate is 58 kW/m^2, which far exceeds the heat flux currently being rejected from PEM fuel cell stacks. The plate wall temperatures range from 47-90 ˚C, depending on heat flux and position on the plate. A thermal hydraulic model has been presented which gives a satisfactory prediction of the mass flow rate, pressure drop, and microchannel plate thermal field while providing a reasonable prediction for the onset of instability. The thermal hydraulic model is suitable for design and analysis applications. To aid in the optimization of the thermosyphon condenser, the performance of three aluminum foam and three carbon foam samples have been evaluated for heat transfer augmentation. Correlations for computing the pressure drop and interstitial heat transfer coefficient based on the geometric properties of the foam are provided. Results show that the D1 carbon foam sample yields the highest heat transfer coefficient while the 10 PPI aluminum foam sample yields the smallest pressure drop. To better quantify the heat transfer performance of these foam samples, further analysis should involve comparison with conventional louvered fin geometries using a coefficient of performance, compactness factor, and power density factor as the basis for comparison.

Patents

No Patent applications.

Publications

Garrity, P., Klausner, J.F., and Mei, R., "A Flow Boiling Microchannel Evaporator Plate for Fuel Cell Thermal Management," Proceedings of the Sixth International Conference on Boiling Heat Transfer," 2006.

Garrity, P., Klausner, J., Mei, R., A Flow Boiling Microchannel Evaporator Plate for Fuel Cell Thermal Management, Heat Transfer Engineering, 28(10):1–8, 2007

Garrity, P., Klausner, J., Mei, R., Performance of Aluminum and Carbon Foams for Heat Transfer Augmentation, Proceedings of 2007 ASME-JSME Thermal Engineering Summer Heat Transfer Conference July 8-12, 2007, Vancouver, British Columbia, CANADA

Students from Research

Pat Garrity, PhD student. Expected graduation date is July 08.

Acknowledgements

References

[1] You, L., Liu, H., A two-phase flow and transport model for the cathode of PEM fuel cells, International Journal of Heat and Mass Transfer 45 (2002) 2277–2287.

[2] Coppo, M., Siegel, N.P., von Spakovsky, M.R., On the Influence of Temperature on PEM Fuel Cell Operation, Journal of Power Sources 159 (2006) 560-569.

[3] Lasbet, Y., Auvity, B., Castelain, C., Peerhossaini, H., A Chaotic Heat-Exchanger for PEMFC Cooling Applications Journal of Power Sources, in press, 2005.

[4] Zuber, N., Findlay, J., Average Volumetric Concentration in Two-Phase Systems, Trans ASME Jul Ht Transfer, Volume 87, p. 453, 1969.

[5] Muller-Steinhagen, H. Heck, K., A Simple Friction Pressure Drop Correlation for Two-Phase Flow in Pipes Chemical Engineering Processes, Vol. 20, pp. 297-308, 1986.

[6] Gungor, K.E., & Winterton, R.H.S., A General Correlation for Flow Boiling in Tubes and Annuli, International Journal of Heat and Mass Transfer, Vol. 29, 3, pp. 351-358, 1986.

[7] Muller-Steinhagen, H., Jamialahmadi, M. Subcooled Flow Boiling Heat Transfer to Mixtures and Solutions, Convective Flow Boiling, Editor John C. Chen, Taylor & Francis, Washington D.C., 1996.

[8] V.V. Calmidi and R.L. Mahajan, Forced convection in high porosity metal foams, J. Heat Transfer 122 (2000), pp. 557–565.

[9] Tzer-Ming Jeng, Li-Kang Liu, Ying-Huei Hung, "A Novel Semi-Empirical Model for Evaluating Thermal Performance of Porous Metallic Foam Heat Sinks," Journal of Electronic Packaging, Volume 127, September 2005.

[10] W. Lu, C. Zhao, S. Tassou, "Thermal analysis on metal-foam filled heat exchangers. Part I: Metal-foam filled pipes," International Journal of Heat and Mass Transfer, Volume 49, Issue 15-16, pp. 2751-2761.

9. Multi-scale Surface Plate Fabrication for Next Generation Fuel Cells

Task PI: Dr. Tony L. Schmitz, Mechanical and Aerospace Engineering, University of Florida
Co-Investigators: Dr. W. Gregory Sawyer, Mechanical and Aerospace Engineering
Dr. John C. Ziegert, Mechanical and Aerospace Engineering, University of Florida

Research Period: August 3, 2004 to April 30, 2007

Abstract
The purpose of this collaborative research was the development and implementation of multi-scale fabrication techniques for the plates (or interconnects) that compose the outer layer of Proton Exchange, or Polymer Electrolyte, Membrane (PEM) fuel cells. The selected rapid fabrication methods, which included high-speed machining, photolithography, and micro-molding, enable low-cost feature production from the nanometer to millimeter scales.

Introduction
Due to their inherent benefits, including zero or very low emissions, high efficiency, quiet operation, scalability, and few moving parts, fuel cells are the topic of many current research efforts. These studies include, for example, hydrogen production/storage techniques, improved cell components, and modeling efforts. Research goals typically include increasing power/energy densities and meeting application-specific requirements (e.g., minimized weight).

In this work, we implemented multi-scale fabrication techniques for the plates (or interconnects) that compose the outer layer of Proton Exchange, or Polymer Electrolyte, Membrane (PEM) fuel cells. These fabrication methods, including high-speed machining, photolithography, and micro-molding, encompass feature production from the nanometer to millimeter scales and were synergistic with thermal management research (J. Klausner), impedance spectroscopy characterization of fuel cell performance (M. Orazem), and computational fluid dynamics modeling work by enabling new geometries to be realized and studied.

We focused on the anode and cathode current collection plates because they currently contain surface patterns and are critical to enhanced fuel cell operation. For example, in order to provide an efficient gas flow field, the side of the plate which faces the backing layer contains a pattern of channels which carries the reactant gas (oxygen on the cathode side and hydrogen on the anode side) from the point at which it enters the fuel cell to the exit. The pattern and size of these channels largely influence the distribution of the gases over the active area of the membrane-electrode assembly. Additionally, the channel geometry affects water supply and removal.

Background
High-speed machining
The conventional manufacturing method used to produce PEM fuel cell graphite plates has been computer numerically-controlled machining at traditional spindle speeds and feed rates. This has yielded acceptable part quality, but at prohibitive costs and low production rates. Alternatives have therefore been explored, including molding blends of graphites, resins, and additives to produce composite plates; constructing a matrix of graphite pins in a polymer matrix; and stacking metal foils and screens, for example. In all cases, a primary consideration is reproducing the ideal properties inherent to the graphite plates, namely inert chemical properties, ability to withstand the fuel cell environment, and electrical conductivity.

Benefits associated with high-speed machining, as opposed to these other methods, include dramatic increases in material removal rates, reduced cycle times, and improved part characteristics (e.g., good surface finish, uniform mechanical properties, and geometric accuracy). Our previous research efforts have led to the ability to predict the machine-spindle-holder-tool dynamics and the use of this information for the analytic and time-domain simulation of process performance, including stability, surface finish, and part geometry error caused by tool vibrations during cutting [1-5].

Micro-molding

Micro-molding of bulk amorphous metals for low cost fabrication of complex three-dimensional components at the nanometer to millimeter scale was investigated. The goal was to demonstrate that it is possible to produce high precision/high aspect ratio metallic components with feature sizes of micrometers or less using an inexpensive process.

The lack of a (regular) crystalline structure for particular amorphous metals leads to a set of characteristic properties which includes high yield strength, hardness, strength/weight ratio, elastic limit, and wear resistance. These alloys have several fundamental characteristics that make them ideal for net shape forming of micro-components. First, they have a comparatively low glass transition temperature (~350 °C), so high molding temperatures are not necessary. Second, since no phase change occurs during molding, there is relatively little shrinkage as the material cools. This enables good tolerance control of the molded features. Finally, due to lack of crystallinity, bulk amorphous metal alloys tend to exhibit good surface finish upon vitrification, which is important because options for secondary finishing operations are limited.

Experimental Description

High-speed Machining

Experiments were carried out on a Mikron UPC 600 Vario high-speed machining center. Tests were completed using the 20000 rpm Step-Tec spindle included with this machine and a second NSK Nakanishi Inc. 50000 rpm micro-spindle (HES500-HSK A63 loaned to the University of Florida Machine Tool Research Center in support of this project).

Micro-molding

An MTS dual column load frame with load capabilities up to 5 kN was instrumented with custom platens to carry out the micro-molding experiments. The bottom platen had a recessed pocket where micro-molding of the bulk metallic glass took place. This pocket provided acceptable heat transfer from the platens to the sample – it is important to have quick heating capabilities to keep the bulk metallic glass amorphous during the molding process. Heating was accomplished using 19 cartridge heaters (6.35 mm in diameter by 63.5 mm long). Each cartridge heater had 250 W of power for a total of 4.75 kW of heating potential. Quick cooling rates are also crucial for maintaining the amorphous structure; this was accomplished using a pump to flow water from a storage tank through parallel channels in both platens. Figure 1 shows the MTS machine with custom platens.

A program was written in *LabView* to work in conjunction with *TestWorks 4*, the operating system designed to control the MTS machine. The *LabView* program signaled *TestWorks 4* at the appropriate moments to control the molding process. A typical molding process consisted of an initial light pre-load applied followed by a temperature increase to the molding temperature (>400 °C). Once the molding temperature was reached, the (higher) molding force was applied for a desired length of time. Finally, the temperature was rapidly lowered while a light post-load was applied. The *LabView* program controlled molding time, temperature to begin molding force, cooling time, and signaled *TestWorks 4* when to continue with the next test segment of the

molding process. The *LabView* program was designed to monitor the temperatures of both platens, apply force, and control the relative positions of the platens.
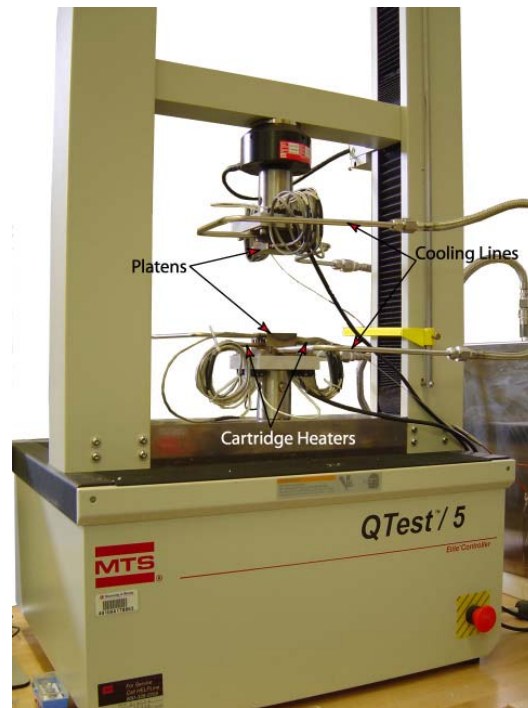

Figure 1: Micro-molding machine.

Results and Discussion

High-speed Machining

To demonstrate feature production at the mm-scale using high-speed machining techniques, initial tests were completed using a 1 mm diameter endmill mounted in the 20000 rpm spindle. Results for an x-direction slotting (100% radial immersion) cut are shown in Figure 2. Measurements were carried out using a scanning white light interferometer. The average roughness, R_a, of the 0.5 mm deep slot floor (6061-T6 aluminum) was 100 nm.

To support the research efforts of J. Klausner (efficient cooling of fuel cells using a pump-less cooling plate that enables fuel cell operation at approximately 75 °C), we high-speed machined a 6061-T6 aluminum cooling plate with 1 mm wide by 1 mm deep channels (56 channels total) which was used for boiling experiments. The engineering drawing and photograph of the finished product/machining setup are provided in Figures 3 and 4.

We also carried out cutting tests using a 350 μm diameter, 2 flute end mill. A microscope image of the tool is provided in Figure 5. Scanning white light interferometry measurements of a micro-machined channel with a 90° corner are displayed in Figure 6. The channel is 350 μm wide and 54 μm deep. The material was 6061-T6 aluminum. Figure 7 shows measurements of a channel with a commanded changed in the depth while micro-machining. The initial depth of 148 μm was decreased to 40 μm during the cut.
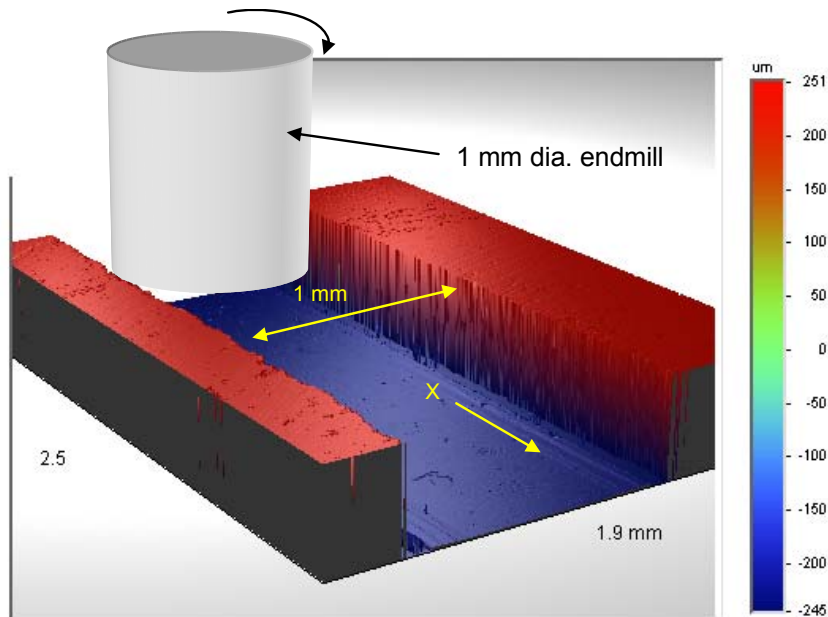
Figure 2: Scanning white light interferometer measurements of high-speed milled slot. Average roughness of the slot floor was 100 nm.

We collaborated with M. Orazem to micro-machine new graphite plates for his experimental fuel cell. The previous serpentine design is shown in Figure 8. We produced new plates with a hollow cavity and raised posts to obtain a more uniform gas distribution over the catalyst face. See Figure 9. The raised posts also provide electrical contact between the graphite plate and catalyst within the cavity, in addition to the area around the cavity perimeter. To produce the plate shown in Figure 9 we used a 1 mm diameter two flute carbide end mill. We performed the cutting at a spindle speed of 10000 rpm with a feed per tooth of 0.05 mm/tooth.
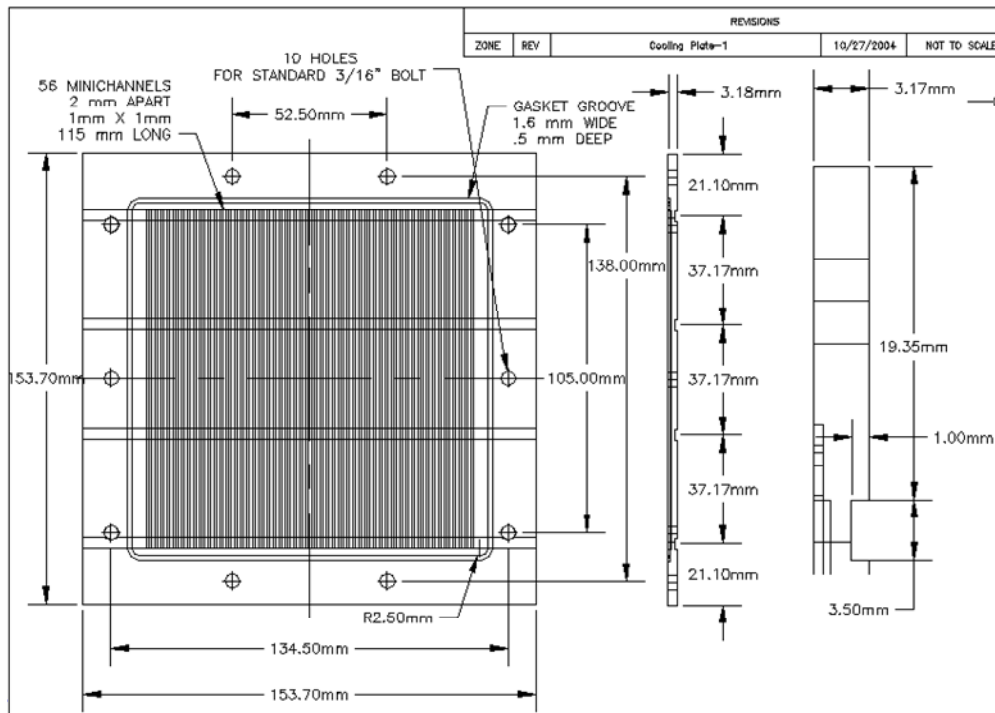
Figure 3: Engineering drawing for Klausner's cooling plate.
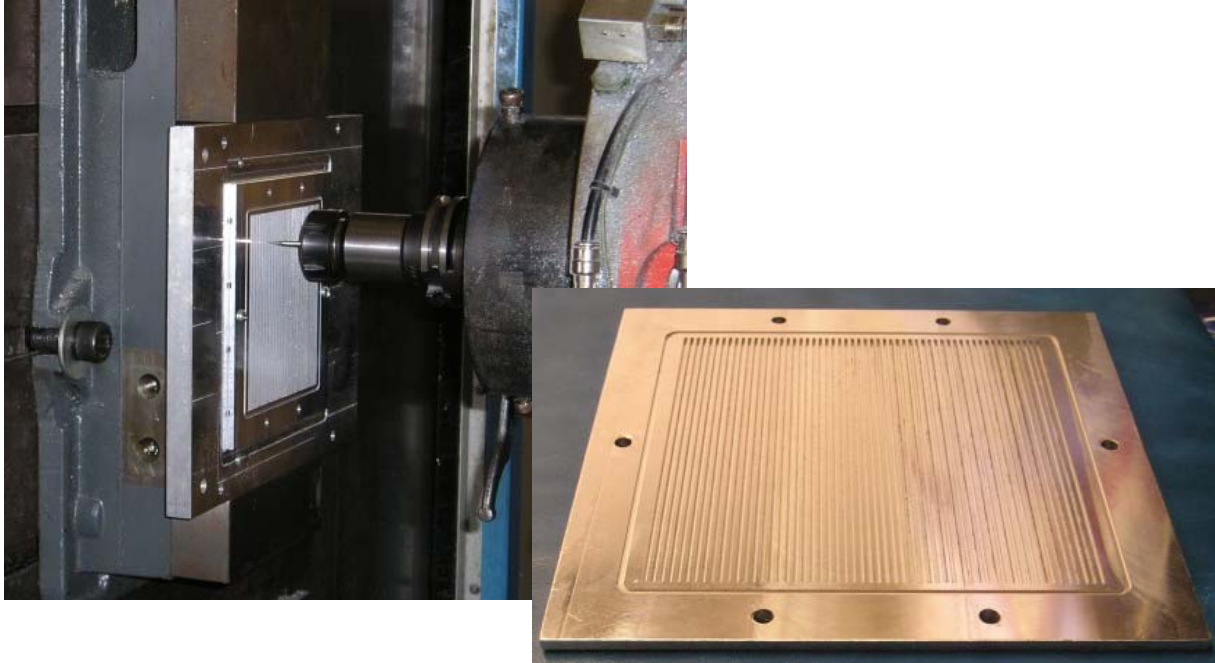
Figure 4: (Left) High-speed machining setup. (Right) Cooling plate with 1 mm channels.
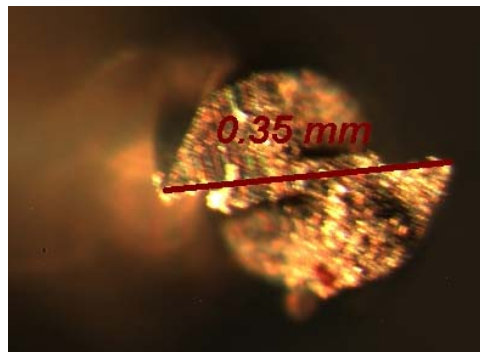
Figure 5: Image of end mill.

As noted, we obtained new high-speed spindles for the micro-machining research from NSK (in addition to the 50000 rpm motorized spindle, we also received an HTS1501S-HSK A63 150000 rpm air turbine spindle). We are currently developing an algorithm to predict the micro-tool dynamics for these and similar spindles using measurements of the spindle alone. This is an important activity because the standard impact testing procedures using for macro-scale tools cannot be applied to micro-scale tools. Specifically, the tool point dynamics are typically obtained by exciting the tool point using an instrumented hammer and the resulting vibrations are recorded using a low-mass accelerometer. For sub-millimeter diameter endmills, this testing procedure can no longer be applied. In our approach, we are using receptance coupling techniques to analytically attach a model of the cutting tool to a measurement of the spindle. The assembly dynamics information is required for any predictive algorithm used to estimate the milling behavior prior to cutting.

Micro-molding

The micro-molding production sequence is illustrated in Figure 10. The individual silicon mold layers were patterned by deep reactive ion etching, which can be used to produce two-dimensional features with aspect ratios as high as 10:1. This parallel fabrication technique is well-suited to our process; for the 5x5 mm square mold sections, over 150 unique designs could be patterned on a single 100 mm diameter wafer.
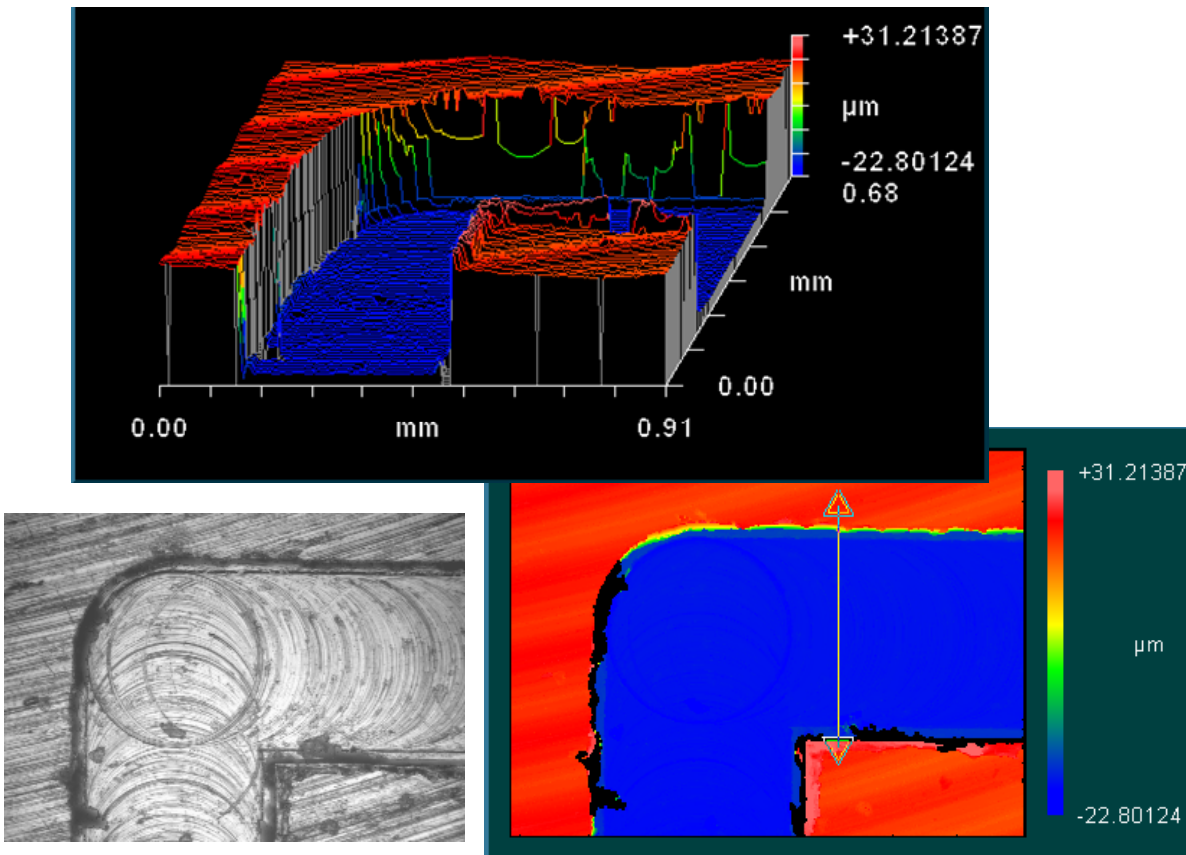

Figure 6: Scanning white light interferometry measurements of a micro-machined channel with a 90° corner.

To create complex non-line-of-sight cavities, we stacked multiple silicon wafers with the desired geometries (Figure 10a). These layers were placed, together with a layer of amorphous metal, into a square pocket machined into a stainless steel block (the block had 4.75 kW of electrical heating power supplied through cartridge-type heaters with integral pathways for water cooling and was attached to the MTS load frame with force and displacement control capabilities). The layered mold and the amorphous metal were heated to the process temperature and pressure was applied to the amorphous metal layer, forcing it into the mold cavities (Figure 10b). This was followed by rapid cooling. A typical process was completed in less than 500 s and the molding pressures were between 100 and 200 MPa (Figure 10c).

The integral part, made up of the silicon layers and the amorphous metal, was then removed from the platform and the silicon was etched away using a heated potassium hydroxide (KOH) solution (Figure 10d), leaving molded structures of amorphous metal attached to the base. We successfully demonstrated fabrication of complex microscale parts made up of seven mold

layers (Figure 10e) that were fully released by abrasively polishing the base down to the silicon mold layer prior to KOH etching (Figure 10f).

The process was able to successfully reproduce the internal cavities created by stacking the silicon layers; in Figure 10e the posts on the seventh layer were 20 μm in diameter, 100 μm tall, and separated by 10 μm. Scanning electron microscopy (SEM) of the released amorphous metal structures and internal surfaces of the mold suggest that this method reproduced the internal surface topography of the silicon mold to better than a micrometer. In order to examine this more quantitatively, a cross-section of the molded stack containing both the amorphous metal and the seven layers of etched silicon was prepared using traditional metallographic techniques (Figure 11a). Examination of the section shows that the amorphous metal filled the mold without visible voids at the mold/metal interface (Figure 11b). This is surprising since the coefficient of thermal expansion of the metallic glass is approximately five times that of silicon. For a post with a nominal diameter of 200 μm and a 400 °C temperature change, the difference in shrinkage between the silicon and the metallic glass should be on the order of 100 nm and visible in the high resolution SEM image. A very thin slice (<200 nm) through the mold/metal interface was collected from this sample by focused ion beam milling. Transmission electron microscopy (TEM) analysis of the slice revealed that a layer of crystallized material approximately 180 nm thick existed at the continuous interface (Figure 11c). The lack of observable separation at the interface due to shrinkage was further supported by the cross-section behavior; the silicon and metal interface remained intact during the slice lift out procedure.

One hypothesis is that the metallic atoms may be chemically reacting with the silicon and oxygen in the mold cavity to create an integral crystallized layer. Such a reaction process may be providing the necessary driving force to follow the intricate surfaces of the mold and surface reactivity may be an important criterion for net shape fabrication of micro-molded components. Semi-quantitative elemental analysis through this region (Figure 11d) suggests that its constituents are primarily from the amorphous metal. An added benefit of the stacked wafer approach is that the flatness of the silicon wafers and the molding pressure appears to completely arrest unintentional flow of amorphous metal between the layers; this ability to mold complex parts without flash negates the need for secondary finishing operations (assuming they were readily available).
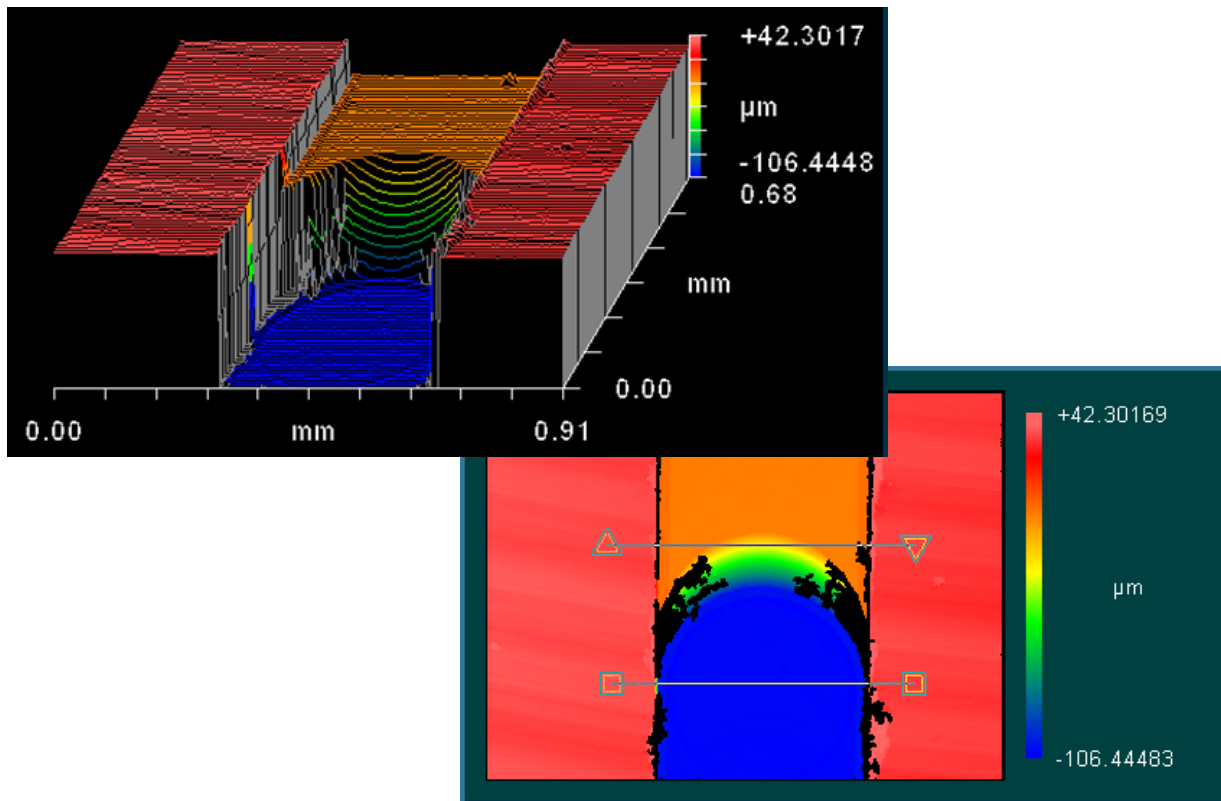
Figure 7: Scanning white light interferometry measurements of a micro-machined channel with variable depth.
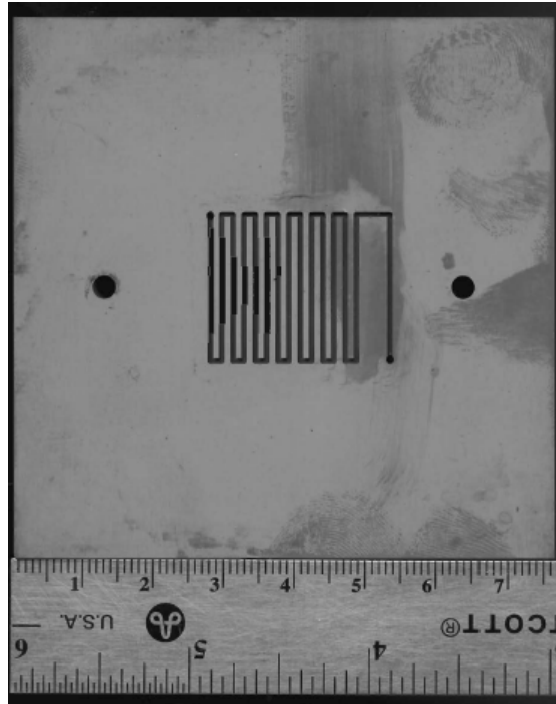
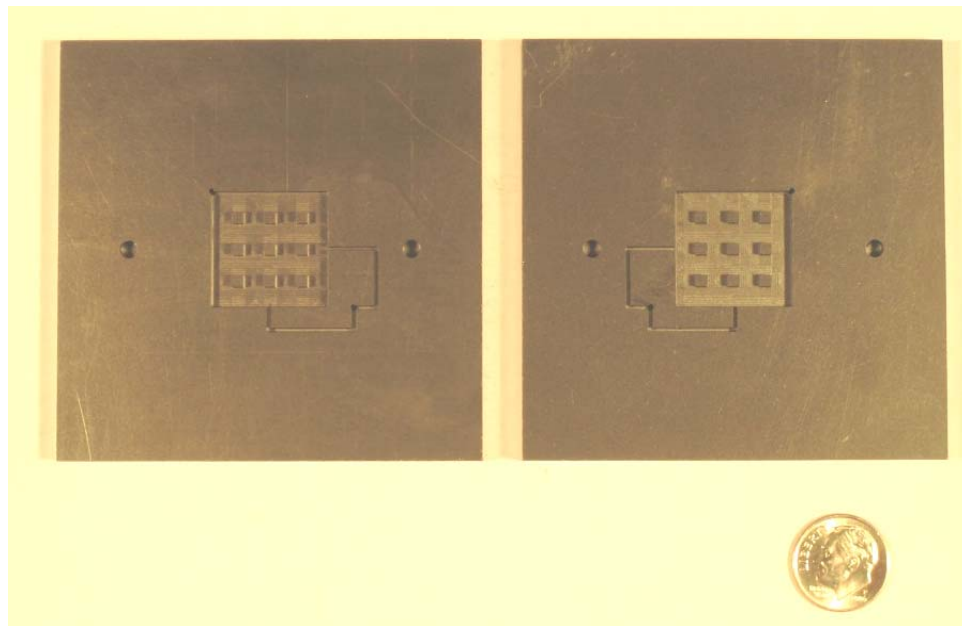*Figure 8: Previous fuel cell graphite plate from M. Orazem.*

Figure 9: New graphite fuel cell plates with raised posts in cavity.

Our next activity was to mold closed channels within a metallic glass structure using the techniques described in the previous paragraphs. In this case, a four layer silicon stack-up was used. Each wafer section was 50 μm thick with appropriate features etched through. The stack-up was composed of wafer sections with: 1) no features (flat); 2) an open square (800x800 μm);

3) three 800x200 μm channels (100 μm spacing); and 4) three 800x200 μm channels (100 μm spacing). The latter three sections were 1.5x1.5 mm square. Figure 12 shows the geometry of the channel sections (the tabbed design enabled easy removal of each section from the larger wafer). The open square section did not include the 100 μm cross members, but was otherwise identical. The overall stack-up is depicted in Figure 13.

Here, the light gray sections indicate the wafers and the dark gray the metallic glass flow through the wafer cavities. In reality, the metallic glass also flowed completely around (as well as through) the 1.5x1.5 mm wafer sections, but this is not shown.
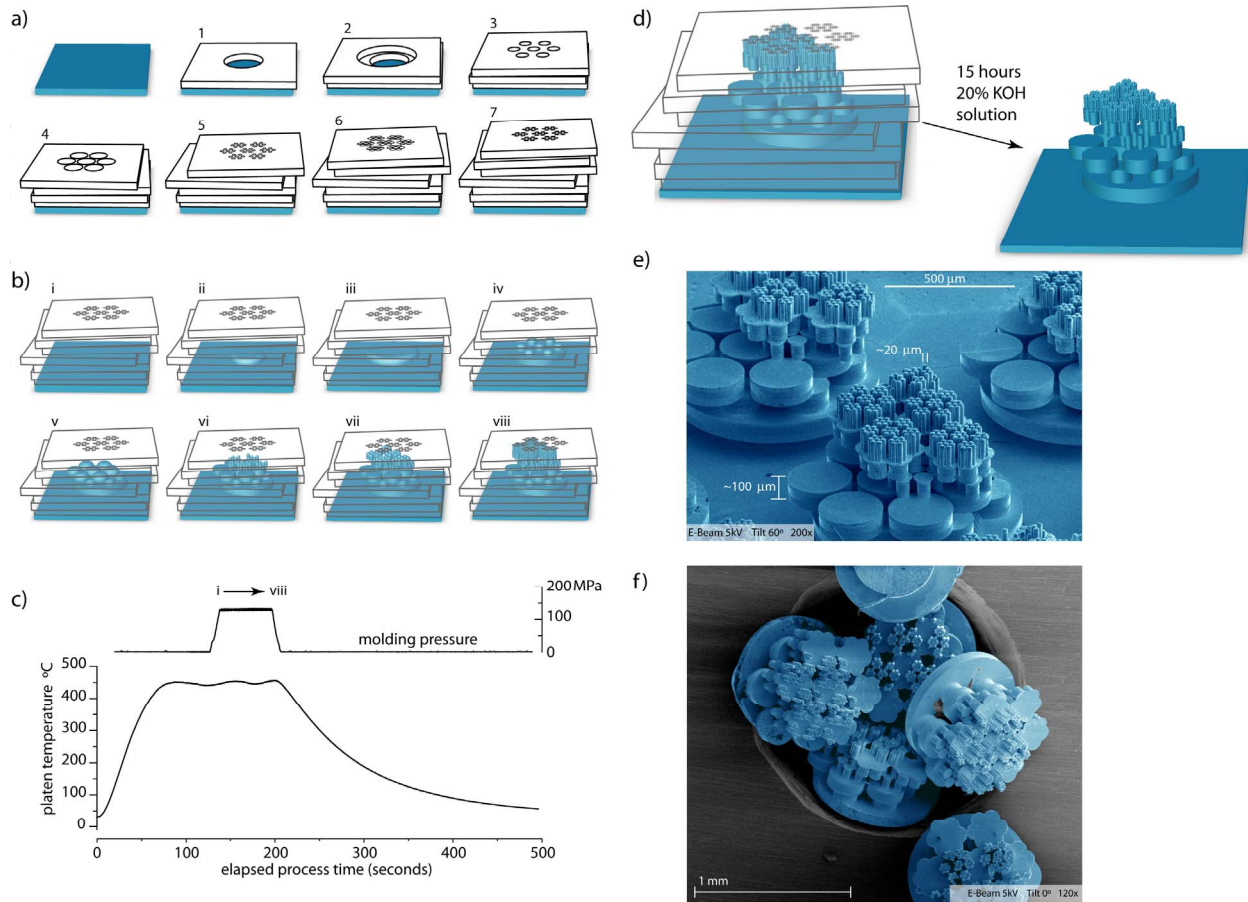
Figure 10: Steps in amorphous metal micro-molding process. a) After patterning by deep reactive ion etching, one or more silicon wafers are stacked to form the sacrificial mold (a seven layer stack was used in the test shown here – the lack of a careful alignment procedure between layers is depicted). The amorphous metal coupon is placed under the mold. b) Once the glass transition temperature of the amorphous metal is exceeded, pressure is applied to force the reduced viscosity metal through the wafer stack. c) The pressure and temperature profiles are displayed. d) After cooling, the silicon-metal composite is removed from the micro-molding platform. The metallic component is visible after etching. e) Scanning electron microscopy (SEM) image of micro-molded features; non-line-of-sight geometries were formed by the selected mold geometry. For this test, it is seen that the imperfect wafer alignments yielded an asymmetric product. f) SEM image of released features after using abrasive polishing method.
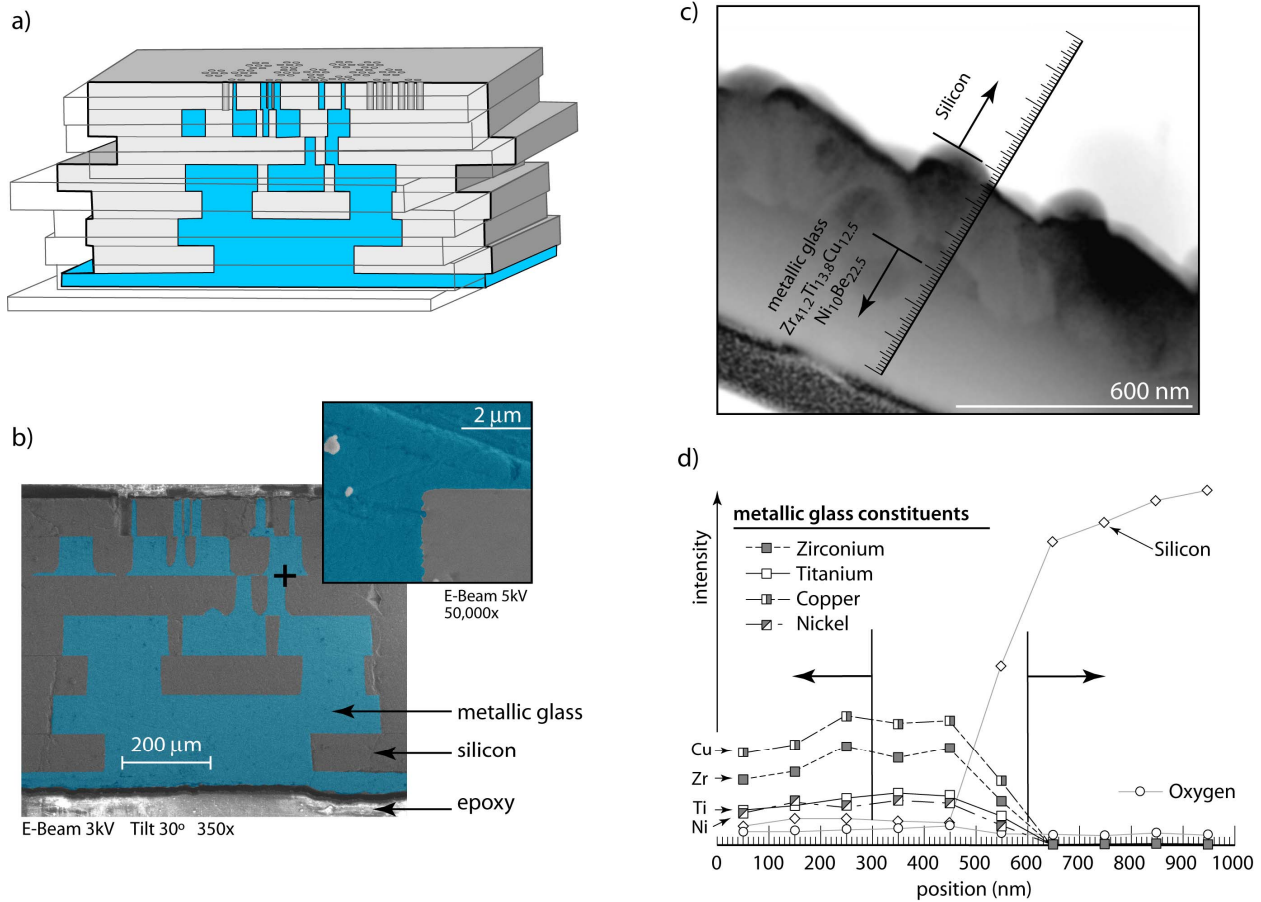
Figure 11: Cross-section of the silicon/metallic glass interface. a) A cross-section of the seven layer mold shown in Figure 1 is depicted. b) SEM image of filled silicon mold. The inset shows the excellent filling capabilities of the process. c) TEM image of the metallic glass (left)/silicon (right) interface. Between the metal and silicon, a crystallized material layer approximately 180 nm thick is observed. This layer may be responsible for the absence of a gap between the silicon and metal after cooling. d) Semi-quantitative elemental analysis through the metallic glass/silicon interface suggesting primarily metallic glass constituents in the integral crystallized region.

To release the part from the silicon, a 2 hour stirred KOH bath at 75 °C was used. To fully etch the captured silicon within the 100x100x800 μm channels, an additional 16 hours was required.

To verify that the enclosed channels indeed extended through the entire part and that the silicon had been completely etched away, a focused ion beam (FIB) was used to mill an 'X' in the metallic glass wall through the right channel. To gain access for the FIB through the channels, the part shown in Figure 14 was diamond sawed along the line indicated in the figure. An SEM image of the FIB 'X' is provided in Figure 15.
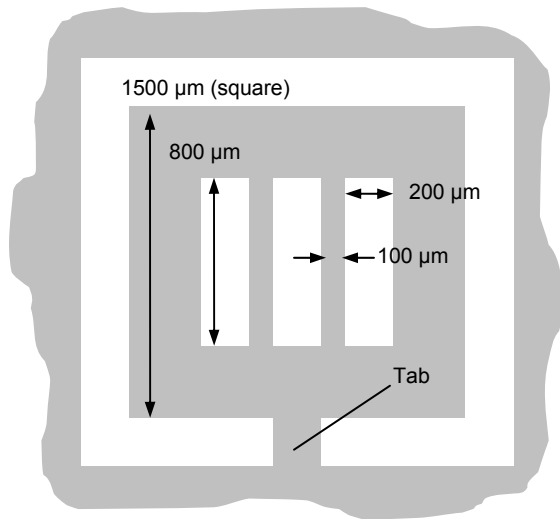
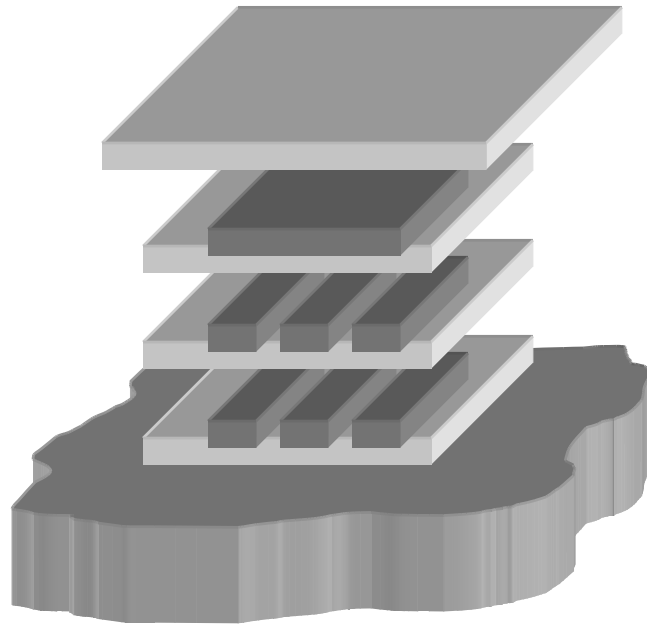Figure 12: Channel section geometry.

Figure 13: Depiction of metallic glass flow through three patterned wafers (two channels and one open cavity).

Finally, we initiated collaboration with Martin Culpepper, Massachusetts Institute of Technology, to micro-mold the HexFlex, a six degree-of-freedom micro-scale flexural manipulator. Figure 16 shows a top view of the manipulator. The hexagonal support structure is approximately 1.5 mm across the flats. The curved support elements supporting the central circular platform (100 μm diameter) have a minimum thickness of approximately 10 μm. The device is actuated by pressing on the six tabs. Figure 17 shows two superimposed images. The gray image shows the device in its free state, while the blue image shows a deformed state created by pressing on one of the tabs.
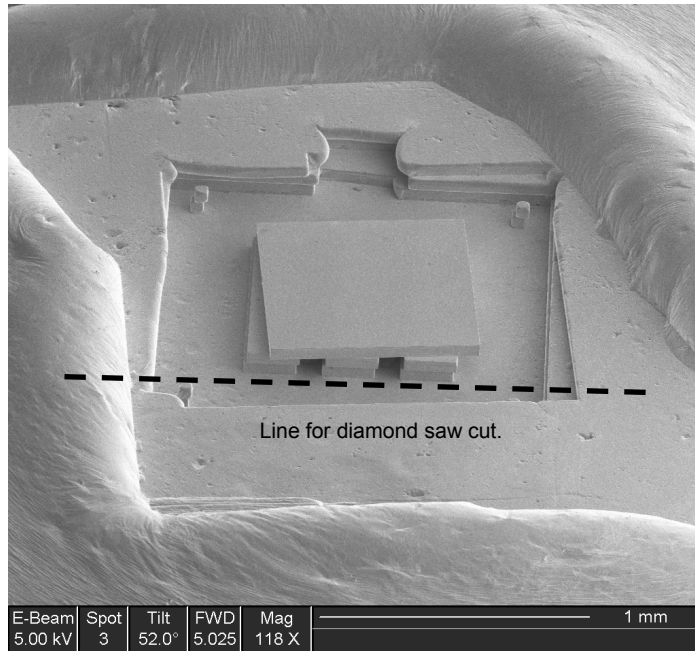
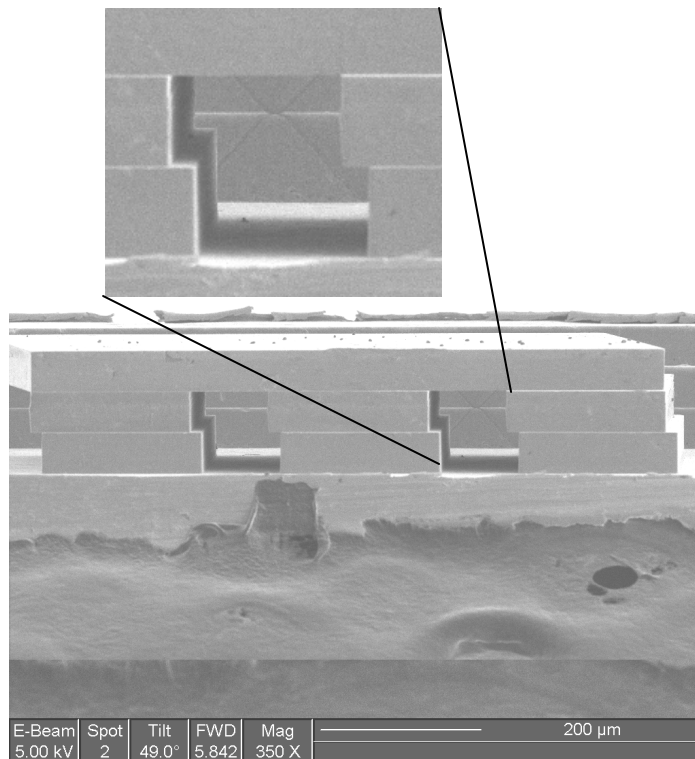*Figure 14: SEM image of micro-molded,*
100x100x800 μm closed channels.

Figure 15: SEM image of micro-molded
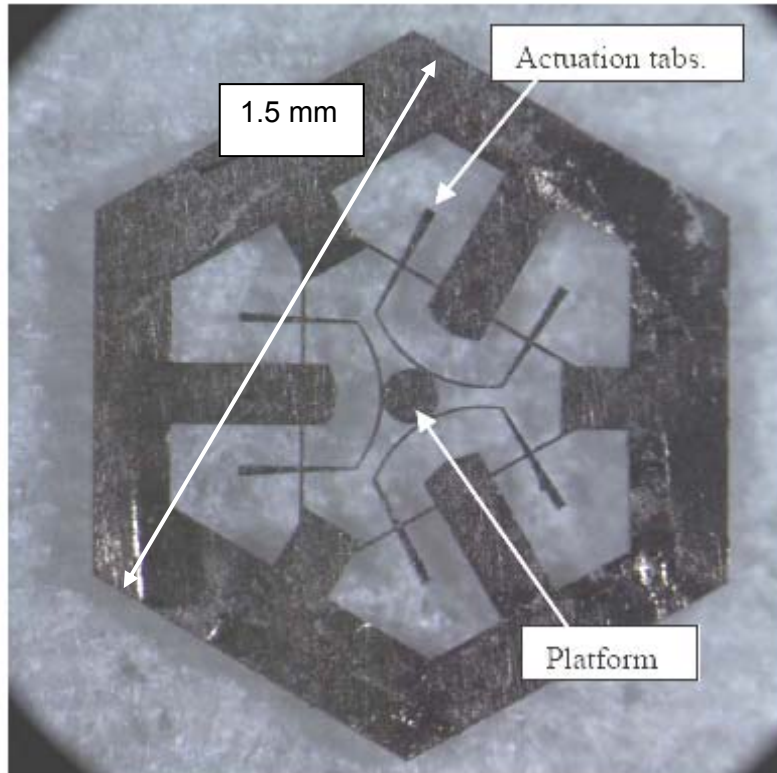*channels with FIB 'X' through the right channel.*

Figure 16: Micro-molded HexFlex manipulator. The platform position is adjusted in six degrees-of-freedom by pressing on the actuators.

Figure 17: HexFlex manipulator shown in free state (gray) and actuated position (blue). Motion was achieved by pressing on the upper right actuator tab with tweezers (also shown).

Conclusions

In this research, experimental platforms were developed and exercised for micro-scale production of features using the techniques of high-speed milling (metals and graphite) and micro-molding (amorphous metals). It was shown that high fidelity, three-dimensional structures could be produced. Example applications were demonstrated that supported other fuel cell research efforts at the University of Florida.

Patents

None.

Publications

1. Bardt, J., Bourne, G., Ziegert, J., Schmitz, T., and Sawyer, W.G., 2007, Micromolding Three-Dimensional Amorphous Metal Structures, *Journal of Materials Research* (accepted).
2. Bardt, J., Bourne, G., Schmitz, T., Sawyer, W.G., and Ziegert, J., 2007, Closed Channel Fabrication using Micromolding of Metallic Glass, to appear in Proceedings of the 2007 International Manufacturing Science & Engineering Conference (MSEC2007), October 15-18, 2007, Atlanta, GA.
3. Cheng, C.-H. and Schmitz, T., 2007, RCSA Application to Micro/Meso-scale Endmills, to appear in Proceedings of the 2007 International Manufacturing Science & Engineering Conference (MSEC2007), October 15-18, 2007, Atlanta, GA.
4. Bardt, J., Ziegert, J., Schmitz, T., Sawyer, W.G., and Bourne, G., 2006, Precision Molding of Complex Metallic Micro-structures, 1st International Conference on Micromanufacturing, University of Illinois, Urbana-Champaign, September 13-15.
5. Bardt, J., Mauntler, N., Ziegert, J., Sawyer, W.G., and Schmitz, T., 2005, Precision Molding of Metallic Micro-components, Proceedings of American Society for Precision Engineering Annual Meeting, October 9-14, Norfolk, VA.
6. Bardt, J., Mauntler, N., Bourne, G., Schmitz, T., Ziegert, J., and Sawyer, W.G., 2005, Metallic Glass Surface Patterning by Micro-molding, Proceedings of American Society of Mechanical Engineers International Mechanical Engineering Congress and Exposition, IMECE2005-81099, Orlando, FL.
7. Bardt, J., Mauntler, N., Bourne, G., Schmitz, T., Ziegert, J., and Sawyer, W.G., 2005, Fuel Cell Collector Plate Fabrication by Micro-molding, 1st Symposium on Manufacturing of MEAs for Hydrogen Applications, August 9-11, Dayton, OH.
8. Cheng, C.-H., Schmitz, T., Arakere, N., and Duncan, G.S., 2005, An Approach for Micro End mill Frequency Response Predictions, Proceedings of American Society of Mechanical Engineers International Mechanical Engineering Congress and Exposition, IMECE2005-81215, Orlando, FL.

Students from Research

J. Bardt, G. Bourne: Received MSc degree. Employed at Texas Instruments.

C.-H. Cheng: Received PhD. Interviewing for faculty positions (no offer yet)

N. Mauntler: Completing PhD at UF

Follow-on Funding

The NASA funds were used to leverage follow-on funding from the National Institute of Standards and Technology (NIST). In this two-year project, the research collaboration is focused on the development of a reference standard for atomic force microscope (AFM) cantilever stiffness calibration. The end goal is production of flexure-based artifacts that exhibit: low fabrication expense, stiffness adjustability by design, insensitivity to load application point, mechanical robustness, and good reproducibility. Experimental determination of the spring constants of AFM cantilevers is important because the measured forces are inferred from the cantilever displacement and the linear relationship between force and displacement.

Rather than rely on the AFM displacement sensor and various other measurements (of geometry and mass, for example) to determine cantilever stiffness, the purpose of this research is to develop a reference artifact that provides a more direct (force) traceability path. Specifically, it is our intent to design an artifact that can be calibrated using the electronic force balance (EFB) developed by J. Pratt *et al*. at NIST and subsequently used as a transfer standard to determine the stiffness of commercial AFM cantilevers. Our final design goals for the artifact are:

1. inexpensive to manufacture;
   We will use the micro-molding process for bulk metallic glass.
2. ability to vary stiffness;
   Multiple artifacts of varying geometry (and, therefore, stiffness) can be produced in a single mold. Our stiffness design range will be 0.5 to 1.0 N/m, which corresponds both to nominal cantilever stiffness values and the preferred range of operation for the EFB.
3. insensitive to load application location;
   Flexure-based geometries will be applied to reduce/eliminate sensitivity of stiffness to the location of the applied load.
4. mechanical robustness; and
   Because the artifact will be metal and have a size scale of ~1 mm, it will be easier to handle and use.
5. good reproducibility
   We anticipate that the micro-molding process is sufficiently accurate and that the bulk metallic glass properties will be acceptably reproducible to produce the "same" artifact(s) from one mold to the next. This could reduce the number of required EFB measurements once the process reproducibility is verified.

References

1. Schmitz, T., 2003, Chatter Recognition by a Statistical Evaluation of the Synchronously Sampled Audio Signal, *Journal of Sound and Vibration*, 262/3: 721-730.
2. Schmitz, T., Davies, M., and Kennedy, M., 2001, Tool Point Frequency Response Prediction for High-Speed Machining by RCSA, *Journal of Manufacturing Science and Engineering*, 123: 700-707.
3. Schmitz, T., Davies, M., Medicus, K., and Snyder, J., 2001, Improving High-Speed Machining Material Removal Rates by Rapid Dynamic Analysis, *Annals of the CIRP*, 50/1: 263-268.
4. Schmitz, T., Davies, M., Dutterer, B., and Ziegert, J., 2001, The Application of High-Speed CNC Machining to Prototype Production, *International Journal of Machine Tools and Manufacture*, 41: 1209-1228.
5. Schmitz, T. and Ziegert, J., 1999, Examination of Surface Location Error Due to Phasing of Cutter Vibrations, *Precision Engineering*, 23/1: 51-62.

Report Date: May 14, 2007

10. Bimetallic Catalysts for the Electrooxidation of Hydrocarbon Fuels

Task PI: Dr. Lisa McElwee-White, Chemistry, University of Florida

Collaborators: Dr. Jason Weaver, Chemical Engineering, Dr. David Hahn, Mechanical & Aerospace Engineering, and Dr. David Mikolaitis, Mechanical & Aerospace Engineering

Graduate Students: Daniel Serra, Jianye Zhang, Marie Correia, Chemistry
Undergraduate Student: Casie Hilliard, Chemistry

Research Period: August 3, 2004 to March 31, 2007

Abstract

Heterobimetallic Ru/Pt, Ru/Pd and Ru/Au complexes and their Fe/Pt, Fe/Pd and Fe/Au analogues were synthesized and confirmed to be catalysts for the electrochemical oxidation of methanol. The liquid organic products were dimethoxymethane (DMM) and methyl formate (MF). Current efficiencies for methanol oxidation were much higher in neat methanol than in less polar organic solvents. Unlike the Ru-containing catalysts, the Fe/Pt complex Cp(CO)Fe(μ-I)(μ-dppm)PtI$_2$ produced CO$_2$ during electrooxidation of methanol. The CO$_2$ was determined by isotopic labeling to be derived from the CO ligand, indicating that these catalysts will not be poisoned by CO. Preliminary experiments on incorporating these catalysts into modified electrodes suggested that carbon paste electrodes will be more successful than dispersing the catalysts in Nafion.

Introduction and Project Goals

The goal of this subtask was to synthesize and study heterobimetallic catalysts for the electrooxidation of methanol and ethanol as models for the use of higher hydrocarbon fuels in fuel cells. We had previously synthesized simple bimetallic Ru/Pt, Ru/Pd and Ru/Au complexes and demonstrated that they are catalysts for the electrochemical oxidation of methanol in homogeneous solution. In this project, we extended these studies in two thrusts: 1) Preparation and study of analogues of these complexes that contain the first row transition metal Fe in place of Ru. Since first row metals are generally more reactive in discrete complexes, these catalysts were screened for increased catalytic activity as compared to our first generation Ru/Pt, Ru/Pd, and Ru/Au electrocatalysts. 2) Incorporation of previously prepared catalysts and their derivatives into modified electrodes to study their alcohol oxidation properties in immobilized environments similar to those found in fuel cell anodes.

Background

One of the important challenges in fuel cell technology is the use of liquid hydrocarbon fuels. Direct conversion of these fuels to CO$_2$ will require electrocatalysts capable of breaking C-H bonds, breaking C-C bonds, and transferring oxygen to carbon-containing fragments. Some inspiration for catalyst design can be found in the literature on direct methanol fuel cells (DMFC),[1,2] for which C-H cleavage and oxo transfer are necessary chemical steps. Although there has been moderate success with platinum anodes for DMFC, it is agreed that the presence of a second metal can decrease the anode overpotential and increase the anode lifetime. Pt/Ru anodes are the most effective of the bimetallic cases.

The Pt portion has been suggested to be the site of methanol binding and dehydrogenation, while the Ru serves as a source of "active oxygen" for the formation of CO$_2$.[3]

Our strategy is to use the lessons from bulk metal DMFC anodes to design discrete bimetallic complexes as catalysts for liquid fuel electrooxidation. These complexes can be viewed as utilizing all of the metal in active sites as opposed to bulk metal anodes, where the reaction occurs at the surface only. If the proposed mechanisms for methanol oxidation at Pt/Ru anodes are correct, the essential features are C-H bond cleavage at Pt and transfer of oxygen from Ru (or another second metal). Both of these reactions are well-precedented for mononuclear complexes of the respective metals. Although binuclear Pt/Ru complexes are not good models of the proposed surface binding site on Pt/Ru anodes, we have demonstrated that it is possible to reproduce the essential functions of the proposed electrooxidation mechanism in heterobinuclear complexes.[4-6]

Results and Discussion

1) Preparation and Study of New Catalysts

Synthesis and Electrochemistry of New Catalysts. The synthesis of new pairs of isostructural Fe and Ru complexes was completed (Scheme 1). We have now prepared catalysts **1-6.** Due to the facile decomposition of Ru/Au complex **6** to $CpRuI(\eta^2\text{-dppm})$, detailed electrochemical studies were carried out only on complexes **1-5**.
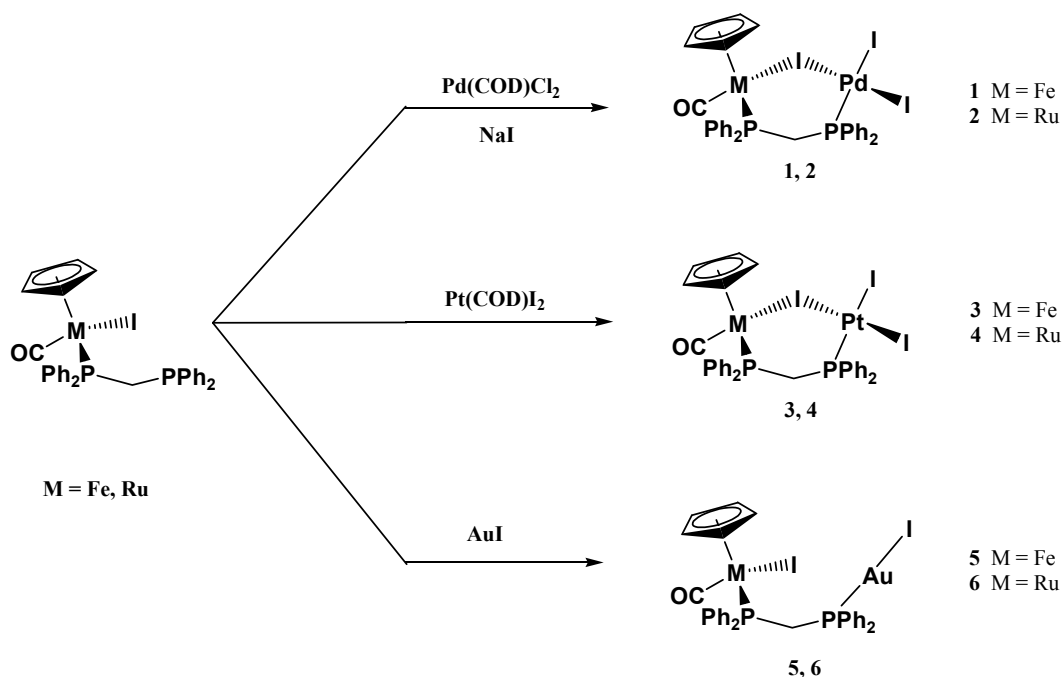

Scheme 1

Cyclic voltammograms for complexes **1**-**6** appear in Figure 1, with the assigned formal potentials for each redox wave in Table 1. All five complexes are catalysts for the electrooxidation of methanol as evidenced by current increases observed upon addition of 50 µL of methanol to the samples during cyclic voltammetry.

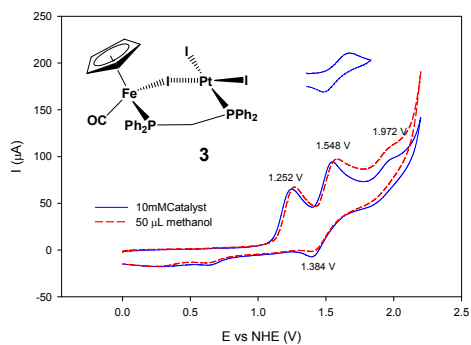**Figure 1.** Cyclic voltammograms for complexes **1-6** in 0.7 M DCE/TBAT with a scan rate of 100 mV/s.
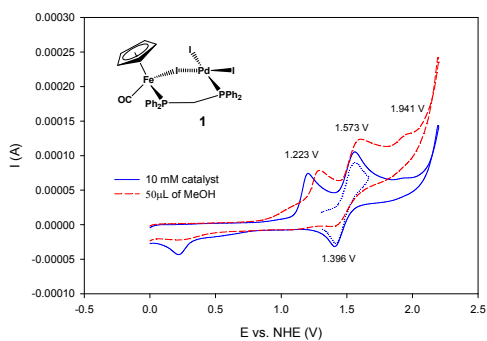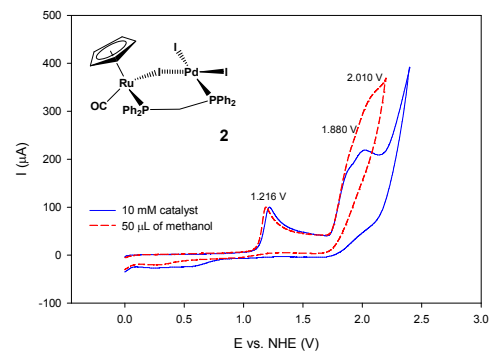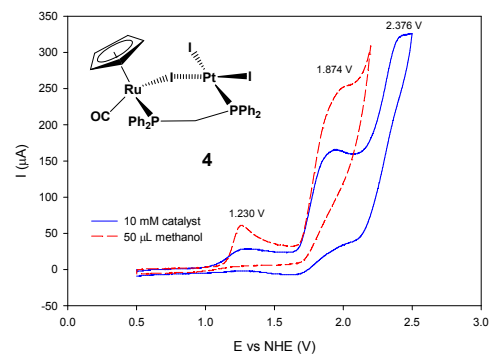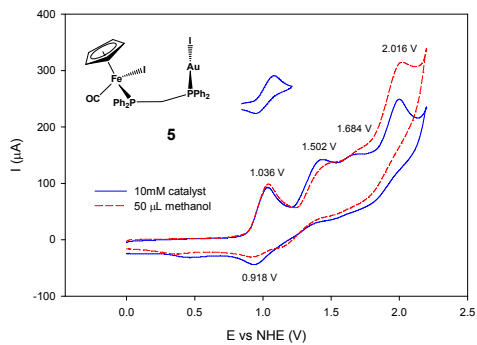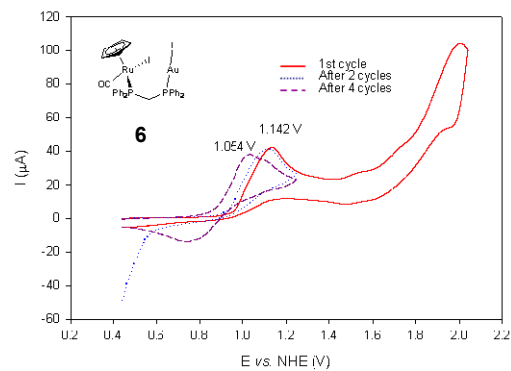
Table 1. Formal Potentials for Complexes **1-7**.[a]

Complex	Couple	E_{pa} (V)	$E_{1/2}$ (V)[b]	Couple	E_{pa} (V)	$E_{1/2}$ (V)[b]	Couple	E_{pa} (V)
1	Fe(II/III)	1.223		Pd(II/IV)	1.573	1.485	Fe(III/IV)	1.941
2	Ru(II/III)	1.216		Pd(II/IV)	1.880		Ru(III/IV)	2.010
3	Fe(II/III)	1.252		Pt(II/IV)	1.548	1.466	Fe(III/IV)	1.972
4	Ru(II/III)	1.230		Pt(II/IV)	1.874		Ru(III/IV)	2.376
5	Fe(II/III)	1.036		Au(I/III)	1.502		Fe(III/IV)	2.016
6	Ru(II/III)	1.142		Au(I/III)	1.552		Ru(III/IV)	2.020
7[c]	Ru(II/III)	1.075		Pt(II/IV)	1.542	1.441	Ru(III/IV)	-

[a]All potentials obtained in DCE/TBAT and reported vs. NHE. [b] $E_{1/2}$ reported for reversible waves. [c]CpRu(PPh$_3$) (μ-I)(μ-dppm)PtI$_2$.

Figure 2. Evolution of liquid organic products (DMM and MF) during bulk electrolysis of methanol with **1**-**5** in 0.7M DCE/TBAT (a) Fe/Pd complex **1**, (b) Ru/Pd complex **2**, (c) Fe/Pt complex **3**, (d) Ru/Pt complex **4,** (e) Fe/Au complex **5**.
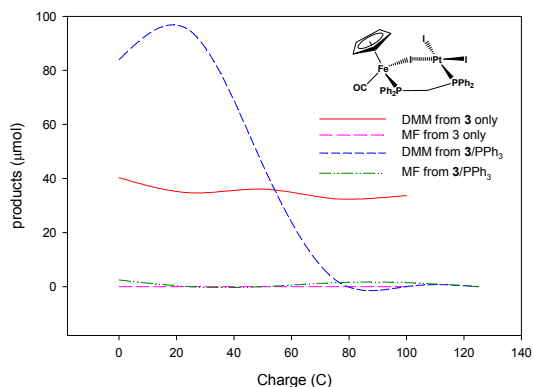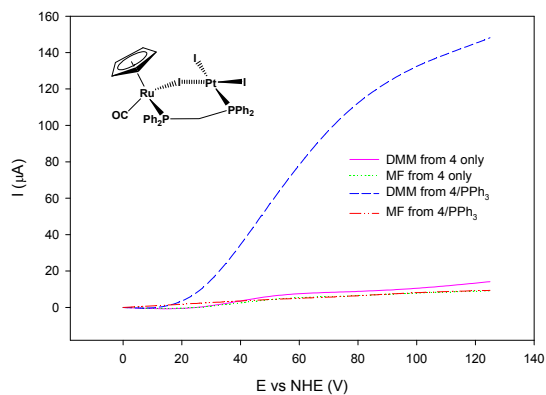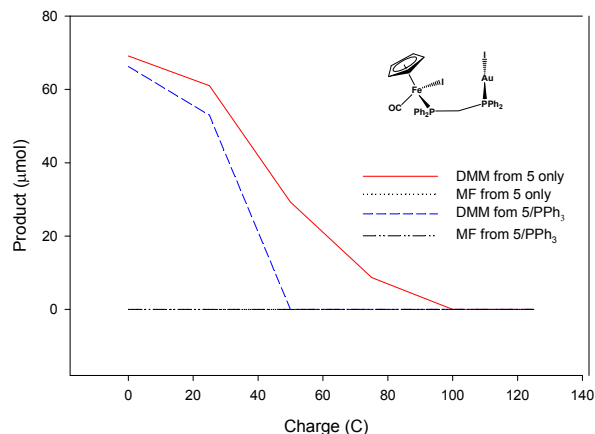
a)
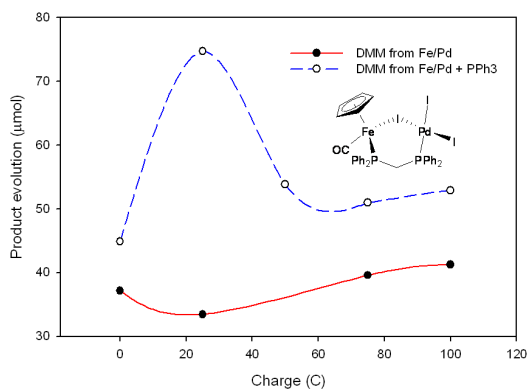
b)
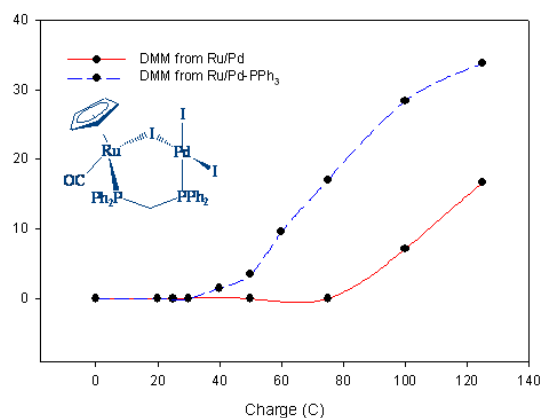
c)

d)

e)

The evolution of liquid methanol oxidation products (dimethoxymethane, DMM and methyl formate, MF) for catalysts **1**-**5** is shown in Figure 2. For the Fe complexes (**1, 3,** and **5**), DMM could be detected before passing any current into the system. This is not typical of our complexes and shows that the iron compounds exhibit different behavior than their ruthenium analogues.

Current efficiencies for the electrooxidation of methanol by catalysts **3** and **4** are summarized in Table 2. These values are the ratio of the charge necessary to produce the observed yields of DMM and MF to the total charge passed during the bulk electrolysis. Although the Fe/Pt (**3**) and Ru/Pt (**4**) complexes afforded relatively low current efficiencies, note that the current efficiencies are significantly higher for the Fe/Pt compound than for its Ru/Pt analogue, indicating that the first row metal Fe produced a more active catalyst in this case. The problems with the low current efficiencies and catalyst stabilities in **3** and **4** appear to be due to facile loss of the CO ligand, which was not present in our earlier Ru/Pt catalysts. This problem can be ameliorated by adding one equivalent of triphenylphosphine (PPh$_3$) to the mixture before passing any current (Table 2, Figure 2). Both the yield of oxidation products and the current efficiencies were improved by the addition of PPh$_3$. For the Ru/Pt complex **4**, the yield of DMM was 10 t times higher in the presence of the phosphine after 125 °C of charge had been passed. When the same experiment was carried out with Fe/Pt complex **3**, again DMM was detected as the major electrooxidation product along with traces of MF. However in that case, instead of having a constant concentration of DMM it seems that the product is consumed during the catalytic process. Since the concentrations of MF do not rise appreciably during the experiment, conversion of DMM to the higher oxidation product CO$_2$ is a strong possibility. Experiments to analyze gas emissions during electrolysis are underway.

Table 2. Current Efficiencies and Products Formed during the Bulk Electrolysis of Methanol Catalyzed by **3** and **4** in the Absence and Presence of PPh_3.

	3			3- PPh_3			4			4- PPh_3		
Charge (C)	DMM (µmol)	MF (µmol)	CE%	DMM (µmol)	MF (µmol)	CE%	DMM (µmol)	MF (µmol)	CE%	DMM (µmol)	MF (µmol)	CE%
0	40.3	-	**-**	83.99	2.48	-	-	-	**-**	-	-	**-**
25	34.7	-	**26.7**	94.42	-	**72.89**	-	-	**-**	8.09	2.23	**9.79**
50	36.1	-	**13.93**	45.13	-	**17.89**	6.10	4.29	**5.17**	56.85	4.36	**25.31**
75	32.5	-	**8.36**	2.73	1.47	**14.59**	8.50	6.17	**5.24**	105.2	6.03	**30.18**
100	33.7	-	**6.50**	-	1.49	**0.57**	10.51	7.92	**4.85**	132.4	8.12	**28.68**
125				-	-	-	14.16	9.14	**5.01**	148.1	9.4	**25.76**

[a] Bulk electrolysis carried out at 1.9V vs. NHE.

Table 3. Current Efficiencies and Products Formed during the Bulk Electrolysis of Methanol Catalyzed by **5** in the Absence and Presence of PPh_3.

	5			5- PPh_3		
Charge (C)	DMM (µmol)	MF (µmol)	CE%	DMM (µmol)	MF (µmol)	CE%
0	69.12	-	-	66.24	-	-
25	61.79	-	-	52.96	-	-
50	29.30	-	-	-	-	-
75	8.66	-	-	-	-	-

[a] Bulk electrolysis carried out at 1.9V vs. NHE.

Bulk electrolysis was also performed for Fe/Au complex **5,** in the absence and presence of PPh_3 (Figure 2, Table 3). For this complex, no MF was detected by GC and again DMM was detected before any current was passed in the system. As for Fe/Pt complex **4,** DMM appears to be consumed during the oxidation process. Addition of PPh_3 did not improve the yields of DMM or MF, but the consumption rate of DMM was increased significantly.

In order to improve the catalyst behavior solvent effects on the CVs were examined. Complexes **1-5** were tested in two additional solvents (acetonitrile and methanol). Results for Fe/Pt **3** and Ru/Pt **4** are presented in Figure 3. Coordination of acetonitrile is demonstrated by the presence of an additional wave and shifts in the redox potentials as compared to the cyclic voltammograms in DCE (Figure 1a,b). Figures 3b,d show the cyclic voltammetry of **3** and **4** in methanol. These studies were particularly important, since they demonstrate that the complexes showed no degradation during electrooxidation in neat methanol, a critical point for use in fuel cell applications.

Figure 3. Effect of solvent on CV of Ru/Pt and Fe/Pt complexes.

Acetonitrile
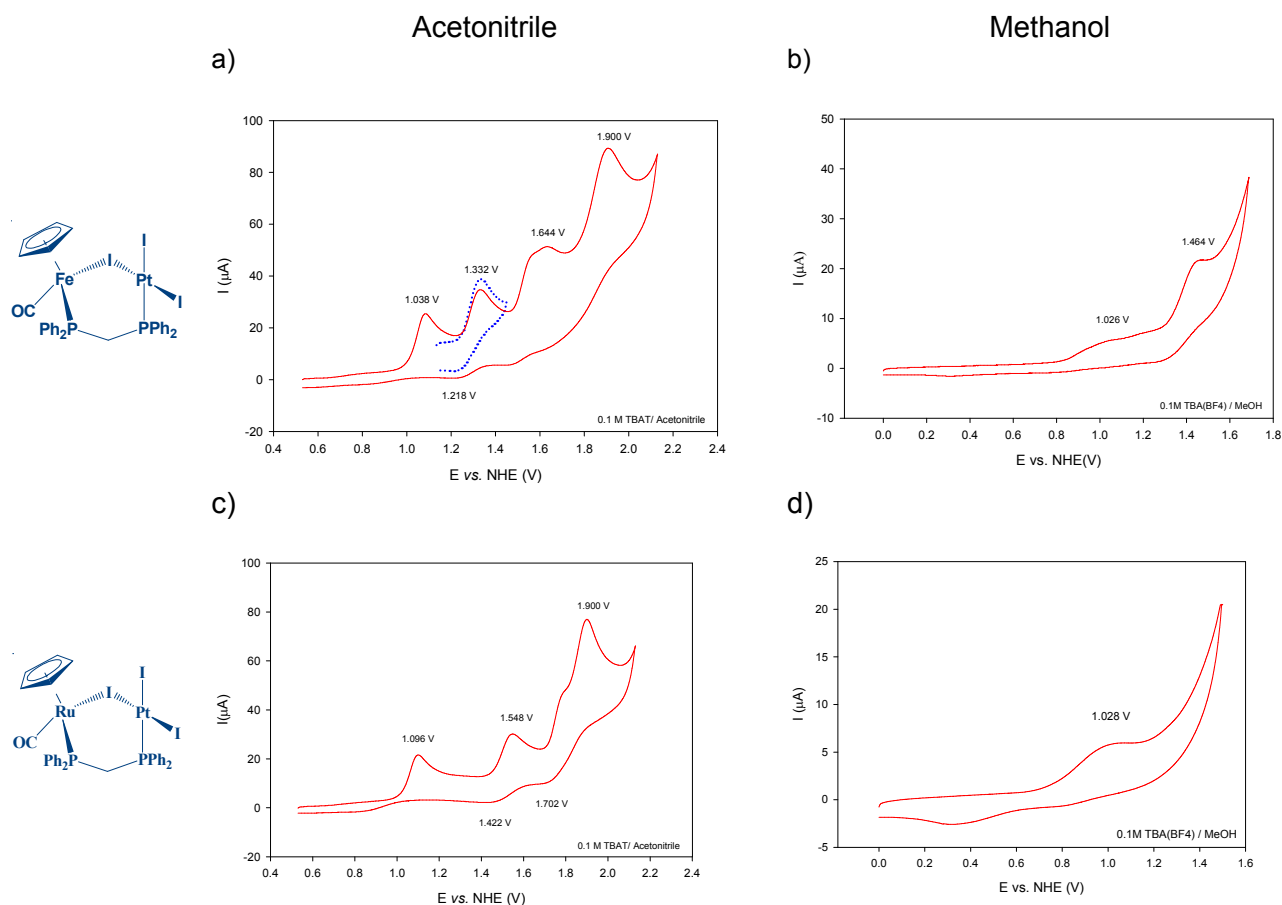
Methanol

a)

b)

c)

d)

Figure 4. Product evolution for electrooxidation of methanol in presence of Ru/Pt **4** and Fe/Pt **3**, in pure methanol, at 1.5 V vs. NHE.
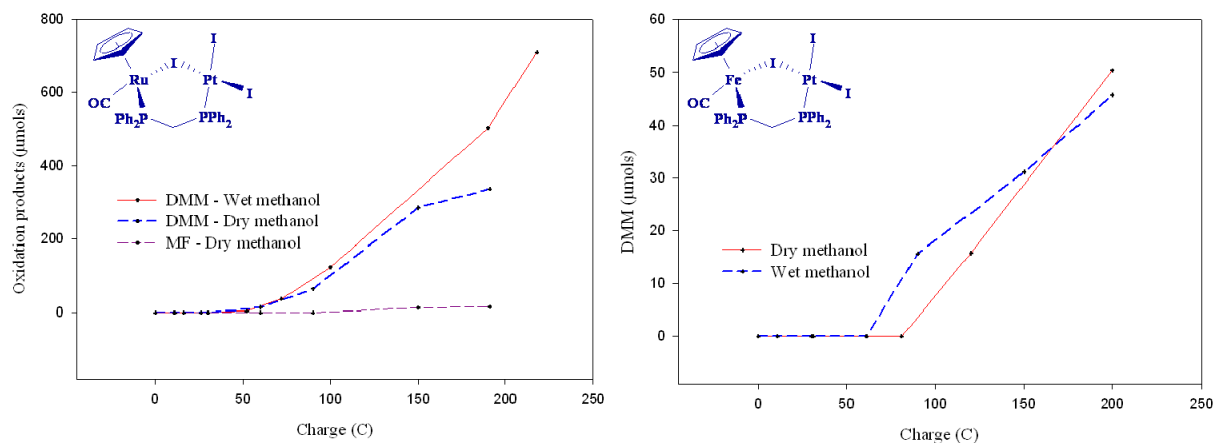

Figure 4 shows the evolution of liquid organic products (DMM and MF) for oxidation by **3** and **4** in pure methanol. No oxidation product was observed before electrolysis, in contrast to the same experiment in DCE. For the bulk electrolysis of methanol in the presence of complex

Ru/Pt **4,** dimethoxymethane **(**DMM) and methyl formate (MF) were both detected in dry methanol while DMM was the only liquid product in wet methanol. For the bulk electrolysis with Fe/Pt complex **3**, DMM was the only liquid oxidation product in both dry and wet conditions. Comparison of the product evolutions in DCE and methanol for these two complexes (Figure 2c,d and Figure 4) shows a significant catalytic improvement, especially for complex **4**.

Figure 5. FTIR of the headspace gases during the electrooxidation of methanol with Fe/Pt **3** in pure methanol.
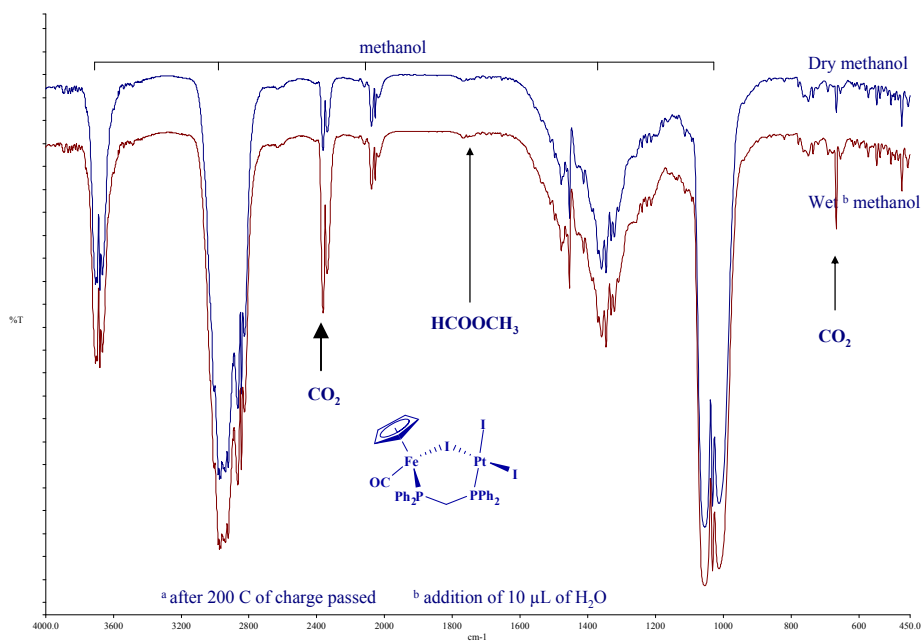
During previous experiments, yields of the liquid organic products DMM and MF had been determined by GC. Such experiments are standard practice for electrooxidation of methanol in homogeneous solution, since gaseous products had not been previously been reported in the literature for homogeneous systems. However, use of our catalysts in fuel cell applications requires that the oxidation go all the way to CO_2. We have now carried out IR spectroscopy experiments designed to detect previously unobserved products such as formaldehyde, formic acid and CO_2. Figure 5 shows FTIR spectra of the headspace gases during the bulk electrolysis in presence of Fe/Pt complex **3**. These first results were promising since the presence of carbon dioxide and methyl formate was detected after 200 °C of charge passed into the system. As shown in Figure 5, formation of CO_2 is also favored by the presence of water. Control IR experiments on the headspace gases before the passage of current did not detect CO_2. In retrospect, the current efficiencies we previously reported for production of the liquid organics DMM and MF are not representative of current utilization by the catalysts that do form the 6 e⁻ oxidation product CO_2, since CO_2 is not reflected in these values. These results represent the first detection of CO_2 from oxidation of methanol by discrete complexes.

Isotopic Labeling Experiments on CO_2 Evolution. In order to determine the origin of the CO_2 formed during the electrolyses with complex **3,** two experiments were required, one using $^{12}CH_3OH$ and the ^{13}CO derivative of the Fe/Pt complex **3**, the other one using the unlabeled ^{12}CO complex and $^{13}CH_3OH$. The synthesis of the ^{13}CO-Fe/Pt complex **3-^{13}C** is illustrated in Scheme 2. In order to incorporate the carbonyl ligands, CpFe^{II}(benzene)PF$_6$ was chosen as the

starting material. Since reduction of the compound by Na/Hg leads to the very reactive intermediate CpFe[I](benzene), substitution of the benzene by ligand such as CO can be carried out. This strategy has been applied to synthesize ^{13}C labeled $[CpFe(CO)_2]_2$ dimer which led to the formation of the $CpFe(^{13}CO)_2I$ precursor after reaction with iodine in refluxing chloroform. The subsequent steps to **3-^{13}C** have been reported for the unlabeled compound.[7]
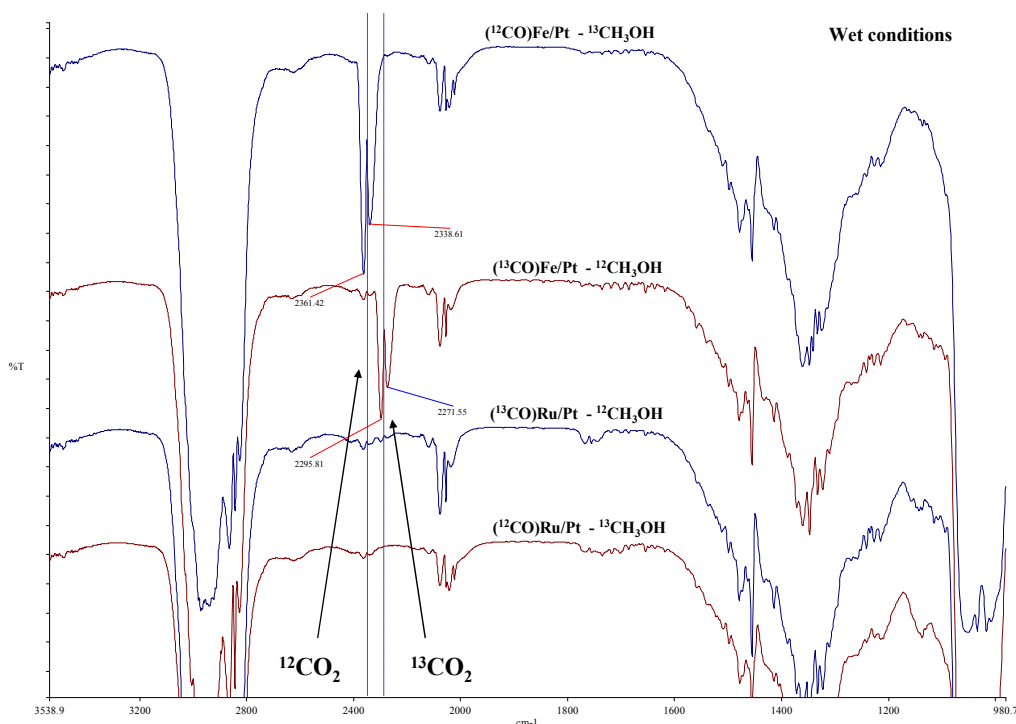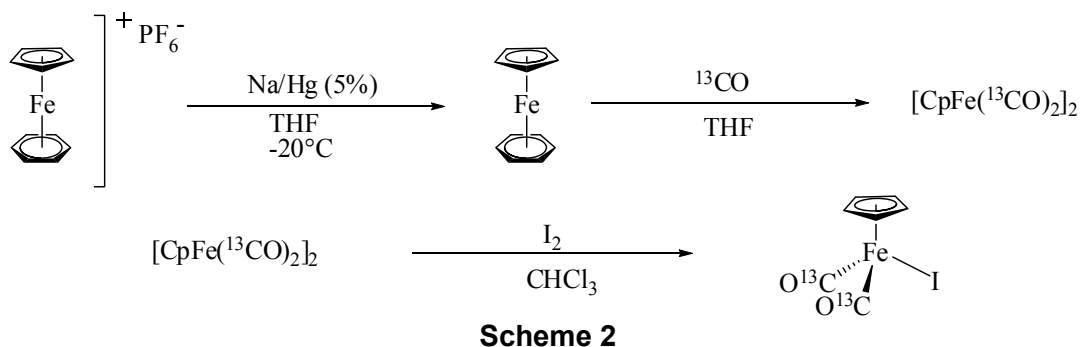

Scheme 2

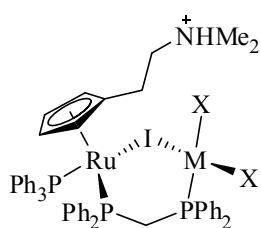**Figure 6.** Isotopic labeling experiments. FTIR spectra of the headspace gases during the electrooxidation of methanol.

Bulk electrolyses have been performed in the presence of a 1:1 mixture of $^{12}CH_3OH$ and $^{13}CH_3OH$ (about 2 mL of $^{13}CH_3OH$ was used for each experiment) for (^{12}CO)-Fe/Pt complex **3**. The same experiment was performed with (^{12}CO)-Ru/Pt complex **4** as a control. If the ^{13}C labeled CO_2 were formed from the electrooxidation of $^{13}CH_3OH$, it would be observed at the theoretical stretching frequency value of 2296 cm^{-1}. However for both complexes **3** and **4,** no $^{13}CO_2$ was detected (Figure 6) which indicates that the origin of CO_2 during the electrolysis is exclusively from the conversion of the CO ligand to CO_2.

Bulk electrolysis was also performed with the Fe/Pt complex **3-^{13}C** in $^{12}CH_3OH$. Again the results confirmed that the CO_2 is coming from the oxidation of the CO ligand by water present during the process since only $^{13}CO_2$ could be observed when the labeled Fe/Pt complex **3-^{13}C** was used for the electrolysis (Figure 6).
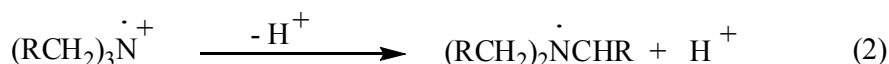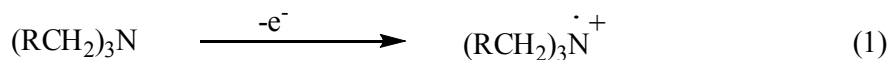
Spectroscopic Studies of Electronic Interactions in New Catalysts. Heterobimetallic complexes **1-6** were characterized by cyclic voltammetry, IR, UV and NMR (^{1}H and ^{31}P) spectroscopy, and elemental analysis. The structures of the I-bridged compounds **1-4** were determined by X-ray crystallography. Electronic interaction between the two metals is significant for the iodide-bridged compounds **1-4** as evidenced by the variation in their carbonyl stretching frequencies and UV-vis spectra, as well as in the shifts of their redox potentials when compared to mononuclear model compounds. In contrast, compounds **5** and **6**, which have only dppm bridges, exhibit limited interactions between the two metals. Full details of this study can be found in the literature.[7]

2) *Incorporation of Catalysts into Modified Electrodes*

Charged Catalysts for Use in Modified Electrodes. As a prelude to incorporation of positively charged catalysts in Nafion films, we carried out a study of the electrochemical oxidation of methanol by amino-substituted cyclopentadienyl complexes **9-12**. The CV data for complexes **9-12** are listed in Table 4. The cyclic voltammetry of the monometallic ruthenium complexes generally exhibits two waves. The first one is assigned to the Ru(II/III) redox couple while the second one is assigned to the Ru(III/IV) couple. In the case of the amino-substituted compounds a third wave is also observed due to the oxidation of the amino moiety. This electrochemical process has been previously described for aliphatic amines. Tertiary aliphatic amines can be oxidized to a radical cation (Eq. 1) which can deprotonate to give a radical (Eq. 2).

Compound	M	X
9	Pt	Cl
10	Pt	I
11	Pd	Cl
12	Pd	I

$$(RCH_2)_3N \xrightarrow{-e^-} (RCH_2)_3\overset{\cdot}{N}{}^+ \qquad (1)$$

$$(RCH_2)_3\overset{\cdot}{N}{}^+ \xrightarrow{-H^+} (RCH_2)_2\overset{\cdot}{N}CHR + H^+ \qquad (2)$$

Protonation of the amine moiety should give electrochemically inactive ammonium ions that exhibit the regular waves observed for the mono and heterobimetallic complexes. However, it appears that the cyclic voltammetry of all the ammonium complexes performed in DCE always exhibits a small wave due to the oxidation of the amine moiety. This phenomenon is probably due to the presence of small amount of non-protonated amine in the samples. The cyclic voltammetry performed in methanol does not show this wave.

Table 4. Formal potentials for complexes **9-12**

Complex	solvent	Couple	E_{pa} V	Couple	E_{pa} V	$E_{1/2}$[b] V	Couple	E_{pa} V	$E_{1/2}$[b] V	Couple	E_{pa} V
N,N-dimethylphen-ethylamine	DCE	amine	1.35	Ru(II/III)			-			Ru(III/IV)	
8	DCE	amine[a]	1.26	Ru(II/III)	1.36	-	Pt(II/IV)	1.72	-	Ru(III/IV)	1.98
	MeOH	amine	-	Ru(II/III)	1.32	-	Pt(II/IV)	[c]	-	Ru(III/IV)	[c]
9	DCE	amine[a]	0.65	Ru(II/III)	0.93	0.82	Pt(II/IV)	1.56	1.45	Ru(III/IV)	2.01
	MeOH	amine	-	Ru(II/III)	0.83	-	Pt(II/IV)	1.55	-	Ru(III/IV)	[c]
10	DCE	amine[a]	1.12	Ru(II/III)	1.35	-	Pd(II/IV)	1.67	1.52	Ru(III/IV)	2.04
	MeOH	amine	-	Ru(II/III)	1.33	-	Pd(II/IV)	[c]	-	Ru(III/IV)	[c]
11	DCE	amine[a]	0.64	Ru(II/III)	1.00	-	Pd(II/IV)	1.57	1.47	Ru(III/IV)	2.09
	MeOH	amine	-	Ru(II/III)	0.93	-	Pd(II/IV)	1.46	-	Ru(III/IV)	[c]

Electronic interactions between the two metals in the I-bridged heterobimetallic complexes **9-12** are evidenced by significant redox potential shifts compared to those of the monometallic model compound $[\eta^5\text{-}C_5H_4CH_2CH_2NMe_2 \cdot HI](PPh_3)Ru(\eta^1\text{-}dppm)I$ (**13**). The cyclic voltammograms of the Ru/Pt complexes **9** and **10** performed in DCE exhibit four redox waves each. The second and fourth waves are due to the Ru(II/III) and Ru(III/IV) couples, while the third wave is assigned to the Pt(II/IV) redox couple of platinum. A small first redox wave is also observed and has been assigned to the oxidation of the residual non-protonated amines. As expected, electronic interactions between the metal centers are observed for those complexes due to the presence of the iodide bridge. The potentials for the Ru(III/IV) waves are not affected by the changes of the ligands around the Pt center for **9** and **10**. In contrast, comparison of the Pt substituted chloride **8** with the iodide complex analogue **10** reveals a significant 430 mV negative shift of the Ru(II/III) redox potential as a result of an increase of the electron density at the Pt center. A similar effect is also observed at the Pt center with the Pt(II/IV) redox couple found to be easier to oxidize by 160 mV, as the chlorides are replaced by iodide ligands. It is very interesting that changing the halides in the ancillary ligand of platinum affects not only the Ru(II/III) and Pt(II/IV) redox waves but also affects the redox potentials of the amine oxidation waves of the cyclopentadienyl ring. A considerable 610 mV negative shift is observed for the oxidation of the amine when the electron density is increased at the Pt center. It is not surprising to observe the same behavior for the palladium analogue complexes **11** and **12**.

Electrochemical Oxidation of Methanol with the Ru/Pt Complexes 9 and 10 and with the Ru/Pd Complexes 11 and 12. One way to determine if these compounds are active catalysts for the electrooxidation of methanol is to observe the effect of addition of methanol during the cyclic voltammetry experiments. The cyclic voltammograms of the heterobimetallic chloride Ru/Pt complex **9**, and the Ru/Pd complexes **11** and **12** show large current increases starting at the oxidation wave of the second metal center (Pt(II/IV) and Pd(II/IV) couples, respectively) indicating that a catalytic process of methanol oxidation is occurring at this point. Figure 7 is typical of the behavior of **9**, **11** and **12**. On the other hand, the cyclic voltammogram of the iodide heterobimetallic Ru/Pt complex **9** shows only a small increase of the current at the Pt(II/IV) wave.
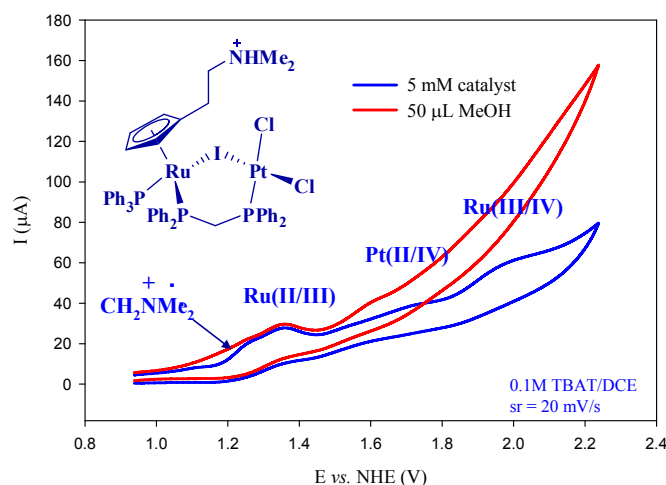
Figure 7. Cyclic voltammograms of complex **9**; glassy carbon working electrode; Ag/Ag⁺ reference electrode.

Previous bulk electrolysis experiments with non-charged heterobimetallic complexes were performed in the non-polar solvents 1,2-dichloromethane or dichloromethane due to poor solubility of the catalysts in polar media. However, in contrast to the original catalysts, compounds **9-12** are soluble in methanol. This allows the use of methanol as both reactant and solvent for the electrolysis experiments. In the case of the neutral complexes, using a high potential of 1.7 V vs. NHE was necessary due to the high overpotentials in DCE. However, a fixed potential of 1.5 V vs. NHE could be used for **9-12** in methanol. Control experiments without catalysts did not show evidence of methanol oxidation at that potential.

As already described, the homogeneous electrochemical oxidation of methanol involves formation of formaldehyde, formic acid, dimethoxymethane (DMM), methyl formate (MF) and CO_2 as oxidation products. Formaldehyde and formic acid are the initial two-electron and four-electron oxidation products from the oxidation of methanol; however in the presence of excess methanol those two undergo fast condensation leading to the formation of DMM, MF and water. The product ratios, current efficiencies and turnover numbers (TON) for the electrooxidation of methanol by catalysts **9-12** and the monomeric model compound **13** are summarized in Table 5.

Table 5. Bulk electrolysis data for the oxidation of methanol by complexes **9-12** and **13**.

| Charge (C) | Product ratios (DMM/MF)[a,b] | | | | |
	Ru/Pt (**9**)	Ru/Pt (**10**)	Ru/Pd (**11**)	Ru/Pd (**12**)	Ru (**13**)
25	-	-	∞	-	
50	0.25	0.41	1.66	0.13	1.59
75	0.48	1.18	1.76	0.45	2.09
100	0.69	1.89	2.34	0.64	2.44
150	0.94	4.39	3.17	0.86	3.80
200	1.08	6.27	3.82	1.01	4.50
Current efficiencies (%) after 200 °C	51.04	15.79	43.65	23.36	9.73
TON after 200 °C	11	4	9	4	2

[a] Electrolyses were performed at 1.5 V vs. NHE in pure methanol. A 10 mM catalyst concentration was used for each experiment.
[b] Determined by GC with respect to n-heptane as an internal standard. Each ratio is reported as an average of 2-3 experiments.

The chloride Ru/Pt complex **9** and Ru/Pd complex **11** gave moderately higher current efficiencies, (51.0 and 43.6%, respectively) when compared to neutral complexes we have previously reported. Experiments in pure methanol have demonstrated that this solvent is more favorable for the catalysis since the electron transfer kinetics are improved in more polar solvent. The product ratios and product evolutions (Figures 8 and 9) from complexes **9** and **10** show also that the partitioning of oxidation products for those two complexes is different. In the early stage of the catalysis, complex **9** forms the four-electron oxidation product MF in higher concentration. However at a late stage of the process it appears that the production of the two-electron oxidation product DMM becomes more favored. Complex **12** shows similar behavior compared to **9** but with a lower activity (23.36% CE and 4 TON for complex **12** versus 51.04% CE and 11 TON for **9**). For Ru/Pd complex **11**, the behavior is different. From the early stage of the catalysis until the end, the two-electron oxidation product DMM is favored as described by the increase of the product ratio from 1.66 to 3.82. This behavior seems to be similar to the monomeric model complex **13** but with better current efficiency for heterobimetallic complex **11**.
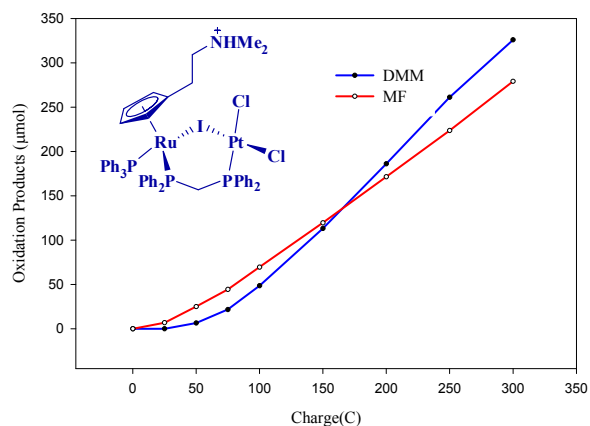

Figure 8. Product evolution for the electrolysis of Ru/Pt complex **9** in 0.1M MeOH/TBABF$_4$.
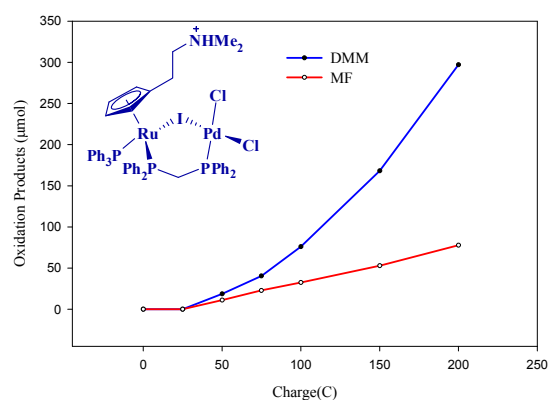

Figure 9. Product evolution for the electrolysis of Ru/Pd complex **10** in 0.1M MeOH/TBABF$_4$.

Construction and Testing of Modified Electrodes. Preliminary efforts to incorporate complexes **9** and **11** into Nafion films were unsuccessful. Doping into Nafion requires aqueous conditions, and these compounds are not sufficiently stable in the presence of water. Because we have a large library of non-charged catalysts and a great deal of information on their electrooxidation of methanol, we instead began to explore fabrication of modified carbon paste electrodes (mcpe) using non-polar binders that dissolve the catalysts. Initial investigations used CpRu(PPh$_3$)$_2$Cl as a model compound since it has similar solubility to the heterobinuclear catalysts. Although it is a much poorer catalyst than the bimetallics for methanol electrooxidation, it does show some water oxidation activity and it is less valuable, making it a prime candidate for initial studies on catalyst incorporation into carbon paste electrodes and electrode stability in aqueous methanol.
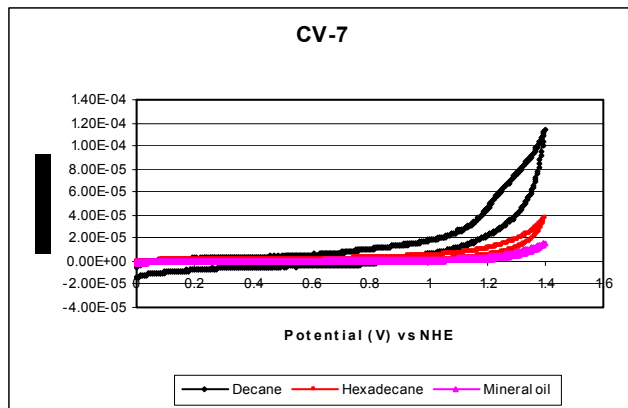
Figure 10. Cyclic voltammograms of mcpe containing CpRu(PPh$_3$)$_2$Cl in different binders. Catalyst loading: 0.10 mmol/g; electrolyte: 1.0M KCl in H$_2$O.

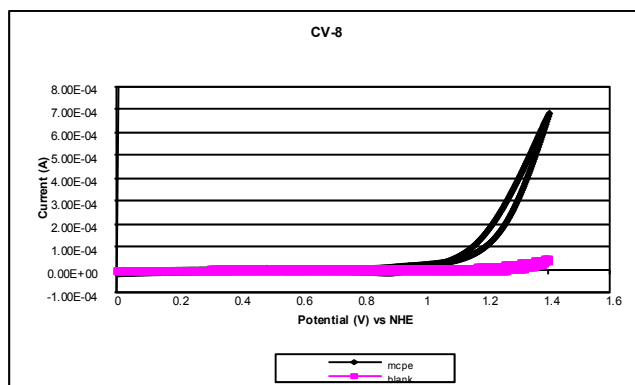**Figure 11.** Cyclic voltammograms of mcpe containing CpRu(PPh$_3$)$_2$Cl vs. a blank electrode. Catalyst loading for mcpe: 0.10 mmol/g; electrolyte: 1.0M KCl in 1:1 CH$_3$OH/H$_2$O.

Electrode preparation has been optimized with respect to catalyst loading and binder choice. Figure 10 shows the comparison of different binder compounds with the catalyst loading and electrolyte composition held constant. As expected, the better kinetics of electrolysis with a lower molecular weight binder compound are reflected in higher catalytic currents for decane-based electrodes. Figure 11 illustrates the catalytic behavior for optimized decane-based mcpe vs. blank (no catalyst) electrodes in 1:1 CH$_3$OH/H$_2$O as a test of electrode stability in aqueous methanol. Experiments with actual heterobimetallic catalysts are continuing.

Conclusions

The heterobimetallic complexes Cp(CO)Ru(μ-I)(μ-dppm)PdI$_2$ (**2**), Cp(CO)Ru(μ-I)(μ-dppm)PtI$_2$ (**4**), and Cp(CO)RuI(μ-dppm)AuI (**6**) and their isoelectronic Fe analogues Cp(CO)Fe(μ-I)(μ-dppm)PdI$_2$ (**1**), Cp(CO)Fe(μ-I)(μ-dppm)PtI$_2$ (**3**), and Cp(CO)FeI(μ-dppm)AuI (**5**) were prepared by the reactions of Cp(CO)M(κ^1-dppm)I (M = Ru, Fe) with Pt(COD)I$_2$, Pd(COD)I$_2$ and AuI, respectively. Heterobimetallic complexes **1-6** were confirmed to be catalysts for the electrochemical oxidation of methanol. The liquid organic products were the 2-electron oxidation product dimethoxymethane (DMM) and the 4-electron oxidation product methyl formate (MF). The cationic catalysts [η^5-C$_5$H$_4$CH$_2$CH$_2$NMe$_2$•HI](PPh$_3$)Ru(μ-I)(μ-dppm)MX$_2$ (M = Pt, Pd; X = I, Cl) (**9-12**) were sufficiently soluble in aqueous methanol to be studied under conditions approximating fuel cells. Current efficiencies for methanol oxidation were much higher in aqueous methanol than in less polar organic solvents, with the efficiency reaching 98% for the Ru/Pd derivative. Unlike the Ru-containing catalysts, the Fe/Pt complex Cp(CO)Fe(μ-I)(μ-dppm)PtI$_2$ produced CO$_2$ during electrooxidation of methanol.

The CO_2 was determined by isotopic labeling to be derived from the CO ligand, indicating that these catalysts will not be poisoned by CO. Preliminary experiments on incorporating these catalysts into modified electrodes suggested that carbon paste electrodes will be more successful than dispersing the catalysts in Nafion.

Publications

1. "Electrochemical Oxidation of Methanol Using Alcohol-Soluble Ru/Pt and Ru/Pd Catalysts," Serra, D.; McElwee-White, L. *Inorg. Chim. Acta*, **2008**, 361, 3237-3246.

2. "Catalysis of the Electrooxidation of Biomass-Derived Alcohol Fuels," Anthony, C.R.; Serra, D.; McElwee-White, L. in *Materials, Chemicals and Energy from Forest Biomass.* Argyropoulos, D.S., Ed. ACS Symposium Series, **2007**, *954*, 296-310.

3. "Electronic Interactions in Fe- and Ru-Containing Heterobimetallic Complexes: Structural and Spectroscopic Investigations," Serra, D.; Abboud, K.A.; Hilliard, C.R.; McElwee-White, L., *Organometallics*, **2007**, 26, 3085-3093.

4. "Electrocatalytic Oxidation of Methanol," Anthony, C.R.; McElwee-White, L., in *Feedstocks for the Future: Renewables for the Production of Chemicals and Materials.* Bozell, J., Ed. ACS Symposium Series No. 921, **2006**, pp. 130-142.

5. "Electrochemical oxidation of methanol using dppm-bridged Ru/Pd, Ru/Pt, and Ru/Au catalysts," Yang, Y.; McElwee-White, L. *Dalton Trans.*, **2004**, 2352-2356.

6. "Selective electrochemical oxidation of methanol to dimethoxymethane using Ru/Sn catalysts," Anthony, C.R.; McElwee-White, L. *J. Mol. Catal. - A: Chem.*, **2004**, *227*, 113-117.

Presentations (invited)

1. University of Mississippi, April 17, 2008

2. University of Illinois, April 2, 2007

3. Washington and Lee University, April 27, 2007

4. "Electrooxidation of ethanol and methanol using heterobimetallic catalysts," Symposium on Feedstocks for the Future, 234th National Meeting of the American Chemical Society, Boston, Massachusetts, August 2007

5. Eastman Chemical Company, May 18, 2006

6. Wayne State University (Frontiers in Chemistry Lecture), April 18, 2005

7. Université Pierre et Marie Curie (Paris 6), September 6, 2005

8. "Heterobimetallic complexes as electrocatalysts for the oxidation of methanol," McElwee-White, L.; Serra, D.; Yang, Y.; Anthony, C.R. Symposium on Materials, Chemicals and Energy from Forest Biomass, 2005 International Congress of Pacific Basin Societies, Honolulu, Hawaii, December 2005

9. University of California, Berkeley, February 10, 2004

10. University of Illinois, Chicago, September 21, 2004

11. Western Kentucky University, November 19, 2004

12. "Electrooxidation of Alcohols Using Heterobimetallic Catalysts,"Symposium on Feedstocks for the Future: Renewables for the Production of Chemicals and Materials,

227th National Meeting of the American Chemical Society, Anaheim, California. Abstract CELL 80, March 2004

13. "Bimetallic catalysts for electrooxidation of methanol," NASA-UF Workshop for Advanced Fuel Cell Research, Gainesville, Florida, May 2004

Invited Conference Presentations

(invited poster, presented by Casie Hilliard) "Synthesis and characterization of ruthenium-containing heterobimetallic complexes: catalytic application in the electrochemical oxidation of ethanol," Symposium on Celebrating Ten Years of Beckman Scholars in Chemistry, 235th National Meeting of the American Chemical Society, April 2008, New Orleans, Louisiana. Abstract PRES 6.

Presentations (contributed)

1. "Heterobimetallic Catalysts for the Electrooxidation of Methanol and Ethanol," Correia, M.; McElwee-White, L. Florida Inorganic Mini-Symposium, September 2007, Gainesville, Florida.

2. "Electrochemical oxidation of alcohols using heterobimetallic catalysts," Sweeney, C.; McElwee-White, L.; Correia, M. 235th National Meeting of the American Chemical Society, April 2007, New Orleans, Louisiana. Abstract CHED 1164.

3. "Electrocatalytic oxidation of methanol by Ru and Fe heterobimetallic complexes," Serra, D.; McElwee-White, L. 231st National Meeting of the American Chemical Society, March 2006, Atlanta, Georgia. Abstract INOR 650.

4. "Electrocatalytic Oxidation of Methanol By Ru And Fe Heterobimetallic Complexes," Serra, D.; McElwee-White, L. 2006 Florida Annual Meeting and Exposition, May 2006, Orlando, Florida.

5. "Electrochemical oxidation of methanol by heterobimetallic Ru and Fe analogue complexes," Serra, D.; McElwee-White, L. 230th National Meeting of the American Chemical Society, September 2006, San Francisco, California. Abstract INOR 679.

6. "Electrochemical oxidation of methanol by heterobimetallic Ru and Re analogue complexes," Serra, D.; McElwee-White, L. Florida Inorganic Mini-Symposium, October 2006, Gainesville, Florida.

7. "Synthesis and Characterization of Heterobimetallic Catalysts for Electrochemical Oxidation of Methanol: Comparative Reactivity Between Ru and Fe Complexes," Serra, D.; McElwee-White, L. Florida Inorganic Mini-Symposium, September 2005, Gainesville, Florida.

8. "Selective electrochemical oxidation of methanol to dimethoxymethane using Ru/Sn catalysts," Anthony, C.R.; McElwee-White, L., Florida Inorganic Mini-Symposium, October 2004, Tampa, Florida.

9. "Selective Electrochemical Oxidation of Methanol to Dimethoxymethane Using Ru/Sn Catalysts," Anthony, C.R.; McElwee-White, L. 2004 Florida Annual Meeting and Exposition, May 2004, Orlando, Florida.

10. "Selective Electrochemical Oxidation of Methanol to Dimethoxymethane Using Ru/Sn Catalysts," Anthony, C.R.; McElwee-White, L. 228th National Meeting of the American Chemical Society, August 2004, Philadelphia, Pennsylvania. Abstract INOR 672.

Students from Research

1. Christina McCall, Undergraduate
2. Casie Hilliard, Undergraduate
3. Marie Correia, Graduate Student
4. Daniel Serra, PhD–Graduation Date: 1/07
5. Corey Anthony, PhD–Expected Graduation Date: 5/06
6. Jianye Zhang, MS–Graduation Date: 05/07
7. Ying Yang, PhD, Graduation Date: 12/04

References

(1) Dillon, R.; Srinivasan, S.; Arico, A.S.; Antonucci, V. *J. Power Sources* **2004**, *127*, 112-126.

(2) Hogarth, M.P.; Ralph, T.R. *Platinum. Met. Rev.* **2002**, *46*, 146-164.

(3) Kua, J.; Goddard, W.A. *J. Am. Chem. Soc.* **1999**, *121*, 10928-10941.

(4) Matare, G.; Tess, M.E.; Abboud, K.A.; Yang, Y.; McElwee-White, L. *Organometallics* **2002**, *21*, 711-716.

(5) Tess, M.E.; Hill, P.L.; Torraca, K.E.; Kerr, M.E.; Abboud, K.A.; McElwee-White, L. *Inorg. Chem.* **2000**, *39*, 3942-3944.

(6) Yang, Y.; McElwee-White, L. *Dalton Trans.* **2004**, 2352-2356.

(7) Serra, D.; Abboud, K.A.; Hilliard, C.R.; McElwee-White, L. *Organometallics* **2007**, in press.

11. Ultrahigh Vacuum Investigations of Bimetallic Catalysts and the Development of Nanoparticle Catalysts for High-Pressure Applications

Task PI: Dr. Helena Hagelin-Weaver and Dr. Jason Weaver, Chemical Engineering, University of Florida

Collaborators: Dr. Lisa McElwee-White, Chemistry, Dr. David Hahn, and Dr. David Mikolaitis, Mechanical and Aerospace Engineering, University of Florida

PI(s): Helena E. Hagelin-Weaver and Jason F. Weaver

Research Period: August 3, 2004 to March 31, 2008

## Hydrogen Production via Steam Reforming of Methanol over Nanoparticle-Oxide-Supported Cu-ZnO Catalysts

Abstract

Methanol steam reforming was studied over several $CuO/ZnO/Al_2O_3$ catalysts supported on nanoparticle alumina with or without ZrO_2 or CeO_2 promoters. The results were compared to those of a commercially available copper, zinc oxide and alumina catalyst. The unpromoted nanoparticle supported catalysts achieved similar hydrogen production rates, but exhibited lower CO selectivities compared with the commercial reference catalyst, although they required slightly higher temperatures to reach the same methanol conversion. In contrast, the ZrO_2-promoted catalysts not only produced more hydrogen per methanol fed to the reactor, but the CO selectivities were significantly lower compared to the commercial catalyst. This is very important for fuel cell applications, where nearly CO-free hydrogen is needed. All nanoparticle-oxide-supported catalysts exhibited higher turnover frequencies, i.e. more hydrogen was formed per surface Cu atom, compared with the commercial reference catalyst. Consequently, the Cu on the surface of the $CuO/ZnO/nano-Al_2O_3$ and $CuO/ZnO/ZrO_2/nano-Al_2O_3$ catalysts is much more active compared with the Cu on the commercial catalyst. In particular, addition of nanoparticle ZrO_2 resulted in very active catalysts. Catalyst characterizations indicate that coking, i.e. carbon deposition, is not a significant deactivation pathway. Instead it appears that ZnO migrates on the surface during the reaction and partly covers the active Cu, which results in loss of activity. Our results suggest that the Cu^+/Cu^0 ratio is important both for the catalytic activity and the CO selectivity. Overall, this project demonstrates that nanoparticle Cu-ZnO catalysts are superior to conventional catalysts in meeting the demands for hydrogen generation for fuel cell applications and should be further studied for large scale processes.

Introduction

This project is part of a collaborative effort with the long term goal of understanding the detailed mechanisms involved in the catalytic reforming of higher hydrocarbons, like JP4. Detailed mechanisms are in turn necessary for the rational design of new catalyst materials and reforming processes. Specific improvement goals that may be met with more complete knowledge of the reforming process and rational catalyst design are higher efficiencies and yields, longer catalyst life and reduced coking, as well as cheaper catalyst cost. Unfortunately the current state of understanding of the kinetic details of the catalytic reforming of even simple fuels like methane, methanol, and ethanol is very incomplete. Hence understanding the details of the reforming process for these simple fuels is an important first step in achieving the long-range goal.

Steam reforming of hydrocarbons can be used to produce hydrogen (Equation 1).

$$C_n H_m + 2nH_2O \rightarrow nCO_2 + (\frac{m}{2} + 2n)H_2 \qquad (m \leq 2n + 2) \qquad (1)$$
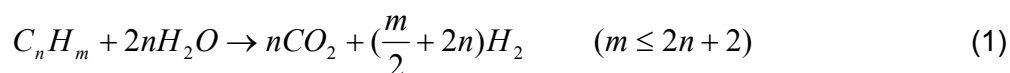
The advantage of steam reforming over partial oxidation (Equation 2) for hydrogen generation is evident when comparing the stoichiometry of the two reactions, since a significant portion of the hydrogen is generated from the water in the steam reforming reaction.

$$C_n H_m + \frac{n}{2}O_2 \rightarrow nCO + \frac{m}{2}H_2 \qquad (2)$$
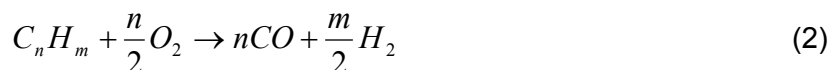
The objectives of this specific project were to develop new and more efficient methanol steam reforming catalysts (Equation 3), as well as to determine the catalytic properties which result in highly active catalysts. In addition to obtaining information about these catalysts for future development of other reforming catalysts, a second goal of this project was to produce hydrogen for fuel cell applications. Methanol is a very promising hydrogen source since 1) it contains a relatively high H:C ratio, 2) it can be reformed at low temperatures (below 300 °C), and 3) it does not lead to extensive coking of the reforming catalysts. Only methane has a higher H:C ratio, but methane requires considerably higher temperatures for reforming, which, in addition to higher energy requirements, can lead to severe catalyst deactivation due to coking. Another advantage of using methanol as a hydrogen source is that it is much safer to store methanol in fuel tanks and produce the hydrogen when needed compared with liquefied or pressurized hydrogen storage on board a vehicle. Furthermore, methanol can be produced using renewable fuels, such as biomass (via biomass gasification and methanol synthesis from the CO_2 containing synthesis gas [CO+H_2] produced during the biomass gasification).

$$CH_3OH + H_2O \rightarrow CO_2 + 3H_2 \qquad (3)$$

For fuel cell applications simply maximizing hydrogen production from methanol is not sufficient. The hydrogen produced also needs to be essentially CO free, since even ppm levels of CO in the hydrogen feed to fuel cells will poison the electrodes and degrade fuel cell performance. Consequently, an effective catalyst must give a high hydrogen yield while at the same time suppress CO formation. This is a complex problem since there are two CO forming reactions of importance in this system, 1) direct decomposition of methanol (Equation 4) and 2) the water-gas-shift reaction (Equation 5).

$$CH_3OH \rightarrow CO + 2H_2 \tag{4}$$

$$CO_2 + H_2 \leftrightarrow CO + H_2O \tag{5}$$

The most common methanol steam reforming catalyst is Cu-ZnO/Al$_2$O$_3$ [1]. Zinc oxide is a promoter added to improve the dispersion of the Cu and the reducibility of the CuO precursor, while Al$_2$O$_3$ is added to supply a high surface area on which to deposit the Cu and to reduce sintering of the Cu on the catalyst surface [2-6]. Our approach was to use nanoparticle Al$_2$O$_3$ as the support for Cu and ZnO and determine if this results in catalysts with unique catalytic properties. The use of nanoparticle support materials is motivated by the high active surface area per mass of catalyst that will be obtained, and the likelihood that the sizes of the active metal clusters will be intrinsically limited, and are therefore controllable by the nanoscopic size of the support oxide. Furthermore, the interactions between the active metal (in this case Cu) and the nanoparticle oxide support (Al$_2$O$_3$) may also be very different from interactions between more conventional supports and result in unique catalytic properties.

Background

Efficient hydrogen production from readily available hydrogen sources is particularly important for NASA to assure an uninterrupted supply of rocket fuel. Furthermore, portable proton exchange membrane fuel cells could be advantageous for several NASA relevant applications. A methanol steam reformer could potentially be placed between a regular fuel tank (filled with methanol instead of gasoline) and a PEM fuel cell to drive motor vehicles. This in turn has potential to reduce the US (and NASA's) dependence on foreign oil.

Experimental

Reactor System – As part of the project the following reactor system was designed and built (Figure 1). During a reaction experiment a mixture of water and methanol is pumped into the system via a syringe pump. Argon (Ar) at a constant flow rate is used to bring the methanol/water mixture to the evaporator. The Ar is also used as the internal standard in the product analysis using the on-line gas chromatograph (GC). After the evaporator the lines to and from the catalytic reactor are wrapped in heating tapes to avoid condensation of the water and methanol. The catalyst is placed in the center of the catalytic reactor, which in turn is placed in a tubular furnace so that the reaction temperature can be varied. After the reactor the unreacted methanol and water are removed before analysis of the reaction products.
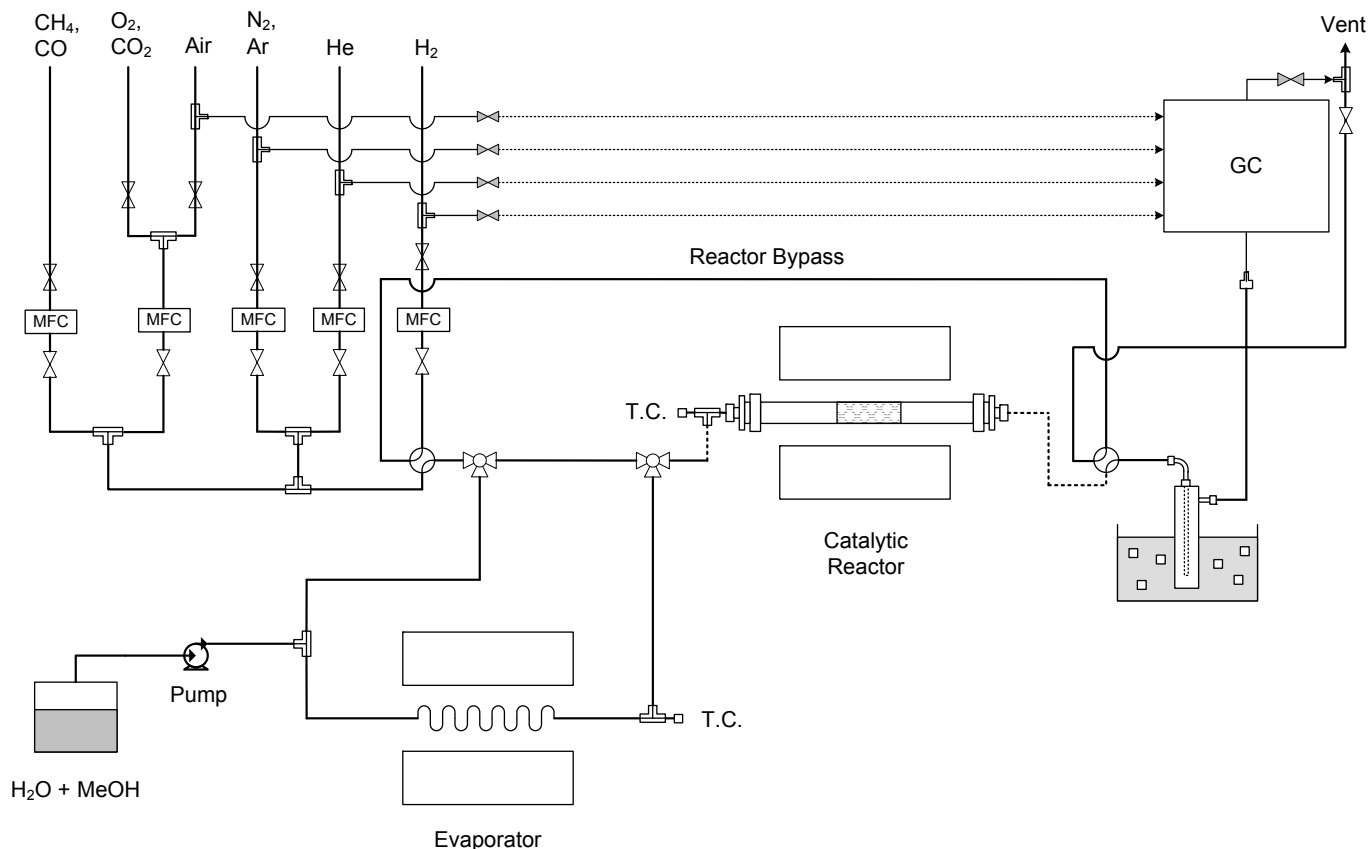
Figure 1. Reactor system for the catalytic steam reforming of methanol.

The reactor bypass was included to allow for calibration of all relevant components (H_2, CO, CO_2, CH_4). Air, nitrogen, helium and hydrogen are also needed to run the GC, which is why lines run directly to the GC, in addition to having the option of using these gases as input to the system.

Catalyst Preparation – Three generations of catalysts were prepared during this project. In the first set, Cu-ZnO catalysts supported on nanoparticle alumina were prepared using different compositions of Cu, ZnO and Al_2O_3 (The exact compositions are given in Table 1, together with preparation procedure). In the second set of catalysts we added CeO_2 and ZrO_2 in an attempt to improve the catalytic activity and lower the CO yields. Work on the third set of catalysts is on-going. In this set we have started preparing catalysts using a microemulsion technique to improve the Cu dispersion on the catalysts.

Table 1. Catalyst compositions, catalyst preparation methods and ZrO_2 or CeO_2 precursors used in the project.

Catalyst Label [a]	Composition [weight%]					Preparation [a]	ZrO_2 or CeO_2 Precursor [b]
	CuO	ZnO	ZrO_2	CeO_2	Al_2O_3		
1:st Generation							
CuZnAl-5/5/90-PR	5%	5%	-	-	90%	Seq. Prec.	N/A
CuZnAl-35/35/30-CI	35%	35%	-	-	30%	Seq. Imp.	N/A
CuZnAl-42/47/11-CI	42%	47%	-	-	11%	Seq. Imp.	N/A
2:nd Generation							
CuZnCeAl-10-CI	15%	15%	-	10%	60%	Co-Imp.	$Ce(NO_3)_2 \cdot 6H_2O$
CuZnZrAl-10-CI	15%	15%	10%	-	60%	Co-Imp.	$ZrO(NO_3)_2 \cdot 6H_2O$
CuZnZrAl-10-SQ	15%	15%	10%	-	60%	Seq. Imp.	$ZrO(NO_3)_2 \cdot 6H_2O$
CuZnZrAl-10-NP	15%	15%	10%	-	60%	Co-Imp.	Nano-ZrO_2
CuZnZrAl-36-CI	14%	14%	36%	-	36%	Co-Imp.	$ZrO(NO_3)_2 \cdot 6H_2O$
CuZnZr-70-NP	15%	15%	70%	-	-	Co-Imp.	Nano-ZrO_2
3:rd Generation							
CuZr-85-ME	15%	-	85%	-	-	μ-Emulsion	Nano-ZrO_2
CuZnZr-70-ME	15%	15%	70%	-	-	μ-Emulsion	Nano-ZrO_2
CuZnZrAl-10-ME	15%	15%	10%	-	60%	μ-Emulsion	Nano-ZrO_2
CuZnAl-35/35/30-ME	35%	35%	-	-	30%	μ-Emulsion	N/A

[a] Seq. Prec.= Sequential Precipitation; Seq. Imp.= Sequential Impregnation; Co-Imp.= Co-Impregnation; μ-Emulsion = micro-emulsion.
[b] N/A = not applicable. Nano-ZrO_2 = nanoparticle ZrO_2.

Most catalysts were either co- or sequentially impregnated. Using the co-impregnation method the catalysts were prepared by dissolving proper amounts of $Cu(NO_3)_2 \cdot 6H_2O$ (Alfa Aesar) and $Zn(NO_3)_2 \cdot 6H_2O$ (Alfa Aesar) [and $ZrO(NO_3)_2 \cdot 6H_2O$ or $Ce(NO_3)_2 \cdot 6H_2O$ where applicable] in deionized water. An aqueous dispersion of commercial nanoparticle Al_2O_3 (NanoScale, surface area ~650 m^2/g) was added to the metal ion solution. The excess water was boiled off under vigorous stirring and the paste was dried at 105 °C overnight. The sample was then calcined at 300 °C for 3 hours (heated in air to decompose the nitrates and form the corresponding metal oxide). In the sequentially impregnated method the ZnO was deposited before the CuO (CuZnAl-35/35/30 and CuZnAl-42/47/11), or the ZrO_2 was deposited before the CuO and ZnO (CuZnZrAl-10-SQ). The CuZnAl-5/5/90 was prepared via sequential precipitation in which the ZnO was deposited before the CuO by forced precipitation from an aqueous dispersion of $Zn(NO_3)_2 \cdot 6H_2O$ and nanoparticle Al_2O_3 using a NaOH solution. After filtration, drying and calcination the resulting $ZnO/nano-Al_2O_3$ was redispersed in an aqueous solution of $Cu(NO_3)_2$ and the precipitation step repeated to deposit the CuO on the $ZnO/nano-Al_2O_3$. The recovered catalyst after filtration was then dried and calcined as above. In some cases, for the second generation catalysts ZrO_2 was added as nanoparticles instead of as an aqueous nitrate solution (CuZnZrAl-10-NP and CuZnZr-70-NP).

Catalyst Characterization – The prepared catalysts were subjected to activity measurements in the reactor system to determine the hydrogen yields as well as the amount of CO formed. The amount of CO formed for each catalyst is presented as the CO selectivity, which is the fraction of CO formed of the total CO plus CO_2 produced (Equation 6, where P_{CO_x} is the partial pressure or molar concentration of CO and CO_2). The catalysts where also characterized using several surface analytical methods. More details on these measurements are given in our manuscripts [7,8]. The following properties where determined for each of the catalysts: BET (Brunauer-Emmett-Teller) surface areas (using N_2 physisorption), Cu surface areas (using N_2O decomposition experiments), CuO reduction properties (using temperature programmed reduction, TPR), surface composition (using X-ray photoelectron spectroscopy, XPS), and catalyst structure (using X-ray diffraction, XRD).

$$S_{CO} = \frac{P_{CO}}{P_{CO} + P_{CO_2}} * 100\% \qquad (6)$$

Results and Discussion

Activity Measurements – For each catalyst, the hydrogen, carbon monoxide and carbon dioxide produced was measured at a water to methanol ratio of 3.1 (mol/mol). In one set of experiments the water/methanol feed was set at a flow rate of (0.8 ml/hour [liquid flow rate]) and the temperature was varied. In the second set of experiments the temperature was fixed at 280 °C, which is the temperature of maximum conversion for the commercial catalyst, and the water/methanol flow rate was varied. Varying the feed rate alters the "contact time", which is a measure of the time that the reactants (methanol and water) are in contact with the catalysts. Increasing flow rates, decreases the contact time, which also decreases the methanol conversion since there is less time to react.

First Generation Catalysts – The hydrogen production rate as a function of temperature at the specified constant feed flow rate is presented in Figure 2a for the first generation catalysts. As can be seen in the figure, the hydrogen produced over this set of catalysts is lower than for the commercial catalyst at temperatures below 280 °C. Only at higher temperatures, where the commercial catalyst exhibits significant deactivation, do the first generation catalysts outperform the commercial reference catalyst. Consequently, the first generation catalysts can produce more hydrogen than the commercial reference, but only at higher temperatures. This is usually undesirable, since higher temperatures also typically lead to higher CO concentrations (See Figure 3).
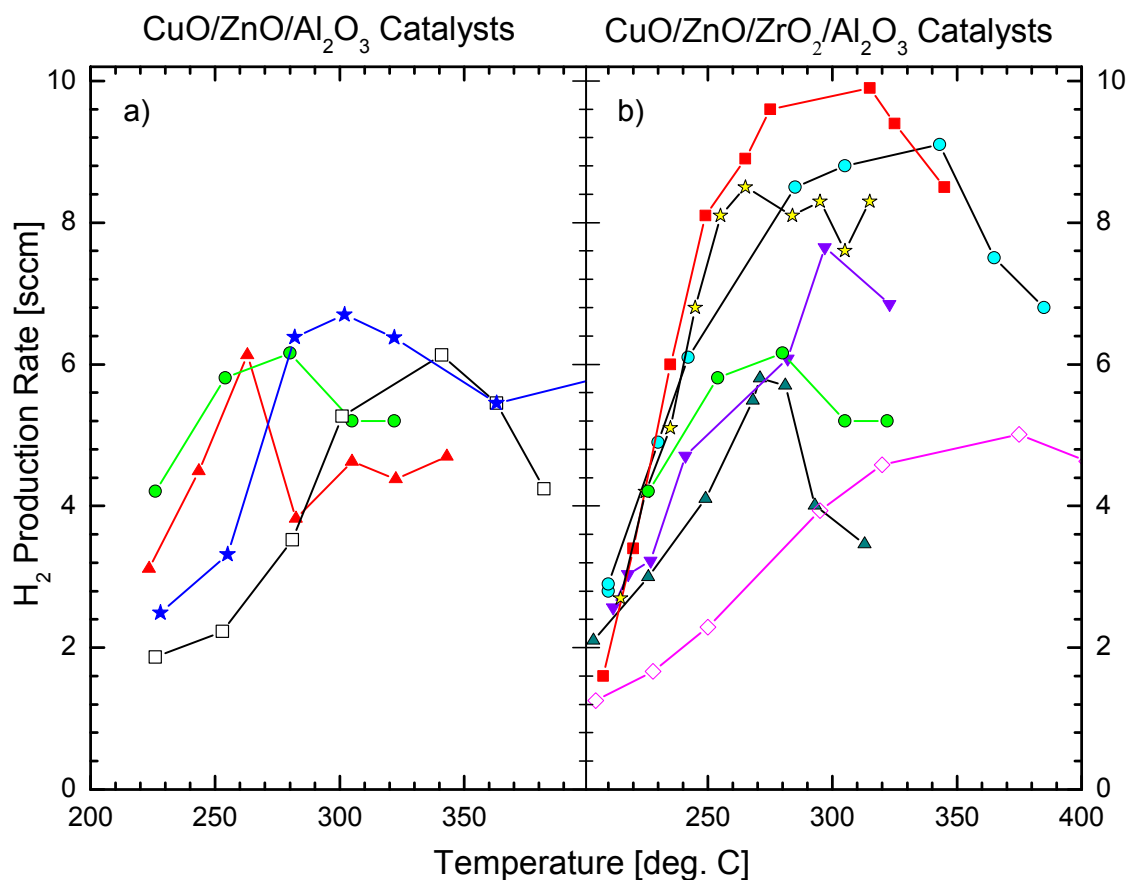
CuO/ZnO/Al$_2$O$_3$ Catalysts   CuO/ZnO/ZrO$_2$/Al$_2$O$_3$ Catalysts

Figure 2. Hydrogen production rate [in standard cubic centimeters, (sccm)] as a function of temperature at water:methanol = 3:1 (mol/mol) and a total liquid flow rate of 0.8 ml per hour for a) the first generation catalysts: CuO/ZnO/Al$_2$O$_3$ and b) the second generation catalysts: CuO/ZnO/ZrO$_2$/Al$_2$O$_3$. a) ●: Commercial Reference, □: CuZnAl-5/5/90-PR, ★: CuZnAl-35/35/30-Cl; ▲: CuZnAl-42/47/11-Cl. b) ●: Commercial Reference, ■: CuZnZrAl-10-NP, ●: CuZnZrAl-10-Cl, ★: CuZnZrAl-10-SQ, ▲: CuZnCeAl-10-Cl, ▼: CuZnZrAl-36-Cl, ◇: CuZnZr-10-NP.

However, the nanoparticle oxide supported catalysts exhibit very interesting CO selectivity behavior below temperatures of 300 °C (below 265 °C for the CuZnAl-42/47/11-Cl catalyst, see Figure 3a). While the CO selectivity of the commercial catalyst increases continuously with temperature, our catalysts exhibit a slight decrease in CO selectivity with increasing temperature up to approximately 300 °C. This is very interesting since both CO producing reactions (the direct methanol decomposition (Equation 4) and the reverse water-gas-shift (Equation 5)) are endothermic, which means that both thermodynamics and kinetics predict an increasing rate of CO production with increasing temperatures. Consequently, the CO$_2$ production rate must increase more than the CO production rate in this temperature range. This is a unique feature of the nanoparticle oxide supported catalysts, and it means that the reaction conditions can be tuned so that our first generation catalysts produce less CO at the same hydrogen production rate.

This is very important since our goal is to both maximize the hydrogen produced and minimize the CO formed. Therefore, when comparing catalysts it is important to consider the CO selectivity at similar H_2 yields, since the catalyst with the highest hydrogen production rate is not necessarily the best catalyst if it also forms significant quantities of CO. One way to "tune" reaction conditions is to alter the feed flow rate, and thus also the "contact time". Data as a function of contact time is better presented in terms of methanol conversion rather than hydrogen production rates. This is due to the fact that the methanol conversion increases with increasing contact time, but since the feed rate is slower at longer contact times, the actual hydrogen production rate is lower (there is less methanol fed to the reactor, but more of the methanol reacts). Therefore, in Figure 4 the CO selectivites are compared at different methanol conversions.
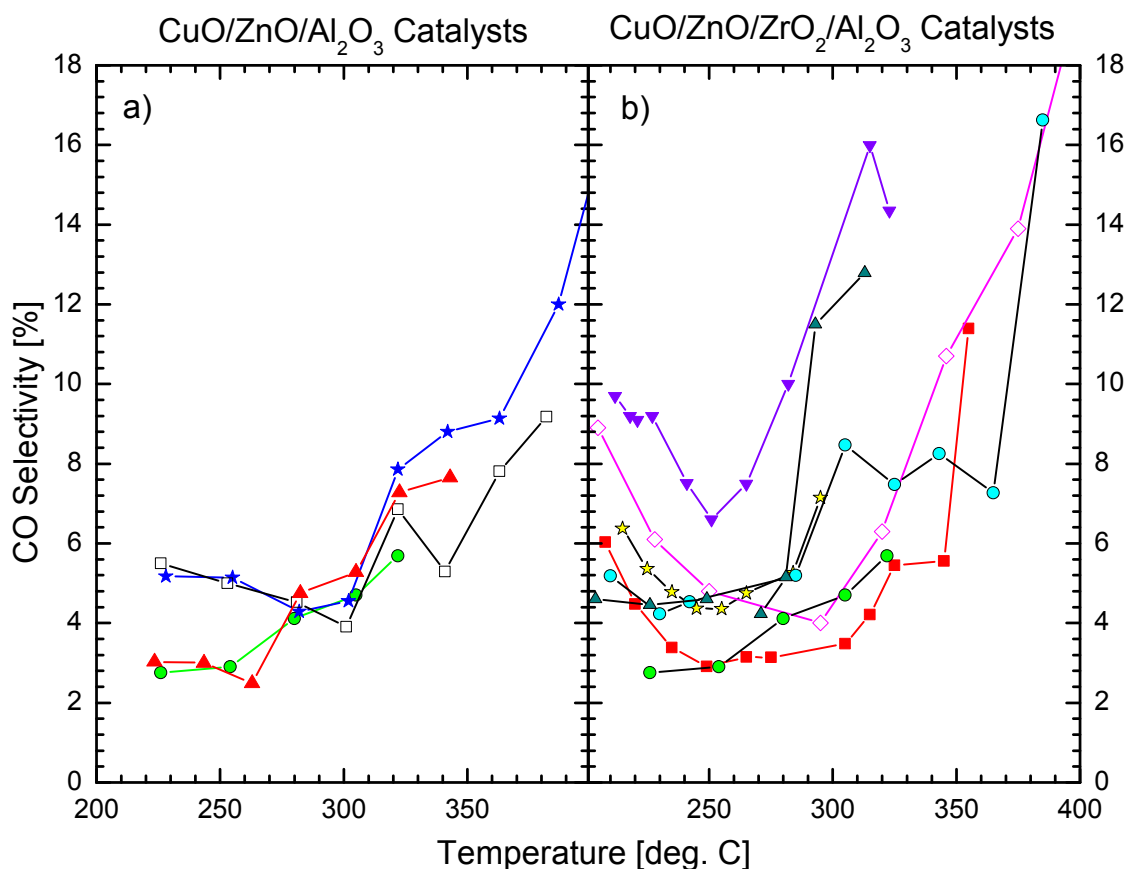
Figure 3. CO selectivity as defined in Equation 6 as a function of temperature (at water:methanol = 3:1 (mol/mol) and a total liquid flow rate of 0.8 ml per hour) for a) the first generation catalysts: $CuO/ZnO/Al_2O_3$ and b) the second generation catalysts: $CuO/ZnO/ZrO_2/Al_2O_3$. a) ● : Commercial Reference, □ : CuZnAl-5/5/90-PR, ★ : CuZnAl-35/35/30-CI; ▲ : CuZnAl-42/47/11-CI. b) ● : Commercial Reference, ■ : CuZnZrAl-10-NP, ● : CuZnZrAl-10-CI, ★ : CuZnZrAl-10-SQ, ▲ : CuZnCeAl-10-CI, ▼ : CuZnZrAl-36-CI, ◇ : CuZnZr-10-NP.
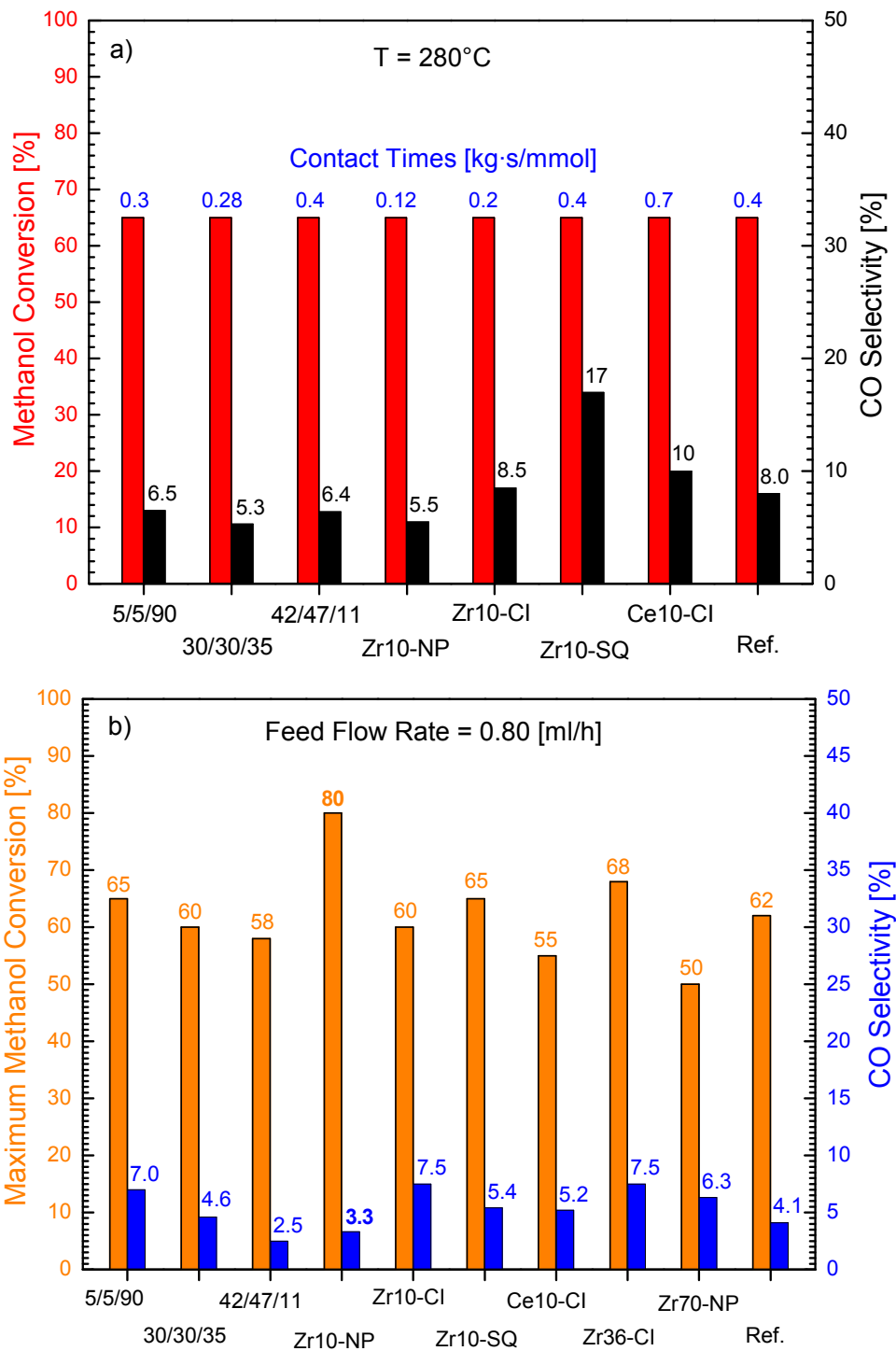
Figure 4. Methanol conversion and CO selectivities for 1:st and 2:nd generation catalysts, a) at 65% methanol conversion and T = 280 °C (contact time for each catalyst given in blue) and b) at the maximum methanol conversion, feed flow rate = 0.8 ml/hour (varying temperature).
5/5/90 = CuZnAl-5/5/90-PR, 35/35/30 = CuZnAl-35/35/30-CI, 42/47/11 = CuZnAl-42/47/11-CI, Zr10-NP = CuZnZrAl-10-NP, Zr10-CI = CuZnZrAl-10-CI, Zr10-SQ = CuZnZrAl-10-SQ, Ce10-CI = CuZnCeAl-10-CI, Zr36-CI = CuZnZrAl-36-CI, Zr70-NP = CuZnZr-70-NP, and Ref. = Reference commercial catalyst.

Second Generation Catalysts – Since literature data has indicated that addition of ZrO_2 can be beneficial to methanol steam reforming catalysts, we prepared a set of ZrO_2–promoted "second generation" catalysts. We tested two ZrO_2 precursors ($ZrO(NO_3)_2 \cdot 6H_2O$ and nanoparticle ZrO_2) and two preparation methods (co-impregnation and sequential impregnation) to determine the best way of adding ZrO_2 to our catalysts (see Experimental Section). The results for these catalysts are presented in Figure 2b, 3b, and 4. As is evident in Figure 2b, addition of ZrO_2 results in very active catalysts. The hydrogen production rates for the CuZnZrAl-10-NP, CuZnZrAl-10-CI, CuZnZrAl-10-SQ catalysts are significantly higher than that of the commercial reference catalyst. These catalysts are thus significantly more effective than the first generation catalysts. Only the CuZnZrAl-36-CI and the CuZnZr-70-NP catalysts exhibit lower H_2 yields (at least below 280 °C for the CuZnZrAl-36-CI) than the commercial reference (Figure 2b). Consequently, addition of ZrO_2 is very beneficial to the methanol steam reforming catalysts, if the concentrations are kept low, such as 10%. The best performing catalyst is prepared via co-impregnation of Cu and Zn nitrates on a physical mixture of nanoparticle ZrO_2 and nanoparticle Al_2O_3. Not only does this catalyst produce the highest amount of H_2, it also forms the lowest amount of CO in the temperature range from 265 to 325 °C (Figure 3b). This is remarkable since the CO selectivity normally increases rapidly with increasing conversion [5,6].

Catalyst Characterization – In an attempt to determine the material properties of importance for highly efficient catalysts, all prepared catalysts were subjected to materials characterization measurements using a number of techniques.

Surface Area Measurements – The first properties to be measured were the overall surface areas and the Cu surface areas of the catalysts. If the catalysts are not structure sensitive it would be expected that the hydrogen production rate, or the methanol conversion, will be proportional to the catalyst Cu surface areas. If on the other hand the reaction is structure sensitive, which means that only certain phases of Cu are active, then there would be no or limited correlation between the activity and the Cu surface area. As can be seen from Figure 5, there is no correlation between the measured Cu surface areas and the catalytic activities under the conditions used in the experiments. In this case the catalytic activity was calculated as turnover frequency, which is mol of H_2 produced per Cu surface atom per second. It is interesting to note that all catalysts have a higher turnover frequency than the commercial reference catalyst, despite the fact that the TOF was calculated at the temperature of maximum conversion for the commercial catalyst. Consequently, the copper on both the first generation and the second generation catalysts is more active than the copper on the commercial reference catalyst. Furthermore, addition of ZrO_2 results in even more active Cu species, particularly if it is in the form of nanoparticle ZrO_2. The most active Cu species is found on the CuZnZr-70-NP catalyst, but this catalyst is limited by its low Cu surface area. These results indicate that the nanoparticle oxide supported catalysts can be improved further by increasing the Cu surface areas, perhaps by using different catalyst preparation techniques. Research has been initiated where a micro-emulsion technique is used to prepare catalysts in an attempt to improve the Cu dispersion (i.e. the Cu surface area).
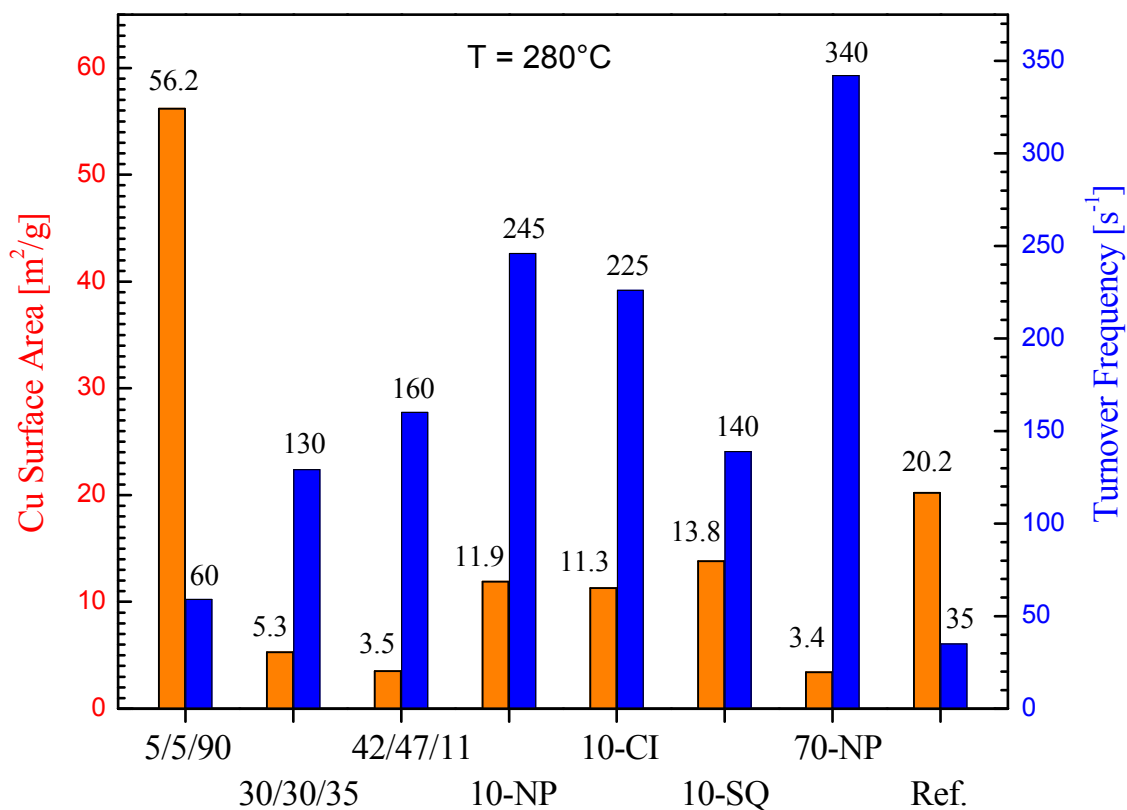
Figure 5. Cu surface areas and catalyst turnover frequencies (TOFs) at T = 280 °C for selected 1:st and 2:nd generation catalysts. 5/5/90 = CuZnAl-5/5/90-PR, 35/35/30 = CuZnAl-35/35/30-CI, 42/47/11 = CuZnAl-42/47/11-CI, 10-NP = CuZnZrAl-10-NP, 10-CI = CuZnZrAl-10-CI, 10-SQ = CuZnZrAl-10-SQ, 70-NP = CuZnZr-70-NP, and Ref. = Reference commercial catalyst.

Temperature Programmed Reduction – Since the catalysts during reaction undergo repeated oxidation-reduction cycles, the reduction properties of the catalysts can be important to attaining a high catalytic activity. The unreduced catalysts (containing CuO on the catalyst surface), were therefore reduced under controlled conditions (the temperature was increased at a fixed rate of 5°/min keeping the catalyst under a stream of H_2). Several studies have shown that catalysts which are easier to reduce, i.e. the CuO on the surface reduces to Cu metal at low temperatures, exhibit higher catalytic activities than catalysts which are more difficult to reduce, i.e. those that require a higher temperature for reduction [6]. However, this is not always the case [9]. The data for the catalysts in this study is presented in Figures 6a and b. While the more active catalysts from the first generation set are easier to reduce compared to catalysts of lower activities, this is not true for the second generation catalysts. In fact, the most active catalyst from the second generation set (CuZnZrAl-10-NP) has the highest reduction temperature of all catalysts. Consequently, there is no simple correlation between the ease of CuO reduction and the catalytic activity for these catalysts.
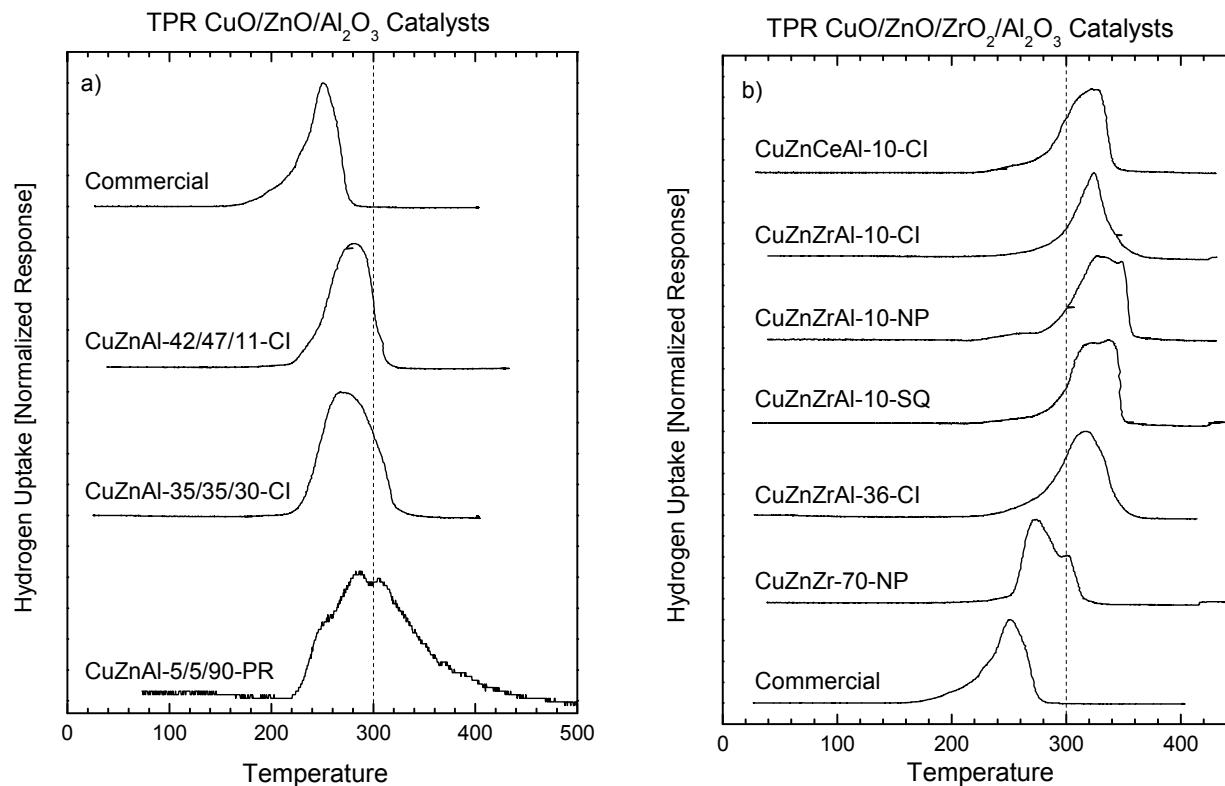
Figure 6. Temperature programmed reduction (TPR) experiments of a) first generation catalysts and b) second generation catalysts.

XRD Measurements – To obtain more information about these catalysts, they were subjected to XRD analysis. While all catalysts will be subjected to these measurements, only the results from the first generation catalysts have been processed at this time. The results from the catalysts before and after reaction are presented in Figures 7a and b. The CuO phase is evident on all catalysts before reaction. ZnO is also visible on the CuZnAl-35/35/30-Cl and CuZnAl-42/47/11-Cl catalysts. Only on the CuZnAl-5/5/90-PR catalyst is the γ-Al$_2$O$_3$ visible (the nanoparticle support). The reason for this is that the alumina phase is poorly crystalline, so the concentration of alumina must be high for the alumina to be visible with XRD. In the presence of other crystalline species, 35% alumina (by weight) is not sufficient.

After reduction and reaction Cu metal is visible on all catalysts and the ZnO phase is unchanged. On the CuZnAl-35/35/30-Cl catalyst another crystalline phase is also present. The peaks in the XRD spectra are consistent with both CuAl$_2$O$_4$ and ZnAl$_2$O$_4$. Our results indicate that ZnAl$_2$O$_4$ is more likely, but we cannot exclude the presence of CuAl$_2$O$_4$. The presence of a spinel (ZnAl$_2$O$_4$ or CuAl$_2$O$_4$) phase may actually be advantageous if it can reduce negative Cu-Al$_2$O$_3$ interactions. Strong metal support interactions between the Cu and the Al$_2$O$_3$ appear to result in catalysts with lower activities. On the CuZnAl-5/5/90-PR catalyst it is possible to identify a Cu$_2$O phase on the catalyst after reaction (Figure 8). This phase is not present after only the pre-reduction before the reaction experiments (see Figure 8). Thus, the Cu$_2$O phase is formed during the reaction, through oxidation by the water. It is possible that this phase is responsible for the catalytic activity in the steam reforming reaction of methanol over these catalysts.
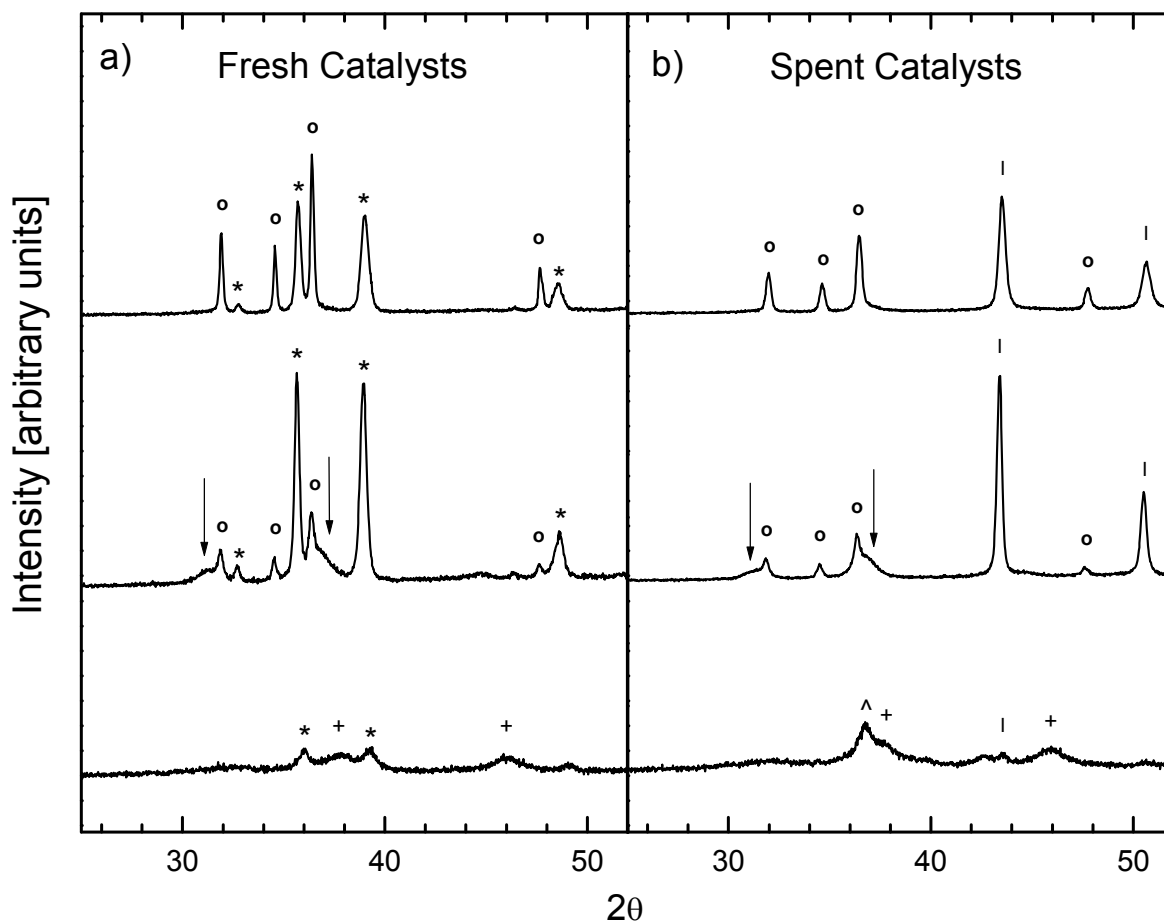
Figure 7. XRD spectra obtained from A) fresh and B) spent $CuO/ZnO/Al_2O_3$ catalysts, a) 5/5/90 $CuO/ZnO/Al_2O_3$ catalysts, b) 35/35/30 $CuO/ZnO/Al_2O_3$ catalysts and c) 42/47/11 $CuO/ZnO/Al_2O_3$ catalysts. +: γ-Al2O3, *: CuO, **o**: ZnO, I: Cu metal, ^: Cu_2O. Arrows indicate peaks due to $ZnAl_2O_4$.

XPS Measurements – The XPS measurements on the first generation catalysts confirm the presence of CuO on the catalysts before reduction and Cu_2O on the surface of the catalysts after reaction.
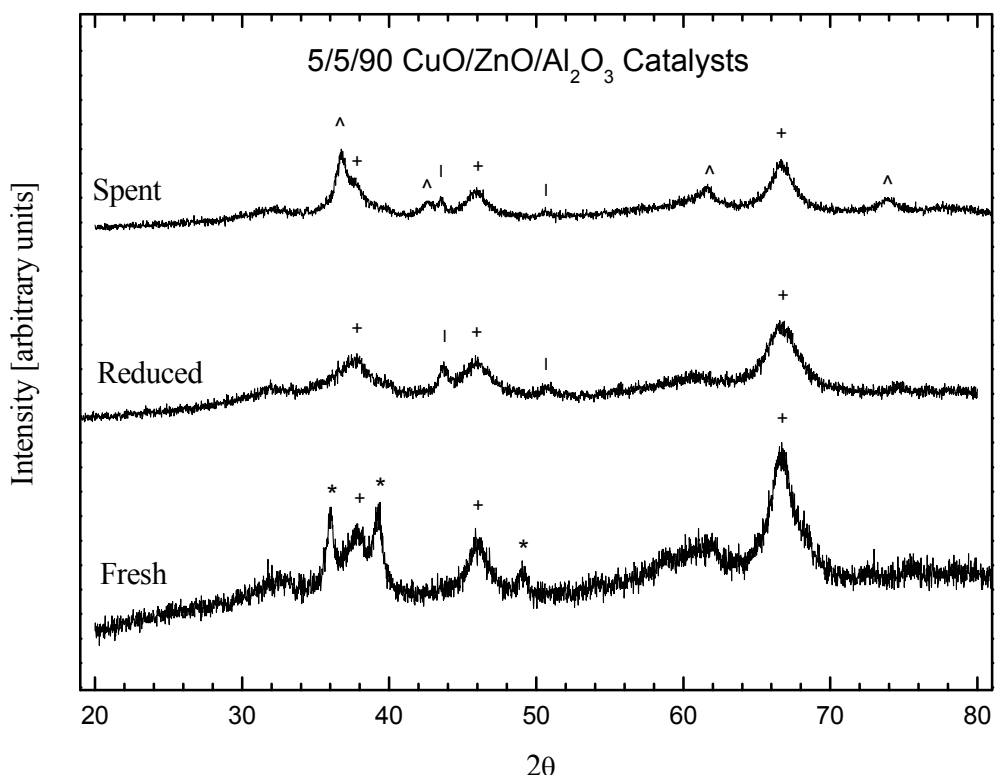
Figure 8. XRD spectra obtained from a) fresh, b) reduced and c) spent 5/5/90 CuO/ZnO/Al$_2$O$_3$ catalysts. . +: γ-Al2O3, *: CuO, I: Cu metal, ^: Cu$_2$O.

Conclusions

The above results demonstrate that the use of nanoparticle oxides as supports can result in highly active and unique methanol reforming catalysts. Addition of alumina is necessary to assure a high Cu surface area, and thus also a high catalytic activity. However, high concentrations of alumina leads to Cu species with a lower activity compared to catalysts with lower alumina concentrations. Addition of ZrO$_2$ to Cu-ZnO catalysts supported on nanoparticle alumina results in catalysts with improved performance. Under similar conditions, our ZrO$_2$-promoted catalysts achieve higher hydrogen production rates and lower CO selectivities in the methanol steam reforming reaction compared to the commercial reference catalyst. Co-impregnation of CuO and ZnO precursors onto a mixture of nanoparticle ZrO$_2$ and Al$_2$O$_3$ results in a catalyst with the best performance of the catalysts tested, i.e. the highest hydrogen production rate with the second lowest CO selectivity. This is remarkable since the undesirable CO concentrations usually increase with increasing hydrogen production rates. Adding CeO$_2$ to the catalysts resulted in lower hydrogen production rates and higher CO selectivities compared with the commercial catalyst.

Catalyst characterization revealed that the Cu on the surface of the nanoparticle-oxide-supported catalysts is more active than the Cu on the commercial reference, i.e. more H_2 was formed per surface Cu atom. It was also found that the Cu on catalysts containing nanoparticle ZrO_2 had even higher turnover frequencies than the Cu-ZnO supported on nanoparticle alumina. On the prepared catalysts there is not a simple correlation between Cu surface area and the catalytic activity. Furthermore, the ease of CuO reduction to Cu on the catalysts does not correlate with the activity. Part of the reason for this may be that the catalytic activity is dependent on the Cu_2O to Cu metal ratio on the surface. Cu_2O was identified on the surface of the catalysts after reaction using XRD and XPS, and it is possible that Cu_2O is needed for methanol adsorption and oxidation and that the Cu metal is required for H_2O decomposition. The ZrO_2 may serve to increase the Cu_2O to Cu metal ratio, which could increase the methanol conversion and thus also the hydrogen production rate. A higher oxidation state is also likely to increase the CO_2 over the CO produced.

In summary, the use of ZrO_2 nanoparticles results in highly active copper phases that promotes the steam reforming reaction and suppresses CO formation well beyond that achieved with a commercial catalyst. The combined effects result in unique, promising catalysts for the methanol steam reforming in fuel cell applications. New catalyst preparation techniques are currently being tested to improve the Cu surface areas, particularly of the nanoparticle ZrO_2 catalysts, and this can increase the activity per unit weight of catalyst and result in even more efficient catalysts.

Publications

Two papers have been submitted at this point (see below). However, two more papers are expected from this project. One of the future papers will contain the catalyst characterization data from the second generation catalysts and the fourth paper will summarize the results for the third generation catalysts.

1) Steam Reforming of Methanol using Cu-ZnO Catalysts Supported on Nanoparticle Alumina, Samuel D. Jones, Luke M. Neal and Helena E. Hagelin-Weaver, *Submitted for Publication*.

2) Steam Reforming of Methanol over CeO_2- and ZrO_2-Promoted Cu-ZnO Catalysts Supported on Nanoparticle Al_2O_3, Samuel D. Jones and Helena E. Hagelin-Weaver, *Submitted for Publication*.

Presentations

1) Role of Copper Spinels in methanol reforming using Cu-ZnO catalysts on Nano-particle Alumina, presented by Samuel D. Jones at the AIChE (American Institute of Chemical Engineers) Annual Meeting in San Francisco, CA on November 15th, 2006.

2) Steam Reforming of CH_3OH over ZrO_2-Promoted Cu-ZnO/Nano-Al_2O_3 Catalysts, presented by Helena Hagelin-Weaver at the Florida AVS (American Vacuum Society) meeting, in Orlando, FL on March 11, 2008.

Students from Research

Samuel D. Jones, Ph.D., anticipated graduation date: Spring 2009.
Luke M. Neal, Ph.D. (partially supported), anticipated graduation date: Spring 2009.

Funding Obtained by Leveraging NASA Grant

Proposals have been submitted and more are planned, but no project has been funded so far.

Collaborations

Dr. Lisa McElwee-White, Department of Chemistry, University of Florida
Dr. David Hahn and Dr. David Mikolaitis, Department of Mechanical and Aerospace Engineering, University of Florida
Dr. Eric Wachsman, Department of Materials Science and Engineering, University of Florida
Dr. Mark Orazem, Department of Chemical Engineering, University of Florida

Acknowledgements

References

1. N.E. Vanderborgh, B.E. Goodby, T.E. Springer, Proc. 32nd Int. Power Sources Symp. (1986) 623-628.
2. B. Peppley, J.C. Amphlett, L.M. Kearns, R.F. Mann, Appl. Catal. A 179 (1999) 21-29.
3. V. Agarwal, S. Patel, K.K. Pant, Appl. Catal. A 279 (2005) 155-164.
4. J. Agrell, H. Birgersson, M. Boutonnet, I. Melian-Cabrera, R.M. Navarro, and J.L.G. Fierro, J. Catal. 219 (2003) 389-403.
5. H. Purnama, T. Ressler, R.E. Jentoft, H. Soerijanto, R. Schlogl, R. Schomacker, Appl. Catal. A 259 (2004) 83-94.
6. J.P. Breen, F.C. Meunier, J.R.H. Ross, Chem. Comm. (1999) 2247-2248.
7. "Steam Reforming of Methanol using Cu-ZnO Catalysts Supported on Nanoparticle Alumina," Samuel D. Jones, Luke M. Neal and Helena E. Hagelin-Weaver, *Submitted*.
8. "Steam Reforming of Methanol over CeO_2- and ZrO_2-Promoted Cu-ZnO Catalysts Supported on Nanoparticle Al_2O_3," Samuel D. Jones and Helena E. Hagelin-Weaver," *Submitted*.
9. C.Z. Yao, L.C. Wang, Y.M. Liu, G.S. Wu, Y. Cao, W.L. Dai, H.Y. He, K.N. Fan. Appl. Catal. A. 297 (2006) 151-158.

Date of Report: 04/07/08

12. In Situ Investigation of Major and Minor Species to Support Detailed Model Development of Catalytic Chemistry in a Reformation Reactor

Task PI: Dr. David Hahn, Mechanical & Aerospace Engineering

Collaborators: Dr. Lisa McElwee-White, Chemistry, Dr. David Mikolaitis, Mechanical & Aerospace Engineering, Dr. Helena Hagelin-Weaver, Chemical Engineering, and Dr. Jason Weaver, Chemical Engineering

Graduate Student: Amy L. Twining, Mechanical & Aerospace Engineering

A final report was submitted for this project. It is given again in this report.

Research Period: August 3, 2004 to April 1, 2006

Abstract

The research project is focused on the development and construction a laboratory-scale reformer/combustor designed for *in situ* Raman along the length of the reactor. This optical access reactor enables measurement of the evolution of reformate gases or reactants/combustion products, thereby providing a clearer picture of the progression of the reforming/reaction progress for various feed stocks, water-gas shift, and carbon build up reactions. As constructed, the system will enable precise, temporally/spatially resolved measurements, providing information as to the mechanisms and effects of fuel impurities. This work supports complementary efforts focused on the development of gas-phase and surface kinetic models for reformation and combustion over various catalytic surfaces.

Project Goals

The research project is focused on the development and construction of a laboratory-scale reformer/combustor designed for in situ Raman spectroscopy and laser-induced fluorescence (LIF) along the length of the reactor. This optical access reactor will enable measurement of the evolution of reformate gases or reactants/combustion products, will provide a clearer picture of the progression of the reforming/reaction progress for various feed stocks, water-gas shift, and carbon build up reactions. Such a system will also enable precise, temporally/spatially resolved measurements, providing information as to the mechanisms and effects of fuel impurities. This work will support complementary efforts focused on the development of gas-phase and surface kinetic models for reformation and combustion over various catalytic surfaces.

Brief Description

The research project is focused on the development and construction a laboratory-scale reformer/combustor designed for *in situ* Raman along the length of the reactor. This optical access reactor enables measurement of the evolution of reformate gases or reactants/combustion products, thereby providing a clearer picture of the progression of the reforming/reaction progress for various feed stocks, water-gas shift, and carbon build up reactions. As constructed, the system will enable precise, temporally/spatially resolved measurements, providing information as to the mechanisms and effects of fuel impurities. This

work supports complementary efforts focused on the development of gas-phase and surface kinetic models for reformation and combustion over various catalytic surfaces.

Reactor Design

As reported in the previous Midterm Report, the optical access reactor was constructed to enable study of the composition of the chemical boundary layer above the catalyst bed in steam methanol reforming. The catalyst bed (24" long by 1" wide) was constructed using Katalco 33-5 catalyst pellets, which are manufactured by Johnson Matthey and are comprised of 64 wt % CuO, 24 wt % ZnO, 10 wt % Al_2O_3, and 2 wt% MgO. The pellets measure 5.2 mm diameter by 5.4 mm length. To form the reactor bed, they were packed end-to-end in a single layer. The bed was housed in a vessel constructed from 2.75" vacuum flanges, as shown in Figure 1. Optical access was obtained through windows mounted on the 6-way flanges. Progress this quarter involves implementation of the laser-based diagnostics and preliminary measurements.
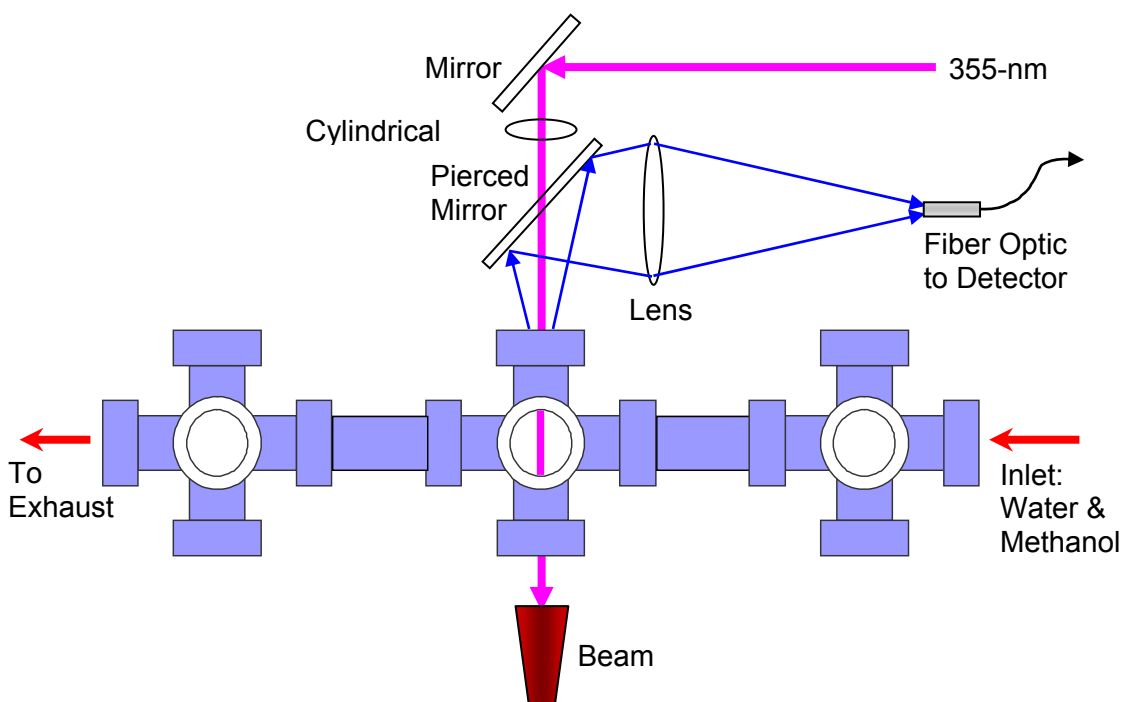
Figure 1. Top View of Optical Access Reactor.

Laser-Diagnostics

The primary diagnostic for this study is Raman spectroscopy. Raman spectroscopy was implemented using a frequency-tripled (355-nm), Nd:YAG laser. The laser was operated in the Q-switched mode, with a pulse width of about 10 ns FWHM, and a pulse repetition rate of 5 Hz. The laser was focused onto the central axis of the reactor using a 250-mm focal length cylindrical lens. This formed a rectangular laser beam above the reactor bed, with a beam height of about 1 mm and a beam width of 6 mm. The laser pulse energy was held constant at 50 mJ/pulse, resulting in a fluence of about 800 mJ/cm^2.

The optical configuration is also shown in Figure 1. The laser beam was passed through a 100-mm square mirror pierced with a 12.5-mm diameter hole. Raman scattered light was

collected in back-scatter, separated from the incident beam path using the pierced-mirror, and launched into a fiber optic bundle using a 100-mm diameter, 250-mm focal length collection lens. Prior to the fiber optic, the collected light was passed through a 375-nm high pass filter, a 440-nm low pass filter, and a 355-nm razor edge filter. The low-pass filter functioned to remove any residual 532-nm light from the tripling process. The fiber optic was coupled to a 0.275-m grating spectrometer (2400 groove/mm grating, 0.12 nm optical resolution), where spectral data were recorded using an intensified CCD detector array. A 250-ns detector gate was centered on the laser pulse, to minimize background light or time-delayed fluorescence signals.

Catalyst Reduction

For reformation to occur, the catalyst must be in the reduced state. That is, the pellets must be heated in a nitrogen/hydrogen environment to reduce (remove oxygen from) the catalyst surface. This was accomplished by heating the catalyst bed in an N_2 atmosphere to an initial temperature of about 130 °C. A hydrogen flow of 10% was then added to the nitrogen, and the temperature was slowly increased to about 180 °C. The hydrogen concentration was then increased to 20%, and the temperature slowly increased to between 215 and 220 °C. At this point, the reduction was observed to begin, as monitored using Raman spectroscopy.

During the reduction process, Raman spectra were recorded about every 5 to 10 minutes. Representative spectra are presented in Figure 2, including spectra corresponding to the beginning, mid-point, and essentially completion of the reduction process. The initial spectrum shows no Raman signal other than the hydrogen band corresponding to the 20% hydrogen flow. The hydrogen band corresponds to the 4156 cm^{-1} fundamental vibrational mode. During the reduction process, the hydrogen signal was observed to decrease, and a water signal was observed at 3654 cm^{-1}, which corresponds to the primary O-H symmetric stretch of gaseous water. Finally, at the end of reduction process, the Raman spectra once again were characterized by primarily hydrogen. The integrated hydrogen and water vapor signals as a function of time are presented in Figure 3 for the reduction process. Overall, the reduction process involves the absorption of H_2 to the catalyst surface, where it reacts with absorbed oxygen to form H_2O, which is then released from the surface resulting in an available active site.
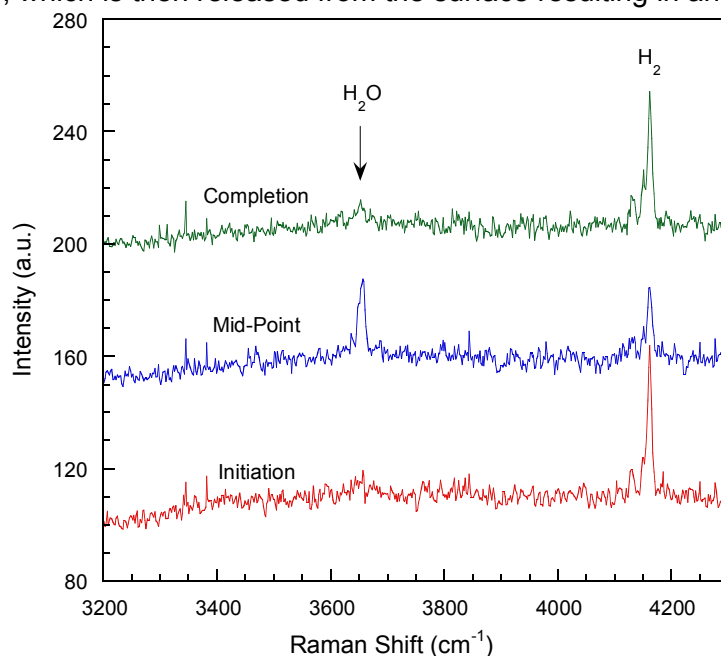

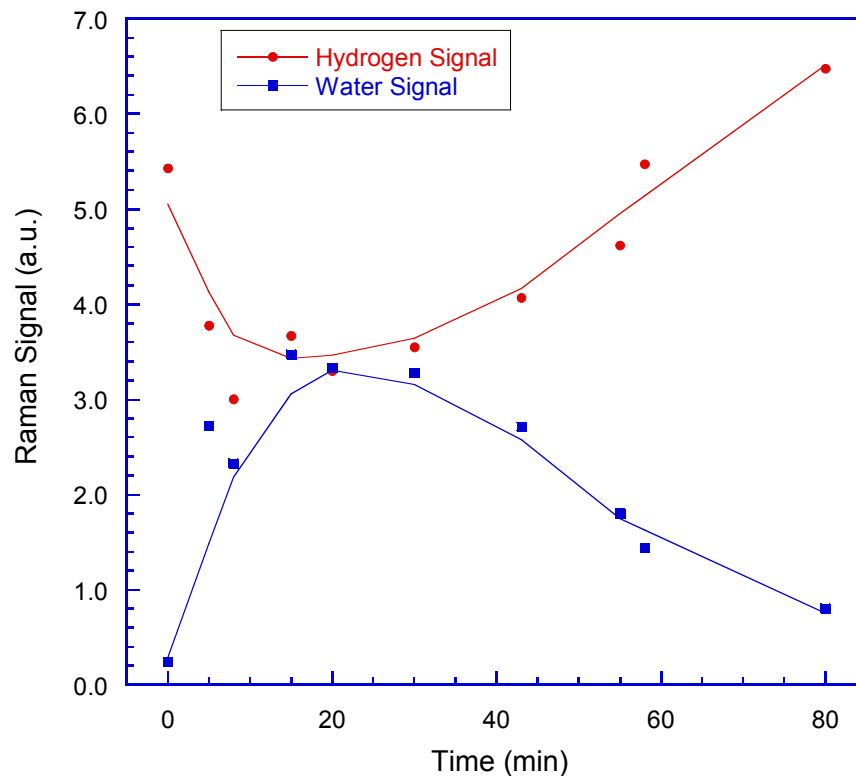Figure 2. **Raman spectra recorded during reduction of the catalyst.**

Figure 3. Integrated Raman signals during the catalyst reduction process.

Raman Scattering Measurements

Upon completion of the catalyst reduction process, measurements were performed to assess the feasibility of the *in situ* optical diagnostics as applied to the reactor geometry. Reformation was initiated using a total flow rate of 2 lpm of nitrogen, of which 1 lpm was passed through the pre-vaporization systems for methanol and water. Pre-vaporized water and methanol flows were initiated at a molar ratio of unity, and reformation was initiated using a reactor bed temperature of 218 °C. A representative Raman spectrum is presented in Figure 4 corresponding to these experimental conditions. The spectrum represents the average of 1500 laser shots, which takes 5 min. to record at the 5 Hz laser repetition rate. The spectrum shows the key Raman bands of interest for reformation, including the CH_3 stretching bands at 2844 and 2955 cm^{-1} and the O-H stretch at 3681 cm^{-1}, all corresponding to methanol, the O-H stretch at 3654 cm^{-1} corresponding to water, and the 4156 cm^{-1} fundamental vibrational mode of hydrogen.
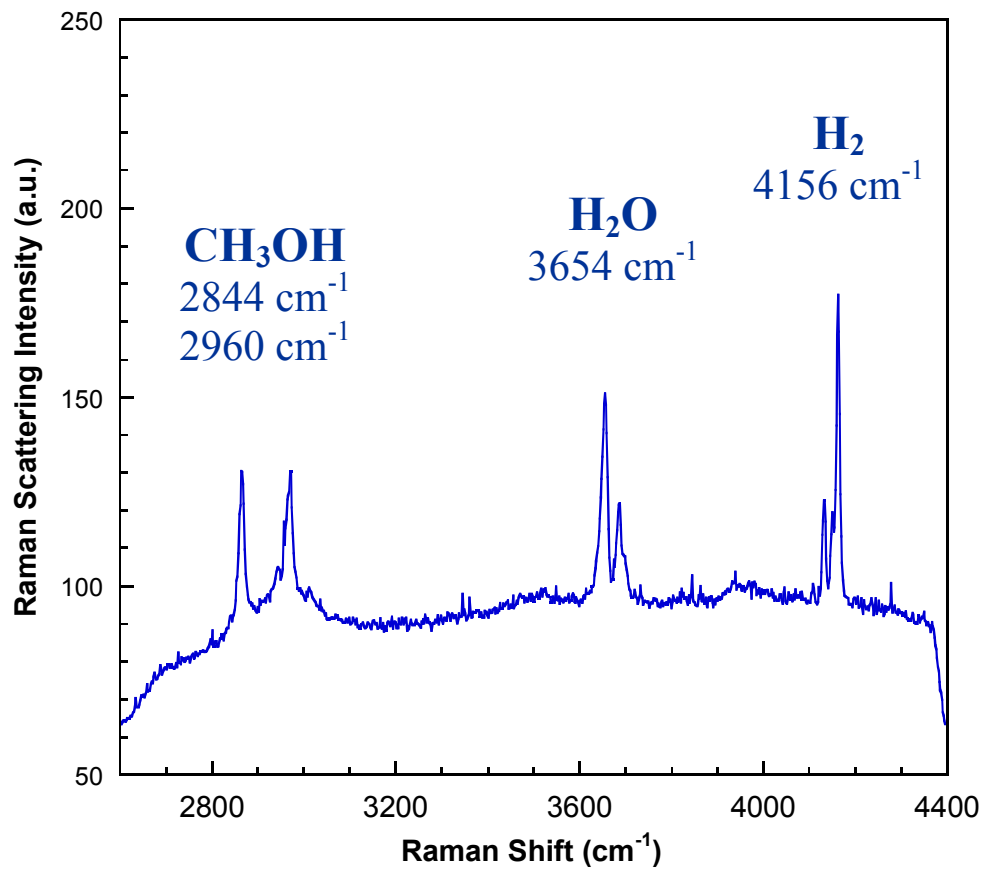
Figure 4. Raman spectrum recorded during methanol reformation.

Calibration

The ability to relate the Raman scattering signals to the actual species concentrations depend on the ability to calibrate the system response. Calibration is accomplished by passing a flow of known analyte concentration (e.g. methane or hydrogen) in a nitrogen balance through the reactor. This enables construction of a calibration curve, which ideally should provide a linear relationship between the analyte Raman signal and the analyte concentration. In addition, it is important to assess the temperature independence of the Raman signal, which ideally should be non-existent. To verify such behavior, calibration measurements were made in an ambient-temperature stream and in an elevated temperature stream. A typical calibration curve is presented below in Figure 5, as recorded for hydrogen in nitrogen at a low temperature (298 K) and at an elevated temperature (450 K). The calibration is very linear, and reveals independence of the hydrogen Raman signal on temperature.
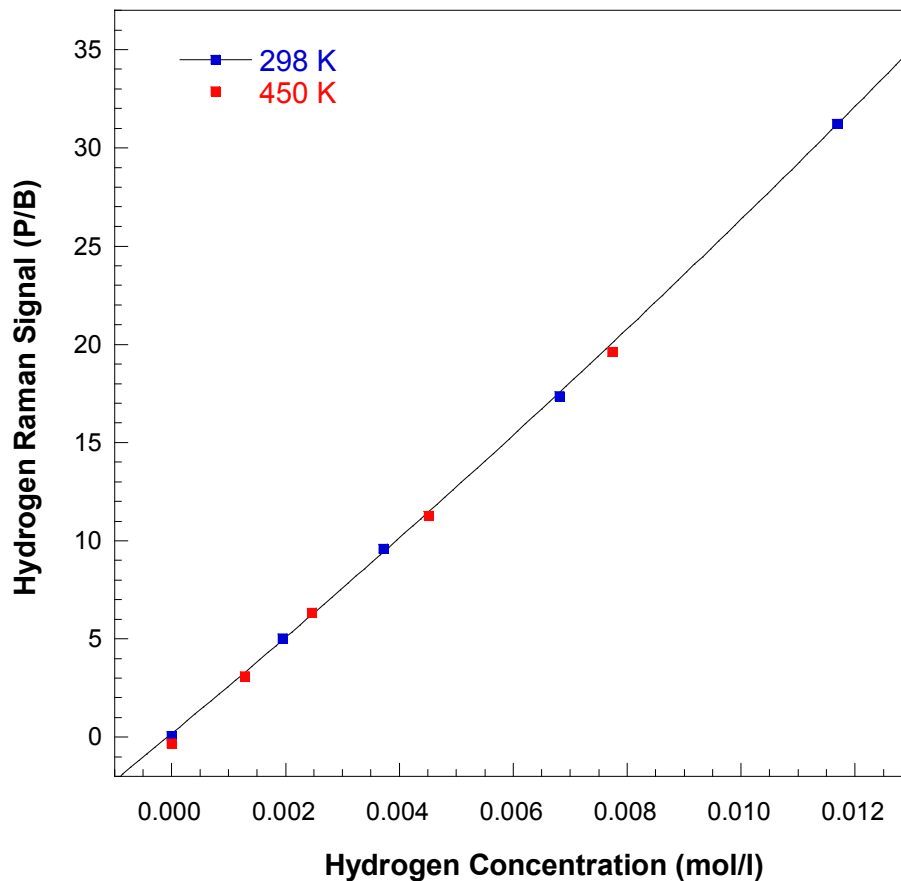
Figure 5. Raman spectrum calibration curve for hydrogen.

Reformation Measurements

The fundamental aspect of the current research project is to perform spatially resolved measurements to support detailed kinetics and fluid flow modeling. As implemented, measurements were recorded at three spatial locations by vertically translating the reactor, while maintaining a static optical set-up. Measurements were performed during steady-state operation, with three 500-shot average spectra recorded at each height above the reactor bed. The lowest position measured corresponds to about 1 mm (center of beam) above the burner surface. The spectra were processed by calculating the total integrated Raman band intensity (full peak area), which were normalized by the local continuum (i.e. background) signal. To assist in calculating the area and background, scaled blanks were used as recorded for a heated flow on only pure nitrogen. Measurements were made for the following conditions:
- ❑ Catalyst bed temperature: 495 K
- ❑ Gas phase temperature: 485 K
- ❑ Steam/Methanol molar ratio: 1.05-1.08
- ❑ 3 axial positions (x/L): 0.08, 0.5, 0.92
- ❑ 4 heights above reactor bed: 1.2-mm spacing
- ❑ Flow velocity: 7.0 & 9.7 cm/s
- ❑ Residence time: 6.3 & 8.4 s

The following figures detail the results obtained with the optical assess reactor.

Figure 6 details the measurement of methanol concentration (i.e. Reactant) as a function of axial location (i.e. residence time). The plot clearly shows the consumption of methanol as hydrogen is formed. As the bulk velocity is increased, the concentration of methanol is reduced at a given location, which is consistent with the increased residence time at lower bulk flow rate.

Figure 7 details the measurement of water vapor concentration (i.e. Reactant) as a function of axial location (i.e. residence time). The plot clearly shows the consumption of water as hydrogen is formed. As the bulk velocity is increased, the concentration of water is reduced at a given location, which is consistent with the increased residence time at lower bulk flow rate.

Figure 8 details the measurement of hydrogen concentration (i.e. Product) as a function of axial location (i.e. residence time). The plot clearly shows the formation hydrogen with residence time. As the bulk velocity is increased, the concentration of hydrogen is reduced at a given location, which is consistent with the increased residence time at lower bulk flow rate, hence less reaction time. In addition, at the last data point (x/L = 0.92), the overall concentration of hydrogen is observed to decrease, which is attributed to diffusion of hydrogen throughout the chamber as the reaction completes.

Figure 9 details the measurement of hydrogen, methanol and water vapor concentrations as a function of height above the reactor bed. The plot clearly shows the diffusion of reactants (methanol and water vapor) toward the surface, and the diffusion of hydrogen (product) away from the surface. With hydrogen, the gradient is small due to the high diffusion coefficient.
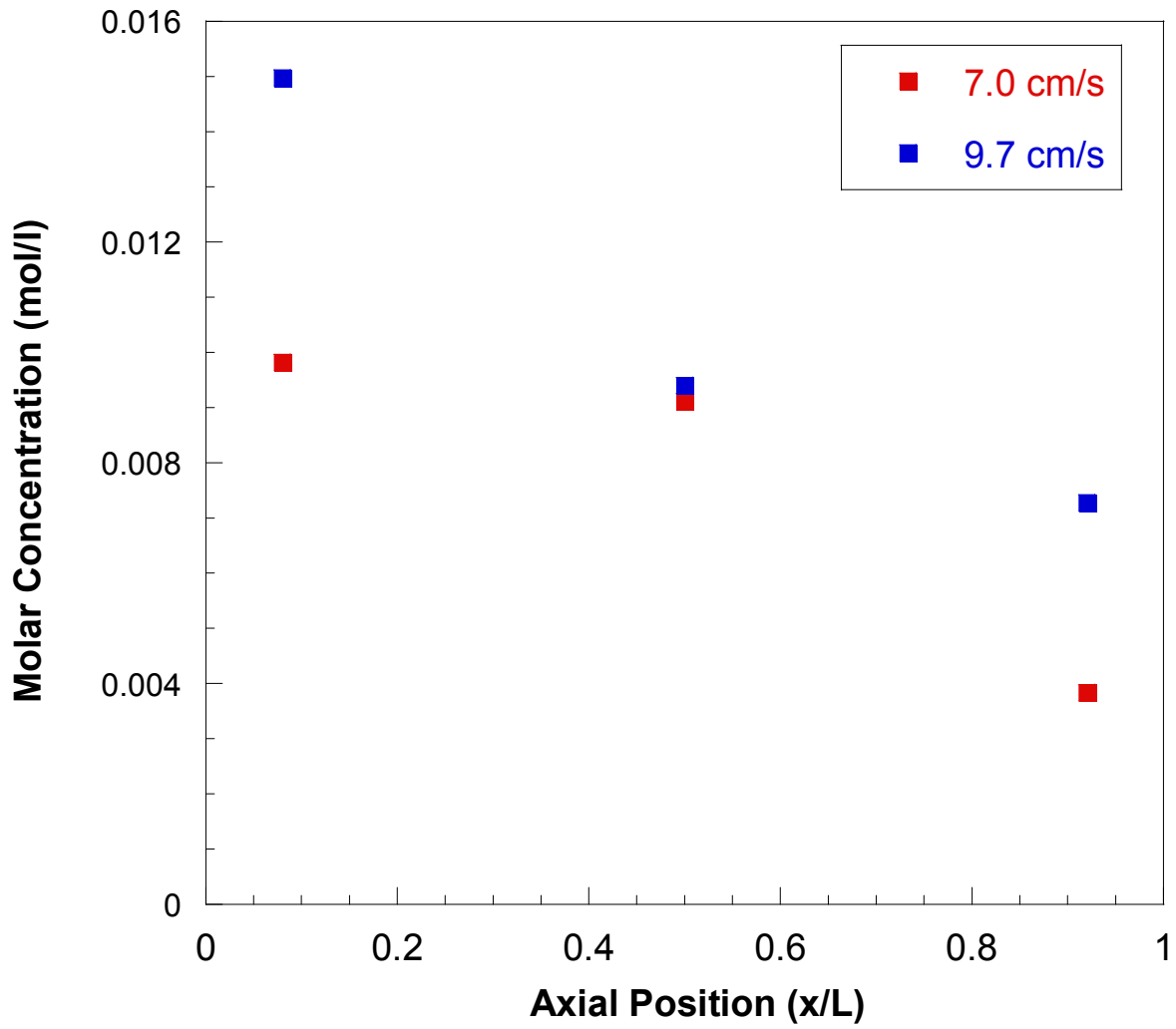
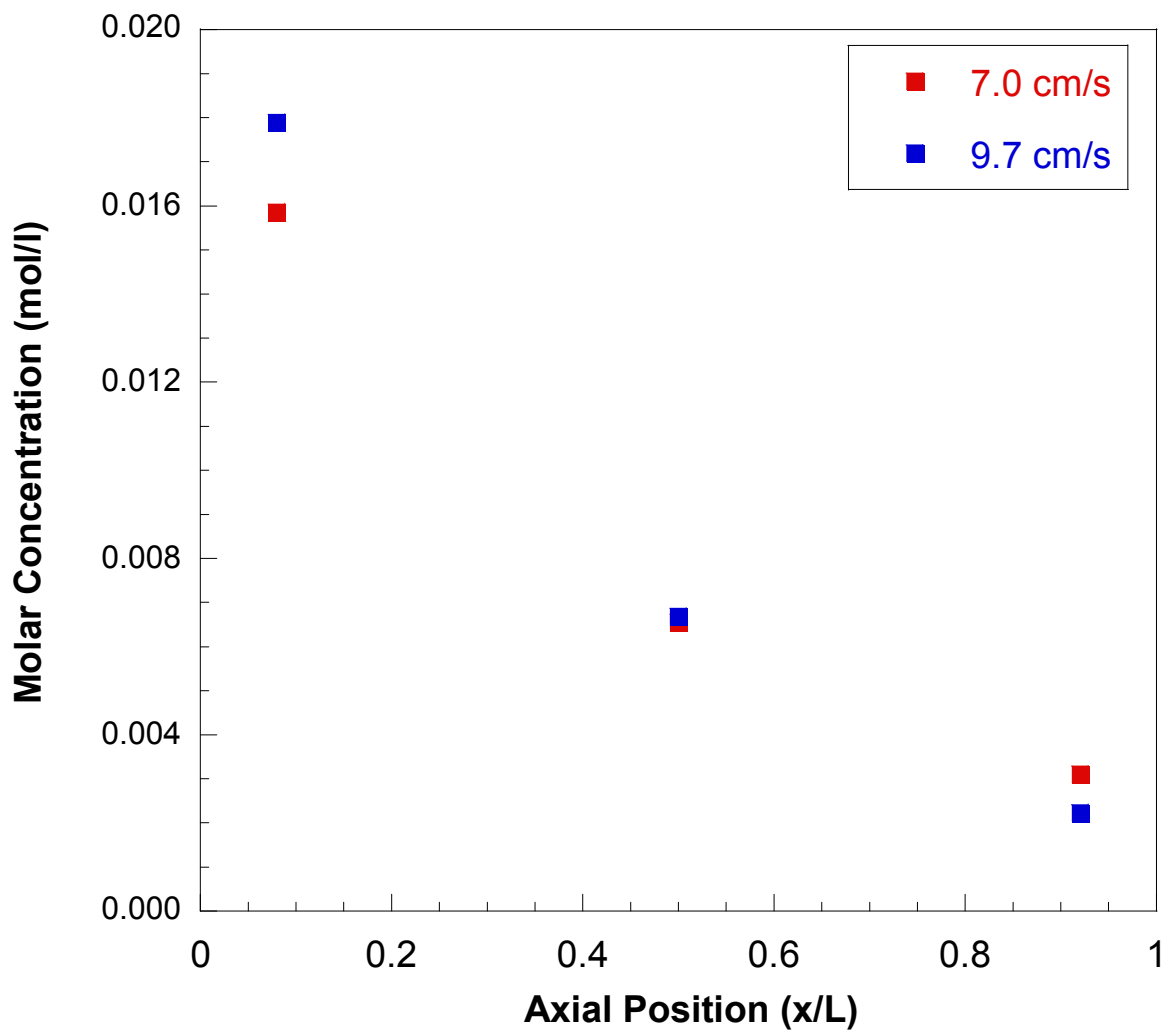**Figure 6. Methanol concentration as a function of axial position.**

Figure 7. Water vapor concentration as a function of axial position.
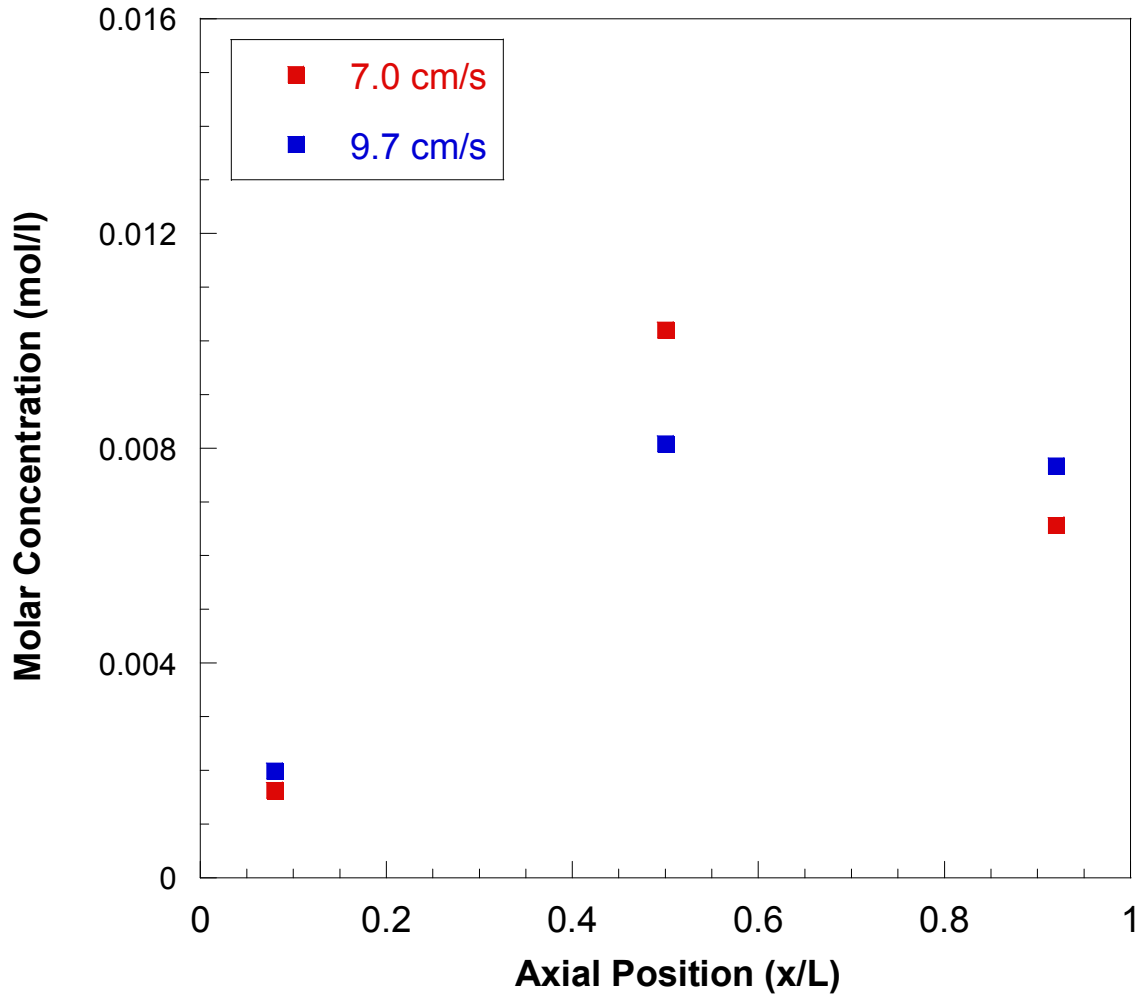
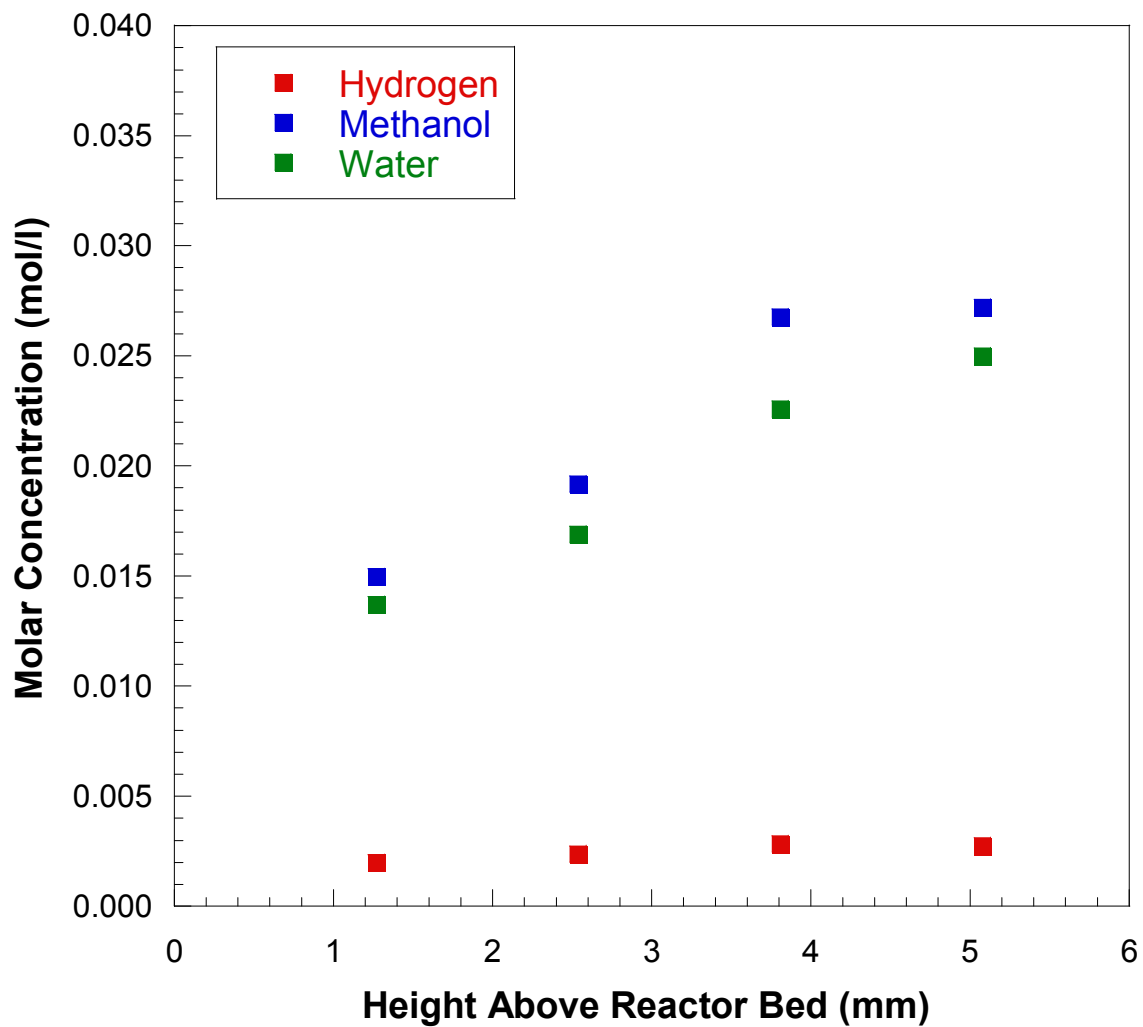**Figure 8. Hydrogen concentration as a function of axial position.**

Figure 9. Species profiles as a function of height above reactor bed at a fixed axial location of x/L = 0.08.

Summary and Conclusions

The current study was undertaken to explore the feasibility of *in situ* measurements of methanol reformation using Raman spectroscopy, with a goal of assessing spatial boundary layers and the overall degree of reaction completion with a suitable residence time-scale. To date, considerable research has been made of methanol reformation; such studies generally utilize a control-volume approach, with only input reactants and output products measured. While much has been learned from such studies, they are of limited use for validation of detailed kinetic models of heterogeneous and gas-phase chemistry. The current study reports some of the first *in situ* Raman measurements of gas-phase reformation species in a catalytic reformation reactor.

Key results of the current study are the successful measurements of the reactants methanol and water vapor and the product hydrogen via Raman spectroscopy. Calibration was used to convert measured spectra to absolute molar concentrations, which revealed a significant conversion of methanol to hydrogen over the residence times (6 to 8 s) used in the current study. While the current reactor design was not optimized for spatial resolution with respect to the Raman measurements, spatial gradients (millimeter-scale) were observed above the catalyst surface under reforming conditions. The key findings of this study are summarized as follows.

1) The Katalco 33-5 (Johnson Matthey) catalyst pellets were an excellent low-temperature (~200 °C) reforming catalyst. These pellets functioned well when configured in a single-layer pellet bed for a laminar flow reactor. This configuration enabled a two-dimensional assessment of the reformation process, providing information about the boundary layer using the height measurements, as well as about the overall kinetics using the axial measurements.

2) Raman spectroscopy using 355-nm excitation was successfully implemented for the *in situ* measurement of hydrogen, methanol and water vapor during actual methanol reformation. While the Raman is a technique characterized overall by relatively low sensitivity as compared to other methods such as laser-induced fluorescence, significant signal levels for the three targeted species were recorded under all reformation conditions for the current study.

3) The current optical access design proved successful for *in situ* Raman analysis. The use of UV-grade fused silica optical windows was successful in minimizing any background fluorescence with 355-nm excitation. However, the current reactor design was based on low-cost, low-build-time design criteria that did not optimize spatial resolution. As a result, Raman signals were diluted by a significant factor with respect to the expected actual gradients above the reactor surface.

13. Detailed Modeling of Methanol and Ethanol Catalytic Reaction

Task PI: Dr. David Mikolaitis, Mechanical & Aerospace Engineering, University of Florida

Collaborators: Dr. David Hahn, Mechanical & Aerospace Engineering, Dr. Lisa McElwee-White, Chemistry, Dr. Jason Weaver, Chemical Engineering, and Dr. Helena Hagelin-Weaver, Chemical Engineering, University of Florida

Graduate Students: Patrick Griffin, Weizhong Zhang, and Hector Leiva, Mechanical & Aerospace Engineering, University of Florida

Introduction

Three different computation models of catalytic combustion were developed. The first two methods were described in earlier reports. A third model describes a reacting gas flow impinging on a catalytic surface. This configuration is well suited for experiments due to the fact that the properties as functions of distance from the catalytic surface only and hence large optical sample paths can be used. Comparisons with experiments conducted by Prof. Hahn are reported.

The most important work here is the development of computational models for the study of coupled gas phase and surface reactions using simple computational tools (Matlab and Cantera) for the eventual comparison with experiments.

Catalytic reactors will play many important roles for NASA. The production of hydrogen by fuel reforming is on obvious place, but it is also important in the eventual production of hydrogen powered aircraft that are flown with gas turbines. Catalytic combustion is a potential key technology in lowered NOx production by keeping the combustion temperatures way below what is found in conventional combustors.

Both methane and syngas are fuels that can be produced from biomass and/or waste. Each of these in turn is a possible feedstock for catalytic reforming for hydrogen production. Hence hydrogen, methane, and syngas are three extremely important fuels to study in the production of energy from biological sources. At the same time catalytic combustion offers the promise of stable low temperature combustion virtually eliminating the production of NOx. Accurate predictions of NOx production in the range of a few parts per million requires accurate detailed kinetic models of the surface chemistry hence the need for accurate kinetic model development and verification.

Background

Prof. Hahn (University of Florida) and I are interested in the development of techniques for directly measuring reaction rates for surface reactions in the high pressure regime. The technique that we are developing is to optically measure the concentrations of chemical species at various points above a catalytic surface with sufficient accuracy that we can measure the gradient in that species. With that information we can therefore deduce the rate of transport into (adsorption) or out of (desorption) of that species.

In order to get enough resolution in the measurement a very strong signal is required. The perfect experimental configuration for this is axi-symmetric stagnation point flow onto a catalytic surface. In this particular flow configuration all the flow properties of interest (concentrations, temperature, pressure, etc.) are functions of distance from the surface only. This allows a laser beam to sample along a long path parallel to the surface in order to generate a very strong signal.

By measuring adsorption and desorption rates at various temperatures we can deduce such important kinetic rate parameters as activation energies and sticking coefficients.

Experimental

The aspect of the project reported here is analytical/computational and does not have an experimental component other than to compare results with those of Hahn.

Results and Discussion

Reaction of Hydrogen, Methane, and Carbon Monoxide in air impinging on a platinum wall

As a first step we have investigated a platinum catalyst surface with different fuel/air mixtures impinging on it. Cooling air is supplied from below to regulate the surface temperature.

In the case shown below a stoichiometric mixture of hydrogen and air impinges on a platinum surface held at 925 K at a pressure of 1 atm. The surface chemistry is modeled with the detailed platinum mechanism of Deutschmann[1] and the gas phase chemistry is described by GRI-Mech 3.0[2]. The blue diamonds give the model predictions for the H2 concentrations while the pink squares are the measured values. The agreement is extraordinarily good.
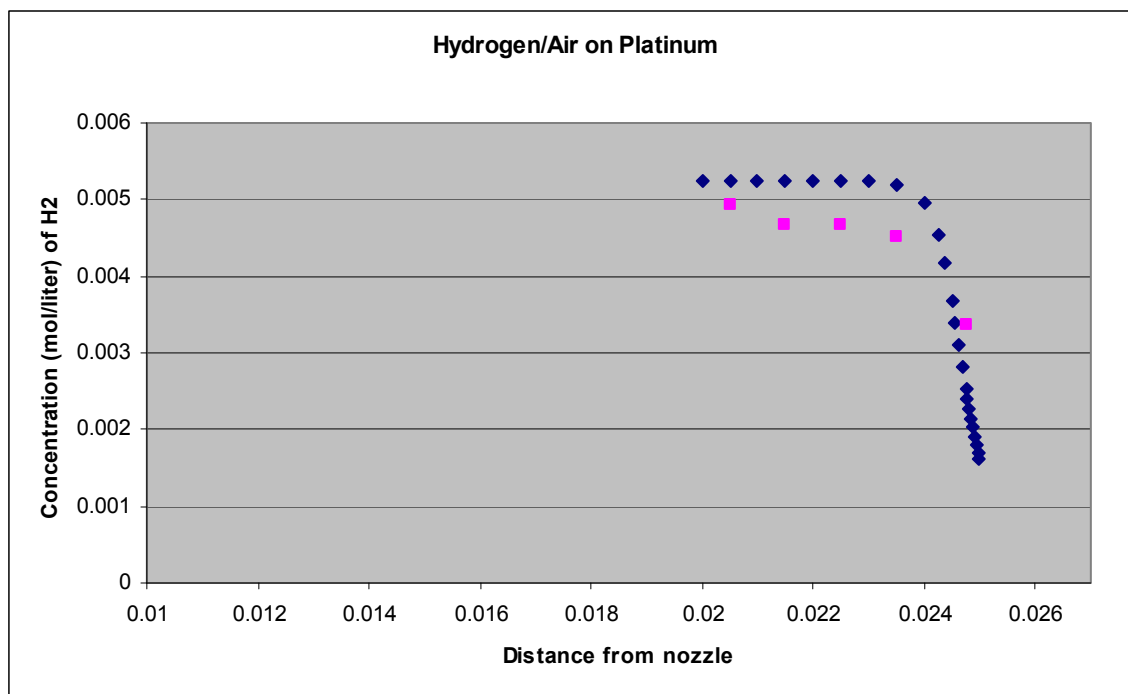
Another case that was analyzed was similar except that the fuel/air stream was a rich Syngas mixture. Syngas is primarily a mixture of carbon monoxide and hydrogen that can be produced from diverse energy sources. Again the detailed platinum mechanism of Deutschmann and the gas phase chemistry as described by GRI-Mech 3.0 is used as the kinetic model.

Once again we see excellent agreement in the H2 predictions as shown below.
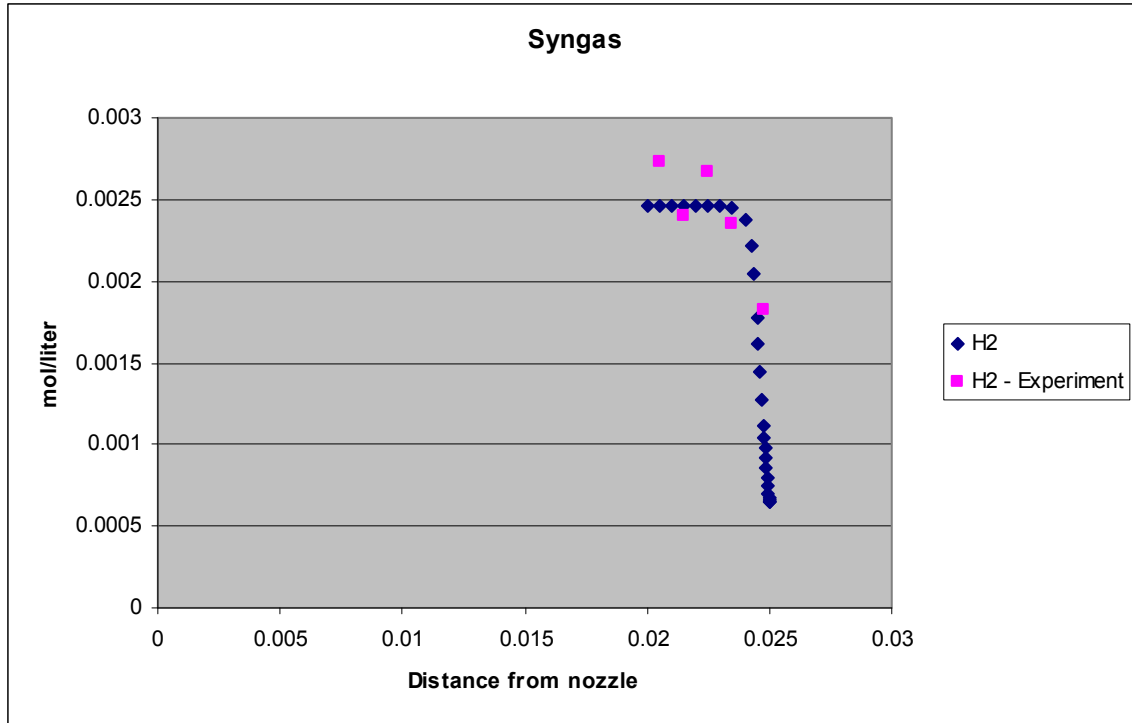
The predictions for carbon monoxide and carbon dioxide are not as favorable as seen here:

Syngas

Syngas
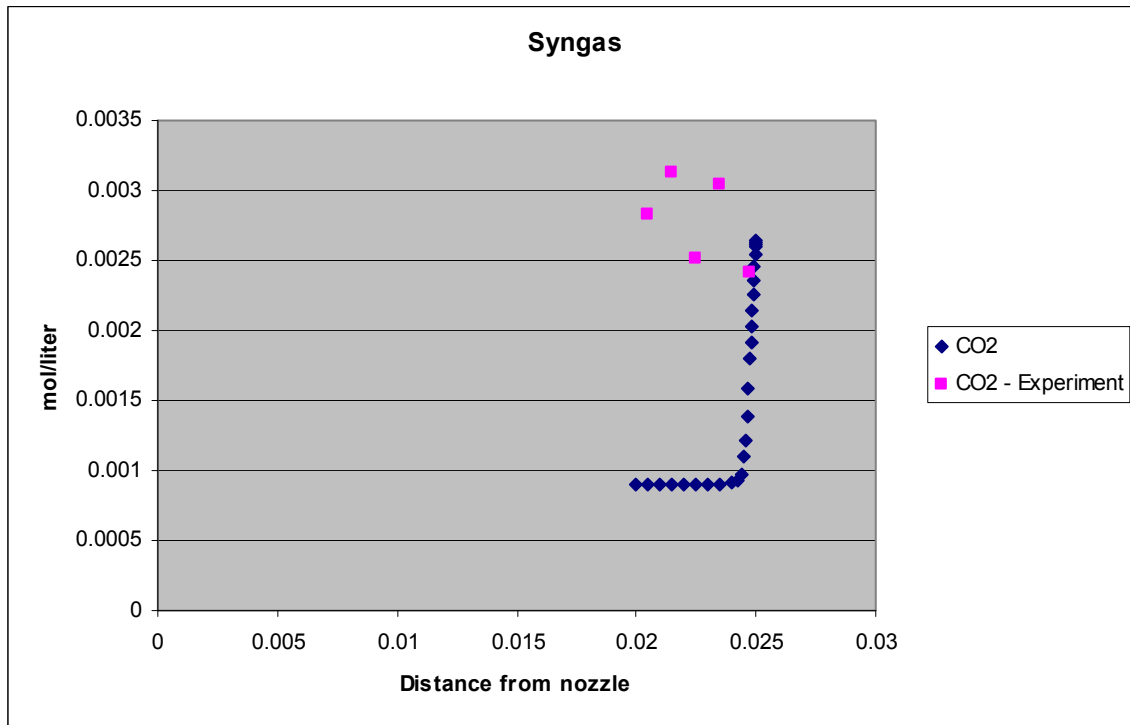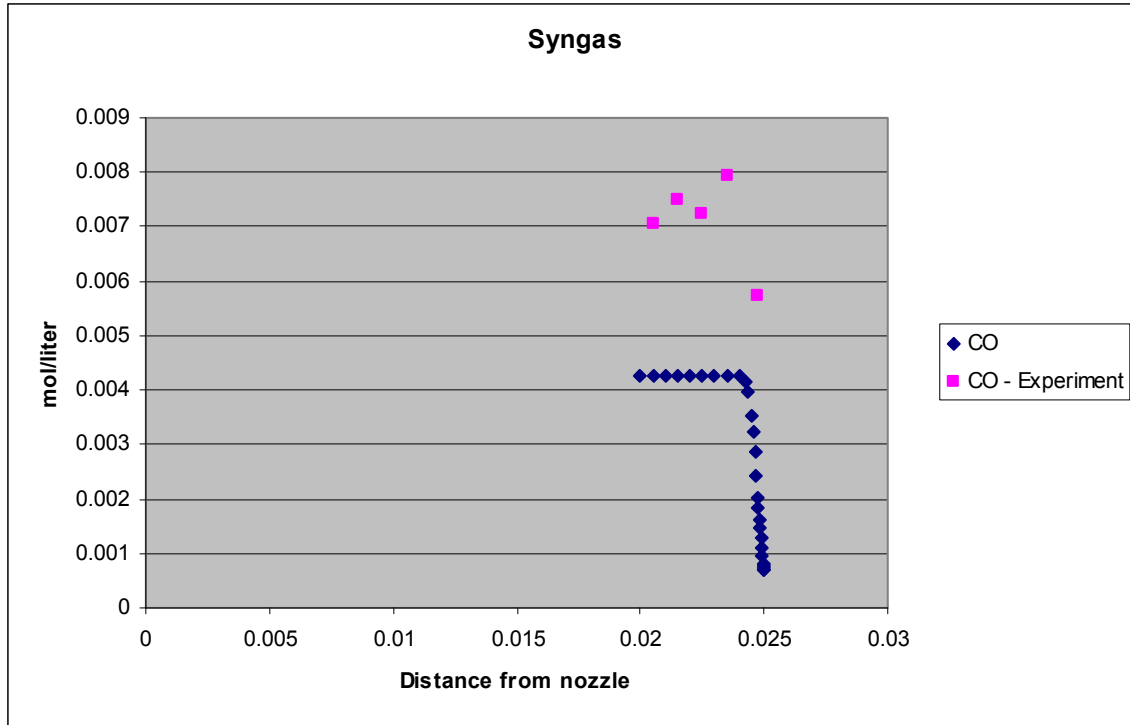
At this point we are uncertain whether the differences are due to shortcoming in the kinetic model or experimental errors and we are doing further investigations.

In addition the code developed for the stagnation point flow reactor is capable of predicting gas phase ignition due to catalytic reaction at the surface. Here are the results for a flow of Syngas

onto a platinum surface with a surface temperature held at slightly less than 1016.8 K. The mass fractions of the incoming mixture are 0.11332 for hydrogen, 0.00146 for methane, 0.13595 for oxygen, 0.505 for nitrogen, 0.00647 for argon, 0.1963 for carbon monoxide, and 0.0415 for carbon dioxide. This mixture is fuel rich. The temperature of the incoming stream is 546 K and the pressure is atmospheric. The mass flux is 8.807 kg/(m²-s).
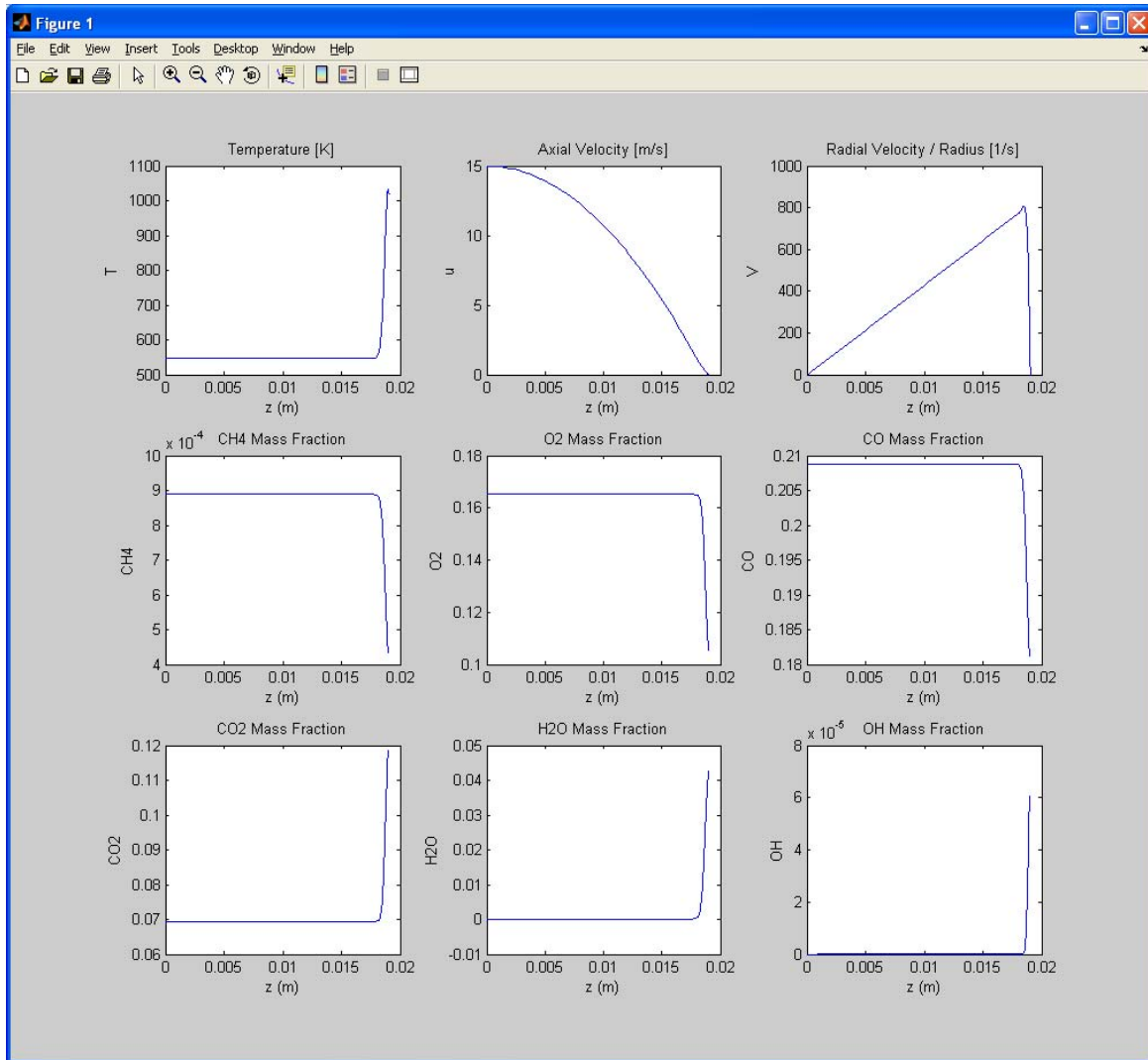
If the surface is held at 1016.9K we get the following result
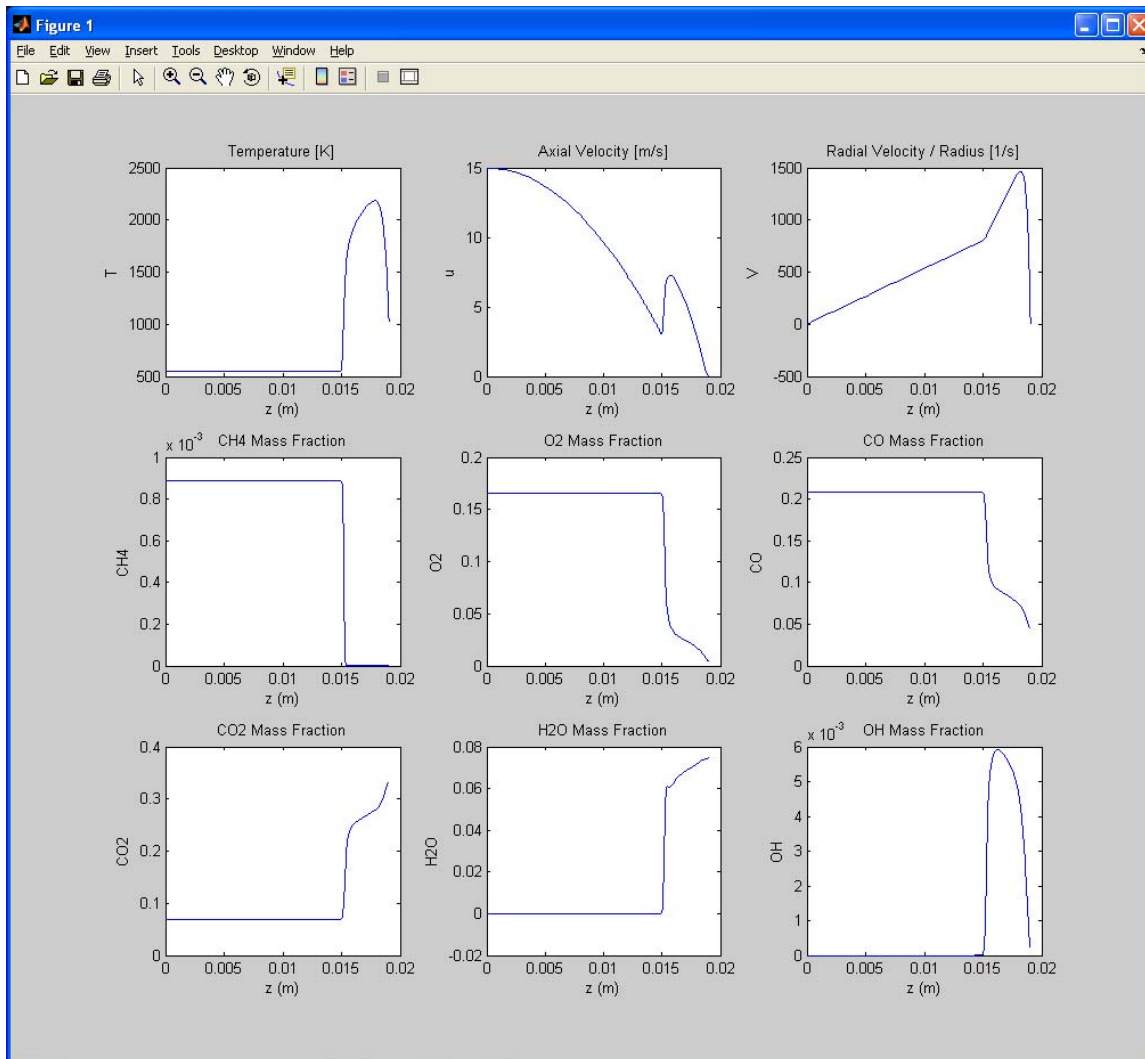
In the first case there is mostly surface reaction with a small amount of reaction in the gas phase near the surface. The production of OH radicals by the surface reaction leads to the small amount of gas phase reaction.

In the second case there is region of strong reaction a few millimeters away from the surface. This is clearly seen by the peak in the OH mass fraction. Not all the carbon monoxide is consumed because this is a case where the incoming is mixture is rich.

Please note that if we are in the second case and then lower the surface temperature a small amount we would not transition to the "unignited" solution. It requires considerably more cooling to extinguish the now established premixed flame in the gas phase. The system has the classic ignition-extinction behavior seen in non-premixed systems where there are ranges of conditions with multiple stable steady-sate solutions. The actual solution seen will depend on the history.

The numerical solution procedure required to obtain the solution with flames in the gas phase is not completely straightforward. In order to get solutions a reasonably good guess was required and then the solution was allowed to evolve in a pseudo-unsteady manner to the final steady-state solution. The method for generating the good guess was to first solve the problem with

hydrogen/air only and then work through a series of problems where the Syngas mixture was slowly turned on and the hydrogen mixture was slowly turned off. The converged solution of the previous case was used as the initial guess for the next case. Solutions for hydrogen/air only are not that difficult to calculate due to the fact that the activation energies involved in the detailed chemical kinetic model are not that large and hence the problem is not extremely "stiff".

Conclusions

We have developed a third catalytic combustion computer model that compliments the two developed earlier. The stagnation point flow code developed here is important in the synergistic research plan for determining kinetic rate data for surface reactions at elevated pressures.

The hydrogen reaction pathways of the detailed platinum mechanism of Deutschmann has been verified, while the carbon monoxide reaction pathways described in that mechanism are in doubt. That is not a condemnation of the model because it is only meant to be applied to the catalytic combustion of methane on platinum and the carbon monoxide pathways play a minor role in that context.

The code developed is suitable for analyzing cases even with strong reaction in the gas phase. This allows for the prediction of gas phase ignition of flames from catalytic reaction at the surface.

Patents

None

Publications

"Two-Dimensional Modeling of a Chemically Reacting Boundary Layer Flow in a Catalytic Reformer", Patrick D. Griffin, Master of Science Thesis, Department of Mechanical and Aerospace Engineering, University of Florida, 2006.

David Mikolaitis and Patrick Griffin, "Reacting Flow in the Entrance to a Channel with Surface and Gas-Phase Kinetics", 2006 58th Annual Meeting of the APS Division of Fluid Dynamics, November 19-21, 2006, Tampa Bay, Florida.

"Gas Phase Ignition and Extinction of Syngas over a Hot Platinum Surface", (In preparation).

Students from Research

Patrick D. Griffin, MS, 2006

Two other students were supported, but have not received degrees: Weizhong Zhang and Hector Leiva.

Funding Received by Leveraging the NASA Grant

Prof. Hahn and I have enjoyed funding from Siemens Corporation to work on catalytic modeling issues due in very large part to the collaboration we developed through this project. Work is continuing on both modeling of the detailed kinetics of catalytic combustion as well as in issues

of heat transfer modification due to surface chemistry. The funding from Siemens Corporation has been around $150K per year.

The collaboration with Siemens Corporation led to a further leverage of funding through the Florida High Tech Corridor Council for approximately $60K.

References

[1] Deutschmann, O., Schwiedernoch, R., Maier, L., & Chatterjee, D. (2001). Natural Gas Conversion in Monolithic Catalysts: Interaction of Chemical Reactions and Transport Phenomena [Electronic version]. *Natural Gas Conversion VI, Studies in Surface Science and Catalysis, 136*, 251-258.

[2] Smith, G.P.; Golden, D.M.; Frenklach, M.; Moriarty, N.W.; Eiteneer, B.; Goldenberg, M.; Bowman, C.T.; Hanson, R.K.; Song, S.; Gardiner, W.C., Jr.; Lissianski, V.V.; Qin, Z. GRI-Mech Home Page. http://www.me.berkeley.edu/gri_mech/

1. REPORT DATE (DD-MM-YYYY) 01-11-2008	2. REPORT TYPE Final Contractor Report	3. DATES COVERED (From - To)

4. TITLE AND SUBTITLE
Hydrogen Research for Spaceport and Space-Based Applications
Fuel Cell Projects

5a. CONTRACT NUMBER

5b. GRANT NUMBER
NAG3-2930

5c. PROGRAM ELEMENT NUMBER

6. AUTHOR(S)
Anderson, Tim; Balaban, Canan

5d. PROJECT NUMBER

5e. TASK NUMBER

5f. WORK UNIT NUMBER
WBS 561581.02.08.03.11

7. PERFORMING ORGANIZATION NAME(S) AND ADDRESS(ES)
University of Florida
1 Univ of Florida
Gainesville, Florida 32611

8. PERFORMING ORGANIZATION REPORT NUMBER
E-16612-1

9. SPONSORING/MONITORING AGENCY NAME(S) AND ADDRESS(ES)
National Aeronautics and Space Administration
Washington, DC 20546-0001

10. SPONSORING/MONITORS ACRONYM(S)
NASA

11. SPONSORING/MONITORING REPORT NUMBER
NASA/CR-2008-215440-PART1

12. DISTRIBUTION/AVAILABILITY STATEMENT
Unclassified-Unlimited
Subject Categories: 25, 28, 33, and 34
Available electronically at http://gltrs.grc.nasa.gov
This publication is available from the NASA Center for AeroSpace Information, 301-621-0390

13. SUPPLEMENTARY NOTES
Faculty Coordinator: Dr. Mark Orazem, Professor, Chemical Engineering

14. ABSTRACT
The activities presented are a broad based approach to advancing key hydrogen related technologies in areas such as fuel cells, hydrogen production, and distributed sensors for hydrogen-leak detection, laser instrumentation for hydrogen-leak detection, and cryogenic transport and storage. Presented are the results from research projects, education and outreach activities, system and trade studies. The work will aid in advancing the state-of-the-art for several critical technologies related to the implementation of a hydrogen infrastructure. Activities conducted are relevant to a number of propulsion and power systems for terrestrial, aeronautics and aerospace applications. Fuel cell research focused on proton exchange membranes (PEM), solid oxide fuel cells (SOFC). Specific technologies included aircraft fuel cell reformers, new and improved electrodes, electrolytes, interconnect, and seals, modeling of fuel cells including CFD coupled with impedance spectroscopy. Research was conducted on new materials and designs for fuel cells, along with using embedded sensors with power management electronics to improve the power density delivered by fuel cells. Fuel cell applications considered were in-space operations, aviation, and ground-based fuel cells such as; powering auxiliary power units (APUs) in aircraft; high power density, long duration power supplies for interplanetary missions (space science probes and planetary rovers); regenerative capabilities for high altitude aircraft; and power supplies for reusable launch vehicles.

15. SUBJECT TERMS
Hydrogen; Cryogenic fluids; Cryogenic storage; Thermodynamics; Sensors; Hydrogen production; Fuel cells

16. SECURITY CLASSIFICATION OF:			17. LIMITATION OF ABSTRACT	18. NUMBER OF PAGES	19a. NAME OF RESPONSIBLE PERSON STI Help Desk (email:help@sti.nasa.gov)
a. REPORT U	b. ABSTRACT U	c. THIS PAGE U	UU	284	19b. TELEPHONE NUMBER (include area code) 301-621-0390